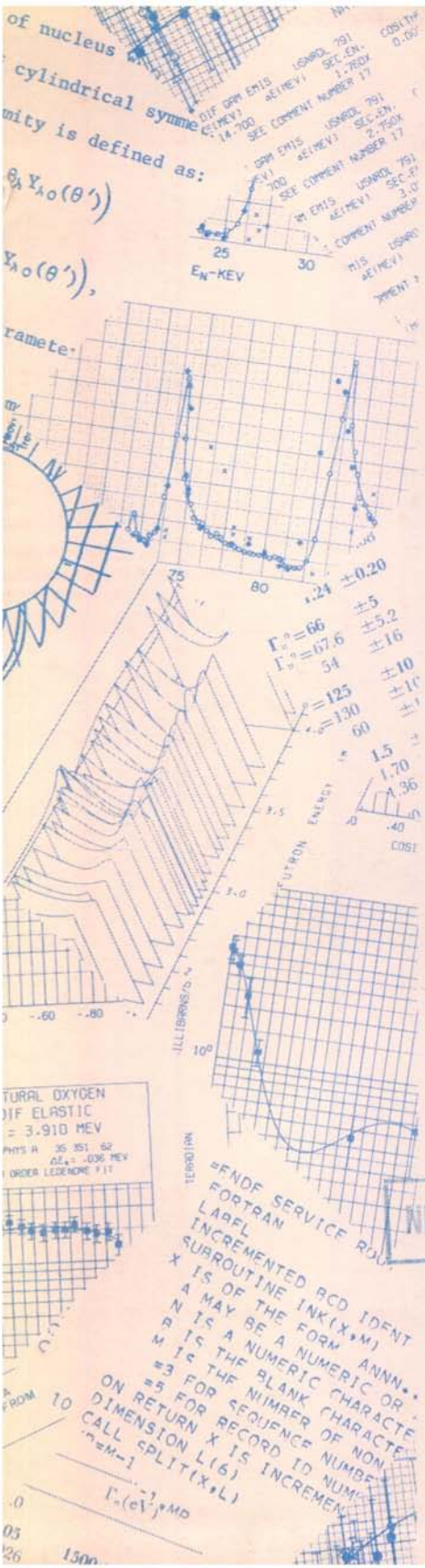

BNL-NCS-51245 - Vol. II of II
DOE/NDC-21/L
NEANDC(US)-208/L
INDC(USA)-84/L

SYMPOSIUM ON NEUTRON CROSS-SECTIONS FROM 10 TO 50 MEV

HELD AT
BROOKHAVEN NATIONAL LABORATORY
UPTON, NEW YORK 11973
May 12-14, 1980

Edited by
M.R. BHAT AND S. PEARLSTEIN

JOINTLY SPONSORED
BY THE OFFICE OF FUSION ENERGY
AND THE DIVISION OF HIGH ENERGY
AND NUCLEAR PHYSICS OF THE
UNITED STATES DEPARTMENT OF ENERGY

July 1980

INFORMATION ANALYSIS CENTER REPORT

NATIONAL NUCLEAR DATA CENTER
BROOKHAVEN NATIONAL LABORATORY
UPTON, NEW YORK 11973

national nuclear data Center

BNL-NCS-51245 - Vol. II of II
DOE/NDC-21/L
NEANDC(US)-208/L
INDC(USA)-84/L
UC-34c
(Physics-Nuclear - TIC-4500)

SYMPOSIUM ON NEUTRON CROSS-SECTIONS FROM 10 TO 50 MEV

HELD AT
BROOKHAVEN NATIONAL LABORATORY
UPTON, NEW YORK 11973
May 12-14, 1980

Edited by
M.R. BHAT AND S. PEARLSTEIN

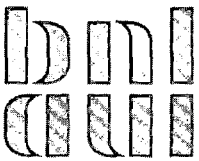

July 1980

JOINTLY SPONSORED BY THE OFFICE OF FUSION ENERGY AND THE DIVISION OF HIGH ENERGY AND NUCLEAR PHYSICS OF THE UNITED STATES DEPARTMENT OF ENERGY

NATIONAL NUCLEAR DATA CENTER

BROOKHAVEN NATIONAL LABORATORY
ASSOCIATED UNIVERSITIES, INC.
UNDER CONTRACT NO. DE-AC02-76CH00016 WITH THE
UNITED STATES DEPARTMENT OF ENERGY

DISCLAIMER

Printed in the United States of America
Available from
National Technical Information Service
U.S. Department of Commerce
5285 Port Royal Road
Springfield, VA 22161
Price: Printed Copy $14.00; Microfiche $3.00

TABLE OF CONTENTS

*Not presented orally.

Page

FUSION MATERIALS IRRADIATION TEST (FMIT) FACILITY RELATED PROBLEMS—SHIELDING AND MATERIALS DAMAGE STUDIES

Session Chairman: R.W. Peelle, ORNL

NUCLEAR DATA RELEVANT TO SHIELD DESIGN OF FMIT FACILITY

L. L. Carter, R. J. Morford, and A. D. Wilcox

Hanford Engineering Development Laboratory
Richland, Washington 99352, U.S.A.

ABSTRACT

Nuclear data requirements are reviewed for the design of the Fusion Materials Irradiation Test (FMIT) facility. This accelerator-based facility, now in the early stages of construction at Hanford, will provide high fluences in a fusion-like radiation environment for the testing of materials. The nuclear data base required encompasses the entire range of neutron energies from thermal to 50 MeV. In this review, we consider neutron source terms, cross sections for thermal and bulk shield design, and neutron activation for the facility.

INTRODUCTION

The FMIT facility [1] will provide the only high-fluence data for a fusion-like radiation environment during the next decade. Groundbreaking ceremonies were held February 22, 1980 to start construction of this accelerator-based facility at Hanford with completion scheduled for 1984.

The neutron source, produced by a 0.1 Amp beam of 35 MeV deuterons incident upon a flowing lithium target, is highly anisotropic with a rapid spectral variation with angle. The spectrum in the forward direction is characterized by a broad peak around $\sim$14 MeV with a high energy tail extending to $\sim$50 MeV. While the broad peak provides the major portion of the source for material damage studies, the contribution from somewhat higher energy neutrons is also important and the extreme high energy portion of the tail impacts shield design.

An adequate design of the facility requires knowledge of the (d,Li) neutron source distribution, neutron cross section data from 20 to 50 MeV (in addition to libraries such as ENDF/B below 20 MeV) for the major isotopic constituents of the shields, extensive neutron activation cross section data, and deuteron activation cross sections along with beam loss criteria within the

accelerator. Integral measurements of neutron and deuteron activation also play an important role. General nuclear data requirements were considered during the previous symposium [2] for (d,Be) and (d,Li) based neutron sources. This session of the current symposium will focus specifically upon the FMIT facility. In this review paper, nuclear data relative to shield design will be considered while the next review paper [3] will focus upon irradiation damage.

NEUTRON SOURCE CHARACTERISTICS

Both shield design and a proper understanding of the material damage of irradiated test specimens require an experimental determination of the neutron source spectrum resulting from 35 MeV deuterons incident upon lithium. From a shielding point of view, there was an early interest in the shape of the high energy tail since there were theoretical reasons to believe that the $^{7}Li(d,n)^{8}Be$ reaction with a Q value of 15 MeV could lead to neutrons with energies up to ∿50 MeV. Transport calculations [4,5] indicated that such neutrons would severely impact shield design even if source strengths were down by two orders of magnitude from the peak around 14 MeV.

The (d,Li) source has been characterized by thick target measurements [6] for ten different angles using time-of-flight techniques and the cyclotron at the University of California at Davis. The spectra at the four angles of Figure 1 (measured data [6] without smoothing) are shown to illustrate neutron energy regimes that impact various aspects of shield design. Particularly significant is the shoulder from 30 to 45 MeV at eight degrees arising from the Q value of 15 MeV. This shoulder is prominent from about six to twenty degrees.

The 35 MeV deuterons impinge upon a flowing lithium target positioned within a 5'x8'x6' test cell (see Figures 2a & 2b). The shoulder in the neutron spectra beyond 30 MeV at forward angles is important for a determination of the shield thickness of the back wall of the test cell since these source neutrons are the dominant neutrons that penetrate the shield. For side walls, the source neutrons between 20 and 40 MeV dominate. This is not to say, however, that the lower energy portion of the spectrum can be ignored in all aspects of shield design. The lower energy neutrons must be considered in the design of the thermal shield and in nuclear heat deposition within the test cell since a low energy neutron has the potential for depositing ∿8 MeV of energy via capture. The entire neutron energy regime is potentially important for neutron activation and must be properly treated to determine shield requirements for positioning and removal of test specimens, maintenance of the accelerator system, and activation of coolants and atmospheres.

The neutron source within the Linear Accelerator (LINAC) and beam transport areas arises from stray deuterons incident upon

materials such as Fe, Cu, Au and Al. While the neutron source strength per unit of deuteron current is less for these materials than for lithium, the general neutron energy regime of Figure 1 is still applicable at the high energy portion of the accelerator. Uncertainties in dose levels within the LINAC, due to both neutron and deuteron activation, are currently dominated by uncertainties in deuteron losses rather than by (d,X) source data or by neutron activation cross sections.

BULK SHIELD DESIGN

Transport calculations have validated the concept presented by a simple removal-theory model of high energy (20-50 MeV) neutron transport through shields. A simple model enables first-order comparisons of shields — both modular and homogeneous — and gives some insights into sensitivities of the dose through the shield to cross section data. Of course, rigorous transport calculations are made to verify the more crucial conclusions.

In the following discussion the outer portion of the shield is assumed to contain enough hydrogenous material so that once the neutron energy is reduced below about one MeV it is rapidly thermalized and captured. A simplified pictorial of the penetration of a high energy neutron source through the shield is shown in Figure 3. Most of the neutrons that eventually emerge from the shield either have a very long first flight, which takes them nearly through the shield, or else suffer one or more small-angle elastic collisions (typically with long flight paths between collisions) before penetrating through most (or all) of the shield. In contrast, neutrons which suffer wide angle collisions prior to deep penetration must travel many more mean free paths or scatter back into the appropriate small solid angle. The neutrons that suffer nonelastic collisions usually lose enough energy so that their probability of penetrating the shield is substantially reduced irrespective of scattering angle.

The microscopic removal cross section is defined as

$$\sigma_r(E) = \sigma_{non}(E) + \alpha\, \sigma_{el}(E) \ , \qquad (1)$$

where $\sigma_{non}(E)$ is the nonelastic cross section, $\sigma_{el}(E)$ is the elastic cross section, and α is the fraction of the elastically scattered neutrons suffering a wide angle ($\gtrsim 25°$) deflection. Such a removal cross section is compared in Figure 4 for iron with two different cross section evaluations. The removal cross section labeled "MCNP" was calculated with Eq. (1) using as a data base the pointwise cross section library that is currently being used for shield design with the Monte Carlo code, MCNP [7,8]. The lower curve was obtained by folding experimental data [9,10] and a priori data using a generalized least squares procedure.

Both removal cross section evaluations of Figure 4 decrease monotonically with increasing neutron energy. Although the

decrease is small, it is important since the macroscopic removal cross section is applied exponentially: the dose through a homogeneous shield of thickness x is approximately

$$D = C \int S(E)\, e^{-\Sigma_r(E)x}\, dE \,, \qquad (2)$$

where S(E) is the energy dependent source and C is a constant for a given shield material. The exponential enhances the worth of the higher energy source neutrons (E>30 MeV) incident upon the back wall so that they are the dominant neutrons that penetrate the thick back wall shield. This is illustrated by the curves in Figure 5 for neutron transport through an eight foot slab of high density magnetite concrete.

The solid (importance) curve in Figure 5 was generated with Monte Carlo calculations [4,11]. A point on the curve gives the dose through eight feet of high density concrete due to a one neutron per cm^2 normally incident source with kinetic energy given by the abscissa. For example, a 40 MeV source neutron is $\sim$250 times as important as a 20 MeV source neutron. Folding this curve with the FMIT spectrum incident upon the back wall results in the future contribution [12] (sometimes called contributon current) curve of Figure 5; i.e., the product of the dose through the slab for unit monoenergetic sources with the source intensity. For the relatively thin eight foot shield, the contributon current at 40 MeV is about seven times that of 20 MeV.

Transport calculations have verified the removal theory interpretation that the nonelastic cross section above 20 MeV is the most sensitive of the nuclear data for bulk shielding. Somewhat less important is the elastic cross section and its associated angular distribution. Even though the elastic cross section is very forward peaked above 20 MeV, treating it as straight ahead results in an overconservatism of at least two orders of magnitude in the dose for the back wall shield thicknesses of interest.

The dose through bulk shields is not very sensitive to the energy- and angular-distribution of neutrons from nonelastic events; however, calculations of neutron flux fields within test assemblies could be sensitive to these distributions. Previous studies [5] have shown that gamma production cross sections for neutron energies above 20 MeV may be neglected in the design of bulk shields. Further confirmation of this is desirable.

The most important elements for the bulk shield analysis are basically the constituents of concrete and iron shields. First priority in nuclear data needs is assigned to iron and oxygen with second priority given to silicon, calcium, and carbon. Recent measurements have been made of the total, nonelastic, and removal cross sections at 40 and 50 MeV [9]. The experimental data points shown in Figure 4 for iron aided in obtaining an updated evaluation of the removal and nonelastic cross sections and assignment of uncertainties in the energy range 20-50 MeV. Better agreement

between the pointwise library being used in the MCNP Monte Carlo code and new evaluations based upon the measurements was obtained for oxygen, calcium, and carbon. Hence our confidence in the nuclear data for these elements has been improved, but much work remains to be done to obtain overall satisfactory agreement between nuclear model codes and experimental data.

TRANSPORT CROSS SECTION LIBRARIES FOR FMIT

The two cross section libraries that are being used in the transport calculations for FMIT are summarized in Figure 6. The pointwise Monte Carlo library is based upon ENDF/B-IV below 20 MeV. Cross sections from 20 to 60 MeV were appended to this library [4, 13] for the elements H, C, O, Si, Ca, Cr, Fe, and Ni using available nuclear data. Nonelastic cross sections from 20 to 60 MeV were taken directly as those recommended by Wilson [14]. Intranuclear-cascade plus Evaporation (IC+E) model calculations [15] at Oak Ridge National Laboratory (ORNL) were used for the number of secondary neutrons from nonelastic scattering events and their energy and angular distributions. Optical model calculations at Hanford Engineering Development Laboratory (HEDL), checked against available experimental data, were used to obtain the elastic scattering cross sections and their angular distributions. An exception is hydrogen, which is based entirely upon experimental measurements.

The coupled neutron-gamma multigroup cross section library is currently being used primarily in one-dimensional discrete ordinates calculations. This library [16] was constructed by Alsmiller and Barish at ORNL by appending multigroup cross sections between 14.9 and 60 MeV to an existing RSIC fusion library [17] for energies below 14.9 MeV. The cross sections above 14.9 MeV are P_5 and, hence, include an adequate expansion for deep penetration calculations. The nonelastic and elastic cross sections above 14.9 MeV were based upon optical model calculations checked against available measurements, while the nonelastic energy and angular distributions were based upon the IC+E model calculations [15]. The fusion cross section library below 14.9 MeV was for infinite dilution. Resonance self-shielding corrections have been made at HEDL to obtain another 0-60 MeV library for iron.

NUCLEAR HEAT DEPOSITION

Nuclear heat deposition from neutron and gamma interactions is important within the material test modules, the thermal shield walls of the test cell (see Figure 2b), and the bulk shield beyond the thermal shield. Calculations of heat deposition are sensitive to neutron transport, neutron KERMA factors, and gamma production cross sections. Nuclear data limitations have been experienced for all three of these categories. The most important element is

iron, although nickel, chromium, calcium, silicon, oxygen, and hydrogen impact various calculations.

Unfortunately, energy balances in ENDF/B continue to have shortcomings for the generation of cross section libraries and for the calculation of KERMA factors [18]. Corrections in the MCNP library have been made over various energy regimes for the more important elements. Los Alamos Scientific Laboratory (LASL) has improved gamma production and energy balances in a new cross section evaluation for iron [19]. This is currently being processed for inclusion in the MCNP master library.

Integral tests of the neutron transport are necessary to establish confidence in the heat deposition calculations. An important example is the back wall of the test cell. The current design of the thermal shield requires about 24 inches of iron and graphite and an inch or two of Boral. Interspaced in this ∿26 inches are some channels for gas cooling of the wall. The bulk shield of concrete is beyond this thermal shield, and an important parameter is the heat deposition within the concrete. This heat deposition is reduced to an acceptable level by an appropriate thermal shield design.

The heat deposition within the concrete is sensitive to the proper treatment of the higher energy (∿14 MeV) neutrons within the thermal shield. This includes (n,2n) and (n,3n) interactions. An integral measurement of the transmission of (d,Li) neutrons through an iron block has recently been made by HEDL to check calculational capabilities [20].

NEUTRON STREAMING

Penetrations through the test cell walls and through the walls of the accelerator require assessments of neutron streaming. Experience to date indicates that calculations of streaming are limited more by geometry models and the two- and three-dimensional aspects of the problem than by nuclear data [11]. The energy regime above 20 MeV has less of an impact upon the results than is true for bulk shields.

ACTIVATION

Approach

Both neutron and deuteron induced activation must be included in the overall assessments for the FMIT facility. Deuteron induced activation is primarily dealt with experimentally as described in a paper of this session [20]. The broader area of neutron activation is treated calculationally and, as the calculations indicate sensitive areas, will include some integral measurements.

The nuclear data base, along with computer codes and linkages, is used to treat neutron activation problems with the general

problem flow shown in Figure 7. The activation problem of concern is first defined. These include the LINAC accelerator with hands-on maintenance being highly desirable, the beam transport area, and activation of the test cell equipment, test cell walls, test assemblies, and the atmosphere within the accelerator and the test cell. After an area of concern is defined, the dozens of possible reactions are sifted through to isolate the most important reactions based upon half-lives, the decay energies of the gamma-rays, and conservative estimates of the relevant cross sections. If cross sections for the most important reactions are not included in the FMIT neutron multigroup activation library, the library is updated. Most of the data in the FMIT activation library has been generated using ENDF/B-V data (when it exists) along with a modified version of THRESH [21]. The modification made at HEDL extends the output of THRESH to 40 MeV with normalization to the ENDF/B-V data at 20 MeV whenever possible.

The energy dependent neutron flux is folded with the cross sections in the activation library to obtain gamma-ray source terms. The resulting gamma flux field is invariably dominated by only a few of the neutron reaction modes for the cooling times of interest. Cross sections for these reaction modes are examined to determine whether there is a need for further refinements. Refinements include the utilization of more exact numerical calculations of the cross sections, with codes such as HAUSER [22], and/or integral measurements of neutron activation.

The activation calculations summarized in the following sections utilized the atom densities shown in Table I and are based upon a one year irradiation at a 0.1 Amp deuteron current. A summary of important reactions is given in Table II.

Neutron Activation of Stainless Steel Within Test Cell

Stainless steel is a very important material since it will be used both structurally and as a major component for the material test modules. Calculations of stainless steel neutron activation have been made for targets located within the prime test region and for various other positions within the test cell.

The summary in Table III gives the volume averaged activation for a 5.5 x 4.0 x 5.0 cm parallelepiped of stainless steel placed within the pristine flux field of the prime test region (see Figure 2b for location and Table I for stainless steel composition). The most important radionuclide for shield design is ^{56}Co because of its hard 3.26 MeV gamma rays and its half-life of 77 days. This leads to a requirement for $\sim$12 inches of lead in the cask for transporting the irradiated test modules.

The most important reactions for activation of stainless steel within the prime test region are ^{58}Ni(n,t)^{56}Co and ^{58}Ni(n,nd)^{56}Co. For cooling times less than a few hours, ^{56}Fe(n,p)^{56}Mn will also be important in some shielding applications. At wide-angle positions within the test cell, the spectra is softer and the concentration of ^{56}Co relative to the other

isotopes will decrease by nominally a factor of four from that of Table III.

Neutron Activation of Important Elements Within Prime Test Volume

The volume averaged pristine neutron flux field, within a 5.5 x 4.0 x 5.0 cm parallelepiped positioned within the prime test region, was also folded with activation cross sections for various elements of interest. The results summarized in Table IV were obtained using the theoretical atom densities of Table I. Since the activities of Tables III and IV were generated using the pristine flux field, extrapolations to configurations with enough material to significantly perturb the flux should be made with care.

Neutron Activation of Aluminum Beam Tube

Neutron streaming back down the beam tube from the lithium target is the dominant mode of neutron activation of the beam tube near the test cell where access to the magnet is essential. An analysis was made to determine the possible advantage of utilizing aluminum rather than stainless steel for the beam tube. The measured neutron spectrum [6] at 150° for a (d,Li) source was used to compare these activations.

The most important radionuclides for the aluminum beam tube were found to be ^{24}Na, ^{65}Zn, ^{46}Sc, ^{60}Co, and ^{48}Sc. The major reaction modes are given in Table II. About one week after shutdown the ^{24}Na will decay to the point where the longer lived nuclides will dominate. Of these, only ^{48}Sc will decay appreciably for the maintenance times of concern.

The overall conclusion is that the aluminum does have advantages over stainless steel, from an activation viewpoint, for cooling time beyond the first few days.

Neutron Activation Along LINAC

Even though deuteron losses are greater at the lower energy end of the accelerator, neutron activation problems are more acute at the higher energy end because the generation rate of neutrons per lost deuteron increases rapidly with increasing deuteron energy. Roughly the same neutron energy regime is of concern along the high energy portion of the accelerator and beam transport area as in the test cell. However, because of the rapid decrease in the neutron source strength beyond ∿20 MeV, activation at energies above ∿30 MeV may usually be neglected. For wide angles, such as side-on at 90 degrees, a 20 MeV limit is usually adequate.

Neutron flux levels within the LINAC were determined from a Monte Carlo calculation [11] with a model of the geometry that included the last ten drift tubes. The results of folding the cross sections of the FMIT activation library with the neutron flux at the high energy end of the accelerator are given in Tables V and

VI for the accelerator tunnel concrete walls and for the LINAC, respectively.

The most important gamma-ray source within the concrete is from ^{24}Na for cooling times beyond a few hours; ^{56}Mn is also important for short cooling times. Since most of the ^{24}Na and ^{56}Mn nuclides are generated by thermal neutrons, a reduction of the gamma field within the accelerator tunnel is obtainable by simply borating the concrete of the LINAC walls.

The neutron activation summary of Table VI includes materials within the drift tubes and the outer tank wall of the accelerator. Point kernel calculations, using appropriate volume weighted source terms for the various materials, were made to obtain radiation fields along the high energy portion of the accelerator tunnel. A dose rate of 4 mrem/hr, at a distance of one foot from the tank, was obtained for a cooling time of one day. This does not include the contribution from the concrete walls of $\sim$5 mrem/hr. This component from the concrete walls can be reduced nearly an order of magnitude by borating the concrete. The dose rate scales linearly with the deuteron loss — assumed to be 3μAmp/m on gold.

This iteration did not include the water coolant of the drift tubes in the model of the geometry for the Monte Carlo calculation of neutron flux levels. An inclusion of the water is expected to increase the thermal flux with a corresponding increase from low energy reaction modes. The 2.6 hour half-life radionuclide ^{56}Mn, from $^{55}Mn(n,\gamma)^{56}Mn$, is expected to increase significantly with an appropriate treatment of the thermal flux.

Air Within Accelerator Tunnel

Preliminary assessments have been made of the activation of air within the accelerator tunnel. The radionuclides of most concern from a maximum permissible concentration (MPC) standpoint are ^{13}N, ^{16}N, ^{14}C, ^{39}Ar, and ^{41}Ar. The important reactions are summarized in Table II.

Experimenters Side Wall

Activation assessments are sometimes sensitive to the neutron transport calculations. An example is the test cell side wall containing plugs for experimental access. Nuclide activation beyond the first $\sim$4 feet of this iron-dominated shield are of concern. Here the flux levels depend upon an appropriate calculation of the transport and slowing down of the higher energy neutrons and the subsequent transport of the lower energy neutrons. There is a wealth of experimental and calculational [13] results for neutron transport within the iron resonance region (20 keV to 2 MeV). An integral measurement [20] of the transmission of (d,Li) neutrons through an iron block has now provided experimental data at higher energies.

SUMMARY

Discrete ordinates and Monte Carlo codes, developed for applications in nuclear reactors, fusion systems, and weapons physics, are applicable for solving neutron and photon transport problems relative to the FMIT facility. Extension of the nuclear data base is a challenging problem. This encompasses the appropriate cross sections for the neutron transport for the energy range 0 to 50 MeV and neutron activation cross sections for dozens of reaction modes over the energy range 0 to ∿30 MeV.

A pointwise library and a multigroup library have been developed for the Monte Carlo and discrete ordinates calculations. These neutron and gamma-ray transport libraries include the neutron energy regime 0 to 60 MeV for the most important elements used in the FMIT facility. Both libraries include adequate angular resolution to serve as data bases for deep penetration calculations. Sensitivity calculations have isolated the nonelastic cross section between 20 and 50 MeV as the most important cross section for the bulk shield design. Next in importance is the elastic scattering cross section for the same energy range with its corresponding angular distribution. Cross section measurements at 40 and 50 MeV for iron, oxygen, calcium, and carbon have enabled improved normalizations of optical model calculations.

A multigroup neutron activation library for FMIT has been created at HEDL. Because of the many reaction modes possible at the high neutron energies, the completeness of the library is examined prior to each calculation involving new isotopes. The dozens of possible reaction modes are sifted through to isolate the most important reactions by examining half-lives, decay energies of the gamma-rays, and conservative estimates of the relevant cross sections. Most of the data in the FMIT activation library has been generated using ENDF/B-V data (when it exists) along with a modified version of the THRESH code. The modification extends the output of THRESH to 40 MeV with normalization to the ENDF/B-V data at 20 MeV whenever possible. More exact treatments, with codes such as HAUSER, are utilized for a limited number of reactions. A few measurements of neutron activation are being planned to provide integral data for direct applications and for verifying calculational techniques.

The current status of calculations have been summarized for activation of stainless steel and other materials within the prime test volume, activation of the beam tube near the lithium target, activation along the LINAC, and activation of air within the accelerator tunnel. The more important reactions were displayed.

The calculation of nuclear heat deposition continues to be a problem due to inaccurate energy balances in ENDF/B and uncertainties in cross section data at higher energies. An important step has been made in a reevaluation of iron by LASL with improved energy balances and gamma production cross sections. A measurement of neutron transmission through an iron block, due to a (d,Li) source, will improve our understanding at the higher energies.

Thick target measurements of the (d,Li) neutron source have established the energy spectrum and yield at ten angles for 35 MeV incident deuterons. Monte Carlo techniques for modeling this anisotropic source, along with three-dimensional models of the test cell geometry, have been used to determine bulk shield thicknesses, neutron streaming through penetrations in the test cell walls, neutron activation, and nuclear heat deposition within the thermal shield.

Source terms due to deuteron loss within the accelerator and beam transport areas are not very well defined. This is primarily due to uncertainties regarding the magnitude of the deuteron loss rather than uncertainties in deuteron activation and neutron production from deuterons incident upon materials.

REFERENCES

1. E. W. POTTMEYER, Jr., "The Fusion Materials Irradiation Test Facility at Hanford", Journal of Nuclear Materials, 85 & 86, 463-465 (1979).

2. M. R. BHAT and S. PEARLSTEIN, editors, "Symposium on Neutron Cross-Sections from 10 to 40 MeV", BNL-NCS-50681, Brookhaven National Laboratory (1977).

3. D. G. DORAN, "Fusion Materials High Energy Neutron Studies — A Status Report", Paper in Session IV of this Symposium.

4. L. L. CARTER and R. J. MORFORD, "Shielding Calculations for the Fusion Materials Irradiation Test Facility", Trans. Am. Nucl. Soc., 30, 618 (1978).

5. R. W. ROUSSIN et al., "Calculations of the Transport of Neutrons and Secondary Gamma Rays Through Concrete for Incident Neutrons in the Energy Range 15 to 75 MeV", Nuclear Engineering and Design, 25, 250 (1973).

6. D. L. JOHNSON et al., "Measurements and Calculations of Neutron Spectra from 35 MeV Deuterons on Thick Lithium for the FMIT Facility", Journal of Nuclear Materials, 85 & 86 (1979). See also paper in Session II of this Symposium, D. L. JOHNSON et al., "Thick Target Neutron Yields and Spectra from the Li(d,xn) Reaction at 35 MeV".

7. LASL GROUP X-6, "MCNP - A General Monte Carlo Code for Neutron and Photon Transport", LA-7396-M, Los Alamos Scientific Laboratory (Revised November 1979).

8. L. L. CARTER and E. D. CASHWELL, "Particle Transport Simulation with the Monte Carlo Method", TID-26607, ERDA Critical Review Series, U. S. Energy Research and Development Administration, Technical Information Center, Oak Ridge, TN (1975).

9. C. I. ZANELLI et al., "Measurements of Neutron Total and Non-elastic Cross Sections for C, O, Ca, and Fe at UC Davis", Paper in Session III of this Symposium.

10. D. C. LARSON et al., "Transmission Measurements Up To 50 MeV for FMIT Design", Paper in Session III of this Symposium.

11. L. L. CARTER et al., "Monte Carlo Applications at Hanford Engineering Development Laboratory", (HEDL-SA-2072-A), Proceedings of a Seminar-Workshop on Theory and Application of Monte Carlo Methods, held at Oak Ridge, Tennessee April 21-23, 1980. To be published as ORNL/RSIC-44.

12. O. L. DEUTSCH and L. L. CARTER, "Simultaneous Global Calculation of Flux and Importance with Forward Monte Carlo", Proceedings of the Fifth International Conference on Reactor Shielding, R. W. Roussin, L. S. Abbott, and D. E. Bartine, editors, Science Press, Princeton (1977).

13. J. S. HENDRICKS and L. L. CARTER, "Computational Benchmark Problem for Deep Penetration in Iron", LA-8193-MS, Los Alamos Scientific Laboratory (1980). Also published in Trans. Am. Nucl. Soc., 33, 663 (1979).

14. W. B. WILSON, "Nuclear Data Development and Shield Design for Neutrons Below 60 MeV", LA-7159-T, Los Alamos Scientific Laboratory (February 1978).

15. R. G. ALSMILLER, JR. and J. BARISH, "NCDATA - Nuclear Collision Data for Nucleon-Nucleus Collisions in the Energy Range 25 to 400 MeV", ORNL-4220, Oak Ridge National Laboratory (1968).

16. R. G. ALSMILLER, JR. and J. BARISH, "Neutron-Photon Multigroup Cross Sections for Neutron Energies $\lesssim$ 60 MeV" ORNL/TM-6486, Oak Ridge National Laboratory (August 1978). Also published in Nuclear Science and Engineering, 69, 378-388 (1979).

17. "VITAMIN-C, 171 Neutron, 36 Gamma-Ray Group Cross Sections in AMPX and CCCC Interface Formats for Fusion and LMFBR Neutronics", DLC-41, Radiation Shielding Information Center (1977).

18. R. E. MACFARLANE, "Energy Balance of ENDF/B-V", Trans. Am. Nucl. Soc, 33, 681 (1979).

19. E. D. ARTHUR and P. G. YOUNG, "Evaluation of Neutron Cross Sections to 40 MeV for ^{54,56}Fe", Paper in Session V of this Symposium.

20. D. L. JOHNSON et al., "Measurements and Evaluations of Nuclear Data to Support Early Design Needs of the FMIT Facility", Paper in Session IV of this Symposium.

21. S. PEARLSTEIN, "Neutron Induced Reactions in Medium Massed Nuclei", Journal of Nuclear Energy, 27, 81-99 (1973). Updated by Proceedings of the Conference on Nuclear Cross Sections and Technology, Washington, DC (1975), NBS Special Publication number 425, page 324 (1975).

22. F. M. MANN, "HAUSER*5, A Computer Code to Calculate Nuclear Cross Sections", HEDL-TME 78-83, Hanford Engineering Development Laboratory (1979).

TABLE I

MATERIAL CONSTITUENTS FOR ACTIVATION STUDIES

Isotope	Density (atoms/barn-cm)	Isotope	Density (atoms/barn-cm)
Ordinary Concrete			
H 1	.42184-002	Ca 40	.44404-002
O 16	.37482-001	Ca 42	.27230-004
Na 23	.10774-002	Ca 43	.56027-005
Mg 24	.16782-002	Ca 44	.84890-004
Mg 25	.20504-003	Ca 46	.13060-006
Mg 26	.21484-003	Ca 48	.75095-005
Al 27	.30626-002	Ti 46	.11819-004
Si 28	.96644-002	Ti 47	.10317-004
Si 29	.47081-003	Ti 48	.10317-003
Si 30	.31475-003	Ti 49	.73789-005
P 31	.38919-004	Ti 50	.72483-005
S 32	.35784-004	Mn 55	.31801-004
S 33	.35915-006	Fe 54	.11493-003
S 34	.17696-005	Fe 56	.17631-002
K 39	.21484-003	Fe 57	.39115-004
K 41	.14692-004	Fe 58	.51913-005
Stainless Steel			
Cr 50	.70009-003	Fe 57	.12112-002
Cr 52	.12971-001	Fe 58	.16922-003
Cr 53	.14517-002	Co 59	.16321-004
Cr 54	.35906-003	Ni 58	.67174-002
Mn 55	.17266-002	Ni 60	.24825-002
Fe 54	.35305-002	Ni 61	.10308-003
Fe 56	.53773-001	Ni 62	.51884-003
		Ni 64	.80059-004
Aluminum Beam Tube			
Al 27	.58003-01	Cr 53	.10132-04
Mg 24	.52984-03	Cr 54	.29800-05
Mg 25	.69732-04	Mn 55	.88804-04
Mg 26	.69732-04	Fe 54	.17880-04
Si 28	.32005-03	Fe 56	.18297-03
Si 29	.20264-04	Fe 57	.41720-05
Si 30	.10132-04	Fe 58	.59600-06
Ti 46	.41720-05	Cu 63	.39932-04
Ti 47	.41720-05	Cu 65	.19072-04
Ti 48	.38144-04	Zn 64	.29800-04
Ti 49	.29800-05	Zn 66	.17284-04
Ti 50	.29800-05	Zn 67	.29800-05
Cr 50	.47680-05	Zn 68	.11920-04
Cr 52	.91784-04	Zn 70	.59600-06

TABLE I (continued)

Isotope	Density (atoms/barn-cm)	Isotope	Density (atoms/barn-cm)
Iron			
Fe 54	.49184-002	Fe 57	.17808-002
Fe 56	.77846-001	Fe 58	.25440-003
Aluminum			
Al 23	.60300-001		
Copper			
Cu 63	.59275-001	Cu 65	.25610-001
Titanium			
Ti 46	.47061-002	Ti 49	.30618-002
Ti 47	.42525-002	Ti 50	.29484-002
Ti 48	.41788-001		
Sodium			
Na 23	.25400-001		
Cobalt			
Co 59	.91000-001		

TABLE II

IMPORTANT NEUTRON ACTIVATION REACTIONS

Target Material	Major Reactions
Stainless Steel (Test Module)	$^{58}Ni(n,t)^{56}Co$
	$^{58}Ni(n,nd)^{56}Co$
	$^{58}Ni(n,2np)^{56}Co$
	$^{56}Fe(n,p)^{56}Mn$
	$^{58}Ni(n,p)^{58}Co$
Aluminum (Beam Tube)	$^{27}Al(n,\alpha)^{24}Na$
	$^{24}Mg(n,p)^{24}Na$
	$^{66}Zn(n,2n)^{65}Zn$
	$^{63}Cu(n,\alpha)^{60}Co$
	$^{46}Ti(n,p)^{46}Sc$
Ordinary Concrete (Accelerator Tunnel)	$^{23}Na(n,\gamma)^{24}Na$
	$^{24}Mg(n,p)^{24}Na$
	$^{27}Al(n,\alpha)^{24}Na$
	$^{23}Na(n,2n)^{22}Na$
	$^{24}Mg(n,t)^{22}Na$
	$^{55}Mn(n,\gamma)^{56}Mn$
	$^{54}Fe(n,p)^{54}Mn$
	$^{56}Fe(n,t)^{54}Mn$
Air (Accelerator Tunnel)	$^{14}N(n,2n)^{13}N$
	$^{16}O(n,p)^{16}N$
	$^{14}N(n,p)^{14}C$
	$^{40}Ar(n,2n)^{39}Ar$
	$^{40}Ar(n,\gamma)^{41}Ar$
Drift Tube and Tank Wall (LINAC)	$^{54}Fe(n,p)^{54}Mn$
	$^{56}Fe(n,nd)^{54}Mn$
	$^{56}Fe(n,t)^{54}Mn$

TABLE III

NEUTRON ACTIVATION OF STAINLESS STEEL WITHIN PRIME TEST VOLUME

(One Year Irradiation with Target Directly in Front of Beam)

Major Reactions	Percentage Contribution To Total	Decay Rate (Curies/cm^3) At Shutdown	Decay Rate (Curies/cm^3) 7 Days Cooling	Dominant Gamma Energies (MeV)	Half-Life (Days)
$^{56}Fe(n,p)^{56}Mn$	97			1.81(29%)	
Total ^{56}Mn		23.3	∿0.	2.11(15%)	0.108
$^{58}Ni(n,p)^{58}Co$	98			0.81(99%)	
Total ^{58}Co		22.7	21.2	1.67(0.6%)	71.
$^{55}Mn(n,2n)^{54}Mn$	25				
$^{54}Fe(n,p)^{54}Mn$	55				
$^{56}Fe(n,t)^{54}Mn$	12				
Total ^{54}Mn		9.65	9.50	0.84(100%)	300.
$^{58}Ni(n,nd)^{56}Co$	10			2.02(11%)	
$^{58}Ni(n,t)^{56}Co$	90			2.60(17%)	
Total ^{56}Co		0.159	0.150	3.26(13%)	77.
$^{60}Ni(n,p)^{60}Co$	92			1.17(100%)	
Total ^{60}Co		0.22	0.21	1.33(100%)	1934.
$^{58}Ni(n,p)^{57}Co$	68				
$^{58}Ni(n,d)^{57}Co$	30				
Total ^{57}Co		1.94	1.91	0.69(14%)	270
$^{58}Ni(n,2n)^{57}Ni$	100			1.37(86%)	
Total ^{57}Ni		1.12	0.039	1.89(14%)	1.5
$^{50}Cr(n,nd)^{48}V$	20				
$^{50}Cr(n,t)^{48}V$	80			1.31(97%)	
Total ^{48}V		0.260	0.193	2.24(3%)	16.2
$^{54}Fe(n,nd)^{52}Mn$	26				
$^{54}Fe(n,t)^{52}Mn$	73			0.94(84%)	
Total ^{52}Mn		0.263	0.111	1.43(100%)	5.6

TABLE IV

NEUTRON ACTIVATION OF ELEMENTS WITHIN PRIME TEST VOLUME

(One Year Irradiation with Target Directly in Front of Beam)

Major Reactions	Percentage Contribution To Total	Decay Rate (Curies/cm^3) At Shutdown	Decay Rate (Curies/cm^3) 7 Days Cooling	Dominant Gamma Energies (MeV)	Half-Life (Days)
IRON					
$^{56}Fe(n,p)^{56}Mn$	98			1.81(29%)	
Total ^{56}Mn		33.6	~0.	2.11(15%)	0.108
$^{54}Fe(n,p)^{54}Mn$	73				
$^{56}Fe(n,t)^{54}Mn$	17				
Total ^{54}Mn		10.3	10.1	0.84(100%)	300.
$^{54}Fe(n,nd)^{52}Mn$	26				
$^{54}Fe(n,t)^{52}Mn$	73			0.94(85%)	
Total ^{52}Mn		0.365	0.156	1.43(100%)	5.7
$^{58}Fe(n,\gamma)^{59}Fe$	100			1.10(56%)	
Total ^{59}Fe		0.014	0.013	1.29(44%)	45.
ALUMINUM					
$^{27}Al(n,p)^{27}Mg$	100			0.84(70%)	
Total ^{27}Mg		28.6	~0.	1.01(30%)	0.007
$^{27}Al(n,\alpha)^{24}Na$	100			1.37(100%)	
Total ^{24}Na		28.3	0.012	2.75(100%)	0.630
COPPER					
$^{65}Cu(n,2n)^{64}Cu$	96			0.51(38%)	
Total ^{64}Cu		77.2	0.0097	1.34(0.5%)	0.54
$^{65}Cu(n,p)^{65}Ni$	100			1.12(16%)	
Total ^{65}Ni		8.08	~0.	1.48(25%)	0.106
$^{63}Cu(n,\alpha)^{60}Co$	98			1.17(100%)	
Total ^{60}Co		1.44	1.43	1.33(100%)	1934.
SODIUM					
$^{23}Na(n,2n)^{22}Na$	100			0.51(180%)	
Total ^{22}Na		2.41	2.39	1.28(100%)	949.
$^{23}Na(n,\gamma)^{24}Na$	100			1.37(100%)	
Total ^{24}Na		0.069	0.00003	2.75(100%)	0.63

TABLE IV (continued)

Major Reactions	Percentage Contribution To Total	Decay Rate (Curies/cm³) At Shutdown	Decay Rate (Curies/cm³) 7 Days Cooling	Dominant Gamma Energies (MeV)	Half-Life (Days)
NICKEL					
$^{58}Ni(n,nd)^{56}Co$	10			2.02(11%)	
$^{58}Ni(n,t)^{56}Co$	90			2.60(17%)	
Total ^{56}Co		1.48	1.39	3.26(13%)	77.
$^{60}Ni(n,p)^{60}Co$	93			1.17(100%)	
Total ^{60}Co		2.02	2.02	1.33(100%)	1934.
$^{60}Ni(n,2p)^{59}Fe$	55				
$^{62}Ni(n,\alpha)^{59}Fe$	45			1.10(56%)	
Total ^{59}Fe		0.91	0.81	1.29(44%)	45.
$^{58}Ni(n,p)^{58}Co$	100			0.81(99%)	
Total ^{58}Co		210.7	197.0	1.67(0.6%)	71.
TITANIUM					
$^{47}Ti(n,np)^{46}Sc$	18				
$^{46}Ti(n,p)^{46}Sc$	65				
$^{48}Ti(n,t)^{46}Sc$	11				
Total ^{46}Sc		9.82	9.27	1.12(100%)	84.
$^{48}Ti(n,p)^{48}Sc$	87			1.04(100%)	
Total ^{48}Sc		11.1	0.77	1.31(100%)	1.8
$^{48}Ti(n,2p)^{47}Ca$	62				
$^{50}Ti(n,\alpha)^{47}Ca$	33				
Total ^{47}Ca		0.79	0.27	1.31(74%)	4.5
COBALT					
$^{59}Co(n,2n)^{58}Co$	100			0.81(99%)	
Total ^{58}Co		216.	201.	1.67(0.6%)	71.
$^{59}Co(n,p)^{59}Fe$	100			1.10(56%)	
Total ^{59}Fe		23.2	20.8	1.29(44%)	45.
$^{59}Co(n,\alpha)^{56}Mn$	100			1.81(29%)	
Total ^{56}Mn		9.49	~0.	2.11(15%)	0.108
$^{59}Co(n,\gamma)^{60}Co$	100			1.17(100%)	
Total ^{60}Co		0.71	0.71	1.33(100%)	1934.

TABLE V

NEUTRON ACTIVATION WITHIN CONCRETE WALLS OF ACCELERATOR TUNNEL

(For 3 μA/m Deuteron Loss)

Major Reactions	Percentage Contribution To Total	Decay Rate (Curies/cm³)[a] At Shutdown	Decay Rate (Curies/cm³)[a] 24 Hours Cooling	Dominant Gamma Energies (MeV)	Half-Life (Days)
$^{23}Na(n,\gamma)^{24}Na$	83.2				
$^{24}Mg(n,p)^{24}Na$	10.2				
$^{27}Al(n,\alpha)^{24}Na$	5.8			1.37(100%)	
Total ^{24}Na		3.5×10^{-9}	1.2×10^{-9}	2.75(100%)	0.630
$^{55}Mn(n,\gamma)^{56}Mn$	96.3			0.85(99%)	
$^{56}Fe(n,p)^{56}Mn$	3.6			1.81(29%)	
Total ^{56}Mn		3.0×10^{-9}	4.9×10^{-12}	2.11(15%)	0.108
$^{54}Fe(n,p)^{54}Mn$	60.8				
$^{56}Fe(n,t)^{54}Mn$	21.6				
Total ^{54}Mn		7.8×10^{-11}	7.8×10^{-11}	0.84(100%)	312.
$^{24}Mg(n,t)^{22}Na$	53.7				
$^{23}Na(n,2n)^{22}Na$	41.5			0.51(180%)	
Total ^{22}Na		2.6×10^{-11}	2.6×10^{-11}	1.28(100%)	956.

[a] Near surface of concrete at high energy end of LINAC.

TABLE VI

NEUTRON ACTIVATION WITHIN DRIFT TUBE AND TANK OF LINAC

(For 3 μA/m Deuteron Loss)

Activation Nuclides	Decay Rate After 24 Hours Cooling		Dominant Gamma Energies (MeV)	Half-Life (Days)
	Drift Tube [a] (Curies)	Tank Wall [a] (Curies)		
^{54}Mn	3.32×10^{-2}	3.74×10^{-3}	0.84(100%)	312.
^{52}Mn	1.41×10^{-3}	1.82×10^{-4}	0.94(85%) 1.43(100%)	5.7
^{56}Mn	3.6×10^{-5}	5.5×10^{-6}	0.85(99%) 1.81(29%) 2.11(15%)	0.108
^{60}Co	2.30×10^{-3}	3.40×10^{-4}	1.17(100%) 1.33(100%)	1934.
^{64}Cu	5.43×10^{-3}	6.51×10^{-3}	0.51(38%) 1.34(0.5%)	0.54
^{58}Co	1.94×10^{-3}	---	0.81(99%) 1.67(0.6%)	71.
^{56}Co	1.71×10^{-4}	---	2.02(11%) 2.60(17%) 3.26(13%)	77.
^{59}Fe	---	1.92×10^{-4}	1.10(56%) 1.29(44%)	45.

[a] Activation of material along a 69.7 cm length at high energy end of LINAC. The FMIT activation library has been updated since this table was generated.

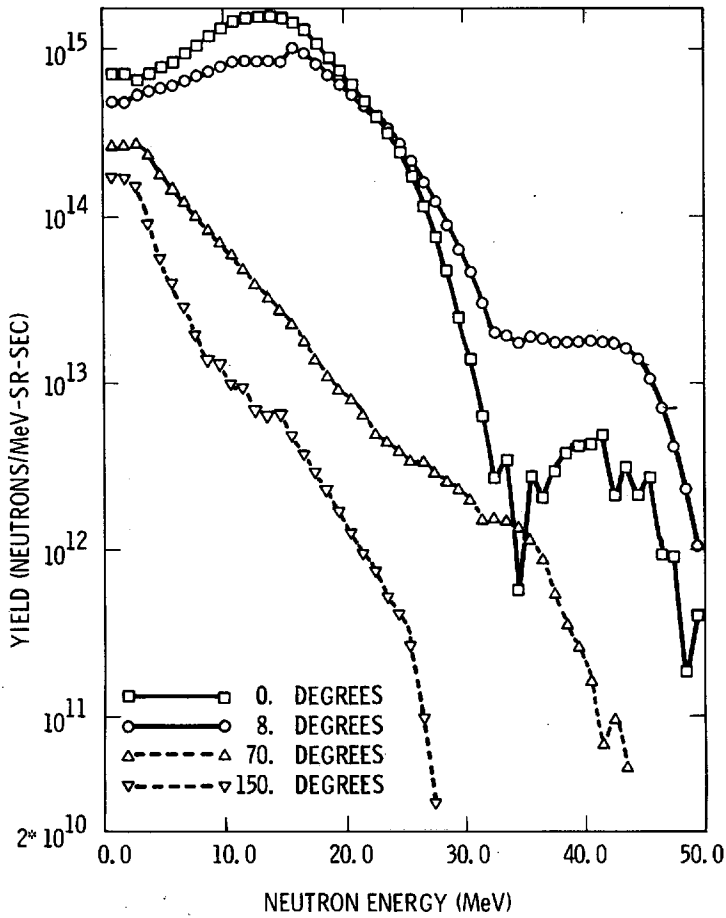

Fig. 1. Neutron spectra from a 0.1 Amp current of 35 MeV deuterons incident upon lithium.

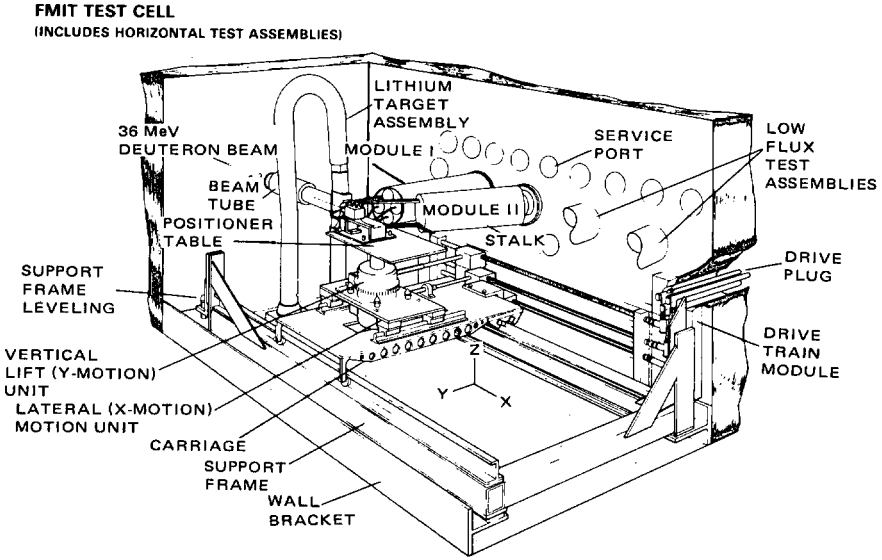

Fig. 2a. Conceptual arrangement of four horizontal test assemblies and a vertical test assembly in the FMIT test cell.

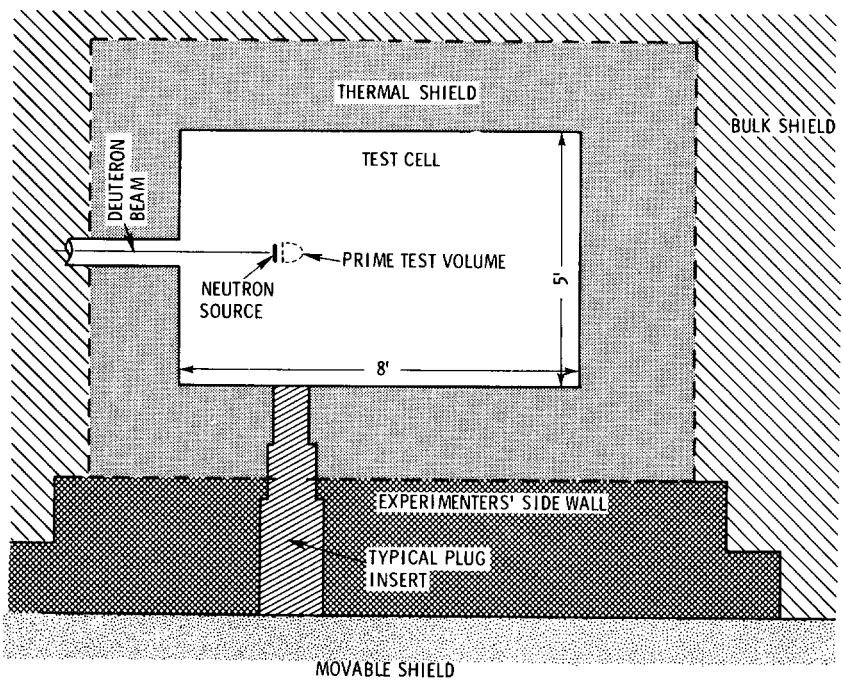

Fig. 2b. Plan view of empty test cell.

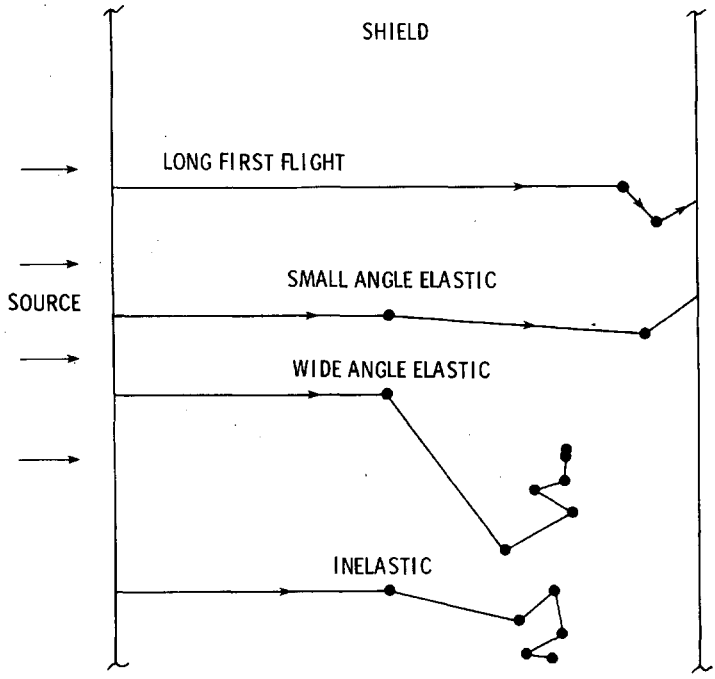

Fig. 3. Penetration of neutrons through a shield for a 20 to 50 MeV incident source.

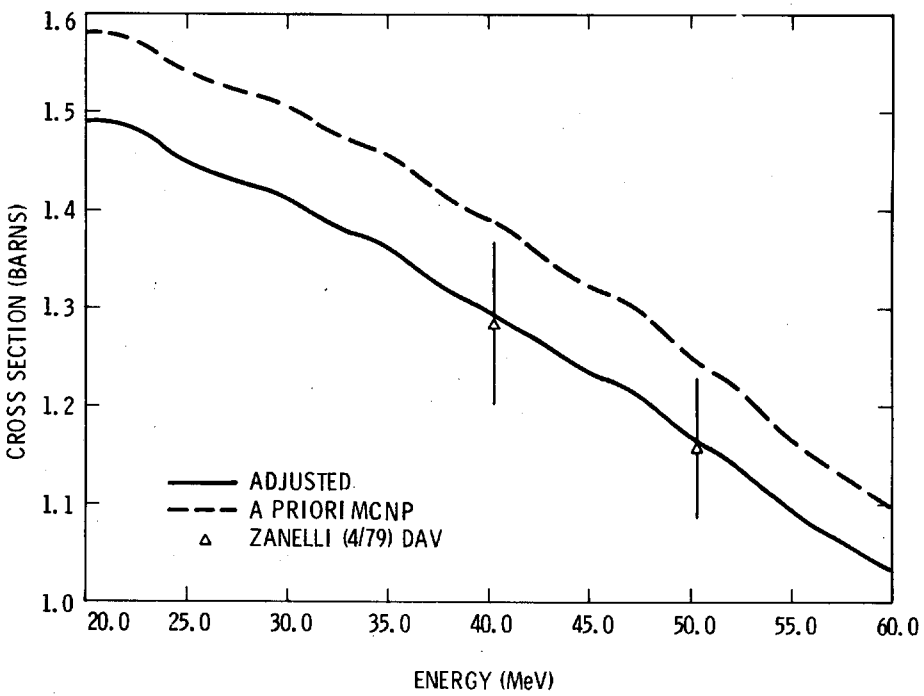

Fig. 4. Removal cross section for two evaluations of iron.

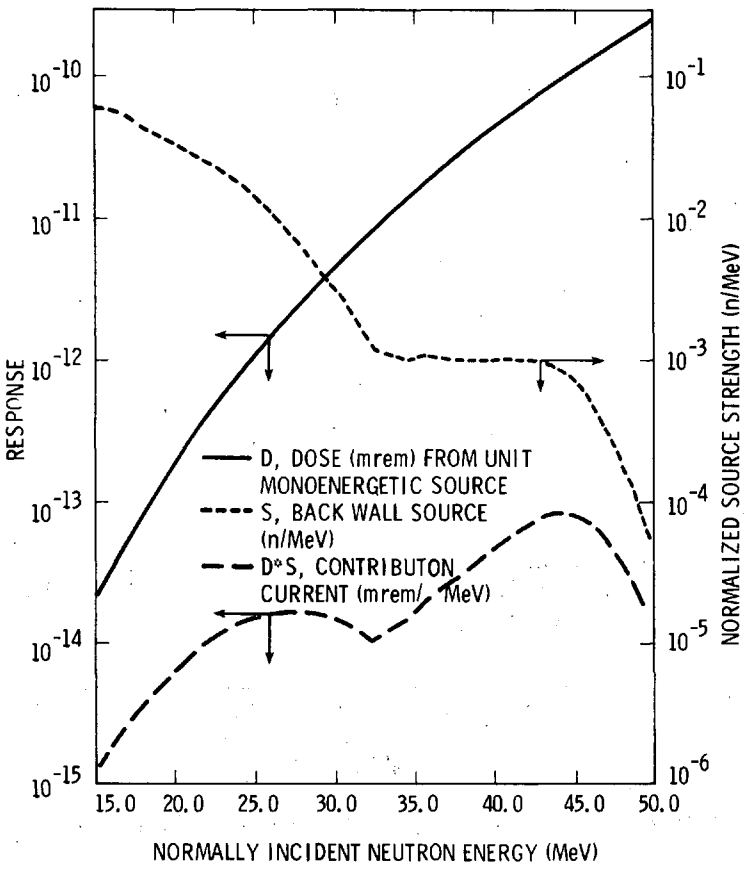

Fig. 5. Dose and contributon current through 8 ft of high density concrete. (3.6 g/cm^3)

	SOURCE OF NUCLEAR DATA
POINTWISE CROSS SECTIONS FOR MCNP MONTE CARLO CODE	
<20 MeV neutron energy including photon production	ENDF/B-IV
20 MeV to 60 MeV (H, C, O, Si, Ca, Cr, Fe, Ni)	
Nonelastic	Ref. 14; based upon optical model [a]
Nonelastic energy-angle distribution	Ref. 15; based upon IC+E
Elastic	Optical model [b]
Elastic angular distribution	Optical model [b]
Gamma production	Ratio of gamma production to total assumed constant above 20 MeV
MULTIGROUP P_5 COUPLED NEUTRON-GAMMA [c]	
(Elements H, ^{10}B, ^{11}B, C, O, Si, Ca, Cr, Fe, Ni)	
<14.9 MeV neutron energy	RSIC fusion cross section library; Ref. 17
14.9 MeV to 60 MeV	
Nonelastic	Ref. 16; optical model
Nonelastic energy-angle distribution	Ref. 15, 16; based upon IC+E
Elastic	Ref. 16; optical model
Elastic angular distribution	Ref. 16; optical model
Gamma production	None above 14.9 MeV

[a] The nonelastic cross section for Ca was based upon the IC+E model.

[b] Hydrogen cross sections above 20 MeV based upon measured values.

[c] 47 neutron groups and 21 gamma groups.

Fig. 6. Cross section libraries for FMIT.

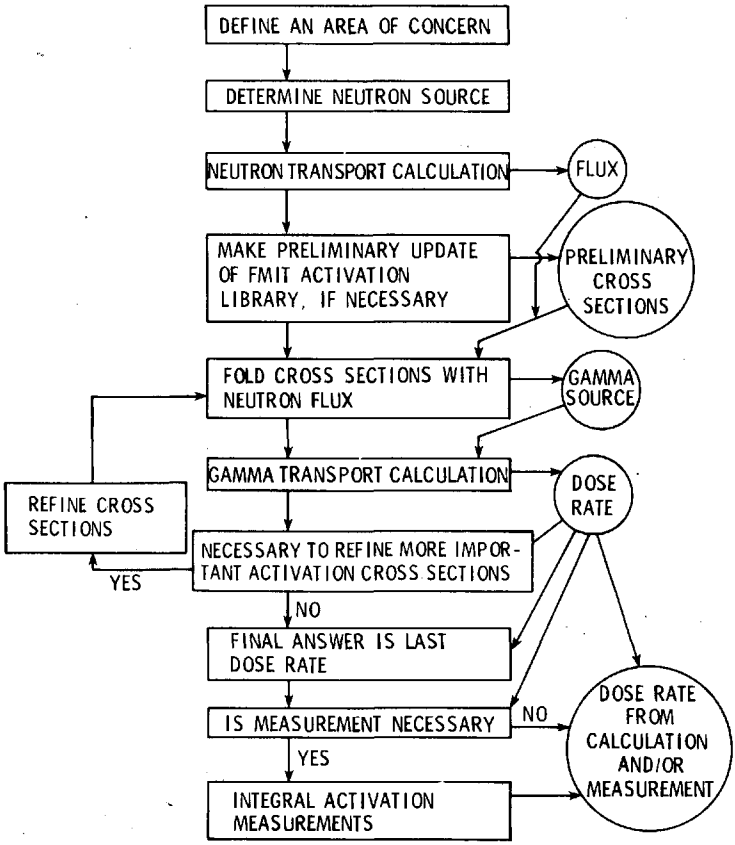

Fig. 7. Calculation of neutron activation.

FUSION MATERIALS HIGH ENERGY NEUTRON STUDIES — A STATUS REPORT

D. G. Doran

Hanford Engineering Development Laboratory
Richland, Washington

M. W. Guinan

Lawrence Livermore Laboratory
Livermore, California

ABSTRACT

The objectives of this paper are (1) to provide background information on the U. S. Magnetic Fusion Reactor Materials Program, (2) to provide a framework for evaluating nuclear data needs associated with high energy neutron irradiations, and (3) to show the current status of relevant high energy neutron studies. Since the last symposium, the greatest strides in cross section development have been taken in those areas providing FMIT design data, e.g., source description, shielding, and activation. In addition, many dosimetry cross sections have been tentatively extrapolated to 40 MeV and integral testing begun. Extensive total helium measurements have been made in a variety of neutron spectra. Additional calculations are needed to assist in determining energy dependent cross sections.

Materials irradiations with high energy neutrons are currently centered at RTNS-II, with emphasis on achieving the highest practical fluences. It has been found possible, generally speaking, to correlate the very low fluence data obtained to date with 14 MeV, d-Be, and fission neutrons by weighting fluences with simple spectrum sensitive parameters. The definition of both the irradiation environment and the associated derived damage parameters still suffer from a serious lack of data and calculated cross sections at high energies.

INTRODUCTION

Let us begin this review by considering what technical areas are common to this conference and to the Fusion Materials Program of the Office of Fusion Energy. Clearly, the purpose of the latter is to develop materials for use in fusion reactors. Assuming that such reactors are shown to be feasible in the next few years, their conversion from a scientific wonder to an important national resource will depend largely on development of improved materials. One of the major considerations, of course, is the effect of the neutron environment on the material. Since the first fussion reactors will employ the D-T reaction, we must determine the effects of neutrons of energies up to and including 14 MeV on materials. The first planned fusion device with provisions for materials studies is the Engineering Test Facility (ETF) [1]. Such studies are not planned until the facility has been in operation for several years, hence not expected before about 1993. In the interim, the only facility that will produce high energy neutrons at high damage rates for materials studies is the Fusion Materials Irradiation Test (FMIT) Facility [2], expected on line in 1984.

To build and use such a facility requires high energy neutron cross sections for facilities design, environmental definition, and damage calculations. Because the FMIT will produce a broad range of neutron energies, these cross sections are required well above the 14 MeV output of the D-T reaction.

Let us be somewhat more specific. FMIT facility design requires neutron cross section data in four areas: source description, shielding, energy deposition, and component activation. A paper in the first session of this symposium described the current status of neutron yields from the D-Li reaction [3]. The status of neutron cross sections for shielding design of FMIT was discussed in the previous review paper by Carter [4].

A primary concern, because of the large impact on facility costs, is the degree to which maintainence must be done remotely. This is determined by the activation of various components by deutrons, the subject of a subsequent paper in this session [5], and by neutrons. Neutron activation is also a concern in the design of the experimental test cell and of associated equipment which must be removed from the test cell such as neutron detectors and experimental modules. Another use for activation cross sections is in estimating the activation of test specimens themselves, a non-trivial concern of the experimenters.

A by-product of the high energy neutron fluxes in FMIT is a high rate of energy deposition in test specimens and test equipment. The high absolute values coupled with strong gradients mean that energy deposition calculations are very important in designing the test modules.

Carter has discussed neutron activation and energy deposition calculations for FMIT in some detail [4]. In particular, he has presented a summary of important activation reactions.

The data analyst, on the other hand, is concerned with the definition of the radiation environment to which the specimens are

exposed. This includes the actual dosimetry and diagnostics needed to determine flux-spectra and fluences and the conversion of these data to damage parameters needed in damage correlation calculations. The status of dosimetry cross sections for FMIT [6] and a description of the FMIT environment in terms of damage parameters [7] are described in subsequent papers in this session.

Most damage calculations have been for metals. However, since the last BNL conference there has been significant work done on damage calculations for insulators.

Before going into more detail regarding high energy studies, let us consider briefly the fusion materials program to which they are being applied.

THE FUSION REACTOR MATERIALS PROGRAM

Program

Changes in Program Emphasis

The US Fusion Program has undergone some changes since the time of the last BNL conference. The logic for the magnetic confinement portion of major device development is indicated in Figure 1 [1]. The Tokamak Fusion Test Reactor (TFTR), currently under construction, is to be in operation in 1982. It is expected to be the first device to demonstrate energy breakeven. The next major fusion facility will be the Engineering Test Facility (ETF) currently being designed at ORNL. The target date for ETF operation is 1990. This is intended to be a multipurpose machine. After a few years of operation as an engineering test facility to qualify technology and components for first generation power reactors, it will also become a materials irradiation test facility. The ETF is to be followed by one or more demonstration reactors, then on to a commercial reactor. It should be added that concurrently with the development of the ETF the U.S. is participating in an international program to design the very similar INTOR machine [8]. The recent concentration of effort on the ETF has had an impact on the fusion materials program as might be expected.

Task Group Reorganization

The Fusion Materials Program is carried out through several task groups. Since the first BNL conference four Program Plans [9] have been completed and implementation of these has begun. The Damage Analysis and Fundamental Studies (DAFS) and Alloy Development for Irradiation Performan (ADIP) task groups have undergone some reorganization since the first conference [10,11]. The current structure is shown in Figures 2 and 3. The reorganization was in part to help stress near-term objectives, particularly those pertaining to ETF and to FMIT. The call for increased and improved nuclear data is from the DAFS Subtask Group on Dosimetry and Damage Parameters, under L. R. Greenwood. This group is responsible for seeing that the irradiation environments associated with fusion materials experiments are adequately and systematically characterized.

A review of this work is included in the symposium [12].

Materials Priorities

As might be anticipated, there have been some changes in the priorities assigned particular materials in the fusion materials program [10]. The current materials emphases in the ADIP program are included in Figure 3. The major changes relative to 1977 are 1) niobium has been pushed to a back burner, 2) the number of titanium alloys has been decreased, and 3) a general class of ferritic steels (9-12% Cr) has been added (new Path E). While it has been known for some time that thermal stresses in a ferritic steel first wall are significantly lower than in an austenitic steel wall, and that ferritic steels exhibit considerable radiation resistance for certain properties, these steels were eliminated from the fusion materials program early on because it was believed that their ferromagnetism precluded their use in a magnetic fusion reactor. Recent studies have concluded that, because the applied magnetic field is well above the saturation value, this concern is not well-founded and these materials are now under intense investigation [13].

Facilities

Rotating Target Neutron Source (RTNS-II)

Description

The RTNS-II facility comprises two independent sources of 14 MeV neutrons [14]. One is currently operating and is the world's most intense 14 MeV source. The design, based on experience with RTNS-I, calls for a 1 cm diameter, 150 ma beam of 400 keV deuterons incident on a water-cooled, titanium tritide target rotating at 5000 rpm. The target, constructed of a copper alloy, is to be 50 cm in diameter and expected to last for about 100 hours. The design yield is 4×10^{13} n/s. The major components of one source are shown in Figure 4 and a schematic of the target and a photograph of an irradiation capsule in place are shown in Figure 5. The method of cooling the target is illustrated in Figure 6.

Facility Status

One source is currently operating 80 hours per week. A 23 cm diameter target (the size used in RTNS-I) is in use with a 40 ma deuteron beam which produces a neutron yield of about 1×10^{13} n/s (peak neutron flux of about 2.5×10^{12} n/cm^2-s). Target life is about 80 hours. Difficulties in fabricating the 50 cm targets are expected to be resolved soon, but large target operation is not expected to begin before April 1981.

Irradiation began at RTNS-II in March 1979; the irradiations carried out to date are summarized in Table I. These experiments can be divided into several categories:

(1) Postirradiation Studies of Metals and Alloys

Two types of specimens have been irradiated at RTNS-II. One is disks for TEM examination and the other is wires for tensile testing. Only a small fraction of these specimens have been tested to date. Very low fluence irradiations of pure elements and simple

alloys have been for the purpose of comparison with model calculations of damage production. The irradiations of more complex materials are intended to be compared with fission reactor irradiations of the same materials to infer the effects of high energy neutrons. In order for these comparison studies to be made at similar damage rates, the Omega-West reactor at Los Alamos will be employed for the fission reactor irradiations. These irradiations are to begin this summer.

(2) In-Situ Studies of Metals and Alloys

The initial change in resistivity of pure metals irradiated near 4°K has been measured at RTNS-II. These experiments are currently being analyzed to infer the number of defects produced for comparison with models. A second type of in-situ experiment concerns the effect of high energy neutrons on creep, from which inference of free defect production rates will be attempted. A feasibility experiment was completed; more irradiations are planned.

(3) Postirradiation Studies of Insulators

Postirradiation examination of insulators includes measurements of mechanical properties, as with metals, plus determination of changes in electrical properties.

(4) Postirradiation Examination of Engineering Materials

Although the flux available at RTNS-II is much lower than that of a fusion reactor, it is nevertheless possible to get engineering data on some materials that will be exposed to low lifetime fluences. Recent examples include window and insulating materials for TFTR and components of superconducting magnets. The latter includes both the superconductor itself and the aluminum or copper matrix material.

Fusion Materials Irradiation Test (FMIT) Facility

Facility Description

The FMIT facility is to comprise basically 1) a linear deuteron accelerator, 2) a flowing lithium target, and 3) test cells in which specimens can be irradiated under a variety of conditions. Neutrons are produced predominantly by a stripping reaction as the 100 ma beam of 35 MeV (or 20 MeV) deuteron is stopped in the 2 cm thick lithium target. The resulting neutron field is strongly forward peaked. The flowing lithium serves also as a heat dump. The configuration of the major components is shown in Figure 7.

The source strength of the FMIT facility is expected to be about 3×10^{16} neutrons per second with a beam area of 1 x 3 cm (fwhm values of Gaussian distributions in both the vertical and horizontal directions). Average flux values of 10^{15} n/cm^2·s are calculated for a volume of 16 cm^3, 10^{14} n/cm^2·s for nearly 1000 cm^3. Put another way, a test volume of 140 cm^3 will provide displacement rates greater than that for a wall loading of about 1 MW/m^2; in 6 cm^3, the rate will exceed that for about 5 MW/m^2.

The facility is designed to have two identical target/test cells in order to reduce outage time during experiment setup

or target maintenance. Each cell provides for routine target access from the side via horizontal test assemblies and access for special equipment from the top. The horizontal test assembly nearest the target provides for simultaneous irradiations at three temperatures in capsules cooled by flowing NaK.

The test cell provides for limited active neutron dosimetry.

Facility Status

Construction of FMIT was initiated on February 22, 1980 at HEDL. The development of the accelerator, the responsibility of the Los Alamos Scientific Laboratory, is proceeding on schedule. An experimental lithium system featuring a full size mock-up of the free-flowing lithium target is about to commence operation. Hydraulic studies with water have been completed. The FMIT facility is at the Title II or final design stage, and is scheduled for completion in 1984.

Characterization of FMIT

The characterization of the FMIT test volume has been carried out as well as can be done with available cross sections in terms of flux-spectra, damage parameters, and energy deposition. The current status of the damage parameter characterization is described in detail in a later paper [7] in this session, and will not be repeated here. The energy deposition calculations, described briefly by Carter in the preceding paper, have yielded heating rates as high as 15 w/g close to the source, about three quarters of which is due to neutrons and one quarter due to gammas. These heating rates have been used in designing the temperature control devices for the horizontal test assemblies that will hold the specimens.

Test Matrix

A preliminary test matrix has been developed for the first few years of FMIT operation [15]. The purpose of this matrix is to guide the design of experimental test facilities, and to aid in the evaluation of certain design features. A portion of the matrix is shown in Table II.

Dosimetry

The formulation of appropriate dosimetry procedures for FMIT has been a lively topic from the outset. One reason for this has been the uncertainty as to how well the neutron source can be defined by deuteron beam diagnostics. Beam stability in both space and time, as well as the ability to characterize these variations on the deuteron side of the target, are in question. Hence, it has been felt necessary that the neutron source be characterizable directly in terms of neutron output. Furthermore, there are dosimetry systems that could be accommodated in the design of the facility that could aid in its future utilization, but which add to costs and which may not be essential for the materials irradiations for which it is being built. A primary source of dosimetry data will be passive monitors included with the experiments. Active systems are being developed for spatial and temporal source characterization and absolute spectrum determination. The strategy and

systems are described in detail by R. Gold, et al. in a paper [6] in this session.

MATERIALS STUDIES WITH HIGH ENERGY NEUTRONS

Purpose

The RTNS-II is the only high energy neutron irradiation facility dedicated to fusion materials research. Until FMIT begins operation in 1984, materials irradiation at RTNS-II will have three objectives. One is to aid in developing models for fusion/fission/charged particle correlations. A second objective, which has become more significant with the advent of the ETF project, is to build up fluences as high as practical for direct correlation with fission reactor irradiations. While practically attainable fluences are less than 10^{20} n/cm^2 (0.3 dpa in iron), this is sufficient, at temperatures below about 200°C, to produce large changes in strength and ductility of candidate alloys for ETF. Saturation property levels are expected to be reached in some cases. A third objective is to actually achieve lifetime exposures at RTNS-II for certain reactor components such as superconductors.

Status

High energy neutron irradiations to date have necessarily been limited to very low fluences, hence have been concerned primarily with damage production and the onset of the evolution of a damage microstructure. The principal diagnostic tools have been resistivity measurements, tensile tests, and transmission electron microscopy. A primary objective has been to correlate observed effects, on a physical basis, with those produced in fission reactor spectra.

The quantitative correlations to date have all been in the form of a simple spectrum dependent factor with which to scale neutron fluence. The universally used procedure is to convert fluences to "damage energy" or, equivalently, to displacements per atom (dpa). The damage energy is that portion of the energy deposited in a material which is available to produce displacement damage. Its value per neutron increases with neutron energy. The common exposure unit, dpa, is proportional to the damage energy.

In reviewing the results of the dozen or so room temperature correlation experiments which had been completed in September 1976, Wiffen and Stiegler [16] summarized as follows: "The quantitative response of a property change to 14 MeV neutron irradiation (as compared to fission reactor irradiation) depends on the sensitivity of that property to various defect configurations. Properties dependent on the total number of defects scale directly with damage energy. Properties which depend on the type and distribution of clustered defects will require more complex analysis of the damage distribution." Now that the available data base has more than doubled and has been extended to more complex materials and to both

elevated and cryogenic temperatures, their summary is still appropriate.

Table III summarizes the quantitative fission-fusion correlation experiments which have been completed since Wiffen and Stiegler's review. Also included are a number of comparisons between irradiations with 14 MeV and D-Be (30-40 MeV deuterons) neutrons. Progress has been made in a number of areas.

Total defect production rates, as measured by electrical resistivity at 4.2 K, are proportional to damage energy for Nb, V, Mo, Cu and Pt. The results for Cu are also in quantitative agreement with the work of Averback, et al [40] on Cu in which ion bombardment was used to study defect production over a wide range of recoil energies.

Free (i.e., mobile) defect production rates near room temperature are also found to scale directly with damage energy in the case of interstitials in Cu and vacancies in α-brass.

Clustered defect size distributions and number densities are still found to show some differences when comparisons are made at equivalent damage energy levels in high purity Cu and Nb. In 316 stainless steel, on the other hand, the cluster density scales more closely with damage energy. Yield stress measurements on pure V, Cu and Nb do not scale with damage energy; high energy neutrons are found to be 1.6 to 2 times more effective than fission reactor neutrons in increasing the yield stress. Measurements on Nb-1% Zr alloy, on the other hand, scale well with damage energy, while measurements on 316 stainless steel seem to scale better than those on pure metals. Further evidence of differences in defect distributions are evident from flux pinning effects in Nb_3Sn and NbTi superconductors, annealing studies in platinum, and positron trapping experiments in Pt.

Disordering by collision cascades in superconducting Nb_3Sn, which leads to decreases in critical temperature and current, appears to scale with damage energy. Flux pinning effects, which lead to initial increases in critical current, do not.

Two experiments on nonmetals are included in Table III. Point defect production (as measured by optical absorption) in Al_2O_3 is consistent with damage energy scaling, as was found earlier in MgO, although uncertainties in both fission reactor exposure and damage energy calculations are high. Only estimates of the damage energy cross section for graphite are available. Recent experiments show that they all underpredict 14 MeV neutron damage relative to fission neutron damage (as indicated by changes in the basal plane shear modulus).

In summary, total defect production in a wide range of materials irradiated by both fission and fusion energy neutrons is directly proportional to damage energy. There is some evidence that, in mid-atomic number materials at least, free defect production also scales with damage energy. Furthermore, there is an indication that the amount of disorder scales similarly.

There is clear evidence of significant differences in the number densities and smaller differences in the size distributions of defect clusters in fission-fusion correlation experiments in pure materials. These differences may be due in part to

the 25-30°C discrepancies in ambient temperatures. In most cases, however, the property changes can be scaled with damage energy if a lower cut-off in recoil energy of about 10 keV is employed, consistent with the expectation that high energy cascades are more effective in producing defect clusters. In Nb-1Zr and, to a lesser extent in 316 SS, damage energy scaling prevails without invoking a low energy cut-off. An assessment of possible differences in the development of irradiation microstructures in pure metals and alloys will have to await the analysis of recently completed irradiations, and the performance of higher fluence experiments at elevated temperatures.

Future Plans

Rotating Target Neutron Source (RTNS-II)

Operation of RTNS-II at 80 hours per week is expected to continue in 1981; the facility should reach design neutron yields by mid-1981. The major emphasis will be on obtaining fluences up to 3×10^{19} or higher at temperatures ranging from 50-500°C.

FMIT

FMIT will not produce materials data until about 1985. By then a correlation methodology [41] will have been developed for applying data obtained in fission reactors to fusion environments. The first experiments in FMIT will be designed to validate that methodology, to fill in vital holes that will undoubtedly exist, and to obtain the first goal exposure data with high energy neutrons on materials of interest to the fusion program. Although it is expected that some types of FMIT data will be directly applicable to fusion reactors through a simple fluence normalization, this is not expected to be true in general. Correlation models will be needed for this transference of data. The displacement rate obtainable at RTNS-II is one-to-two orders of magnitude below that expected in a fusion reactor first wall. Early low exposure experiments in FMIT will be compared with experiments performed in RTNS-II to see if flux effects are as predicted.

NUCLEAR DATA FOR MATERIALS STUDIES

Damage Calculations

Descriptions of displacement damage in irradiated materials begin with the calculation of primary knock-on spectra. For high energy neutrons, this requires knowledge of the cross sections of essentially all nuclear reactions because they all result in sufficient energy transmitted to the target nucleus to displace it from its normal lattice site. Required information is differential angular cross sections for elastic and inelastic scattering and the energy and angular distributions of emitted particles. Damage energy cross sections are the result of

combining primary knock-on atom spectra with an energy partition model that designates the fraction of recoil energy available to cause further displacements.

Damage energy and displacement cross sections have been standardized as calculated from ENDF/B-IV, although these will be updated shortly to ENDF/B-V. Therefore, they extend only to 20 MeV. Recently, Greenwood [42] has added some approximations to high energy cross sections developed by Alsmiller and Barish [42] and extended the damage energy cross sections for Fe, Cr, and Ni to 50 MeV (see Figure 8). Still lacking are sufficient experimental data to tie down the calculated nuclear cross sections at high energies.

In the first BNL conference, the need for evaluating the usual assumption of isotropic emission of secondary particles was discussed [11]. This need still exists.

The program to make total helium measurements in a variety of neutron spectra is continuing at Rockwell International. It has a twofold objective: 1) helium production rates must be known for experiment design and analysis, and 2) once the cross sections are known, total helium production measurements in various materials provide a good measure of neutron fluence. Papers on both topics are included in this conference. Measurements at 14.8 MeV have been made on C, Al, Ti, V, Fe, Ni, Cu, Zr, Nb, Mo, Pt, Au, and 316 SS [44]. Measurements in a Be (30 MeV d, n) field have been made for Al, Fe, Ni, and Cu [45]. The helium production cross section for copper has been extended theoretically to high energies by Mann using the code HAUSER *5 [46]. Good agreement with experiment is obtained at 14 MeV; further comparisons will be made with measurements made in D-Be spectra when the spectral definition is completed. Calculations are needed for many other materials.

No attempt has yet been made to extend the cross sections needed to calculate other transmutation products in FMIT spectra.

It is expected that ceramic insulators that will be exposed to the plasma in a magnetic fusion reactor will be tested at FMIT. Relevant cross sections have not been extended above 20 MeV. However, a significant new development is the extension to polyatomic insulators of the methodology for calculating damage energy cross sections [47].

A brief summary of nuclear data needs for damage calculations is given in Figure 9.

Dosimetry

The status of nuclear data for the characterization of the FMIT test environment is described in detail in other papers in this symposium [6,12]. Three complementary approaches to FMIT dosimetry have been identified, viz., passive, active and calculational. As shown in the paper by Greenwood [12], a good start has been made on developing radiometric monitors for passive, in-situ dosimetry. He has had gratifying success in extrapolating cross sections above 20 MeV and integrally testing them in high energy neutron spectra [48,49]. The set of cross sections used is given in Table IV and the good agreement obtained with time-of-flight measurements in a d-Be spec-

trum is shown in Figure 10.

Other cross sections also need better definition at high energy for dosimetry application. Two examples are total helium cross sections and fission cross sections. The former provide stable product monitors for measuring high fluences. The latter, for use with track recorders, provide high energy thresholds for spectral definition.

While the most obvious nuclear data need is high energy cross section data and associated nuclear parameters, there is a continuing need for better monitors below 1 MeV. This region is important for damage production in mixed spectrum reactors and in fusion reactors for components outboard of the shielding. As pointed out by Gold, et al [6], such monitors will be needed in FMIT because the rear of the test cell will be useful for testing materials for such components.

A number of systems are being considered for active dosimetry in FMIT; the associated nuclear data needs are discussed by Gold, et al [6].

The nuclear data needs for neutronic calculations are essentially the same as discussed by Carter for shielding calculations [4,6].

For in depth discussions of the application of dosimetry techniques in the fusion materials program, see the recent reviews by Greenwood [50] and Smith [51].

Neutron Activation

Neutron activation calculations for FMIT have been described in detail by Carter [4]. A neutron activation library has been established at HEDL [52]. The cross sections are tied to ENDF/B-V below 20 MeV, and extended to higher energies using THRESH. As critical reactions are identified, more accurate calculations will be made.

Source/Shielding for Facility Design

In calculations needed for FMIT design, use has been made of all available high energy neutron data. In some cases, data were developed with FMIT in mind. The most extensive data are the total neutron cross section measurements made at Oak Ridge National Laboratory on many materials, including C, O, Al, Si, Ca, Cr, Fe, Ni, Cu, Au, and Pb [53]. Total and nonelastic cross sections for C, O, Ca and Fe have also been made at UC-Davis [54]. These data and their application to FMIT have been discussed by Carter [4].

Nuclear Models

A discussion of developments in nuclear modeling is beyond the scope of this paper. Some relevant work is described in a recent review paper by Haight [55]. A productive approach is to search for systematics that can be used to extend data from one material to another. Considerable success has been achieved for (n, x) reactions [56].

SUMMARY

We have attempted to describe briefly the current status of high energy neutron studies within the framework of the fusion materials program. Materials irradiation experiments are centered on RTNS-II, the only high energy neutron facility dedicated to fusion materials research. Nuclear data development, on the other hand, is focused on FMIT. This does not imply, however, that all data needs are in the 10-50 MeV range addressed explicitly by this symposium. Some progress has been made on meeting nuclear data needs since the last symposium. Much of this was obtained under the pressure of design milestones for FMIT. While some of these data are applicable to damage calculations, most of the needs described at the 1977 symposium still exist. With respect to dosimetry needs, early testing of some radiometric monitors has met with considerable success and significant progress has been made in developing helium accumulation fluence monitors suitable for use in FMIT spectra. As plans for FMIT characterization progress, however, new nuclear data needs are surfacing, and accuracy requirements are becoming better defined.

It is clear that, as vital as some key measurements are, a sustained effort must be mounted to evaluate existing and forthcoming data and to incorporate such data into calculations of necessary nuclear quantities.

ACKNOWLEDGEMENTS

The authors gratefully acknowledge assistance provided by L. L. Carter, H. Farrar, R. Gold, L. R. Greenwood, D. L. Johnson, F. Mann, W. N. McElroy, E. K. Opperman, and R. E. Schenter and the many accounts of research provided prior to publication by authors whose work is cited in Table III.

This work was supported by the Office of Fusion Energy of the U. S. Department of Energy.

REFERENCES

1. F. E. Coffman, "Fusion Technology Development," U.S. Dept. of Energy Report DOE/ET-0116/1, August 1979.

2. E. W. Pottmeyer, Jr., "The Fusion Materials Test Facility at Hanford," Fusion Reactor Materials, F. W. Wiffen, J. H. Devan and J. O. Stiegler, eds., North Holland Publ. Co., p. 463-465 (1979).

3. D. L. Johnson, F. M. Mann and R. E. Schenter, "Neutron Yields from D-Li Reactions," this conference.

4. L. L. Carter, "Nuclear Data Relevant to Shield Design of FMIT Facility," this conference.

5. D. L. Johnson, F. M. Mann and R. E. Schenter, "Deuteron Induced Activation for E_d = 5-35 MeV," this conference.

6. R. Gold, et al., "Cross Sections Required for FMIT Dosimetry," this conference.

7. F. M. Mann, et al., "Neutron Environment in the FMIT Facility: Theoretical Predictions," this conference.

8. W. M. Stacey, Jr., et al., "General Characteristics and Assessment of the Scientific/Technical Feasibility of the Next Major Device in the Tokamak Fusion Program," U.S. Dept. of Energy Report DOE/ET-0117/1, September 1979.

9. The Fusion Reactor Materials Program Plan, Section I, II, III and IV, U.S. Dept. of Energy Report DOE/ET-0032/1, 2, 3, 4, July 1978.

10. J. O. Stiegler and T. C. Reuther, "The Program for Alloy Development for Irradiation Performance in Fusion Reactors", Symposium on Neutron Cross Sections from 10-40 MeV," M. R. Blat and S. Pearlstein, eds., DNL-NCS-50681, p. 51.

11. D. G. Doran, et al., "MFE Damage Analysis Program Nuclear Data Needs," ibid, p. 323.

12. L. R. Greenwood, "Review of Source Characterization for Fusion Materials Irradiation," this conference.

13. S. N. Rosenwasser, et al., "The Application of Martensitic Stainless Steels in Long Lifetime Fusion First Wall/Blankets," ibid, Reference 2, p. 177-182.

14. "RTNS: A Tool for Studying Neutron Damage," Energy and Technology Review, Lawrence Livermore Laboratory Report UCRL-52000-78-3, March 1978. See also, "RTNS-II Utilization Plan," U.S. Dept. of Energy Report DOE/ET-0066, September 1978.

15. R. E. Nygren, "Considerations on Experiments in FMIT," Proc. IEEE 8th Symposium on Engineering Problems in Fission Reactors, November 1979 (also Hanford Engineering Development Laboratory HEDL-SA-1928).

16. F. W. Wiffen and J. O. Stiegler, "Recent Progress in CTR Bulk Radiation Effects Studies," in Proc. of Second Topical Meeting on the Technology of Controlled Nuclear Fusion, CONF-76093, Volume 1, p. 135 (1976).

17. J. B. Roberto, et al., J. Nucl. Mat., 73, 97 (1978).

18. M. A. Kirk and L. R. Greenwood, J. Nucl, Mat., 80, 159 (1979).

19. J. A. Goldstone, D. M. Parkin, and H. M. Simpson, "Differential Neutron Cross Section for Free Interstitial Production in Copper," ibid, Reference 2, p. 617.

20. J. Narayan and S. M. Ohr, "The Nature of High Energy Neutron Damage in Copper and Gold," ibid, Reference 2, p. 515.

21. J. B. Roberto, "X-Ray Studies of Fusion-Energy Neutron Damage in Copper," in Solid State Division Annual Progress Report, Oak Ridge National Laboratory Report ORNL-5328 (1977).

22. J. B. Mitchell, "Exploratory Experiments Comparing Damage Effects of High-Energy Neutrons and Fission-Reactor Neutrons in Metals," Lawrence Livermore Laboratory Report UCRL-52388 (1978).

23. R. R. Coltman, C. E. Klabunde, and J. M. Williams, (quoted in Reference 18), (1979).

24. M. W. Guinan and C. E. Violet, (quoted in Reference 18), (1978).

25. M. W. Guinan and C. E. Violet, "Initial Damage Rates in Nb, V and Mo", in Proc. of Symposium on High Energy Neutrons, 10 to 40 MeV, Brookhaven National Laboratory Report BNL-NCS-50681 (1977).

26. R. H. Jones, et al., "Microstructure and Tensile Properties of T(d,n) Neutron Irradiated Nickel, Niobium and 316 SS," ibid., Reference 2, p. 889.

27. R. H. Jones, "Correlation of 16 MeV Protons with Fusion Neutrons," Damage Analysis and Fundamental Studies Quarterly, Progress Report, U.S. Dept. of Energy Report DOE/ET-0065/6, p. 186 (1979).

28. R. R. Vandervoort, W. L. Barmore and A. K. Mukherjee, Rad. Effects, 41, 113 (1979).

29. W. L. Barmore, A. W. Ruotola and E. L. Raymond, "In-Situ Creep Testing During Irradiation with High-Energy Neutrons," Damage Analysis and Fundamental Studies Quarterly Progress Report, U.S. Dept. of Energy Report DOE-ET-0065/7, p. 55 (1979).

30. M. W. Guinan, et al., "A Comparison of Experimental Defect Production Efficiency in Mo with Computer Simulations in W.," ibid., Reference 27, p. 71 (1979).

31. C. L. Snead, Jr., et al., in Proc. 5th International Conference on Positron Annihilation, Japan, R. R. Hasiguti and K. Fugiwara, eds., p. 725 (1979).

32. M. W. Guinan, et al., Rad. Effects, 40, 209 (1979).

33. R. R. Vandervoort, E. L. Raymond and C. J. Echer, Rad. Effects, 45, 191 (1980).

34. C. L. Snead, Jr., et al., "Determination of the Damage-Energy Cross Section of 14-MeV Neutrons from Critical Property Changes in Irradiated Nb_3Sn," ibid., Reference 16, p. 229.

35. R. M. Scanlan and E. L. Raymond, "Low Temperature Irradiations of Nb_3Sn with 14-MeV Neutrons," in Proc. of 1978 Applied Superconductivity Conference, Pittsburgh, Pennsylvania (1979).

36. B. S. Brown, et al., J. Appl. Phys., 49, 4144 (1978).

37. B. D. Evans and M. Stapelbrook, "Fusion/Fission Damage Ratio for Alumina," ibid., Reference 2, p. 497.

38. W. J. Gray and W. C. Morgan, "Damage Function for Carbon at Neutron Energies up to 15 MeV," ibid., Reference 2, p. 237.

39. W. J. Gray and W. C. Morgan, "Experimental Determination of Radiation Damage Function for Graphite," Pacific Northwest Laboratory Report PNL-2836 (1979).

40. R. S. Averback, R. Benedek and K. L. Merkle, Phys. Rev., B18, 4156 (1978).

41. C. R. Odette and D. Frey, "Development of Mechanical Property Correlation Methodology for Fusion Environments," ibid., Reference 2, p. 817.

42. L. R. Greenwood, "Calculation of Damage Cross Sections for Cr, Fe, Ni, Cu and Nb to 50 MeV," Damage Analysis and Fundamental Studies Quarterly Progress Report, U.S. Dept. of Energy Report DOE/ET-0065/4, p. 59, May 1979.

43. R. G. Alsmiller, Jr., and J. Barish, "Neutron-Photon Multigroup Cross Sections for Neutron Energies $\leq$60 MeV," ORNL/TM-6486, August 1978.

44. H. Farrer IV and D. W. Kneff, Tran. ANS 28, 197 (1978).

45. D. W. Kneff, H. Farrar IV, and M. M. Nakata, "Helium Accumulation Neutron Dosimetry for the Be (d,n) Irradiation Environment," ibid., Reference 29, p. 21.

46. F. M. Mann and C. Kalbach, "Cross Section Prediction," ibid., Reference 42, p. 39.

47. C. A. Coulter and D. M. Parkin, J. Nucl. Mat. 88, 249 (1980).

48. L. R. Greenwood, "Extrapolation of Neutron Activation Cross Sections for Dosimetry to 44 MeV," Argonne National Laboratory Report ANL-FPP-TM-115, November 1978.

49. L. R. Greenwood, "Integral Cross Section Testing in a $^{9}Be(d,n)$ Field at E_d = 40 MeV," Damage Analysis and Fundamental Studies Quarterly Progress Report, U.S. Dept. of Energy Report DOE/ET-0065/2, p. 23, May 1979.

50. L. R. Greenwood, "The Status of Neutron Dosimetry and Damage Analysis for the Fusion Materials Program," Proc. International Conference on Nuclear Cross Sections for Technology, Knoxville, Tennessee, October 1979.

51. D. L. Smith, "Neutron Dosimetry for Radiation Damage in Fission and Fusion Reactors," ibid.

52. F. M. Mann, "FMIT Activation Library," Damage Analysis and Fundamental Studies Quarterly Progress Report, U.S. Dept. of Energy Report DOE/ET-0065/8, p. 18, February 1980.

53. D. C. Larson, D. M. Hetrich, and J. A. Harvey, Bull. APS, Volume 25, p. 543 (1980).

54. C. I. Zanelli, et al., "Measurements of Neutron Total and Nonelastic Cross Sections for C, O, Ca and Fe at UC Davis," this conference.

55. R. C. Haight, "Neutron Cross Sections for Fusion," ibid., Reference 50.

56. F. M. Mann and C. Kalbach, "Cross Section Prediction," Damage Analysis and Fundamental Studies Quarterly Progress Report, U.S. Dept. of Energy Report DOE/ET-0065/7, p. 10, November 1979. See also C. Kalbach and F. M. Mann, "Phenomenology of Pre-equilibrium Angular Distribution," this conference.

TABLE I

Irradiation Experiments Performed at RTNS-II

DATE STARTED	MATERIALS IRRADIATED	MEASUREMENT	LABORATORY	MAXIMUM FLUENCE n/cm^2
3/19/79	Ni, Nb & SS	Mechanical Properties	PNL	3.4×10^{17}
3/19/79	TFTR Glass	Density & Optical Properties	ANL	$\sim 2.0 \times 10^{18}$
3/19/79	A15 Superconductors	Transision Temperature Critical Field & Current	BNL/LLL	$\sim 9.0 \times 10^{17}$
3/19/79	Nb Sn	Critical Current	LLL	$\sim 8.0 \times 10^{17}$
3/19/79	Ni, Nb & SS	Mechanical Properties	PNL	2.0×10^{18}
4/03/79	Au TEM Foils	Sub-Cascade Structure	ANL	4.9×10^{15}
4/03/79	TFTR SS	Hydrogen Trapping	SANDIA	1.4×10^{16}
4/05/79	Cu, Ni, V, Nb, Ti & SS TEM Disks	Microstructure/ Microhardness	HEDL/UCSB	3.9×10^{17}
6/06/79	Cu, Ni, V, Nb, Ti & SS TEM Disks	Microstructure/ Microhardness	HEDL/UCSB	1.2×10^{18}
6/06/79	Ni-Al & Ni-Si TEM Disks	Nucleation Studies	LLL/ANL	5.4×10^{17}
7/02/79	Zr Al TEM Disks	Cascade Size & Structure	UW/LLL	6.5×10^{15}
8/14/79	Nb	In-Situ Creep 400°-600°C	LLL	7.5×10^{16}

TABLE I
(cont'd)

9/24/79	MACOR Ceramic (TFTR Insulators)	Thermal/Mechanical	LASL	1.0×10^{16}
9/24/79	Glass-Bonded Mica (TFTR Insulators)	Thermal/Mechanical	LASL	1.0×10^{18}
9/24/79	MACOR Ceramic (TFTR Insulators)	Thermal/Mechanical	LASL	1.0×10^{18}
10/29/79	Binary Alloys Based on Ni and Cu	Microstructure/ Microhardness	HEDL	$\sim 1.0 \times 10^{18}$
2/20/80	SS Strips	Microstructure/Tensile	U.Va	1.0×10^{18}
2/27/80	316 SS, Ni, Ti-6 Ti-6Al-4V	Microstructure/ Microhardness/Tensile	HEDL	$\sim 1.2 \times 10^{18}$
3/13/80	Fiber Optic Cables	Optical Attenuation	LLL	$\leq$25 krad
5/07/80	NbTi Cu, Al	Critical Current. 4°K Magnetoresistance and Initial Damage Rates (Resistivity)	LLL	$\sim 1.0 \times 10^{17}$

TABLE II

A Sample of the Proposed FMIT Test Matrix

HIGH FLUX	# MATERIALS	REDUNDANCY	FLUENCES	SUBTOTAL	# TEMPS
TEM (Chemical Variation, Micro, Rate)	30	4	(5, 10, 20, 50, 100 dpa)	600	4
Creep (Rate Effect)	5	2	(Interim to 100)	10	3
MODERATE FLUX					
TEM (Micro, Rate)	15	10	(2, 5, 10 dpa)	450	4
Creep/Rupture	15	5	(Interim to 50)	75	3
Stress Relax (In-Situ)	15	2	(3 Preirradiated)	90	3
In-Situ Cyclic Flux (Specimen Oscillated)	10	2	(5, 20, 50)	60	3
LOW FLUENCE					
TEM (Seed Microstructure)	15	6	(0.2, 0.5, 2)	270	3
Creep (Rate Effect)	5	2	(Interim to 5 dpa)	10	3

TABLE III.

High Energy Neutron Correlation Studies

Material	Ref.	Property Measured	Sensitivity	Neutron Spectrum	Maximum Fluence (n/cm^2)	Relative Response Per Unit Damage Energy	Comments
Cu	(17)	Resistivity at 4.2K	Total defects	BSR	3×10^{17}	1.0	Annealing to 300K similiar.
				40MeV d-Be	4.5×10^{17}	$0.9 \pm .2$	
	(18)	"	"	CP-5(VT53)	$> 10^{18}$	$0.9 \pm .2$	
	(19)	Modulus changes from $\perp$ pinning at 330K	Free interstitials	14.1 MeV	10^{11}- 10^{12}	1.0	Mono-energetic neutrons.
				1.9 "	"	$1.6 \pm .4$	
				3.9 "	"	$1.2 \pm .6$	
				5.9 "	"	$1.1 \pm .4$	
				23.4 "	"	$0.9 \pm .2$	
	(20)	TEM	Defects retained in clusters	BSR	1.0×10^{18}	1.0	Comparable size and number distributions.
				RTNS	1.8×10^{17}	1	
				40MeV d-Be	1.8×10^{17}	1	
	(21)	X-ray diffuse scattering	Defect cluster size distribution	BSR	1.0×10^{18}	See Comments	Some differences in size and number distributions.
				RTNS	1.8×10^{17}		
				40MeV d-Be	2.0×10^{17}		
	(22)	Yield stress at ambient and 480K	Defect clusters	LPTR	5×10^{18}	1.0	Two stage hardening at 480K for LPTR.
				RTNS	7×10^{17}	$2.0 \pm .2$	
				30MeV d-Be	1.2×10^{18}	$2.0 \pm .2$	

TABLE III. (continued)

Material	Ref.	Property Measured	Sensitivity	Neutron Spectrum	Maximum Fluence (n/cm^2)	Relative Response Per Unit Damage Energy	Comments
Nb	(23)	Resistivity	Total	BSR	2.6×10^{17}	1.0	Nb-.03%Zr
	(24)	at 4.2K	defects	LPTR(FNIF)	8.4×10^{14}	$1.2 \pm .2$	Nb-.03%Zr
	(25)	"	"	30MeV d-Be	1.3×10^{16}	$0.9 \pm .2$	Nb-.03%Zr
		"	"	RTNS	8.6×10^{15}	$0.9 \pm .2$	Nb-.03%Zr
	(17)	"	"	BSR	$> 10^{17}$	$1.1 \pm .2$	
		"	"	40MeV d-Be	3.7×10^{15}	$0.9 \pm .2$	
	(18)	"	"	CP-5(VT53)	$> 10^{18}$	$0.8 \pm .2$	
	(22)	Yield stress	Defect	LPTR	5×10^{18}	1.0	
		"	clusters	RTNS	1.2×10^{17}	$1.6 \pm .3$	
				30MeV d-Be	9×10^{17}	$1.6 \pm .3$	
	(26)	Yield stress	Defect	RTNS	2×10^{17}	See	Two stage hardening,
	(27)	and TEM	clusters	40MeV d-Be	1×10^{18}	Comments	levels differ.
	(28)	Creep	Clustered and	30MeV d-Be	2.0×10^{12}/s	See	Qualitatively
	(29)	750-900K	free defects	RTNS-II	1.2×10^{12}/s	Comments	similiar response.
Mo	(23)	Resistivity	Total	BSR	2.4×10^{17}	1.0	Mo-.03%Zr
	(30)	at 4.2K	defects	LPTR(FNIF)	8.4×1014	$1.1 \pm .2$	Mo-.03%Zr
	(25)	"	"	30MeV d-Be	1.3×10^{16}	$0.9 \pm .2$	Mo-.03%Zr
		"	"	RTNS	8.6×10^{15}	$1.0 \pm .2$	Mo-.03%Zr
	(18)	"	"	CP-5(VT53)	$> 10^{18}$	$0.7 \pm .2$	

TABLE III. (continued)

Material	Ref.	Property Measured	Sensitivity	Neutron Spectrum	Maximum Fluence (n/cm^2)	Relative Response Per Unit Damage Energy	Comments
V	(23)	Resistivity	Total	BSR	5.2×10^{17}	1.0	V-.03%Zr
	(24)	at 4.2K	defects	LPTR(FNIF)	8.4×10^{14}	$1.2 \pm .2$	V-.03%Zr
	(25)	"	"	30MeV d-Be	1.3×10^{16}	$0.9 \pm .2$	V-.03%Zr
		"	"	RTNS	8.6×10^{15}	$1.0 \pm .2$	V-.03%Zr
	(22)	Yield stress	Defect	LPTR	4×10^{18}	1.0	
		"	clusters	RTNS	3×10^{17}	$2.1 \pm .2$	
				30MeV d-Be	1×10^{17}	$2.1 \pm .2$	
Pt	(17)	Resistivity	Total	BSR	$> 10^{17}$	1.0	Less annealing at 300K for d-Be.
		at 4.2K	defects	40MeV d-Be	4.1×10^{15}	$0.8 \pm .2$	
	(18)	"	"	CP-5(VT53)	$> 10^{18}$	$0.9 \pm .2$	
	(31)	Positron	Vacancy-like	HFBR	$> 10^{18}$	1.0	
		trapping	defects	30MeV d-Be	3.4×10^{16}	$0.8 \pm .2$	
Au	(20)	TEM	Defects in	BSR	1.0×10^{18}	1.0	
		"	clusters	40MeV d-Be	6.0×10^{16}	5	
Ni	(26)	Yield stress	Defect	RTNS	2×10^{17}	1.0	
	(27)	and TEM	clusters	40MeV d-Be	1×10^{18}	$1.0 \pm .3$	

TABLE III. (continued)

Material	Ref.	Property Measured	Sensitivity	Neutron Spectrum	Maximum Fluence (n/cm^2)	Relative Response Per Unit Damage Energy	Comments
Nb-1%Zr	(22)	Yield stress	Defect clusters	LPTR	5×10^{18}	1.0	
		"		RTNS	7×10^{17}	1.0 ± .1	
α-Brass	(32)	Resistivity/ SRO	Free vacancies	LPTR	2×10^{17}	1.0	
				RTNS	7×10^{16}	1.1 ± .2	
316 SS	(33)	Yield stress ductility and TEM	Defect clusters	LPTR	2.6×10^{19}	1.0	Similiar scaling for all three properties.
				RTNS	2.2×10^{17}	1.1 ± .3	
				30MeV d-Be	3.8×10^{18}	1.1 ± .3	
Nb_3Sn	(34)	Transition temperature	Disordering	HFBR	8×10^{19}	1.0	
				RTNS	2×10^{18}	1.1 ± .2	
	(35)	Critical current	Fluxoid pinning	RTNS	7×10^{16}	1.0	Corrected to same temperature and transverse field
				30MeV d-Be	7×10^{17}	1.0 -1.6	
	(36)	4.2K-6K	"	CP-5(VT53)	2×10^{18}	0.6 ± .2	
Al_2O_3	(37)	Optical absorbtion	Point defects	NRLR	1×10^{18}	1.0	
				RTNS	1×10^{17}	1.0 ± .3	
Graphite	(38) and (39)	Basal plane shear modulus	Defect pinning	BNLR	1.2×10^{17}	1.0	Ratios based on ENDF/III-B damage analysis.
				RTNS	1.1×10^{17}	1.5 ± .3	
				5.5MeV d-Be	4.6×10^{16}	2.0 ± .4	

TABLE IV

Ratio of Measured-to-Calculated Activities
Using Time-of-Flight Spectra

Relative errors are 1.5%, absolute errors ±10%, except as noted.

REACTION	90% Energy[a] Range (MeV)	Ratio at 0° (∿3.5°)	Ratio at 15° (∿17°)
	(0° Spectrum)		
$^{45}Sc(n,\gamma)^{46}Sc$	7.6^{-3} - 25.0	1.00[b]	1.17[b]
$^{59}Co(n,\gamma)^{60}Co$	1.6^{-4} - 22.7	1.26[b] ±10%	1.35[b] ±10%
$^{197}Au(n,\gamma)^{198}Au$	2.5^{-4} - 19.5	1.03[b]	1.10[b]
$^{238}U(n,\gamma)^{239}Np$	4.3^{-4} - 4.2	1.02[b]	0.88[b]
$^{235}U(n,f)$	0.6 - 29.7	0.99[c]	0.94[c]
$^{238}U(n,f)$	5.0 - 30.8	1.00[c]	0.94[c]
$^{115}In(n,n^{1})^{115m}In$	1.8 - 23.1	1.04	0.96
$Ti(n,p)^{46}Sc$	9.0 - 33.0	*1.84 (0.83)[d]	*1.93 (0.88)[d]
$Ti(n,p)^{47}Sc$	12.0 - 33.0	*8.82 (1.18)[d]	*7.14 (1.13)[d]
$^{48}Ti(n,p)^{48}Sc$	9.9 - 26.6	0.97	0.99
$Fe(n,p)^{54}Mn$	6.0 - 33.0	*1.89 (0.94)[d]	*1.88 (1.04)[d]
$^{56}Fe(n,p)^{56}Mn$	8.6 - 23.5	1.05	1.02
$^{59}Co(n,p)^{59}Fe$	8.1 - 24.2	0.85 ±15%	0.95 ±15%
$^{58}Ni(n,p)^{58}Co$	4.4 - 23.4	0.93	0.88
$^{60}Ni(n,p)^{60}Co$	7.9 - 23.0	0.97 ±5%	0.98 ±7%
$^{27}Al(n,\alpha)^{24}Na$	9.0 - 21.5	1.02	0.96
$^{54}Fe(n,\alpha)^{51}Cr$	9.5 - 28.0	*1.28	*1.43
$^{59}Co(n,\alpha)^{56}Mn$	9.3 - 24.4	1.05	1.02
$^{45}Sc(n,2n)^{44m}Sc$	13.9 - 27.5	0.95	0.98
$^{59}Co(n,2n)^{58}Co$	12.8 - 26.6	1.06	1.04
$^{58}Ni(n,2n)^{57}Ni$	14.8 - 28.2	0.82 (1.26)[e]	0.84 (1.34)[e]
$^{90}Zr(n,2n)^{89}Zr$	14.1 - 28.1	0.99	1.02
$^{93}Nb(n,2n)^{92m}Nb$	11.2 - 22.0	0.93	0.94
$^{169}Tm(n,2n)^{168}Tm$	10.4 - 23.3	0.91	0.92

TABLE IV
(cont'd)

$^{169}Tm(n,3n)^{167}Tm$	17.9 - 30.6	1.05	1.08
$^{197}Au(n,2n)^{196}Au$	10.7 - 23.5	0.99	0.98
$^{197}Au(n,3n)^{195}Au$	18.0 - 29.4	0.87 ±4%	1.06 ±7%
$^{197}Au(n,4n)^{194}Au$	27.2 - 39.8	1.03 ±10%	0.88 ±13%
$^{238}U(n,2n)^{237}U$	7.7 - 16.4	1.21	1.10
Std. DeV. (%)		*9.7	*10.8
Total Flux (n/cm^2 - sec)		6.26×10^{10}	3.21×10^{10}

*Reactions not included in standard deviation.

[a]90% of the activation integral falls within this energy range. 7.6^{-3} means 7.6×10^{-3}. The range at 15° is only slightly changed.

[b](n,γ) ratios are somewhat arbitrary since the time-of-flight data stops at 2 MeV. A smooth extrapolation was chosen to give a reasonable fit to the data.

[c]14 MeV fission yields were used.

[d]Ratios not in parentheses were calculated assuming mono-isotropic production [e.g. $^{54}Fe(n,p)$]; ratios in parentheses include production from higher mass isotops based on THRESH calculations. Energy limits are for total production.

[e]Cross-section from ENDF/B-IV and LASL; values in parentheses from ENDF/B-IV only.

FUSION FACILITY DEVELOPMENT

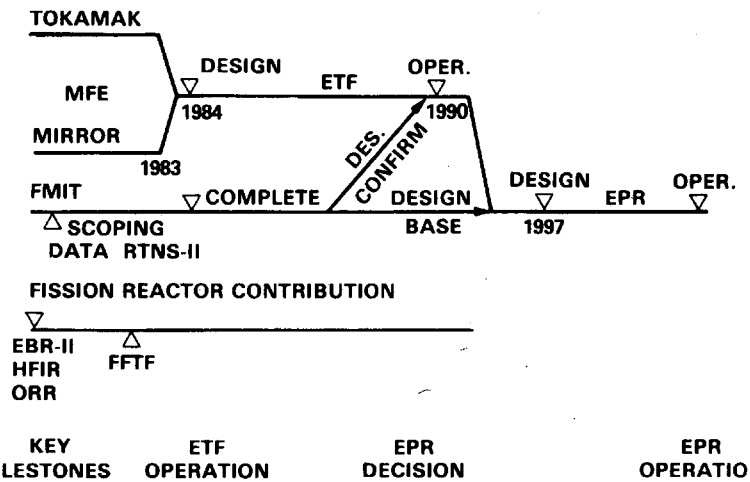

Fig. 1. Magnetic Fusion Facility Development.

ORGANIZATION OF DAFS PROGRAM

Task Group

D. G. Doran, Chairman

M. M. Cohen, DOE/OFE

L. R. Greenwood, Chairman, Subtask Group A, Dosimetry and Damage Parameters

R. H. Jones, Chairman, Subtask Group B, Fundamental Mechanical Behavior

G. R. Odette, Chairman, Subtask Group C, Correlation Methodology

W. G. Wolfer, Consultant

Program Participants

OFE programs in the three areas currently exist at:

Subtask Group A	Subtask Group B	Subtask Group C
ANL	ANL	ANL
BNL	HEDL	HEDL
HEDL	MIT	LLL
LASL	NRL	MIT
LLL	PNL	PNL
ORNL	UCSB	USCB
RI	U.Va.	U.Wisc.
	U.Wisc.	W-R&D
	W-R&D	

There is significant participation from outside the OFE programs.

Fig. 2. Organization of Damage Analysis and Fundamental Studies (DAFS) Program.

ORGANIZATION OF THE ADIP PROGRAM

Task Group

E. E. Bloom, Chairman

T. C. Reuther, DOE/OFE

R. E. Gold, Chairman, Subtask Group A, Alloy Development for Near Term Application

F. W. Wiffen, Chairman, Subtask Group B, Alloy Development for Long Term Application

J. J. Holmes, Chairman, Subtask Group C, Analysis and Evaluation

Materials of Primary Interest

Subtask Group A - Solid solution strengthened austenitic stainless steels (Path A alloys, i.e., AISI 316 and modifications thereof)

- Ferritic stainless steels (Path E alloys, e.g., HT-9)

Subtask Group B - Precipitation hardened developmental austenitic steel alloys (Path B)

- Vanadium and titanium alloys (Path C)

- Innovative materials (Path D), e.g., long-range-order alloys

Fig. 3. Organization of the Alloy Development for Irradiation Performance (ADIP) Program.

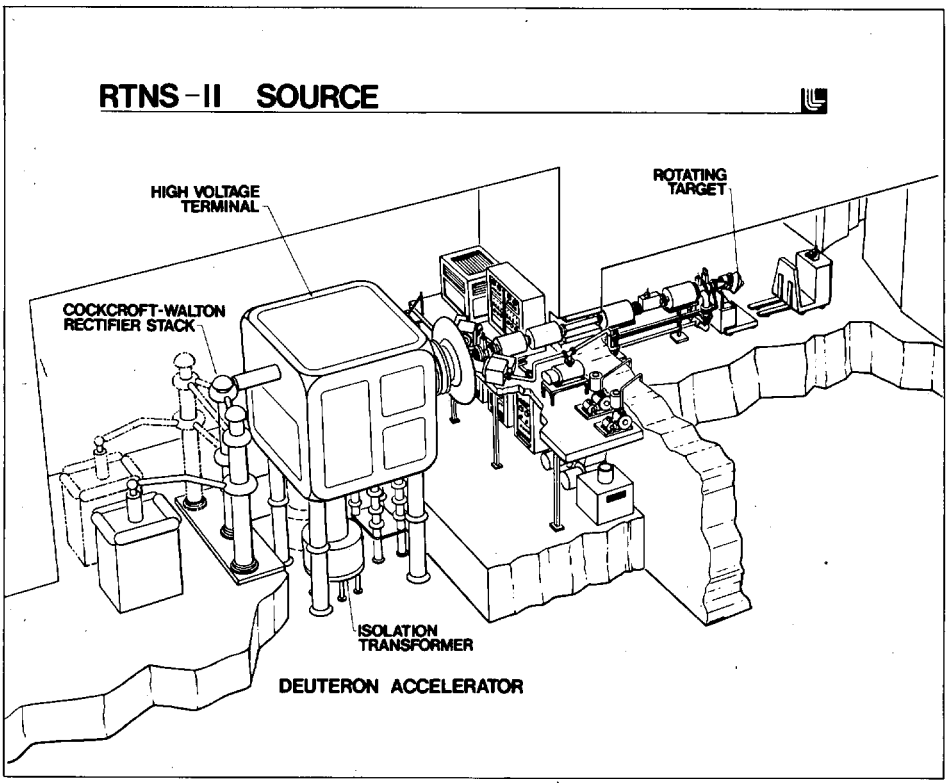

Fig. 4. Major Components of a Single Neutron Source at the RTNS-II Facility.

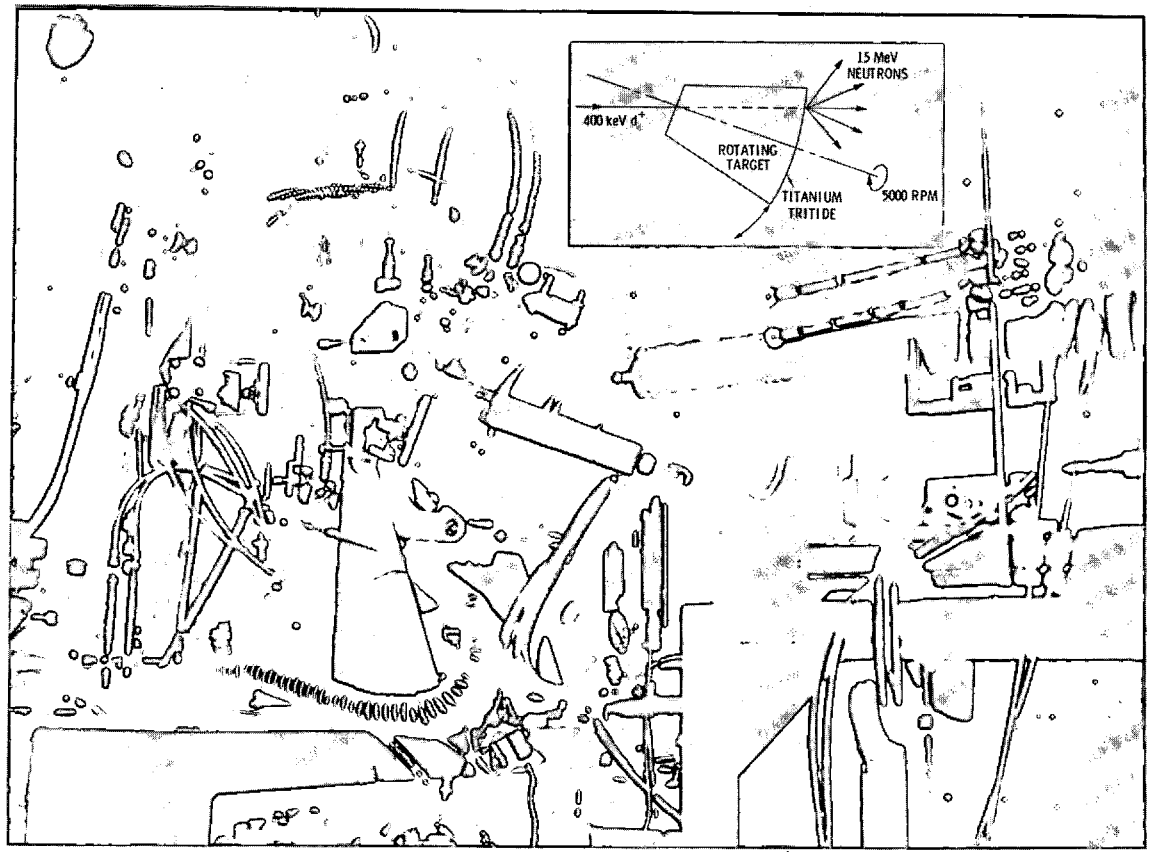

Fig. 5. Cylindrical Specimen Capsule Positioned Close to the Rotating Target at RTNS-II.

CHANNEL PATTERN FOR COOLING WATER IN TARGET

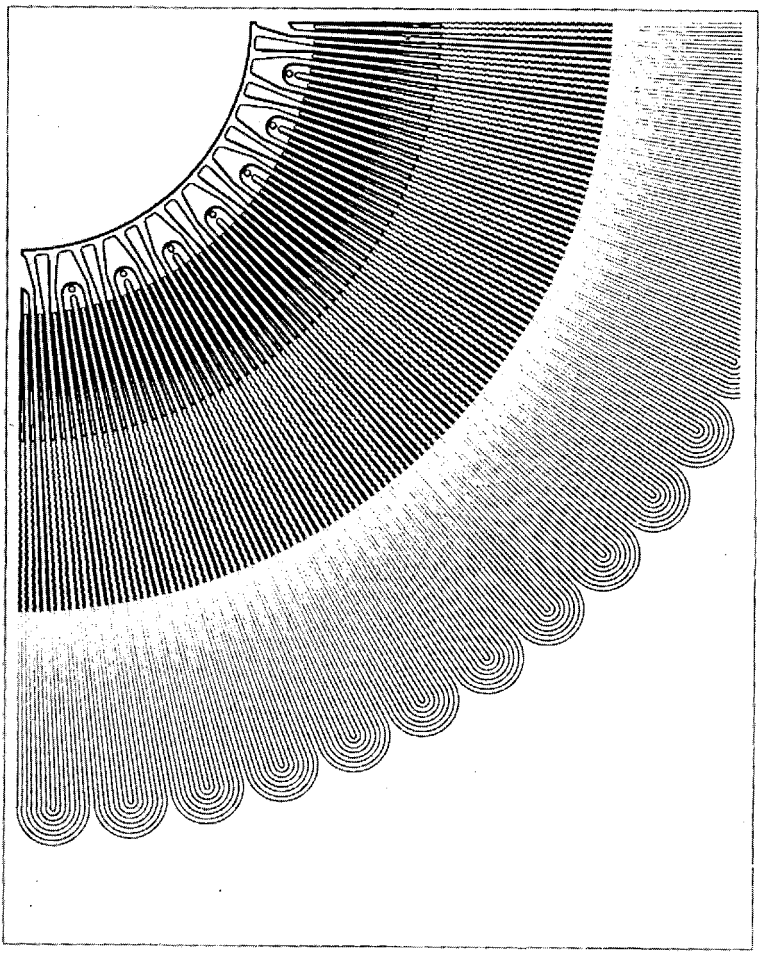

Fig. 6. A Section of the Etching Mask Used to Produce Water-Cooling Channels Within a Rotating Target. The dark lines are etched into a sheet of copper alloy, which is then covered by diffusion bonding a second sheet to the first to produce convoluted channels.

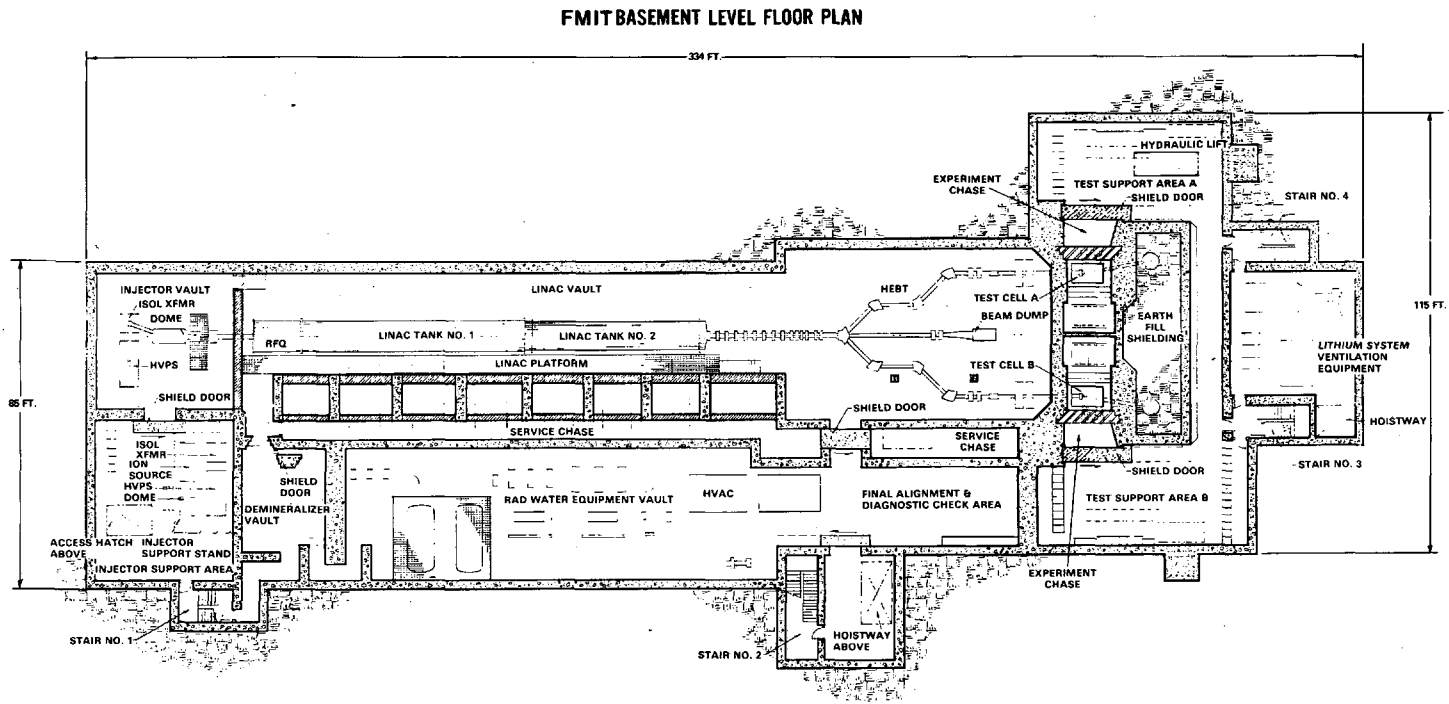

Fig. 7. Major Components of the Fusion Materials Irradiation Test (FMIT) Facility. HVPS = High Voltage Power Supply; RFQ = Radio Frequency Quadrupole; HEBT = High Energy Beam Tunnel.

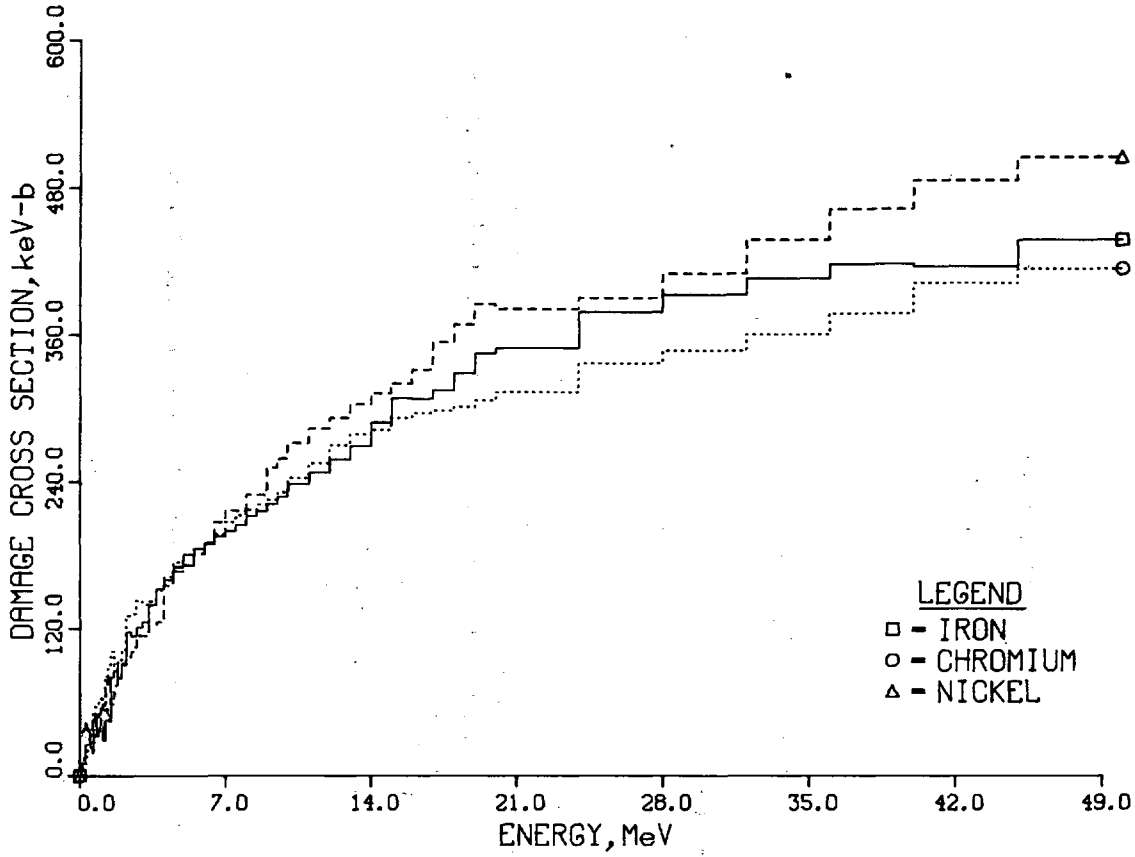

Fig. 8. Damage Energy Cross Sections for Fe, Cr, and Ni Extended to High Energies by Greenwood.

BRIEF SUMMARY OF
NUCLEAR DATA NEEDS FOR
DAMAGE CALCULATIONS

Materials

Fe, Ni, Cr, Al, Cu, W, V, Nb, Ti

Energy Range

15-35 MeV

Data Needed

Differential angular cross sections for all reactions.

Angular and energy distributions of emitted particles (especially first particle out).

Total helium cross sections.

Total hydrogen cross sections.

Note

Some work done on some materials - see text.

Fig. 9. Brief Summary of Nuclear Data Needs for Damage Calculations.

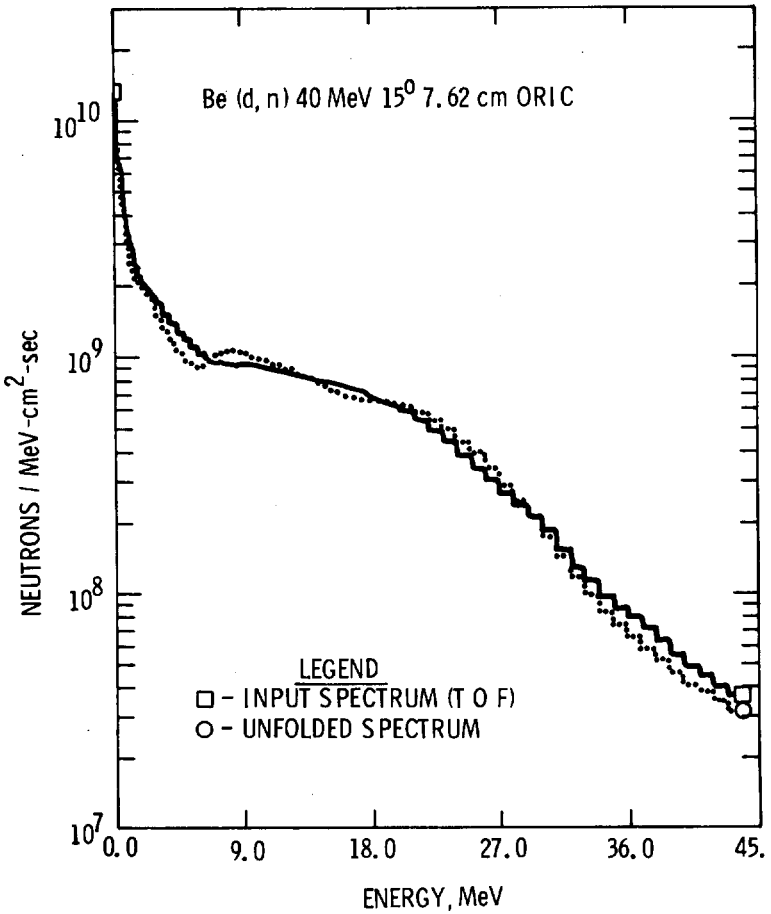

Fig.10. Comparison of a Time-of-Flight (input) Be (d,n) Spectrum with the Spectrum Adjusted Using Extrapolated Reaction Cross Sections in the SAND-II Code.

MEASUREMENTS AND EVALUATIONS OF NUCLEAR DATA TO SUPPORT EARLY DESIGN NEEDS OF THE FMIT FACILITY

D.L.Johnson, F.M.Mann, and R.E.Schenter

Hanford Engineering Development Laboratory
Richland, Washington 99352

ABSTRACT

The Fusion Material Irradiation Test (FMIT) facility is currently being designed for use in the study of neutron radiation effects in fusion reactor materials. This facility will make use of the intense source of high energy neutrons produced by a beam of 35 MeV deuterons incident upon a thick target of liquid lithium. In the forward direction, the neutron spectrum from this source peaks near 14 MeV as in a fusion device. However, the neutron energy spectrum in the FMIT facility will be broader and there will be a significant number of neutrons emitted with energies up to about 30 MeV. A small fraction will be emitted with even higher energies, up to a maximum of 50 MeV. Since ENDF/B evaluations of neutron-cross section data extend only to 20 MeV (with little data above 15 MeV) there is a great need for neutron data from 15 to 50 MeV for the FMIT facility. Furthermore, nuclear reaction cross sections induced by deuterons up to 35 MeV are a vital part of design and operation considerations, and are even less well understood than the neutron data. The time scale of the design of the FMIT facility has been so rapid that it has precluded large amounts of new nuclear data coming from outside the project. This report outlines work carried out within the FMIT project to supply the most immediate nuclear data needs. Nuclear data needs for remaining design considerations and for long term operational uses will be discussed.

INTRODUCTION

The Fusion Materials Irradiation Test (FMIT) facility is being designed for construction at the Hanford Engineering Development Laboratory (HEDL) with accelerator design by Los Alamos Scientific Laboratory (LASL). Figure 1 shows a schematic diagram of the general layout of the facility. Deuterons are accelerated in a linear accelerator to an energy of 35 MeV. The design specifies a beam current of 100 mA on target. The beam will be transported to one or the other of two targets via a series of bending and focusing magnets as shown.

Those familiar with acceleration of deuterons know that a major design consideration is the enormous quantities of prompt neutron and gamma radiation, and also residual gamma radiation, that will be associated with even tiny fractional losses of the deuteron beam which will occur during acceleration and transport to the target.

The beam will be normally incident upon a target of liquid lithium ($\sim$ 2 cm thick) within which the deuterons are stopped (range $\sim$ 1.5 cm), the neutrons are produced, and the deposited heat is carried away. A stainless steel plate, (about 0.16 cm thick) backs the lithium and separates it from the test cell where neutron irradiation experiments will be conducted. In the vicinity of the target and lithium systems, major design considerations are associated with the huge yield of very energetic neutrons from the Li(d,xn) reaction. Also important is deuteron induced activation of the liquid target material.

The major objective of the work described here was to provide data for immediate design needs. There is considerable overlap between design needs and needs for operation and analysis of irradiation experiments. However, because of the short time scale we have gone no further than was absolutely required for design purposes.

A preliminary design (Title I) for the FMIT facility was completed in late 1979 and cost estimates were based on that design. Since final design (Title II) is now being done and will be complete in early 1981, relatively little new data can be incorporated beyond what is described here. Data associated with operation and interpretation of irradiation experiments is not required as urgently, however, much of that data should be available before initial operation of the facility, which is currently scheduled for late 1984.

There are three general categories of nuclear data that will be discussed in the body of this report. They are (1) sources of prompt neutron, gamma ray, and charged particle radiation induced by deuterons; (2) neutron and gamma ray transport and radiation heating data; and (3) neutron and deuteron induced activation data. Particular data that have been emphasized will be described. Plans for obtaining data for remaining design needs will be discussed as well as data needs for operation and interpretation of irradiation experiments.

Sources of Prompt Radiation Induced by Deuterons

A. Deuterons on Lithium

Neutron source data were required to (1) allow maximizing the volume within the test cell having a neutron flux of 10^{15}n/cm^2-s or greater resulting from a 100mA beam of 35 MeV deuterons incident on a thick target of lithium, and (2) provide the source for use in evaluations of shielding requirements, radiation heating, activation, effects on instrumentation and dosimeters and estimates of radiation damage in irradiation experiments and facility components in the vicinity of the test cell.

The data required for evaluating the high neutron flux region ($\sim 10^{15}$n/cm^2-s) in the test cell are the double differential neutron production cross sections $(d\sigma(E_d)/d\Omega dE_n)$ as a function of deuteron energy up to 35 MeV. These data are needed (rather than thick target data) to take explicit account of the spatial distribution of source neutrons for distances very close to the target. The spatial distribution is about 3 cm wide because of the need to spread the beam to reduce lithium flow requirements. Such differential data are not directly available either from experiment or theory. The approach that has been taken is to obtain the needed differential data by fitting a simple model of the microscopic differential cross section to integral data obtained from measurements with thick lithium targets (in which an integral over deuteron energy is obtained). This approach is described more fully in references [1] and [2].

To partially meet the need for experimental data at the FMIT energy, measurements were conducted at the University of California at Davis of the neutron yield and spectra from 35 MeV deuterons on a 2 cm thick target of natural lithium. The spectra covered a range of emission angles from 0° to 150°and an energy range from $\sim$ 1 MeV to 50 MeV, the maximum kinematically allowed energy. Additional measurements were made to study the very low energy portion of the spectra ($E_n < 1$ MeV) and also with a target enriched in the isotope ^{6}Li. The measurements and results are described in more detail in reference[3]. Figure 2 shows the spectra as a function of emission angle as obtained from these measurements.

The double differential neutron production cross sections were then obtained as a function of deuteron energy by fitting to the measurements described above and in reference [3] for 35 MeV deuterons and also to data obtained at other energies from deuterons on targets of thick lithium. The results of this procedure and calculations of the neutron flux-spectra at various positions (unperturbed by the presence of test samples) within the FMIT test cell, based on this model, are described in reference [1] (earlier versions are described in references [2] and [4].

Measurements of the prompt gamma ray yields and spectra were made simultaneously with the neutron measurements described above and in reference [3]. The interest in these data was potential gamma heating in the FMIT test samples. Only preliminary analysis

has been performed so far, largely because it was observed that the gamma production consisted of very weak production of low energy gamma rays. The dominant gamma ray is $\sim$ 0.5 MeV and is emitted approximately isotropically. The most likely candidates for this are the .478 MeV gamma ray from deuteron inelastic scattering to the first excited state of ^{7}Li and possibly the 0.428 MeV decay of the first excited state of ^{7}Be formed by both the ^{7}Li(d,2n) and ^{6}Li(d,n) reactions. Both of the candidate gamma decays are isotropic.

Calculations of the proton emission from deuterons on lithium have been made with the assumption that it is identical to the neutron emission except for the high energy shoulder portion of the spectrum (neutrons $\gtrsim$ 30MeV in Figure 2), which, for protons, is limited to 40MeV. The concern was that a large flux of protons could significantly increase the rate of heating and damage to the stainless steel backing plate or even penetrate to the test samples. Protons having energies up to 40 MeV can be produced from deuterons on lithium (the ^{6}Li(d,p) reaction has the highest positive Q- value of about 5 MeV). Fortunately the protons are rapidly degraded in the lithium and a flux only about 1% or less of the neutron flux is expected to hit the backing plate, if one assumes the proton yield is identical to the neutron yield. Hence no significant increase in heating or damage is expected from the proton flux. Furthermore, the maximum proton energy emerging from a 2 cm lithium target will be only about 24 MeV which is insufficient to penetrate the backing plate.

B. Deuterons on Accelerator and Beam Transport System Materials

Sources of prompt radiation are required as input to calculations to determine (1) shielding requirements when the beam is on, and (2) neutron and gamma radiation fields which effect beam diagnostic and control instrumentation when the beam is on, (3) radiation damage to accelerator and beam transport components, (4) neutron activation of the accelerator, beam transport system, and surrounding materials, and (5) radiation induced gas production which affects the accelerator vacuum.

Prompt neutron and gamma production will be directly dependent upon the small losses of the beam which will occur along the linear accelerator during acceleration and throughout the system used to transport it to the target. After beam tuneup, it is expected that the losses will be greatest at the low energy end and will diminish the farther the beam travels toward the high energy end. Neutron flux levels are expected to be much higher at the high energy end than at the low energy end, however, despite the reduction in losses as the beam is transported through the machine. This is because neutron production rates increase dramatically with increasing deuteron energy and they are emitted predominantly in forward directions.

No measurements of (d,xn) yields and spectra from accelerator materials have been done for the FMIT project and very little eval-

uation has been done. This is primarily because there is some data already in the open literature, and because the trends in the cross sections and spectra as a function of deuteron energy and target mass are fairly well understood and reasonably smooth for the energies of importance. For example, the Serber model of deuteron breakup reactions [5] can be used here to provide a method for interpolating and/or extrapolating experimental data. Currently, the primary source of (d,xn) yields and spectra that is being used for FMIT design is the experimental data of Meulders et al,[6] which is for deuterons of 16, 33, and 50 MeV incident on thick targets of Be, C, Cu, Mo, Ta, and Au. The choice of these targets is fortunate since the linear accelerator will have large quantities of copper. Furthermore, thin pieces of gold and tantalum are under consideration as materials to prevent the beam from hitting copper or for beam collimation. This is because the (d,xn) yields from gold and tantalum are smaller than lighter mass materials such as copper and their activation may be acceptably low. The current feeling is that for steady state operation, the uncertainty in the neutron sources due to deuteron beam losses is dominated by uncertainties in predicting the beam losses rather than by uncertainties in (d,xn) data. In situations where the beam loss is better defined, (e.g. while tuning a known beam current into a collimator or beam stop), then more accurate (d,xn) data may be desirable.

There is a great need for (d,xγ) yields and spectra for materials in the FMIT accelerator and beam transport system. The main application is to define prompt gamma radiation fields that will effect instrumentation used for beam diagnostics and control. In particular, current plans are to observe the gamma radiation produced by deuteron loss during accelerator tuning (e.g. on a collimator) in order to minimize beam loss and maximize transmission. It is believed that observation of prompt gamma radiation will be a much better indication of local beam losses than observation of neutrons. Unfortunately, there is very little (d,xγ) data. In fact we are unaware of any experimental data in the literature which could be applied directly to FMIT needs as (d,xn) data can be. No measurements or calculations of (d,xγ) data have been done in support of the FMIT project to date, however plans are being developed to fill this important need.

There may also be a need for data on production of gases within the FMIT accelerator and vacuum system. For example, nuclear reactions such as (d,α) and (n,α) on materials within the FMIT vacuum system could generate quantities of helium and other gases that would be difficult to pump with conventional vacuum pumping systems. Scoping calculations have not yet been made to evaluate this question.

Neutron and Gamma Ray Transport and Radiation Heating Data

Data for calculations of neutron and gamma transport and radiation heating are required for the same reasons as listed in

the previous section, which described sources of prompt radiation induced by deuterons.

The types of data include cross sections for differential elastic scattering, nonelastic scattering, neutron emission spectra, charged particle emission spectra, gamma ray emission spectra, and KERMA factors. Neutron total cross sections are of use to aid in evaluation of the data above.

Data were needed for energies up to 50 MeV because, as shown in Figure 2, the spectra from the Li(d,xn) reaction extend that high. Furthermore, although the fraction of neutrons emitted in the Li(d,xn) spectra with energies greater than $\sim$ 30 MeV is only about 1% of the total, the transport properties of these highest energy neutrons are extremely important because they dominate the penetration of thick shields made of ordinary and high density concrete. This is explained in more detail by Carter and Morford in reference [7].

A major effort has been expended by the FMIT project to minimize the requirements and hence the cost for shielding, particularly near the test cell where the source is largest, the shielding is thickest and uncertainties due to neutron transport data are largest.

Initial calculations for shielding, radiation heating, and activation, were made with a combination of transport data primarily from the following sources: (1) ENDF/B-IV data for neutron energies less than 15 MeV, (2) Optical model calculations of elastic scatterings for E_n>15 MeV, (3) Nonelastic cross sections and neutron emission spectra and distributions from evaluations by Wilson [8] and Alsmiller and Barish [9] for E_n>15-20 MeV. The details of the data used and its application are given in ref. [7].

Most of the transport data used for neutron energies greater than 15 MeV were based on some nuclear model calculation with very little experimental data available for comparison and establishment of uncertainties. Data on neutron total cross sections were the notable exception to this generalization. Unfortunately, it is the components of the total cross section (elastic and nonelastic cross sections) which are actually used and the division between the two is often uncertain. It was determined that uncertainties in transport data for neutrons on the constituents of ordinary and high density concrete were large enough that significant cost increases would result from designing conservatively to account for such uncertainties.

A collaborative program was initiated with the neutron physics group at the University of California at Davis to measure some of the most important cross sections for concrete in the energy region of 20 - 50 MeV. The primary goal was to measure nonelastic cross sections at a few energies for the important shielding materials C, O, Ca, and Fe. In addition, the removal cross section was desired for "back of the envelope" calculations of neutron penetration in thick shields. This cross section is the sum of the nonelastic cross section plus the fraction of the elastic scattering cross section which leads to scattering to angles greater than 25°

(see ref. [7] for further description). An accurate knowledge of the neutron total cross section was needed at each energy that the nonelastic cross section was measured. For targets of Ca and Fe it was necessary to measure the total cross sections in order to determine them with sufficient accuracy. The nonelastic cross sections were measured at energies of about 40 and 50 MeV and the total cross sections were measured at about 35, 40, and 50 MeV. The experiments and results are reported in another contribution to this symposium [10].

The data obtained from the measurements described above were then used to aid in updating the evaluation of the total, nonelastic, elastic, and removal cross sections over the energy range of 20 - 60 MeV for neutrons on C, O, Si, Ca, and Fe. Additional experimental data, which were obtained from the CSISRS file at Brookhaven National Laboratory, were also used in the evaluation. Other new total cross section data by ORNL [11] were only in preliminary form at the time of this evaluation.

An example of the updated evaluation is shown in Figure 3 of the nonelastic cross section for neutrons on iron. The dashed curve is the cross section used in initial Monte Carlo calculations and corresponds to the evaluation of Wilson [8]. The solid curve is the new evaluation which is the result of a generalized least squares fit to the experimental data and the a priori data using the code FERRET [12]. Note that the previous evaluation is outside the error bars of the new data and is about 13% higher than the new evaluation. Therefore, use of the older evaluated data for the iron in high density concrete would have lead to wall thicknesses that would be too thin to reduce the dose sufficiently. Further updates of these data are planned if time is available, to take into account such things as optical model systematics, proton data, and new neutron data. A recent evaluation by LASL [13] for neutrons up to 40 MeV on iron may be sufficient for current needs.

As noted by Carter and Morford in reference [7], calculations of heat deposition are sensitive to neutron transport, neutron KERMA factors, and gamma production cross sections. The shortcomings and improvements in KERMA factors have been noted in ref. [7 & 14]. Data on (n,xγ) reactions for many materials are reasonably well understood below 20 MeV. Recent theoretical evaluations have provided some (n,xγ) data for higher energies (see ref. [13]). Experimental data is extremely sparce for energies above 20 MeV.

One area where an integral measurement has been employed to understand a design question is related to heat deposition in the FMIT test cell walls. An early design of the walls had thick iron surrounded by concrete with gas cooling channels passing through. A major concern was whether the cooling design was adequate to remove the heat deposited in the concrete. Transport calculations indicate that the source spectra as in Figure 2 is degraded in thick iron (∿ 30 cm (12") or more) such that most of the neutrons emerging have energies less than 1 MeV. The transport data, KERMA factors, and (n,xγ) data for such low energy

neutrons are fairly well understood for the constituents of concrete [14]. Therefore, a primary uncertainty that remains in calculations of heating in test cell walls is in the transport of the high energy source neutrons through the thick iron.

An experiment was conducted at the University of California at Davis to measure the transmission of FMIT-like neutrons through thick iron. The neutrons were produced by a beam of 35 MeV deuterons incident upon a lithium target that was 2.5 cm diameter x 2 cm thick. The same target was used for measurements of the Li(d,xn) data shown in Figure 2,and the evaluation in ref. [1] has provided source data suitable for transport calculations. The source was placed approximately at the center of a nearly cubical block of solid iron that was about 60 cm (2 feet) on a side.

Neutron spectra were measured with detectors placed about 10 cm (4 in.) outside the block at 0° and 90° with respect to the beam direction. Proton recoil spectrometers were used to observe the portion of each spectra from $\sim$ 10 KeV to $\sim$ 1.5 MeV, where most of the neutrons were expected. An NE213 liquid scintillator was used to observe the high energy portion of the spectra which overlapped with the proton recoil spectral data. Additional data on gamma dose fields were obtained with thermoluminescent dosimeters (TLD's). Also a few solid state track recorders (SSTR's) and nuclear emulsions were exposed to observe the neutron spectra.

This experiment is similar to measurements and calculations of the transmission of 14 MeV neutrons through a 76 cm diameter sphere of iron as described in reference [15]. In that work, discrepancies between experiment and calculation in the low energy portion of the leakage neutron spectrum were found. When the data from the present experiment have been analyzed, they will be compared to predictions by the same code used for calculations of heat depositions. Adjustments in such calculations may then be necessary, depending upon the magnitude of a possible discrepancy.

Neutron and Deuteron Induced Activation Data

Activation data is needed to establish gamma radiation levels: (1) When the beam is on in places where such levels are dominated by decay radiation rather than prompt radiation, and (2) During shutdown after operation.

A. Activation Data for Radiation Levels During Operation

There will be locations within the FMIT facility where access is limited or excluded during operation because of high levels of decay radiation rather than prompt radiation. Short-lived nuclides are of most importance and both deuteron and neutron-induced activation are significant.

Examples where activation data plays a role are as follow:

(1) Rooms containing lithium piping and nearby spaces will experience large gamma radiation fields due to decay of short-lived isotopes produced in the liquid lithium primarily by deuteron induced reactions in the lithium and its contaminants. An example would be $^{23}Mg(T_{\frac{1}{2}} \sim 11$ s) produced by a reaction on a contaminant ($^{23}Na(d,2n)^{23}Mg$).

(2) Rooms containing cooling water piped from the accelerator and beam transport system will have large decay gamma fields due to short-lived radioisotopes produced by neutron-induced activation of the water and its contaminants. For example, a large contributor to this radiation is due to decay of ^{16}N, which has a half life of $\sim$7 sec. and emits very penetrating gamma rays of $\sim$ 6 MeV. It is produced via the $^{16}O(n,p)^{16}N$ reaction.

(3) Spaces containing an atmosphere which has been exposed to the neutron flux in either the accelerator tunnel (air) or test cell (nitrogen).

B. Activation Data for Radiation Levels after Shutdown

A major goal of the FMIT project is to minimize maintenance time in order to maximize availability of the facility for irradiation exposures. An availability of 80% is desired but will be challenging to meet because of the high activation levels that can be expected from both deuteron and neutron induced reactions. Current plans are for remote maintenance of the components in the test cell and hands-on maintenance, wherever practical, elsewhere. Here the problem is long-lived radionuclides.

Examples of cases where activation data are important are as follow:

(1) Maintenance of the lithium system where radionuclides such as ^{7}Be (from $^{7}Li(d,2n)$ and $^{6}Li(d,n)$ reactions) and ^{22}Na (from the contaminant $^{23}Na(d,t)$ reaction) will remain on the walls of the piping even after draining. Reference [16] describes evaluation of shielding requirements for maintenance of the lithium system.

(2) Maintenance of the accelerator and beam transport system where large quantities of radioactive nuclides will be produced directly from deuteron induced activation and also from activation by the secondary neutrons that are prolifically produced whenever a high energy deuteron hits any material. It is desired to minimize the radiation dose that results from the sum of both deuteron and neutron induced contributions to activation levels for a particular location in the facility. This would tend to discourage the use of some materials which might otherwise be useful. An example is the use of graphite (carbon) as a beam collimator. Al-

though the deuteron induced activation of graphite is known to be very low, the deuteron induced neutron production from such a light material is high compared to heavier materials. Hence, the neutron induced activation of components surrounding the graphite could be prohibitively high.

(3) Maintenance in spaces containing an atmosphere which has been exposed to the neutron flux in either the accelerator tunnel (air) or the test cell (nitrogen) and release of this atmosphere to outside of containment. A few reactions such as $^{14}N(n,nT\alpha)^{7}Be$, $^{14}N(n,p)^{14}C$, and $^{40}Ar(n,2n)^{39}Ar$ lead to very long-lived products and have cross sections large enough for concern.

C. Deuteron Induced Activation Data

In general there is less data available on deuteron activation at the high energies of interest than on neutron activation. On the other hand, only those materials directly exposed to deuterons can be activated, which considerably limits the number of materials that must be considered. Those materials are (1) the lithium target plus contaminants (Na, Ca, K, etc.) and corrosion products (Fe, Ni, Cr, etc.) that may be in it, and (2) the materials near the beam centerline in the accelerator and beam transport system. The linear accelerator has large quantities of copper but consideration is being given to coating those parts exposed to deuterons with a material such as gold or tantalum in order to reduce activation. The high energy beam transport system has not yet been finalized, however materials that have been considered for the beam tube are stainless steel and aluminum. Furthermore, beam scrapers or collimators made from materials such as carbon, tantalum or gold are under consideration.

One feature of activation in the FMIT facility that may not be widely appreciated is that the quantity of deuteron induced activation can far exceed that produced by the secondary neutrons that are associated with the incident deuterons. For example, with 35 MeV deuterons on a thick lithium target, only about 5 neutrons are emitted for every 100 incident deuterons. There are even fewer neutrons emitted when deuterons hit heavier mass targets. Hence the deuterons have a much greater chance for inducing activation reactions. The preponderance of deuteron induced activation would not necessarily remain in a situation where the neutron activation cross sections are much larger (e.g. for thermalized neutrons), or where the quantity of material that neutrons are exposed to is very much larger than deuterons are exposed to. However, that is not believed to be the case near the accelerator or beam transport system. Activation from the secondary neutrons will of course be more spatially diffuse than from the deuteron induced activation and will dominate radiation dose levels in some locations.

There was some data in the literature on cross sections for deuteron induced activation that lead to medium and long-lived

products. Very little data is available on production of very short-lived isotopes that are of interest for the lithium system when the beam is on.

The initial design of the shielding around the lithium system is based upon rough estimates of upper limits of activation cross sections plus a measurement of the ^{7}Be production. This was necessary because of the large number of reactions and limited experimental data and time. The differential cross section for each unknown deuteron induced activation reaction was assumed to be a constant 0.5 barns for deuteron energies above the Coulomb barrier or threshold energy, which ever is greater. Thick target yields were then evaluated using such cross sections for each reaction that could occur with 35 MeV deuterons on a target of thick lithium plus estimated trace contaminants. Measured data for production of ^{7}Be (the most abundantly produced radionuclide) were used instead of an estimate. Furthermore, comparisons were made to some data available in the literature to verify that under-estimates of the activation were not being made. This procedure is expected to result in a very conservative design since such activation cross sections are not generally as large as 0.5 barns.

Initial scoping evaluation of deuteron induced activation of accelerator and beam transport materials was done using a simple extension of the THRESH code (ref. [17]) which is used for estimation of neutron induced activation cross sections. Comparisons were made with available experimental activation data such as given by Fulmer and Williams for deuterons up to 40 MeV on copper [18]. The comparison indicated that the model calculations were only accurate enough for order of magnitude scoping studies. Figure 4 shows the dose as a function of decay time calculated from the estimated activation cross sections. The relative doses calculated for activation of C, Al, Fe, Cu, and Ta tend to agree roughly with previous dose calculations [19] for the same elements which were based upon experimental activation data.

A program to measure deuteron induced activation was begun for the following reasons: (1) There were no reliable data available for some elements of known importance for energies of interest. For example, the production of ^{7}Be by deuterons on lithium had not been measured up to 35 MeV; (2) Previous experiments may have missed some weakly produced radionuclides having long half lives which could be important for dose considerations because of their buildup in long irradiations. For example, we are not aware of previous observation of the long lived isotopes ^{58}Co, ^{60}Co, and ^{59}Fe produced by deuterons on copper, however, for 35 MeV deuterons they are energetically allowed via such reactions as $^{63}Cu(d,\alpha T)^{58}Co$, $^{63}Cu(d,\alpha p)^{60}Co$, and $^{65}Cu(d,2\alpha)^{59}Fe$; (3) There is a need to find materials having very low deuteron activation doses for special applications such as for beam scrapers or collimators, beam tube liners, and low activation coatings of accelerator parts that are exposed to deuterons.

Measurements were conducted on stacked foil targets using

a beam of 35 MeV deuterons from the cyclotron at the University of California at Davis. Targets included Li, C, Al, Fe, Ni, Cu, Mo, Ta, Au and Pb. Other measurements are planned on targets of Na, K, Ca, Cr, and Mn and possibly other materials estimated to have low activity for special applications.

An example of preliminary results from this program is shown in Figure 5 which illustrates the thick target activation of copper as a function of deuteron energy. Note that the long-lived isotopes ^{58}Co, ^{60}Co, and ^{59}Fe were indeed observed at 35 MeV with production rates that are large enough to be significant for dose considerations.

D. Neutron Induced Activation Data

The major need for neutron activation cross sections is for energies above 20 MeV. There are extensive sets of neutron activation cross sections up to 20 MeV in ENDF/B and other libraries, although not all activation cross sections that might be important are included.

Scoping studies of neutron induced activation have been done for such varied materials as air, water, concrete, iron, copper, and aluminum in spectra that have significant portions of the spectra above 20 MeV. This work is described more fully in ref. [7] and will only be outlined here.

First, the most important reactions are selected by calculating the dose for a particular neutron flux-spectrum exposure, irradiation time and decay time using estimated upper limits to the activation cross sections as a function of energy. Then improved dose calculations are made using cross sections estimated by the THRESH code (ref. [17]) which was extended to 40 MeV. These cross sections were joined at 20 MeV to ENDF/B-V activation cross sections when they were available. Next, improved calculations of a few selected reaction cross sections have been made using the code HAUSER*5 [20] which treats the reactions in the formalism of Hauser-Feshbach statistical reaction theory with pre-equilibrium emission.

Some neutron induced activation reactions are not expected to be reliably calculated by any of the methods described above and they have not been measured. An example is the production of ^{7}Be from neutrons on ^{14}N. Nitrogen will be in the test cell and accelerator tunnel. A likely path for this reaction involves the following cascade, $^{14}N(n,nT\alpha)^{7}Be$ which has a threshold of $\sim$ 32MeV.

Plans are being considered for integral measurements of such neutron activation cross sections in spectra that will be prototypic of the FMIT facility. Note that measurements in Be(d,xn) spectra with 35 MeV deuterons would not be suitable for the ^{14}N reaction described above, since the d,Be spectrum extends only to $\sim$ 40 MeV and is not prototypic of the Li(d,xn) spectra which extends to 50 MeV. A lithium target, which will be cooled to allow high deuteron beam currents and corresponding high neutron flux levels is being designed for possible use in activation measure-

ments at the University of California at Davis.

Remaining Needs and Plans

There is much nuclear data that is still needed for completion of design. Plans are being developed within the FMIT project to provide for immediate needs as much as possible within the time limits as stated earlier. Primary areas where work is being considered are:

(1) Measurements and evaluation of (d,xγ) and (d,xn) data for accelerator and beam transport materials.

(2) Further calculations and possible integral measurements of neutron activation cross sections.

(3) Completion of measurements and evaluations of deuteron induced activation cross sections.

(4) Updating evaluation of neutron transport and heating data for FMIT structural materials.

(5) Providing data for evaluation of neutron radiation damage for key FMIT structural components.

(6) Providing data on deuteron and neutron induced production of gases in materials exposed to the FMIT vacuum system.

For operation of the FMIT facility and interpretation of irradiation experiments, nuclear data needs are largely related to neutron dosimetry and damage prediction in irradiation experiments. Detailed discussions of these needs are given in other contributions to this conference [21 & 22]. Important needs include the following:

(1) Neutron activation cross sections for dosimetry applications.

(2) Neutron transport data for prediction of neutron flux-spectra in experimental samples.

(3) Neutron data for prediction of displacement damage, gas production, and transmutation in experimental samples.

(4) Neutron KERMA factors and gamma production data for prediction of radiation heating in experimental samples.

A more complete list of needs is given in reference [23].

Acknowledgements

This work is funded by U.S.D.O.E. under contract DE-AC14-76FF02170.

We would like to acknowledge the major contributions to this effort which have been made by the following people: F.P.Brady, J.W.Watson, J.L.Ullmann, J.L.Romero, C.M.Castaneda, C.I. Zanelli, M.L.Johnson, W.G.Wyckoff, G.L.Woodruff, F.Schmittroth, R.J.Morford,

L.L.Carter, A.D.Wilcox, and L.G.McWethy.

REFERENCES

1. F. M. Mann and F. Schmittroth, "Neutron Environment in d+Li Facilities," proceedings of this symposium (also HEDL-SA-2123).

2. D. L. Johnson et al, "Measurements and Calculations of Neutron Spectra from 35 MeV Deuterons on Thick Lithium for the FMIT Facility," Jour. of Nucl. Mat'ls. 85 & 86 (1979) 467.

3. D. L. Johnson et al, "Thick Target Neutron Yields and Spectra from the Li(d,xn) Reaction at 35 MeV," proceedings of this symposium (also HEDL-SA-2141).
D.L.Johnson et al, "Measurements of Neutron Spectra from 35 MeV Deuterons for the FMIT Facility," proceedings of the International Conference on Nuclear Cross Sections for Technology, Knoxville,TN., Oct. 22-26, 1979 (also HEDL-SA-1905).

4. J. O. Schiffgens, et al., "Spatial Variations of Damage Parameters in FMIT and Their Implications," Jour. of Nucl. Mat'ls 85 & 86 (1979) 491.

5. R. Serber, Physical Review 72 (1947) 1008.

6. J. P. Meulders, et al., "Fast Neutron Yields and Spectra from Targets of Varying Atomic Number Bombarded by Deuterons from 16 to 50 MeV," Phys. Med. Biol. 20 (1975) 235.

7. L. L. Carter and R. J. Morford, "Nuclear Data Relevant to Shield Design of FMIT Facility," proceedings of this symposium.

8. W. B. Wilson, "Nuclear Data Development and Shield Design for Neutrons Below 60 MeV," LA-7159-T Los Alamos Scientific Laboratory, Los Alamos, NM, Feb. 1978.

9. R. G. Alsmiller, Jr., and J. Barish, "Neutron-Photon Multigroup Cross Sections for Neutron Energies < 60-MeV," Nuclear Science and Engineering 69, 378-388 (1979) (also ORNL/TM-6486 Aug. 1978).
R. G. Alsmiller, Jr., and J. Barish, "NCDATA-Nuclear Collision Data for Nucleon-Nucleus Collisions in the Energy Range 25 to 400MeV," ORNL-4220, Oak Ridge, TN, 1968.

10. C. I. Zanelli, F. P. Brady, J. L. Romero, C. M. Castaneda, M. L. Johnson, G. A. Needham, J. L. Ullmann, P. P. Urone, D. L. Johnson, "Measurements of Neutron Total and Nonelastic Cross Sections for C, O, Ca, and Fe at UC Davis," proceedings of this symposium.

11. D. C. Larson, J. A. Harvey and N. W. Hill, "Transmission Measurements up to 50 MeV for FMIT Design," proceedings of this symposium.

12. F. Schmittroth, "FERRET Data Analysis Code," HEDL-TME-79-40, Hanford Engineering Development Laboratory, Sept. 1979.

13. E. D. Arthur and P. G. Young, "Evaluation of Neutron Cross Sections to 40 MeV for ^{54,56}Fe," proceedings of this symposium.

14. R. E. MacFarlane, "Energy Balances of ENDF/B-V," Trans. Am. Nuclear Society, 33, 681 (1979).

15. N. E. Hertel, R. H. Johnson, J. J. Dorning, and B. W. Wehring, "Measurements and Analyses of Neutron Transport Through Iron," proceedings of the International Conference on Nuclear Cross Sections for Technology, Knoxville, TN, Oct. 22-26, 1979.

16. S. T. Huang, A. M. Shapiro, W. C. Miller, and J. B. Lee, "Shielding Consideration for a Deuteron Activated Liquid Lithium System," proceedings of the 8th Symposium on Engineering Problems of Fusion Research, San Francisco, CA, Nov. 13-16, 1979 (also HEDL-SA-1904).

17. S. Pearlstein, "Neutron Induced Reactions in Medium Mass Nuclei," Journal of Nuclear Energy, 27, 81-99 (1973). Updated by Proceedings of the Conference on Nuclear Cross Sections and Technology, Washington DC (1975), NBS special publication number 425, page 324 (1975).

18. C. B. Fulmer and I. R. Williams, "Excitation Functions for Radioactive Nuclides Produced by Deuteron Induced Reactions in Copper," Nuclear Physics A155(1970) 40.

19. C. B. Fulmer and G. Kindred, "Calculated Residual Radiation Levels for Some Elements Used in Cyclotron Structures," ORNL-TM-2834, Oak Ridge National Laboratory, Oak Ridge, TN. (Aug. 1970).

20. F. M. Mann, "HAUSER*5, A Computer Code to Calculate Nuclear Cross Sections," HEDL-TME-78-83 (1979).

21. R. Gold, W. N. McElroy, E. P. Lippincott, D. L. Oberg, J. H. Roberts, F. H. Ruddy, and F. M. Mann, "Cross Sections Required for FMIT Dosimetry," proceedings of this symposium.

22. D. G. Doran, "Fusion Materials High Energy Neutron Studies--A Status Report," proceedings of this symposium.

23. R. E. Schenter, F. M. Mann, and D. L. Johnson, "Nuclear Data Needs for FMIT," proceedings of the International Conference on Nuclear Cross Sections for Technology, Knoxville, TN., Oct. 22-26, 1979.

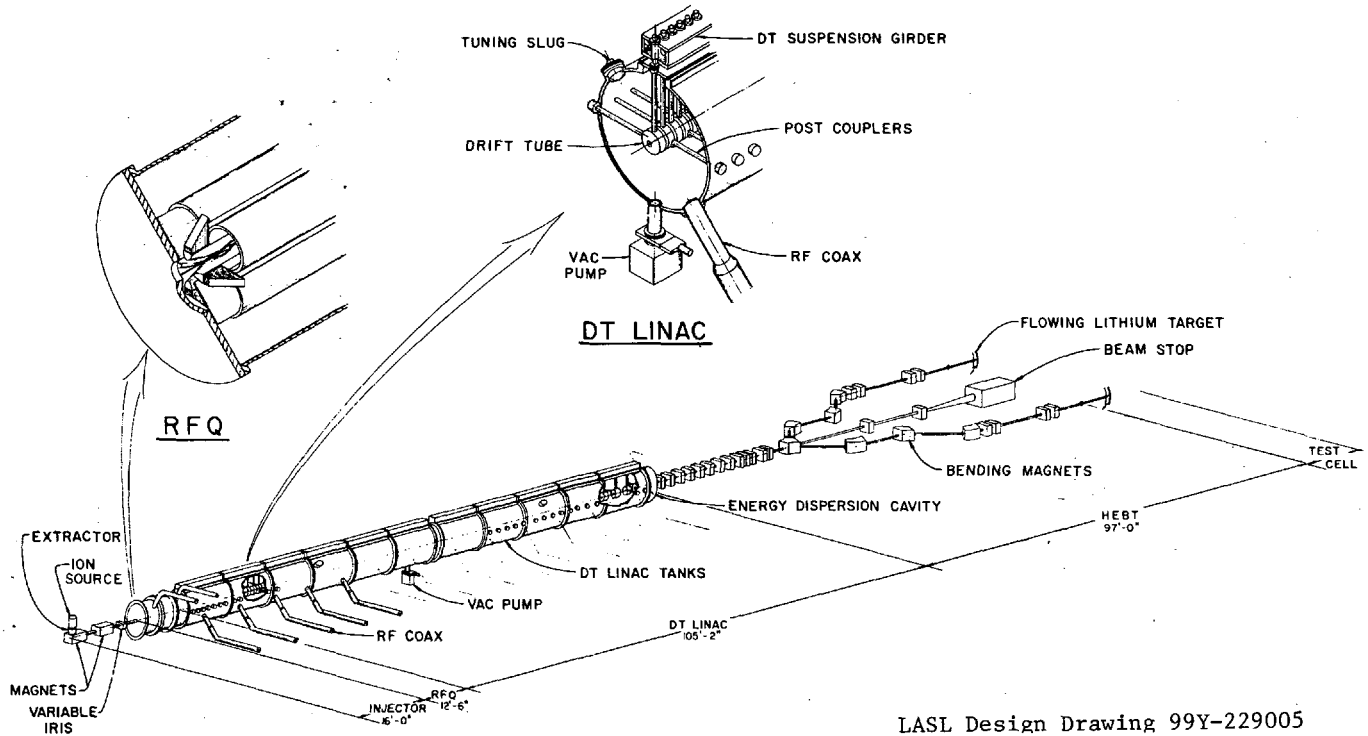

Fig. 1 General layout of FMIT linear accelerator, high energy beam transport system, and targets.

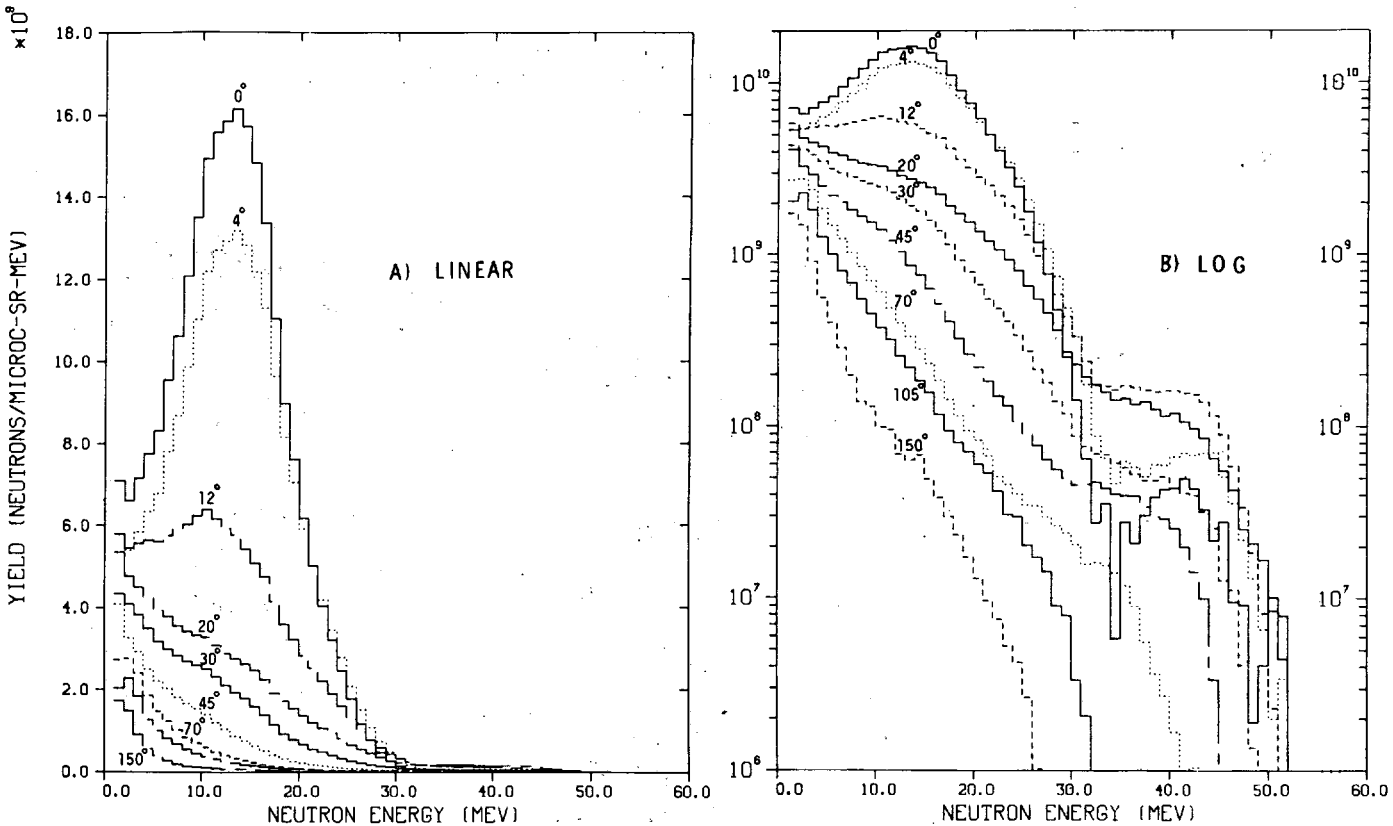

Fig. 2 Measured neutron yield spectra as function of emission angle in the laboratory for 35 MeV deuterons on thick natural lithium.

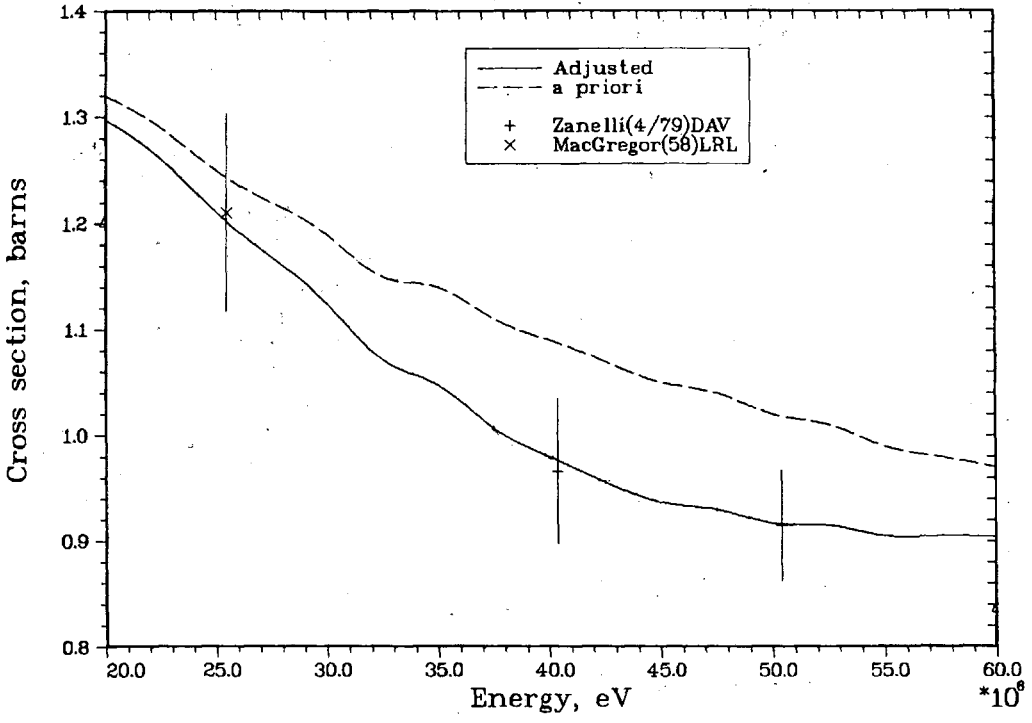

Fig. 3 Updated evaluation of the non-elastic cross section for neutrons between 20 and 60 MeV on iron. A priori data were from the previous evaluation by Wilson [8].

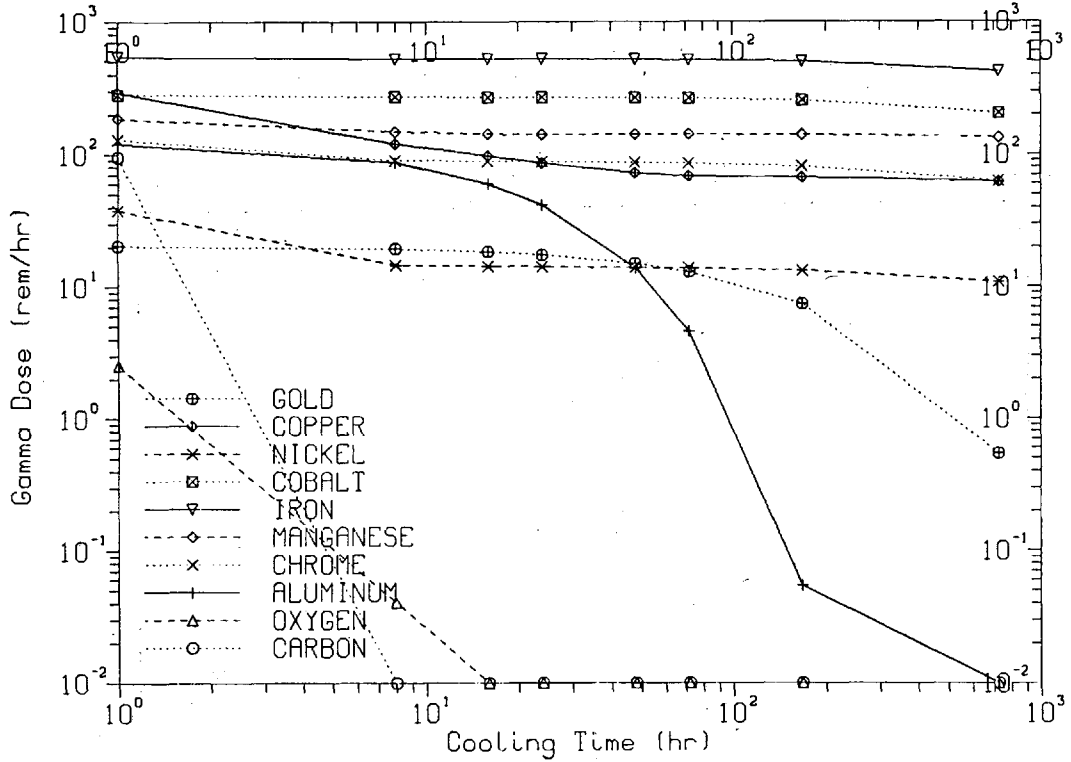

Fig. 4 Residual unshielded gamma ray doses at a distance of 1 meter for deuteron induced activation of various thick targets. Irradiation was with a 1 mA current of 35 MeV deuterons for a period of 1 year. Activation cross sections were estimated using an extension of the THRESH code [17].

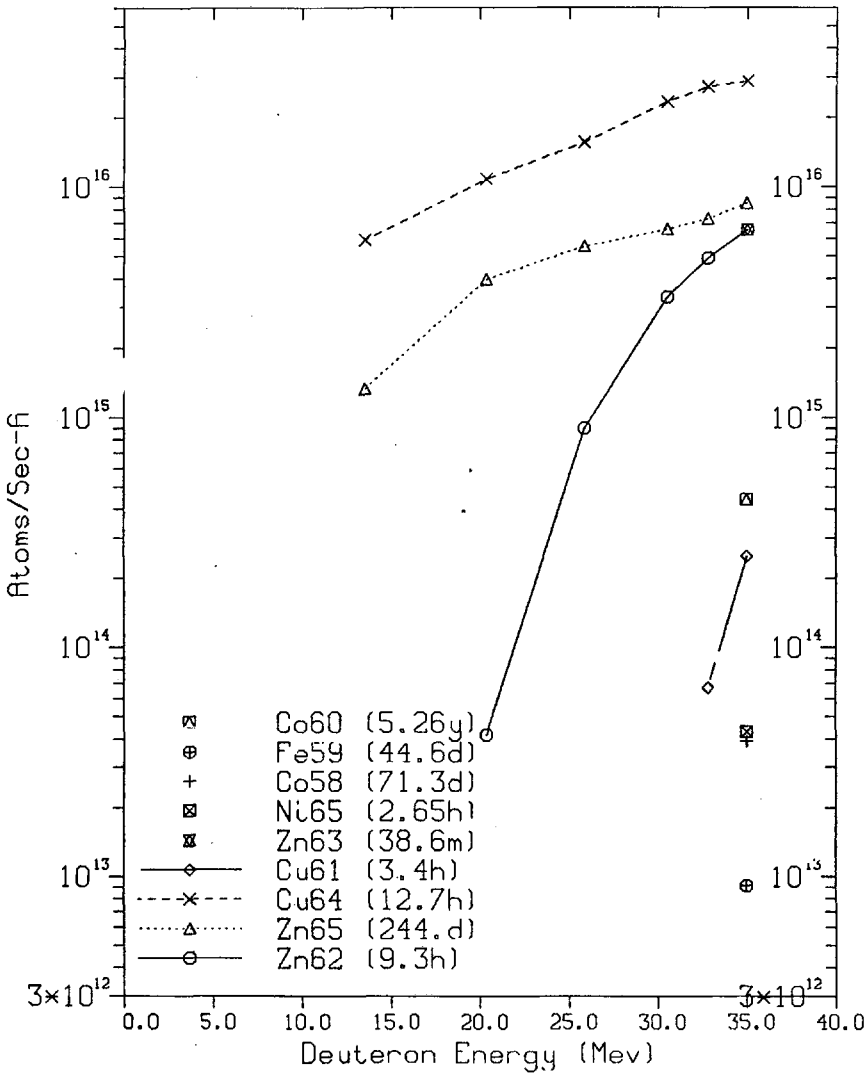

Fig. 5 Rates measured for production of various gamma decaying radionuclides from deuterons up to 35 MeV incident upon a thick copper target.

NEUTRON ENVIRONMENT IN d + Li FACILITIES

F. M. Mann and F. Schmittroth
and L. L. Carter
Hanford Engineering Development Laboratory
Richland, Washington 99352

ABSTRACT

A microscopic d + Li neutron yield model has been developed based upon classical models and experimental data. Using equations suggested by the Serber and evaporation models, a generalized least squares adjustment procedure generated angular yields for E_d to 40 MeV using the available experimental data. The HEDL-UCD experiment at E_d=35 was used to adjust parameters describing the neutron spectra. The model is used to predict yields, spectra, and damage responses in the FMIT Test Cell.

I. INTRODUCTION

With the continuing progress toward breakeven fusion facilities, more thought is being directed toward the materials that will be used in power-producing fusion reactors. Unfortunately, there presently does not exist any facility capable of producing very large peak fluxes ($>10^{15}$ n/cm^2-s) of high energy neutrons ($\sim$14 MeV) or of large fluxes ($>10^{14}$ n/cm^2-s) of high energy neutrons over large volumes (500 cm^3). Because of the severe limitation of producing dense targets of deuteron or tritium, the RTNS (Rotating Target Neutron Source) or any other d+t source is restricted to much lower fluxes ($\sim10^{13}$ n/cm^2-s) in small volumes ($\sim$1 cm^3).

Such high fluxes are necessary as can be seen from previous material programs. Materials must be tested to end-of-life conditions because material property changes are not only nonlinear with neutron dose, but also can be nonmonotonic. Thus, displacements of 75 to 300 dpa (displacements per atom) and helium productions of 500 to 2500 appm (atomic parts per million) must be achieved before the first fusion engineering test reactor is constructed. Fission reactors can produce the desired displacements but cannot match the helium production to displacement rate. Ion bombardment is also suspect because of its concentration of damage near the surface.

High fluxes of high energy neutrons can be produced from d+Li reactions. The Fusion Material Irradiation Test Facility (FMIT)[1] now being designed at the Hanford Engineering Development Laboratory for the U.S.Department of Energy will produce high energy neutrons with sufficient fluxes in large volumes. This paper describes, using relatively simple yet accurate models, the neutron environment (including expected displacement and helium production rates) of such d+Li facilities [2,3] with particular attention to the nominal operating parameters of FMIT. The effects of changing various FMIT design parameters will also be described as well as the perturbing effects of samples. A preliminary report has been published elsewhere [4].

II. BACKGROUND

FMIT will have 35 MeV deuterons striking a flowing liquid lithium target 1.9 cm thick. In order to reduce heating problems in the lithium jet, the beam will be disbursed with present designs being Gaussian in shape with full widths at half maximum values (FWHM) of 3 cm in width and 1 cm in height. Over 99.9% of the beam will hit the Li jet. A stainless steel backing plate of $\sim$.16 cm will contrain the Li and will separate the target space from the experimental volume in the test cell.

Since the peak fluxes of greater than 10^{15} n/cm^2-s will occur within 3 cm of the rear of the backing plate, the source of neutrons cannot be modeled as a point. Persiani [5] has analyzed the neutron environment using the experimental data of Daruga et al., [6] and of Saltmarsh et al., [7] but treating the source as a point. For a more accurate description, the cross sections for producing neutrons are needed as a function of distance into the lithium and of the angle between the incident beam direction and the neutron's path. Since the position within the lithium is related to the deuterons' instantaneous energy (ignoring small straggling effects), the dependence of cross section on position can be converted into a dependence on deuteron energy. In addition, since most material property changes will depend on the energy distribution of the neutrons striking the material, the dependence of the cross section on neutron energy must also be known. Thus, the unperturbed energy dependent neutron flux as a function of neutron energy at a point in the test cell can be found from

$$\frac{d\phi}{dE_n} = \int_0^{E_{d\text{-inc}}} dE_d \int \frac{d^2\sigma}{d\Omega\, dE_n} \frac{I(y,z)}{(dE_d/dx)\, r^2} \, dydz \qquad (1)$$

where $d^2\sigma/d\Omega dE_n$ is the differential cross section for producing neutrons, E_{d-inc} is the incident deuteron energy, dE_d/dx is the relationship between energy loss and the position parallel to the beam (x), $I(y,z)$ is the deuteron current distribution, and r is the distance between the neutron source point and the point of interest in the test volume. Note that Equation 1 ignores scat-

tering (both neutron and deuteron) within the target as well as neutron scattering outside the target. The equation also ignores the slight loss of deuteron intensity (less than 5%) as they pass through the lithium due to nuclear reactions and the extremely slight divergence of the deuteron beam.

III. NEUTRON SOURCE TERM

a. Introduction

All the quantities in Equation 1, except the differential cross sections, are known from geometry, target design, or well established physics. Unfortunately, there is not enough experimental data to determine these cross sections. Instead, models tested against experiment must be used.

The d+Li interaction can be modeled in four ways, stripping of the deuteron's proton, formation of a compound nucleus followed by the evaporation of neutrons, the breaking up of the deuteron by the long range Coulomb potential, and the interaction of the deuteron with only one of the neutrons in the lithium nucleus. Fortunately, because of the low atomic number of lithium and the relatively low deuteron energies used in FMIT, the latter two processes are relatively unimportant.[8] However, over 40 reactions are possible for the deuteron energies of interest, thus requiring a simplified approach. The approach taken here is to use two semi-classical models, the Serber stripping model and the evaporation model, and adjust their parameters to obtain agreement with experiment.

b. Angular Yields

Although for most applications the energy dependent neutron flux is needed, there are several important applications where only the energy integrated flux (or angular yield) is needed, such as total neutron yield either of the source as a whole or at points in the FMIT Test Cell. Also it is easier to incorporate experimental data into angular yield models since these are the quantities experimenters normally report.

Using the least squares adjustment computer code FERRET [9] the energy dependence of 5 angular functions forming the angular yields were determined using all the experimental data for deuterons on lithium with $14 < E_d < 45$ MeV. A major problem in using experimental data is that the data do not span all neutron energies; rather only neutrons above some threshold energy are observed. Therefore, using a preliminary version of the model and the energy dependence from the very low energy measurement of the HEDL-UCD (threshold = .4 MeV at E_d = 35 MeV), all the data were corrected to zero neutron energy.

In addition, in order to compare the experimental data, the

data were put onto a common angle and deuteron energy grid (θ = 0, 4, 7, 12, 20, 30, 45, 70, 90° and E_d = 5, 10, 15, 19, 22, 25, 30, 35, and 40 MeV. For measurements where no uncertainties were given a normalization uncertainty of 20% and a statistical uncertainty of 10% were used. Other experimental uncertainties were increased by uncertainties because of data modifications to the standard grid. The uncertainties due to the use of a standard grid were unimportant, but the corrections for neutron energy thresholds were important, especially at large angles. The input data is summarized in Table I and Figure 1. The data of Goland, et al,[15] were not used because their inclusion caused a lack of convergence in the adjustment procedure. For the data of Saltmarsh, et al,[7] the time-of-flight data were used instead of the dosimetry corrected data as it is now thought that the correction is wrong.[16]

To explain the neutron yield and spectra from 160 MeV deuteron bombardment of thin targets, Serber [17] in 1947 treated the deuteron as very weakly bound with the energy and angle of the spectator neutron being determined by the average internal motion of the target nucleus. Although slight differences exist depending upon whether the target nucleus is opaque or transparent, these differences are relatively minor. The resulting formula is

$$\left.\frac{d\sigma}{d\Omega}\right|_{\text{Serber}} = \frac{1.}{[1 + (\theta/\theta_s)^2]^{3/2}}. \qquad (2)$$

where $\theta_s = (5720/E_d).^{1/2}$ However, the theory presupposes that $E_d >> E_B$, the deuteron binding energy ($\sim$2.2 MeV). Thus it is not surprising that a slightly different formula was more successful in the preliminary model.

$$\left.\frac{d\sigma}{d\Omega}\right|_{\text{Pre}} = \frac{1.}{1 + (\theta/\theta_p)^2} \qquad (3)$$

where $\theta_p = (1800/E_d).^{1/2}$ For an isotropic angular distribution in the center of mass system for a given neutron energy, the laboratory angular distribution would be a linear combination of unity and cosine (θ). However, an analysis of the HEDL-UCD data for E_n = 1 to 2 MeV shows a 1 + cos $^5\theta$ dependence. Therefore, maximum ($\cos^5\theta$,0) was added to form the five angular functions. Functions peaking at $\sim$20° and 90° were also tried but their parameters were too uncertain to be meaningful.

So as not to presuppose the deuteron energy dependence of each of the six angular functions, the energy range was broken into 9 groups, 0 - 5 MeV, 5 - 10 MeV, 10 - 15, 15 - 19, 19 - 22, 22 - 25, 25 - 30, 30 - 35, and 35 - 40 MeV. Thus 45 parameters were adjusted by FERRET, which at the same time kept track of the 32 data points. By requiring a smooth variation as a function of deuteron energy, the parameters and their covariance matrix were found.

The most important result of this analysis is the total number of neutrons produced in the d + Li reaction. For example, the volume having flux greater than 10^{15} n/cm^2-s for the current FMIT design is 7.6 $\pm$ 1.8 cm^3, while the volume having an average flux of 10^{15} n/cm^2 is 21 $\pm$ 4 cm^3. Figure 2 shows the volume with flux greater than ϕ as a function of ϕ as well as the volume with an average flux of ϕ. Since flux is linearly related to deuteron current, Figure 2 can be used to determine such relations as a function of deuteron current as well. Not only may the deuteron current be different when the FMIT facility begins operation, but other design variables may also change.

c. Neutron Spectra

The determination of the neutron spectra is much more difficult because so much more data are required. Even if experimental neutron spectra were available, the magnitude of the quantity of the data and the need to use non-linear parameters make the use of a code like FERRET unadvisable. Instead, simple models for stripping and for evaporation are used with their parameters being adjusted to fit the HEDL-UCD experiment at E_d = 35 MeV.

The model for stripping relies mainly on the Serber model. As noted above, the Serber model pictures the deuteron as weakly bound with the energy and angular dependence of the emerging neutron dependent on the average motion of nucleons in the target nucleus. August, et al,[18] have shown that this model which was developed to explain results using 160 MeV deuterons gives the proper shape of the high energy distribution ($E_n > E_d/2$) at 0° for a thick target for incident deuteron energies of interest at FMIT. The equations used are

$$\frac{d^2\sigma}{d\Omega dE_n} = \frac{d\sigma(E_d,\Theta)}{d\Omega} \quad S(E_d,E_n) \qquad 0 < E_n < E_d$$

$$\frac{d\sigma}{d\Omega}(E_d,\Theta) = a(E_d) \left.\frac{d\sigma}{d\Omega}\right|_{\text{Serber}} + b(E_d) \left.\frac{d\sigma}{d\Omega}\right|_{\text{Pre}}$$

$$a(E_d) = K_1 * \text{Max}(41.4,\ 24.6 + E_d) * 6.426$$

$$b(E_d) = K_2 * \text{Max}(106.,\ 87 + E_d) * 2.761$$

$$S(E_d,E_n) = Nf(E_n,E_d) \frac{E_d E_B}{[(E_n - E_d/2)^2 + E_B E_d]^{3/2}}$$

$$f(E_n,E_d) = \text{MIN}\left(\frac{E_n^2}{(.35\ E_d)^2},1\right)$$

where $d\sigma/d\Omega|_{Serber}$ is defined in Equation 2, $d\sigma/d\Omega|_{Pre}$ is defined in Equation 3, E_B is the binding energy of the deuteron. The functions $a(E_d)$ and $b(E_d)$ come from smoothing the results from the angular yields analysis and are not part of the Serber model which assumes a cross section independent of deuteron energy. Neither is the function $f(E_n,E_d)$ which ensures that the cross section for zero or negative energy neutrons is zero, not finite as predicted by the Serber model. Remember that the Serber model assumed $E_n > E_B$. The form of f was chosen to match the low energy ($E_n < E_d/2$) part of HEDL-UCD data. The normalization constant N is chosen so that

$$\int_0^{E_d} \frac{S(E_d,E_n)}{f(E_d,E_n)}\, dE_n = 1$$

For the highest neutron energies ($E_n > E_d$) the Serber model breaks down for d + Li. Here the dominant reaction is the stripping of ^{7}Li to the ground and first excited states of ^{8}Be. Because only two states are involved (and both are unbound), the classical picture fails and one must resort to a quantum mechanically treatment or to experiment. The latter choice is taken with a deuteron energy independent microscopic cross section $\sigma(\Theta)$ used for each state for $E_d < E_n < E_d + Q(\Theta)$.

The evaporation part of the model is also in two parts. The first part is the classical evaporation model [19] which predicts the energy spectrum of the neutrons which are boiled off as the first particle out after a compound nucleus is formed. The second part, a linear term in neutron energy, represents all succeeding evaporations. Thus the formulas that result are

$$\frac{d\sigma}{dE_d d\Omega dE_n} = \frac{d\sigma}{d\Omega}(E_d,\Theta) \quad * S(E_d,E_n)$$

$$\frac{d\sigma}{d\Omega}(E_d,\Theta) = a(E_d) + b(E_d)\cos\Theta + d(E_d)\cos^5\Theta$$

$$a(E_d) = K_3 * (282. - E_d) \quad * .875$$

$$b(E_d) = K_4 * (342. + E_d) * .881$$

$$d(E_d) = K_6 * MIN\ (125.,\ 105. + E_d) * (06.191)$$

$$S(E_d,E_n) = \frac{1}{T} \exp(-E_n/T) + f(E_d,E_n)$$

$$T = .55 * E_d^{\frac{1}{2}}$$

$$f(E_d,E_n) = \left[.1 * E_d - 2 * MIN(E_n,.05\ E_d)\right] * .1$$

d. Comparison with Experiment

Figure 3 presents a comparison between the model results (corrected for the experimental neutron detection threshold) and the measurements between 15 and 40 MeV. The calculation passes through the data of Nelson, et al.,[11] Daruga, et al.,[6] Amols et al., [13] Johnson, et al.,[14] and Saltmarsh, et al.[7] The calculations are lower than the measurements of Lone, et al.,[10] and Weaver, et al.,[12] but higher than those of Goland et al. It should be noted that the data of Lone, et al., show a very large yield for low energy neutrons ($E_n < 2$), which is very uncertain due to uncertainties in detection efficiency. If the 2.3 MeV detection threshold of Lone, et al., is used instead of their 0.3 MeV threshold, the C/E's change to .89, .92, .85 respectively. The data of Goland, et al., on the other hand, show a drastic fall off for neutrons below 5 MeV, maybe explaining why the model predicts more neutrons than they observed. Overall, there seems to be little deuteron energy dependence or angular dependence in the differences between the model and the measurements.

The HEDL-UCD experiment is the most detailed and precise experiment for the deuteron energy of FMIT. Figure 4 shows a comparison of the neutron spectrum for the 12° HEDL-UCD measurements using a logarithmic axis. Table I displays a summary of the comparisons for the HEDL-UCD measurements. It should be noted that the 0 - 1 MeV experimental value is assumed to be (1.5 $\pm$ 1.5) of the values between 1 and 2 MeV in agreement with the trend of the HEDL-UCD data below 1 MeV. In general, the model accurately describes the measurement.

IV. APPLICATIONS

a. Unperturbed Neutron Spectra

Two different methods are used to determine the unperturbed neutron spectra in the FMIT test cell. The first method which

treats the source volume as a set of discrete sources is very fast and flexible, allowing not only spectra, but also displacement rates, helium production rates, and volumes involving such quantities, to be inexpensively calculated. The other method, based on the Monte Carlo technique [20] allows an easy extension to the calculation of perturbed fluxes. The difference in the calculated unperturbed fluxes by the two methods is less than 1%.

The discrete method uses planes corresponding to equal ΔE_d steps, with surface elements on the planes chosen to have equal beam density. The source is assumed to be concentrated at the midpoint of the surface element. Typically 35 planes (ΔE_d=1MeV) planes with 80 surface elements are used to evaluate the integral in Equation 1. Experience has shown that the calculated flux values are not sensitive if the number of source elements in each plane is above 50 but are very sensitive if only one direction in the plane is used. The calculations of volumes having flux greater than a given value are insensitive to the treatment of the vertical (1cm FWHM) direction, while the value of flux at a given point is quite sensitive.

The source for the Monte Carlo method is treated as 6 separate volumes corresponding to E_d=0 to 15MeV, 15MeV to 20MeV, 20 to 25, 25 to 30, 30 to 33, and 33 to 35MeV, whose source strength was calculated using the discrete model. Neutrons are assumed to be born uniformly in the direction parallel to the beam and according to the beam profile in directions perpendicular to the beam. Both plane and point detectors have been used. However, great care must be exercised in the use of planar detectors near the source because of the rapid variation of the flux near the source.

Figure 5 shows the predicted unperturbed spectra for four representative points, the point of the highest flux, a point further along the axis of the deuteron beam, a point on the backing plate which is off-axis, but in the midplane, and finally a point on the backing plate but off midplane. The shapes of the spectra above 15MeV are remarkably similar. Also there is a significant number of neutrons below 10MeV for points near the backing plate resulting from neutrons from wide-angle effects.

b. Damage Parameters

Although much attention is paid to flux, the experimentalists who will use FMIT will be more interested in predicting damage rates, such as displacement and helium production.

Unfortunately, the nuclear data needed for such calculations are in very poor shape. Data is needed past 40MeV, but ENDF/B,[21] the main U.S. nuclear data library, extends only to 20MeV. Therefore, data for isolated materials but not for iron or stainless steel, have been obtained over the desired energy range. To provide an idea of the usefulness of FMIT, damage parameters for Cu, the evaluated material closest to iron, have been used. The displacement cross sections are from ORNL[22] with E_{damage} = 30eV.

Because the ORNL calculations for helium production do not agree with measured values [23,24] and do not include processes such as $(n,2n\alpha)$, new calculations using the computer code HAUSER*5 [25] were performed.

Since the main reason for the FMIT facility is to expand the damage data base from fission reactors to fusion reactors, the damage response in FMIT should peak around 14MeV. Figures 6 and 7 show the predicted damage rates (displacement and helium productions, respectively) for the four points of Figure 5. As can be seen, there is relatively little response at low energies and that the damage rates do peak in the region of interest.

V. CONCLUSION

The unperturbed neutron spectra, displacement rate, and helium production in the FMIT test cell have been calculated using a source term which agrees well with experimental results. The predicted values show that there exists significant volumes having damage rates greater than that of the first wall of a fusion reactor.

REFERENCES

1. E. W. Pottmeyer, Jr., "The Fusion Materials Irradiation Test Facility at Hanford," presented at the 1st Topical Meeting on Fusion Reactor Materials, Miami Beach, Fla., Jan. 1979; Journal of Nuclear Materials, 85 & 86 (1979) 463.

2. M. J. Saltmarsh and R. E. Worsham, "INGRID - an Intense Neutron Generator for Radiation-Induced Damage Studies in the CTR Material Program," ORNL-TM-5233, Oak Ridge National Laboratory Oak Ridge, Tenn. (Jan. 1976).

3. F. Grand and A. N. Goland, "An Intense Neutron Source Based Upon the Deuterium - Stripping Reaction," Nucl. Instl. Meth. 145 (1977) 49. P. Grand (ed.), "Accelerator - Based Neutron Generator," BNL-20159 and addendum BNL-2048, Brookhaven Nat'l Laboratory, Upton, NY (Jan. 1975 and Jan. 1976).

4. J. O. Schiffgens, R. L. Simons, F. M. Mann, and L. L. Carter, "Spatial Variations of Damage Parameters on FMIT and their Implications," presented at the 1st Topical Meeting on Fusion Reactor Materials, Miami Beach, Fla., Jan. 1977; Journal of Nuclear Materials, 85 & 86 (1979) 491.

   F. Schmittroth and F. M. Mann, "Flux-Volume Review for the Fusion Materials Irradiation Test Facility (FMIT)," TC-1375 Hanford Engineering Development Laboratory, Richland, WA., (May 1979).

5. P. J. Persiani, W. Becker, and J. Donahue, "Neutron Spectra for the 40-MeV Deuteron Lithium Source System," Trans Am Nucl Soc (1977) 795.
   P. J. Persiani, W. Becker, and J. Donahue, "Neutron Spectra and Basic Data Requirements for (d,Li) and (d,Be) Target Systems," in BNL-NCS-50681, Brookhaven National Laboratory, Upton, NY (1977).

6. V. K. Daruga and N. N. Krasnov, "Production of Strong, High-Energy Neutron Fluxes by a Cyclotron by Irradiating Thick Lithium and Beryllium Targets with 22-MeV Deuterons," Atomic Energy 30 (1971) 493, translated from the Russian Atomnaya Energiya 30 (1971) 399.

7. M. J. Saltmarsh, C. A. Ludemann, C. B. Fulmer, and R. C. Styles, "Neutron Yields and Dosimetry for Be (d,n) and Li (d,n) Neutron Sources at E_d = 40 MeV," in NBSIR 77-1279, National Bureau of Standards, Washington, DC, (July 1977).

8. G. W. Schweimer, "Fast Neutrons Production with 54 MeV Deuterons," Nucl. Phys. A100 (1967) 537.

9. F. Schmittroth, "Generalized Least-Squares for Data Analysis" HEDL-TME 77-51, Hanford Engineering Development Laboratory, Richland, WA., (March 1978).

10. N. A. Lone, "Neutron Spectral Distributions from Proton and Deuteron Bombardment of Thick Li & Be Targets at 14.8, 18, & 23 MeV," in NBSIR 77-1279, National Bureau of Standards, Washington, DC, (July 1977).

11. C. E. Nelson, F. O. Purser, P. Von Behren, and H. W. Newson, "Neutron Spectra from Deuteron and Proton Bombardment of Thick Lithium Targets," in BNL-NCS-50681, Brookhaven National Laboratory, Upton, NY (1977).

12. K. W. Weaver, J. D. Anderson, H. H. Barschall, and J. C. Daves, "Neutron Spectra from Deuteron Bombardment of D, Li, Be, and C," Nucl. Sci. Eng., 52 (1973) 35.

13. H. I. Amols, J. F. Dicello, M. Awschalon, L. Coulson, S. W. Johnson, and R. B. Theus, "Physical Characterization of Neutron Beams Producted by Protons and Deuterons of Various Energies Bombarding Beryllium and Lithium Targets of Several Thicknesses," Med. Phys. 4 (1977) 486.

14. D. L. Johnson, F. M. Mann, J. W. Watson, J. Ullmann, and W. G. Wyckoff, "Measurements and Calculations of Neutron Spectra from 35 MeV Deuterons on Thick Lithium for the FMIT Facility" presented at the 1st Topical Meeting on Fusion Reactor Materials, Miami Beach, Fla., (Jan 1979);
Journal of Nuclear Materials, 85 & 86 (1979) 467.

15. A. N. Goland, C. L. Snead, Jr., D. M. Parker, and R. B. Theus, "Use of Li (d,n) Neutrons for Simulation of Radiation Effects in Fusion Reactors," IEEE Transactions on Nuclear Science, NS-22 (1975) 1776. Also see first article under Reference 2.

16. L. R. Greenwood, R. R. Heinrick, M. J. Saltmarsh, and C. B. Fulmer, "Integral Tests of Neutron Activation Cross Sections in a ^{9}Be (d,n) Field at E_d = 40 MeV,"Nucl. Sci.&Eng. 72 (1979) 175.

17. R. Serber, "The Production of High Energy Neutrons by Stripping," Phys. Rev. 72 (1947) 1008.

18. L. S. August, F. H. Attip, G. H. Herling, P. Shapiro, and R. B. Theus, Phys. Med. Bio. 6 (1976) 931.

19. See, for example, P. Marmier and E. Sheldon, Physics of Nuclei and Particles, Vol. 2, p. 1233, Academic Press Inc., New York (1970).

20. LASL Group TD-6, "MCNP - A General Monte Carlo Code for Neutron and Photon Transport," LA-7396-M, Los Alamos Scientific Laboratory, Los Alamos, NM, (July 1978).

21. The Evaluated Nuclear Data File, maintained at the National Nuclear Data Center, Brookhaven National Laboratory, Upton, NY. The current version is ENDF/B-V.

22. C. Y. Fu and F. G. Perey, Journal of Nuclear Material, 61 (1976) 153.

23. S. M. Grimes, R. C. Haight, J. D. Anderson, K. R. Alvar, and R. R. Borchers, "Development of a Spectrometer for the Measurement of (n,xp), (n,xd) and (n,xα) Cross Sections, Angular Distributions, and spectra at E_n = 15 MeV," in BNL-NCS-50681, Brookhaven National Laboratory, Upton, NY. (May 1977).

24. H. Farrar IV, D. W. Kneff, R. A. Britten, and R. R. Heinrick, "Fluence Mapping of RTNS-I by Helium Accumulation and Foil Activation Methods," in BNL-NCS-50681, Brookhaven National Laboratory, Upton, NY, (May 1977).

25. F. M. Mann, "HAUSER*5, A Computer Code to Calculate Nuclear Reaction Cross Sections," HEDL-TME 78-83, Hanford Engineering Development Laboratory, Richland, WA (1979).

TABLE I

NEUTRON YIELDS FROM d + Li

Experimenter	As Measured				As Used in Fit		
	E_d	$E_{n\text{-}min}$	θ	Value	E_d	θ	Value[c]
Lone, et al.	14.8	0.3	0	3.1	15	0	3.70[a]
	18.0	0.3	0	4.9	19	0	5.87[a]
	23.0	0.3	0	10.3	22	0	9.20[a]
Nelson, et al.	15.0	1.0	0	2.5	15	0	2.9[a]
	15.0	1.0	10	2.0	15	12	2.1[a]
	15.0	1.0	20	1.3	15	20	1.6[a]
	15.0	1.0	30	.82	15	30	1.02[a]
	15.0	1.0	45	.58	15	45	.75[a]
Weaver, et al.	16.0	3.0	3.5	3.6±.6	15	4	3.9[b]
	19.0	3.0	3.5	5.8±.9	19	4	7.2[b]
	19.0	3.0	10	4.3±.7	19	12	5.0[b]
	19.0	3.0	18	2.9±.5	19	20	3.7[b]
	19.0	3.0	25	2.0±.3	19	20	3.5[b]
	19.0	3.0	32	1.5±.2	19	30	2.4[b]
Doruga, et al.	22.0	0.0	0	7.3±1.2	22	0	7.3[c]
	22.0	1.8	90	.6±.1	22	90	.9[c]
Amols, et al.	35.0	5.0	0	21±5	35	0	24.9[a]
Johnson, et al.	35	1.0	0	23.5±3.8	35	0	24.5[d]
	35	1.0	4	21.0±3.4	35	4	22.0[d]
	35	1.0	8	16.5±2.7	35	7	18.5[d]
	35	1.0	12	12.1±2.0	35	12	12.9[d]
	35	1.0	20	7.13±1.17	35	20	7.80[d]
	35	1.0	30	5.08±.83	35	30	5.70[d]
	35	1.0	45	3.12±.51	35	45	3.61[d]
	35	1.0	70	1.85±.30	35	70	2.22[d]
Saltmarsh, et al. (TOF data)	40	2.0	0	36.7±5.5	40	0	39.0[c]
	40	2.0	7	24.7±3.7	40	7	26.6[c]
	40	2.0	15	11.4±1.7	40	12	15.8[c]
	40	2.0	30	6.28±.9	40	30	7.55[c]
	40	2.0	45	3.61±.5	40	45	4.5[c]
	40	2.0	60	2.41±.4	40	70	2.83[c]
	40	2.0	90	1.43±.22	40	90	2.01[c]

)Yield from 0-1 MeV assumed 1.5 Yield 1-2 MeV

a)Normalization uncertainty = 20%, statistical uncertainty = 10%

b)Normalization uncertainty = 16%, statistical uncertainty = 10%

c)Normalization uncertainty = 15%, statistical uncertainty = 5%

d)Normalization uncertainty = 15%, statistical uncertainty = 6.5%

e)Uncertainties due to corrections are 100% of $E_{n\text{-}min}$ correction for $E_n \leq 2.0$ MeV, 50% for $E_n \geq 2.0$ MeV, 10% of E_d and θ correction are added to above uncertainties

TABLE II

Comparison of HEDL-UCD Experiment and Model

Yield[a] (10^{16}n/sec-A)

Angle	Exp.[6]	Model	Ratio	Maximum Deviation[b,c]
0	24.3 ± 1.1	25.6	1.06±.05	1.00 ± .03 - 1.08 ± .05
4	20.8 ± 1.3	22.4	1.08±.07	1.00 ± .05 - 1.11 ± .06
12	12.0 ± 0.8	12.8	1.07±.07	1.04 ± .05 - 1.08 ± .06
20	7.13 ± 0.43	8.07	1.13±.07	1.11 ± .06 - 1.20 ± .06
30	5.07 ± 0.30	5.35	1.05±.06	1.01 ± .06 - 1.16 ± .04
45	3.11 ± 0.19	3.32	1.07±.07	1.02 ± .07 - 1.15 ± .04
70	1.85 ± 0.11	2.10	1.14±.07	1.11 ± .03 - 1.18 ± .06
105	1.31 ± 0.08	1.38	1.06±.07	1.04 ± .03 - 1.07 ± .04
150	0.65 ± 0.04	0.73	1.13±.07	1.08 ± .06 - 1.25 ± .12

[a] The yield is for E_n >1 MeV.

[b] There is a 15% normalization uncertainty in the experimental data.

[c] Only that energy range having Yield (Θ) >.05* MAX Yield (Θ) is considered.

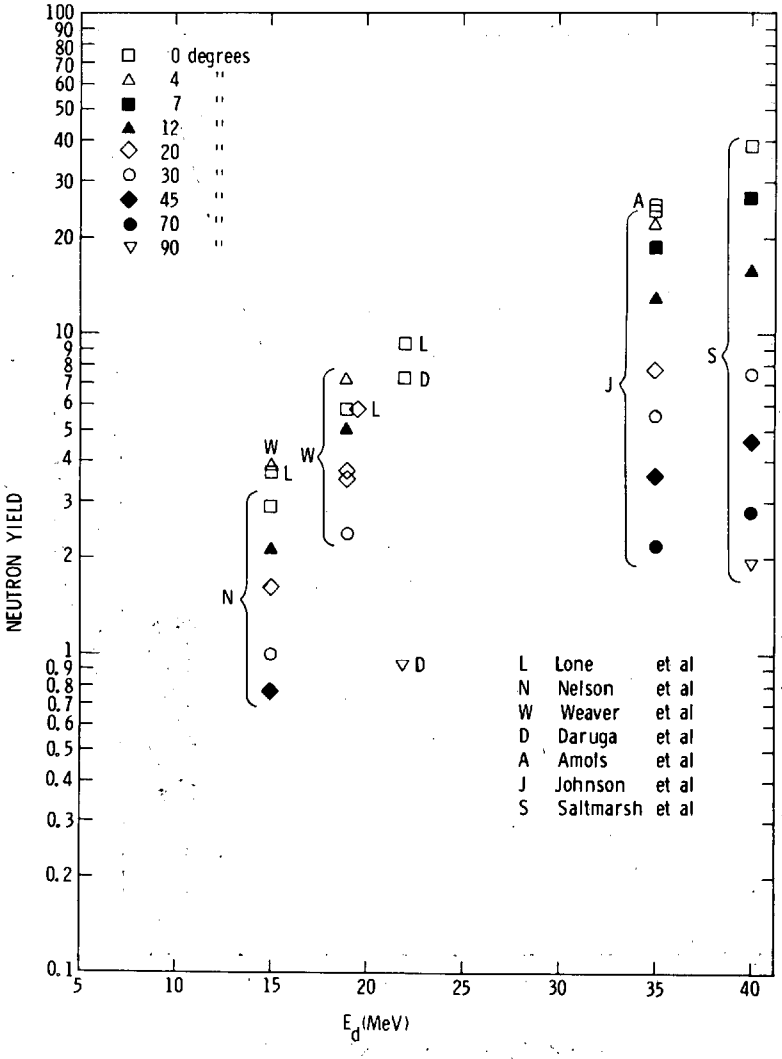

Fig. 1 Input Data

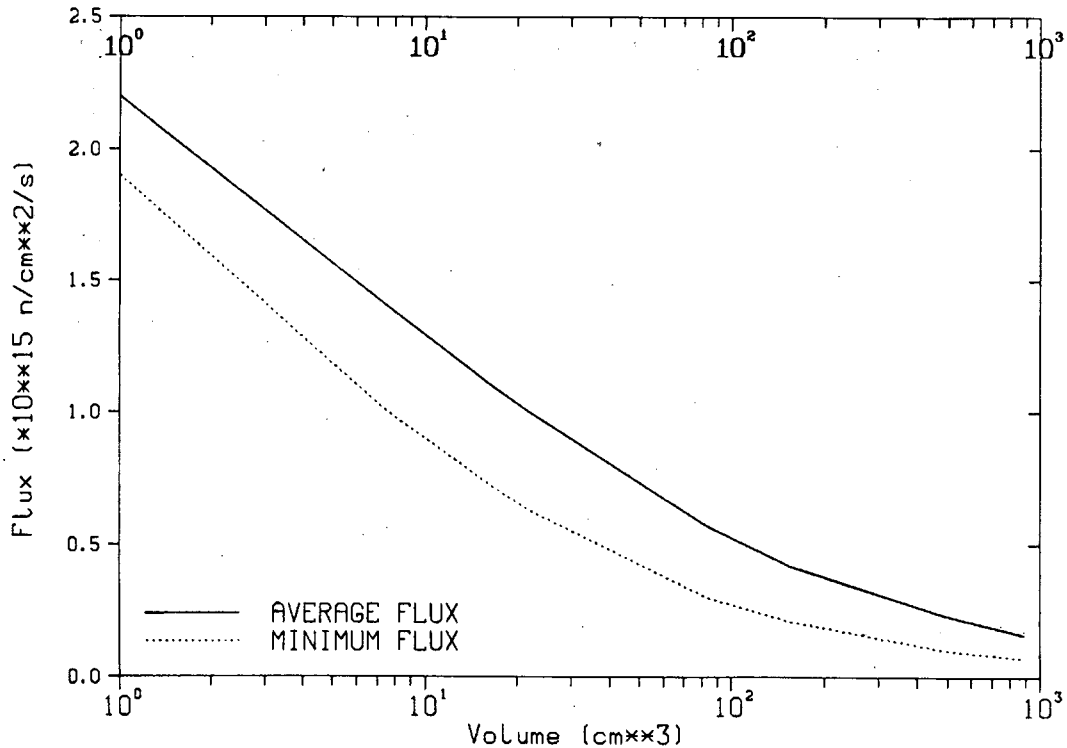

Fig. 2 Relationship between Flux and Volume

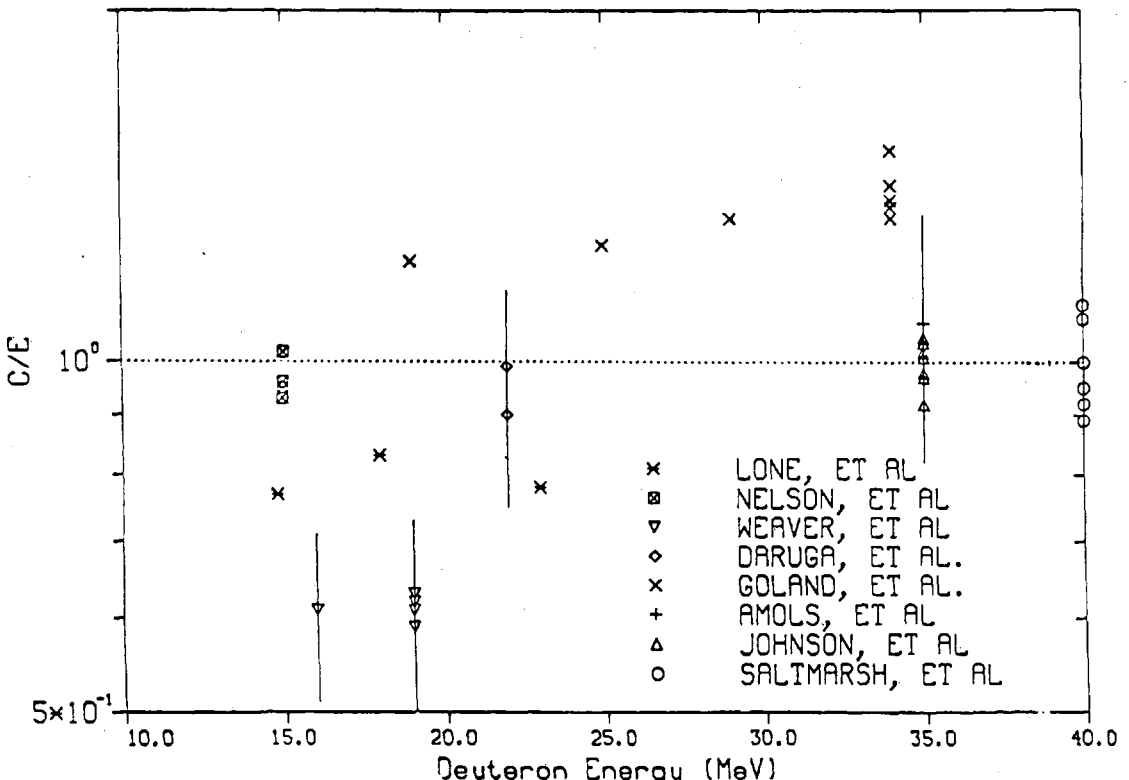

Fig. 3 Comparison between Model and Measurement

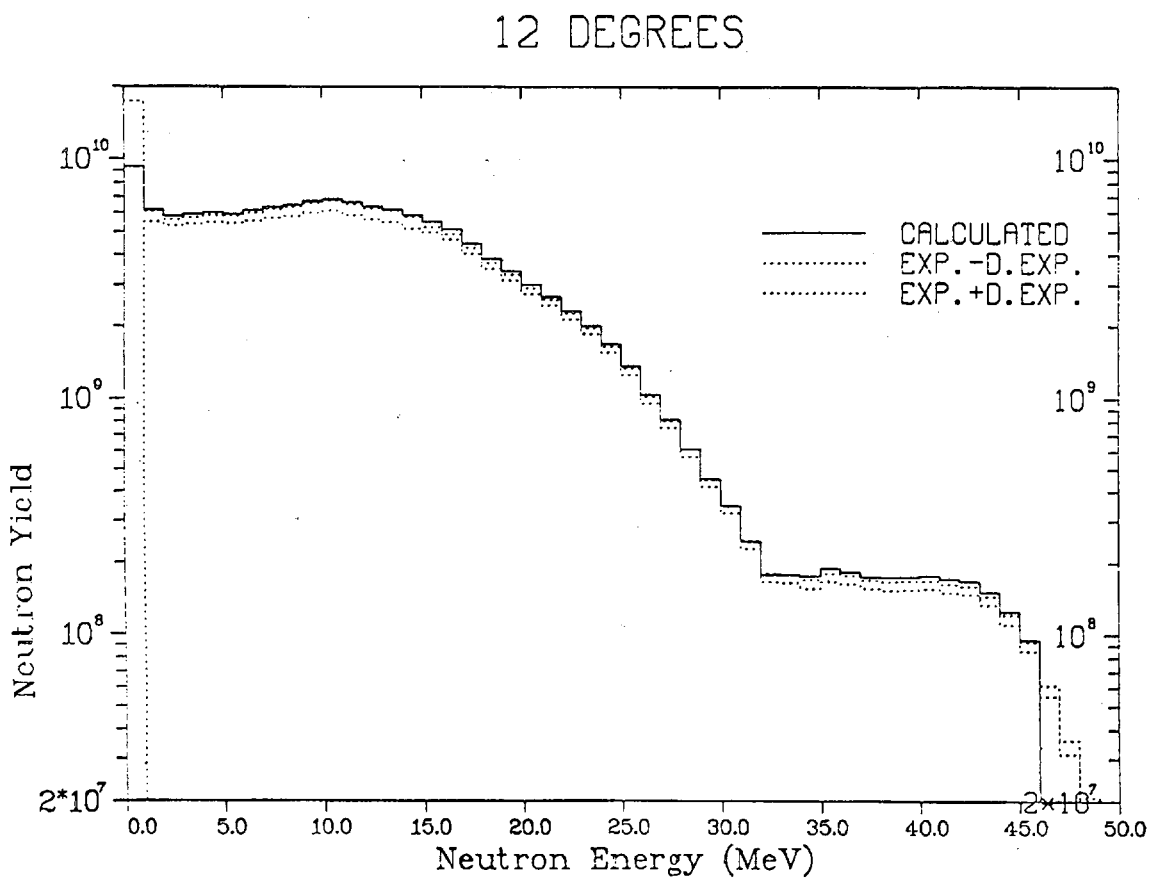

Fig. 4 Comparison between Model and UCD-HEDL Experiment

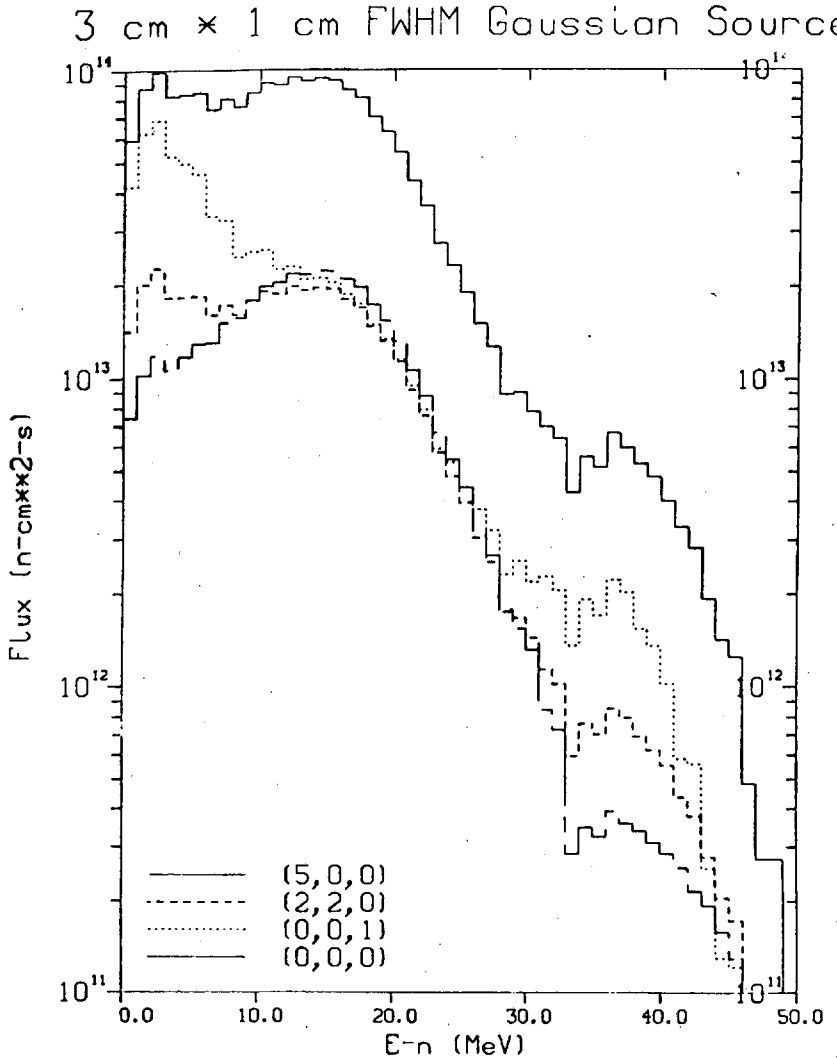

Fig. 5 Predicted Unperturbed Neutron Spectra E-d=35 MeV, I-d=0.1 A

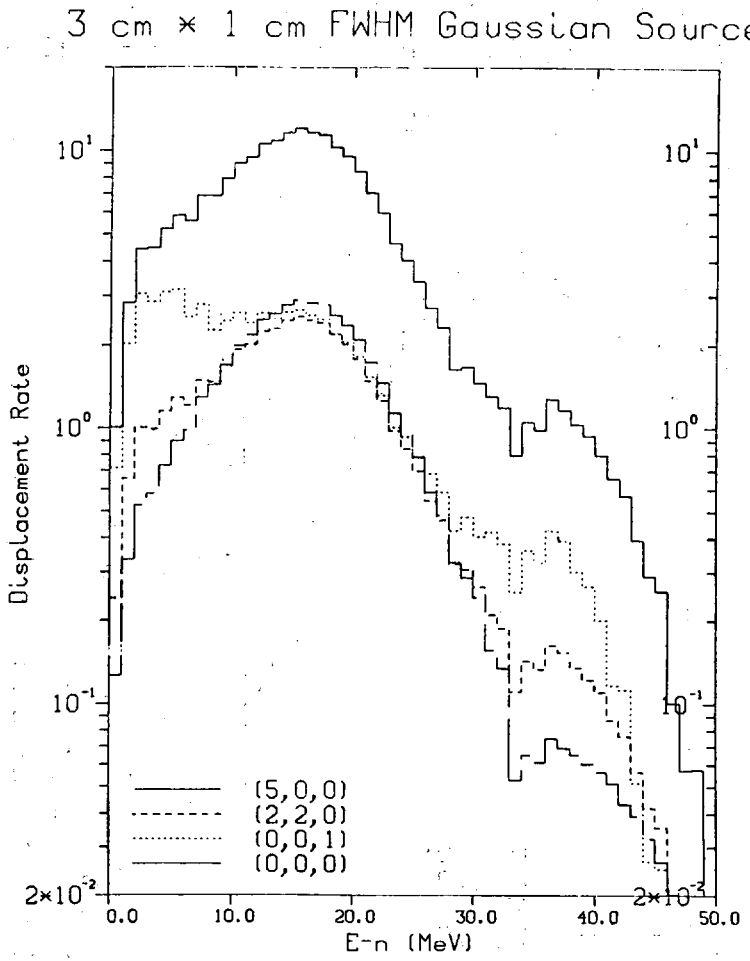

Fig. 6 Predicted Displacement Response for Copper E-d=35 MeV, I-d=0.1 A

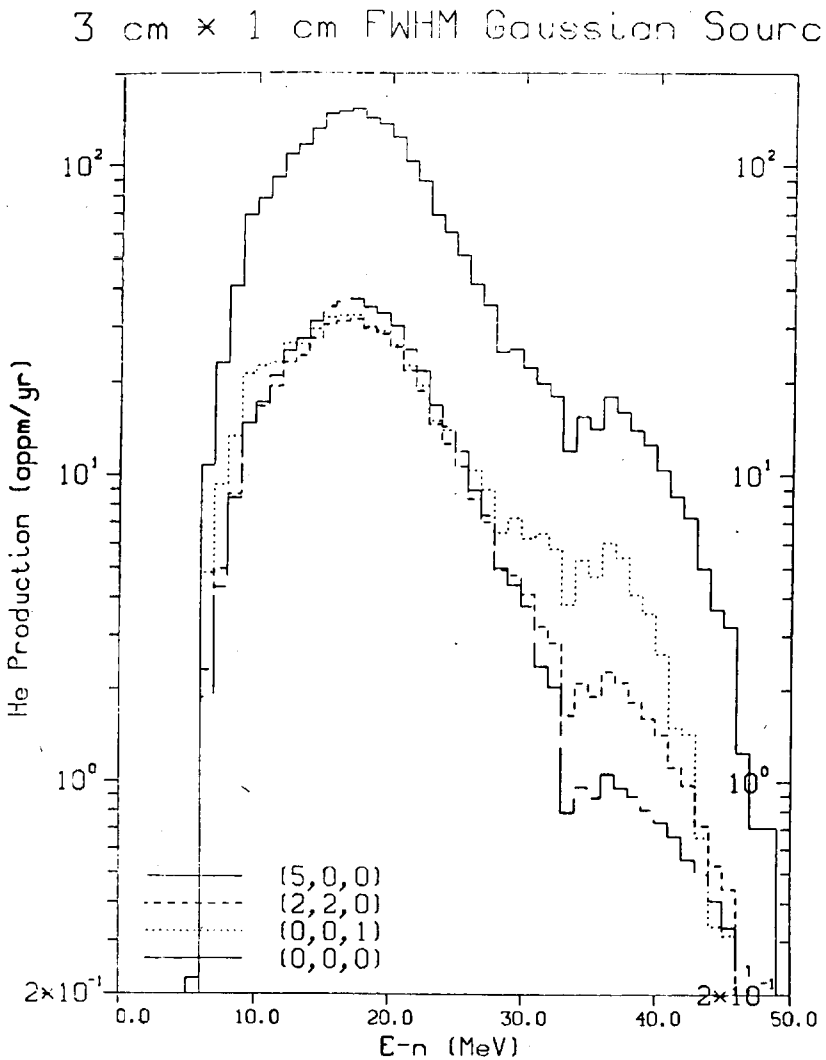

Fig. 7 Predicted Helium Production Response E-d=35 MeV, I-d=0.1 A

INTEGRAL CROSS SECTION MEASUREMENTS ON (n,x) REACTIONS INDUCED BY 30 MeV d(Be) BREAK-UP NEUTRONS ON FRT WALL AND STRUCTURAL MATERIALS

S.M. Qaim, S. Khatun* and R. Wölfle

Institut für Chemie 1 (Nuklearchemie)
Kernforschungsanlage Jülich GmbH, 517 Jülich, FRG

ABSTRACT

Integral cross sections were measured by the activation technique for some 30 MeV d(Be) break-up neutron induced (n,2n), (n,3n), (n,p), [(n,n'p)+(n,d)], (n,α), (n,n'α) and (n,^{3}He) reactions on isotopes of the elements Al, Ti, V, Cr, Mn, Fe, Co, Ni, Cu, Nb and Mo. Tritium formation cross sections were determined for the elements Al, Cr, Mn, Fe, Co, Ni and SS by vacuum extraction and gas counting of tritium. The integral cross section data agree within 20% with the average cross section values deduced from the known excitation functions of a few reactions. Some preliminary systematic trends observed in the cross section data are described. A comparison of the 30 MeV d(Be) neutron cross sections with those available at 14.5 MeV is given and some of the possible consequences of the use of a 30 MeV d(Be) neutron source for radiation damage studies, instead of a 14 MeV d-t source, especially with regard to hydrogen and helium gas production in wall and structural materials, are discussed.

---

* IAEA-Fellow, on leave from Bangladesh Atomic Energy Commission, Dacca, Bangladesh

INTRODUCTION

In view of the difficulties associated with the construction of high intensity d-t neutron sources for radiation damage studies on fusion reactor wall and structural materials, the proposal of using d(Be) and d(Li) intense neutron sources is gaining increasing importance. However, for an interpretation of the radiation damage effects brought about by deuteron break-up neutron spectra an extensive knowledge of fast neutron induced reaction cross sections up to about 40 MeV will be required. Some recent surveys [1-3] have shown that the cross section data base at energies above 15 MeV is very weak. Cross section measurements at discrete neutron energies require considerable effort but would yield valuable information for testing nuclear models and developing computational codes, especially in the energy region above 30 MeV. For immediate use, integral cross section measurements with deuteron break-up neutron spectra could yield information useful for various calculations.

In connection with our fundamental studies on the emission of ^{3}H and ^{3}He particles in fast neutron induced reactions, using activation, tritium counting and mass spectrometric techniques, we carried out extensive integral cross section measurements with a 53 MeV d(Be) neutron source [4-6]. The present paper describes integral cross section measurements on several potential FRT materials with a 30 MeV d(Be) neutron source.

NEUTRON SPECTRUM AND IRRADIATIONS

Fast neutrons were produced by bombarding a 1 cm thick Be target with 30 MeV deuterons at the Jülich isochronous cyclotron (JULIC). The experimental arrangement is given schematically in Fig. 1(A).

The high energy part of the neutron spectra produced in the interactions of high energy deuterons (E_d> 30 MeV) with Be is known [7,8]. In the low energy region of the neutron spectrum, however, there are some discrepancies. For characterizing the 30 MeV d(Be) neutron spectrum in the forward direction, Nethaway et al [9] used the multiple foil activation technique and reported the spectrum given in Fig. 1(B). By applying the same technique of spectrum unfolding through the use of threshold reactions and correcting for the angle dependent

intensity of the neutrons [8,10] incident at our irradiation position as well as for the decrease in their intensity due to passage through beryllium, copper and the irradiation samples we obtained the shape of the spectrum at the Be-converter which was very similar to that given in Fig. 1(B). Some small deviations observed are being investigated further but for cross section measurements the spectrum given in Fig. 1(B) was adopted. The neutron spectrum has a strong low energy component. Its exact origin is not known. Presumably some contribution is furnished by secondary effects. The spectrum can be divided roughly into three groups with energy regions and relative intensities: 2 to 8 MeV (39.5%), 8 to 13.5 MeV (25.5%) and 13.5 to 30 MeV (35.0%).

Irradiations were carried out at a distance of about 6 cm from the Be-converter. For measurements involving ß-counting or γ-ray spectroscopy about 0.1 g of the high purity target material, generally in the form of an enriched isotope, was sandwiched between two aluminium foils (each 1.0 x 1.0 x 0.03 cm) and irradiated for periods varying between 2 min and 5 h, depending on the half-life of the activation product. Beam currents were around 2.5 μA. The $^{27}Al(n,\alpha)^{24}Na$ reaction served as a monitor on the experimental conditions during each irradiation. In measurements involving tritium counting, for each investigated metal about 10 foils (each 1.0 x 1.0 x 0.1 cm) were stacked together, with an aluminium foil separating each metal foil, and the irradiation was done for about 10 h.

CROSS SECTION MEASUREMENTS

Cross sections were measured by activation and identification of the radioactive products as described in several publications from this Institute [cf. 11-13]. In the case of soft radiation emitters as well as low-yield reaction products radiochemical separations were performed [11,14]. The radioactivity of the activation product was generally determined by Ge(Li) detector γ-ray spectroscopy or Si(Li) detector X-ray spectroscopy. In some cases, low-level anticoincidence β^--counting as well as $4\pi\beta\gamma$-coincidence method was also used. Cross sections were obtained by applying the usual corrections like those for decay, β^- and γ-ray branching ratios, counting efficiency, geometry, absorption, etc.

The tritium formation cross sections were determined by vacuum extraction of tritium from the irradiated metal foils at 1000 °C followed by gas phase counting using an anticoincidence system [4].

RESULTS AND DISCUSSION

Cross Section Data and Systematics

The measured activation cross sections for some of the relatively strong reaction channels (n,2n), (n,p), (n,α) and [(n,n'p)+(n,d)] are plotted in Fig. 2 as a function of the asymmetry parameter (N-Z)/A. The cross section data and the preliminary trends described here for 30 MeV d(Be)-break-up-neutrons have been observed for the first time. The trends are somewhat similar to those at 14 MeV [1,3]. As is evident, in the light mass region the reactions involving the emission of charged particles compete strongly with the (n,2n) process. With increasing asymmetry, however, the cross section of the (n,2n) process increases and, as a general feature, those of processes involving the emission of charged particles decrease. For a detailed analysis of the systematic trends more data are needed.

Cross sections for some of the other high threshold processes like (n,3n), (n,n'α) and (n,^{3}He) investigated by the activation technique are given in Table I. As yet the data are too few to discern any systematic trends.

The tritium formation cross sections of some of the constituents of potential first wall and structural materials, determined by tritium counting, are given in Table II. It seems worth mentioning that the tritium formation cross section for stainless steel determined experimentally agress well with that estimated from the tritium formation cross sections of the individual constituents of SS.

Integral Data and Average Cross Section Values deduced from the Excitation Functions

For a few nuclear reactions we obtained average cross sections $\bar{\sigma}$ (effective for the neutron spectrum given in Fig. 1) by an integration of the known excitation functions [15-17]. The values are given in Table III and are compared with our experimental data obtained by integral measurements. Both sets of data agree within about 20%. This may be considered as rather good

since in the energy region above 20 MeV some of the excitation functions have large errors. This adds confidence to our experimental data, especially in those cases where the excitation functions are not known.

Comparison of 30 MeV d(Be) and 14.5 MeV Data

The ratios of cross sections for 30 MeV d(Be) neutrons measured in this work to those reported for 14.5 MeV neutrons [18] are shown as a function of the asymmetry parameter (N-Z)/A in Fig. 3: (A) for (n,2n) reactions, (B) for [(n,n'p)+(n,d)] reactions, (C) for (n,p) reactions and (D) for (n,α) reactions. Whereas for (n,α) reactions the ratio is practically constant, in the case of (n,2n) and (n,p) reactions, with increasing (N-Z)/A the ratios decrease, apparently due to increasing competition from the (n,3n) and (n,n'p) processes, respectively. The ratios for the [(n,n'p)+(n,d)] reactions increase with increasing (N-Z)/A.

From Fig. 3 it is apparent that, due to the generally lower (n,2n) cross sections of potential structural materials with 30 MeV d(Be) neutrons than with 14.5 MeV neutrons, the neutron multiplication factor will be slightly lower in the fusion materials irradiation test facility (FMIT) than in the case of intense 14 MeV neutron sources. This will, however, be partly compensated by the (n,3n) process (cf. Table I) which at 14.5 MeV is energetically not possible.

As far as hydrogen production in structural materials is concerned, at 14.5 MeV the major contribution is furnished by (n,p) reactions (with the exception of some light mass nuclides which have high (n,n'p) cross sections). With the 30 MeV d(Be) neutrons, however, both (n,p) and [(n,n'p)+(n,d)] reactions will contribute almost equally.

Helium production in structural materials constitutes a very serious problem from the point of view of radiation damage. At 14.5 MeV the major source of helium production is the (n,α) reaction (with about 20% contribution from the (n,n'α) process [3]). With the 30 MeV d(Be) neutrons the (n,α) cross section is only about half of the 14.5 MeV value. On the other hand, the two (n,n'α) cross sections reported (Table I) show that the (n,n'α) contribution in the case of 30 MeV d(Be) neutrons is comparable to that of (n,α) reactions.

The (n,t) and (n,^{3}He) reaction cross sections with 30 MeV d(Be) neutrons are appreciably higher than those with 14.5 MeV neutrons. In terms of absolute magnitudes, however, these reactions constitute only weak reaction channels even at high excitation energies.

From the above discussion it appears that the total radiation damage caused in FRT materials via hydrogen and helium gas production may be the same whether 30 MeV d(Be) neutrons or 14.5 MeV neutrons are used. For a detailed interpretation of the end effects, however, in the former case a much stronger cross section data base is needed.

ACKNOWLEDGEMENTS

It is a pleasure to thank Prof. G. Stöcklin for his active support of this research programme. Acknowledgement is made to the Isochronous Cyclotron Group for their counsel and help in the construction of the Be-target and to the machine operators for performing numerous irradiations. Mr. H. Ollig and Mrs. A. Schleuter assisted appreciably in the experimental measurements. One of us (S.K.) thanks the IAEA for a fellowship and the Bangladesh Atomic Energy Commission for granting leave of absence.

REFERENCES

1. S.M. QAIM, "A Survey of Fast Neutron Induced Reaction Cross Section Data", in Proc.Conf. on Nuclear Cross Sections and Technology, Washington, D.C. (1975), NBS Special Publication 425 (1975), p. 664.

2. R.C. HAIGHT, "Review of Neutron Data: 10 to 40 MeV", in Proc.Symposium on Neutron Cross Sections from 10 to 40 MeV, Brookhaven (1977), BNL-NCS-50681 (1977), p. 201.

3. S.M. QAIM, "Recent Advances in the Study of some Neutron Threshold Reactions", in Proc.Int.Conf. on Neutron Physics and Nuclear Data for Reactors and other Applied Purposes, Harwell (1978), OECD-Nuclear Energy Agency, Paris (1979), p. 1088.

4. S.M. QAIM, R. WÖLFLE and G. STÖCKLIN, "Fast Neutron Induced [(n,t)+(n,n't)] Reaction Cross Sections in the Medium and Heavy Mass Regions", J.Inorg.Nucl.Chem., 36, 3639 (1974).

5. S.M. QAIM and R. WÖLFLE, "Triton Emission in the Interactions of Fast Neutrons with Nuclei", Nucl.Phys., A295, 150 (1978).

6. C.H. WU, R. WÖLFLE and S.M. QAIM, "Activation and Mass Spectrometric Study of ^{3}He-Particle Emission in the Interactions of Fast Neutrons with Medium Mass Nuclei", Nucl.Phys., A329, 63 (1979).

7. G.W. SCHWEIMER, "Fast Neutron Production with 54 MeV Deuterons", Nucl.Phys., A100, 537 (1967).

8. J.P. MEULDERS et al., "Fast Neutron Yields and Spectra from Targets of Varying Atomic Number Bombarded with Deuterons from 16 to 50 MeV", Phys.Med.Biol., 20, 235 (1975).

9. D.R. NETHAWAY et al., "Neutron Spectra from 30 MeV Deuterons on a Thick Beryllium Target", in Proc. Symposium on Neutron Cross Sections from 10 to 40 MeV, Brookhaven (1977), BNL-NCS-50681 (1977), p. 135.

10. M.A. LONE, "Intense Fast Neutron Source Reactions", in Proc.Symposium on Neutron Cross Sections from 10 to 40 MeV, Brookhaven (1977), BNL-NCS-50681 (1977), p. 79.

11. S.M. QAIM and G. STÖCKLIN, "A Systematic Investigation of (n,t) Reactions at 14-15 MeV on Medium and Heavy Mass Nuclei", J.Inorg.Nucl.Chem., 35, 19 (1973).

12. S.M. QAIM, "Total (n,2n) Cross Sections and Isomeric Cross Section Ratios at 14.7 MeV in the Region of Rare Earths", Nucl.Phys., A224, 319 (1974).

13. N.I. MOLLA and S.M. QAIM, "A Systematic Study of (n,p) Reactions at 14.7 MeV", Nucl.Phys., A283, 269 (1977).

14. S.M. QAIM, R. WÖLFLE and G. STÖCKLIN, "Radiochemical Methods in the Determination of Nuclear Data for Fusion Reactor Technology", J.Radioanalyt. Chem., 30, 35 (1976).

15. D.I. GARBER and R.R. KINSEY, "Neutron Cross Sections, Volume II, Curves", BNL 325 (1976).

16. A. PAULSEN, "Status Report about some Activation, Hydrogen and Helium Producing Cross Sections of Structural Materials", in Proc.Specialist Meeting on Neutron Data of Structural Materials for Fast Reactors, Geel (1977), Pergamon Press, Oxford (1979), p. 261.

17. D.R. NETHAWAY, "The $^{93}Nb(n,2n)^{92m}Nb$ Cross Section", J.Inorg.Nucl.Chem., 40, 1285 (1978).

18. S.M. QAIM, "14 MeV Neutron Activation Cross Sections", in Handbook of Spectroscopy, Vol. III, CRC Press, Palm Beach, in press.

TABLE I

Cross Sections of some weak Reaction Channels induced by Fast Neutrons

Nuclear Reaction	Q-value[a] (MeV)	Cross Section for 30 MeV d(Be) neutrons (mb)	Cross Section at 14.5 MeV[b] Exp. or [Systematics] (mb)
$^{47}Ti(n,3n)^{45}Ti$	22.07	1.10 ± 0.25	
$^{50}Cr(n,3n)^{48}Cr$	23.58	0.07 ± 0.03	
$^{53}Cr(n,3n)^{51}Cr$	20.11	10.56 ± 1.6	
$^{59}Co(n,3n)^{57}Co$	19.03	11.22 ± 1.8	
$^{58}Ni(n,3n)^{56}Ni$	22.46	0.02 ± 0.01	
$^{63}Cu(n,3n)^{61}Cu$	19.74	4.26 ± 1.21	
$^{51}V(n,n'\alpha)^{47}Sc$	10.29	3.5 ± 0.8	[2.5]
$^{65}Cu(n,n'\alpha)^{61}Co$	6.79	5.1 ± 1.3	1.7 ± 0.3
$^{51}V(n,^{3}He)^{49}Sc$	12.50	0.25 ± 0.08	[0.006]
$^{53}Cr(n,^{3}He)^{51}Ti$	12.41	0.26 ± 0.08	[0.006]

[a] All Q-values are negative.

[b] From measurements and systematics developed at Jülich [cf. 3].

TABLE II

Tritium Formation Cross Sections of some Constituents of Potential First Wall Materials in the Interactions with 30 MeV d(Be) neutrons

Target	Cross Section[a] (mb)	Target	Cross Section[a] (mb)
Al	1.51	Cr	0.33
Mn	1.40	Fe	0.41
Co	0.49	Ni	0.28
Nb	0.49	SS[b]	0.37[c]

[a] All cross sections have experimental errors of about ±20%.

[b] Stainless steel V2A (DIN 10 Cr Ni Ti 18 9) has the composition: Cr(18.00%), Ni(10.00%), Mn ($\leq$2.00%), Fe(70.00%).

[c] This experimentally determined cross section is comparable to the value of 0.38 mb obtained by taking into account the various constituents of SS.

TABLE III

Comparison of Cross Section Data obtained by Integral Measurements with Values deduced from some known Excitation Functions

Nuclear reaction	$\bar{\sigma}$ obtained by integral measurement[a] (mb)	$\bar{\sigma}$ deduced from the known excitation function[b] (mb)
$^{27}Al(n,\alpha)^{24}Na$	45 ± 8	49.2
$^{46}Ti(n,p)^{46}Sc$	126 ± 24	143.5
$^{60}Ni(n,p)^{60}Co$	82 ± 16	66.8
$^{65}Cu(n,p)^{65}Ni$	12 ± 3	9.2
$^{93}Nb(n,2n)^{92m}Nb$	178 ± 24	178

[a] Values obtained in this work.

[b] Excitation function taken from the literature [15-17].

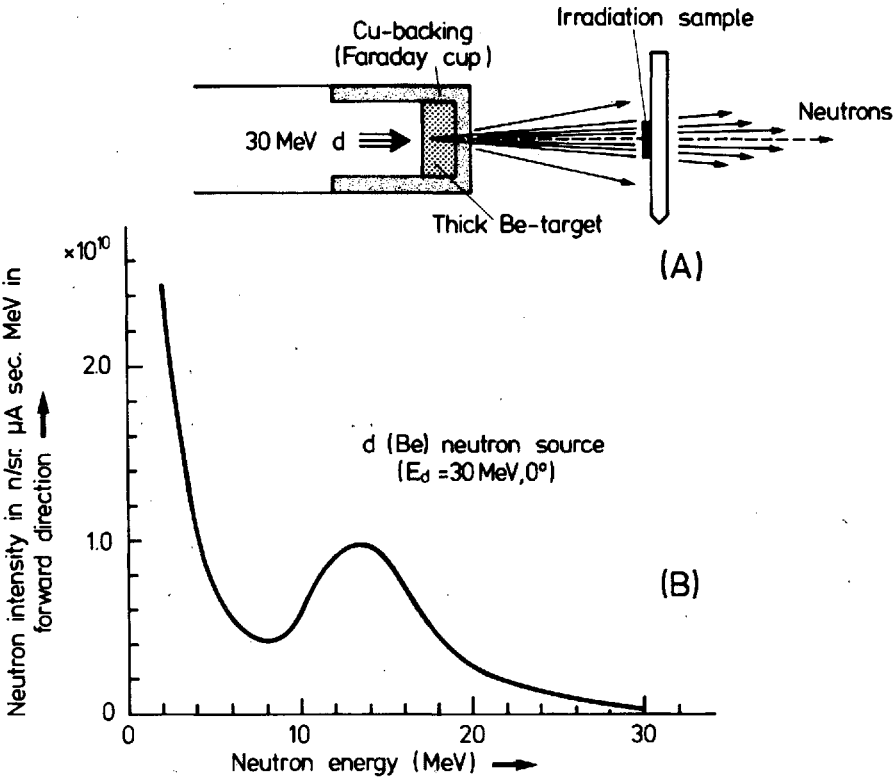

Fig. 1 (A) Experimental set-up for neutron irradiations.
(B) Yields of neutrons (n/sr. μA sec. MeV) produced in the forward direction by bombarding a thick beryllium target with 30 MeV deuterons.

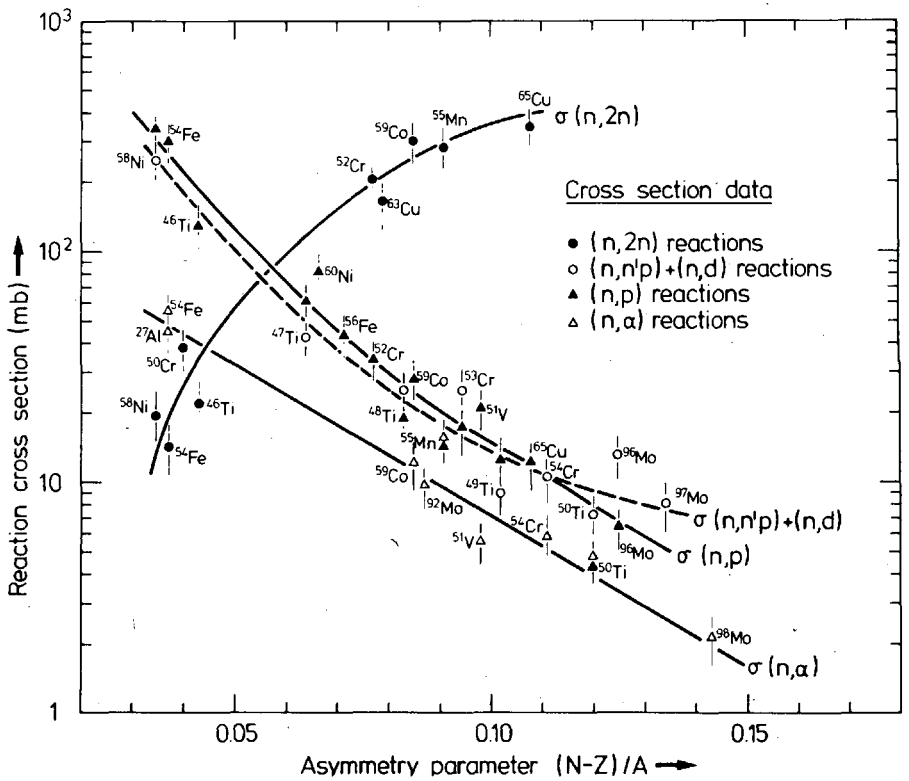

Fig. 2 Systematic trends in cross sections of (n,2n), (n,p), [(n,n'p) + (n,d)] and (n,α) reactions induced by 30 MeV d(Be) neutrons on some structural materials.

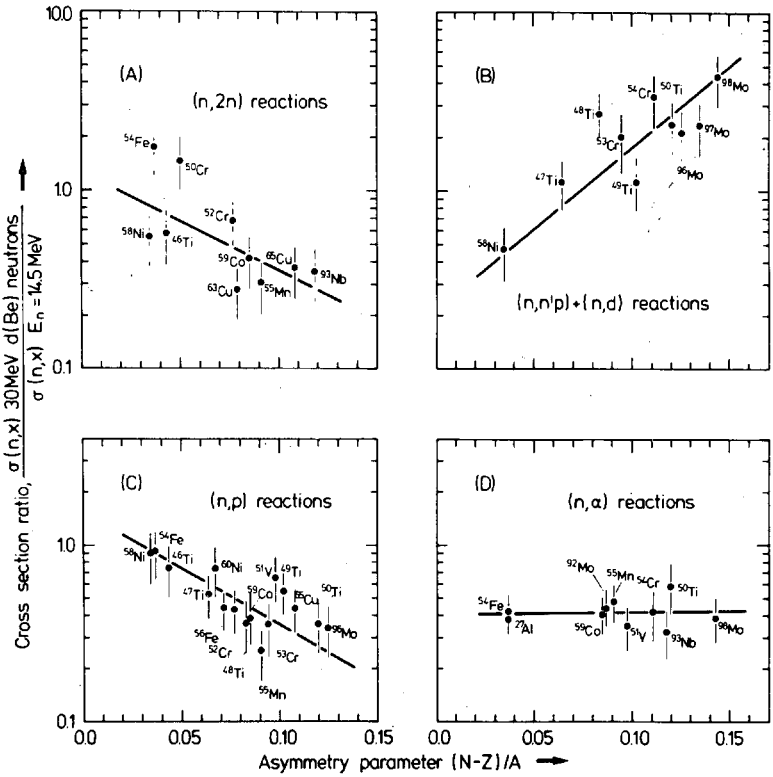

Fig. 3 $\frac{\sigma(n,x)\ 30\ MeV\ d(Be)\ neutrons}{\sigma(n,x)\ E_n = 14.5\ MeV}$ as a function of the asymmetry parameter (N-Z)/A for (A): (n,2n) reactions, (B): [(n,n'p) + (n,d)] reactions, (C): (n,p) reactions and (D): (n,α) reactions.

CROSS SECTIONS REQUIRED FOR FMIT DOSIMETRY

R. Gold, W. N. McElroy, E. P. Lippincott, F. M. Mann
D. L. Oberg, J. H. Roberts, F. H. Ruddy

Westinghouse Hanford Company
Hanford Engineering Development Laboratory
Richland, Washington 99352

ABSTRACT

The Fusion Materials Irradiation Test (FMIT) facility, currently under construction, is designed to produce a high flux of high energy neutrons for irradiation effects experiments on fusion reactor materials. Characterization of the flux-fluence-spectrum in this rapidly varying neutron field requires adaptation and extension of currently available dosimetry techniques. This characterization will be carried out by a combination of active, passive, and calculational dosimetry. The goal is to provide the experimenter with accurate neutron flux-fluence-spectra at all positions in the test cell. Plans have been completed for a number of experimental dosimetry stations and provision for these facilities has been incorporated into the FMIT design. Overall needs of the FMIT irradiation damage program delineate goal accuracies for dosimetry that, in turn, create new requirements for high energy neutron cross section data. Recommendations based on these needs have been derived for required cross section data and accuracies.

INTRODUCTION

In support of materials development for the Magentic Fusion Energy (MFE) program, the United States Department of Energy is constructing an intense neutron source known as the Fusion Materials Irradiation Test (FMIT) facility.[1,2] The FMIT facility will generate an intense source of high energy neutrons for the systematic study, evaluation and development of fusion reactor materials. The Li(d,n) reaction will be used to produce this intense neutron source. A prototype linear accelerator will provide a high current deuteron beam (~100mA, 15-35 MeV) that will impinge on a target of flowing liquid lithium. The objective for

FMIT is a maximum flux intensity of 10^{15} neutrons/(cm^2·sec) with a mean energy of 14 MeV. The unperturbed steady state neutron volume/flux goals are approximately 10 cm^3 at 10^{15} n/(cm^2·sec) and 500 cm^3 at 10^{14} n/(cm^2·sec).

With these capabilities, FMIT will provide entry into a new realm of fusion reactor material testing. No irradiation facility yet built approximates the irradiation environment planned in FMIT, and full exploitation of this unique facility demands characterization of the irradiation environment to a degree consistent with MFE materials testing program objectives. For proper characterization in the required 10 to 30% (1σ) accuracy range, FMIT facility design must be flexible enough to include both present and future dosimetry needs. These neutron and gamma ray dosimetry needs, in turn, impact on the design of the FMIT test cell and associated facilities.

To this end, design efforts have gone forward and overall dosimetry needs have been incorporated into formal FMIT design plans and specifications.[3,4] While adequate facilities are obviously necessary for dosimetry efforts at FMIT, attainable characterization accuracy also depends in good measure upon the general nuclear data base. In particular, the accuracy of selected high energy neutron cross sections is crucial in defining the limiting accuracy of neutron dosimetry attained at FMIT.

Wherever possible, methods developed and used for fission reactor environments will be relied upon for FMIT dosimetry. However, the dosimetry task for FMIT is considerably more complex. Characterization of the FMIT test volume is complicated by the following factors:

(1) Large flux component of very high energy neutrons.

(2) Steep flux and energy spectrum gradients within the test volume.

(3) Highly directional neutron flux, as opposed to the essentially isotropic flux in a fission reactor.

(4) Irregular production of secondary neutrons within the test assembly.

(5) Great sensitivity of the preceding factors to source instabilities.

As a result of extensive planning and reviews,[3,5-9] and current ASTM recommended practices,[10] it has been concluded that present state-of-the-art active, passive and calculational neutron dosimetry methods have significant shortcomings if individually applied to the characterization of the FMIT test volume environment. For example, except for the hydrogen (n,p) reaction, cross section data are barely adequate in the 2-28 MeV energy range and there is virtually no data above 28 MeV. Further, conventional active detectors may not be reliable, considering the high flux levels and large angular, spatial, and local

temporal variations of the neutron energy spectrum. Passive detectors, while more suitable for high flux environments, do not provide the necessary real time information such as temporal variations of the (d, Li) neutron source. Flux gradients, directionality and source instability militate against a characterization based largely on a calculational approach. While it is reasonable to expect technical advances tending to improve this situation over the long term, it is not reasonable to assume that these advances will eliminate the need for a multifaceted approach for FMIT dosimetry. It has, therefore, been concluded that characterization of the FMIT radiation environment will be accomplished by a prudent combination of three general approaches, namely:

(1) passive dosimetry (PD)

(2) active dosimetry (AD)

(3) calculational dosimetry (CD).

These three general approaches must be supported by evaluation and benchmarking in low intensity neutron fields [11-15] as well as by longer range efforts to improve the accuracy of general nuclear data, such as cross sections, that have a vital impact upon neutron exposure and damage correlation parameter accuracies.

Each general approach, namely Passive Dosimetry (PD), Active Dosimetry (AD), and Calculational Dosimetry (CD), calls for special program elements. The general relationship amongst PD, AD, and CD program elements is shown by block diagram in Figure 1. To implement these program elements, a number of experimental stations have been recommended for specific dosimetry purposes at FMIT. These dosimetry stations are summarized in Table I. Specific FMIT dosimetry activities which are associated with these dosimetry stations, have been identified. To provide some insight into the range of these specialities, these dosimetry activities are briefly summarized in Table II.

Clearly this range of activities encompasses a need for General Nuclear Data (GND) which extends beyond high energy neutron cross sections. These more general requirements can be easily demonstrated by citing some of the more apparent examples. Use of radiometric monitors (RM) for in-situ test assembly dosimetry (PD-2) demands the application of decay scheme branching ratios and half-lives in absolute nuclear metrology. Fission product yields are a particularly significant example, although these reactions can be regarded as partial neutron cross sections. Characteristics of (d, Li) neutron production must be adequately defined in order to develop FMIT lithium targets of high yield (GND-1). In particular, this activity includes knowledge of the straggling distribution of deuterons in liquid lithium. Application of the lithium flow dosimetry station (AD-4) for a variety of FMIT dosimetry related tasks[3] requires knowledge of specific

charged particle cross sections as well as certain decay scheme branching ratios and half-lives.

Benchmark field testing (AD-7 and PD-4) will be employed to evaluate candidate active and passive FMIT dosimetry techniques. The pragmatic utility of benchmark fields can not be over-emphasized.[6-15] State-of-the-art dosimetry techniques are as often limited by systematic effects as by lack of neutron cross section data. In benchmark field calibration experiments, these systematic effects arise in a natural way, i.e. in the same effective way which occurs in the actual application of the given dosimetry technique. Consequently, the value of such calibration experiments is that they can empirically account for very complex systematic effects and can significantly reduce or eliminate the need for precise knowledge of the absolute magnitude of many secondary dosimetry cross sections. As opposed to the absolute scale, the shape of these cross sections becomes the dominant uncertainty.

In view of the sparsity of high intensity fusion neutron fields, FMIT will be used as a benchmark. Current in-situ passive dosimetry efforts for fission reactors emphasize the need for such benchmark field referencing.[16-17] Because the fusion reactor dosimetry data base is not comparable with the fission reactor dosimetry data base, benchmark referencing is even more essential for FMIT in-situ passive dosimetry efforts. Rabbit tubes are planned at a number of key locations in the FMIT facility (see the section on Passive Dosimetry) in order to implement benchmark field calibration work.

Required neutron cross section data generated by AD, PD, and CD activities for FMIT are reviewed in the next three sections, respectively. Time and space restrictions permit inclusion of the needs of only the more relevant dosimetry activities, as enumerated in Table II. Recommendations are summarized in the last section for the high energy neutron cross section data needs of FMIT dosimetry.

ACTIVE DOSIMETRY

Active dosimetry plans for FMIT have been separated into six distinct activities (see Table II). Those activities impacting most on nuclear data requirements and singled out for emphasis here are Active Radiography (AD-1), Differential Dosimetry (AD-2), Integral Dosimetry (AD-3), and the Lithium Flow Dosimetry Station (AD-4).

Active Radiography

Active two dimensional (2D) neutron radiography is planned for the 0° dosimetry station. The 0° port will contain a pinhole collimator to produce a very narrow neutron leakage beam. The general layout of this 0° port is shown in Figure 2 and a more detailed view of a typical pinhole collimator can be found in Figure 3. The equipment vault and access plugs shown in Figure 2 provide necessary space for the 2D position sensitive detector and accessories. Active differential dosimetry can be simultaneously conducted in the 0° dosimetry station, as described below.

The active radiography systems provide the potential for extremely important on-line FMIT dosimetry information, such as:

(1) A slow response to permit feedback for determining flux time history information and integrated fluence for most test assembly irradiations.

(2) A moderately fast response (1-2 seconds) to permit feedback for operator control of focusing and beam spot position, if required.

(3) A very fast time response to also permit the generation of signals for an interlock control system which could protect both the target and accelerator, if required.

It has already been emphasized in the introduction that the intensity distribution of the source term plays a crucial role in calculations of neutron flux-fluence-spectra throughout the test cell.

Spatial resolution of active neutron-imaging systems is determined largely by the distance traveled or range of the nuclear reaction products used to infer the detection of a neutron. Nearly all active position-sensitive detectors for radiation are gas-filled ionization detectors. Quite high gas pressure is required to achieve position resolution in a neutron detector approaching one millimeter. Recently, a one dimensional proportional counter neutron detector with a spatial resolution in the 1-2 mm range has been developed.[18]

The existing 1-D position-sensitive detector could be suitably adapted for the FMIT environment by filling the tube with neon gas at modest pressure. The intent would be to detect the energy from Ne recoils, but to make the gas filling low enough so that alpha particles, protons, etc. from the walls could be biased out. In this manner, temporal and spatially dependent data could be generated for FMIT dosimetry characterization. Such a

system may also be sufficiently sensitive to detect abnormal FMIT beam behavior for the purpose of short response accelerator shutdown. Based on the experience and successful use of this 1-D detection system, a 2-D proportional counter system for FMIT application is already under development.[19-20]

The use of a 2D proportional counter using high pressure neon requires accurate knowledge of the Ne(n,n') cross section for both elastic and inelastic processes. Presumably, enriched ^{20}Ne would be used in the filling gas. Of secondary importance would be knowledge of data for high energy neutron reactions in other possible constituents of the filling gas (C, O, Xe) as well as constituents of the counter walls (e.g., Fe).

The use of ^{3}He is limited due to interference of the ^{3}He (n,n') ^{3}He recoils with the primary reaction products from the $^{3}He(n,p)\ ^{3}H$ reaction at energies above about 2.3 MeV. The use of recoils in high pressure ^{4}He is also precluded by the long range of the ^{4}He recoils which in turn will limit spatial resolution. Similarly, operational experience may dictate the use of a heavier noble gas other than Ne (such as Ar or Kr) to improve the spatial resolution. In such an event, knowledge of the (n,n') cross section and angular distribution data for these heavier noble gases becomes necessary.

Differential Dosimetry

Neutron energy differential dosimetry is planned for the 0° port using various configurations of ex-test cell detectors with signal output related to incident neutron energy. The energy spectrum of neutrons passing through the 0° collimator would be measured in near real time. Even though the 0° collimator would be configured primarily for 0° radiography (spatial distribution measurements), it would be adequate for active differential spectrometry without modification.

The specific detector system(s) to be employed for active differential dosimetry have not as yet been selected. Indeed, such systems can be expected to change over the life of the facility. The goal parameters of the spectrometer system are summarized as:

dynamic range: sub-MeV to 40 MeV

energy resolution: <10%

efficiency: $>10^{-5}$

background sensitivity (to gamma radiation):

operation in 1-10 R/hr fields

lifetime > 9 months

Several candidate systems are under consideration. They include:

(1) ^{3}He (n,p) ^{3}H gas proportional counters

(2) ^{1}H and ^{4}He recoil proportional counters

(3) Organic scintillators

(4) (n,p) magnetic spectrometer

(5) ^{6}Li (n,α) ^{3}H coincident spectrometer

(6) (n,p) thin radiator telescope[21]

(7) Two-detector, short path time-of-flight[22]

The relative advantages and disadvantages of each of these systems are summarized in Table III.

Although ^{3}He gas proportional counters can make unambiguous use of the ^{3}He (n,p) ^{3}H reaction only up to about 2.3 MeV, sufficient knowledge of reaction cross sections for this and other energetically possible reactions as well as knowledge of ^{3}He (n,n') cross sections can extend the usefulness of this technique to somewhat higher energies. Similarly, ^{6}Li (n,α) ^{3}H coincident spectrometers would be limited by competing reactions unless adequate data are available at higher energies. At higher energies such as those expected for FMIT, the ^{3}He (n,p) and Li (n,α) reactions decrease rapidly, enhancing the importance of knowing the cross sections for competing charged particle emitting reactions. A summary of expected cross section needs for FMIT differential dosimetry is contained in Table IV.

Many candidate leakage neutron spectrometers are based on (n,p) scattering in hydrogen by incorporating a hydrogenous radiator foil in the leakage beam. The thickness of such radiator foils is dictated by a trade-off between efficiency and energy resolution. In addition to hydrogen, such radiator foils invariably contain carbon and often contain oxygen. Consequently the ^{12}C(n,p) and ^{16}O(n,p) reactions can produce background in such spectrometry systems. Proper correction of these background contributions requires a knowledge of the ^{12}C(n,p) and ^{16}O(n,p) cross sections over the entire energy domain of the spectrometer system. Similar concerns have already been noted for high energy neutron spectrometry with nuclear research emulsions.[23] These needs are briefly touched upon in the Passive Dosimetry section.

Integral Dosimetry

In-cell dosimetry assemblies are planned that incorporate active integral detectors to provide time-dependent neutron intensity as well as fluence data during test irradiations. In addition, neutron and gamma heating will be measured with calorimeters.

Detectors considered for active integral dosimetry include the following:

(1) Long Counters - In a long counter[24], a detector sensitive to thermal neutrons is surrounded by sufficient moderator to thermalize the fast neutrons. Long counters have been used as reliable active integral monitors for many years; however, they have not usually been employed where the neutron energy is greater than 14 MeV. Typically, the neutron detectors have been BF_3 and ^3He proportional counters.[25] The FMIT environment with its high gamma fluxes and high energy neutrons may necessitate some variation in moderator design or some alternate detector such as a fission chamber. Such design parameters can be resolved in benchmark field tests.

(2) Fission Chambers - These are ionization chambers coated internally with ^{235}U or ^{238}U. ^{235}U coated chambers are primarily sensitive to low energy neutrons while ^{238}U chambers are more sensitive to fast neutrons. Fission chambers have high efficiency, fast response time and by using ^{235}U and ^{238}U chambers together, some degree of spectral information can be obtained. The need for gamma compensation and the effect of charged particles produced in the chamber walls by high energy neutrons will be determined by benchmark field testing.

(3) Self-Powered Neutron Detectors - In a self-powered neutron detector, charged particles produced when a neutron interacts with the emitter, are collected to produce a current proportional to the rate of neutron absorption. Self-powered neutron detectors are very small in size, simple to operate and, by use of various emitter materials, provide some degree of spectral information. Although the small size of the detector causes the efficiency to be low, they are a viable candidate for test assembly "steering" detectors. As "steering" detectors they would be mounted in pairs, one to either side and one above and below the test assembly. Their response can therefore be used to "steer" the test assembly so as to attain maximum exposure fluence over an irradiation cycle. The experimental test assembly would be moved to maintain a constant ratio of the detector pair signal difference to the detector pair signal sum. This technique normalizes the detector output variations for changes in detector sensitivity, energy spectrum, and intensity to give a first order output of position.

The use of these integral detector systems impacts on data needs primarily in the area of fission cross sections. A minimum requirement is that the total fission cross sections for $^{235}U(n,f)$ and $^{238}U(n,f)$ be known over the entire range of FMIT neutron energies. Other fission reactions, such as $^{232}Th(n,f)$ and possibly higher threshold fission reactions such as $^{226}Ra(n,f)$ could also prove useful. The usefulness of high threshold (n,f) reactions is discussed further in the section on Passive Dosimetry.

Lithium Flow Dosimetry Station

A lithium flow dosimetry station is being considered for FMIT that utilizes either high resolution Ge detectors or high efficiency NaI scintillators to measure radioactivants in the flowing lithium. The role of this lithium flow station is significant for FMIT dosimetry in that it provides:

(1) Time history information on the total neutron yield.

(2) Source neutron spectrum stability information.

(3) Li target impurity information.

(4) Li flow stability information.

At the Li-flow dosimetry station, as shown in Figure 4, gamma detectors view the lithium transport pipe through appropriate gamma-ray collimators at selected distances downstream of the target. The need for two spaced collimators is dictated by the complexity of the FMIT system. The intensity attained by a particular radioactivant depends principally upon several factors, namely:

(a) Total neutron yield

(b) Lithium impurities

(c) Lithium flow rate

(d) Deuteron beam characteristics*

Since different radioactivants can be selected for specific purposes by the on-line analysis of gamma-ray spectral data, this system possesses considerable power and versatility. The fundamental utility of the Li flow station for FMIT dosimetry will be illustrated using some typical radioactivants. However, an exhaustive study of this system has not as yet been performed, including Li flow characteristics downstream from the target.

---

*In particular, absolute beam intensity and beam energy distribution are the most pertinent characteristics.

Consequently, the examples presented here cannot be rigorously defended, but rather serve as only illustrations of overall system capability.

A. ^{8}Li Activity - The direct interaction of the FMIT deuteron beam in the flowing liquid lithium target will produce 0.844 sec ^{8}Li activity. This nuclide possesses an exceptionally strong β^- decay, $E_{max} \cong 13$ MeV. Hence through high energy bremstrahling production, it is a suitable candidate for time-history total neutron yield monitoring. The upper end of observed gamma spectra say $E_\gamma \gtrsim 10$ MeV, can be used to isolate the ^{8}Li activity with improved signal-to-background-ratio.

Corrections due to variable lithium flow rate can be readily performed, since such corrections depend only on the response ratio of the two detectors. The 0.844 sec half-life of the ^{8}Li decay is almost ideal for two collimators spaced approximately one meter apart. The upper collimator should obviously be located as close as possible to the external face of the test cell floor, as indicated in Figure 4. Actually the ratio of these responses supplies the lithium flow rate in terms of the known ^{8}Li half-life. This observed flow rate can then be used as a normalization factor for the time-history total neutron yield data. As opposed to monitoring from the fixed in-cell dosimetry assemblies as previously described, this method is essentially independent of beam location and effectively integrates over the entire 4π solid angle subtended by the source.

B. ^{16}N Activity - The interaction of the FMIT neutron source with oxygen impurity in the lithium will produce 7.13 sec - ^{16}N activity through the ^{16}O(n,p) reaction. This nuclide has an extremely energetic β^- decay, $E_{max} \cong 10.4$ MeV, and possesses very energetic gammas at 6.13 MeV (100%) and 7.11 MeV (7%). The ^{16}N activity observed at either collimator will obviously depend upon factors (a)-(d), above. Factors (a) and (c) can be accounted for using the ^{8}Li data as described above. In order to ascertain factors (b) and (d), one can measure activities that arise from alternative reactions in the oxygen impurity.

The (n,2n) and (n,3n) reactions on ^{16}O produce 122 sec - ^{15}O and 70.6 sec ^{14}O, respectively. Both these nuclides possess β^+ decay, with $E_{max} = 1.72$ and 1.81 MeV, respectively. However, ^{15}O does not possess any characteristic gamma transitions whereas ^{14}O has an intense gamma at 2.31 MeV (99%). The thresholds of these three reactions on ^{16}O, namely (n,p), (n,2n) and (n,3n) are approximately 11 MeV, 18 MeV, and 29 MeV, respectively. Hence observation of the relative intensities of ^{14}O to ^{16}N at either or both gamma-ray collimators would provide information on the spectral stability of the source, independent of long-term fluctuations in oxygen impurity.

In order to determine absolute oxygen impurities, the absolute efficiency of the gamma detectors must be measured and cross sections for the above mentioned reactions must be known. It would be preferable to measure this efficiency over the entire gamma energy region of applicability to FMIT, ~0.1-13 MeV. A simple alternative for oxygen impurity observations would be to spike the lithium with a known addition of ^{16}O and observe the increases in ^{14}O and ^{16}N activities.

In many cases, only relative counts are required between the two detectors, coupled with accurate knowledge of the half-life. However, to determine flow characteristics and relative source intensity, a minimum requirement for absolute source characterization is to know the production cross sections for all energetically possible reactions of deuterons on lithium that will result in detectable activation products. The half lives of the products of these reactions, which are summarized in Table V must also be known.

PASSIVE DOSIMETRY

Passive dosimetry plans for FMIT have been separated into three distinct activities (See Table II). The complexity of FMIT characterization as described in the introduction makes extensive use of in-situ passive neutron dosimetry essential. The adaptation and extension of currently used multiple foil techniques for this environment are important efforts because of the need to determine neutron flux-fluence-spectra over a very large region. The specific need, however, will depend on the application; i.e., interpretation of dosimetry results, calculation of damage exposure values and units, and facility operation. Passive dosimetry will be used both in short term exposures, such as with individual foil benchmark field calibrations associated with the rabbit tube system, and long term test assembly exposures lasting from weeks to months to years.

Multiple Foil Flux-Fluence-Spectra Determination

The multiple foil dosimetry technique utilizes a group of reactions which selectively sample neutrons of different energies. A well chosen set will provide data sensitive to the neutron flux-fluence-spectrum over the entire energy range of interest. In the case of FMIT the energy range extends from thermal to 40-50 MeV. The measured reactions or reaction rates are then used, together with a calculation or best estimate of the neutron spectrum (see the Section on Calculational Dosimetry), to determine a solution that is self-consistent with the available data.

The energy range over which a given reaction possesses a ... neutron response is one of the more important characteristics used in the selection of multiple foil dosimetry sets.

If we define E_f using the equation

$$f = \frac{1}{\bar{\sigma}\ \Phi_{tot}} \int_0^{E_f} \Phi(E)\ \sigma(E)dE, \qquad (1)$$

where f is the fraction of energy sensitivity below E_f for a given reaction,

Φ_{tot} is the total flux, and

$$\bar{\sigma} = \frac{1}{\Phi_{tot}} \int_0^{\infty} \sigma(E)\ \Phi(E)dE, \qquad (2)$$

then we can calculate E_{min} as the energy above which 95% of the sensitivity lies (f=.05), E_{mid} as the median sensitivity (f=.50), and E_{max} as the upper energy for 95% of the sensitivity (f=.95). In order to carry out these calculations, the cross sections and fluxes must be known within reasonable accuracies over the entire energy range of importance.

A limited number of high energy neutron induced reaction cross sections have been experimentally measured in recent years.[5-9, 26-30] Some have been reported at this conference[31]. The cross sections used in the following study are from Greenwood.[26] Improved integral and differential cross section measurement results will be used, along with better calculated cross sections, as they become available. Extension of ENDF/B-V data to a higher energy range (up to about 50 MeV) is presently required for FMIT applications.

The neutron flux spectrum has been calculated using Monte Carlo programs [32-34] for various positions within the FMIT test cell, both with and without simulated test modules in place. In spectral regions of relatively low flux the errors in these calculations are large. This problem is particularly important for the low flux test positions in the rear of a loaded test cell where significant amounts of flux are below 1 KeV.

Sensitivity calculations have been carried out using Equations (1) and (2) with cross sections and neutron spectra taken from the referenced sources. The results are presented in Table VI for sensitivity limits in the neutron spectrum at the position closest to the front of the forward Horizontal Test Assembly (HTA), which is Monte Carlo Zone 1. This table also includes the reaction product half-lives which are discussed below.

Table VII gives characteristics of the total flux and neutron spectra at various positions calculated for a partially loaded test cell. As described in Table VII, Zone 1 is at front and center, Zone 5 is slightly above the beam spot (FWHM 1x3 cm), Zone 51 is

at the rear of the second HTA, and Zone 108 is at the rear of the test cell with a substantial amount of material (assumed to be stainless steel) between it and the lithium target. Spectral averaged cross sections for these four locations are given in Table VIII.

Some examples of plots of sensitivity vs. energy are shown in Figure 5. These examples are only for the neutron spectrum in Zone 1; sensitivity plots at the rear of the test space in the cell are not presented due to the uncertainties noted above. However, it is expected that the dosimetry techniques which have been developed by Greenwood et al.[5-8] for MFR programs and others for LWR and FBR applications[11-17] will be sufficient, for the most part, to characterize the flux-fluence-spectrum at such positions.

For similar reasons, one should be cautious of several of the (n,γ) reactions which seem to show sensitivity limits of 20 MeV or so. The cross sections for (n,γ) reactions on ^{23}Na, ^{45}Sc, ^{59}Co, ^{63}Cu, and especially ^{58}Fe show substantial excitation of the giant dipole resonance at about 20 MeV; however, the flux averaged cross sections are relatively low. Thus, any thermal component could very likely overshadow this effect.

The goal of FMIT dosimetry is to provide the experimenter with accurate neutron flux-fluence-spectra at all positions in the test cell. Passive radiometric monitors (RM), solid state track recorders (SSTR), and helium accumulation fluence monitors (HAFM) will be used to provide measured integral reaction and reaction rate input data for SAND[35-37], STAYSL[38], FERRET[39] or other codes to determine absolute values of flux-fluence-spectra. Since these adjustment codes do not yield unique results, and to paraphrase a recent review by D. L. Smith[9], "it is reasonable to ask how one can deduce from in-situ passive dosimetry the most likely spectrum representation and estimate its uncertainty from available integral data and evaluated differential dosimetry cross sections". Perey[38] and Schmittroth[39] addressed this problem and developed least squares procedures which answer this question in a rigorous manner. A variation of the FERRET least squares approach has been used for performing evaluations of iron dosimetry cross section data.[40]

The least squares approach uses matrix alegbra techniques and covariance matrices must be provided for the trial spectrum, for the differential cross sections, and for the integral reaction rates. To again paraphrase D. L. Smith for flux-fluence-spectra determination, "this requirement is both a source of strength and of weakness in this approach. The strength lies in the fact that all uncertainties in the unfolding procedure are considered and the unfolded spectrum is the best estimate (in the least-squares sense) which the available information can provide. The weakness is that it is very difficult to provide realistic covariance

matrix elements (especially off diagonal elements representing cross correlation effects). Use of inadequate matrix elements can thwart the process and lead to unreasonable results. It is generally accepted that this formalism is the logical way to proceed, at least, for the long run. Steps are being taken to implement it (e.g. inclusion of covariance matrices in ENDF/B-V). Experience gained over the next few years should establish whether it is a practical approach for routine dosimetry. In the meantime, it is likely that many other methods will continue to be used."

The adjusted flux-fluence-spectra which such codes produce have uncertainties and errors from several sources: measured RM,SSTR, and HAFM total reactions or reaction rates, cross sections, and the non-uniqueness associated with solving a set of reaction (or reaction rate) equations. Goal accuracies for neutron fluence-spectra have been established in support of FMIT design activities and are listed in Table IX.

In order to meet these goal fluence accuracies, cross sections must be known to an accuracy approximately as good as the best goal accuracy for fluence determination at energies at which they have a significant sensitivity. Required accuracies and priorities have been called out in Table VI. It should be noted that these requirements basically refer to relative accuracies; suitable integral measurements in high intensity benchmark fields, together with validation of calculational techniques, can provide the required absolute and relative correlations necessary for FMIT dosimetry and materials damage studies.

Using ENDF/B-V, an ENDF/A adjusted dosimetry cross section file will be established for RM, SSTR, and HAFM sensors for FMIT Passive Dosimetry. The procedures that will be used for adjustment are discussed elsewhere,[11-15] and it is anticipated that codes such as SAND II, FERRET, and STAYSL will be used for making the adjustments and developing a consistent uncertainty and error* file together with the basic energy dependent cross section file.

Passive Reaction and Reaction Rate Measurements

Passive reaction and reaction rate measurements can be made using several techniques which will be described below. These measurements depend on locating monitors at positions in the neutron field, removing the monitor after the irradiation, sectioning the monitor as required, and measuring the number of reactions that occured.

*Uncertainty in the sense treated here is a scientific characterization of the reliability of a measurement result and its statement is the necessary premise for using these results for applied investigations claiming high or at least stated accuracy. The term error will be reserved to denote a known deviation of the result from the quantity to be measured. Errors are usually taken into account by corrections.[41]

Techniques that can be applied include radiometric, solid state track recorders, and helium accumulation fluence monitors. These techniques possess complementary capabilities and selection criteria for a particular application include:

(1) Sensitivity

(2) Time response

(3) Energy response

(4) Spatial resolution

(5) Absolute accuracy and precision

The sensitivity is of particular importance for short (or low fluence) irradiations where detection of reactions may be difficult. These measurements can be made using short half-life reaction products or SSTR. For longer irradiations, sensitivity is not usually a problem but long half-life or stable products must be used to provide a good integration over the exposure. SSTR are particularly valuable for measurement of long, low-fluence exposures, while HAFM will be valuable for high-fluence.

To determine neutron flux- or fluence-spectra, it is necessary to use several reactions to measure neutrons of various energies. In contrast to fission reactors where a few (as little as two or three) reactions can, in some cases, provide a reasonable response that provides broad range adjustments of the flux-spectrum, the rapidly changing spectrum in FMIT and the need to attain higher spatial resolution will necessitate using a larger number of reactions.

Radiometric Techniques

Measurements of reactions using radiometric techniques depend on production of an unstable product that decays with a convenient half life. Short half-lives are useful to obtain high sensitivity (large number of disintegrations per second) for shorter irradiations whereas long half-life products provide better integrations over long exposures. The optimum lifetime is therefore about the same as the run duration. Table VI lists half-lives for a number of candidate reactions. From this list, foil sets can be selected to provide complete neutron energy coverage (as depicted in Figure 5).

It has been noted above that there is a paucity of very high energy cross section data, especially at short and long half-lives. Bayhurst, et al,[27] and Vesser, et al,[28] present cross section data up to 28 MeV and 24 MeV for several (n,xn) reactions leading to products with relatively long half-lives (Table X). However, these cross sections need to be extended to still higher energies. Two reactions which might be useful for very long term (service life of FMIT) exposures would be ^{159}Tb (n,2n) ^{158}Tb and ^{109}Ag (n,2n) ^{108m}Ag.

The test cell dosimetry systems for FMIT will include provision for a rabbit system for rapid transfer of monitors from referenced (benchmark field) irradiation positions to a service cell and in- and ex-service cell counting systems. A few of the possible candidates for investigating high energy neutron fluxes at short half-lives are shown in Table X.

It has been stated that there will be considerable damage to the magnets in a MFE power plant resulting from long term exposures of energies between 0.1 and 1 MeV.[42] For this region, boron shielded RM, SSTR, HAFM, and inelastic scattering reactions leading to isomeric states would be very useful. Reactions of this type are characterized by a rather low threshold energy. A candidate reaction used in fission reactors is $^{93}Nb(n,n')^{93m}Nb$. ^{93m}Nb has a half-life of 13.6 years and a threshold energy of 30 KeV. Many other reactions of this type exist with varying threshold energies. Some of these are listed in Table X. It will be noted that many of these have very short half-lives and thus are good candidates for use with the previously mentioned rabbit system. During FMIT irradiation cycles, the rabbit tube will usually be used in the rear of the test cell where the neutron spectrum will be substantially moderated by the forward test assemblies as well as wall return neutrons. It is just such a spectrum as this where neutrons of lower energies can be very important in producing damage to magnets and structural components.

Solid State Track Recorders

Solid State Track Recorder (SSTR) dosimeters consist of an appropriate dielectric material such as mica or quartz crystal placed in firm contact with a deposit of fissionable material as shown in Figure 6. In the case of SSTR dosimeters, the total fission cross section is the quantity of interest. In addition to cross section data for conventionally used thermal and threshold reactions, such as $^{235}U(n,f)$, cadium and boron covered $^{235}U(n,f)$, $^{237}Np(n,f)$, $^{238}U(n,f)$, and $^{232}Th(n,f)$, cross section data for higher threshold fission reactions will undoubtedly be of value in the FMIT spectrum.

^{226}Ra with an approximate fission threshold of about 3 MeV is a good candidate for further and more accurate cross section measurements. The available data for neutron induced fission of nuclides lighter than ^{226}Ra is sparse. Fission barrier systematics[43] indicate that $^{209}Po(109y)$ and $^{210}Po(138d)$ have fission thresholds of 13 MeV and 15 MeV, respectively. The half-lives of these target nuclides limits their use to all but the highest fluence applications. Table XI contains fission threshold data for a number of convenient target nuclides. These fission thresholds were estimated by using mass data and Z^2/A trends in the

height of the fission barrier. Although the use of these threshold reactions will be limited by anticipated low cross sections and concomitant problems from contamination of dosimeters with more fissionable naturally occurring nuclides, such as ^{232}Th and isotopes of uranium, data on any or all of these reactions would undoubtedly be of value.

Helium Accumulation Fluence Monitors

Although HAFM have only been used to a limited extent in fission reactors, increased applicability has been forecasted for high energy neutron fields. Applications have already been made and measurements in a Be(d,n) neutron field are reported at this conference.[44]

Application of the HAFM technique involves measurement of total helium produced in a sample. In contrast to helium production cross sections in fission spectra, cross sections in FMIT will be nearly the same in magnitude. This simplifies the need to have such high purity materials (expecially low in boron) but limits the use of capsules for helium containment since generation in the capsules may be comparable to the sample. However, bare wire samples can be used, provided they can be shown to retain the helium at irradiation temperatures. The outer layers of the wire, from which helium is lost to, or implanted from, the surroundings must be etched away prior to measurement.

Helium production cross sections are poorly known at high energies. A variety of reactions must be included to determine the total helium produced, e.g. (n,α), $(n,n\alpha)$, $(n,2\alpha)$, etc. Much of the cross section evaluation in the FMIT energy region will depend on integral measurements using HAFM.

Flux Contour Mapping

As stated above, the rapid variation of flux and spectrum in FMIT makes mapping a particular challenge. All of the techniques discussed above (RM, HAFM, and SSTR) will be used. Reactions will be selected which are less sensitive to spectral changes for fluence measurements and reactions of higher efficiency can be used to monitor beam variations.

In the highest flux test assembly, volume for materials testing will be severely limited as will the space for available dosimetry. Therefore, single dosimeters that can provide multiple reactions will be particularly valuable. Examples are $^{197}Au(n,\gamma)$, (n,p), (n,2n), (n,3n), (n,4n), (n,α) and $^{59}Co(n,\alpha)$, (n,p), (n,2n), (n,3n), and (n,4n). Sensitivity plots for the gold reactions are presented in Figure 7.

Passive flux contour maps of the FMIT neutron source will be needed for maximizing test assembly exposure fluences. These passive techniques will complement active dosimetry methods that have already been described. RM[6] and HAFM[44] have been used to

provide neutron intensity contour maps of high energy neutron sources. SSTR can also be employed to this end. Indeed, these three passive techniques possess complimentary capabilities for mapping neutron source intensity contours. In fact, of these complimentary attributes perhaps the most important for contour mapping are those general selection criteria already cited for passive reaction rate measurements.

While these neutron intensity contour maps are useful, what is actually needed for FMIT calculational dosimetry is the angular flux, $\phi(\underline{r},\underline{\Omega},E)$, emitted from the source. In this context, a neutron source intensity contour map represents a complex folding of this angular flux over the geometry and energy sensitivity of the particular passive monitor.

An important example of SSTR contour mapping is the use of isotopes such as ^{226}Ra for neutron activation alpha autoradiography. In the FMIT neutron field, the following reactions will be induced in ^{226}Ra:

$$^{226}Ra(n,2n)^{225}Ra \xrightarrow[14.8d]{\beta^-} {}^{225}Ac \xrightarrow[10.0d]{\alpha}$$

$$\beta^- \swarrow 3.9m$$

$$^{226}Ra(n,pn)^{225}Fr$$

The ^{225}Ac alpha particles with an energy of 5.83 MeV can be easily discriminated from ^{226}Ra 4.78 MeV α particles by differential etching of the SSTR or the use of absorbers. Furthermore, the induced alpha activity becomes greater than the ^{226}Ra alpha activity after about five hours. After exposure to FMIT neutrons, the foil containing ^{226}Ra would be placed in firm contact with a suitable SSTR (e.g., CR-39 polymer, cellulose nitrate, or makrofol E), and the spatial distribution of the resultant α-track density can be related to the source neutron intensity distribution. Usable track densities can be obtained from the FMIT source in as little as 30 minutes.

For exposure periods greater than about 10 days, sensitivity decreases due to the fact that an increasingly larger fraction of the activity results from times near the end of the exposure. For these cases, the following reaction becomes most useful:

$$^{233}U(n,2n)^{232}U \xrightarrow[72y]{\alpha}$$

This reaction provides the necessary sensitivity for irradiation periods from days through the total lifetime of FMIT.

Although the use of SSTR is planned to give an autoradiographic image of the neutron source contours, an appropriate scintillator coupled to a videcon could be used to give a more rapid readout from the autoradiography foil for both dosimetry and

diagnostic purposes. Source movement (due to beam drift) or serious source anisotropies could be rapidly detected using ^{225}Ac autoradiographs and this information can then be used for correcting calculational dosimetry codes. It could also be supplied to FMIT operations in order to correct such undesirable effects.

For longer term operation, ^{233}U containing foils could be placed on all available surfaces of test assemblies to provide intensity contours for the neutrons that are entering and leaving the test assemblies. This information will aid in interpreting the data obtained from passive in-situ dosimeters that are contained inside the test assemblies.

Absolute neutron flux determinations using ^{225}Ac autoradiography will require accurate knowledge of both the $^{226}Ra(n,2n)$ and $^{226}Ra(n,pn)$ cross sections (a determination of the sum of these two cross sections will suffice in this case) as well as accurate knowledge of the half-lives for β^- decay of ^{225}Fr and ^{225}Ra and for α decay of ^{225}Ac. Similarly, the $^{233}U(n,2n)$ cross section must be accurately known along with the ^{232}U half-life.

Passive Spectrometry

Passive spectrometry can be carried out using the well known cross section for neutron scattering from hydrogen. Emulsion techniques for observations of high energy angular neutron flux have already been reviewed at the first of these symposia.[23] Included in that review were emulsion cross section requirements for charged particle reactions useful in high energy neutron spectrometry as well as for reactions which produce background in emulsion observations. To date, the status of these needs have not changed.

The potential uses of CR-39 polymer SSTR for FMIT passive dosimetry are discussed in detail in a companion paper at this conference.[45] In addition to H(n,p) cross section, specific SSTR applications may make use of other charged particle emitting reactions such as $^{6}Li(n,\alpha)^{3}H$ and $^{10}B(n,\alpha)^{7}Li$. The need for better $^{6}Li(n,\alpha)$ and $^{10}B(n,\alpha)$ cross sections and data for other alpha particle emitting reactions has already been cited for HAFM applications.

CALCULATIONAL DOSIMETRY

Calculational dosimetry plans for FMIT have been separated into four distinct activities (see Table II). The methods to be used in calculational dosimetry will be very similar to those used in the design of FMIT.[46] There are, however, three important differences:

(1) the need for increased accuracy,

(2) the need to include the spatial distribution of the source,

(3) the varied contents of the test modules.

The needs of design, chiefly shielding, are mainly met with conservative assumptions. In contrast, for calculational dosimetry all assumptions must be as accurate as possible. Actual deuteron beam distributions and actual sample compositions must be included. The methods are in place for such calculations; the main uncertainties lie in nuclear data.

The samples will be very near the neutron source (∿0.7 to 10 cm) which itself is distributed in space (∿1.5 cm thick x ∿3 cm wide x ∿1 cm high). Thus thick target yields at one bombarding energy are not sufficient, rather the neutron spectra for thin target thicknesses are needed. This need has been met for design purposes by taking the available thick target measurements (E_d=15 to 40 MeV) and fitting classical models to the results.[47] The accuracy of this procedure awaits thin target measurements and/or flux measurements near the distributed source.

The last major difference, the need to accurately include the composition of the test modules, is probably the most significant. Current designs indicate that the volume fractions will be 39% Na, 25% samples, 25% void, 11%K. Since the bulk of the samples will be iron or nickel based alloys, the neutron transport cross sections for Na, Fe, K, and Ni will be the most important. The iron cross sections are the best known, having total elastic cross sections over the main energy range of interest (∿1 Mev to ∿30 MeV). The situation is much worse for Na and K where no such data exists above 20 MeV, and the data above fast breeder reactor energies is skimpy. Much work is needed for these isotopes as well as for non-elastic cross sections for all isotopes. It is very likely that model calculations[31] verified by a few experiments will form the bulk of the nuclear data base. In particular, recent descriptions based on preequilibrium angular distribution will greatly aid this task.[48]

RECOMMENDATIONS

As recommended above, characterization of the neutron field in FMIT requires dosimetry reaction cross section data at selected energies in the 1 to 50 MeV range. Data are needed as soon as possible to improve the accuracy of design calculations and planning for dosimetry systems and by 1983 to support initial FMIT operation. Requests for some of these data have already been tabulated.[49-50] Tables IV, VI, and X present updated information related to such requests.

To meet various measurement requirements (sensitivity, half-life, etc.) cross section data on a rather large number of reactions must be developed. In addition, since all the requested cross section data accuracies will not be attained, redundancy is required to reduce the errors in flux-fluence-spectral unfolding. To maximize the data value, a plan for cross section measurements should be developed. This plan should include provision for combining differential measurements with integral reaction rates

in the best characterized (benchmark) high energy neutron fields to produce a self-consistent cross section set with well defined accuracies (covariances). In this way a relatively few well-planned measurements coupled with calculations could produce the desired cross section information and accuracies.

ACKNOWLEDGEMENT

This work was performed at HEDL in support of the Fusion Materials Irradiation Test (FMIT) facility under contract to the U. S. Department of Energy.

REFERENCES

1. E. W. Pottmeyer, Jr., "Construction of a High Intensity Deutron Linac with an Energy 35 MeV and an Intensity of 100mA CW", HEDL-SA 1652, Sixth All-Union National Conference on Particle Accelerators, Dubna, USSR, October 11-13, 1978.

2. E. W. Pottmeyer, Jr., "The Fusion Materials Irradiation Test Facility at Hanford", HEDL-SA 1734, Hanford Engineering Development Laboratory, Richland, WA, 1979.

3. R. Gold, W. N. McElroy, J. L. Fuller, E. M. Sheen, and R. Dierckx, "Dosimetry Program for Characterization of the FMIT Facility", Third International ASTM-EURATOM Symposium on Reactor Dosimetry, Ispra (Varese), Italy, October 1-5, 1979.

4. R. E. Schenter, F. M. Mann, and D. L. Johnson, "Nuclear Data Needs for FMIT", Proceedings of the International Conference on Nuclear Cross Sections for Technology, October 22-26, 1979.

5. R. R. Heinrich, L. R. Greenwood, G. R. Odette, H. Farrar, IV, R. Dierckx and R. Gold, "Dosimetry Needs for the Magnetic Fusion Materials Program", Proceedings of the Second International ASTM-EURATOM Symposium on Reactor Dosimetry, Vol. 3, NUREG/CP-0004, Palo Alto, CA, p. 1017, October 3-7, 1977.

6. L. R. Greenwood, "Status of Current, Routine Dosimetry at Existing Irradiation Facilities: Flux-Spectrum Mapping at ORR, RTNS II, and U.C. Davis Facilities", Third International ASTM-EURATOM Symposium on Reactor Dosimetry, Ispra (Varese), Italy, October 1-5, 1979.

7. L. R. Greenwood, et al., "Integral Tests of Neutron Activation Cross Sections in a $^{9}Be(d,n)$ Field at E_d=40MeV", Nucl. Sci. Engr. 72, 175-190 (1979).

8. L. R. Greenwood, "The Status of Neutron Dosimetry and Damage Analysis for the Fusion Materials Program", Proceedings of the International Conference on Nuclear Cross Sections for Technology, Knoxville, Tenn., October 22-26, 1979.

9. D. L. Smith, "Neutron Dosimetry for Radiation Damage in Fission and Fusion Reactors", Proceedings of the International Conference on Nuclear Cross Sections for Technology, Knoxville, Tenn., October 22-26, 1979.

10. ASTM Standard Practice for Conducting Irradiations at Accelerator-Based Neutron Sources, ASTM E10.08 Standard, October 1979.

11. Proceedings of Consultants' Meeting on Integral Cross-Section Measurements in Standard Neutron Fields for Reactor Dosimetry, Vol. I and II, IAEA-208, Vienna, Austria, 1978.

12. J. Grundl and C. Eisenhauer, "Benchmark Neutron Fields for Reactor Dosimetry", Proceedings of Consultants' Meeting on Integral Cross-Section Measurements in Standard Neutron Fields for Reactor Dosimetry, Vol. I, IAEA-208, Vienna, Austria, p. 53, 1978.

13. A. Fabry, J. A. Grundl, E. P. Lippincott, W. N. McElroy, and H. Farrar, IV, "Status Report on Dosimetry Benchmark Neutron Field Development, Characterization and Application", Proceedings of the Second ASTM-EURATOM Symposium on Reactor Dosimetry, Vol. 3, NUREG/CP-0004, Palo Alto, CA, p. 1141, October 3-7, 1977.

14. W. N. McElroy, R. Gold, E. P. Lippincott, A. Fabry, and J. H. Roberts, "Spectral Characterization by Combining Neutron Spectroscopy, Analytical Calculations, and Integral Measurements", Proceedings of Consultants' Meeting on Integral Cross-Section Measurements in Standard Neutron Fields for Reactor Dosimetry, Vol. I, IAEA-208, Vienna, Austria, 1978.

15. A. Fabry, W. N. McElroy, L. S. Kellogg, E. P. Lippincott, J. A. Grundl, D. M. Gilliam, and G. E. Hansen, "Review of Microscopic Integral Cross Section Data in Fundamental Reactor Dosimetry Benchmark Neutron Fields", Proceedings of Consultants' Meeting on Integral Cross-Section Measurements In Standard Neutron Fields for Reactor Dosimetry, Vol. I, IAEA-208, Vienna, Austria, 1978.

16. W. N. McElroy, et al., "Development and Testing of Standardized Procedures and Reference Data for LWR Surveillance", HEDL-SA 1719 and Proceedings of an "IAEA Specialist's Meeting on Irradiation Embrittlement, Thermal Annealing and Surveillance of Reactor Pressure Vessels", Vienna, Austria, February 26-March 1, 1979.

17. W. N. McElroy, et al., "LWR Pressure Vessel Surveillance Dosimetry Improvement Program", HEDL-SA 1949 and Proceedings of the Third ASTM-EURATOM International Symposium on Reactor Dosimetry, Ispra, Italy, October 1-5, 1979.

18. J. W. Behrens, R. A. Schrack, and C. D. Bowman, "Resonance Neutron Radiography Using a Position Sensitive Proportional Counter", Trans. Am. Nuc. Soc., 32, 207 (1979).

19. J. W. Behrens, R. G. Johnson, and C. D. Bowman, "Pin-Hole Camera Imaging of Neutrons Using a Position-Sensitive Proportional Counter", Annual Meeting of the American Nuclear Society, Las Vegas, June 8-13, 1980.

20. R. G. Johnson, J. W. Behrens, and C. D. Bowman, "Source Imaging for FMIT Using a Neutron Pin-Hole Camera", Symposium on Neutron Cross Sections from 10-50 MeV, Brookhaven National Laboratory, Upton, N.Y., May 1980.

21. R. Dierckx, "Neutron Monitoring and Neutron Measurements; Experimental Possibilities at the INS Source", LASL 6792-MS, May 1977.

22. R. Madey and F. Waterman, "Time-of-Flight Spectrometer for Neutrons from 1 to 500 MeV", Nucl. Instr. and Methods, 106, 89 (1973).

23. J. H. Roberts and R. Gold, "Nuclear Emulsion Techniques for Fast Neutron Angular Spectrometry", Symposium on Neutron Cross Sections from 10 to 40 MeV, BNL-NCS-50681, Brookhaven National Laboratory, Upton, N.Y., May 1977.

24. A. O. Hanson and J. L. McKibben, "A Neutron Detector Having Uniform Sensitivity from 10 keV to 3 MeV", Phys. Rev., 72, 673 (1947).

25. G. Grosshoeg, "Neutron Ionization Chambers", Nucl. Instr. and Methods, 162, 125 (1979).

26. L. R. Greenwood, "Extrapolated Neutron Activation Cross Sections for Dosimetry to 44 MeV", ANL/FPP/TM-115, September 1978.

27. B. P. Bayhurst, J. S. Gilmore, R. J. Prestwood, J. B. Wilhelmy, Nelson Jarmie, B. H. Erkkila, and R. A. Hardekopf, "Cross Sections for (n,xn) Reactions Between 7.5 and 28 MeV", Phys. Rev. C 12, 451 (1975).

28. L. R. Veeser, E. D. Arthur, and P. G. Young, "Cross Sections for (n,2n) and (n,3n) Reactions Above 14 MeV", Phys. Rev. C 16, 1792 (1977).

29. T. B. Ryves, P. Kolkowski, and K. J. Zieba, "Cross Section Measurements of $^{14}N(n,2n)^{13}N$, $^{19}F(n,2n)^{18}F$, $^{54}Fe(n,2n)^{53}Fe$, $^{27}Al(n,p)^{27}Mg$, and $^{27}Al(n,\alpha)^{24}Na$ Between 14.7 and 19.0 MeV", J. Phys. G: Nucl. Phys. 4, 1783 (1978).

30. Proceedings of Symposium on Neutron Cross Sections from 10 to 40 MeV, BNL-NCS-50681, Brookhaven National Laboratory, Upton, N.Y., May 1977.

31. Proceedings of the Symposium on Neutron Cross Sections 10-50 MeV, Brookhaven National Laboratory, Upton, N.Y., 1980.

32. L. L. Carter, "Neutron Environment in the Fusion Materials Irradiation Test Facility", Proceedings of the Third ASTM-EURATOM International Symposium on Reactor Dosimetry, Ispra, Italy (October, 1979).

33. F. M. Mann, F. Schmittroth, L. L. Carter, and J. O. Schiffgens, "Neutron Environment in the FMIT Facility: Theoretical Predictions", Proceedings of the Symposium on Neutron Cross Sections 10-50 MeV, Brookhaven National Laboratory, Upton, N.Y., 1980.

34. LASL Group TD-6, "MCNP - A General Monte Carlo Code for Neutron and Photon Transport", LA-7396-M, Los Alamos Scientific Laboratory, Los Alamos, N.M., July 1978.

35. C. A. Oster, W. N. McElroy, J. M. Marr, "A Monte Carlo Program for SAND-II Error Analysis", HEDL-TME 73-20, 1973.

36. G. L. Guthrie and R. L. Simons, "Analysis and Extension of the SAND-II Code in Damage Function Unfolding Applications", HEDL-SA 1475 and Proceedings of the 9th ASTM International Symposium on Effects of Radiation on Structural Materials, July 11-14, 1978, Richland, Washington.

37. G. L. Guthrie, F. Schmittroth, R. L. Simons, and E. P. Lippincott, "Use of HEDL Codes in the Sensitivity and Uncertainty Analysis of the Pressure Vessel Embrittlement Damage Function Problem", ORNL/RSIC-42, Proceedings of the Conference on Theory and Applications of Uncertainty Analysis, Oak Ridge, Tennessee, August 22-24, 1978.

38. F. G. Perey, "Least-Squares Dosimetry Unfolding: The Program STAYSL", ORNL-TM-6062, 1977.

39. F. Schmittroth, "FERRET Data Analysis Code", HEDL-TME 79-40, September 1979.

40. R. E. Schenter, F. Schmittroth, and F. M. Mann, "Evaluations of the $^{58}Fe(n,\gamma)^{59}Fe$ and $^{54}Fe(n,p)^{54}Mn$ Reactions for the ENDF/B-V Dosimetry File", Proceedings of the International Conference on Nuclear Cross Sections for Technology, Knoxville, Tennessee, October 22-26, 1979.

41. S. R. Wagner, "The Treatment of Systematic Errors Which Cannot Be Quantitatively Assessed with the Aim to Characterize the Accuracy of a Measurement", Proceedings of the Symposium on "Measurement Theory-Measurement Error Analysis", Enschede, The Netherlands, December 11-13, 1975, International Measurement Confederation, IMEKO Secretariat, Budapest, Hungary.

42. L. J. Baker and G. Constantine, "Dosimetry Requirements for a Fusion Reactor Blanket and Shield", Proceedings of the Third ASTM-EURATOM International Symposium on Reactor Dosimetry, Ispra, Italy (October 1979).

43. R. Vandenbosch and J. Huizenga, Nuclear Fission, Academic Press, New York, p. 255, 1973.

44. D. W. Kneff, H. Farrar, IV, L. R. Greenwood, and M. W. Guinan, "Characterization of the Be(d,n) Neutron Field by Passive Dosimetry Techniques", Symposium on Neutron Cross Sections 10-50 MeV, Brookhaven National Laboratory, Upton, N.Y., May 1980.

45. F. H. Ruddy, C. C. Preston, R. Gold, E. V. Benton, and J. H. Roberts, "CR-39 Polymer: A Promising New Solid State Track Recorder for High Energy Neutron Applications", Symposium on Neutron Cross Sections from 10-50 MeV, Brookhaven National Laboratory, Upton, N.Y., May 1980.

46. L. L. Carter, "Nuclear Data Relevant to Shield Design of FMIT Facility", Symposium on Neutron Cross Sections 10-50 MeV, Brookhaven National Laboratory, Upton, N.Y., May 1980.

47. F. M. Mann, F. Schmittroth, L. L. Carter, and J. O. Schiffgens, "Neutron Environment in the FMIT Facility: Theoretical Predictions", Symposium on Neutron Cross Sections 10-50 MeV, Brookhaven National Laboratory, Upton, N.Y., May 1980.

48. C. Kalbach and F. M. Mann, "Phenomenology of Preequilibrium Angular Distribution", Symposium on Neutron Cross Sections from 10-50 MeV, Session V: Nuclear Model Codes and Data Evaluation, Brookhaven National Laboratory, Upton, N.Y., May 1980.

49. "Compilation of Requests for Nuclear Data", BNL-NCS-51005, DOE/NDC-16/U, April 1979.

50. D. W. Muir, IAEA Editor, "WRENDA 79/80, World Request List for Nuclear Data", INDC(SEC)-73/URSF, October 1979.

TABLE I

Active and Passive FMIT Dosimetry System Stations

Dosimetry Station	Category	CANDIDATE DETECTORS Active	Passive
Ex-Test Cell Neutron Radiography Station - 180°	PD,AD	To Be Determined	SSTR
Ex-Test Cell Neutron Radiography Station and Differential Dosimetry - 0°	AD,PD	(a) Charged Particle Telescope (b) Associated-Particle TOF System (c) Position Sensitive Proportional Counter or Spark Counter	SSTR
In-Test Cell Active Dosimetry Assemblies (Fission and/or Ionization Chamber Sensors)	AD	(a) Long Counters (b) Fission Chambers - Current and Pulse Mode (c) Neutron and Gamma Ray Calorimeters (d) Gamma Ionization Chambers (e) Self-Powered Detectors	N/A
In-Test Cell Passive Dosimetry Assemblies (Fission and Non-fission Reaction Sensors: Radiometric Monitors (RM) Solid State Track Recorders (SSTR), and Helium Accumulation Fluence Monitors (HAFM)	PD	N/A	RM, SSTR, HAFM
Lithium Flow Dosimetry	AD	Ge-Intrinsic	N/A
Service Cell Counting Stations (Primarily for Passive Sensors)	PD	Ge-Intrinsic	RM

TABLE II

FMIT Dosimetry Activities

Dosimetry Activity Designation[a]	Title
AD-1	Active Radiography
AD-2	Differential Dosimetry
AD-3	Integral Dosimetry
AD-4	Lithium Flow Dosimetry Station
AD-5	Data Acquisition
AD-6	Neutron and Gamma Heating
PD-1	Passive Radiography
PD-2	Test Cell Dosimetry
PD-3	In-Situ Dosimetry
AD-7 and PD-4	Benchmark Field Testing
CD-1	Source Spectrum Calculations
CD-2	Transport Calculations
CD-3	Spectral Modification Codes
CD-4	Sensitivity Studies
GND-1	Li Target Studies
GND-2	Dosimetry, Damage Analysis, and Shielding Cross Sections

[a]Active Dosimetry (AD), Passive Dosimetry (PD), Calculational Dosimetry (CD), and General Nuclear Data (GND).

TABLE III

Summary of Advantages/Disadvantages of Candidate Active Spectrometer Systems

System	Advantages	Disadvantages
1. $^{3}He(n,p)t$ proportional counters	•High efficiency •Inexpensive •Long history of use	•Dynamic range: thermal to 1-2 MeV (limited by elastic scatter interference) •Microphonic
2. Recoil proportional counters	•^{4}He usable to 15 MeV •Self-contained, small size •Pulse shape discrimination of gamma rays	•^{1}H limited to energy <3 MeV •Resolution probably >10-15% •Requires development work •Very high voltage bias required
3. Organic scintillators (OS)	•Very fast •Pulse shape γ discrimination possible •Self-contained •High energy spectrometry (>50 MeV) straightforward •High efficiency	•High gamma ray efficiency
4. (n,p) magnetic spectrometers	•Good resolution possible based on well-known hydrogen $\sigma(n,p)$ •Good high energy response	•Large size, increased expense •Cumbersome design
5. $^{6}Li(n,\alpha)t$ coincident spectrometer	•High Q reaction, good potential for γ-ray discrimination •Geometry adds additional background suppression	•Limited to low energy portion of spectrum due to low efficiency as well as lack of knowledge of σ and charged particle angular distribution, and competing reactions

TABLE III (Cont'd)

System	Advantages	Disadvantages
6. (n,p) thin radiator telescopes	•Basic method well developed •5% resolution plausible •Good high energy response	•Correction for inelastic C interactions cumbersome •Dynamic range - resolution limited by radiator thickness •Low efficiency
7. Two-detector TOF	•Would use OS (#3 above) •Wide dynamic range: 1-500 MeV with short flight path (<10 m) •Real time correction for inelastic scattering in C possible	•Resolution poor •Probably not feasible to put first detector in beam

TABLE IV

Cross Section Requirements for Differential Dosimetry[a]

$^{3}He\ (n,p)\ ^{3}H$

$^{3}He\ (n,2p)\ 2n$

$^{3}He\ (n,pn)\ ^{2}H$

$^{3}He\ (n,n')\ ^{3}He$

$^{6}Li\ (n,\alpha)\ ^{3}H$

$^{6}Li\ (n,n')\ ^{6}Li$

$^{6}Li\ (n,p)\ ^{6}He$

$^{6}Li\ (n,pn)\ ^{5}He$

$^{6}Li\ (n,2np)\ ^{4}He$

$^{6}Li\ (n,2n)\ ^{5}Li$

$^{6}Li\ (n,\alpha n)\ ^{2}H$

TABLE V

Reactions of Deuterons on Lithium Which Result in Detectable Activation Products at the Lithium Flow Dosimetry Station[a]

$^{6}Li\ (d,n)\ ^{7}Be$	(53.28d)
$^{6}Li\ (d,2p)\ ^{6}He$	(0.805 sec)
$^{7}Li\ (d,p)\ ^{8}Li$	(0.844 sec)
$^{7}Li\ (d,2pn)\ ^{6}He$	(0.805 sec)
$^{7}Li\ (d,2n)\ ^{7}Be$	(53.28d)

[a]Desired reaction cross section accuracy level is 10 percent (1σ).

TABLE VI

Reactions for FMIT Passive RM and SSTR Dosimetry[a]

REACTION	PRIORITY/ ACCURACY[b]	HALFLIFE	EMIN (MeV)	EMID (MeV)	EMAX (MeV)
AG107(N2N)AG106M	1	8.27 D	11.50	16.50	23.00
AL27(N A)NA24		15.00 H	8.00	12.50	19.00
AU197(N2N)AU196	1	6.18 D	10.00	14.00	21.00
AU197(N3N)AU195	1	183.00 D	17.50	21.00	28.00
AU197(N4N)AU194	1*	1.65 D	26.00	31.00	39.00
AU197(N G)AU198		2.70 D	.00	.90	14.50
CO59(N P)FE59	1	44.60 D	6.00	13.50	21.00
CO59(N A)MN56		2.60 H	8.00	13.50	21.00
CO59(N 2N)CO58	1	70.80 D	12.00	16.50	24.00
CO59(N 3N)CO57	1	271.00 D		27.00	
CO59(N 4N)CO56	1*	78.50 D		35.00	
CO59(N G)CO60		5.25 Y	.01	1.75	18.50
CU63(N A)CO60		5.25 Y	7.50	11.50	19.00
CU63(N G)CU64		12.70 H	.00	1.75	16.50
CU65(N 2N)CU64		12.70 H	11.50	16.00	22.00
FE (N X)MN54	1	314.00 D	4.00	10.50	27.00
FE54(N A)CR51	1	27.70 D	7.50	14.00	23.00
FE56(N P)MN56		2.60 H	7.00	12.50	20.00
FE58(N G)FE59		44.60 D	.70	16.50	27.00
IN115(N N)IN115M	1	4.50 H	1.50	6.00	16.00
IN115(N G)IN116		54.20 M	.02	1.00	4.50
IR191(N3N)IR189		13.10 D	17.00	21.00	27.00
IR191(N2N)IR190		11.80 D	9.50	13.50	20.00
LU175(N G)LU176		3.69 H	.00	.25	5.50
MG24(N P)NA24	1	15.00 H	7.50	12.50	19.50
NA23(N G)NA24		15.00 H	.00	5.00	22.00
NB93(N 2N)NB92M	1	10.20 D	10.50	14.50	21.00
NI58(N P)CO58	1	70.80 D	3.50	9.00	18.50
NI58(N 3N)NI56	1*	6.10 D		29.00	
NI58(N 2N)NI57	1	1.53 D	14.00	19.00	26.00
NI60(N P)CO60	1	5.25 Y	6.50	11.50	20.00
NP237(N G)NP238		2.12 D	.00	.35	5.00
NP237(N F)FSPR			1.25	10.00	23.00
PU239(N F)FSPR			.70	9.00	23.00
SC45(N A)K42		12.40 H	7.50	13.50	22.00
SC45(N G)SC46		83.80 D	.01	1.25	20.00
SC45(N 2N)SC44		2.44 D	13.00	17.50	25.00
TA181(N G)TA182		115.00 D	.00	.60	8.50
TH232(N F)FSPR			3.00	13.50	26.00
TI (N X)SC47		3.43 D	5.50	19.00	29.00
TI (N X)SC46		83.80 D	6.00	15.00	28.00

TABLE VI (Cont'd)

REACTION	PRIORITY/ ACCURACY[b]	HALFLIFE	EMIN (MeV)	EMID (MeV)	EMAX (MeV)
TI48(N P)SC48		1.83 D	8.00	14.00	23.00
TL203(N3N)TL201		3.05 D	18.00	22.00	29.00
TL203(N2N)TL202		12.50 D	9.50	14.50	21.00
TM169(N3N)TM167	1	9.25 D	17.50	21.00	28.00
TM169(N2N)TM168	1	93.10 D	9.50	14.00	20.00
U235(N F)FSPR			.60	10.00	24.00
U238(N G)U239		23.50 M	.01	.90	5.00
U238(N 2N)U237	1	6.75 D	7.00	10.50	15.00
U238(N F)FSPR	1		2.25	12.00	25.00
W186(N G)W187		23.90 H	.01	1.00	16.50
Y89(N 3N)Y87	1*	3.35 D	23.00	28.00	38.00
Y89(N 2N)Y88	1	107.00 D	13.00	17.50	24.00
ZR (N X)ZR89	1	3.26 D	13.50	18.00	26.00

[a]Cross section data used are from Greenwood, Reference 7.

[b]All required accuracies are 10% (1σ) except those high energy reactions indicated by (*) for which the required accuracies are 20%(1σ). Those reactions indicated by a (1) should be given the highest priority.

TABLE VII

Calculated Flux Characteristics at Several Positions in the FMIT Test Cell[a]

	Zone 1	Zone 5	Zone 51	Zone 108
Distance from Lithium target	0.25cm	0.25cm	14.5cm	147.0cm
Horizontal distance from beam center	0.30cm	0.30cm	0.5cm	0.0cm
Vertical distance from beam center	0.25cm	1.75cm	1.0cm	0.0cm
Total flux (n/cm^2-sec)	1.83×10^{15}	5.70×10^{14}	3.50×10^{13}	1.49×10^{12}
Relative flux greater than 0.001 MeV	1.00	1.00	1.00	0.94
.01 MeV	1.00	1.00	0.98	0.87
.1 MeV	0.99	0.99	0.84	0.60
1.0 MeV	0.91	0.84	0.67	0.10
3.0 MeV	0.75	0.60	0.46	0.017
10.0 MeV	0.40	0.23	0.096	--
20.0 MeV	0.083	0.025	--	--
30.0 MeV	0.006	0.009	--	--

[a]Reference 32.

TABLE VIII

Flux-Averaged Cross Sections at Several Positions in the FMIT Test Cell[a]

REACTION	SIG AVG(B) ZONE 1	ZONE 5	ZONE 51	ZONE 108
AG107(N2N)AG106M	.1836	.0906	.2327	.0018
AL27(N A)NA24	.0416	.0286	.0417	.0003
AU197(N2N)AU196	.6358	.3926	.7236	.0051
AU197(N3N)AU195	.1884	.0498	.2389	.0020
AU197(N4N)AU194	.0141	.0185	.0137	.0002
AU197(N G)AU198	.0371	.0571	.0615	.5547
CO59(N P)FE59	.0237	.0158	.0244	.0003
CO59(N A)MN56	.0092	.0061	.0097	.0001
CO59(N 2N)CO58	.2113	.1023	.2686	.0021
CO59(N 3N)CO57				
CO59(N 4N)CO56				
CO59(N G)CO60	.0033	.0045	.0046	.0213
CU63(N A)CO60	.0145	.0104	.1365	.0001
CU63(N G)CU64	.0062	.0085	.0090	.0696
CU65(N 2N)CU64	.2762	.1408	.3500	.0027
FE (N X)MN54	.3795	.2891	.3365	.0075
FE54(N A)CR51	.0354	.0225	.0379	.0003
FE56(N P)MN56	.0386	.0263	.0385	.0003
FE58(N G)FE59	.0048	.0030	.0060	.0044
IN115(N N)IN115M	.1815	.1950	.1381	.0212
IN115(N G)IN116	.0474	.0767	.0691	.3868
IR191(N3N)IR189	.1882	.0491	.2411	.0020
IR191(N2N)IR190	.5974	.3836	.6579	.0047
LU175(N G)LU176	.0344	.0605	.0716	.9226
MG24(N P)NA24	.0720	.0494	.0714	.0006
NA23(N G)NA24	.0003	.0003	.0004	.0046
NB93(N 2N)NB92M	.1467	.0847	.1734	.0012
NI58(N P)CO58	.3333	.2892	.2582	.0088
NI58(N 3N)NI56				
NI58(N 2N)NI57	.0178	.0067	.0236	.0002
NI60(N P)CO60	.0602	.0434	.0552	.0006
NP237(N G)NP238	.0652	.1134	.1275	1.3480
NP237(N F)FSPR	1.9854	1.7300	1.9300	.3122
PU239(N F)FSPR	2.1353	2.0010	2.1430	1.7570
SC45(N A)K42	.0155	.0100	.0166	.0002
SC45(N G)SC46	.0031	.0043	.0047	.0300
SC45(N 2N)SC44	.0376	.0167	.0495	.0004
TA181(N G)TA182	.0413	.0684	.0743	.7131
TH232(N F)FSPR	.2737	.1926	.2743	.0088
TI (N X)SC47	.2679	.1402	.3098	.0042
TI (N X)SC46	.2006	.1230	.2084	.0023
TI48(N P)SC48	.0212	.0130	.0232	.0002
TL203(N3N)TL201	.1703	.0470	.2103	.0017

TABLE VIII(Cont'd)

REACTION	SIG AVG(B) ZONE 1	ZONE 5	ZONE 51	ZONE 108
TL203(N2N)TL202	.6664	.4066	.7622	.0056
TM169(N3N)TM167	.1716	.0488	.2179	.0019
TM169(N2N)TM168	.6160	.3848	.6960	.0051
U235(N F)FSPR	1.6723	1.4970	1.7350	1.8210
U238(N G)U239	.0263	.0434	.0419	.2973
U238(N2N)U237	.4474	.3533	.3545	.0039
U238(N F)FSPR	.8419	.6414	.8179	.0364
W186(N G)W187	.0149	.0228	.0235	.1776
Y89(N 3N)Y87	.0162	.0151	.0174	.0002
Y89(N 2N)Y88	.2883	.1248	.3781	.0031
ZR (N X)ZR89	.2695	.1136	.3544	.0030

[a]The position and flux characteristics are given in Table VII.

TABLE IX

FMIT Dosimetry Goal Accuracy Requirements

Neutron Energy Range (MeV)	Estimated Percent Contribution to Displacements for 35 MeV Deuterons[a]	Broad Group Fluence Accuracies % (±)
0-3	5	30-60
3-5	5	20-40
5-10	15	10-20
10-15	25	10-20
15-20	25	10-20
20-25	15	10-20
25-30	5	20-40
30-50	5	40-80

[a]Based on Copper.

TABLE X

Additional Reactions Required for FMIT RM and HAFM Dosimetry

Radiometric (n,x)	Priority & Accuracy[d]	Observed Threshold Energy (MeV)	Maximum Measured Energy (MeV)	Halflife -State- Ground	Metastable
Na23 (n,2n) Na22	1	--	--	2.6Y	
Fe54 (n,t) Mn52	1	--	--	5.6D	21M
Mn55 (n,2n) Mn54	1	12	15[a]	312D	
Y89 (n,p) Sr89	1	--	--	50.5D	
Zr90 (n,p) Y90	1	--	--	3.2H	64H
Zr90 (n,3n) Zr88	1	23	28[c]	83.4D	
Rh103 (n,2n) Rh102		10	24[b]	207D	3Y
Rh103 (n,3n) Rh101		18	24[b]	3Y	4.5D
Ag107 (n,3n) Ag105	1	--	--	41D	7M
Ag109 (n,2n) Ag108		--	--	2.4M	130Y
Eu151 (n,3n) Eu149		15	28[c]	93D	
Eu151 (n,4n) Eu148	*	25	28[c]	54D	
Tb159 (n,2n) Tb158		--	--	150Y	10S
Tm169 (n,4n) Tm166	1*	26	28[c]	7.7H	
Tm169 (n,5n) Tm165	1	--	--	30H	
Lu175 (n,2n) Lu174		8	28[b,c]	3.3Y	142D
Lu175 (n,3n) Lu173		15	28[b,c]	1.4Y	
Lu175 (n,4n) Lu172	*	25	28[c]	6.7D	37M
Ta181 (n,2n) Ta180		8	24[b]	Stable	8.1H
Ta181 (n,3n) Ta179		15	24[b]	1.8Y	
Ir191 (n,4n) Ir188	*	25	28[c]	41.4H	
Ir193 (n,2n) Ir192		8	28[c]	74.2D	241Y
Tl203 (n,4n) Tl200	*	26	28[c]	7.4H	
Bi209 (n,2n) Bi208		8	24[b]	3.7×10^5Y	
Bi209 (n,3n) Bi207		16	24[b]	38Y	

TABLE X (Cont'd)

Radiometric (n,n')	Priority & Accuracy[d]	Observed Threshold Energy (MeV)	Maximum Measured Energy (MeV)	Halflife -State- Ground	Halflife -State- Metastable
Br79		.21			4.9S
Y89		.91			15.7S
Nb93	1	.030			13.6Y
Rh103	1	.040			56M
Ag107		.093			44S
Ag109		.088			40S
Au197		.41			7.8S
HAFM (Total Helium)					
Li6	1	0	15[a]	(Stable-HAFM)	
B10	1	0	15[a]		
Al		6	15[a]		
Fe		5	15[a]		
Ni		3	15[a]		
Cu		5	15[a]		
Au		13	15[a]		

[a]From ENDF/B-V.

[b]From Veeser, et al., Reference 28.

[c]From Bayhurst, et al., Reference 27.

[d]All required accuracies are 10% (1σ) except those high energy reactions indicated with (*) for which the required accuracies are 20% (1σ). Those reactions indicated by a (1) should be given the highest priority.

TABLE XI

Calculated Neutron-Induced Fission Thresholds for Selected Nuclides for SSTR Dosimetry[a]

Target Nuclide	Fissioning Nuclide	Fission Barrier (MeV)	Neutron Binding Energy (MeV)	Threshold Energy (MeV)
^{209}Bi	^{210}Bi	26	4.36	22
^{205}Tl	^{206}Tl	22	6.43	16
^{203}Tl	^{204}Tl	21	6.57	14
^{197}Au	^{198}Au	23	6.30	17
^{193}Ir	^{194}Ir	25	6.10	19
^{191}Ir	^{192}Ir	24.5	6.14	18
^{181}Ta	^{182}Ta	29	5.98	23
^{169}Tm	^{170}Tm	33.6	9.76	24

[a]The fission thresholds listed represent theoretical estimates only. Cross section measurements on as many of the listed threshold reactions as possible are desirable to cover the FMIT energy range. Cross sections for those reactions found to have thresholds less than 20 MeV should be measured to an accuracy of about ±10% whereas those with thresholds higher than 20 MeV should be measured to an accuracy of ±20%.

FMIT DOSIMETRY SYSTEM PROGRAM ELEMENTS AND INFORMATION FLOW

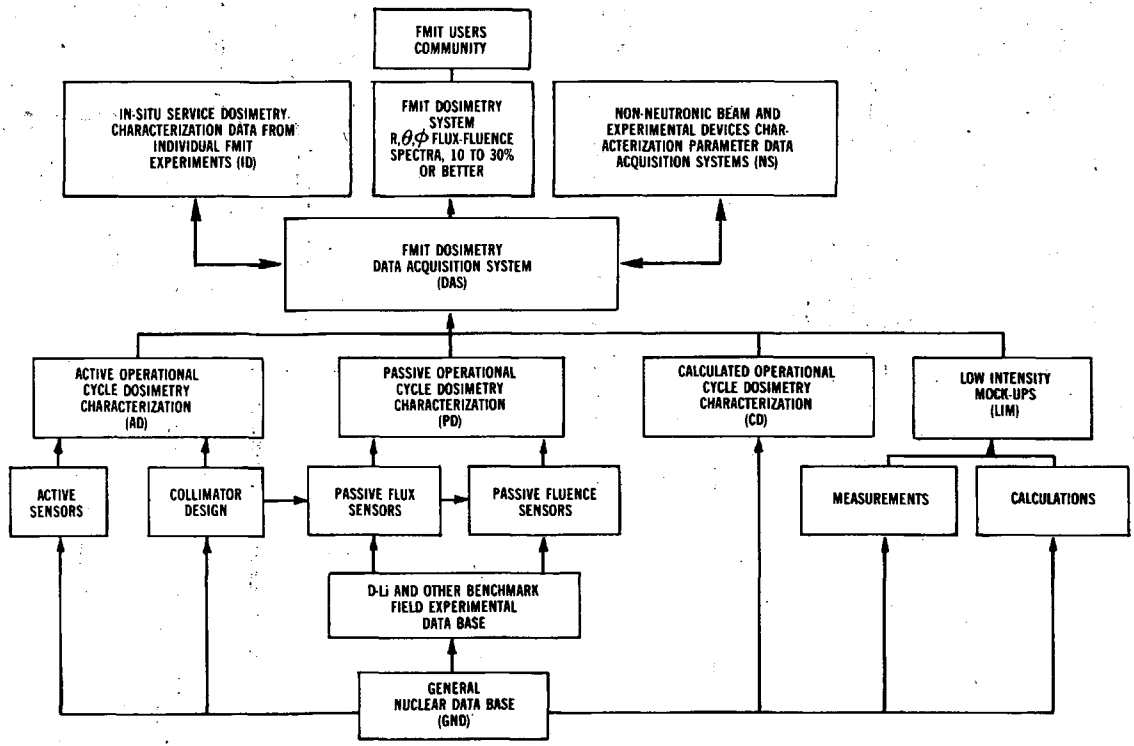

Figure 1: Relationships Amongst FMIT Dosimetry Program Elements.

0° DOSIMETRY STATION

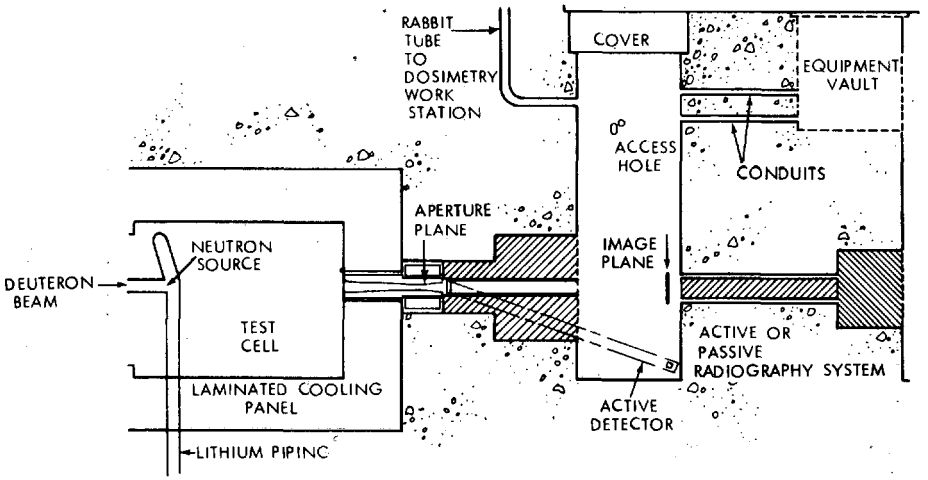

Figure 2: Side View of the 0° Dosimetry Station Showing the Neutron Pinhole Collimator and Access for Radiography/Spectrometry Activities.

COLLIMATOR DETAIL

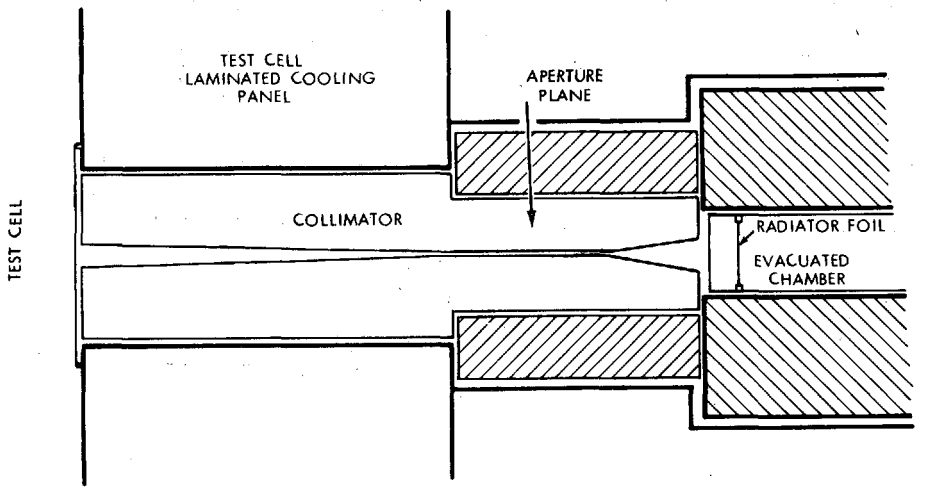

Figure 3: Detailed View of the Pinhole Neutron Collimator.

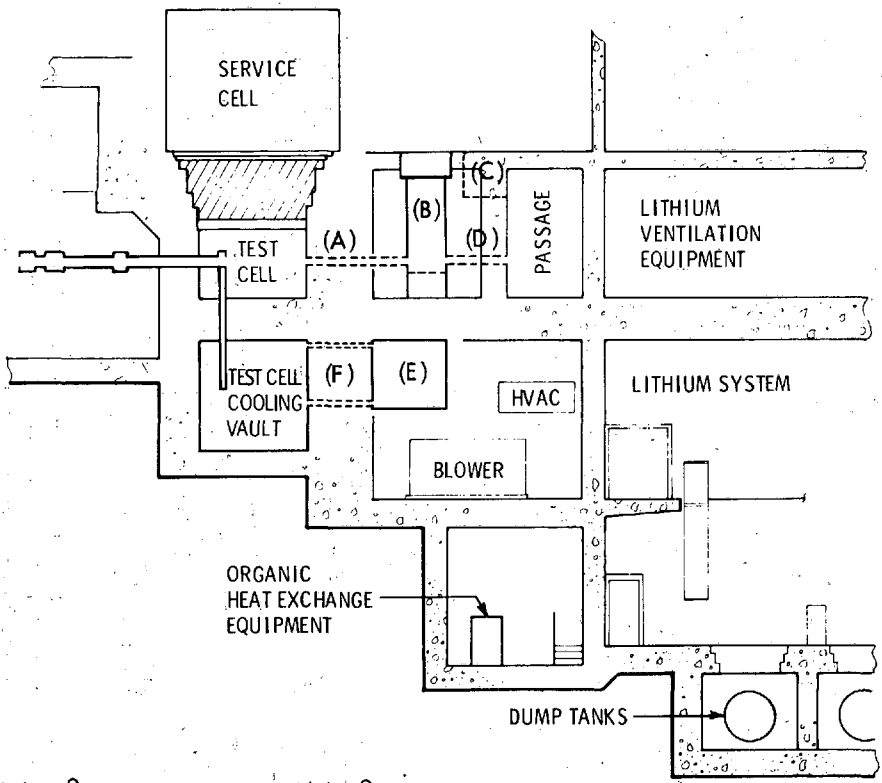

(A) 0°DOSIMETRY PORT (B) 0°DOSIMETRY ACCESS PIT
(C) EQUIPMENT VAULT (D) 0°DOSIMETRY PORT ACCESS
(E) LITHIUM FLOW DOSIMETRY STATION (F) PLUGS FOR GAMMA RAY COLLIMATORS

Figure 4: Lithium Flow Dosimetry Station (E) with Collimator Plugs (F).

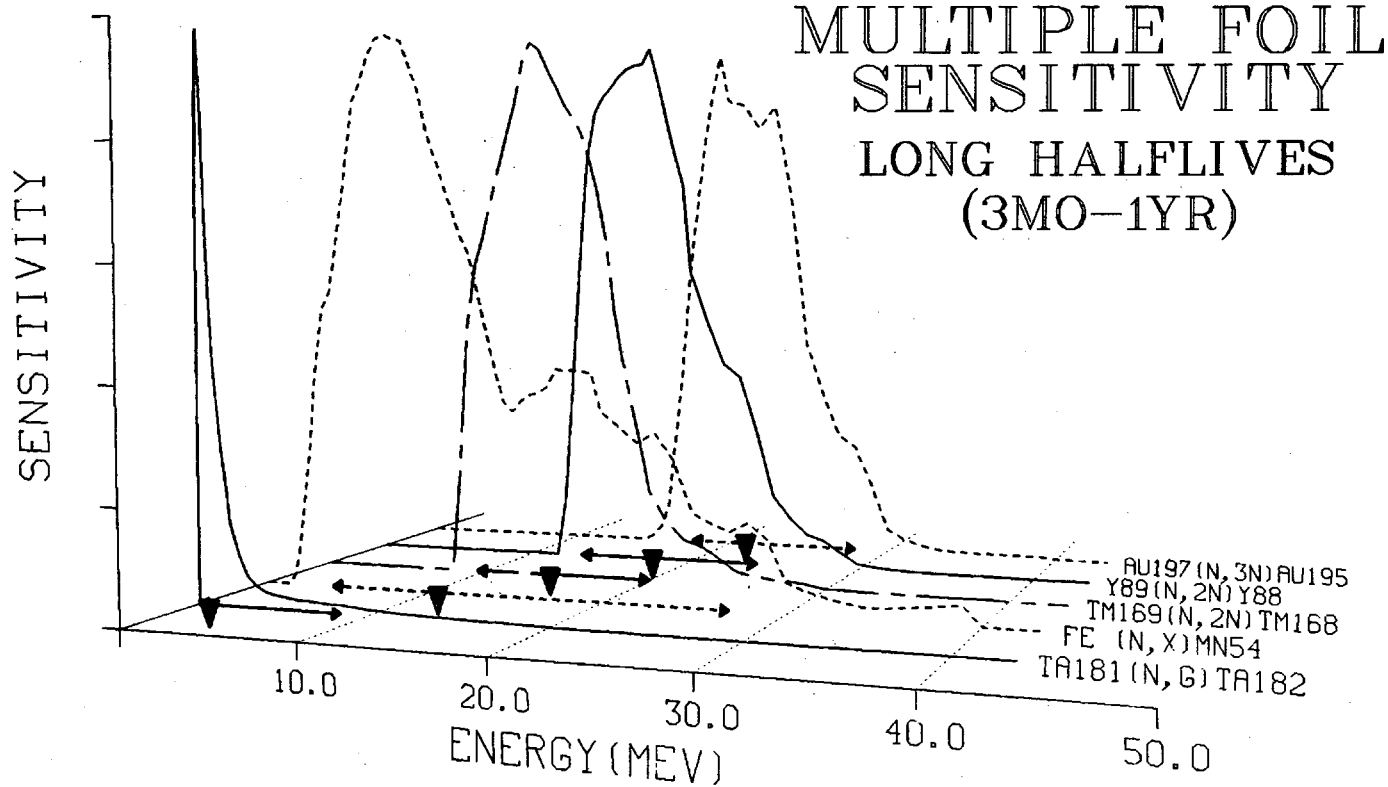

Figure 5: Plots of Sensitivity as a Function of Neutron Energy For A Candidate Set of Reactions with Long Half Lives Using the Flux Calculated for Zone 1 of Table VII. The Arrows Indicate Sensitivity Limits of 5%, 50%, and 95%. Sensitivity Plots are Normalized to a Maximum of Unity.

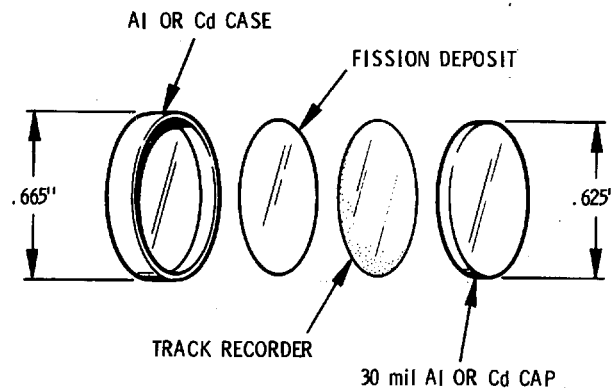

Figure 6: Typical Geometrical Configuration Used for SSTR Neutron Dosimetry [Dimensions can be scaled depending upon application.]

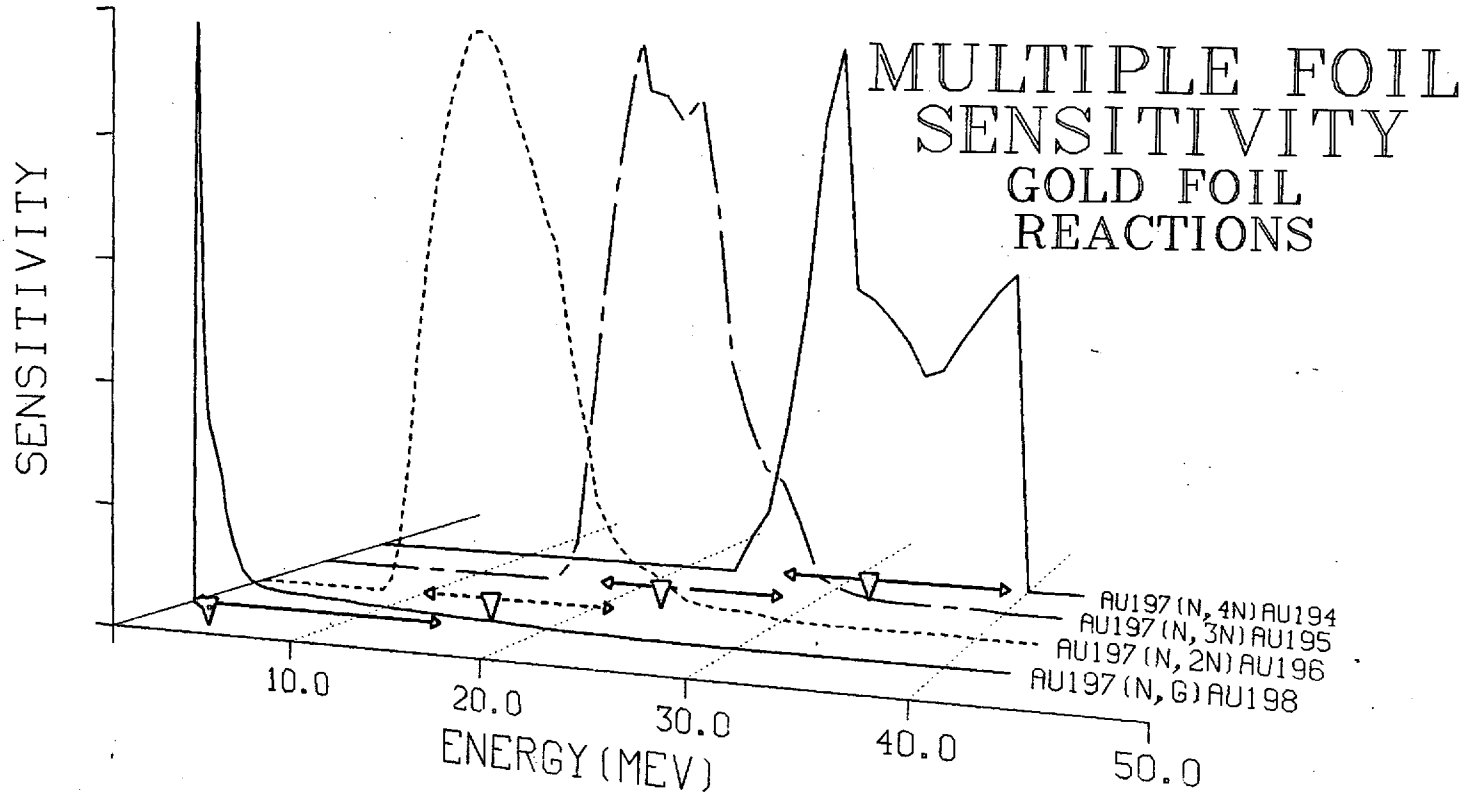

Figure 7: Plots of Sensitivity as a Function of Neutron Energy for Gold Foil Reactions Using the Flux Calculated for Zone 1 of Table VII. The Arrows Indicate Sensitivity Limits of 5%, 50%, and 95%. Sensitivity Plots are normalized to a Maximum of Unity.

CR-39 POLYMER, A PROMISING NEW SOLID STATE TRACK RECORDER FOR HIGH ENERGY NEUTRON APPLICATIONS

F. H. Ruddy, C. C. Preston, and R. Gold

Hanford Engineering Development Laboratory
Richland, Washington 99352, U.S.A.

E. V. Benton

University of San Francisco
San Francisco, California 94117, U.S.A.

J. H. Roberts

Macalester College
St. Paul, Minnesota 55105, U.S.A.

ABSTRACT

CR-39 Polymer, a new solid state track recorder with unprecedented sensitivity to lightly ionizing particles (such as protons) is being developed for eventual neutron dosimetry applications in the Fusion Materials Irradiation Test Facility and elsewhere. The diameters of proton tracks have been found to vary smoothly and reproducibly as a function of energy from 0.20 to 18.0 MeV. Preliminary results on the response of CR-39 polymer to proton tracks as a function of angle show a rapid decrease of the registration efficiency from 100% to 0 for angles of incidence less than 75°. Proton recoil track size distributions in CR-39 polymer irradiated with monoenergetic neutrons of varying energy are presented. Some proposed high energy neutron dosimetry and radiography systems using CR-39 polymer are discussed.

INTRODUCTION

Since the recent discovery of the track recording properties of CR-39 polymer [1, 2], this solid state track recorder (SSTR)

has been shown to have a number of unique and useful properties not found previously. Among these properties, those most advantageous for neutron applications are:

(1) High sensitivity to lightly ionizing particles. A measure of this sensitivity is the broad energy range of proton track registration [3].

(2) Homogeneous bulk etch rate. Samples of CR-39 polymer SSTR may be etched for periods of time resulting in tens of microns of surface removal, and the surface of the SSTR retains its excellent optical quality.

(3) High resistance to β and γ radiation. Samples of CR-39 polymer have been exposed to a total β-γ dose of 10^7 Rads and were still found to record discernible tracks from a lithium foil [4].

(4) The response to lightly ionizing particles can be changed by altering the etching conditions [5]. In neutron fields, for example, tracks from alpha particles and heavier ions can be revealed while at the same time discriminating against neutron induced proton recoil tracks.

These properties make CR-39 polymer an excellent SSTR candidate for neutron applications. The heretofore unavailable capability for proton track registration over a wide energy range makes possible many dosimetry applications which rely on the H(n,p) reaction. This is a particular advantage, since the H(n,p) cross section and angular distribution are quite well known over a broad energy range (including the entire neutron energy spectrum range of the Fusion Materials Irradiation Test [FMIT] Facility).

The response of CR-39 polymer is being calibrated for eventual neutron dosimetry in FMIT and also for other applications in U.S. nuclear reactor energy programs.

EXPERIMENTAL

CR-39 polymer SSTR have been exposed to proton beams using 90° scattering through a thin ($100\mu g/cm^2$) gold foil. For protons of energy greater than 10 MeV, protons scattered forward at 45° have been analyzed using a magnetic spectrometer to avoid contamination due to inelastically scattered protons and reaction products.

For protons, the CR-39 polymer is etched in 6.25N NaOH solution to which 0.5 mole % Dowfax Surfactant has been added. The temperature of the etchant is maintained at 70.0±0.1°C and the SSTR are typically etched for 16 hours.

Track densities and track size distributions are obtained with the aid of a computerized Quantimet 720 system coupled to an optical microscope.

RESULTS AND DISCUSSION

Results on the response of CR-39 polymer to protons in the energy range from 0.2 to 6 MeV and to alpha particles in the energy range from 3.2 to 6.1 MeV have been reported previously [3]. The diameters of normally incident tracks were measured as a function of energy, resulting in an integral response for alpha particles and a rapidly varying response for protons. The proton results have since been extended to an energy of 18 MeV. Figure 1 shows microphotographs of normally incident proton tracks with energies of 9.0, 12.0, 15.0, and 18.0 MeV. The mean diameters of these tracks, measured with the aid of the Quantimet, are plotted as a function of energy in Figure 2. The line in Figure 2 is a result of a computer code which simulates etching in CR-39. CR-39 polymer continues to show a differential energy response as a function of proton energy up to 18 MeV. Experiments are in progress to extend this calibration to higher proton energies.

Experiments have been initiated to calibrate the proton response of CR-39 polymer as a function of angle of proton incidence. CR-39 polymer SSTR have been exposed to scattered proton beams at incidence angles of 90°, 85°, 80°, 75°, 70°, 65°, and 60°. Microphotographs of 5 MeV protons incident at 90°, 85°, 80°, 75°, and 70° are shown in Figure 3. At 80° and 75° the track profiles become more elipsoidal and at 70° the tracks become very faint. At 65° and 60°, the proton tracks were not visible. Preliminary results on the etching efficiency as a function of angle are shown in Figure 4. The track fading at 70° is accompanied by a 50% reduction in registration. For angles greater than or equal to 75°, the response is essentially unity, whereas for angles less than 65°, the response is zero. The response at all angles has been normalized to unity at 90°. Normally incident protons register with 100% efficiency up to at least 5 MeV [3]. The angular response of CR-39 polymer SSTR to 8 MeV protons has been found to be quite similar to the response at 5 MeV. This similarity is to be expected, since for a 16 hour etch, the cone angles for 5 and 8 MeV protons are nearly the same. This rather simple, "step function" angular response should simplify the use of CR-39 polymer under conditions of isotropic track incidence. On the other hand, it may be possible to use this response to provide some angular information in non-isotropic neutron fields.

Further angular response measurements are in progress.

APPLICATIONS OF CR-39 POLYMER SSTR IN NEUTRON DOSIMETRY

Several applications of CR-39 polymer SSTR for neutron dosimetry in FMIT have been proposed. In the simplest of these, CR-39 polymer could be used to record proton recoils from a hydrogenous radiator exposed to neutrons as shown in Figure 5. The response of CR-39 polymer above 18 MeV is still under investigation, but by using a large scattering angle from the radiator, the range of expected recoil proton energies can be compressed from the 40 MeV range of neutron energies down to less than 18 MeV. The resulting proton recoil diameter spectrum can be converted into an energy spectrum using the calibration curve in Figure 1, and the proton energy spectrum can be unfolded to reveal the incident neutron energy spectrum.

Other reactions may offer unique advantages for FMIT neutron spectrometry. Among these are the $^{6}Li(n,\alpha)$ and $^{10}B(n,\alpha)$ reactions [6,7]. CR-39 polymer SSTR have been shown to provide an integral response (constant diameters) to alpha particles in the range from 3-6 MeV [3]. For the $^{6}Li(n,\alpha)$ reaction, an integral response would be expected for the alpha particles whereas the product tritons would result in smaller tracks with differential energy response. When etched under less sensitive chemical conditions, proton tracks are not revealed in CR-39 and the alpha particle energy response becomes differential [5]. Thus, with proper calibration alpha spectrometry measurements can be made in high energy neutron fields that would otherwise result in a background of proton recoils from neutron interactions with the hydrogen atoms in the CR-39 polymer.

The concept of neutron pinhole radiography has been advanced for FMIT [8] and calculations have shown that adequate spatial resolution can be obtained with such a device [9]. Passive radiometric foils can be placed in the image plane of the collimator and the spatial distribution of the reaction products can be determined to map the image of the neutron source. Alternatively, SSTR may be placed in the image plane, and the resultant track densities can be related to neutron fluence at a given point. Figure 6 shows a sample of CR-39 polymer that was exposed using a D-T 14 MeV neutron source. It is encouraging to note that most of the proton recoil tracks have circular profiles indicating that they are incident nearly normal to the surface (as is expected from angular calibration data) and that most of the tracks have small diameters corresponding to energies near 14 MeV (compare with Figure 1). The unexpected simplicity of this 14 MeV neutron induced proton recoil response augers well for the prospects of unfolding the proton recoil spectrum to determine the incident neutron energy spectrum. Additionally, the spatial distribution of proton recoil tracks should be proportional to the

intensity of incident neutrons so that a two dimensional inverse image of the neutron source is obtained.

An alternative to in-beam pinhole neutron imaging as described above is to use the arrangement shown in Figure 7. A proton radiator of some suitable material such as polyethylene ($[CH_2]_n$) is placed in the image plane of the pinhole collimator and the resultant proton recoils are viewed through a proton pinhole collimator using CR-39 polymer. In order to obtain normal incidence for the recoil protons, the CR-39 is placed at an angle to the proton image plane, so that corrections for projection angle and small geometric efficiency differences must be made to obtain an inverted image of the proton recoil distribution which is, in turn, an inverted image of the source neutron distribution.

In the event that the background caused by neutron induced proton recoils in the CR-39 polymer becomes a problem, ^{6}Li or ^{10}B could be used as an alpha radiator and an alpha particle image can be obtained with the SSTR. Alternatively, the recoil protons can be degraded to lower energies (which are not present in great abundance from direct interactions of neutrons with the CR-39 polymer) and the larger diameter tracks from the low energy protons can be easily distinguished from the smaller neutron induced proton recoil background tracks in the polymer.

This latter method has resulted in the concept of a radiographic neutron camera. [10] A prototype model of this radiographic neutron camera is shown in Figures 8 and 9. The prototype camera will be used to explore neutron source imaging using benchmark fields and low intensity mockups. The camera is shown in position next to a sealed tube D-T 14 MeV neutron generator. Protons produced in a proton radiator placed next to the neutron source will be degraded by passing through pressurized gas and a pinhole image of the degraded proton recoils will be projected on a CR-39 polymer track recorder.

A Fresnel zone plate[11,12] could also be used in place of the pinhole collimator to provide higher efficiency. The three dimensional Fresnel shadowgraph image would, in this case, only provide an image of the two dimensional image from the proton radiator. Through benchmark testing and optimization, the prototype radiographic camera will evolve into a neutron imaging device suitable for use at FMIT and other fusion environments.

The encouraging response for 14 MeV proton recoils in CR-39 polymer shown in Figure 6 has led to attempts to quantify the response to incident neutrons. The proton track diameter distributions as obtained by the Quantimet are shown in Figure 10 for incident neutron energies of 0.57, 2.1, 5.3, and 15.1 MeV. A 1 mm thick high density polyethylene radiator was used in surface contact with the CR-39 for these exposures. For the three higher energy exposures, peaks are found at diameters corresponding to slightly less than the diameter expected for a direct knock-on proton. This apparent shift to higher energy is caused by etching of

proton recoils formed within the CR-39 polymer. These tracks are not exposed to the etchant for the full 16 hours resulting in smaller diameters. The increase in intensity of these peaks with increasing neutron energy corresponds to an increase in effective thickness of the radiator due to the larger range of the recoil protons. The absence of a peak near the maximum proton energy in the 0.57 MeV neutron irradiation is probably due to a combination of the decreased effective thickness of the radiator foil and lack of contrast for the shallow proton recoil tracks resulting in a loss of optical efficiency for detection of the tracks. This latter effect is enhanced by the fact that the recoil protons are emitted isotropically (in the center of mass system) resulting in shallower tracks within the angular range of registration. Also, the dominant source of proton recoils at this energy is the hydrogen atoms in the CR-39 polymer so that all tracks will not be etched for the full 16 hours. This loss of efficiency at low energy is also apparent in the higher energy exposures where low energy incident tracks are expected due to proton recoil energy degradation in the radiator.

A major peak at approximately 3μm is present in all of the diameter spectra. This peak is due to either incompletely etched low energy protons or to carbon or oxygen recoils from neutron inelastic scattering within the CR-39 polymer.

On the basis of these results, further exposures are being conducted with 14 MeV neutrons to attempt to simplify the characteristics of the diameter spectra by optimizing the radiator thickness and etch time. It is likely that the optimum radiator may be no radiator at all in the case of high intensity, high energy neutron exposures.

CONCLUSIONS

CR-39 polymer is an extremely promising material for use in high energy neutron dosimetry applications. Its unprecedented wide energy response for protons, variable response characteristics, radiation resistance, and high optical quality make it ideal for this purpose. Because of these unique characteristics, applications of CR-39 polymer in the FMIT, as well as other Magnetic Fusion Energy, Light Water Reactor, and Fast Breeder Reactor environments are currently being developed.

REFERENCES

1. B. G. CARTWRIGHT, E. K. SHIRK, and P. B. PRICE, "CR-39: A Nuclear Track Recording Polymer of Unique Sensitivity and Resolution," Nuclear Instruments and Methods 153, 457 (1978).

2. R. M. CASSOU and E. V. BENTON,"Properties and Applications of CR-39 Polymeric Nuclear Track Detector," Nuclear Track Detection 2, 73 (1978).

3. E. V. BENTON, C. C. PRESTON, F. H. RUDDY, R. GOLD, and J. H. ROBERTS, "Proton and Alpha Particle Response Characteristics of CR-39 Polymer for Reactor and Dosimetry Applications," in Proceedings of the Tenth International Conference on Solid State Nuclear Track Detectors, Lyons (1979).

4. R. GOLD, F. H. RUDDY, E. P. LIPPINCOTT, W. N. MCELROY, and J. H. ROBERTS, "Spent Thermal Reactor Fuel Assembly Characterization with Solid State Track Recorders," HEDL-TME 78-89, 1979.

5. G. SYMOGI and I. HUNYADI, "Etching Properties of CR-39 Polymer Nuclear Track Detector," in Proceedings of the Tenth International Conference on Solid State Nuclear Track Detectors, Lyons (1979).

6. R. GOLD and J. H. ROBERTS, "SSTR Measurements of the $^{6}Li(n,\alpha)$ Angular Differential Cross Section," in LMFBR Reaction Rate and Dosimetry 11th Progress Report, HEDL-TME 77-34 (1977).

7. J. H. ROBERTS AND R. GOLD, "SSTR Measurements of (n,α) Reactions for Reactor Applications," in LMFBR Reaction Rate and Dosimetry 11th Progress Report, HEDL-TME 77-34 (1977).

8. R. GOLD, W. N. MCELROY, J. L. FULLER, E. M. SHEEN, and R. DIERCKX, "Dosimetry Program for Characterization of the FMIT Facility," in Proceedings of the Third ASTM-EURATOM International Symposium on Reactor Dosimetry, Ispra (1979).

9. R. J. MORFORD, "Neutron Pinhole Radiography for the Fusion Materials Irradiation Test Facility," in Proceedings of the Third ASTM-EURATOM International Symposium on Reactor Dosimetry, Ispra (1979).

10. R. GOLD, F. H. RUDDY, C. C. PRESTON, J. H. ROBERTS, and W. N. MCELROY, "Neutron Camera for Fusion Diagnostics," Third APS Topical Conference on High Temperature Plasma Diagnostics, Los Angeles (1980).

11. N. M. CEGLIO and C. W. COLEMAN, "Spatially Resolved α-Emission from Laser Fusion Targets," Phys. Rev. Letters 39, 20 (1977).

12. E. V. BENTON and N. M. CEGLIO, "Diagnosis of High-Density Implosions of Laser Fusion Targets Using High-Sensitivity Nuclear Track Detectors," in Proceedings of the Tenth International Conference on Solid State Nuclear Track Detectors, Lyons (1979).

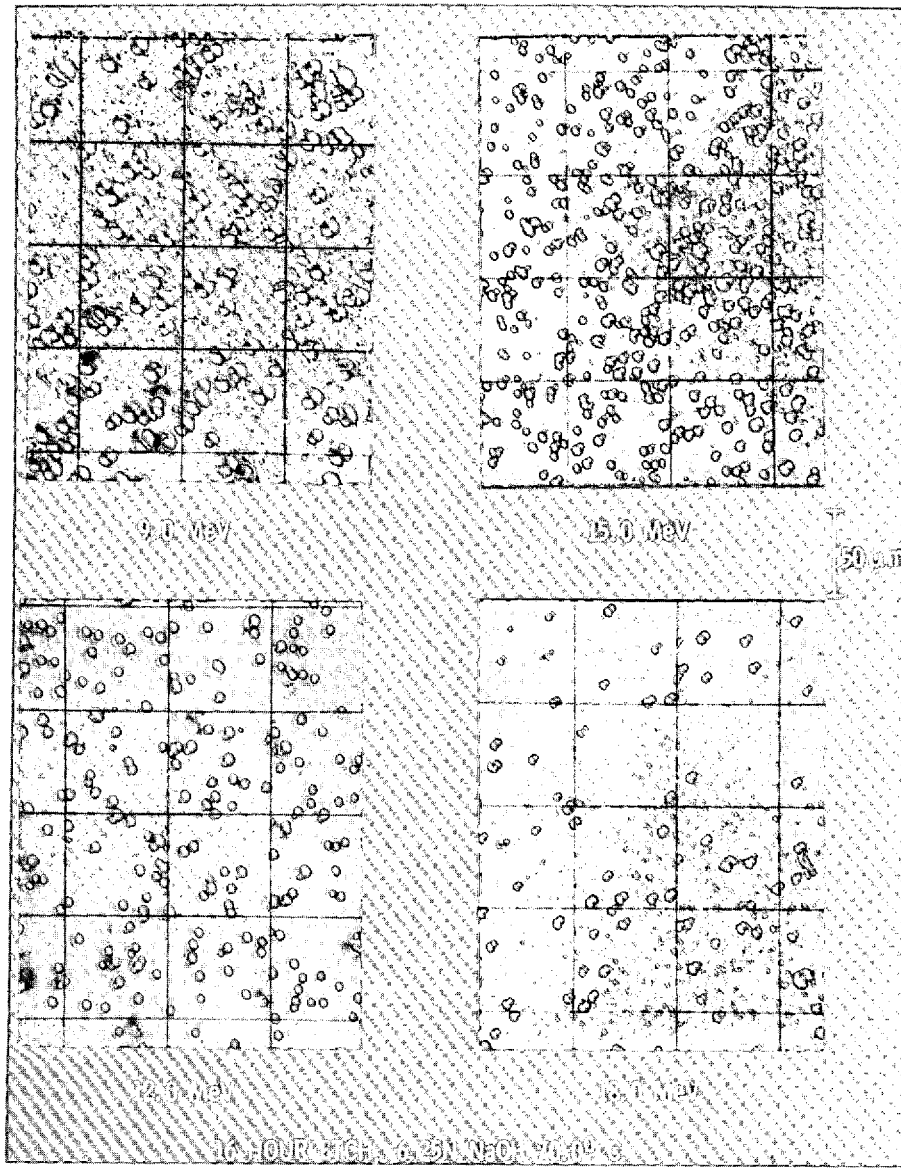

Figure 1. Tracks from normally incident protons in CR-39 polymer solid state track recorders.

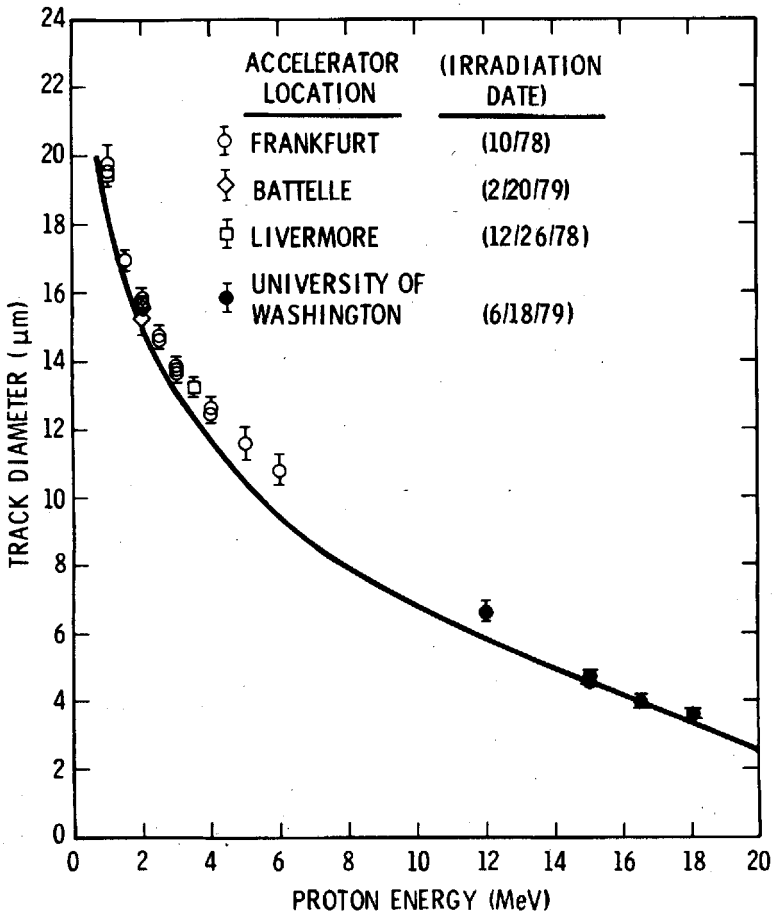

Figure 2. Proton track diameter as a function of energy for CR-39 polymer solid state track recorders etched in 6.2N NaOH for 16 hours at 70°C.

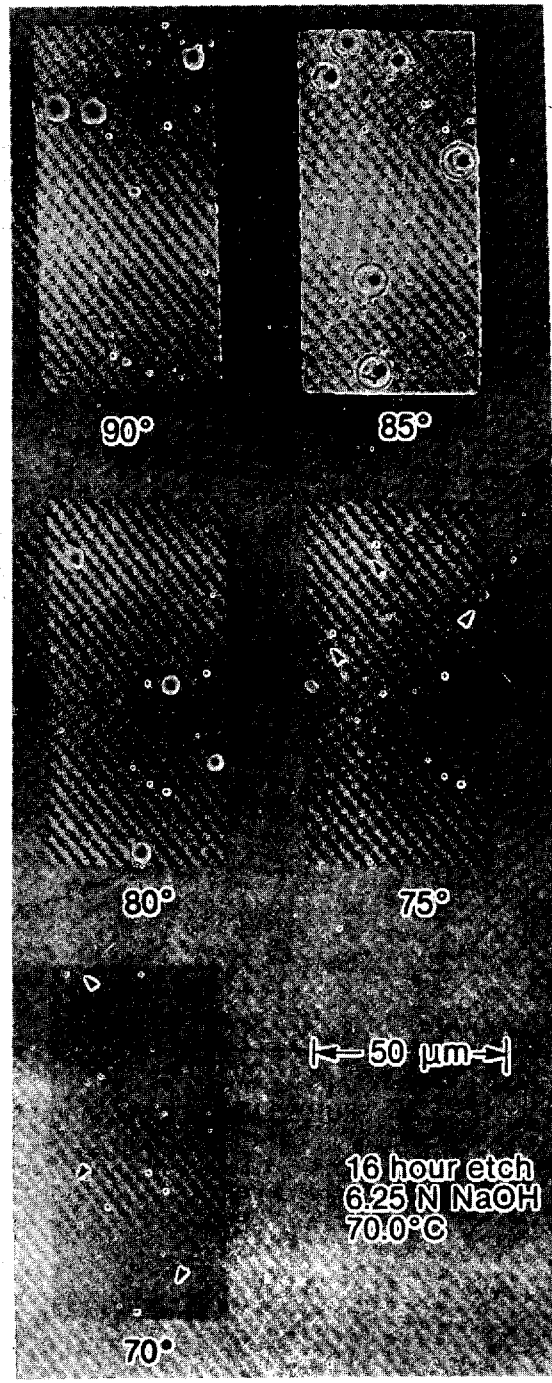

Figure 3. Microphotographs of tracks in CR-39 polymer from 5.00 MeV protons with the indicated incidence angles. The arrows indicate faint tracks at 75° and 70° incidence.

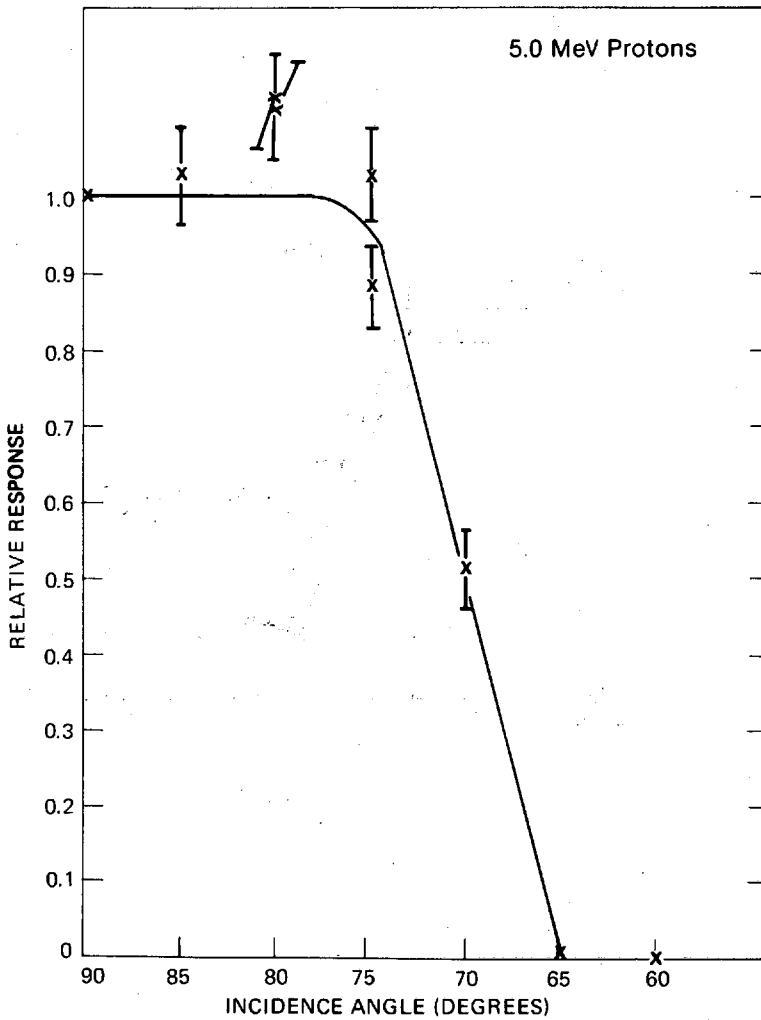

Figure 4. Relative track response of CR-39 polymer as a function of incidence angle for 5.00 MeV protons.

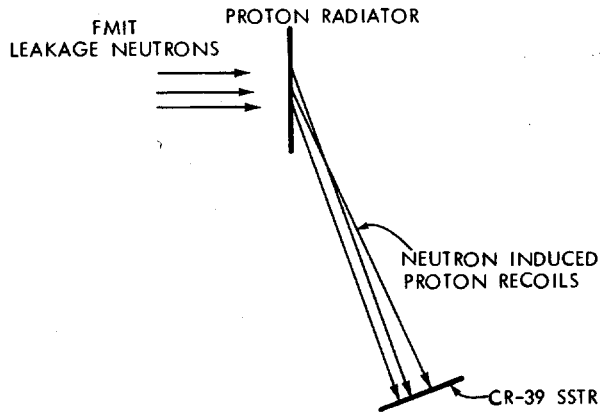

Figure 5. CR-39 polymer neutron-induced proton recoil spectrometry using large angle scattering.

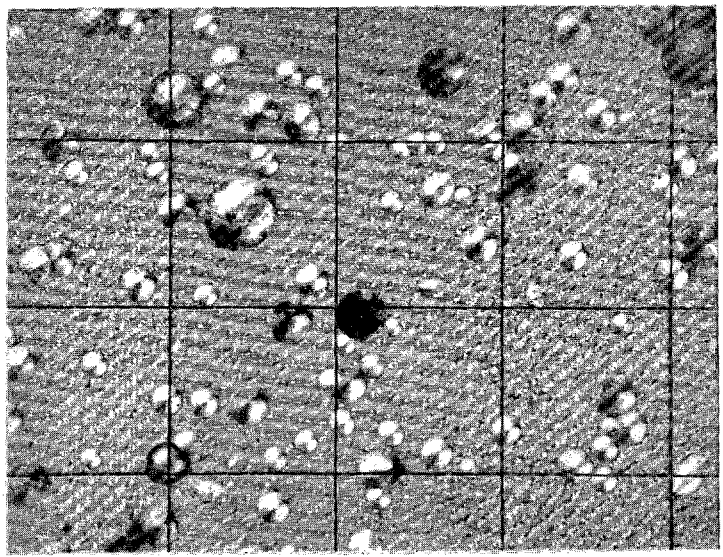

Figure 6. Proton recoil tracks resulting from 14 MeV neutrons. The extremely large track near the center of the field is probably an α particle track produced by the decay of ^{222}Rn or one of its daughters.

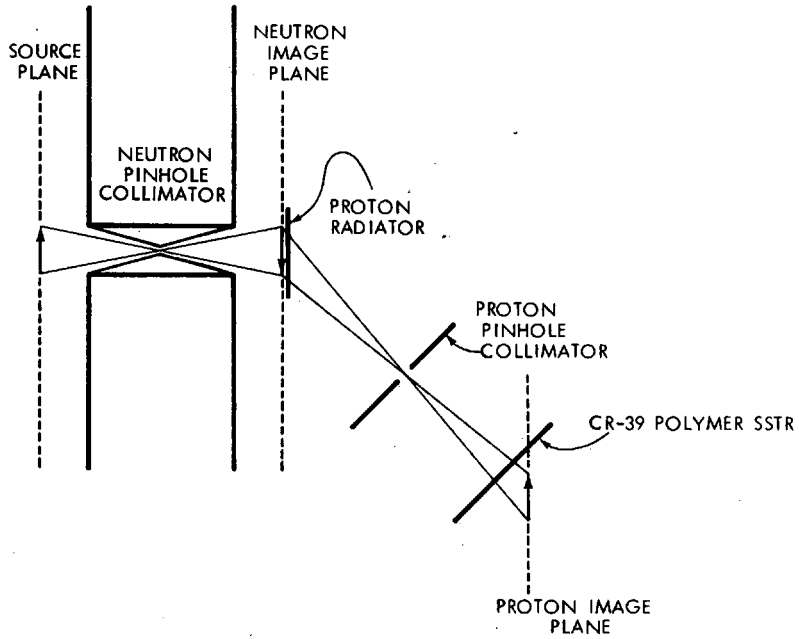

Figure 7. Double pinhole radiography using neutron and proton pinhole collimators.

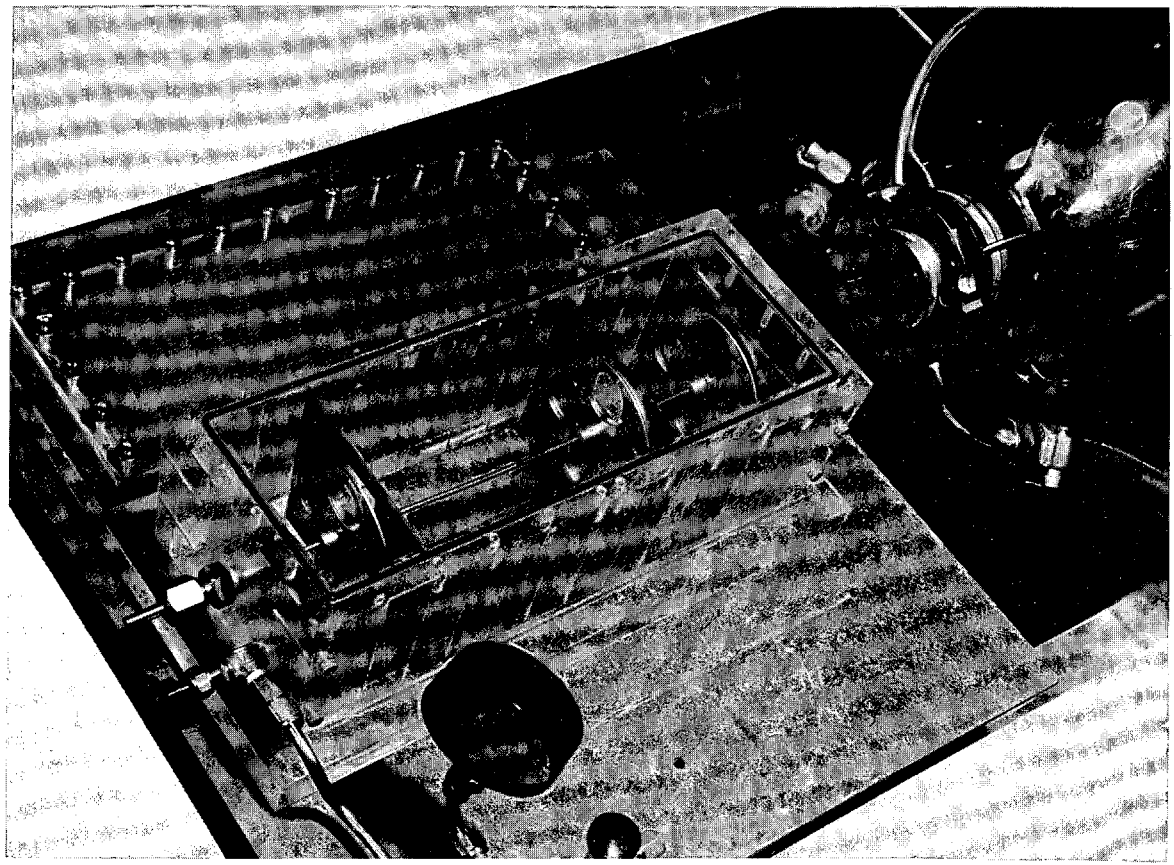

Figure 8. Radiographic neutron camera showing holders for mounting of radiators, collimators, and CR-39 polymer track recorders.

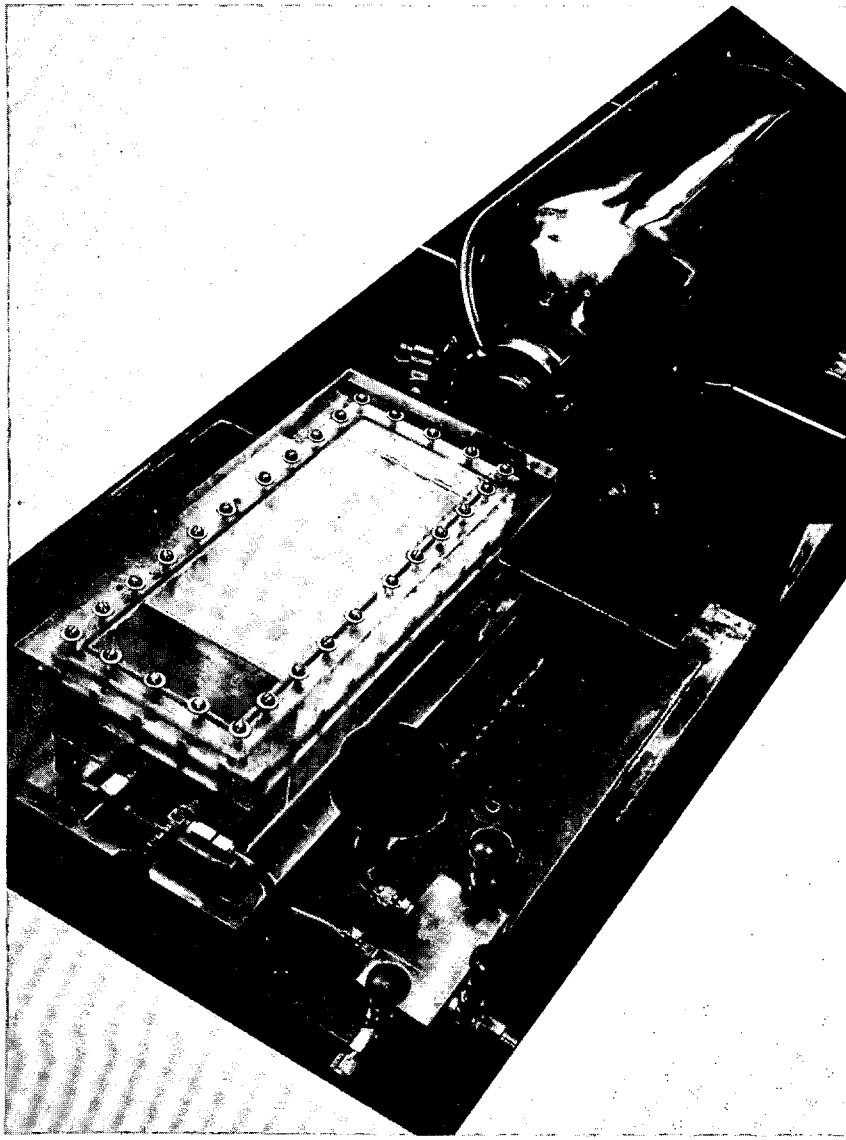

Figure 9. Radiographic Neutron Camera. Camera (foreground) is placed adjacent to a 14 MeV (D-T) neutron generator.

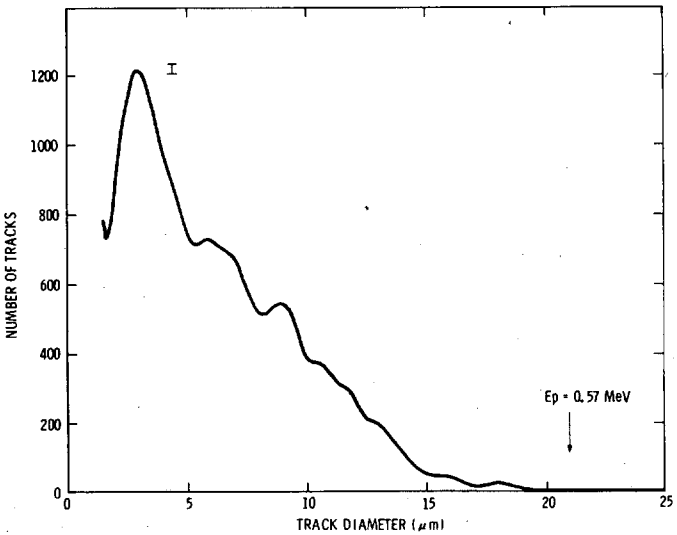

Figure 10a. Diameter distribution for tracks produced in CR-39 polymer irradiated with 0.57 MeV neutrons. The curve represents a smooth fit to a histogram with a bin size of 0.25μm. The CR-39 polymer was etched for 16 hours at 70.0°C in 6.25 NaOH. The diameter corresponding to the maximum proton recoil energy is indicated with an arrow.

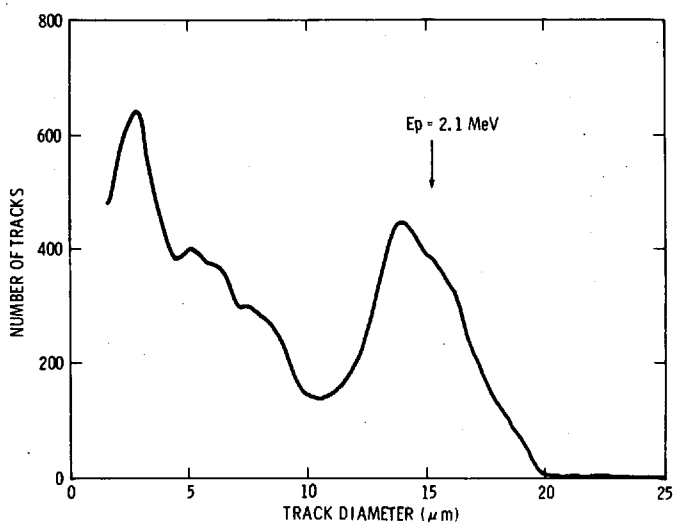

Figure 10b. Track diameter distribution for CR-39 polymer irradiated with 2.1 MeV neutrons.

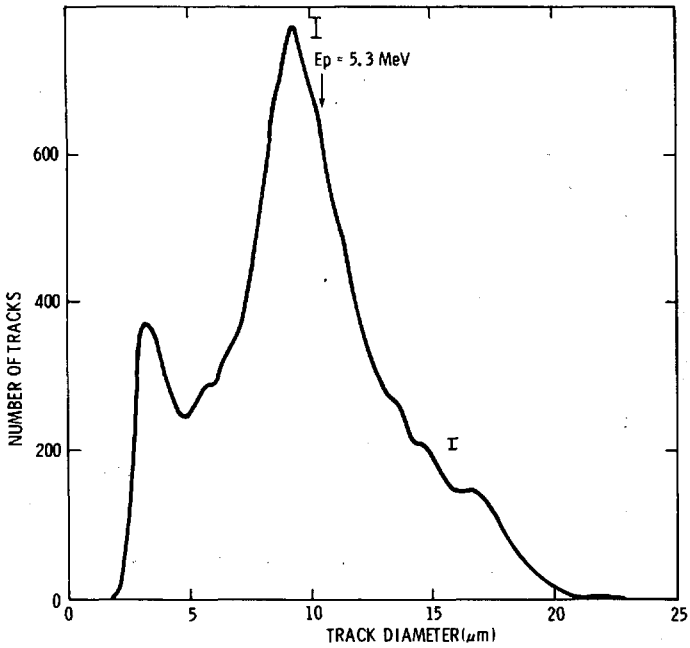

Figure 10c. Track diameter distribution for CR-39 polymer irradiated with 5.3 MeV neutrons.

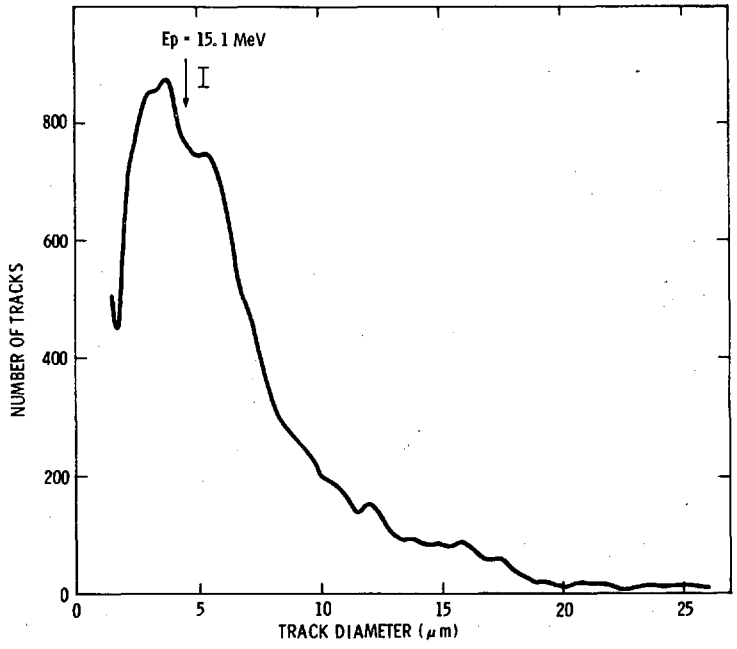

Figure 10d. Track diameter distribution for CR-39 polymer irradiated with 15.1 MeV neutrons.

DAMAGE PARAMETERS FOR NON-METALS IN A HIGH ENERGY NEUTRON ENVIRONMENT

G. F. Dell, H. C. Berry, O. W. Lazareth, and A. N. Goland

Brookhaven National Laboratory*
Upton, New York 11973, U.S.A.

ABSTRACT

Simulation of radiation damage induced in monatomic and binary non-metals by FMIT and fusion neutrons is described. Damage produced by elastic scattering of recoil atoms and by ionization-assisted processes has been evaluated using the damage program DON. Displacement damage from gamma rays has been evaluated by using the technique of Oen and Holmes. A comparison of damage for an anticipated FMIT radiation environment generated by a coupled n-γ transport calculations and a fusion spectrum is made. Gamma-induced displacement damage is sufficiently small that it is dominated by neutron-induced recoil processes. Ionization-assisted displacements may be important depending upon the ionization cross section of the particular non-metal under consideration.

INTRODUCTION

A realistic materials development program for fusion reactors requires the ability to expose samples to environments similar to that in a fusion reactor. The FMIT facility at HEDL will provide a means for performing needed irradiations. However, the volume in FMIT over which the neutron flux exceeds $1.0 \cdot 10^{15}$ n/cm^2·s will be modest ($\sim$10 cm^3), whereas the number of samples to be irradiated will be large and many samples will have to be exposed to a high fluence ($\geq 10^{22}$ n/cm^2). Even in the highest flux region of the FMIT, irradiations lasting a year will be required, and there will most likely be a backlog of samples to irradiate. Therefore it is desirable to expedite the test program by identifying promising materials prior to irradiation. It is also desirable to compare anticipated results from materials exposed to an FMIT radiation environment with the corresponding anticipated results for materials

*Supported by the U.S. Dept. of Energy.

exposed to a fusion reactor environment in order to ascertain whether the results are equivalent. The different nature of the flux spectra coupled with the reasons previously stated justifies a program to calculate expected damage to materials exposed to high fluences of neutrons and gamma rays.

The understanding of processes governing radiation damage in non-metals is an important aspect of the special materials development program for fusion reactors. Some typical uses of non-metals include use in the first wall, as insulators for neutral beam injectors, as insulators in power supplies, and in magnets. In this paper the status of our program in simulating damage in insulator materials is reported. Evaluations have been made for a hypothetical first-wall spectrum as well as for the neutron-gamma ray environment anticipated for the FMIT facility. Similarities and differences are noted as are limitations introduced by incomplete knowledge of cross sections and displacement energies.

FMIT FLUX CHARACTERIZATION

The FMIT radiation environment was generated by using the MORSE Monte-Carlo transport code to perform coupled n-γ transport calculations for a problem having geometry similar to that of an FMIT test facility. This geometry is shown in Fig. 1. A test module containing samples is positioned immediately downstream of a lithium target. The test module is 30 cm wide, 20 cm high, and 20 cm deep, and it is filled uniformly with quarter-density iron. These dimensions were selected arbitrarily and differ somewhat from the 15 cm depth of half-density iron used in calculations at HEDL. The fluxes are slightly different for the two geometries, but the conclusions we reach are unaffected by these flux differences.

Neutrons are generated in a volume 3 cm wide, 1 cm high, and 2 cm thick that corresponds to the dimensions of the lithium target. The deuteron beam is assumed to have uniform intensity along the 3 cm width of the target and to have a gaussian profile in the vertical direction. Neutrons are generated randomly with depth in the target. The energy of the deuteron at the point of interaction is obtained from the range-energy relation for 35 MeV deuterons in lithium. The initial direction and energy of each neutron is generated randomly using Serber's [1] transparent nucleus model as well as the evaporation model. The ratio between stripping and evaporation neutrons was adjusted to give a reasonable fit to the neutron spectra measured by Saltmarsh et al. [2]

The high-energy neutron cross sections of Alsmiller and Barish [3] were used in performing the transport calculations. These cross sections extend to 60 MeV, but only eleven materials, including high-density concrete, are included in the set. As lithium is not among them, the lithium target was assumed to be transparent to neutrons.

The neutron and gamma ray fluxes were determined at several points along the central axis of the test module. Flux characterizations were performed for the test module located within a 5' × 6' × 8' cave having 1 m thick walls of high density concrete.

The fluxes generated by MORSE have units of flux per primary neutron. Conventional units are obtained by multiplying the MORSE fluxes by the neutron yield from 35 MeV deuterons in a thick lithium target. A value of $2.75 \cdot 10^{17}$ n/Coulomb has been deduced by interpolating between the yield at 40 MeV measured by Saltmarsh et al. [2] and the yields at lower energies [4]. The FMIT spectrum at a distance of 4 cm from the lithium target and the fusion spectrum used in the present evaluations appear in Fig. 2.

DAMAGE ANALYSIS

The high-energy neutron cross sections of Alsmiller and Barish were used for characterizing the radiation environment in the test module, and then ENDF/B-V cross sections were used with the damage program DON [5] to evaluate damage parameters in various materials. For the FMIT neutron spectrum used in the present evaluation, 38% of the neutrons have energy greater than 14.9 MeV, and 21% have energy above 20 MeV. For those neutrons having energy above 20 MeV, a high-energy extrapolation of the cross section is made by the DON program.

The neutron and gamma-ray flux spectra generated during the transport calculation were used to evaluate neutron-induced recoil atom damage, gas production rates, recoil damage initiated by energetic electrons produced by gamma-rays, and damage induced by a particular ionization process involving L shell ionization of atoms by primary knock-on atoms. These types of damage are discussed below.

Neutron-Induced Recoil Damage

For monatomic materials we have used the Robinson [6] form of the Lindhard function L(T) to relate recoil energy T to damage energy in the DON program, and we have used the Kinchin-Pease relation to relate damage energy to displacements $\nu(T)$

$$\nu(T) = \frac{0.8\,T\,L(T)}{2E_d} \qquad (1)$$

where E_d is the displacement threshold energy.

For multicomponent materials the division of damage energy between the different species of atoms is complicated, and different atomic species can have different displacement energies. Parkin and Coulter [7] have obtained numerical solutions to the integro-differential equation of Lindhard [8] for several binary materials of interest to us. They have generated tables of displacement functions for Al_2O_3, Si_3N_4, and CaO. These tables

have been incorporated in the damage program DON and serve as lookup tables for relating displacements to PKA energy.

Evaluation of displacement cross sections for a binary material requires four separate calculations; displacements of each species of atom by each species of PKA must be evaluated. As an example, for Al_2O_3, it is necessary to determine the number of oxygen atoms displaced by aluminum PKA's, n(Al,O), as well as by oxygen PKA's, n(O,O). The results are then combined according to the atomic fraction of each species of PKA:

$$n(Al) = 0.4\ n(Al,Al) + 0.6\ n(O,Al)$$
$$n(O) = 0.4\ n(Al,O) + 0.6\ n(O,O). \quad (2)$$

The spectrum-averaged displacement cross sections for Al_2O_3 and Si_3N_4 have been evaluated for the FMIT and fusion reactor first wall spectra of Fig. 2, and the results are listed in Table I.

TABLE I

Spectrum Averaged Displacement and Gas Production Cross Sections for Al_2O_3 and Si_3N_4

Al_2O_3			Si_3N_4		
	FMIT	FUSION		FMIT	FUSION
$\bar{\sigma}_d$(Al) (b/atom)	1111.5	723.6	$\bar{\sigma}_d$(Si) (b/atom)	392.9	220.1
$\bar{\sigma}_d$(O) (b/atom)	428.8	280.1	$\bar{\sigma}_d$(N) (b/atom)	452.4	255.0
$\bar{\sigma}_H$ (mb/atom)	39.0	18.5	$\bar{\sigma}_H$ (mb/atom)	156.0	75.2
$\bar{\sigma}_{He}$ (mb/atom)	53.6	33.0	$\bar{\sigma}_{He}$ (mb/atom)	151.0	61.1
H/dpa(Al) (appm)	35.1	25.5	H/dpa(Si) (appm)	397.0	341.7
He/dpa(Al) (appm)	53.6	45.6	He/dpa(N) (appm)	384.3	277.6

The large difference in displacement cross sections for aluminum and oxygen in Al_2O_3 is a direct result of the different displacement energies used in the evaluation. The displacement energies were measured by Pells and Phillips [9] with a HVEM, and were found to be 18 and ∿75 eV for aluminum and oxygen, respectively. A displacement energy of 60 eV was used for both silicon and nitrogen in Si_3N_4 in the absence of experimental values.

Gas Production

Spectrum-averaged cross sections for hydrogen and helium production are evaluated by the damage program DON. The spectrum-

averaged gas cross sections for Al_2O_3 and Si_3N_4 have been obtained by weighting the contribution from each species according to its atomic percentage in the compound.

The He/dpa ratio can vary with position in the test module. In Fig. 3 the dependence of the He/dpa ratio in silicon upon depth in the module and upon average density of the module is compared to the He/dpa ratio for the fusion spectrum. The decrease of the He/dpa ratio with increasing material thickness results from a decrease in the average energy of the neutron spectrum. As there are many high-energy neutrons in the high flux region near the lithium target, neutron cross sections above 20 MeV are needed for calculations of He/dpa ratios in this important region.

Gamma Ray-Induced Displacements

Displacement cross sections for recoil atom damage initiated by energetic electrons that are produced during gamma-ray interactions have been evaluated using the method of Oen and Holmes [10] for Compton and photoelectric processes and of Cahn [11] for the pair-production process. Their calculations, made for gamma-ray energies up to 5 and 7 MeV, respectively, have been extended to 15 MeV. The displacement functions of Parkin and Coulter were used to obtain the displacement cross sections for aluminum and oxygen in Al_2O_3 exposed to the FMIT gamma-ray spectrum shown in Fig. 4. This spectrum was generated for a point 0.5 cm from the lithium target and represents the most intense gamma-ray flux in the test module. The gamma-ray flux, average energy, and spectrum averaged displacement cross sections for aluminum and oxygen in Al_2O_3 are listed in Table II.

TABLE II

Gamma-ray Induced Damage in Al_2O_3

γ-Flux ($\gamma/cm^2 \cdot s$)	$3.0 \cdot 10^{14}$
$\bar{E}_\gamma$ (MeV)	1.83
$\bar{\sigma}_d^{\gamma}$(Al) barns/atom	0.90
$\bar{\sigma}_d^{\gamma}$(O) barns/atom	0.57

The spectrum-averaged cross sections for gamma-ray initiated recoil-atom damage in the test module is insignificant compared with neutron-initiated recoil-atom damage [9] while the gamma

heating at this position is $1.25 \cdot 10^{13}$ MeV/g·s. It is to be stressed that our present gamma-ray fluxes are probably low. The Alsmiller-Barish cross sections do not include gamma-ray production or gamma-ray downscatter for neutrons whose energies are above 14.9 MeV. Since nearly 40% of the neutrons in the FMIT spectrum of Fig. 2 have such energies, they have not contributed to the calculated spectrum of gamma rays. It is anticipated that inclusion of gamma production and downscatter for neutrons above 14.9 MeV would substantially increase the gamma-ray flux and the average energy of the gamma-ray spectrum. Moreover, the spectrum-averaged displacement cross section could easily increase due to this effect, although gamma-ray initiated displacements induced by energetic electrons should still be much smaller than neutron-induced recoil-atom displacements.

Ionization-Assisted Displacement Processes

A displacement mechanism involving ionization of atoms by a PKA, and subsequent repulsion between the PKA and the ionized atom has been described by Yarlagadda and Robinson [12].

The role of such ionization-assisted damage processes involving L-shell ionization of carbon and Al_2O_3 has been evaluated for the fusion spectrum and for the FMIT spectrum of Fig. 2. These calculations require a knowledge of the cross section for L-shell ionization of an atom by the recoil atom. Unfortunately, few experimental data exist for L-shell ionization in ion-atom collisions. Consequently, we have used the model of Fortner et al. [13] to evaluate cross sections of interest to us. The experimental data of Fortner et al. for L-shell ionization in Ar-Ar interactions were used to estimate the values of the parameters needed to evaluate L-shell ionization cross sections for Al-Al, Al-O, O-Al, and O-O interactions.

The ionization-assisted stopping cross section $S_I(T)$ was expressed by Yarlagadda and Robinson as:

$$S_I(T) = \sigma_I^L(T)\Delta E_d \tag{3}$$

where $\sigma_I^L(T)$ is the L-shell ionization cross section at energy T, and ΔE_d is the energy lost in displacing an atom.

The importance of the ionization-assisted mechanism was assessed by constructing functions, L'(T), similar to the Lindhard function, expressing the fraction of the total energy that is lost through ionization-assisted processes.

$$L'(T) = \frac{\sum_{T'=0}^{T} S_I(T)\Delta T'}{\sum_{T'=0}^{T} [S_n(T)+S_e(T)]\Delta T'} \tag{4}$$

where $S_n(T)$ and $S_e(T)$ are the Lindhard nuclear stopping cross section and the electronic stopping cross section, respectively.

The functions L'(T) were incorporated in DON, and the displacement cross section was evaluated for each ion-atom combination.

The ionization-assisted displacement cross sections for carbon as well as for aluminum and oxygen in Al_2O_3 are listed in Table III along with the corresponding cross sections for neutron-induced damage.

TABLE III

Comparison of Spectrum Averaged Displacement Cross Sections for Ionization-Assisted and Neutron-Induced Recoil Atom Damage in Al_2O_3 and Carbon

$\bar{\sigma}_d$ (barns/atom)	Al_2O_3				CARBON	
	FMIT		FUSION		FMIT	FUSION
	Al	O	Al	O		
Ionization Assisted	79	201	37	94	1200	548
Recoil Atom	1112	429	724	280	730	642
$\frac{\text{dpa(Ion)}}{\text{dpa(Recoil)}}$	0.071	0.469	0.051	0.336	1.64	0.854

Based on these values it is concluded that ionization-assisted damage can be important in non-metals. At present our estimates of this type of damage are crude due largely to uncertainties in ionization cross sections and displacement energies, but these initial results indicate that further consideration of this mechanism is warranted for nonmetals.

CONCLUSIONS

Neutron-initiated recoil atom damage and ionization-assisted damage are coupled to the neutron cross sections through the primary knock-on atom. Gas production depends directly upon the hydrogen and helium production cross sections, and gamma-ray initiated damage depends upon gamma-ray production and downscatter probabilities. Hence any extensions of the neutron cross sections to energies above 20 MeV will have direct impact on our simulations. In addition, ionization cross sections for ion-atom

interactions are needed as are displacement threshold energies for multicomponent materials.

REFERENCES

1. R. SERBER, "The Production of High Energy Neutrons by Stripping," Phys. Rev. 72, 1008 (1959).

2. M. J. SALTMARSH et al., "Characteristics of an Intense Neutron Source Based on the d+Be Reaction," Nucl. Inst. and Methods 145, 81 (1977).

3. R. G. ALSMILLER, JR. and J. BARISH, "Neutron-Photon Multigroup Cross Sections for Neutron Energies ≤60 MeV," Nucl. Sci. and Eng. 69, 378 (1979).

4. P. J. PERSIANI, W. BECKER, and J. DONAHUE, "Neutron Spectra and Basic Data Requirements for (d,Li) and (d,Be) Target Systems," Symposium on Neutron Cross Sections from 10-40 MeV, Brookhaven National Laboratory, May 3-5, 1977, BNL-NLS-50681, p. 151.

5. D. M. PARKIN and A. N. GOLAND, "Calculation of Radiation Effects as a Function of Incident Neutron Spectrum," Radiation Effects 28, 31 (1976).

6. M. T. Robinson, "The Energy Dependence of Neutron Radiation Damage in Solids," in Proc. Brit. Nucl. Energy Soc. Conf. on Nucl. Fusion Reactors, British Nuclear Energy Society, London (1970) p. 364.

7. D. M. PARKIN and C. A. COULTER, "Displacement Functions for Diatomic Materials," J. of Nucl. Materials 85 & 86, 611 (1979).

8. J. LINDHARD et al., "Integral Equations Governing Radiation Effects," Kgl. Dansk, Vedenskab. Selsk, Mat.-Fys. Medd. 33 #10 (1963).

9. G. P. PELLS and D. C. Phillips, "Radiation Damage of α-Al_2O_3 in the HVEM," J. of Nucl. Materials 80, 207 (1979).

10. O. S. OEN and D. K. HOLMES, "Cross Sections for Atomic Displacements in Solids by Gamma Rays," J. Appl. Phys. 30, 1289 (1959).

11. J. H. CAHN, "Irradiation Damage in Germanium and Silicon due to Electrons and Gamma Rays," J. Appl. Phys. 30, 1310 (1959).

12. B. S. YARLAGADDA and J. E. ROBINSON, "Assessment of Ionization-Assisted Damage Processes in CTR First-Wall Materials," J. of Nucl. Materials 63, 466 (1976).

13. R. J. FORTNER et al., "X-Ray Production in C^+-C Collisions in the Energy Range 20 keV to 1.5 MeV," Phys. Rev. 185, 164 (1969).

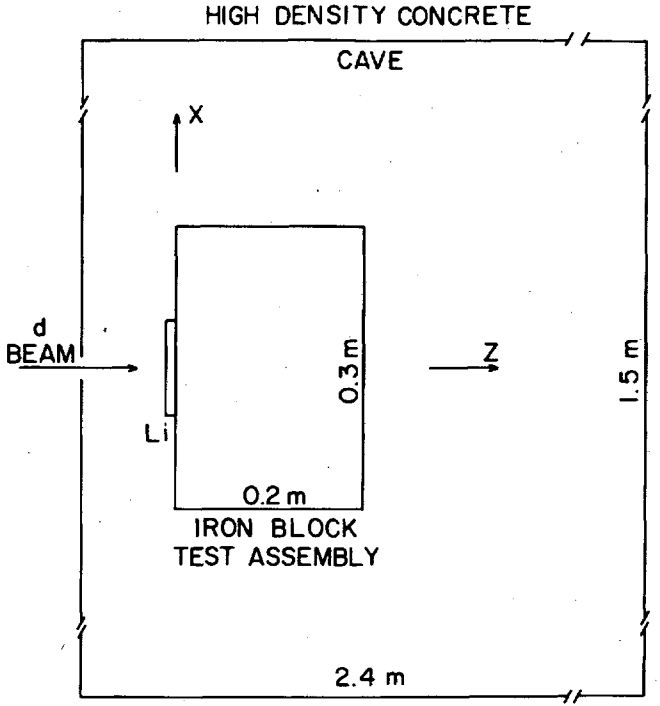

Fig. 1 Geometry used for characterizing the neutron-gamma ray radiation environment in a FMIT irradiation cave with the MORSE transport code. A beam of 35 MeV deuterons (d BEAM) is incident on a volume (Li) representing the dimensions of the lithium target. The iron block test assembly consists of quarter-density iron.

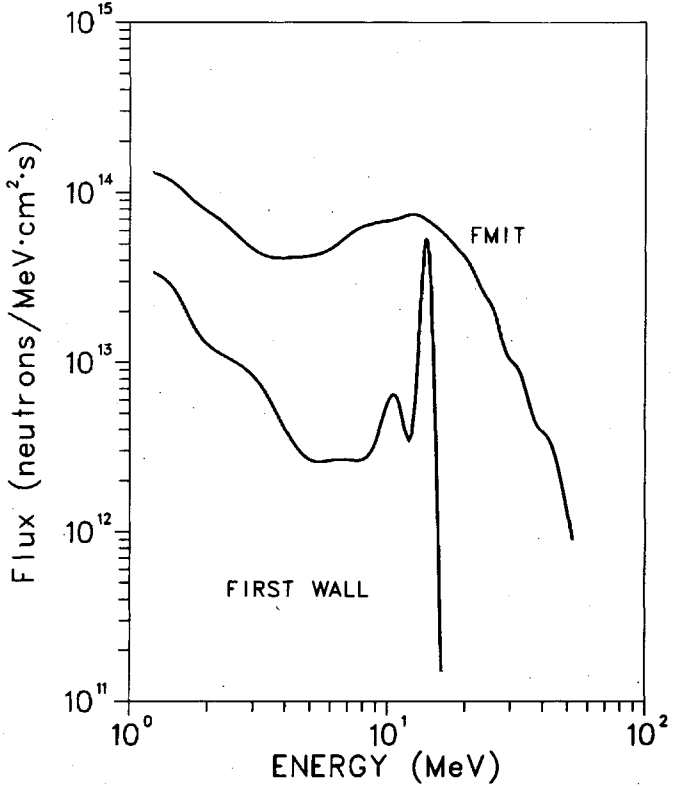

Fig. 2 Neutron spectra used to assess radiation damage. The "First Wall" spectrum corresponds to a 1 MW/m^2 wall loading and has a total flux of $3.81 \cdot 10^{14}$ $n/cm^2 \cdot s$. The "FMIT" spectrum corresponds to the neutron flux at a point on the beam axis 4 cm from the lithium target. Total flux is $1.56 \cdot 10^{15}$ $n/cm^2 \cdot s$.

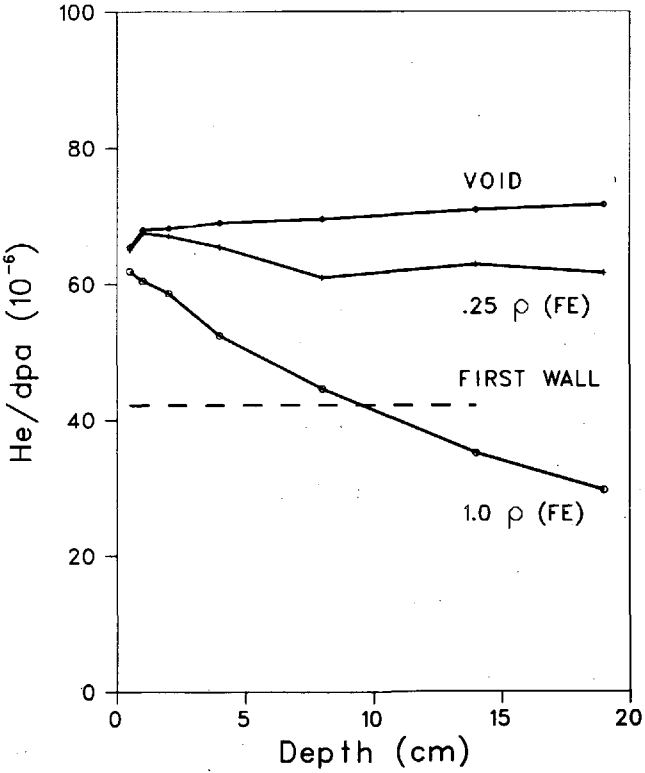

Fig. 3 Dependence of the He/dpa rates upon the depth within the test assembly as well as on the average density of the test assembly.

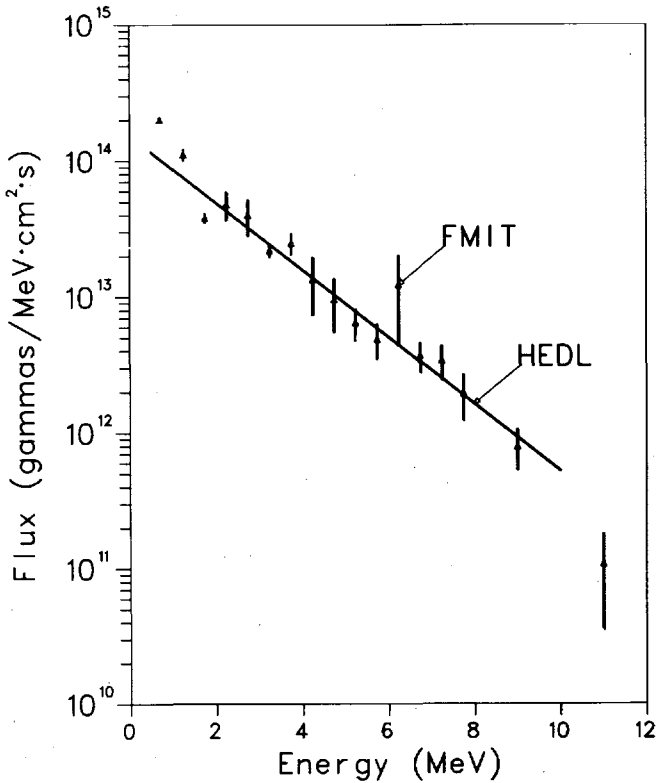

Fig. 4 FMIT-gamma ray spectrum generated with MORSE for a point on the beam axis at a distance of 0.5 cm from the lithium target. HEDL-gamma ray spectrum generated at HEDL for a point on the beam axis and 0.25 cm from the target backing plate.

SOURCE IMAGING FOR FMIT USING A NEUTRON PIN-HOLE CAMERA

R. G. Johnson, J. W. Behrens, and C. D. Bowman

National Bureau of Standards
Washington, D.C. 20234, U.S.A.

ABSTRACT

A pin-hole camera technique has been used to measure the variation in neutron emission intensity over the area of the neutron-producing target of the NBS Electron Linac. The method uses a linear position-sensitive proportional counter (PSPC) with an intrinsic spatial resolution of 1.0 mm. The pin hole is made in a thick sheet of cadmium and neutron energy (< 0.3 eV) selection is achieved by time-of-flight. Both one-dimensional and two-dimensional detectors are now available for this work. In a completely separate experiment the neutron cone obtained from the (d,t) reaction using the associated-particle technique was imaged by a two-dimensional PSPC. This second measurement demonstrated the use of the two-dimensional detector for imaging high energy (14 MeV) neutrons.

INTRODUCTION

The Fusion Materials Irradiation Test (FMIT) Facility being constructed at the Hanford Engineering Development Laboratory is providing some unique challenges in engineering and physics. An average beam power of 3 MW is planned for a flowing Li target with 10-cm^2 area. The effective and safe use of this facility will require accurate real-time beam intensity and position information for use in accelerator operation. Also accurate measurements of neutron fluence [1] and spectral information will be facilitated with real-time measurements of the neutron source term from the target. This information could be obtained by operation of a neutron pin-hole camera at a back angle and perhaps also in the forward direction.

The NBS Neutron Measurements and Research Group has had for the past several years an interest in developing and using neutron detectors which can provide position sensitivity with a 1-2 mm resolution. Such detectors can be used in a variety of measurements including neutron pin-hole camera systems, thermal and resonance neutron radiography [2], small angle scattering measurements, etc. As part of this program in using spatially-resolved neutron detectors, the present paper describes two experiments in this area. In the first experiment the variation in neutron emission intensity over the area of the neutron-producing target of the NBS Electron Linac using the pin-hole camera technique is described. In the second experiment the neutron cone from the (d,t) reaction as defined by the associated-particle technique and imaged by a two-dimensional position-sensitive proportional counter (PSPC) is described. This measurement was performed at the NBS Positive Ion Van de Graaff Accelerator.

EXPERIMENT I

In Fig. 1 the experimental set-up for the first measurement is illustrated. This neutron-producing target of the NBS Electron Linac consists of water-cooled tungsten plates followed by a 5 cm by 18 cm by 20 cm rectangular container filled with water for neutron moderation. The linac which was operated at a repetition rate of 360 Hz, an electron pulse width of 1 μs, and an electron energy of 106 MeV delivered 4 kW of power on the target. The evacuated time-of-flight tube was perpendicular to one of the large flat faces of the water container and was collimated to view a 13-cm diameter circle at the target. At a distance of 4.0 m from the neutron target a 1.6-mm thick Cd sheet with 2.0-mm hole in the center was placed to serve as the pin hole. The one-dimensional position-sensitive proportional counter was oriented for horizontal position sensitivity.

The PSPC, designed and built in collaboration with Oak Ridge National Laboratory, has a sensitive length of 50 mm and a spatial resolution of 1.2 mm. Position sensitivity is obtained by RC-encoding [3]. The detector contains 3 atm ^3He, 7.5 atm Xe, and 0.5 atm CO_2. To obtain spatial information in the vertical direction the detector could be remotely positioned in that direction. The detector was therefore moved in 1.6-mm steps with separate runs taken at each step.

Since Cd was used to define the pin hole, only neutrons with energy below the Cd cut-off were used to produce the image. Neutron-energy selection was obtained by placing a gate on the neutron time-of-flight to accept neutrons with energy below 0.3 eV.

A total of 11 vertical steps of the detector were taken to image the neutron target. The horizontal information from the PSPC was collected by a 256-channel pulse-height analyzer. Analysis of these pulse-height distributions was quite simple. A small background (approximately 5% of the signal, obtained in separate

runs with Cd covering the neutron target) was subtracted. The data were then grouped in four-channel sums and plotted both in a three-dimensional representation and in a grey-scale representation as shown in Fig. 2. In the grey-scale representation of Fig. 2 the number of dots per pixel is proportional to the counts in the respective channel of the pulse-height distribution. The circle represents the field-of-view imposed by the flight-path collimation. Also shown in Fig. 2 are the pixel size and resolution. The pixel size was 0.8 mm by 1.6 mm at the detector. The resolution in the horizontal direction was 1.5 mm and was determined by the 1.2-mm resolution of the PSPC and the 1.0-mm radius of the pin hole. The vertical resolution was $\sim$ 1.7 mm at the PSPC, determined primarily by the 1.6-mm displacement of each step. Recalling the object distance (4.0 m) and image distance (0.5 m) of the experimental set-up, the magnification of the pin-hole camera is 1/8. This then implies a resolution at the neutron target of $\sim$ 1.3 cm in either direction. For this initial experiment the magnification was kept smaller than ultimately necessary in order that the background outside the field-of-view of the pin-hole camera could be readily assessed. A factor of three larger magnification (with approximately the same improvement in resolution) can be obtained with no loss in field-of-view.

Several improvements in this type of measurement are now possible and further studies are planned. A two-dimensional PSPC is now available and its use would both shorten the beam time necessary for this measurement (obviously eliminating the need for stepping in the vertical direction) and improve the resolution in the vertical direction. To reach higher neutron energies will require a more complicated pin-hole collimator. Design studies for such a collimator are now underway.

EXPERIMENT II

Recently the Neutron Measurements and Research Group at NBS has been working on a measurement of the $^{235}U(n,f)$ cross section at 14 MeV. To perform this measurement an associated-particle system using the (d,t) reaction has been set up at the 3-MV Positive Ion Van de Graaff Accelerator at NBS. The experimental arrangement is shown in Fig. 3. Molecular deuterium ions accelerated by the Van de Graaff strike a tritiated Ti target. Alpha particles are detected by a surface-barrier detector at an angle of 82.5° relative to the incident deuteron beam. Neutrons (E_n = 14 MeV) in coincidence with these alpha particles are therefore kinematically defined to a cone centered at 90° relative to the incident beam and with a half angle defined by the collimation of the alpha detector.

A two-dimensional PSPC was placed in the position normally occupied by the fission chamber. Although the original intent was to use a high-pressure ($\sim$ 15 atm) detector filled with ^4He, Xe, and CO_2, electronics problems forced replacement of this detector

with one of the same design but filled with 1.0 atm ^3He, 1.5 atm Xe, and 0.1 atm CO_2. This latter detector was designed for low-energy neutrons and consequently had significantly larger resolution at 14 MeV than the desired detector. Nevertheless, the results of the measurement show a proof-in-principal for the concept.

The two-dimensional PSPC, again designed and developed in collaboration with ORNL, has an active area of 50 mm by 50 mm. Three crossed wire arrays are contained within the counting gas volume. The center plane is the anode while the outer planes of mutually perpendicular wires are the cathodes. Position sensitivity is obtained by RC-encoding [3]. The thickness of the active volume of the detector is 10 mm.

To define a valid event a three-fold coincidence between the alpha detector and the two cathodes of the PSPC was demanded. A coincidence resolving time of 400 ns was allowed. Valid events were then collected in a 64 channel by 64 channel array through a two-parameter data collection system. The results of the measurement are shown directly in Fig. 4 both in a three-dimensional representation and in a grey-scale representation. The neutron cone of the associated-particle system is readily apparent.

The resolution of the low pressure PSPC used in this measurement was estimated from the range of ^3He recoils and the geometrical limits of the detector to be 8 mm. This compares very well with the measured resolution as determined by the known full angle of the neutron cone and the width of the peak in Fig. 4, i.e., a resolution of approximately 9 mm.

CONCLUSIONS

In the two measurements described in this report, the concept of active neutron dosimetry using a pin-hole camera technique and a two-dimensional position-sensitive proportional counter for high or low energy neutrons has been demonstrated. In the first experiment low-energy neutrons from an extended neutron source were imaged through a pin-hole camera arrangement. The resolution at the detector was $\sim$ 1.6 mm. Although in this preliminary measurement a small magnification was chosen in order to observe the backgrounds, so that the resolution at the source was rather poor, it is clear that the resolution at the source can easily be made to approach that of the detector.

In the second experiment the use of a two-dimensional PSPC for the measurement of positional information for high-energy (14 MeV) neutrons was demonstrated. Although non-fundamental experimental problems caused a rather poor positional resolution to be obtained, the calculated resolution for high-pressure ^4He filled PSPC is 2.1 mm.

The only major missing element required for a high-energy pin-hole camera system is the pin-hole collimator. A preliminary design which can provide a 1-2 mm pin-hole has been made and no major problems in its construction are foreseen. Once the collimator is constructed the whole system will be tested at the NBS Positive Ion Van de Graaff Accelerator.

ACKNOWLEDGMENTS

The authors are pleased to acknowledge the fruitful collaboration with M. K. Kopp, J. A. Williams, and H. N. Hill (Instrumentation and Controls Division of Oak Ridge National Laboratory) in the design and construction of the PSPC detectors used in these measurements. The authors also want to thank O. A. Wasson for his invaluable help in the Van de Graaff measurement.

REFERENCES

1. C. D. BOWMAN, "Evaluation of Proposed FMIT Neutron Dosimetry System," Report to Hanford Engineering Development Laboratory, (1979)

2. J. W. BEHRENS, R. A. SCHRACK, and C. D. BOWMAN, "Resonance Neutron Radiography Using a Position-Sensitive Proportional Counter," Trans. Am. Nucl. Soc. 32, 207 (1979).

3. C. J. BORKOWSKI and M. K. KOPP, "Design and Properties of Position-Sensitive Proportional Counters Using Resistance-Capacitance Position Encoding," Rev. Sci. Instrum. 46, 951 (1975).

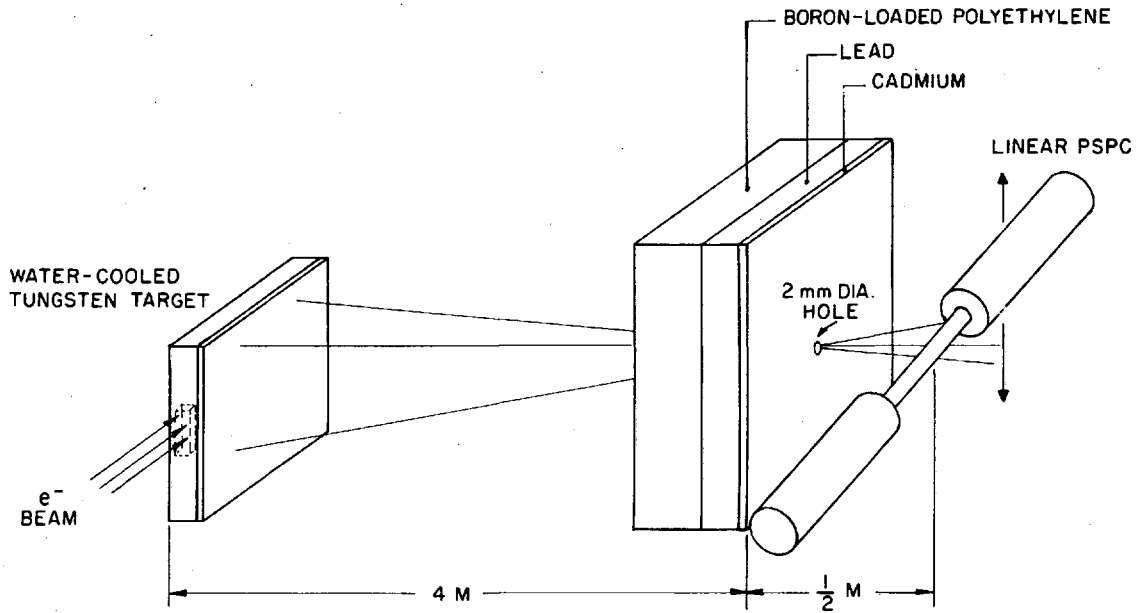

FIG. 1. Experimental arrangement for imaging the neutron emission from the neutron-producing target of the NBS Electron Linac.

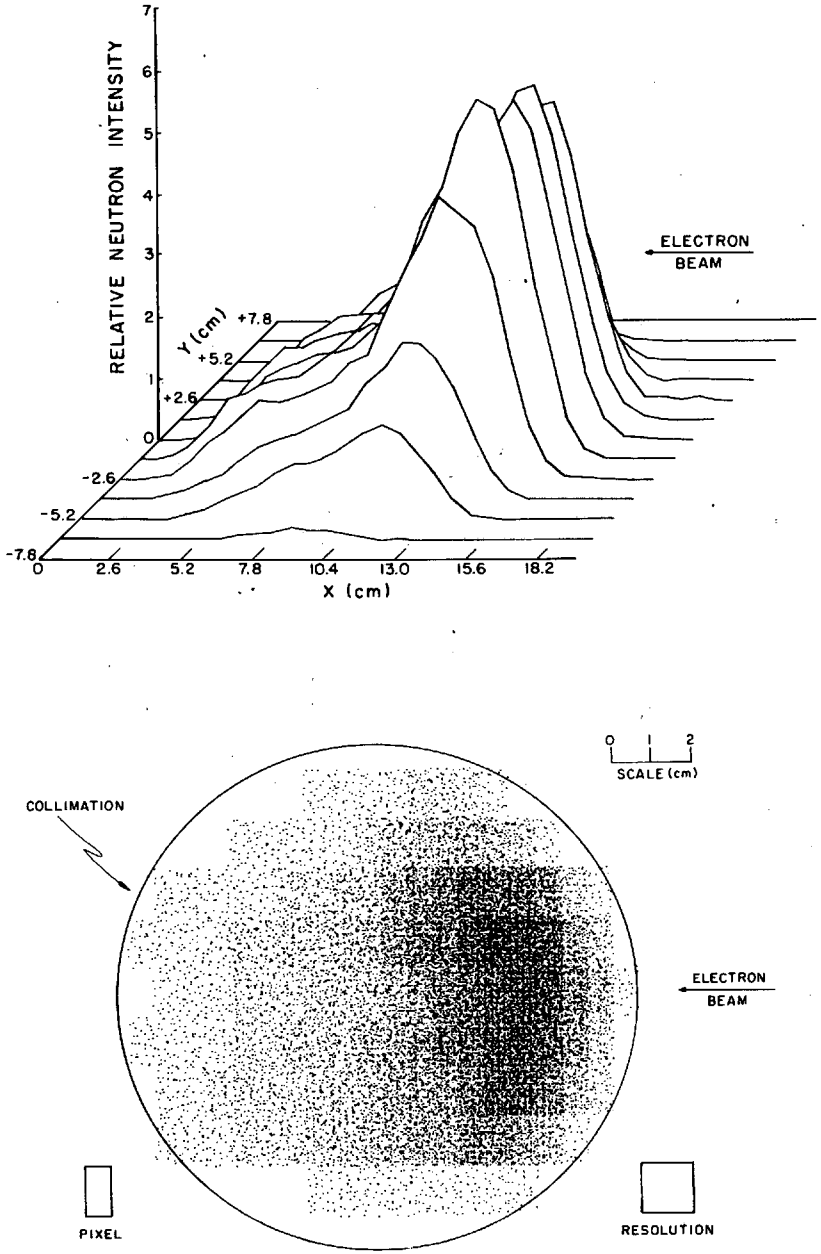

FIG. 2. Pin-hole camera image of the linac neutron-producing target. Both a three-dimensional representation and a grey-scale representation are shown. See text for details.

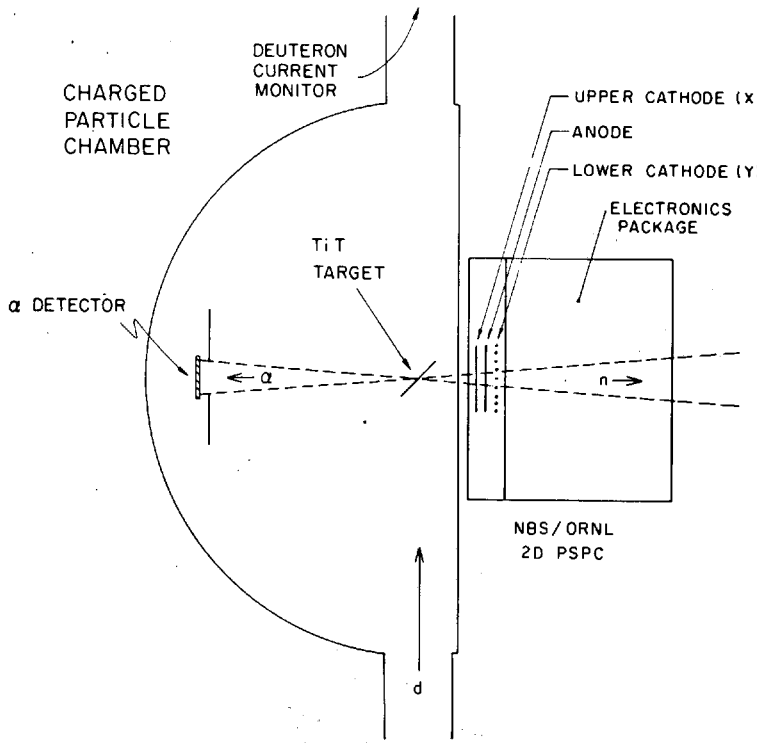

FIG. 3. Schematic diagram of the imaging system using the associated-particle technique and two-dimensional PSPC.

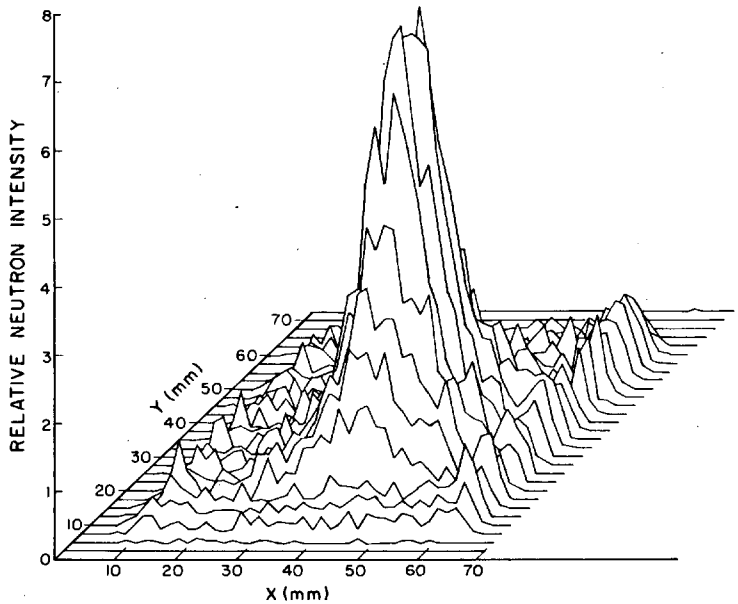

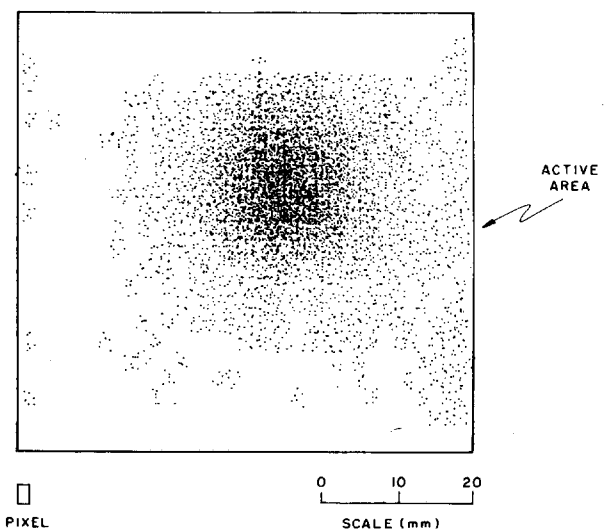

FIG. 4. Image of the associated-particle neutron cone. Both a three-dimensional representation and a grey-scale representation are shown.

NUCLEAR MODEL CODES AND DATA EVALUATION

Session Chairman: E.D. Arthur, LASL

RECENT DEVELOPMENTS IN NUCLEAR REACTION THEORIES AND CALCULATIONS

D. G. Gardner

Lawrence Livermore Laboratory
Livermore, California 94550, U.S.A.

ABSTRACT

A brief review is given of some recent developments in the fields of optical model potentials; level densities; and statistical model, precompound, and direct reaction codes and calculations. Significant developments have occurred in all of these fields since the previous Conference in 1977, which will greatly enhance our ability to calculate high-energy neutron-induced reaction cross sections in the next few years.

INTRODUCTION

Selecting subjects and material for this review paper has presented certain difficulties. At this conference we already have had the opportunity to be exposed to many excellent status reports on high-energy cross sections, on various data bases related to dosimetry, shielding design, and on other nuclear data needs of the fusion community. At the recent International Conference on Nuclear Cross Sections for Technology, Knoxville, Oct. 1979, R. C. Haight reviewed the subject of neutron cross sections for fusion [1], P. G. Young, E. D. Arthur, and D. G. Madland spoke on the use of nuclear models and calculations to supplement our various evaluated data libraries [2], and D. L. Smith [3] covered neutron dosimetry for radiation damage in fission and fusion reactors. In addition, M. R. Bhat has made an extensive review of evaluated nuclear cross sections for fusion reactor calculations [4]. And, as Haight [1] points out, it is de rigueur to include in reviews a summary or at least a table of all pertinent previous reviews.

To avoid the pitfall of merely summarizing previous reviews, I will avoid any discussion of data needs or data bases. Instead, I will try to concentrate either on topics which were not covered in this session of the 1977 Conference on Neutron Cross Sections from 10 to 40 MeV, or where significant advancements have occurred. If

the person making such an advancement has contributed a paper to this session, I will defer and let the expert speak for (him/her) self. The topics that I will touch upon, subject to the above restrictions, are: the optical model, level densities, some aspects of statistical model codes and calculations, some aspects of precompound and direct reactions, and suggestions for new data libraries.

THE OPTICAL MODEL

For those of us involved in making detailed Hauser-Feshbach (HF) cross-section calculations, one of our primary sources of exasperation involves the search for an adequate set of optical model parameters for use in calculating transmission coefficients. We require a neutron optical model potential that is valid not only at the maximum incident particle energy of interest, but for all lower energies, usually down to the tens of keV region. Hopefully the potential is adequate at least for several neighboring nuclei, such as adjacent isotopes of a given element, and the more global the parameter set is, the greater is its convenience.

On the other hand, if one is interested only in a rough survey of a large number of reactions, or if the incident particle energy is high enough so that the cost of detailed HF calculations becomes prohibitive, then perhaps calculations of the Weisskopf-Ewing type, where only inverse cross sections are involved and angular momentum is not explicitly considered, may be adequate. In this case it is quite acceptable to patch together inverse cross-section sets calculated in different energy regions with different optical model parameters. For example, one might create such a cross-section set for incident neutrons by using the parameters of Moldauer [5] for neutrons up to about 2 MeV, the parameter set of Wilmore and Hodgson [6] to span the range from 2 to 25 MeV, and finally, one of the optical models described by Becchetti and Greenlees [7] to carry one up to 50 or 60 MeV. It has been suggested that the proton potential of Becchetti and Greenlees, with the Coulomb term removed from the real potential and the signs of the isospin terms reversed, may be preferable to their neutron potential in certain cases.

Perhaps the single most important qualification for any optical model is that it reproduce well the total cross section over the entire energy range. In a paper by T. W. Phillips and H. Camarda, in this session, we will hear about their total cross-section measurements for neutrons up to 50 MeV on a number of elements in the mass range from Ba to Nd, together with the resulting optical model parameters. I would like, in addition, to direct your attention to recent reviews in this area. One by D. Wilmore and P. E. Hodgson [8] discusses a number of the older, more commonly used neutron potentials, including their own [6], and those of Moldauer [5], Becchetti-Greenlees [7], and Englebrecht and Fiedeldey [9]. This last is of particular interest as it was

designed to extend Moldauer's neutron results beyond 1 or 2 MeV, in fact, up to 200 MeV. Furthermore, Ref. 8 also lists a large number of optical model and statistical model codes which have been used in recent years.

Delaroche, Lagrange and Salvy [10] give an excellent review of the optical model with particular emphasis on the coupled-channel model, and describe the "SPRT" method used at Bruyères-le-Châtel for the determination of neutron optical model parameters that fit experimental data over a wide range of energies. The "S" and "P" refer to s-wave and p-wave neutron strength functions, the "R" is the potential scattering radius, while the "T" comes from the total cross-section data used in the analysis. Two more recent reviews are those of Lagrange [11] and Rapaport, Kulkarni, and Finlay [12]. The latter describes a global parameter set for neutrons in the energy range 7-26 MeV, and for spherical nuclei in the mass range 24 to 209. In the former paper, Lagrange is particularly concerned with the energy and isospin dependence of the potential. The isospin dependence is necessary for the construction of a general nucleon-nucleus potential that will fit both neutron and proton data, as specified in the Lane model [13].

The paper in this session by Hansen, Grimes, Pohl, and Wong will describe an attempt to obtain a "Lane-consistent" potential for neutrons and protons in the heavy mass region around Th and U. The general approach is mentioned in the above review papers of Delaroche [10], Lagrange [11], and Rapaport [12]. One of the first attempts to get such a global, nucleon-nucleus optical potential was described by Patterson, Doering, and Galonsky [14]. They added an imaginary surface energy-dependent isovector term to the Coulomb-corrected proton parameter set of Becchetti and Greenlees [7], and modified the parameters to fit some (p,n) isobaric analog state (IAS) data. The resulting potential provided reasonable fits to neutron scattering data, and was stated to be useful for the entire mass range from Al to Bi and for energies in the 7-24 MeV range.

Of all the work mentioned above, only that of the Bruyères-le-Châtel group [10,11] has addressed itself to providing potentials that span a wide enough energy range and are valid down to the 10 keV region, to be fully useful to those of us making statistical model calculations. A further example of the SPRT method combined with the Lane-model approach was given by Lagrange [15] for nucleons interacting with ^{93}Nb, in the energy range of 10 keV to 50 MeV. In Fig. 1, I show some of Lagrange's calculations for protons near 50 MeV. The top dashed line was obtained using a potential that was derived from 18-MeV (p,n) data for a pure surface imaginary potential and energy independent isovector terms. The improvement shown in the dash-dot curve resulted from the inclusion of a volume imaginary term, while the best fit (solid curve) required the further addition of an energy dependence in the isovector component of the real potential. Recall that Patterson [14] had also introduced an energy dependence in one of the isovector terms, but he chose the imaginary potential instead.

Perhaps all that is necessary is a redistribution of the isovector strength between the real and imaginary potentials, and this may be parameterized effectively by a linear energy dependence in either one of the isovector terms.

The parameter sets of Lagrange and colleagues often show a surface imaginary potential that increases with energy up to about 10 MeV, at which point the potential either remains constant or decreases with energy as a volume imaginary component grows in. As Delaroche [10] points out, imaginary potentials that continually decrease with increasing energy, such as Wilmore-Hodgson [6] and Becchetti-Greenlees [7] simply do not work well at very low energies. This has also been reported recently by Fitzgerald, et al. [16] in a study of (p,n) IAS measurements on ^{119}Sn. Here the imaginary potential for the neutrons was observed to increase for at least 6 MeV before leveling off or possibly decreasing. Their results are shown in Fig. 2. This type of imaginary potential, although not common, has been used a number of times in the past for neutrons, and Delaroche's [10] paper gives four additional references besides those listed here. The work that I've cited regarding the Lane-type potential is relevant for this conference because much of the neutron optical model information required for the study of reactions up to 50 MeV may be derived from proton reaction studies.

If the situation is unsatisfactory for global spherical optical-model sets, the situation for coupled-channel calculations is, of course, much worse. Recent efforts of several laboratories to obtain parameter sets for deformed potentials have been discussed by Delaroche, et al. [10]. One important problem always has been how to determine the proper deformation parameters, say β_2 and β_4, to use for rotational nuclei. A thorough review of this problem was given recently by Haouat [17], who points out that deformation parameters derived from different experimental methods can have different values. Quite a few sets of experimental and theoretically-calculated parameter values are compared in his paper.

I'd like to make two more comments before leaving the subject of coupled-channel calculations. The first concerns the determination of an initial or trial set of deformed well parameters. Madland and Young [18] made a study of six actinide elements from ^{232}Th to ^{239}Pu, and developed a method of deriving parameters for a deformed potential from a local, energy and isospin dependent spherical potential. They observed that the geometric parameters remained unchanged from the spherical fit, and that the imaginary surface potential required by the deformed well was about 70% of the spherical imaginary depth. The real well depth was increased by about 3% over the spherical case. Lanier [19] at Livermore reports success with the same approach in the Ta mass region. At first glance the results are somewhat surprising, because one might expect offhand that the direct inelastic strength in the coupled-channel calculation would come mainly from the shape elastic cross section. It would be important to know if the method works in

other deformed mass regions, because of the great savings in time a spherical search code has over a deformed code.

My last comment concerns the calculation of transmission coefficients with a deformed potential. Several coupled-channel codes will provide such transmission coefficients, but not when they are run under the adiabatic approximation. Recently V. Madsen of Oregon State University solved this problem, and his results will be published in the near future [20]. Again, a great savings in computer time will be the result.

LEVEL DENSITIES

Statistical model calculations require, in addition to transmission coefficients, level density information for the residual nuclei. Many of us use the Gilbert-Cameron formulation [21], with the updated parameters of Cook, et al. [22], which we further adjust to fit the latest discrete level and resonance information. The Cook parameters have recently been reexamined [23], but the spin cut-off expression used by Gilbert and Cameron has been retained:

$$\sigma^2(E) = \frac{6}{\pi^2} \langle m^2 \rangle (aU)^{1/2} \tag{1}$$

where the mean square spin projection was taken as

$$\langle m^2 \rangle = 0.146\ A^{2/3}. \tag{2}$$

Here a is the level density parameter and U is the excitation energy above the pairing gap. Reffo [24] and other investigators have suggested that a better average representation for $\langle m^2 \rangle$ would be:

$$\langle m^2 \rangle = 0.24\ A^{2/3}. \tag{3}$$

I have examined a number of cases in the mass 90 region, and a few other cases where the spins of the first 25 to 30 levels were known. The spin cut-off parameter may be calculated from the spins of discrete levels with the expression

$$\sigma^2 = \frac{1}{2N} \sum_{i=1}^{N} (I_i + 1/2)^2. \tag{4}$$

Fig. 3 gives the results for ^{93}Nb. We are plotting in the histogram the calculated σ^2, that arises from the summing of additional levels in groups of five, against level energy. Also shown are the values calculated from Eqs. 2 and 3. The pairing gap and the energy of the last level are indicated on the figure. This is perhaps a more sensitive test than comparing the shape of a calculated spin distribution with the experimental distribution of the low-lying levels. My limited experience supports the opinion of Reffo. Since the spin cut-off parameter comes into the expression for the state density as well as the level density, the new

parameters of Cook [23] that are used to calculate the level density parameter a would have to be modified to compensate for the approximately 28% decrease in the level density which results from the choice of Eq. 3 rather than Eq. 2.

The use of ad hoc parameterizations of level densities, such as that of Gilbert and Cameron, have proved rather successful for nuclei near the line of stability, particularly beginning a few MeV above the pairing gap. There is no good substitute for knowledge of the first 20 or 30 discrete levels above the ground state, particularly when the levels tend to favor one parity state or if the nucleus is deformed and rotational bands are in evidence. I will return to this point in a later section of this paper. As one departs from the line of stability, large uncertainties develop in our knowledge of the level densities. Another problem arises with reactions induced by 50 MeV neutrons. Not only can you produce nuclei far from stability, but you must trust your level density expression up to high energies, usually way above any direct experimental measurements. There now appears to be hope that we may have, in the not too distant future, a better method to estimate these level densities.

At a recent conference [25] devoted to spectral distribution theory [26], the application of this approach to the determination of nuclear level densities was explored. Many problems that arise in the Fermi gas model, such as the ad hoc inclusion of pairing, shell, and collective effects, are due to the neglect of the two-body force. Spectral distribution theory allows one to include the full two-body force in the moment calculation of level densities. The level distribution in a finite basis set is assumed to be Gaussian, and can be characterized in terms of the total number of states N, the average energy of the states $\langle H \rangle$, and the average energy squared of the states $\langle H^2 \rangle$. The first moment of the distribution is its centroid, while the second moment defines its width.

$$\rho(E) = \frac{N}{\sqrt{2\pi}\sigma_H} \exp\left[-\frac{(E-\langle H\rangle)^2}{2\sigma_H{}^2}\right] \tag{5}$$

where $\sigma_H = [\langle H^2\rangle - \langle H\rangle^2]^{1/2}$. (6)

The level distribution may be expanded first in terms of energy, and then, at each specified energy, expanded again in terms of the angular momentum projection J_Z, or the distribution expansion can be done first in J_Z and then in energy. Previous work by Ratcliff [27] and Grimes, et al. [28] has shown that the assumption of a Gaussian form for the distribution is approximately correct, but that higher moments will be required to achieve the desired accuracy, particularly at low energies.

As an example of the method, I present in the next figure some results from a report by Grimes [29]. Here ^{21}Ne is considered to consist of a ^{16}O core with five valence particles in the $d_{5/2}$, $s_{1/2}$ and $d_{3/2}$ orbitals. This generates 8580 states with spins from 1/2

to 19/2. Fig. 4 shows a Gaussian expansion of the energy distribution for all spins, compared to the exact values obtained from diagonalization. Also shown is the expansion obtained with moments as high as the eighth. The improvement appears modest but it is important at low energies. Further tests are now underway to determine the importance of such higher moments in much larger basis spaces.

Currently a collaborative effort between S. M. Grimes and co-workers at Livermore, and B. J. Dalton of Iowa State University is underway to test the validity of various expressions for the two-body force used in the calculations. As its strength and form is better determined through comparison of calculations with experiment, extrapolation to nuclei off the stability line may be made with increased confidence. Level densities for deformed nuclei can thus be calculated without prior knowledge of the deformation parameter, and other information, such as the spin cut-off parameter and its energy dependence, will come from the calculation. If high enough moments can be included, it is possible to consider spin projection expansions for each parity state, and so the parity ratio as a function of energy may become available. Once the detailed calculation is made for a given nucleus, the results may be parameterized, in the Gilbert-Cameron approach for example, to allow ease of use in statistical model codes. It appears that we can look forward to exciting developments in the field of level densities in the near future!

THE STATISTICAL MODEL

There are three papers in this session concerned with cross-section evaluations, and one with aspects of fission barriers. These include the work of Arthur and co-workers on neutron cross sections up to 40 MeV for ^{54,56}Fe and ^{59}Co; the evaluation to 20 MeV of Bi cross sections by Smith, et al.; and the prediction of heavy element fission barrier features by Cusson, et al. Optical model and statistical model considerations have played an important role in this work. At the previous Conference in 1977, this session was mainly concerned with descriptions of Hauser-Feshbach-type codes and examples of their calculations. In this review I will limit myself to some remarks on two codes currently under development, on the results from the intercomparison of the three codes currently in use at Livermore and Los Alamos, and about some recent comparisons of calculations with experiments.

The first code I will mention is a version of the ALICE code [30], which is currently under development at Livermore by Blann and colleagues [31]. The new code is called "RECOIL ALICE: a Code for Estimating Radiation Damage." It is a statistical model code which has been modified to include recoil energy spectra and to produce radiation damage curves for incident particles up to 50 MeV. The code considers precompound decay, multiple particle (n,p,α) emission following precompound decay, and is currently

being modified to include the recoil/radiation-damage spectra from the elastic channel. The code uses a forward-peaked angular distribution function for the precompound contribution, which is based on (p,n) data, while isotropic angular distributions were assumed for all compound decay modes. The output includes the recoil energy spectra and the radiation damage spectra for each nuclide. Additionally, a total differential damage spectrum over all product nuclides is given, as well as a running sum of the total radiation damage. It is hoped that the code will be completed and debugged this year.

Most of us doing cross-section calculations have been frustrated at times by not having a single code or system that will do all of the types of calculations desired, over the entire energy range of interest, correctly and in an efficient manner. Usually we must patch together results obtained in different energy ranges from several codes that were running not quite the same problem. A code that has been designed to address these inadequacies is currently under development by M. Uhl [32]. It was begun in 1978 at Livermore and the work has continued in Vienna. The general specifications of the code are listed in Table I, while the operational sequence is given in Table II. The material in Tables I and II was kindly supplied by Dr. Uhl. Besides encompassing essentially all of the features one would want in a cross-section code, another attractive feature is that it will be a single code that can be run at various levels of sophistication. For example, it will be run routinely in the Weisskopf-Ewing mode to supply a rough survey of all possible reactions that may occur with a given incident particle and incident energy. Then one may specify particular daughter products or certain reaction paths, and do a full-blown HF calculation. Other approximations that may be chosen include the neglect of parity selection rules, and the use of approximate forms of gamma-ray competition in those cases where gamma-ray spectra or isomer populations are not desired. A non-linear integration scheme is employed, so that the restriction of dividing the energy range into equal-sized energy bins is avoided. Every effort is being made to make the numerical procedures as efficient as possible, so that computer time will be minimized. I'm sure that we are all looking forward to the completion of this code.

Once Uhl's master code is completed, it will require extensive testing through comparisons with existing codes. Three such codes, two at Livermore and one at Los Alamos, were carefully compared during the summer of 1978. At Livermore these codes were the latest versions of COMNUC-CASCADE [33] and STAPRE [34], while the Los Alamos code was GNASH [35]. The comparison was enlightening, because unsuspected errors were discovered in each code. The problem was ^{90}Zr + n, for neutrons in the energy range from 3 to 25 MeV. The calculations were made without precompound evaporation, but both with and without gamma-ray competition. The complete set of reactions calculated is given in Table III, although

each code did not necessarily calculate all of them. At Livermore we found that without gamma-ray competition our two codes produced essentially identical results, while with gamma-ray competition the results agreed to better than 5-10% in all cases except for the (n,n') reaction at energies above 20 MeV. Figs. 5, 6, and 7 show some of the Livermore results. Arthur [36] at Los Alamos finds the same sort of agreement. He says "This represents one of the most stringent comparison tests made [among] statistical codes and the agreement is gratifying in light of the different techniques used for integration, treatment of cascades, etc." Efforts are now underway, between the two laboratories, to compare the GNASH and STAPRE codes when precompound evaporation is allowed.

There are a number of very sophisticated HF codes now in use, and we all know how well they can reproduce cross sections [2], at least for stable targets where there is a lot of data to compare with. But what about unstable targets, off from the stability line? How well can their cross sections be calculated? This is an important question for this Conference, but one to which there is no unique answer. I've indicated above the progress that has been made in obtaining good optical model and level density parameters. One test of our confidence in the codes and in our methods for obtaining good input data might be sited. M. Gardner [37] at Livermore and E. Arthur [38] at Los Alamos have recently completed cross-section libraries for neutron-induced reactions on a number of stable and unstable Zr isotopes. Fig. 8 shows two of Arthur's (n,2n) calculations, for the unstable Zr nuclei ^{88}Zr and ^{89}Zr. The preliminary experimental measurements, shown prior to publication, were made by Nethaway, Smith, Rego, and Prestwood [39] on ^{88}Zr, and by Delucchi [40] on ^{89}Zr. The agreement can certainly be viewed as satisfactory.

Zirconium has been used on occasion, in the past, to measure the neutron fluence in thermonuclear fuels. In this situation of extremely intense fields of neutrons that exist for relatively short lengths of time, the population of isomeric states and the subsequent reactions on such isomeric states becomes important. For example, M. Gardner [37] has estimated that as much as 20% of the total ^{90}Zr (n,2n) ^{89}Zr reaction can occur first by producing the 0.81 sec., (5^-) isomer of ^{90}Zr by inelastic neutron scattering, followed by an (n,2n) reaction on that isomer. This is obviously an extreme situation, but the production and destruction of longer-lived isomers must be considered when radiation effects on reactor materials are estimated.

A number of codes are available, such as STAPRE [34] and GNASH [35], that do a detailed gamma-ray cascade and can be used to calculate isomer populations. However, the necessity of using sufficient discrete level information is not always appreciated. An interesting example is a Livermore calculation of the reaction ^{175}Lu (n,2n) ^{174}Lu^{m,g}, where m refers to the 140-day, (6^-) isomer, and g corresponds to the 3.6-year, (1^-) ground state. In order for the calculated isomer ratio to agree with experiment [41], it was necessary to use about 90 discrete states in ^{174}Lu. The

nucleus is deformed, and there are eight or so rotational bands that have band heads in the first several hundred keV of excitation, in addition to the ground-state band and the band built on the (6^-) isomeric state. It proved necessary to run each band up to about spin 12 or 13, in order that each band might fairly sample the spin distribution that developed in ^{174}Lu following the (n,2n) reaction. Fig. 9 shows the experimental value of the m/g ratio, together with the results of a number of calculations with various numbers of ^{174}Lu levels. The high-spin isomer would always receive an unfairly large proportion of the cross section until the ground state and other bands were allowed to have high-spin members themselves. This implies that the high-spin states are fairly pure, and that once a gamma-ray cascade starts down a band there will be little interband crossing until levels near the bottom of the band are reached.

It might appear strange to mention isospin at a neutron cross-section conference, but I believe information required for neutron calculations will come in substantial measure from the analysis of proton reaction data. The optical model discussed above is an example. Level densities, gamma-ray strength functions, and the importance of precompound reactions are other examples. The analysis of proton spectra from inelastic scattering experiments or gamma-ray transition probabilities following (p,p') reactions are among the types of measurements particularly sensitive to isospin considerations. Fig. 10 shows calculations made by Koopman [42] using the STAPRE code, compared with two sets of experimental data for the ^{62}Ni (p,p') reaction. In the top portion of the figure the solid lines are the calculations, while in the lower portion the calculations are shown as dashed lines. The calculations ignoring isospin are grossly in error, while those with isospin completely conserved are somewhat too high. Studies such as these can be used to determine the systematics of isospin mixing of the $T_>$ states into the $T_<$ states. Even for reactions less sensitive to isospin, one might as well include the simple isospin Clebsch-Gordon coefficients given by Grimes, et al. [43] in both the statistical and the precompound portions of one's cross-section calculations.

PRECOMPOUND AND DIRECT REACTIONS

It's interesting to me that the three papers in this session related to precompound models (by Fu, Kalbach and Mann, and Gruppelaar) and the multistep direct reaction model (Tamura) all emphasize their model's capability to calculate angular distributions. To me this is indicative of the rapid advances that seem to be occurring in these areas.

It's quite possible to combine the results from separate statistical model and precompound model calculations and fit experimental cross sections and particle spectra rather well, in spite of the many inherent inconsistencies involved. This can even be

done with the Weisskopf-Ewing model for the statistical part, and simple, closed-form approximations for the precompound part. If you wish only to fit or interpolate experimental data, there is little need for a more sophisticated approach. The problem is that the parameters so obtained probably have little physical meaning, and cannot be depended upon for use where experimental data are scarce or absent. Thus, it becomes very important to strengthen and enlarge the physics of the precompound model and to attempt to join it in a consistent manner to a statistical model where angular momentum is conserved.

A major advance occurred in precompound calculations in 1975, before the first conference in this series, with the work of Mantzouranis et al. [44], who generalized the master-equation model for fast nucleons incident on a nucleus. The nuclear states were characterized as a function of time by an exciton number n and an angle or direction Ω of the fast particle. In a series of binary scattering events the fast particle gradually looses energy and directional correlation. When a nucleon is emitted from a given exciton state formed by the scattering event, it is assumed to have the direction Ω. The lower energy, recoil nucleon is not considered. The internal transition rate between exciton states is assumed to be factorable into a product of the usual transition rate and an angle-dependent part that is not a function of exciton number.

$$\lambda(n,\Omega;n',\Omega') = \lambda(n,n') \times G(\Omega,\Omega') \qquad (7)$$

Here G is supposed to be proportional to the differential free nucleon-nucleon scattering cross section. This results in a complicated generalized master equation, that Mantzouranis solved numerically. Recently Akkermans [45] and co-workers [46] simplified the mathematical formulation and have greatly eased the computational difficulties. The generalized master equation now includes changes of exciton number $\Delta n = 0,\pm 2$, and treats the precompound and the compound parts in a consistent way. However, the model does not, as yet, include angular momentum effects, discrete levels, gamma-ray competition, or multiparticle emission.

An interesting side light of the above work [46] is related to inelastic neutron scattering. They found that they could get good overall fits (even at back angles) to the Hermsdorf [47] angular distribution data for 34 nuclei using only two free global parameters. The angular distributions are somehow rather simple. A similar observation has been made by Kalbach [48], who studied a wide range of experimental data for incident particles including p, d, t, and α particles. She observed that the angular distributions were not very sensitive to incident particle energy or target mass, and the results for different outgoing particles could be correlated if they were compared at the same outgoing energy (rather than momentum). The end result was a Legrendre expansion where the coefficients of the polynomial are given by simple

expressions involving the energy of the outgoing particle. No adjustable parameters are involved. A recent unpublished study at the University of California, Davis [49] of the (p,n) reactions on isotopes of Ni and Zr confirmed the accuracy of this type of parameterization.

The problem of including angular momentum conservation in precompound calculations has been under study in recent years by C. Y. Fu and others. The successful results of Fu were summarized in a recent report [50]. In it is described how the master-equation exciton model is modified such that it automatically reduces to the Hauser-Feshbach formulation after equilibrium has been reached. This removes many of the shortcomings of the previous treatments because, in addition to angular momentum conservation, one may now have discrete levels, gamma-ray competition and multiple particle emission. Another feature is that the compound nucleus level densities are obtained from direct summation of the particle-hole state densities used for the precompound component. When angular distributions have been included into the treatment, and I understand that this is currently underway [51], the result will represent a remarkable achievement.

Internuclear cascade calculations were described at the previous Conference in 1977, but I'm not aware of any recent work. However, Alsmiller and Barish [52] describe the construction of a multigroup neutron-photon cross-section library in which previously made internuclear cascade calculations were used to infer nonelastic scattering cross sections for neutron energies from 15 to 60 MeV. The internuclear cascade model has, of course, provided angular distributions for many years when the early precompound models could not. It appears, however, to be less successful at low and medium energies, particularly at backward angles [53,54], and I'm not aware of its use below 15 MeV.

The last topic that I would like to mention in this section is the multistep direct reaction (MSDR) approach of T. Tamura and T. Udagawa that was described at the 1977 Conference. I understand [55] that the development work on the ORION code should be completed this summer, and the code itself should be available in the fall. The results from two additional studies of the method have been published [56, 57] since the previous Conference.

You may recall that the MSDR approach considered one-step and two-step direct reactions to single-particle shell-model states grouped in rather large energy bins. A basic assumption was made that one could use an average or "collective" form factor that was independent of the j values of the shell-model orbitals. The model was applied only to the high-energy end of the continuum particle spectrum, with the suggestion that the lower energy portion of the spectrum would more appropriately come from a HF calculation.

Further study [58] has indicated the need for certain improvements in the approach. For example, the (p,p') differential cross sections previously calculated were often too small at very small angles, and also at all angles for those emitted particles which were low in energy and which thereby gave rise to residual nuclei

at high excitation energy Ex. It has since been found that some of the first difficulty could be removed if (p,2p) and (p,np) reactions were added to the (p,p') calculation, but it was necessary to scale the calculated pick-up cross sections by an arbitrary factor. This is shown in Fig. 11 for proton reactions on ^{208}Pb. The pickup cross section is called $\sigma_{q,f}$, and required scaling by a multiplicative factor of 2.5 to get agreement with the experimental measurements.

The disagreement found when Ex was high might have been due to the approximation of a "collective" form factor. To check this a number of calculations were made with microscopic form factors to a variety of one-particle one-hole states. The end result was that, for a given L value, the shape of the angular distributions produced by the microscopic and the "collective" form factors were rather similar, but the absolute magnitude of the cross sections differed for the higher L values. The "collective" form factors tended to underestimate the magnitude of the cross sections. Further progress on these and other problems is anticipated before the code is released this year.

POSSIBLE NEW DATA LIBRARIES

As my final topic, I would like merely to raise the question as to whether evaluated libraries of parameters and/or data required by code calculations be produced and made available like ENDF? A number of examples come to mind -- such as sets of level density parameters, particularly for neutron-deficient species. A library of tested inverse cross sections required for Weisskopf-Ewing calculations might be of interest to people who did not require detailed calculations at high energies. Another valuable library would contain evaluated sets of nuclear levels, including information on energy, spin, parity, gamma-ray decay branching ratios, and half lives (in particular for isomers). We would need the complete set of levels, not just those accessible to experiment, and so the experimental decay and reaction data would have to be supplemented by theory. I believe such data bases would be of great value for high-energy calculations, which often require an enormous amount of input information.

ACKNOWLEDGMENTS

This work was performed under the auspices of the U. S. Department of Energy by the Lawrence Livermore Laboratory under contract number W-7405-ENG-48.

REFERENCES

1. R. C. Haight, "Neutron Cross Sections for Fusion," UCRL-83005, Oct. 1979; Int. Conf. Nuclear Cross Sections for Technology Knoxville, TN (Oct. 1979).

2. P. G. Young, E. D. Arthur, and D. G. Madland, "Applications of Nuclear Models," LA-UR-79-2862, 1979. Int. Conf. Nuclear Cross Sections for Technology, Knoxville, TN (Oct. 1979).

3. D. L. Smith, "Neutron Dosimetry for Radiation Damage in Fission and Fusion Reactors," Int. Conf. Nuclear Cross Sections for Fusion Reactor Calculations," BNL-NCS-25295 (Oct. 1979).

4. M. R. Bhat, "Evaluated Files of Nuclear Cross Sections for Fusion Reactor Calculations," BNL-NCS-25295 (1979).

5. P. Moldauer, Nucl. Phys. 47, 65 (1963).

6. D. Wilmore and P. E. Hodgson, Nucl. Phys. 55, 673 (1964).

7. F. D. Becchetti, Jr. and G. W. Greenlees, Phys. Rev. 182, 1190 (1969).

8. D. Wilmore and P. E. Hodgson, "Neutron Optical Potentials," Nuclear Theory in Nuclear Data Evaluation, Vol. II, IAEA-190, Vienna, p. 131 (1976).

9. C. A. Engelbrecht and H. Fiedeldey, Ann. Physics 42, 262 (1967).

10. J. P. Delaroche, C. Lagrange, J. Salvy, "The Optical Model with Particular Consideration of the Coupled-Channel Optical Model," Nuclear Theory in Nuclear Data Evaluation, Vol. I, IAEA-190, Vienna, p. 251 (1976).

11. C. Lagrange, "On Optical Model Calculations in the Mass Region A=80 to A=170," Specialists' Meeting on Neutron Cross Sections on Fission Product Nuclei, Bologna, (Dec. 1979).

12. J. Rapaport, V. Kulkarni, and R. W. Finlay, Nucl. Phys., A330, 15 (1979); and J. Rapaport and R. W. Finlay, IEEE Trans. Nucl. Sci., Vol. NS-26, 1196 (1979).

13. A. M. Lane, Phys. Rev. Lett. 8, 171 (1962); Nucl. Phys. 35, 676 (1962).

14. D. M. Patterson, R. R. Doering, and A. Galonsky, Nucl. Phys., A263, 261 (1976).

15. C. Lagrange, "Optical Model Calculations of Nucleon Interactions with ^{93}Nb, from 10 keV to 50 MeV," Int. Conf. Nuclear Cross Sections for Technology, Knoxville, TN (Oct. 1979).

16. D. H. Fitzgerald, et al., Phys. Rev., C16, 2181 (1977).

17. G. Haouat, "Nuclear Deformation from Fast Neutron Scattering," Proc. Second Int. Symposium on Neutron Induced Reactions, Smolenice, Czechoslovakia (June 1979).

18. D. G. Madland and P. G. Young, "Neutron-Nucleus Optical Potential for the Actinide Region," LA-UR-78-2510; Proc. Int. Conf. on Neutron Physics and Neutron Data for Reactors and Other Applied Purposes, Harwell (Sept. 1978).

19. R. G. Lanier, Lawrence Livermore Laboratory, private communication.

20. V. Madsen, "Nuclear Absorption Cross Section in the Adiabatic Approximation," to be issued as a UCRL report.

21. A. Gilbert and A. G. Cameron, Can. J. Phys. 43, 1446 (1965).

22. J. L. Cook, H. Ferguson, and A. R. de L. Musgrove, "Nuclear Level Densities in Intermediate and Heavy Nuclei," AAEC/TM 392 (1967).

23. E. K. Rose and J. L. Cook, "An Evaluation of the Gilbert-Cameron Level Density Parameters," AAEC/E419 (1977).

24. G. Reffo, "Parameter Systematics for Statistical Theory Calculations of Neutron Reaction Cross Sections," CNEN-RT/FI (78) 11 (1978).

25. International Conference of Theory and Applications of Moment Methods in Many Fermion Systems, Ames, Iowa (Sept. 1979).

26. J. B. French and K. F. Ratcliff, Phys. Rev. C3, 94 (1971).

27. K. F. Ratcliff, Phys. Rev., C3, 117 (1971).

28. S. M. Grimes, et al., Phys. Rev. C19, 2378 (1979).

29. S. M. Grimes, "Calculation of Spin Cutoff Parameters Using Moment Techniques," UCRL-83463 (1979); Int. Conf. on Theory and Application of Moment Methods in Many Fermion Systems, Ames, Iowa (Sept. 1979).

30. M. Blann, "Corrections to Overlaid Alice, through July, 1978," UR-NSRL-181 (1978).

31. M. Blann, T. Komoto, and R. Howell, Lawrence Livermore Laboratory, private communication.

32. M. Uhl, Institut für Radiumforschung and Kernphysik, Boltzmanngasse 3, 1090 Wien IX, Austria.

33. C. L. Dunford, "A Unified Model for Analysis of Compound Nucleus Reactions," AI-AEC-12931 (1970).

34. M. Uhl, Physica Austriaca 31, 245 (1970); and M. Uhl and B. Strohmaier, "STAPRE - A Computer Code for Particle Induced Activation Cross Sections and Related Quantities," IRK-76/02 (1976).

35. P. G. Young and E. D. Arthur, "GNASH: A Preequilibrium, Statistical Nuclear - Model Code for Calculation of Cross Sections and Emission Spectra," LA-6947 (1977).

36. Applied Nuclear Data Research and Development, July 1-Sept 30, 1978, C. I. Baxman and P. G. Young, editors, LA-7596-p9, p. 5 (1978).

37. M. A. Gardner, Lawrence Livermore Laboratory, private communication.

38. E. D. Arthur, "Calculation of Neutron Cross Sections on Isotopes of Yttrium and Zirconium," LA-7789-MS (1979).

39. D. R. Nethaway, N. L. Smith, J. H. Rego, and R. J. Prestwood, "Cross Section Measurements for the Radioactive Targets ^{88}Y and ^{88}Zr," abstracts of Am. Chem. Soc. Meeting, Miami Beach, Sept. 1978.

40. A. Delucchi, Lawrence Livermore Laboratory, private communication.

41. D. G. Gardner and D. R. Nethaway, "Isomer Ratio for the ^{175}Lu (n,2n) ^{174}Lu Reaction at 14.8 MeV," UCRL-79073-Abstract (1977).

42. R. P. Koopman, "Systematics of Gamma Decay through Low-Lying Vibrational Levels of Even-Even Nuclei Excited by (p,p') and (n,n') Reactions," Ph.D. Thesis, University of California (1977); UCRL-52275 (1977).

43. S. M. Grimes, et al., Phys. Rev. C5, 85 (1972).

44. G. Mantzouranis, D. Agassi, and H. A. Weidenmuller, Phys. Lett. 57B, 220 (1975); see also Z. Physik A276, 145 (1976).

45. J. M. Akkermans, Phys. Lett. 82B, 20 (1979).

46. J. M. Akkermans, H. Gruppelaar, and G. Reffo, "Angular Distributions in a Unified Model of Preequilibrium and Equilibrium Neutron Emission," ECN-79-161 (1979).

47. D. Hermsdorf, et al., ZFK-277 (1974).

48. C. Kalbach-Walker, "Calculating Angular Distributions for Preequilibrium Particle Emission," HEDL Report TC-1544 (1979).

49. Department of Physics, University of California, Davis, Progress Report to the National Science Foundation, UCD-CNL-192 (1979).

50. C. Y. Fu, "A Consistent Nuclear Model for Compound and Precompound Reactions with Conservation of Angular Momentum," Int. Conf. on Nuclear Cross Sections for Technology, Knoxville, TN (Oct. 1979).

51. C. Y. Fu, Oak Ridge National Laboratory, private communication.

52. R. G. Alsmiller and J. Barish, Nucl. Sci. Eng. 69, 378 (1979).

53. G. Mantzouranis, Phys. Rev., C14, 2018 (1976).

54. M. Blann, "Nuclear Equilibrium Models for Nuclear Reactions at Moderate Excitations," Univ. of Rochester Report COO-3494-4 (1972).

55. T. Tamura, University of Texas, private communication.

56. T. Tamura and T. Udagawa, Phys. Lett. 71B, 273 (1977).

57. T. Tamura and T. Udagawa, Phys. Lett. 78B, 189 (1978).

58. Progress Report for 1979, Theoretical Nuclear Physics Group, Dept. of Physics, University of Texas, unpublished (Jan. 1980).

TABLE I

Specifications of the Uhl Code

Purpose

Calculate nuclear reaction cross sections for:

projectile:	arbitrary
energy range:	$\lesssim$50 MeV
decay modes:	emission of n,p,α,d,t,^{3}He,γ, and fission
end products:	all nuclei populated by all reaction paths with up to six emitted particles chosen among (n,p,α,d,t,^{3}He)

Calculated Cross Sections

A. For First Chance Processes

1. Differential and total cross sections for exciting individual levels:

$$\frac{\partial\sigma}{\partial\Omega}(E_i,\Omega),\ \sigma(E_i) \quad \text{(including elastic scattering)}$$

2. Differential and total cross sections for exciting the continuum:

$$\frac{\partial^2\sigma}{\partial E\partial\Omega}(E,\Omega),\quad \frac{\partial\sigma}{\partial E}(E,\Omega)$$

B. For Higher-Chance Processes (for all end products)

1. Activation cross sections.

2. Isomeric state production cross sections.

3. Production cross sections for gamma-ray transitions between discrete levels.

4. Spectra of populating particle and gamma-rays (no angular distributions).

5. Multiple fission cross section.

C. Total Production Spectra: of particles and gamma rays

Models

A. Coupled Channels or Single-Channel Optical Model

- elastic scattering.
- inelastic scattering exciting rotational bands and vibrational levels.
- transmission coefficients.

TABLE I (Continued)

B. Preequilibrium Model

1. First chance only, hybrid or excitation model, simple form for angular distribution.

2. Higher chance preequilibrium decay.
DWBA - or multistep direct reactions into continuum.

C. Statistical CN Model

- Angular momentum and parity conservation (in general).
- Level density: 1. parameterized level density formula
2. microscopic calculation
- First chance processes: 1. correction for width fluctuation
2. isospin conservation (+ mixing)
- Particle emission: optical model transmission coefficient: $T_j(\varepsilon)$
- Gamma-ray emission: transmission coefficients related to to gamma-ray strength functions:

$$T_{\chi L}(\varepsilon) = 2\pi\, \varepsilon^{2L+1} f^{\gamma}_{\chi L}(\varepsilon)$$

- Fission: Single- or double-humped barrier transition states:
1. discrete (rotational bands)
2. continuum

For a double-humped barrier:
1. complete damping for higher chance fission
2. partial damping for first chance fission

- Gamma-ray cascades: considered for all relevant nuclei.

Libraries

- nuclear masses
- inverse cross sections (Weisskopf-Ewing, preequilibrium)
- nuclear decay schemes
- global optical potentials
- gamma-ray strength function parameters
- level-density parameters
- single-particle states (microscopic level density)

TABLE II

Operational Sequence of the Uhl Code

Three sections

1. Set up problem and create input file.
2. Prepare CN-model calculations.
3. Calculate cross sections.

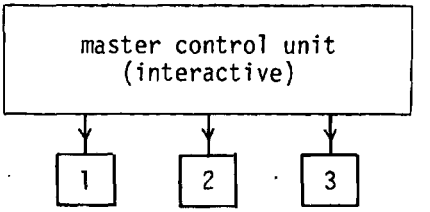

1. Set up problem and create input file.

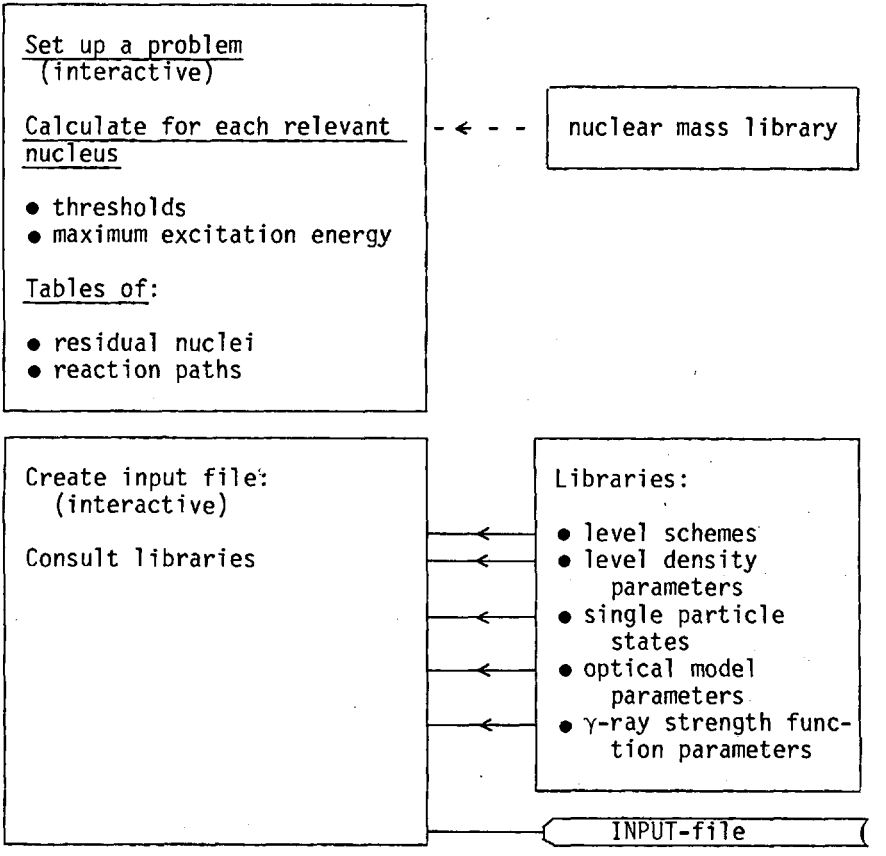

TABLE II (Continued)

2. Prepare CN-model calculations

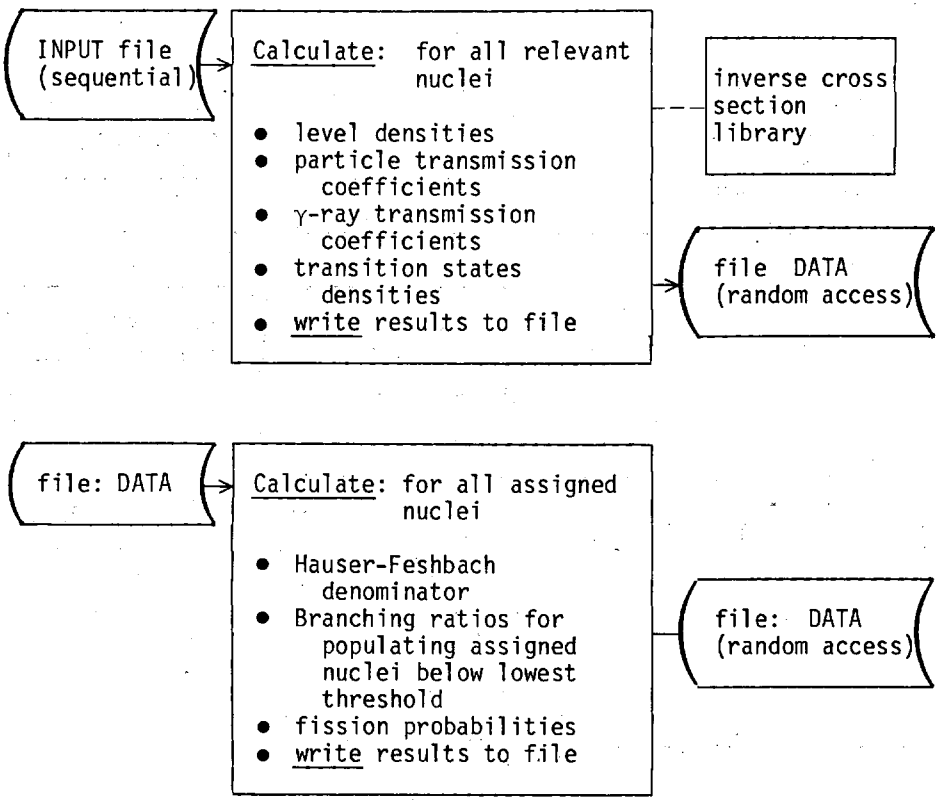

TABLE II (Continued)

3. Calculate cross sections

Set up loop over incident energies.

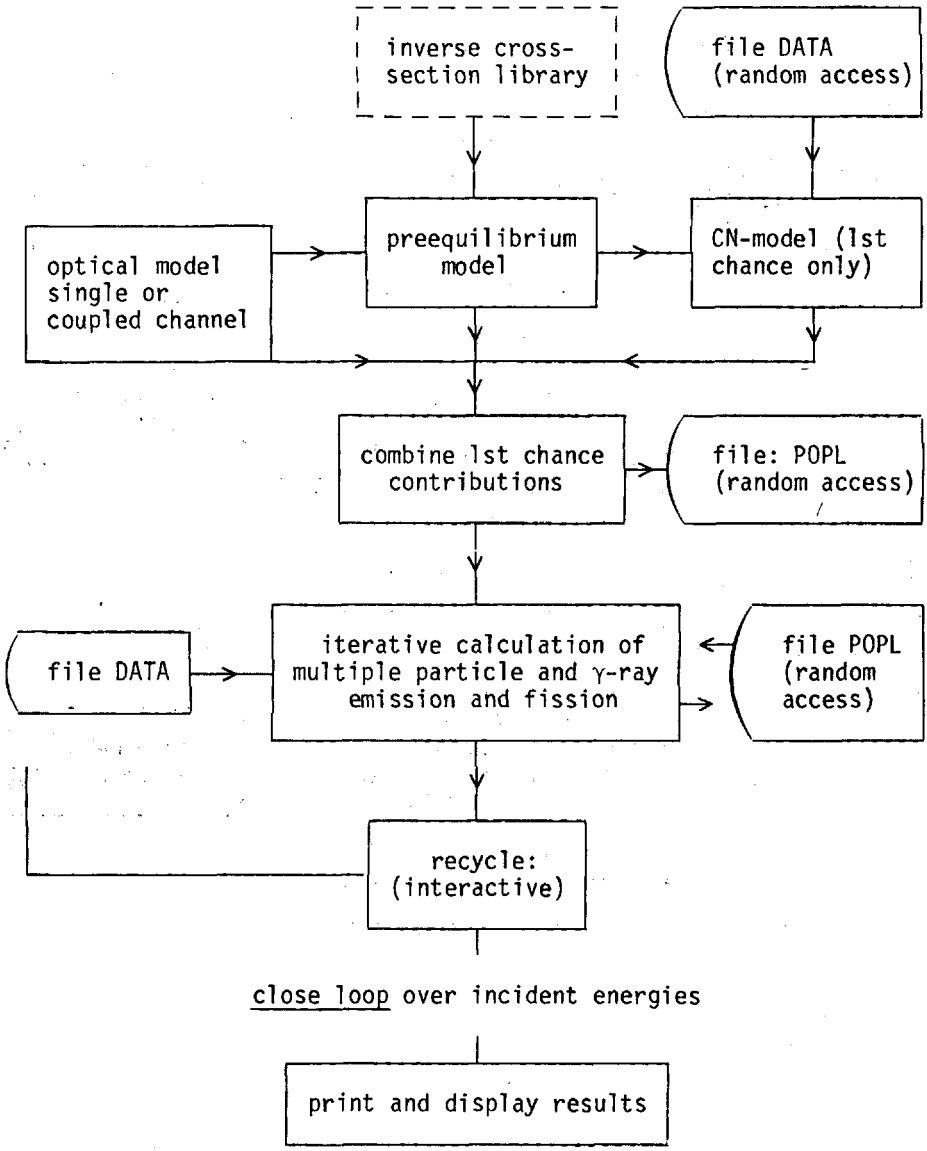

TABLE III

Reactions Studied in Code Comparison

^{90}Zr + n	
total	(n,3n)
reaction	(n,p)
shape elastic	(n,np)
compound elastic	(n,pn)
capture, compound	(n,2np)
(n,γn')	(n, alpha)
capture, direct	(n,n alpha)
(n,2n)	(n, alpha n)

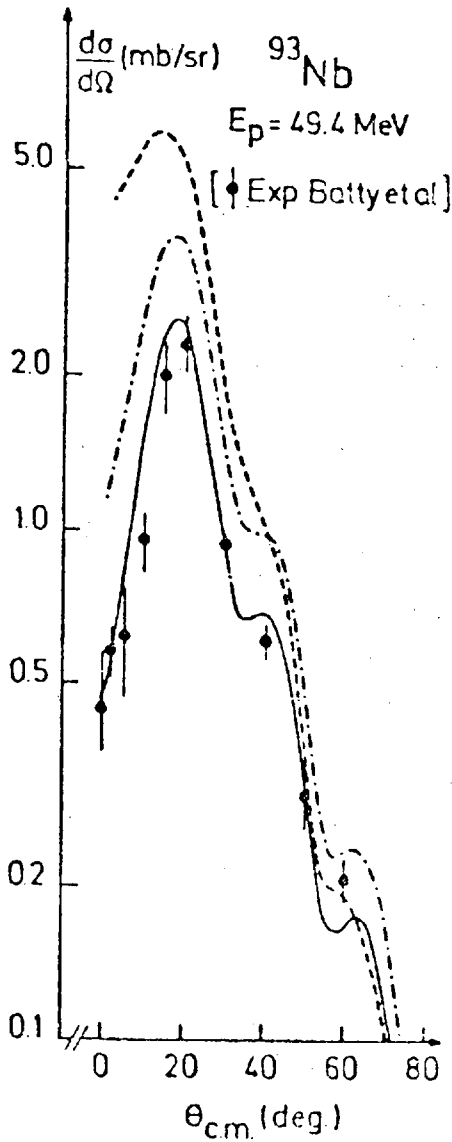

Fig. 1. From Ref. 15. Comparison of coupled channel calculations with (p,n) IAS differential cross-section data. See text for details.

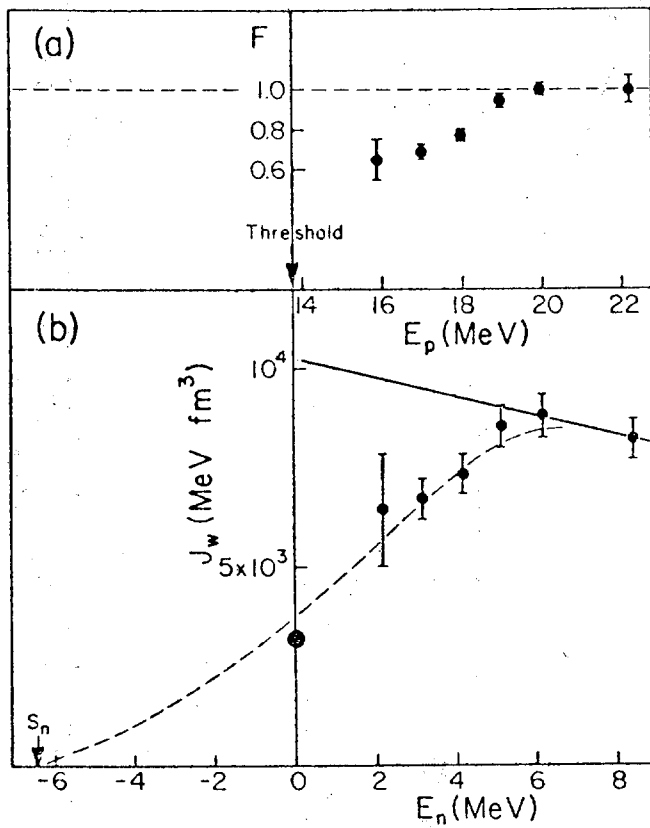

Fig. 2. From Ref. 16. (a) Values of the neutron imaginary potential scaling factor F, required to fit data. (b) Volume integral of the neutron imaginary potential versus c.m. neutron energy.

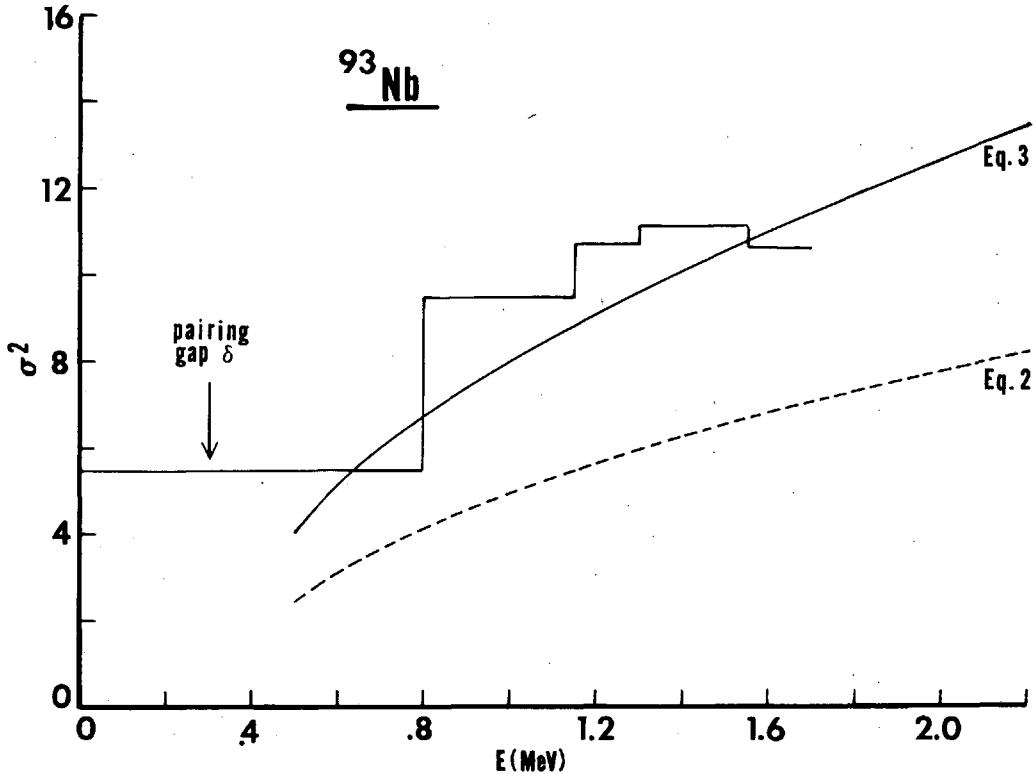

Fig. 3. Spin cut-off factor determined from discrete levels of ^{93}Nb (histogram), compared with calculations from Eq. 2 and 3.

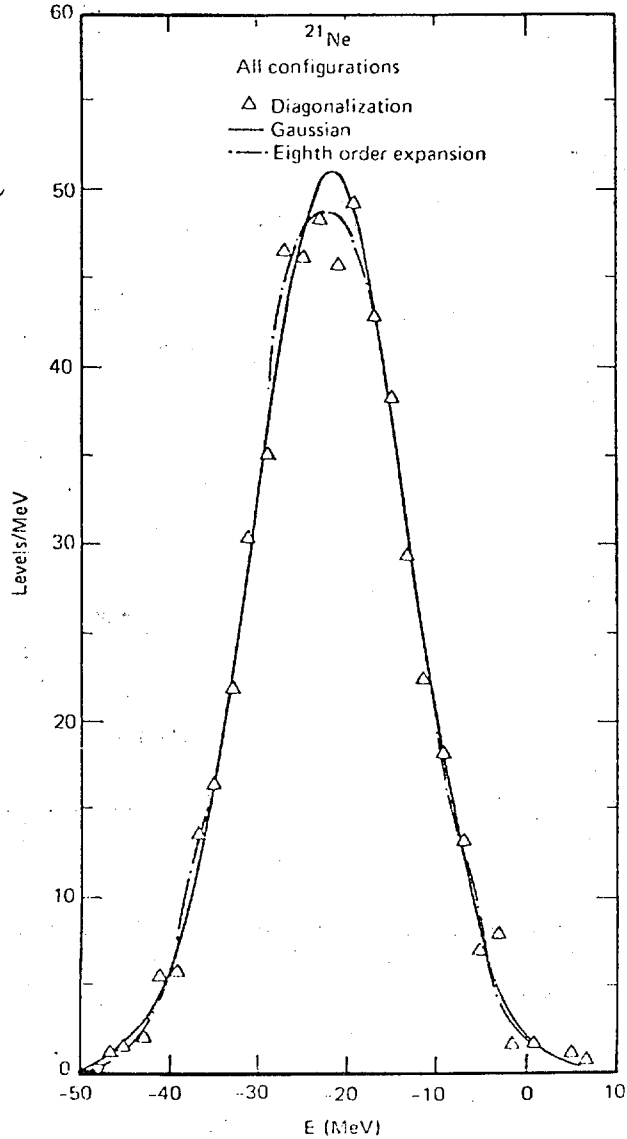

Fig. 4. From Ref. 29. Expansions of the energy level distributions for ^{21}Ne, compared with diagonalization values. Energies relative to ^{16}O.

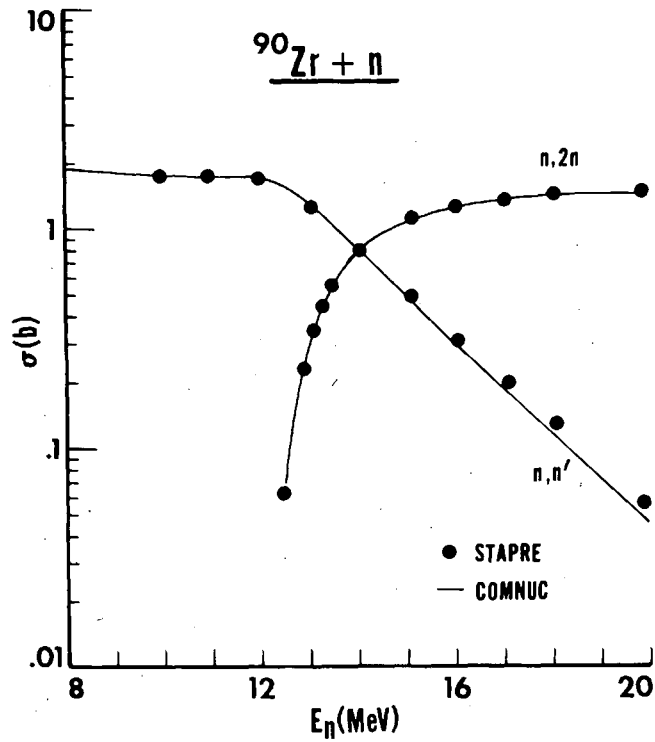

Fig. 5. Comparison of cross sections for some reactions of fast neutrons with ^{90}Zr calculated with the two codes COMNUC and STAPRE. Gamma-ray competition was included, but not precompound evaporation.

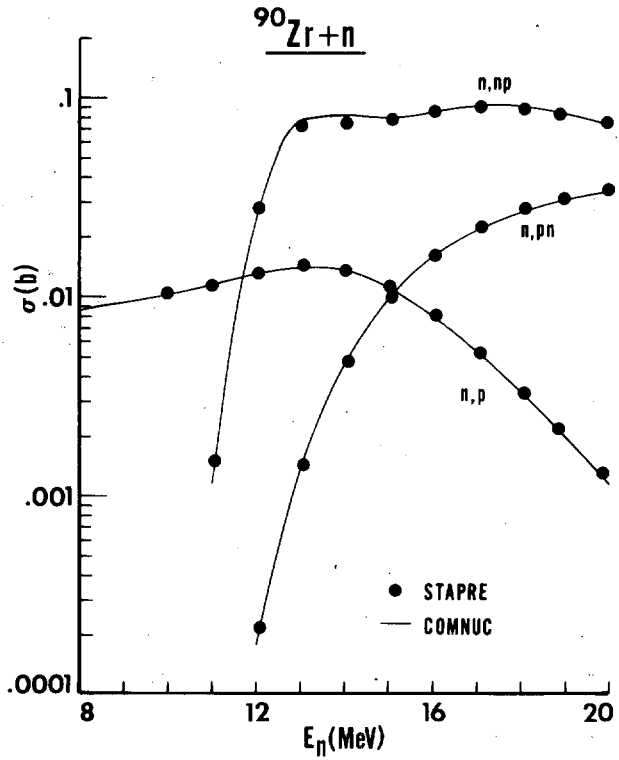

Fig. 6. Comparison of cross sections for some reactions of fast neutrons with ^{90}Zr calculated with the two codes COMNUC and STAPRE. Gamma-ray competition was included, but not precompound evaporation.

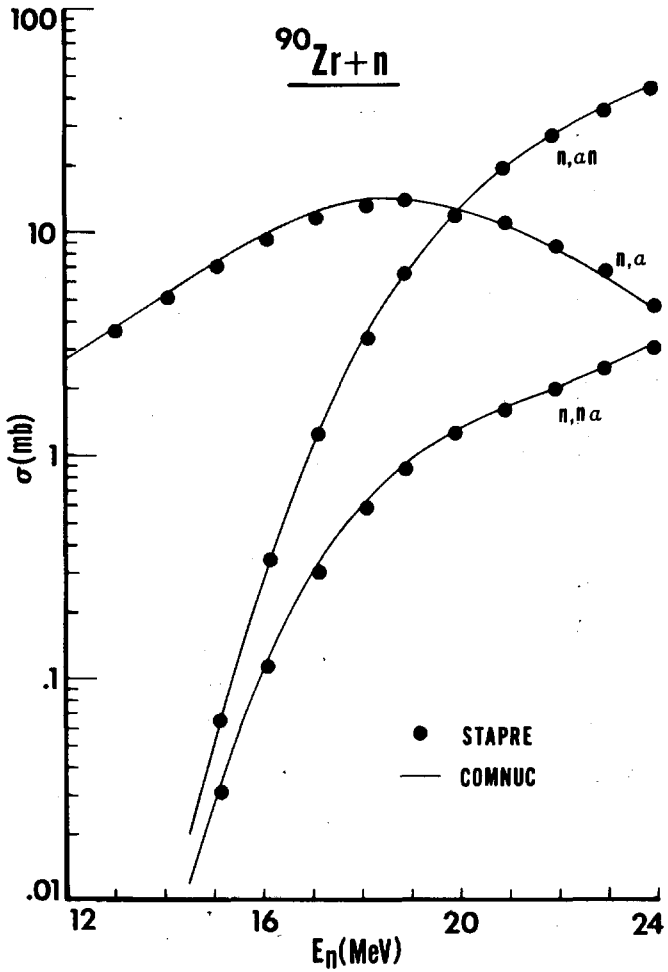

Fig. 7. Comparison of cross sections for some reactions of fast neutrons with ^{90}Zr calculated with the two codes COMNUC and STAPRE. Gamma-ray competition was included, but not precompound evaporation.

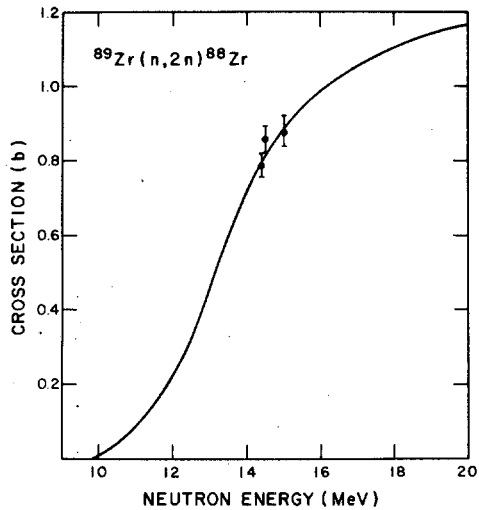

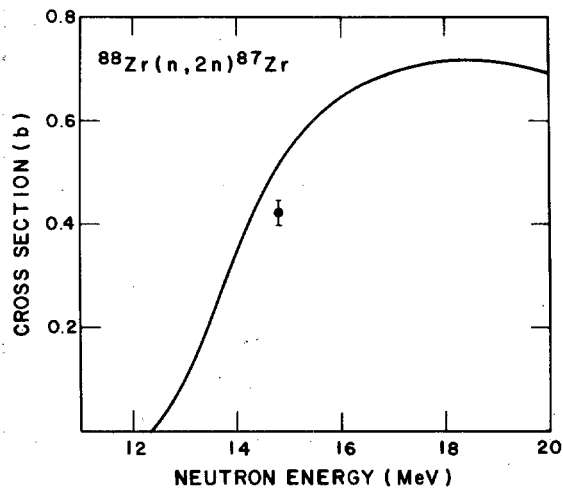

Fig. 8. From Ref. 38. Comparison of calculated and experimental values for the (n,2n) reaction on the unstable targets ^{88}Zr and ^{89}Zr.

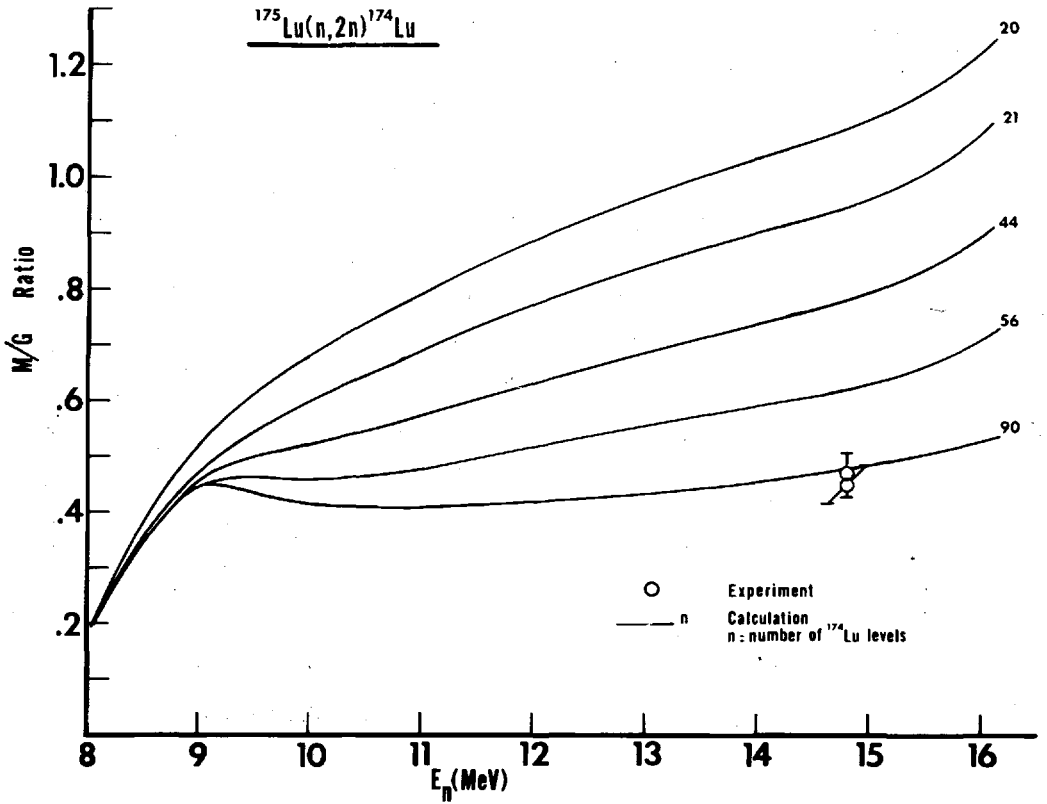

Fig. 9. Calculations of the isomer ratio in ^{174}Lu following the (n,2n) reaction on ^{175}Lu, using various numbers of discrete levels in ^{174}Lu, compared with experimental values.

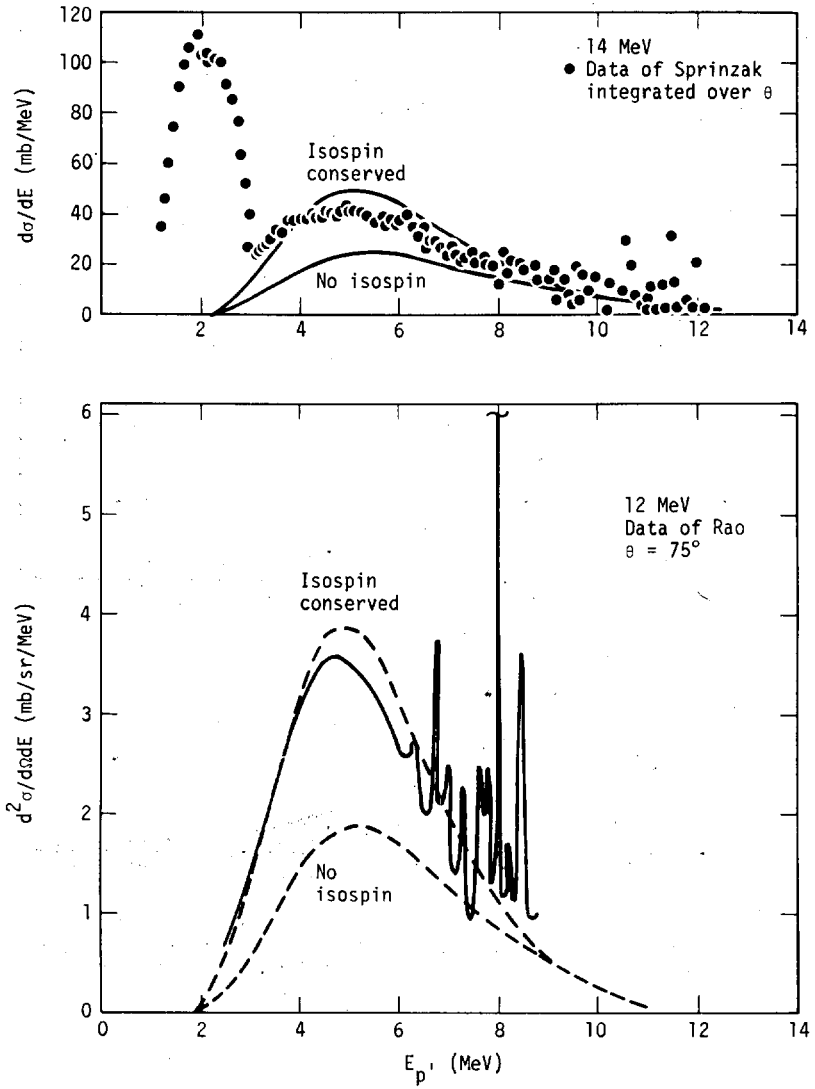

Fig. 10. From Ref. 42. Comparison of calculated proton energy spectra from the ^{62}Ni (p,p') reaction with experimental data at two incident energies. In the top figure the experimental data are the filled circles, while in the bottom figure the solid curve represents the data. The calculations show the effect of conserving isospin.

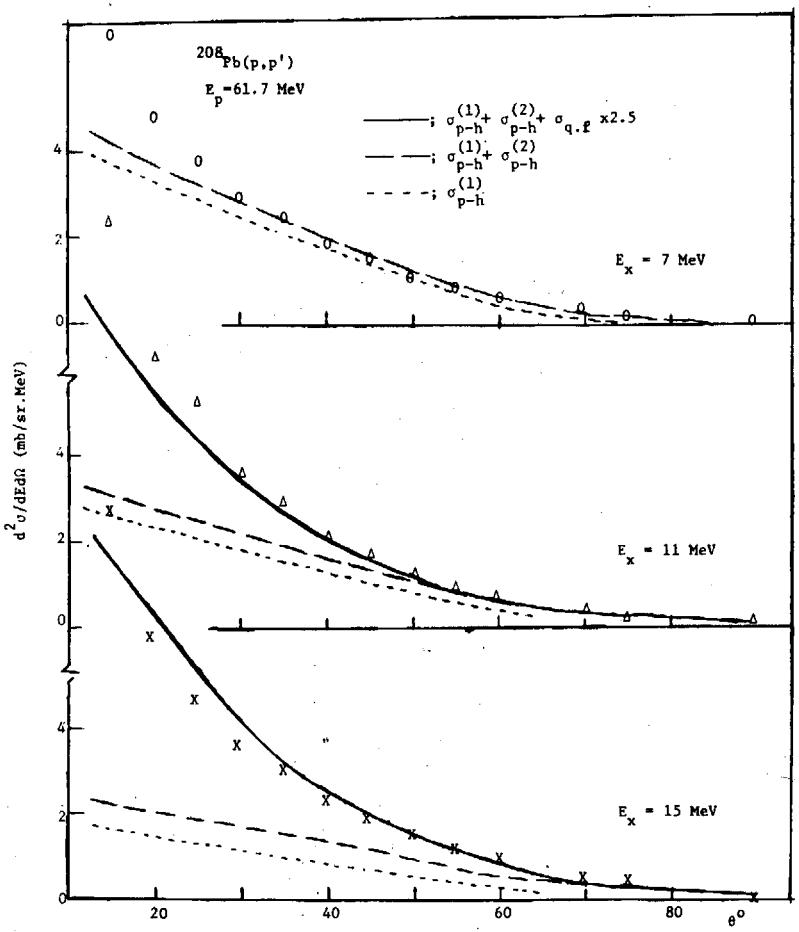

Fig. 11. From Ref. 58. Comparison of experimental angular distributions for the reaction ^{208}Pb (p,p') with incident 61.7-MeV protons (o,Δ,x) with calculations from the MSDR approach.

DEVELOPMENT AND APPLICATIONS OF MULTI-STEP HAUSER-FESHBACH/PRE-EQUILIBRIUM MODEL THEORY

C. Y. Fu

Oak Ridge National Laboratory
Oak Ridge, Tennessee 37830, U.S.A.

ABSTRACT

A recently developed model that combines compound and precompound reactions with conservation of angular momentum is discussed. This model allows a consistent description of intermediate excitations from which tertiary reaction cross sections can be calculated for transitions to the continuum as well as to the discrete residual levels with known spins and parities. Predicted neutron, proton, and alpha-particle production cross sections and emission spectra from 14-MeV neutron-induced reactions are compared favorably with angle-integrated experimental data for 12 nuclides. The model is further developed to include angular distributions of outgoing particles. The random phase approximation used for the compound stage is partially removed for the precompound stages, allowing off-diagonal terms of the collision matrix to produce both odd and even terms in the Legendre polynomial expansion for the angular distribution. Calculated double differential cross sections for the 14.6-MeV $^{23}Na(n,n'x)$ reaction are compared with experimental data.

I. INTRODUCTION

Development of fusion energy technology calls for substantial improvement in the knowledge of neutron cross sections in the energy range from a few MeV to about 40 MeV [1]. In this energy range, the multi-step Hauser-Feshbach model with precompound effects is the most versatile and is considered an indispensible theoretical tool for cross-section evaluations [2]. In analyzing cross sections such as hydrogen and helium production from 14-MeV neutron-induced reactions, we showed [3] that spin and parity effects are more important in the second step (tertiary reaction) of the calculation than in the first step, requiring conservation

of angular momentum in the precompound stages in a manner consistent with the Hauser-Feshbach model used for the compound stage.

We have recently developed a model [4] that treats compound and precompound reactions consistently with conservation of angular momentum. The main features of this development are summarized in Section II.

The fact that angular momentum is conserved in both the precompound stages and the compound stage of our calculation provides the possibility of calculating angular distributions of outgoing particles. Progress in this respect is reported in Section III.

Our aim is to develop a model code, with ever-improving physics content, that can be used to calculate a large variety of nuclear cross sections over a wide energy range. Much work needs to be done, but in the meantime many uses of the code have been made. Some examples of applications are briefly discussed in Section IV.

II. THE CONSISTENT COMPOUND AND PRECOMPOUND MODEL WITH CONSERVATION OF ANGULAR MOMENTUM

Detailed derivation of the model will be published elsewhere [4]. Here we present the final formula and summarize its essential features. The cross-section formula for outgoing particle of type b and energy ε is given by

$$\sigma_b(E,\varepsilon)d\varepsilon = \pi \lambda^2 \sum_{J\pi} g_J \sum_{s\ell} T^J_{s\ell} \frac{d\varepsilon}{D_{J\pi}} \sum_{s'\ell'} T^J_{s'\ell'} \Omega_b(I,E,U), \quad (1a)$$

where

$$\Omega_b(I,E,U) = \sum_p D_b(p,E)\, \rho_b(p-1,h,I,U') + C(E)\, \rho_b(I,U') \quad (1b)$$

with

$$D_b(p,E) = \int_0^T P_b(p,h,t)dt/\omega(p,h,E) \quad (1c)$$

$$C(E) = \int_T^\infty P(p,h,t)dt/\omega(p,h,E) \quad (1d)$$

$$\rho_b(I,U') = \sum_p \rho_b(p-1,h,I,U') \quad (1e)$$

Equation (1a) has a form much like the Hauser-Feshbach formula except the quantity $\Omega_b(I,E,U)$ defined in Eq. (1b). E is the excitation energy of the composite nucleus. The quantity I [summed implicitly in Eq. (1a)] is the spin of a group of residual levels at excitation energy U. The effective excitation energy U' is related to U by $U' = U - U_{p,h}$ where $U_{p,h}$ accounts for the pairing effects. The righthand side of Eq. (1b) contains two terms, the first corresponds to the precompound component and the second the compound. Occupation probabilities P_b and P for the particle-hole pairs, (p,h), at time t are obtained from a set of new master equations which ensures consistency between the precompound and

the compound stages of the calculation. The equilibration time T is the time when all allowed states are equally populated. The level density $\rho_b(p\text{-}1,h,I,U)$ and the state density $\omega_b(p\text{-}1,h,I,U)$ are related by $\omega_b(p\text{-}1,h,I,U) = (2I+1)\ \rho_b(p\text{-}1,h,I,U)$.

The following features of Eq. (1) may be noteworthy.

1. Equation (1) reduces to the Hauser-Feshbach formula if instantaneous equilibration is assumed.

2. The occupation probabilities, P_b, for the precompound stages depend on the relative distribution of neutrons, protons, and alpha-particles in the excitons. This dependence is particularly strong for $t \ll T$ when the incident particle contributes predominantly to the particle-type distribution. On the other hand, there is no such dependence in the occupation probability, P, for the compound stage.

3. The spin dependences in ω, P_b, and P are assumed to be similar and therefore cancel in their ratios in Eqs. (1c) and (1d), allowing the use of spin-independent master equations for solving P_b and P. This assumption needs to be examined, but we do not expect it to cause a serious problem for nucleon-induced reactions above a few MeV.

4. The level density used for the compound stage of the calculation is obtained from summing those used for the precompound stages, removing a large source of uncertainty in defining the ratios of the precompound to compound cross sections often found in the literature.

5. Because (p,h) states have fewer high-spin stages than (p+1,h+1) states, conserving angular momentum in the precompound calculation results in spin populations different from those of the compound calculation, changing calculated cross sections accordingly.

Calculations of neutron, proton, and alpha-particle production spectra for 14.6-MeV neutrons incident on thirteen isotopes have been compared with experimental data [4]. Our calculated results for ^{56}Fe are compared in Fig. 1 with the (n,xn) spectrum measured by Hermsdorf *et al.* [5] and the (n,xp) and (n,xα) spectra measured by Grimes *et al.* [6]. The histograms in the calculated (n,xn) spectrum in Fig. 1 represent DWBA calculations for some discrete levels [7]. These cross sections correspond to rotational and vibrational excitations which are very weakly taken into account by the compound and precompound calculations. The dashed curves in Fig. 1 include calculated results from the binary step only. Twelve other comparisons similar to that shown in Fig. 1 can be found in reference 4.

III. ANGULAR DISTRIBUTIONS

The use of Eq. (1) in our multi-step Hauser-Feshbach code for the calculation of angular distributions yields front-back symmetry in the center-of-mass coordinates. This is of course incorrect

because the random phase approximation used for the compound stage is invalid for the precompound stages.

We know that an incident particle enters a nucleus as a single particle. After initiating a certain number of collisions, creating $\bar{h}$ holes, the incident particle as well as any excited particles will have lost all traces of the incoming single-particle coherent motion and the random phase approximation becomes valid. On the other extreme, if an incident particle traverses the nucleus without suffering a collision, fully correlated phases for any connected pairs of the collision matrix elements should be assumed instead.

Knowing the two extremes at $h = 0$ and $h = \bar{h}$, we may be able to guess what happens in between by examining some experimental data. This is done in two steps. First we derive a formula for differential cross sections that assumes random phases for the compound stage but fully correlated phases for the precompound stages. Then a weighting function that depends on the number of collisions is used to require the formula to satisfy the two extreme cases. We obtain the following:

$$\frac{d\sigma}{d\Omega} = \frac{\lambda^2}{4(2I_0+1)(2i+1)} \sum_L (B_L+B'_L)\, P_L(\cos\theta) \tag{2a}$$

$$B_L = \sum_{s_a\, s_b\, J\, \ell_a\, \ell_b} (-1)^{s_a-s_b}$$

$$Z(\ell_a\, J\, \ell_a\, J;\, s_a\, L)\, Z(\ell_b\, J\, \ell_b\, J;\, s_b\, L)$$

$$T^J_{s_a\ell_a}\, T^J_{s_b\ell_b}\, \Omega_b(I,E,U)/D_{J\pi} \tag{2b}$$

$$B'_L = \sum_{s_a s_b\, J\, J'\, \ell_a\, \ell'_a\, \ell_b\, \ell'_b} (-1)^{s_a-s_b}$$

$$(J\neq J' \text{ and/or } \ell_a\neq\ell'_a \text{ and/or } \ell_b\neq\ell'_b)$$

$$i^{\ell_a-\ell'_a-L}\, Z(\ell_a\, J\, \ell'_a\, J';\, s_a\, L)$$

$$i^{\ell_b-\ell'_b-L}\, Z(\ell_b\, J\, \ell'_b\, J';\, s_b\, L)$$

$$(T^J_{s_a\ell_a}\, T^{J'}_{s_a\ell'_a}\, T^J_{s_b\ell_b}\, T^{J'}_{s_b\ell'_b})^{1/2}\, (D_{J\pi}\, D_{J'\pi'})^{-1/2}$$

$$\sum_{\substack{p \\ (h<\bar{h})}} Y(h)\, D_b(p,E)\, \rho_b(p-1,h,I,U') \tag{2c}$$

where

$$Y(h) = \left(\frac{\bar{h}-h}{\bar{h}}\right)^{y} \qquad (2d)$$

Here the Z's are the Z coeffients defined by Biedenharn, Blatt, and Rose [8]. The phase correction due to Huby [9] corrects an error in the derivation given by Blatt and Biedenharn [10]. The collision matrix elements in the formula given by Blatt and Biedenharn [10] have been replaced by transmission coefficients in the manner described by Satchler [11]. The first term in Eq. (2a) produces even Legendre coefficients L = 0, 2, 4, ... The second term gives L = 1, 2, 3, 4, ... and is present for $h < \bar{h}$ and $t < T$. For $h \geq \bar{h}$ and $t \geq T$, the random phase approximation is valid and the second term approaches zero. This is achieved by using the weighting function Y(h) which we tentatively assume to take the form of Eq. (2d).

Calculated results using Eq. (2) for the 14.6-MeV ^{23}Na(n,n'x) are compared in Fig. 2 with the data of Hermsdorf *et al.* [5]. For this calculation, $\bar{h}$ was taken to be the most probable hole number in the excited composite nucleus and is equal to 2.7 for ^{24}Na. This number of course increases with increasing excitation energy and increasing mass number of the composite nucleus. The parameter y was determined to be 2.0 from fitting the data but can probably be derived from a theoretical model. From Fig. 2 it is clear that the model did what we wanted it to do – a forward peaking that increases with increasing outgoing particle energy and a backward peaking that exhibits angular momentum effects. Such backward peaking cannot be obtained from calculations that ignore angular momentum effects.

Extensive tests of the model are planned. Refinements of the model are anticipated.

IV. APPLICATIONS

While development of our model theory and code continues, many applications have been made. A summary of rather broad applications was given previously [3]. Here we describe our latest efforts.

A critical review of neutron emission spectra induced by 14-MeV neutrons from ENDF/B-V files was made by Hetrick *et al.* [12]. It became clear from this review why advanced nuclear model codes need to be developed and applied to cross-section evaluations. In 14-MeV neutron-induced reactions, several neutron-producing reactions compete. These reactions usually include (n,n'γ), (n,2n), (n,np), (n,nα), (n,pn), and (n,αn). Barring a sudden advancement in experimental techniques, cross sections of these competing reactions as well as the secondary particle and gamma-ray energy distributions can only be evaluated in a consistent fashion through the use of multi-step Hauser-Feshbach codes with precompound effects. The fact that such codes were not available several years ago explains the poor agreement of many ENDF/B-V

neutron emission spectra with available experimental data shown in the review.

We have started to redo some of our evaluations for ENDF/B-V that were made without the aid of an advanced nuclear model code. An example is given here for the reevaluation of neutron and gamma-ray-production cross sections for calcium from 8 to 20 MeV [13]. The original evaluation [14] made extensive use of a multistep Hauser-Feshbach code that had no precompound effects. For this reason, the neutron emission spectrum shown in the review [12] is typical of a pure compound component. We have made new calculations using our present model for all reaction cross sections of ^{40}Ca from 8 to 20 MeV. The same parameters as determined previously were used. The parameters required for the precompound mode of calculation were those determined in reference 4. Our calculated 14.6-MeV $^{40}Ca(n,xn)$ spectrum is compared in Fig. 3 with the data measured by Hermsdorf *et al.* [5]. The calculation is in much better agreement with the experiment than those used for ENDF/B-V.

Simultaneous calculations of neutron and gamma-ray-production cross sections will ensure consistency between the two and ensure energy balance between the incident neutron and the outgoing particles and gamma rays. For this reason, gamma-ray-production cross sections and spectra need also be calculated at the same time and be used for the new evaluation. Two such calculations, induced by 8.75- and 15.5-MeV neutrons respectively, were compared in Figs. 4 and 5 with the data measured by Dickens [15]. These calculated results deviate somewhat from those obtained previously for ENDF/B-V but remain in good agreement with the experimental data.

V. SUMMARY AND CONCLUSIONS

A model that treats compound and precompound reactions consistently with conservation of angular momentum is summarized. This model was extended, also in a consistent manner, to calculate angular distributions of outgoing particles from combined compound and precompound reactions. The importance of including spins in the precompound mode of calculation became apparent from the agreement between the calculated and the observed backward peaking in the angular distributions. The practical need of advanced nuclear model theory and code was reiterated.

Further developments in both theory and code are needed. Tests of the angular distribution method should be made for (n,xp) and (n,xα) reactions and more (n,xn) reactions. A scheme is needed to extrapolate the precompound effects in the angular distributions from the continuum to the discrete levels. Radiative capture should be incorporated in a consistent manner as one of the competing precompound reactions.

ACKNOWLEDGEMENT

Research sponsored by the Division of Basic Energy Sciences, U. S. Department of Energy, under contract W-7405-eng-26 with the Union Carbide Corporation.

REFERENCES

1. M. R. BHAT and S. PEARLSTEIN, editors, "Symposium on Neutron Cross Sections from 10 to 40 MeV," in BNL-NCS-50681, Brookhaven National Laboratory, Upton, New York (1977).

2. L. STEWART and E. D. ARTHUR, "Neutron Cross-Section Evaluation at High Energies — Problems and Prospects," *ibid.*, 435.

3. C. Y. FU, "Multi-Step Hauser-Feshbach Codes with Precompound Effects: A Brief Review of Current and Required Developments and Applications up to 40 MeV," *ibid.*, 453.

4. C. Y. FU, "A Consistent Nuclear Model for Compound and Precompound Reactions with Conservation of Angular Momentum," ORNL/TM-7042 (1980) and submitted to Physical Review C.

5. D. HERMSDORF, A. MEISTER, S. SASSONOFF, D. SEELIGER, K. SEIDEL, and F. SHAHIN, Zentralinstitut für Kernforschung, Rossendorf Bei Dresden, ZfK-277 (U), (1975).

6. S. M. GRIMES, R. C. HAIGHT, K. R. ALVAR, H. H. BARSCHALL, and R. R. BORCHERS, Phys. Rev. C19, 2127 (1979). R. C. HAIGHT and S. M. GRIMES, Lawrence Livermore Laboratory Report UCRL-80235 (1977) and private communication.

7. C. Y. FU, in Nuclear Cross Sections and Technology, Proceedings of a Conference, Vol. I, p. 328, National Bureau of Standards Special Publication SP-425, Washington, DC (1975).

8. L. C. BIEDENHARN, J. M. BLATT, and M. E. ROSE, Rev. Mod. Phys. 24, 249 (1952).

9. R. HUBY, Proc. Phys. Soc. (London) A67, 103 (1954).

10. J. M. BLATT and L. C. BIEDENHARN, Rev. Mod. Phys. 24, 258 (1952).

11. G. T. SATCHLER, Phys. Rev. 94, 1304 (1954); 104, 1198 (1956); 111, 1747 (1958).

12. D. M. HETRICK, D. C. LARSON, and C. Y. FU, in Proc. Conf. on Nucl. Cross Sections for Technology, Knoxville, Tennessee, October 22-26, 1979.

13. C. Y. FU and D. M. HETRICK, "Reevaluation of Neutron and Gamma-Ray-Production Cross Sections for Calcium from 8 to 20 MeV," ORNL/TM (to be published).

14. C. Y. FU, Atomic Data and Nucl. Data Tables 17, 127 (1976).

15. J. K. Dickens, Nucl. Sci. Eng. 48, 78 (1972).

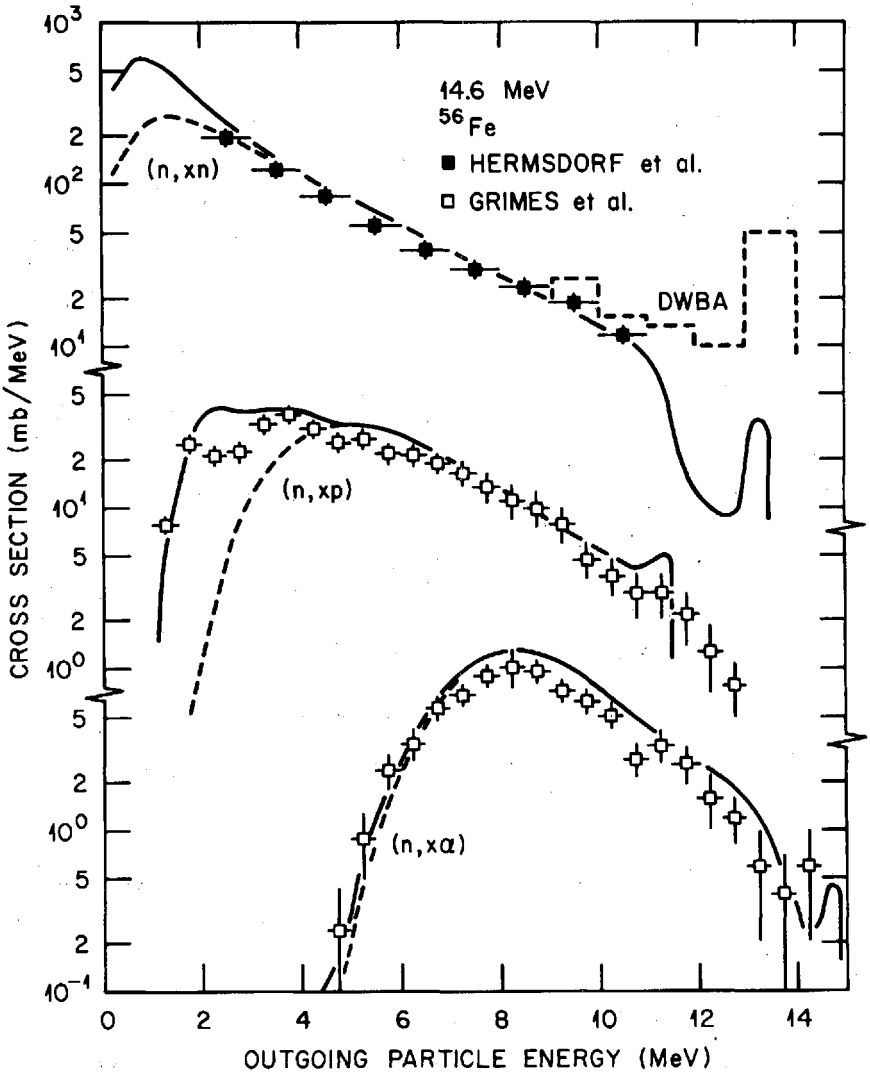

Fig. 1. Calculated and experimental angle-integrated neutron, proton, and alpha-particle production spectra from 14.6-MeV neutrons on ^{56}Fe. The solid curves are calculations. The dashed curves include calculated contributions from the binary step only. The histograms represent DWBA calculations of (n,n') cross sections for 15 discrete levels.

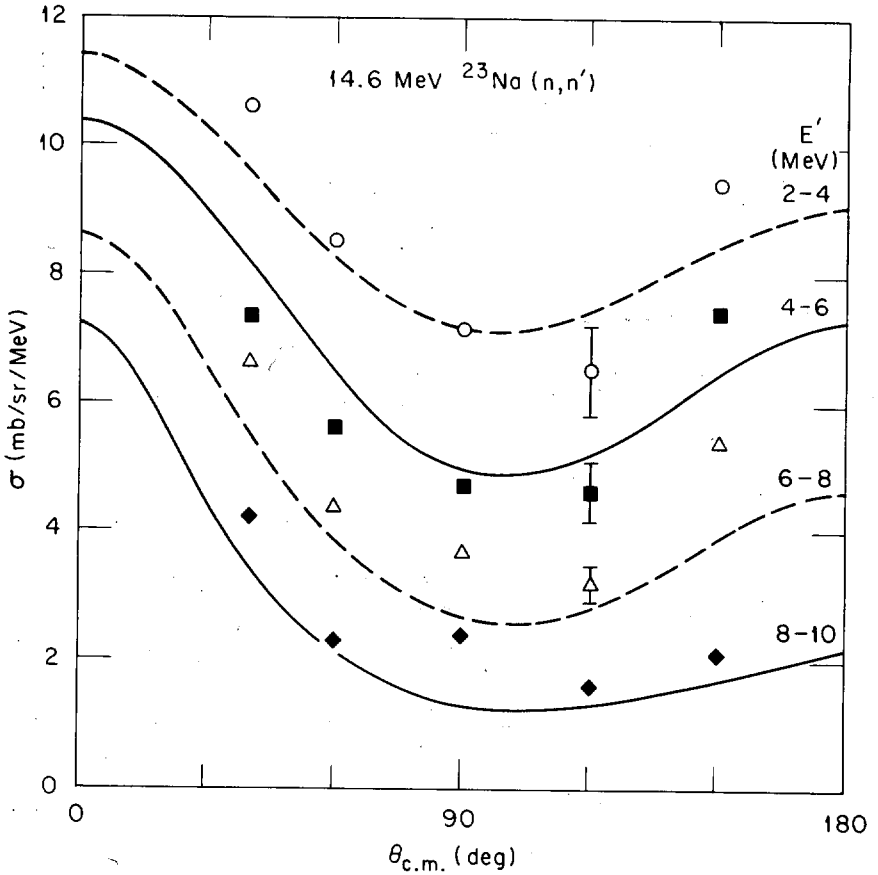

Fig. 2. Calculated and experimental double differential cross sections of the 14.6-MeV ^{23}Na(n,n'x) reaction. The data are due to Hermsdorf *et al.* [5]. Backward peaking in the calculated and observed angular distributions exhibits angular momentum effects.

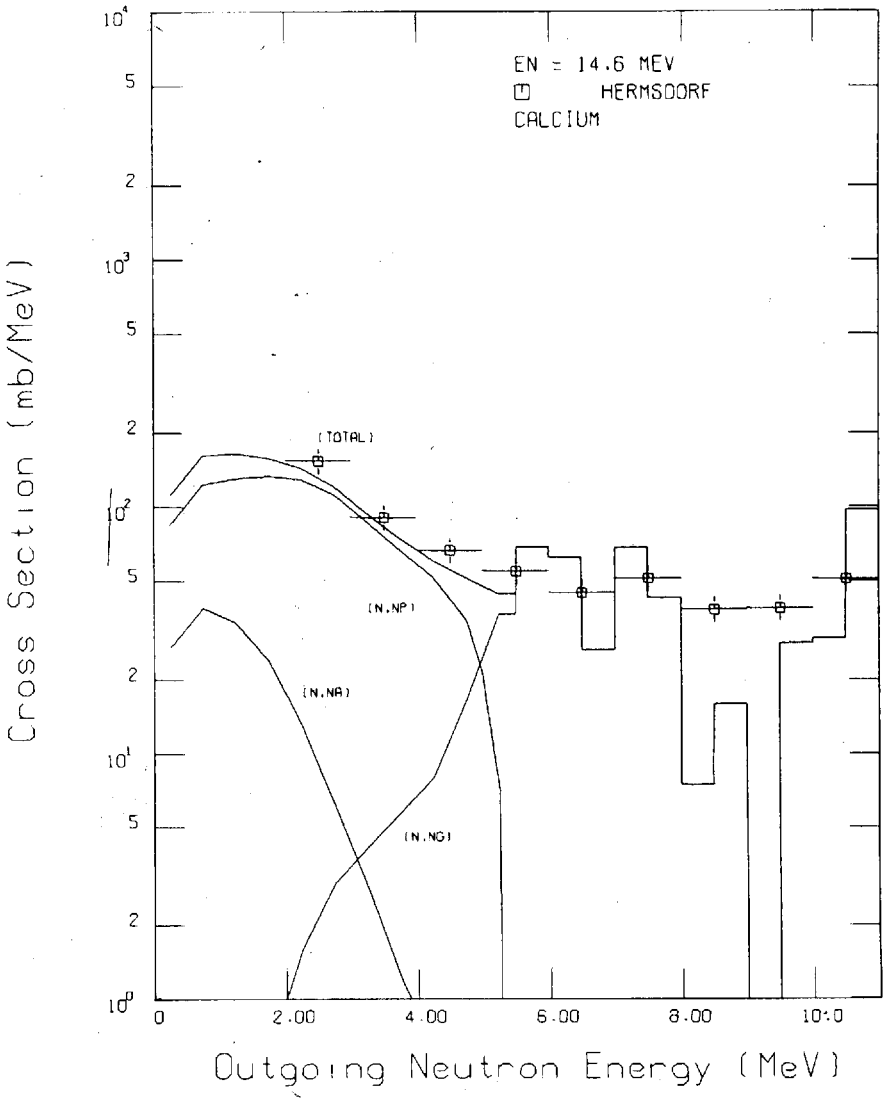

Fig. 3. The sum of partial neutron emission spectra calculated from various competing reactions for calcium is compared with the data measured by Hermsdorf *et al.* [5]. Correction due to DWBA calculations for the discrete levels has been applied.

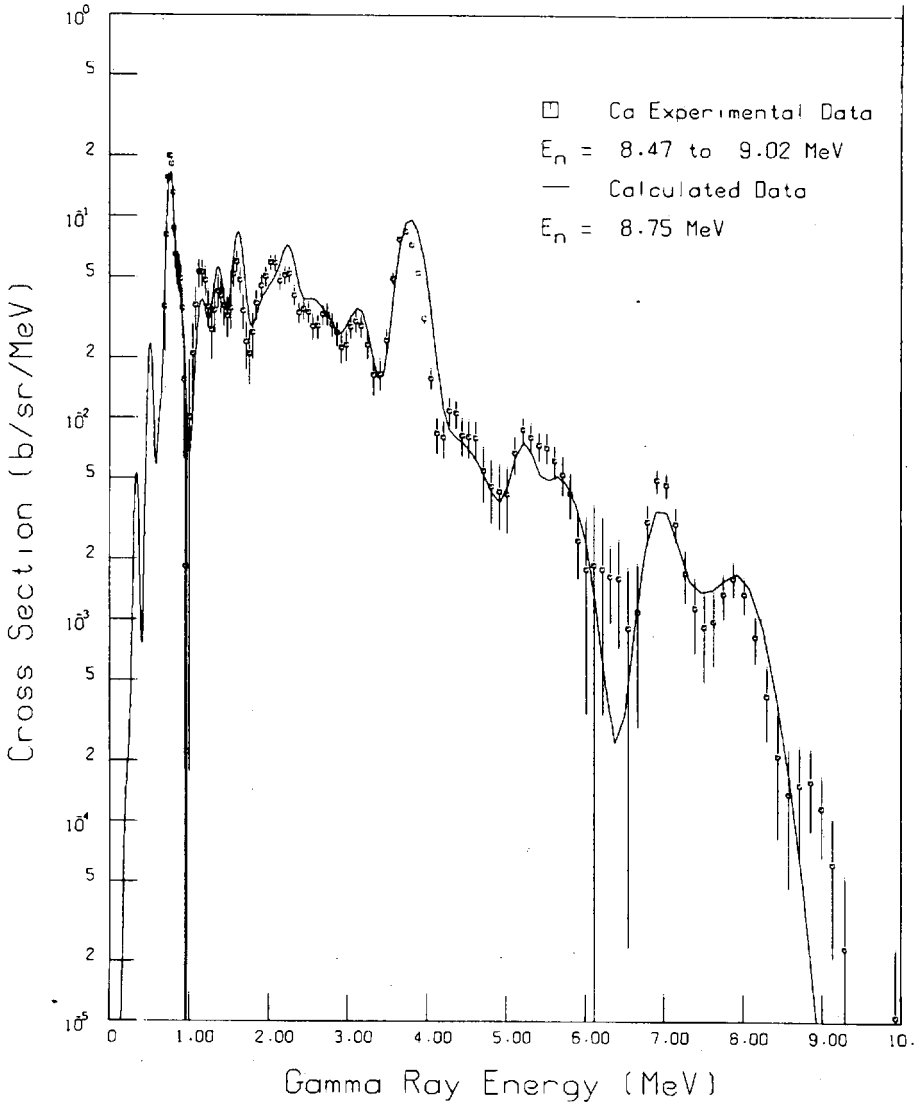

Fig. 4. Comparison of calculated and experimental [15] gamma-ray production spectra from 8.75-MeV neutrons on calcium. The calculation was done for ^{40}Ca while the observed 1.158-MeV gamma ray was produced in $^{44}Ca(n,n'\gamma)$ reaction.

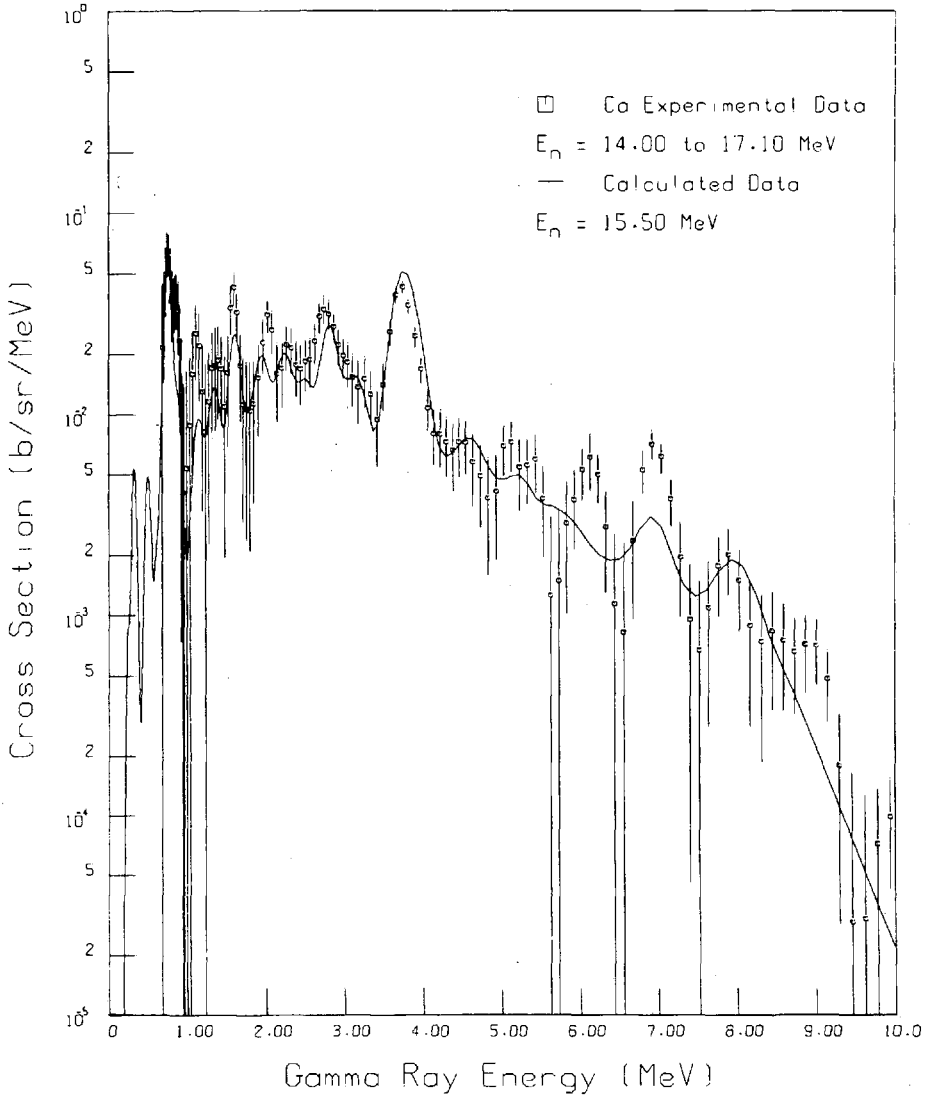

Fig. 5. Comparison of calculated and experimental [15] gamma-ray production spectra from 15.5-MeV neutrons on calcium. Some of the observed discrete gamma rays have not yet been identified.

PHENOMENOLOGY OF PREEQUILIBRIUM ANGULAR DISTRIBUTIONS

C. Kalbach

Triangle Universities Nuclear Laboratory
Durham NC 27706

and

F. M. Mann

Hanford Engineering Development Laboratory
Richland WA 99352

ABSTRACT

The systematics of continuum angular distributions from a wide variety of light ion nuclear reactions have been studied. To first order, the shapes of the angular distributions have been found to depend only on the energy of the outgoing particle and on the division of the cross section into multi-step direct and multi-step compound parts. The angular distributions can be described in terms of Legendre polynomials with the reduced polynomial coefficients exhibiting a simple dependence on the outgoing particle energy. Two integer and four continuous parameters with universal values are needed to describe the coefficients for outgoing energies of 2 to 60 MeV in all the reaction types studied. This parameterization combined with a modified Griffin model computer code permits the calculation of double differential cross sections for light ion continuum reactions where no data is available.

INTRODUCTION

In recent years work has begun on extending models for preequilibrium particle emission in nuclear

reactions to the calculation of angular distributions. The approaches proposed so far [1-10] are quite diverse. All involve some serious approximations and/or computational complexity. They disagree as to the important physical quantities involved in determining the shapes of the angular disstributions, and none has been shown to reproduce data under a sufficiently varied set of reaction conditions to be useful in applied areas where many unmeasured angular distributions must be predicted.

In light of this, we have chosen to approach the problem phencmenologically. A broad range of data have been studied to identify the reaction parameters governing the shapes of continuum angular distributions. This knowledge has then been used in developing a simple parameterization which can be incorporated into existing preequilibrium model codes such as PRECO. Such codes traditionally calculate only angle integrated cross sections.

THE DATA

The data [11-17] used in this work are listed in Tables I and II. Those systems above the dashed lines were used in determining the systematics. Those below the dashed lines were used to check the predictive ability of the final parameterization. They cover a wide range of target mass, incident and outgoing energy, and reaction mechanism. Only light ion ($A \leq 4$) reactions are considered. In several cases, particularly for inelastic scattering, data from extreme forward angles were rejected because of experimental difficulties. In addition, data from different laboratories might be expected to show slightly different behavior due to different estimates of background contributions. This is a common problem in continuum data.

MSD AND MSC PROCESSES IN THE GRIFFIN MODEL

Continuum angular distributions tend to be smoothly varying with angle, and the amount of forward peaking for a given reaction increases regularly with the energy of the outgoing particle. Because of these qualitative similarities, the detailed reaction mechanism would seem not to play an important role. On the other hand, there must be some smooth way of going from the strongly forward peaked angular distributions characteristic of direct reactions to the nearly

isotropic ones associated with compound nucleus processes.

To accomplish this transition we have considered the ideas suggested by Feshbach et al [10] and adapted them for use in the Griffin (or exciton) preequilibrium model. They define as statistical multi-step direct (MSD) those processes in which there is at least one particle in the continuum at each stage of the reaction. This definition has been retained. The MSD reactions are expected to exhibit forward peaked angular distributions. The other class of reactions, statistical multi-step compound (MSC), are expected to yield angular distributions which are symmetric about 90 degrees. They have been defined [10] as those in which all of the particles are bound in each stage of the reaction. In the Griffin model, however, only states which have continuum particles are considered to undergo particle emission, and transitions from bound to unbound configurations are allowed. Thus MSC processes have been redefined to include all reactions in which the system passes at different stages through both bound and unbound configurations.

The Griffin model has been extended by deriving the rates for particle-hole pair creation and annihilation in a formalism in which bound and unbound configurations are considered separately. (An unbound configuration is one in which at least one particle degree of freedom is in the continuum.) Thus, for example, in place of the average pair creation rate, $\lambda_+(p,h,E)$, for a state with p particle and h hole degrees of freedom at excitation energy E, we now have the four pair creation rates $\lambda_+^{(uu)}(p,h,E)$, $\lambda_+^{(ub)}(p,h,E)$, $\lambda_+^{(bb)}(p,h,E)$, $\lambda_+^{(bu)}(p,h,E)$. Here the super scripts u and b denote the bound and unbound character of the initial and final states of the interaction. In general it is found that

$$\lambda_+(p,h,E) \cong \lambda_+^{(uu)}(p,h,E) + \lambda_+^{(ub)}(p,h,E) \cong \lambda_+^{(bb)}(p,h,E) + \lambda_+^{(bu)}(p,h,E) \qquad (1)$$

Particle emission rates must also be modified. If $\omega(p,h,E)$ is the density of states specified by p, h, and E, and $\omega^{(u)}(p,h,E)$ is the density of such states with at least one continuum particle, then we find that the average emission rate for particles of type b and energy ϵ from unbound states is

$$W_b^{(u)}(p,h,\epsilon)\, d\epsilon = W_b(p,h,\epsilon)\, d\epsilon \frac{\omega(p,h,E)}{\omega^{(u)}(p,h,E)} \qquad (2)$$

Here $W_b(p,h,\epsilon)$ is the conventional emission rate averaged over bound and unbound states alike. It is assumed that emission rates for bound states are zero.

All reaction calculations are performed in the closed form approximation using PRECO-D [18], a new version of the Griffin model code PRECO. All input parameters are the same as in earlier versions. Output includes the energy differential cross sections for preequilibrium MSD, preequilibrium MSC and first chance evaporation (also MSC) components. Subroutines are available to calculate direct nucleon transfer cross sections and cross sections for inelastic and knockout processes involving cluster degrees of freedom. An improved version of a semi-empirical formalism [19] is used for these direct reactions. Their cross sections are included in the overall MSD component. Where later chance evaporation occurs, these components should be included in the MSC cross section. They are not currently calculated in PRECO but have been included in this work whenever they were available.

ANGULAR DEPENDENCE

It was decided at the outset to describe the angular distributions in terms of Legendre polynomials because we were confident of being able to obtain good fits to the data using a relatively small number of parameters. The systematics of the data would be quantitatively displayed in the systematics of the Legendre polynomial coefficients.

Since existing models predict the magnitude of the cross sections, the present work centers on the <u>shape</u> of the experimental angular distributions. These, in turn, are given not by the usual Legendre coefficients, a_ℓ, but by the reduced coefficients, $b_\ell = a_\ell / a_0$. If the distinction between MSD and MSC processes is not important then the double differential cross section for the reaction A(a,b) is given by

$$\frac{d^2\sigma}{d\Omega\, d\epsilon}(a,b) = a_0(TOT)\sum_{\ell=0}^{\ell_{max}} b_\ell \; P_\ell(\cos\theta) \qquad (3)$$

where $a_0(TOT)$ is the energy differential cross section divided by 4π. We have assumed in this work that if the MSD/MSC distinction is meaningful, then the same b_ℓ systematics will apply for both processes but with only the even order polynomials contributing to the MSC cross section. The double differential cross section

will then become

$$\frac{d^2\sigma}{d\Omega\, d\epsilon}(a,b) = a_0(MSD)\sum_{\ell=0}^{\ell_{max}} b_\ell\, P_\ell(\cos\vartheta) + a_0(MSC)\sum_{\substack{\ell=0 \\ \Delta\ell=2}}^{\ell_{max}} b_\ell\, P_\ell(\cos\vartheta) \qquad (4)$$

which reduces to eq. (3) in the limit of pure MSD. The choice between the two equations will be made based on the data.

SYSTEMATICS

All of the systems above the dashed lines in Tables I and II were run through a Legendre polynomial fitting routine, with all fits done in the center of mass. Because of the small number of angles at which data were measured for some of the reactions, only polynomials up through order 4 were considered. A dependence of the form of eq. (3) is assumed in the code.

Figure 1 shows the reduced coefficients for (p,p') and (p,^{4}He) reactions plotted as a function of the square root of the outgoing energy. Initially only systems with at least 95% of their cross section predicted to come from MSD processes are considered since in this limit eqs. (3) and (4) become identical. In the pure MSD limit we see from the figure that the incident energy and the target mass do not seem to affect the shape of the angular distributions. Comparison of the (p,p') and (p,^{4}He) results shows that the reduced coefficients agree well when compared for the same energy (or $\epsilon^{1/2}$) rather than for the same momentum. These observations are generally supported by the other data.

The (complex,p) results are shown in Fig. 2 and have more scatter than the points in Fig. 1 for proton induced reactions. This is due partly to the smaller cross sections and partly to the smaller number of data points in many of the angular distributions. The reduced coefficients appear to be somewhat larger than those for proton induced reactions at the same outgoing energy, and the possibility of a projectile dependence is investigated in the parameterization step.

PARAMETERIZATION

In seeking to parameterize the systematics observed above for the reduced Legendre coefficients, the energy dependence was assumed to be that of transmission coefficients for a parabolic barrier [20]. By analogy to $(2\ell+1)\ T_\ell$ we define

$$b_\ell(\epsilon) = \frac{(2\ell+1)}{1+\exp[\,A_\ell\,(B_\ell-\epsilon)\,]} \qquad (5)$$

where A_ℓ and B_ℓ are free variables.

New Legendre polynomial fits were done on the 62 MeV (p,p') data of Bertrand and Peelle [13], varying the maximum order of the fits from 2 to 12. These data are indicated in Table I in the column labelled "stage 1". The coefficients from the fits with the lowest reduced chi-square values were selected and those corresponding to at least 98% MSD were analyzed graphically to determine preliminary values for A_ℓ and B_ℓ. The maximum order polynomial actually needed was ℓ=8, but A_ℓ and B_ℓ values could only be estimated for ℓ=1 to 5.

These preliminary values were used to investigate the mixed MSD and MSC region. Angular distributions for systems in this region were calculated using both eqs. (3) and (4). The results shown in Fig. 3 indicate the validity of distinguishing between MSD and MSC processes, and eq. (4) has been adopted in the rest of this work.

The A_ℓ and B_ℓ values themselves seem to show a simple variation with ℓ. Dependences of the form

$$A_\ell = k_1 + k_2\,[\,\ell(\ell+1)\,]^{m_1/2}$$

$$B_\ell = k_3 + k_4\,[\,\ell(\ell+1)\,]^{m_2/2}$$

have been investigated using a least square fitting routine on a subset of the data including both proton and alpha particle induced reactions. The data used are indicated under "stage 2" in Tables I and II. Values of $m_1 = 2$ and $m_2 = -1$ were found. The final forms for the A and B parameters are

$$A_\ell = 0.036\ \text{MeV}^{-1} + 0.0039\ \text{MeV}^{-1}\ \ell(\ell+1) \qquad (6a)$$

$$B_\ell = 92.\ \text{MeV} - 90.\ \text{MeV}\,[\,\ell(\ell+1)\,]^{-1/2} \qquad (6b)$$

The b_ℓ values obtained from using eq. (6) in eq. (5) are shown in fig. 4 along with the values determined from Legendre fitting of the 62 MeV (p,p') data.

Equations (4)-(6) have been used to calculate the angular distributions for all the reaction systems shown in Tables I and II. The sum $a_0(MSD)+a_0(MSC)$ is adjusted to facilitate comparisons between the shapes of measured and calculated curves while the ratio $a_0(MSD)/a_0(MSC)$ is taken from the output of PRECO-D. The data fall into three categories:

(i) data used in optimizing parameter values,
(ii) data used in studying systematics, and
(iii) data included just to test the predictive ability of the parameterization.

Typical results for the three categories are shown in Figs. 5, 6 and 7, respectively. More examples are shown for high emission energies since these are generally harder to reproduce than the more nearly isotropic angular distributions at low emission energies.

In almost all cases the agreement is quite good and is comparable for the three categories of data. The greatest exception to this is the higher emission energy data from [14] where the experimental distributions show more forward peaking than the calculated ones. Because of the success of the parameterization with similar data from other laboratories, an experimental difficulty in the data of [14] is suspected. The reaction $^{232}Th(d,d')$ [17] is also a problem, but the other (d,d') data from the same reference is adequately reproduced.

Aside from these data there appears to be no evidence that different systematics are needed for complex and nucleon projectiles. The parameterization seems quite general within the range of data included in the tables. The fundamental limitation comes at high emission energies where the cross section may drop by several orders of magnitude in going from forward to backward angles. At $\epsilon \geq 50$ MeV the forward angle data, representing most of the cross section, is well reproduced, but at the more backward angles, beginning at levels of a few percent of the peak cross section, the agreement breaks down. This is not very important for most practical applications but suggests that for $\epsilon > 60$ MeV some mathematical form other than Legendre polynomials would be more appropriate to describe continuum angular distributions.

SUMMARY AND CONCLUSIONS

This work shows that to first order the shapes of continuum angular distributions for light ion induced reactions depend on the energy of the outgoing particle and on the percent of the cross section which is MSD. Target mass, projectile mass and energy, and the detailed reaction mechanism (eg. stripping vs knockout) seem not to be important.

The angular distributions can be described in terms of Legendre polynomials with the reduced coefficients being a simple function of the outgoing energy and the order, ℓ, of the polynomial as shown in eqs. (4)-(6).

The present systematics, while quite general, seem to do best at explaining data for reactions where only nucleons and alpha particles are involved. Only proton and alpha particle induced reactions have been studied here, but the results have now been confirmed [21] for (n,p) data at U. C. Davis. For reactions involving mass 2 and mass 3 particles, the degree of forward peaking in the data is sometimes slightly underestimated. The systematics seem to work for targets ranging in mass from 12 to 200 and for bombarding energies of from 18 MeV up to at least 80 MeV. They do well for emission energies up to about 40 or 45 MeV. For emission energies of 50 to 60 MeV they do well only at forward angles where the bulk of the cross section is located. At still higher emission energies, where the cross section varies over many orders of magnitude, a different mathematical form for the angular distributions would seem to be needed.

In summary, this work has given experimentalists and people in applied areas a useful way to calculate unmeasured angular distributions for light ion reactions populating a statistical number of final states.

ACKNOWLEDGEMENTS

This work was supported by Hanford Engineering Development Laboratory. HEDL is operated by Westinghouse Hanford Company, a subsidiary of Westinghouse Electric Corporation, under DOE contract number DE-AC-76FF02170. One of the authors (CK) would like to acknowledge the hospitality of the Triangle Universities Nuclear Laboratory.

REFERENCES

1. G. MANTZOURANIS, H. A. WEIDENMUELLER, and D. AGASSI, Z. Phys. A 276, 145 (1976).

2. G. MANTZOURANIS, Phys. Rev. C 14, 2018 (1976).

3. J. M. AKKERMANS, Phys. Lett. 82B, 20 (1979).

4. H. MACHNER, Phys. Lett. 86B, 129 (1979).

5. V. A. PLYUIKO, Sov. J. Nucl. Phys. 27, 623 (1978) (Yad. Fiz. 27, 1175 (1978)).

6. Y. IBIE, M. HYAKUTAKE, M. MATOBA, and M. SONODA, Phys. Lett. 62B, 9 (1976).

7. T. TAMURA, T. UDAGAWA, D. H. FENG and K.-K. KAN, Phys. Lett. 66B, 109 (1977)

8. T. TAMURA, T. UDAGAWA, Phys. Lett. 71B, 273 (1977).

9. A. D. DUISEBAEV, V. I. KANASHEVICH, E. M. SAPRYKIN, I. B. TEILOV, D. A. SHALBAEV, and N. P. YUDIN, Sov. J. Nucl. Phys. 27, 613 (1978) (Yad. Fiz. 27, 1156 (1978)).

10. H. FESHBACH, A. KERMAN and S. KOONIN, Ann. Phys. 125, 429 (1980).

11. C. KALBACH, S. M. GRIMES, and C. WONG, Z. Phys. A 275, 175 (1975)

12. S. M. GRIMES, J. D. ANDERSON and C. WONG, Phys. Rev. C 13, 2224 (1976).

13. F. E. BERTRAND and R. W. PEELLE, Phys. Rev. C 8, 1045 (1973).

14. J. BISPLINGHOFF, J. ERNST, R. LOHR, T. MAYER-KUCKUK, and P. MEYER, Nucl. Phys. A 269, 147 (1976).

15. F. E. BERTRAND, R. W. PEELLE, and C. KALBACH-CLINE, Phys. Rev. C 10, 1028 (1974).

16. R. W. WEST, Phys. Rev. 141, 1033 (1966).

17. J. R. WU, C. C. CHANG, H. D. HOLMGREN, Phys. Rev. C 19, 370 (1979).

18. C. KALBACH, "PRECO-D: Program for Calculating Preequilibrium and Direct Reaction Double Differential Cross Sections", informal report available from author.

19. C. KALBACH, Z. Phys. A 283, 401 (1977).

20. D. L. HILL and J. A. WHEELER, Phys. Rev. 89, 1102 (1953).

21. J. ULLMAN et al, "Progress Report to the National Science Foundation on Medium Energy Neutron Scattering and Reactions, July 1, 1977 to June 30, 1979" Univ. of California at Davis, Crocker Nuclear Laboratory (1979) pp 89,117-126.

TABLE I

Data for Nucleon Induced Reactions

Reaction	Proj. Ener. (MeV)	Ejec. Ener. (MeV)	# of Ener.	# of Ang.	Ref.	Stage 1	Stage 2
^{103}Rh(p,n)	18	5.5-12.5	4	10	11		x
^{107}Ag(p,n)	18	4.5-12.5	4	10	12		x
^{107}Ag(p,n)	25	6.5-18.5	5	16	12		x
^{54}Fe(p,p')	39	5-28	7	7	13		
^{54}Fe(p,p')	62	4-52	13	19	13	x	
^{120}Sn(p,p')	62	8-55	11	18	13	x	x
^{54}Fe(p,d)	39	7-16	4	7	13		
^{54}Fe(p,d)	62	5-35	7	21	13		
^{120}Sn(p,d)	62	8-42	10	20	13		
^{54}Fe(p,t)	39	10-12	2	7	13		
^{54}Fe(p,t)	62	10-35	6	21	13		
^{120}Sn(p,t)	62	8-42	8	20	13		
^{54}Fe(p,^{3}He)	62	14-33	6	21	13		
^{54}Fe(p,^{4}He)	39	8-24	5	7	13		
^{54}Fe(p,^{4}He)	62	10-48	10	21	13		
^{120}Sn(p,^{4}He)	62	12-55	10	21	13		
^{12}C(p,p')	62	30-40	2	18	13		
^{27}Al(p,p')	62	30-50	2	17	13		
^{54}Fe(p,p')	29	4-20	5	4	13		
^{197}Au(p,p')	29	20	1	4	13		
^{197}Au(p,p')	62	20-40	2	5	13		
^{209}Bi(p,p')	62	30-50	2	17	13		
^{54}Fe(p,d)	29	4-7	2	5	13		
^{12}C(p,^{4}He)	62	30	1	18	13		
^{27}Al(p,^{4}He)	62	30	1	17	13		
^{54}Fe(p,^{4}He)	29	8-20	4	5	13		
^{197}Au(p,^{4}He)	29	22	1	4	13		
^{197}Au(p,^{4}He)	62	25	1	6	13		
^{209}Bi(p,^{4}He)	62	20-40	2	18	13		

TABLE II

Data for Complex Particle Induced Reactions

Reaction	Proj. Ener. (MeV)	Ejec. Ener. (MeV)	# of Ener.	# of Ang.	Ref.	Stage 1	Stage 2
^{63}Cu(d,p)	25	4.3-24.8	3	7	14		
^{63}Cu(d,d')	25	5.3-18.8	3	7-9	14		
^{63}Cu(d,t)	25	5.8-18.3	3	7-9	14		
^{63}Cu(d,^{4}He)	25	10.3-27.8	3	8	14		
^{62}Ni(^{3}He,p)	24	4.3-24.8	3	7	14		
^{62}Ni(^{3}He,d)	24	5.3-18.8	3	7	14		
^{62}Ni(^{3}He,t)	24	5.8-11.3	2	7	14		
^{62}Ni(^{3}He,^{3}He')	24	9.3-18.3	3	7	14		
^{62}Ni(^{3}He,^{4}He)	24	10.3-27.8	3	7	14		
^{54}Fe(^{4}He,p)	59	6-40	10	6	15		
^{59}Co(^{4}He,p)	42	10-32	5	8	16		x
^{61}Ni(^{4}He,p)	36	4.3-24.8	3	7	14		
^{103}Rn(^{4}He,p)	42	10-32	5	8	16		x
^{54}Fe(^{4}He,d)	59	6-33	8	6	15		
^{61}Ni(^{4}He,d)	36	5.3-18.8	3	7-8	14		
^{54}Fe(^{4}He,t)	59	8-31	5	6	15		
^{61}Ni(^{4}He,t)	36	5.8-18.3	3	7-8	14		
^{54}Fe(^{4}He,^{4}He')	59	7-45	9	6	15		x
^{61}Ni(^{4}He,^{4}He')	36	10.3-27.8	3	7	14		
^{27}Al(d,p)	80	60	1	7	17		
^{27}Al(d,d')	80	50	1	7	17		
^{58}Ni(d,d')	80	30	1	8	17		
^{208}Pb(d,d')	70	50	1	9	17		
^{232}Th(d,d')	70	40	1	8	17		
^{27}Al(d,t)	80	20	1	7	17		
^{58}Ni(d,t)	80	40	1	7	17		
^{90}Zr(d,t)	70	30	1	8	17		
^{232}Th(d,t)	70	40	1	8	17		
^{27}Al(d,^{4}He)	80	40	1	7	17		
^{58}Ni(d,^{4}He)	80	60	1	8	17		
^{90}Zr(d,^{4}He)	70	50	1	8	17		
^{208}Pb(d,^{4}He)	70	50	1	9	17		
^{12}C(^{4}He,p)	59	20	1	5	15		
^{12}C(^{4}He,^{4}He')	59	20	1	5	15		

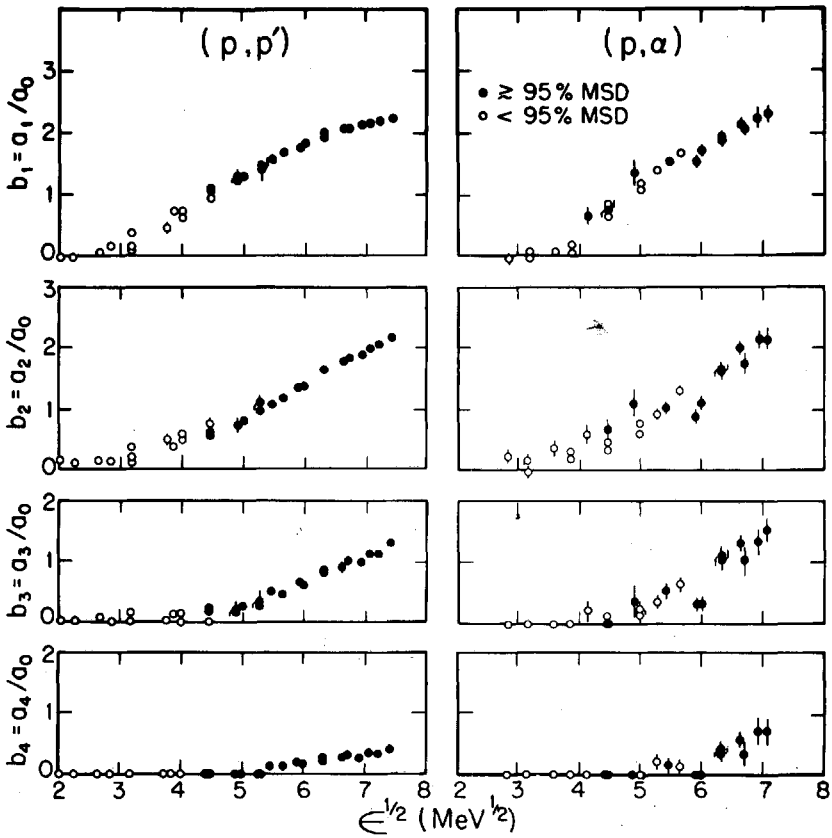

Fig. 1. Experimental reduced Legendre coefficients for proton induced reactions.

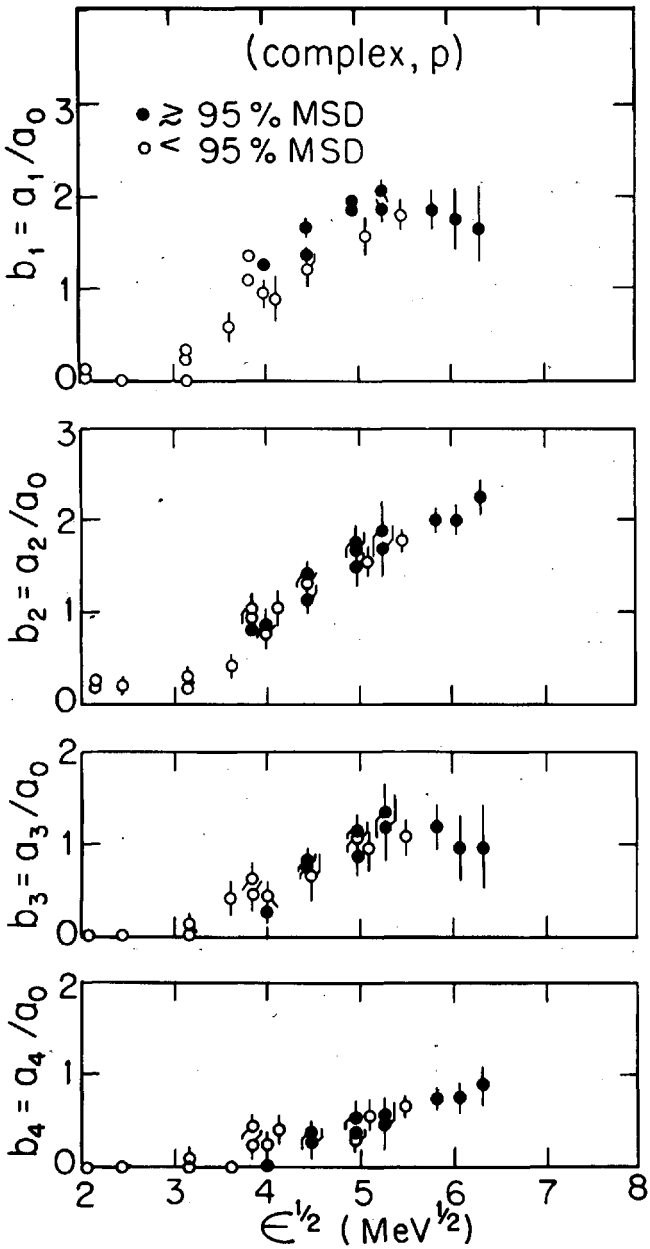

Fig. 2. Experimental reduced Legendre coefficients for complex particle induced reactions.

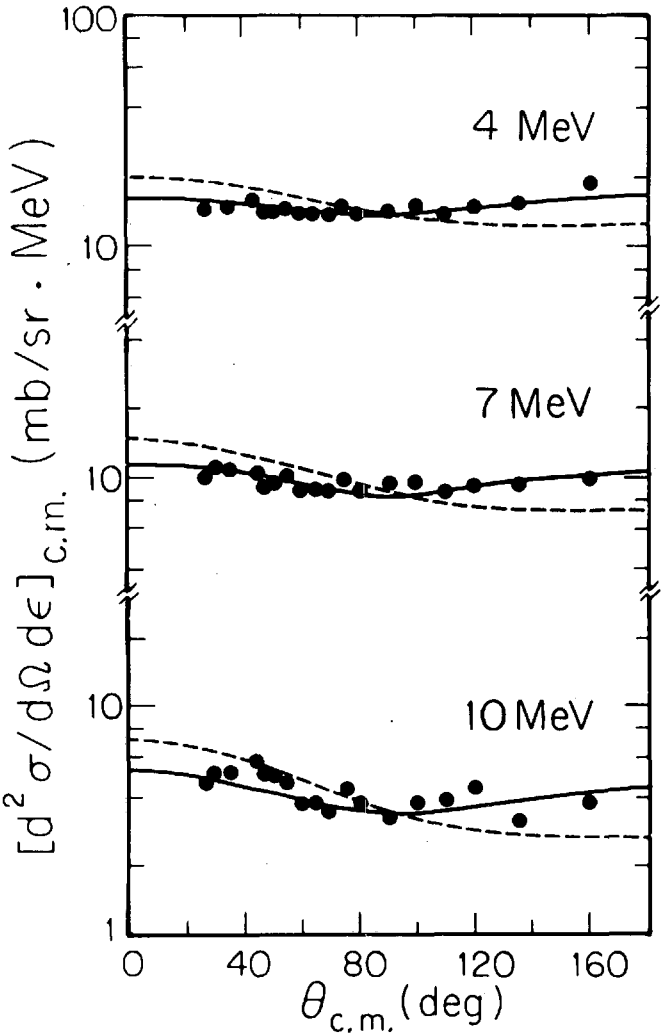

Fig. 3. Importance of distinguishing MSD and MSC processes. The points represent data for the $^{54}Fe(p,p')$ reaction at 62 MeV incident energy and the indicated outgoing energies. The dashed and solid curves are calculated with eqs. (3) and (4), respectively.

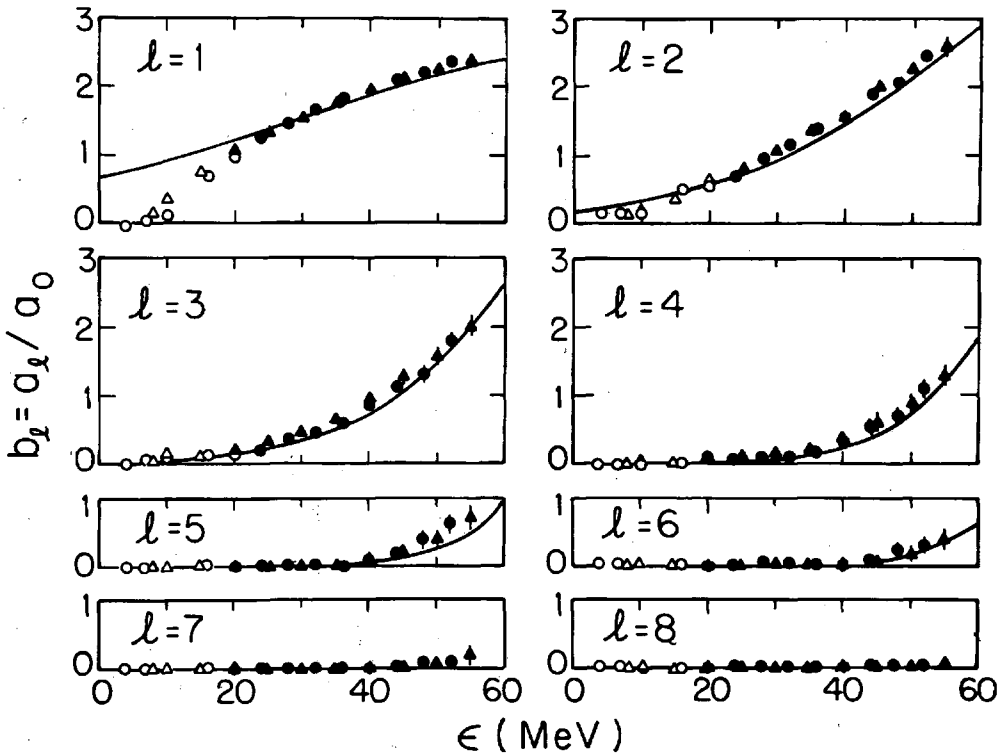

Fig. 4. Systematics of the reduced Legendre coefficients. The points result from fitting the 62 MeV (p,p') data with polynomials of order up through 12, assuming eq. (3). The curves show the systematics derived here and given by eqs. (5) and (6). They are to be used in eq. (4). For odd ℓ they are directly comparable to the points only in the pure MSD limit.

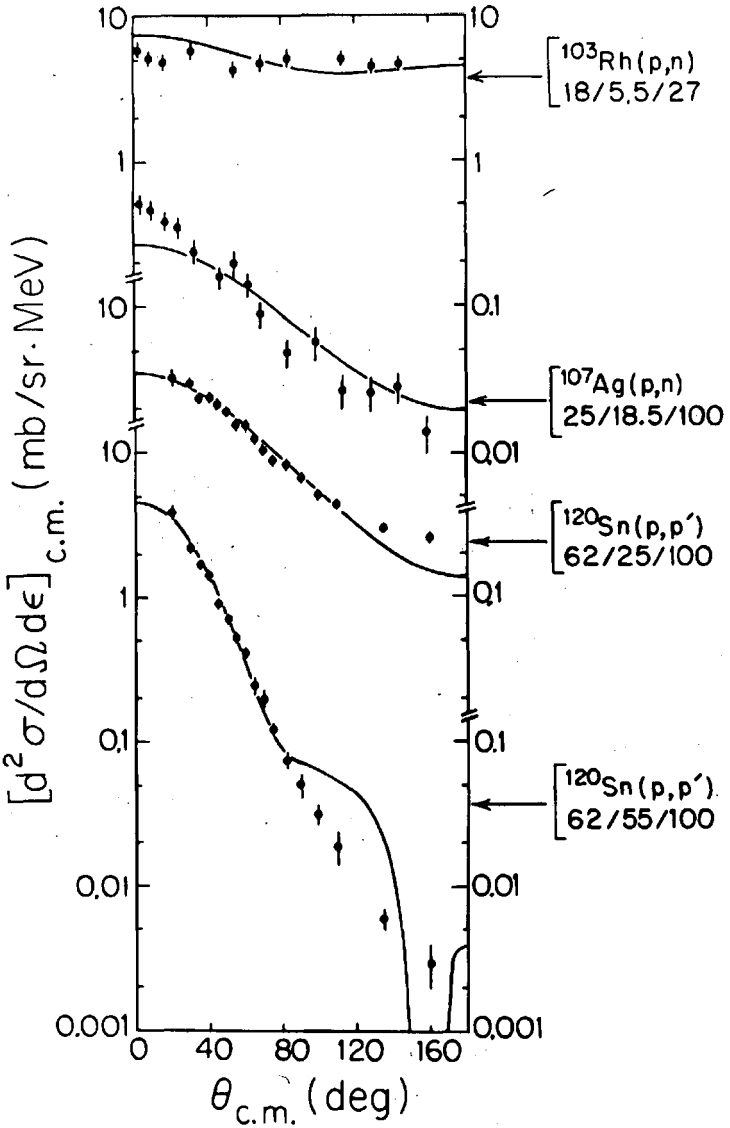

Fig. 5a. Sample angular distributions for data systems used in the least squares fitting to determine parameter values. The points show the data while the curves are calculated using the final parameterization derived here. The three numbers beneath the reaction designations for each curve give the incident (lab) energy, the emission (cm) energy, both in MeV, and the %MSD.

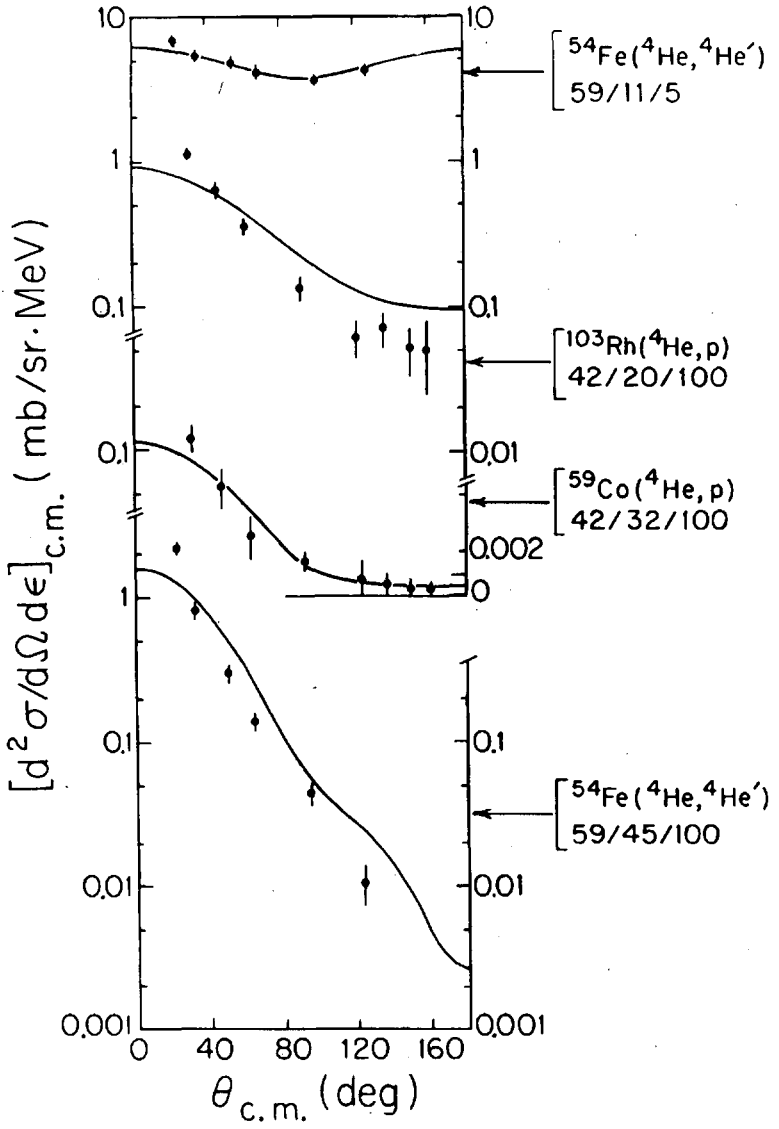

Fig. 5b. Sample angular distributions for data systems used in the least squares fitting to determine parameter values. The points show the data while the curves are calculated using the final parameterization derived here. The three numbers beneath the reaction designations for each curve give the incident (lab) energy, the emission (cm) energy, both in MeV, and the %MSD.

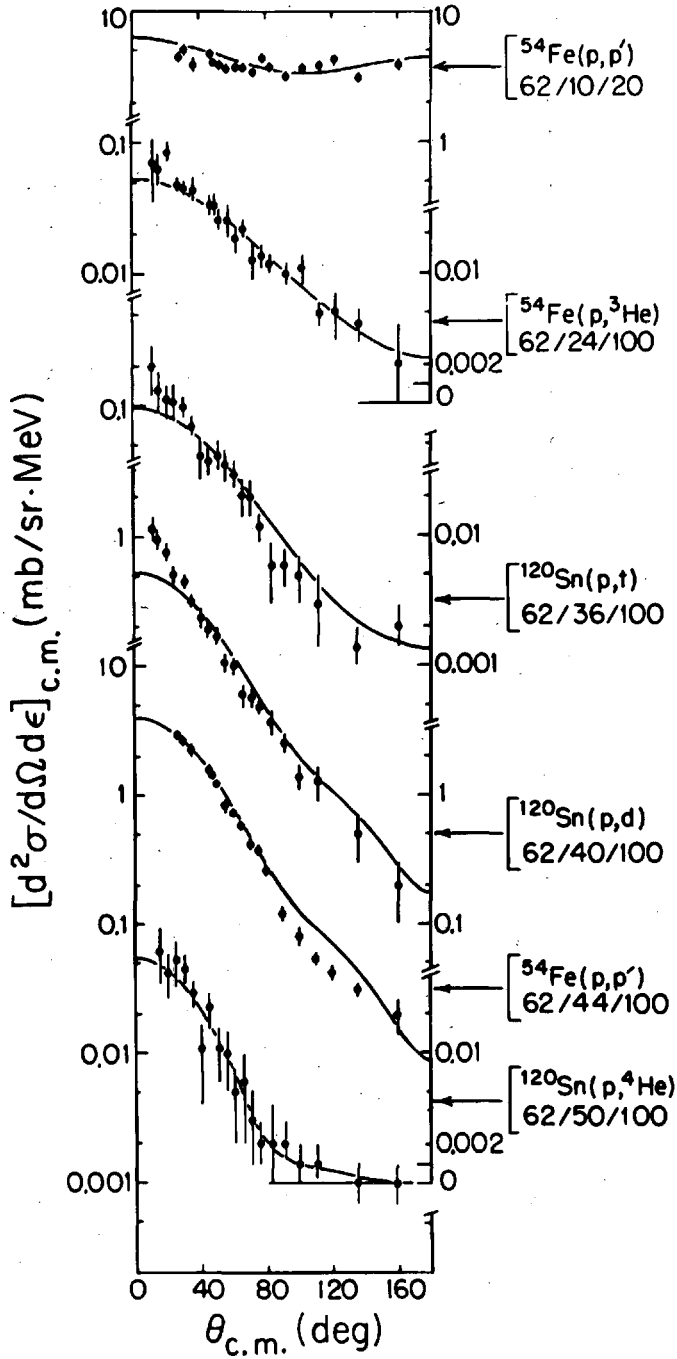

Fig. 6a. Sample angular distributions for data systems used in the determination of the general systematics but not in the setting of parameter values. Points and curves have the same significance as in Fig. 5.

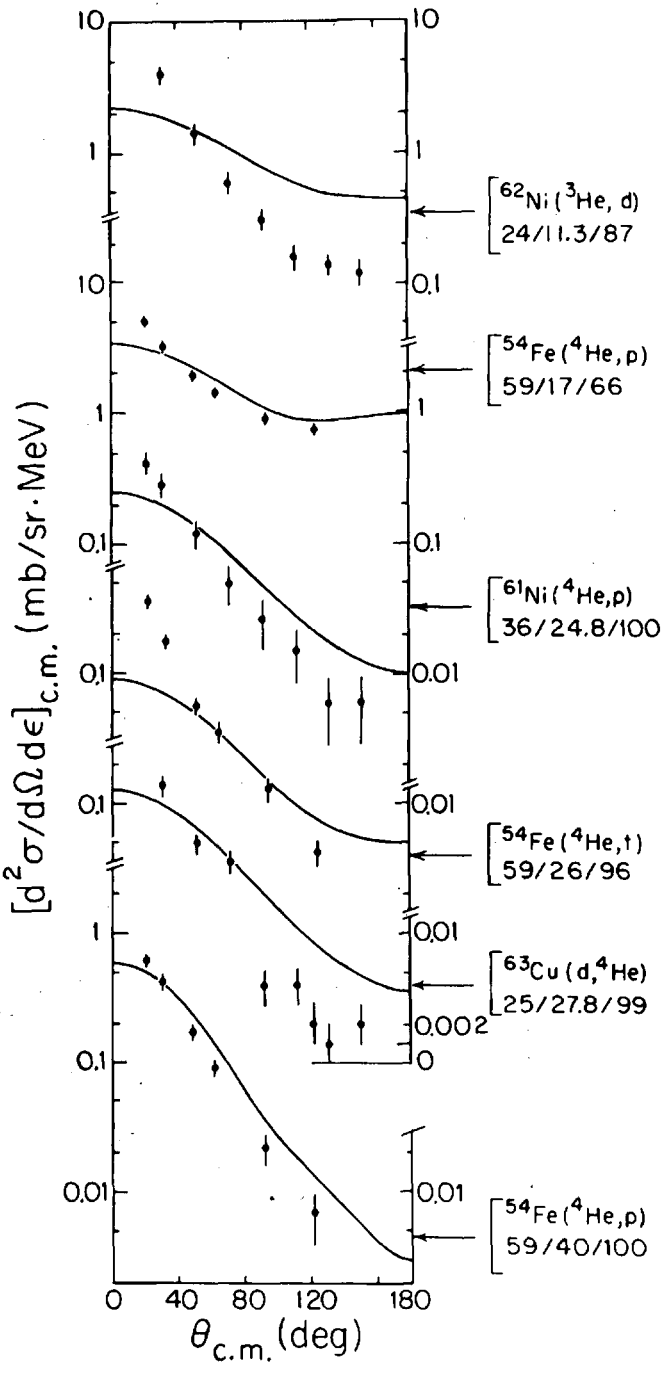

Fig. 6b. Sample angular distributions for data systems used in the determination of the general systematics but not in the setting of parameter values. Points and curves have the same significance as in Fig. 5.

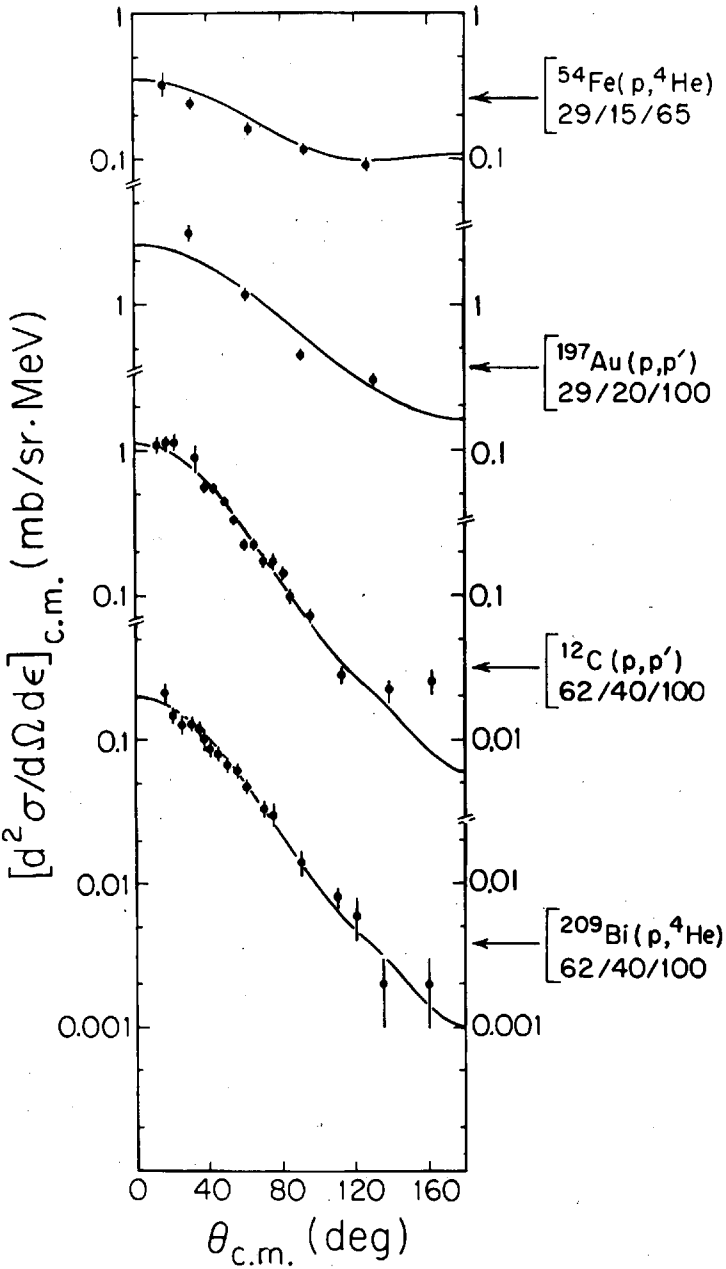

Fig. 7a. Sample angular distributions for data systems used to test the predictive ability of the parameterization derived here. Points and curves have the same significance as in Fig. 5.

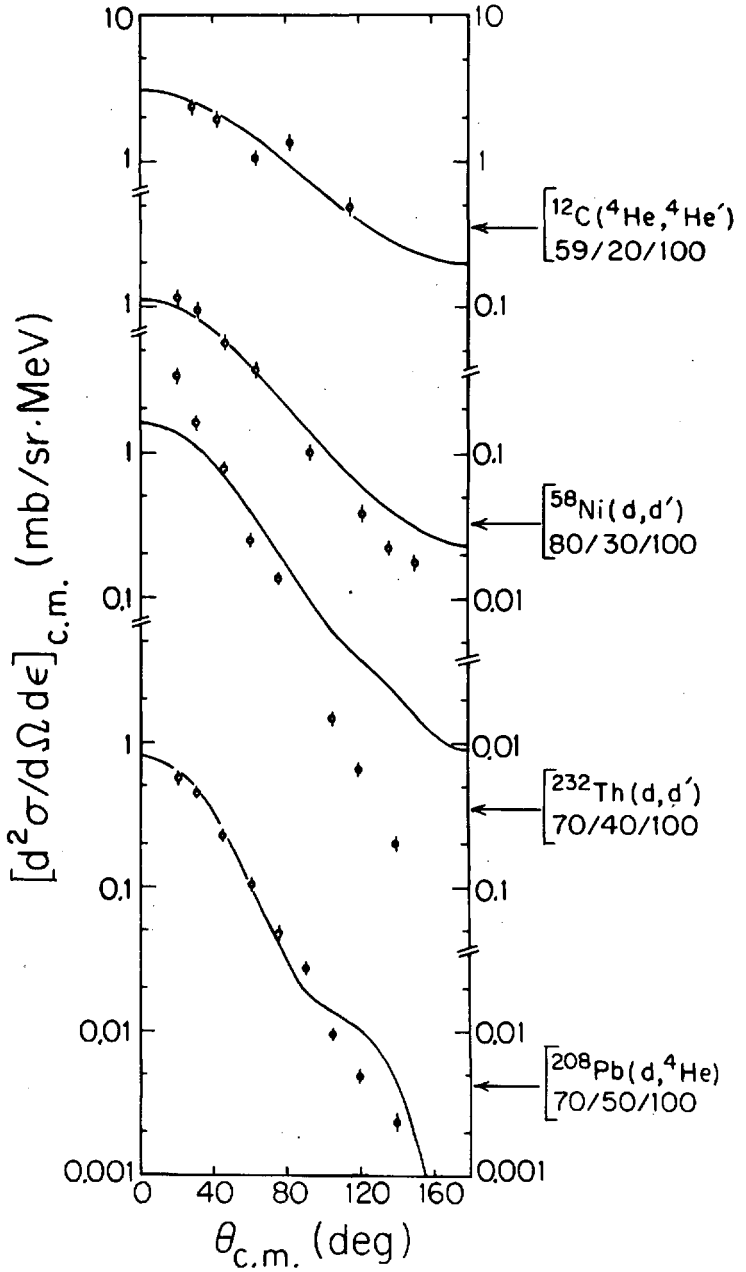

Fig. 7b. Sample angular distributions for data systems used to test the predictive ability of the parameterization derived here. Points and curves have the same significance as in Fig. 5.

COMPARISON OF EXPERIMENTAL AND CALCULATED NEUTRON EMISSION SPECTRA AND ANGULAR DISTRIBUTIONS

H. Gruppelaar and J.M. Akkermans *

Netherlands Energy Research Foundation (ECN), P.O. Box 1, 1755 ZG Petten, The Netherlands

ABSTRACT

Experimental and calculated neutron emission spectra and angular distributions have been intercompared for 14.6 MeV neutron-induced reactions. The experimental data, measured by Hermsdorf et al., cover 34 elements in a large mass range. To calculate the differential neutron scattering cross sections a unified model of preequilibrium neutron emission was used, in which the generalized master equation of Mantzouranis et al. was solved with a fast exact matrix method, recently introduced by Akkermans. For the scattering kernel a three-term Legendre polynomial representation was adopted, which was either derived from the differential free nucleon-nucleon scattering cross section or fitted to obtain optimal agreement with the set of experimental data of Hermsdorf et al. The results of the last-mentioned calculation are quite acceptable in view of the fact that only two global parameters have been used to describe the angular distributions of all experimental data. It is further shown that improvements in the energy and angular distributions could be obtained by means of adjustment of the level-density parameters of the individual residual nuclei. Finally a short discussion is devoted to the problems of fitting angular distributions at backward angles by varying the model parameters or the specification of the initial condition.

* Present address: FOM-Institute for Plasma Physics, "Rijnhuizen", P.O. Box 7, 3430 AA Nieuwegein, The Netherlands.

1. INTRODUCTION

In this paper the results of an intercomparison between experital and calculated neutron emission spectra and angular distributions of neutron-induced reactions at about 14.6 MeV are discussed. The experimental data were taken from the work of Hermsdorf et al. [1], who have measured emission spectra at several angles for 34 elements, spanning the mass range from Beryllium to Bismuth. The calculations were performed with the code PREANG [2], which is based upon a statistical model predicting both equilibrium and preequilibrium contributions. In this model the generalized master equation, introduced by Mantzouranis et al. [3] is solved according to the exact matrix method given by Akkermans [4]. The method is a generalization of the solution of Luider [5] for the angle-integrated master equation, which has been introduced [6] into the code of Běták [7].

Our adopted model and initial-condition specifications differ from those of Mantzouranis et al. [3] in the following aspects [8]:

- a fast and exact calculation method is used to compute both energy and angular distributions;
- Legendre coefficients of angular distributions are directly calculated;
- a unified description of both preequilibrium and equilibrium emission is followed;
- transitions with $\Delta n=0$ have been accounted for;
- a rough estimate for refraction effects of the incident wave has been included.

In all our calculations we have assumed that the angular distribution of the initial condition and that of the internucleon scattering kernel are the same. We have used a three-term Legendre polynomial representation for this distribution, which was either derived from the differential free nucleon-nucleon scattering cross section [3] or fitted to obtain optimal agreement with the set of experimental data of Hermsdorf et al.

In Ref. [8] a rather extensive discussion of this "unified model of preequilibrium and equilibrium neutron emission" has been given, together with some examples of comparisons between calculated and experimental data. A large number of tables and graphs of these comparisons is given in a laboratory report [9]. In this paper the results of this systematic intercomparison are summarized and discussed with emphasis on backward-angle scattering.

2. CALCULATIONS

The experimental data of Hermsdorf et al. [1] have been used to calculate Legendre coefficients (ℓ=0,1 and 2) by means of a least-squares fitting procedure. The experimental coefficients, summed over outgoing neutron energies in the range $\Delta\varepsilon$=6 to 11 MeV are given in the first columns of Tables I to III. The coefficients have been defined as follows:

$$\frac{d\sigma_{nn'}(\Delta\varepsilon,\theta)}{d\Omega} = \frac{\sigma_{nn'}(\Delta\varepsilon)}{4\pi}\{1 + 3f_1P_1(\cos\theta) + 5f_2P_2(\cos\theta)\}. \qquad (1)$$

Theoretical coefficients were calculated with the code PREANG [2], using neutron-optical model parameters of Wilmore and Hodgson [10] and the usual value for the average internal transition matrix element: $M^2 = 190/A^3E$ [11]. A more detailed description of the adopted parameters has been given in Refs. [8,9]. Here we only summarize the various calculations of which the results are given in Tables I to III.

In *Calculation 1* we have used standard global parameters, i.e. $g = A/13$ MeV^{-1} for the single-particle level-density parameters [11], pairing energy shifts from Gilbert and Cameron [12] and the following Legendre coefficients describing the initial angular distribution and scattering kernel [8,9]: $\mu_0 = 1$, $\mu_1 = 2/3 - \beta/2 - 2\beta^2/15$ and $\mu_2 = 1/4 - 4\beta/5 + \beta^2/4$, where $\beta = 1/A$. These coefficients have been derived by assuming that the nucleon-nucleon scattering cross section inside the nucleus is isotropic in the nucleon-nucleon c.m. system [3].

In *Calculation 2* the same parameters were used, except that $\Delta n = 0$ and $\Delta n = -2$ transitions were neglected in the calculation of angular distributions by inserting the simple closed-form expression of Ref. [4], assuming isotropic contributions from states with $n \geq \bar{n}$, where $\bar{n} = \sqrt{2gE}$ denotes the equilibrium exciton number.

The results of *Calculation 3* were obtained by multiplying μ_1 and μ_2 with constants $c_1 = 0.87$ and $c_2 = 1.74$, which were obtained from a least-squares procedure giving the minimum value of χ^2 for the coefficients f_1 and f_2. All other parameters were the same as in Calc. 1.

Shell effects were investigated in *Calculation 4* by modification of level-density parameters according to $g = \frac{6}{\pi^2}(0.00917S + 0.142)A$ [12]; other model parameters were the same as those of Calc. 1.

In *Calculation 5* the same parameters were used as in Calc. 1, except that no pairing energy shift was assumed in the final-state level-density formula and that the parameter g_r was adjusted to fit $\sigma_{nn'}$ and f_1 for each individual element. It was not possible to obtain agreement also for f_2.

Therefore, in *Calculation 6* the parameter μ_2 was multiplied with a constant $c_2 = 1.95$ to fit the experimental f_2-values in a global fashion.

3. COMPARISON WITH EXPERIMENTAL DATA

Calculation 1 (standard global parameters) gives a surprisingly good overall result for the integrated cross sections, although the f_1- and f_2-coefficients are systematically too high and too low, respectively (see Table IV). It has to be noted that in all our calculations the contribution of secondary emitted neutrons has been neglected. This contribution would lead to increased values of angle-integrated spectra [8] and to less-pronounced angular distributions

at low emission energies ($\varepsilon \lesssim 6$ MeV). The largest discrepancies in f_1 occur for the elements in the mass range A = 60 to 80.

Calculation 2 (simple closed-form expression) shows larger discrepancies with experimental f_1- and f_2-coefficients (Table IV), mainly because the neglect of $\Delta n = 0$ and $\Delta n = -2$ transitions leads to further underestimation of backward-angle scattering. The mass-dependence of the calculated values for f_1 and f_2 turns out to be much weaker than in Calc. 1; especially for light masses ($A \lesssim 90$) the results are quite different (Tables II and III). A possible explanation is given in Sec. 5(c).

The results of *Calculation 3* were obtained by fitting only two global parameters (c_1 and c_2), to minimize deviations between experimental and calculated f_1- and f_2-coefficients. The overall comparison (Table IV) looks quite good and is completely in line with the present status of preequilibrium theory where effective parameters are used to describe the angle-integrated spectra. Since the f_1- and f_2-coefficients differ almost constant factors with those of Calc. 1 the largest discrepancies are also found at A = 60 to 80.

From graphs showing the energy dependence of the Legendre coefficients (e.g., Fig.1; see further Ref. [9]) it follows that for many nuclides f_1 and f_2 are calculated within the range of their experimental uncertainties, matching the experimental energy dependence surprisingly well. In fact, the fits of the angle-integrated cross sections (f_0) are often less satisfactory than those of f_1 and f_2, particularly at the highest emission energies for light even-mass nuclides. This could be ascribed to a faulty level-density description at the lowest excitation energies, cf. Sec. 4. Inspecting the angular distributions (graphs given in Ref. [9]), it follows that the largest improvements could be obtained by small renormalizations of the angle-integrated cross sections. Only for some nuclei (e.g. with A = 60 to 80) the actual angular dependence needs significant improvement. In the next section we demonstrate that many of these remaining discrepancies in $\sigma_{nn'}$, f_1 and f_2 could be ascribed to level-density effects.

4. LEVEL DENSITY EFFECTS

The adopted level-density formula [13,14] and the parameter choice $g = A/13$ MeV^{-1}, with pairing energy corrections of Gilbert and Cameron gives a rather poor description of the experimental level-density, e.g. because:

- shell corrections have not been introduced;
- pairing-energy corrections have been included in a very rough way, leading to vanishing high-energy tails in the spectra (see graphs in Ref. [9]);
- the level-density parameters have not been fitted to match experimental data (level schemes, neutron resonance spacings);
- a Fermi-gas type formula badly reproduces the observed energy dependence of low-lying levels [12], probably leading to unsatis-

factory representations of the spectra.

In *Calculation 4* an attempt was made to introduce shell corrections. However, the results (Table IV) for the angle-integrated cross sections are not very encouraging, mainly because in pre-equilibrium theory the value of the transition matrix element $M^2 = 190/A^3E$ has been determined empirically [11] by assuming that the level-density parameter g equals $A/13\ MeV^{-1}$. Because of the intimate connection between the compound-state level-density parameter g_c and M^2, it was decided to leave these parameters unchanged, assuming that there are no shell effects in the internal transition rates.

Thus, the next step was to vary the level-density parameters of the residual nucleus only. These parameters occur in the emission rates and directly affect the spectrum shapes. Because in previous calculations the high-energy tails of the calculated spectra were strongly reduced for many nuclides as a result of pairing-energy corrections, it was decided to drop P_r while adjusting g_r. In this way it was tried in *Calculation 5* to find fits for $\sigma_{nn'}$ and f_1 without using the global correction factors c_1 and c_2 introduced before. The results given in Table IV show standard deviations of about 30% for $\sigma_{nn'}$ and f_1. Furthermore, the mass-fluctuations in f_1 are reproduced quite well (Table II) and the energy dependence of $\sigma_{nn'}$ and f_1, f_2 is significantly improved (e.g., for Fe, see Fig. 2). Drawbacks of this calculation are that the level-density parameters seem not very realistic (see Table I), whereas also the absolute values of f_2 could not be fitted.

From the above-mentioned experience it is concluded that, although level-density parameters certainly affect angular distributions, the present model does not reproduce the experimental data by adjustment of level-density parameters only. Therefore, in *Calculation 6* the parameter c_2 was fitted to match the experimental f_2-coefficients (see Table IV). The results show significant improvements compared with Calc. 3, regarding both energy and angular distributions. Striking examples are given in Ref. [9] for those elements where the pairing energy correction is large (e.g., for S, Ca and Se). For other elements the spectral shape of f_1 was largely improved [e.g.,for Fe(Fig. 2), Ni, Br, Zr]. In some cases the improvements refer both to the angle-integrated cross section (f_0) and f_1 (e.g., for Cr, Fe, Ni, Ta and Hg).

It has to be noted, that the exercises presented in this section were only performed to study the possible influence of level-density effects and should not be taken as serious attempts to improve the model. For that purpose it might be better to introduce a more realistic level-density formula into the model in combination with refitted global parameters c_1 and c_2.

5. DISCUSSION ON BACKWARD SCATTERING

From all calculations with the adopted model it has become very clear that without adjustment of the parameters μ_1 and μ_2 the backward-angle scattering is seriously underestimated. This is illustrated in Fig. 3, where the angular distribution of the adopted scattering kernel (full line), its three-term Legendre polynomial representation (dashed-dotted line) and the adjusted Legendre representation used in Calc. 3 (dotted line) have been plotted. The last-mentioned curve shows a strong enhancement at backward angles. Although this adjustment of the scattering kernel is not based upon physical arguments, it indicates that the present angular distribution theory needs further improvement. Some effects which may enhance large-angle scattering are summarized in this section; assuming that the concept of "following only the fast particle" is justified (c.f. Ref. [15]).

a. Refraction effects

In our version of the generalized model we have made a crude attempt to include refraction of the *incident wave* through simple quasi-classical considerations, which are in fact rather similar to the procedure used in the VEGAS-code of the intranuclear-cascade model [16] for a square potential well. In addition we have taken the limit of a large refractive index; this leads to a simple result and is more justified at the considered low incident energy (14.6 MeV) than neglecting refraction completely. Straightforward geometrical considerations then yield that refraction acts like an additional collision (in addition to the intranuclear collision that forms the 2p-1h configuration). Thus by taking $n_0 = 1$ (instead of $n_0 = 3$) and suppressing elastic scattering the effect of refraction at the nuclear surface is simulated, whereas the angle-integrated spectra are not affected. Fig. 4 illustrates this effect for ^{127}I, from which it is seen that the backward scattering is significantly enhanced. The effects of reflection and refraction of the outgoing wave have not been accounted for in this simple model.

b. Finite-size effect

Another geometry effect neglected in the model is due to the finite size of the nucleus which limits the angular momentum of the fast particle. Mantzouranis et al. [15] have proposed an empirical formula for the initial condition to account for this effect, which compensates the effects of the Pauli exclusion principle. In our model these effects are not explicitly considered. It may well be, however, that the proposed fitted global parameters of Calc. 3 partially result from finite size effects. A difference with the empirical formula of Mantzouranis et al. is that their formula depends on the mass of the target nucleus, whereas our adjusted scattering kernel is almost independent of the nuclear mass.

c. $\Delta n = 0$ and $\Delta n = -2$ transitions

It has been shown before [4] that λ^0-transitions ($\Delta n = 0$) explicitly appear in the generalized master equation. The numerical influence of neglecting λ^0- and λ^--transitions follows from the differences between Calcs. 1 and 2. This is illustrated in Fig. 5 for ^{27}Al and ^{127}I, where we have also indicated the effect of neglecting λ^0-transitions only (dashed curve). If the equilibrium exciton number $\bar{n}$ is close to n_0 (which occurs for light nuclides or at low energies), the system would reach $\bar{n}$ without having reached isotropy, as a result of the "never come back" hypothesis. This clearly leads to a too much forward-peaked "preequilibrium part" of the spectrum. Therefore, for light nuclides (or low energies) inclusion of λ^0- and λ^--transitions gives rise to strongly enhanced backward scattering, although the experimental data are still underestimated.

d. Deviations from isotropy of nucleon-nucleon cross section

A fundamental quantity in the model is the scattering kernel describing the angular distribution of an intranuclear collision. This kernel is supposed to be equal to the differential free nucleon-nucleon cross section normalized to unity, which in the model is taken to be isotropic in the nucleon-nucleon c.m. system. However, it is experimentally known that the free nucleon-nucleon scattering is not quite isotropic, in particular at higher energies and for n-p scattering. It is straightforward to show that small deviations from isotropy may enhance μ_2 and thus backward scattering [9].

e. Clustering effects

The overestimation of the forward peaking could be reduced due to clustering effects in the nucleus, or due to assigning a somewhat higher effective mass to the target nucleons as a result of effective intranuclear forces (in reality they are not free particles). Assuming for simplicity that the scattering cross section is isotropic in the c.m. system, it follows from geometrical considerations that increasing the mass of the target particles leads to a strong decrease of μ_1, although μ_2 is also decreased [9]. The total effect, however, is an enhancement of the emission into the backward hemisphere. Therefore we expect that clustering effects could be important, although they are not able to account for the underestimation of the second-order coefficients.

f. "Multi-step direct" and "multi-step compound" emission

According to the ideas of Feshbach et al. [17] the observed forward-peaked angular distribution originates from a "multi-step direct" reaction type, to be distinguished from a "multi-step

compound" reaction type, which leads to angular distributions symmetric about 90°.

In preequilibrium theory one commonly utilizes two time scales: a fast (preequilibrium) time scale in which the energy is not yet statistically distributed over all nucleons and which produces the high energy tails, and a slow (equilibrium) time scale which comprises the evaporational stage of the reaction. One might ask whether this picture must be changed when considering angular distributions: another time scale enters, viz. the time scale on which isotropy is reached. Considering the eigenvalues of the operators of the generalized master equation we conclude [18] that there are *three rather than two* time scales:

1. A very fast anisotropic preequilibrium time scale; this is the first part of the preequilibrium phase in which most of the preequilibrium spectrum is emitted and the angular distributions are strongly forward-peaked.
2. An isotropic preequilibrium time scale; this is the second part of the preequilibrium phase in which angular distributions are essentially isotropic but the energy is not yet statistically distributed over all nucleons.
3. The statistical evaporation phase.

In this picture, the so-called preequilibrium phase is to be divided in two parts. However, according to the present model the contribution of the second phase is quite small. Therefore this distinction may not be very practical. To a certain extent of the proposed dichotomy of the preequilibrium phase reminds of the proposed multi-step direct and multi-step compound emission mechanisms [17].

6. CONCLUSION

The generalized exciton model is able to describe the global characteristics of experimental preequilibrium angular distributions and emission spectra. However, the model shows underestimation of the angular distributions at backward angles. In this respect it resembles the semi-classical intranuclear cascade model (with which it has many physical ideas in common), although the generalized exciton model is reported to do much better in describing backward-angle scattering than the intranuclear cascade model [19].

We have demonstrated that a good fit of all angular distributions can be obtained within the present model by adjustment of only two global parameters. We believe, therefore, that the defects of the model are mainly due to a not very correct specification of initial condition and scattering kernel, which at present is essentially based upon classical considerations.

In view of this, the effects of the nuclear geometry seem to be very important (refraction and reflection at the nuclear surface; the finite size of the nucleus). A very simple estimate for

the refraction of the incident wave already leads to considerable improvement. Secondly, the description of the intranuclear collision process could be improved. For instance, the existence of correlated clusters of nucleons within the nucleus might enhance the predicted backward scattering. Another suggestion could be to use for the scattering kernel the expressions derived by Kikuchi and Kawai [20] for collisions in nuclear matter.

It has also been shown that the description of level densities in the exciton model is not very realistic and needs to be improved. Much of the observed structure in the first-order Legendre coefficient as a function of mass might be ascribed to level-density effects.

7. REFERENCES

1. D. Hermsdorf et al., "Differentielle Neutronenemissionsquerschnitte $\sigma_{nM}(E_o,E,\theta)$ bei 14.6 MeV Einschussenergie für die Elemente Be, C, Na, Mg, Al, Si, P, S, Ca, Ti, V, Cr, Mn, Fe, Co, Ni, Zn, Ga, Se, Br, Zr, Nb, Cd, In, Sn, Sb, J, Ta, W, Au, Hg, Pb und Bi", ZfK-277, Zentralinstitut für Kernforschung, Rossendorf bei Dresden (1974).
2. J.M. Akkermans and H. Gruppelaar, "Calculation of preequilibrium angular distributions with the exciton model code PREANG", ECN-60, Netherlands Energy Research Foundation (1979).
3. G. Mantzouranis, D. Agassi and H.A. Weidenmüller, Phys. Lett. 57B, 220 (1975).
4. J.M. Akkermans, Phys. Lett., 82B, 20 (1979).
5. F.J. Luider, Z. für Physik A284, 187 (1978).
6. F.J. Luider, "Preequilibrium theory and slaves of the master equation", ECN-17, Netherlands Energy Research Foundation (1977).
7. E. Běták, Comp. Phys. Comm. 9, 92 (1975) and 10, 71 (1975).
8. J.M. Akkermans, H. Gruppelaar and G. Reffo, "Angular distributions in a unified model of preequilibrium and equilibrium neutron emission", Phys. Rev. C (to be published).
9. H. Gruppelaar and J.M. Akkermans, "Comparison of experimental and calculated neutron emission spectra and angular distributions", ECN-report (to be published), Netherlands Energy Research Foundation.
10. D. Wilmore and P.E. Hodgson, Nucl. Phys. 55, 673 (1964).
11. C. Kalbach-Cline, Nucl. Phys. A120, 590 (1973).

12. A. Gilbert and A.G.W. Cameron, Can. J. of Phys. 43, 1446 (1965).
13. F.C. Williams, Nucl. Phys. A166, 231 (1971).
14. E. Běták and J. Dobeš, Z. für Physik A279, 319 (1976).
15. G. Mantzouranis et al., Z. für Physik A276, 145 (1976).
16. K. Chen et al., Phys. Rev. 166, 949 (1968).
17. H. Feshbach et al., Ann. Phys. (N.Y.) 125 (1980) 429.
18. J.M. Akkermans and H. Gruppelaar, to be submitted for publication in Z. für Physik.
19. G. Mantzouranis, Phys. Rev. C14, 2018 (1976).
20. K. Kikuchi and M. Kawai, Nuclear matter and nuclear reactions, North-Holland Publishing Company, Amsterdam (1968).

Table I

Experimental and calculated inelastic scattering cross sections integrated from 6 to 11 MeV[a].

Element	$\sigma_{nn'}$ (6-11 MeV) mb				g_r (MeV^{-1})			A[b]
	Exp.	Calc. 1-3	Calc. 4	Calc. 5,6	Calc. 1-3	Calc. 4	Calc 5,6	
Be	211±16	172[c]	162[c]	237	0.69	0.78	0.41	9
C	146± 6	182[c]	166[c]	258	0.92	1.04	0.76	12
Na	192± 8	176	82	259	1.77	2.58	1.02	23
Mg	181± 5	102[c]	48[c]	257	1.85	2.52	1.20	24
Al	167± 3	196	122	237	2.08	2.56	1.46	27
Si	141± 4	133[c]	102[c]	198	2.15	2.33	1.01	28
P	199±10	199	145	239	2.38	2.52	1.86	31
S	180±13	125	95	231	2.46	2.47	1.99	32
Ca	263±25	100	56	239	3.08	3.30	2.50	40
Ti	183± 6	141	110	247	3.69	4.21	2.97	48
V	146± 7	211	191	209	3.92	3.89	2.53	51
Cr	212± 8	162	169	231	4.00	3.74	3.07	52
Mn	154± 9	212	187	208	4.23	4.05	2.67	55
Fe	132± 5	162	167	151	4.31	3.86	1.87	56
Co	95± 4	207	198	202	4.54	4.29	2.88	59
Ni	114± 3	142	214	143	4.46	3.31	2.25	58
Cu	131± 7	192	169	203	4.85	4.72	2.54	63
Zn	123± 6	159	132	155	4.92	4.88	2.47	64
Ga	206±10	194	113	191	5.31	6.21	3.21	69
Se	233±16	165	126	235	6.15	7.23	4.49	80
Br	193± 8	183	97	174	6.08	7.59	3.14	79
Zr	198±21	190	259	178	6.92	5.93	3.15	90
Nb	180± 7	227	224	181	7.15	6.62	5.50	93
Cd	185± 4	201	98	187	8.62	10.50	5.00	112
In	217± 6	218	121	170	8.85	10.60	6.00	115
Sn	236± 8	209	195	177	9.23	9.85	5.00	120
Sb	189±16	219	175	177	9.31	10.4	6.79	121
I	247± 7	222	221	180	9.77	10.3	7.44	127
Ta	211±17	280	214	230	13.9	15.3	11.7	181
W	301±13	287	227	302	14.2	15.3	12.4	184
Au	239± 9	251	611	201	15.2	12.1	12.5	197
Hg	347±29	257	1014	307	15.5	8.70	14.0	202
Pb	350±21	386	1091	406	16.0	4.02	14.2	208
Bi	356±23	369	1025	355	16.1	5.38	15.1	209

[a] See Sect. 2 for meaning of various calculations.

[b] Mass number assumed in calculations.

[c] Extrapolations have been used to obtain values at the highest emission energies, due to large pairing energy corrections. For Be and C pairing energy corrections of 2.5 MeV and 5.0 MeV have been assumed, respectively.

Table II

Experimental and calculated first-order Legendre coefficients of angular distributions of inelastic scattering cross sections integrated from 6 to 11 MeV[a].

Element	f_1 (6-11 MeV)					
	Exp.	Calc. 1	Calc. 2	Calc. 3	Calc. 4	Calc. 5,6
Be	0.21±0.03	0.28[b]	0.37[b]	0.21[b]	0.26[b]	0.23
C	0.19±0.02	0.20[b]	0.39[b]	0.14[b]	0.16[b]	0.29
Na	0.13±0.02	0.25	0.38	0.18	0.15	0.13
Mg	0.25±0.01	0.24[b]	0.41[b]	0.18[b]	0.17[b]	0.22
Al	0.18±0.01	0.27	0.38	0.20	0.20	0.18
Si	0.16±0.02	0.26[b]	0.40[b]	0.19[b]	0.25[b]	0.13
P	0.23±0.02	0.27	0.37	0.20	0.28	0.21
S	0.32±0.04	0.30	0.39	0.22	0.29	0.27
Ca	0.28±0.04	0.32	0.40	0.24	0.31	0.29
Ti	0.34±0.02	0.33	0.39	0.24	0.32	0.29
V	0.24±0.03	0.33	0.38	0.24	0.32	0.20
Cr	0.25±0.02	0.33	0.39	0.25	0.33	0.28
Mn	0.19±0.02	0.33	0.38	0.24	0.31	0.19
Fe	0.14±0.02	0.34	0.39	0.25	0.33	0.16
Co	0.16±0.03	0.33	0.38	0.24	0.32	0.19
Ni	0.18±0.01	0.34	0.39	0.25	0.37	0.17
Cu	0.09±0.03	0.33	0.38	0.25	0.32	0.13
Zn	0.19±0.02	0.35	0.39	0.26	0.34	0.18
Ga	0.17±0.03	0.34	0.38	0.25	0.32	0.19
Se	0.17±0.04	0.37	0.40	0.28	0.37	0.31
Br	0.16±0.02	0.35	0.39	0.26	0.34	0.14
Zr	0.17±0.05	0.37	0.40	0.28	0.38	0.15
Nb	0.36±0.02	0.36	0.39	0.27	0.36	0.32
Cd	0.22±0.01	0.38	0.40	0.29	0.38	0.26
In	0.22±0.02	0.37	0.39	0.28	0.37	0.30
Sn	0.21±0.02	0.38	0.40	0.29	0.39	0.25
Sb	0.32±0.04	0.38	0.39	0.28	0.37	0.33
I	0.24±0.02	0.38	0.39	0.28	0.38	0.34
Ta	0.38±0.04	0.38	0.39	0.28	0.38	0.38
W	0.32±0.02	0.39	0.40	0.28	0.38	0.37
Au	0.15±0.02	0.39	0.39	0.28	0.39	0.38
Hg	0.31±0.04	0.39	0.40	0.29	0.43	0.38
Pb	0.27±0.03	0.38	0.39	0.28	0.43	0.37
Bi	0.26±0.03	0.37	0.38	0.27	0.42	0.37

[a] See Sect. 2 for meaning of various calculations.

[b] Extrapolations have been used to obtain values at the highest emission energies, due to large pairing energy corrections. For Be and C pairing energy corrections of 2.5 MeV and 5.0 MeV have been assumed, respectively.

Table III

Experimental and calculated second-order Legendre coefficients of angular distributions of inelastic scattering cross sections integrated from 6 to 11 MeV[a].

Element	f_2 (6-11 MeV)						
	Exp.	Calc. 1[a)]	Calc. 2	Calc. 3	Calc. 4	Calc. 5	Calc. 6
Be	0.10±0.04	0.017[b]	0.027[b]	0.054[b]	0.015[b]	0.013	0.053
C	0.14±0.02	0.013[b]	0.034[b]	0.043[b]	0.011[b]	0.021	0.086
Na	0.09±0.03	0.028[b]	0.038[b]	0.077[b]	0.015[b]	0.012	0.050
Mg	0.12±0.01	0.023[b]	0.045[b]	0.075[b]	0.017[b]	0.021	0.087
Al	0.07±0.01	0.027[b]	0.038[b]	0.086[b]	0.020[b]	0.018	0.074
Si	0.06±0.02	0.027[b]	0.043[b]	0.086[b]	0.025[b]	0.014	0.055
P	0.11±0.03	0.028	0.038	0.090	0.024	0.022	0.090
S	0.03±0.04	0.032	0.043	0.099	0.030	0.028	0.11
Ca	0.18±0.07	0.036	0.045	0.11	0.034	0.031	0.13
Ti	0.07±0.02	0.038	0.045	0.12	0.037	0.032	0.13
V	0.18±0.02	0.037	0.042	0.12	0.036	0.022	0.090
Cr	0.08±0.02	0.038	0.045	0.12	0.038	0.031	0.13
Mn	0.09±0.03	0.037	0.042	0.12	0.036	0.022	0.088
Fe	0.06±0.02	0.040	0.046	0.13	0.039	0.019	0.075
Co	0.06±0.02	0.038	0.043	0.12	0.037	0.023	0.090
Ni	0.07±0.02	0.040	0.045	0.13	0.044	0.021	0.081
Cu	0.12±0.03	0.039	0.043	0.12	0.037	0.015	0.060
Zn	0.05±0.02	0.041	0.046	0.13	0.040	0.022	0.085
Ga	0.09±0.03	0.040	0.044	0.13	0.037	0.022	0.088
Se	0.13±0.04	0.045	0.049	0.14	0.045	0.037	0.15
Br	0.11±0.02	0.042	0.045	0.13	0.040	0.018	0.070
Zr	0.10±0.05	0.045	0.048	0.14	0.046	0.018	0.072
Nb	0.11±0.02	0.042	0.045	0.14	0.043	0.038	0.15
Cd	0.09±0.01	0.047	0.050	0.15	0.046	0.033	0.13
In	0.11±0.01	0.045	0.047	0.14	0.044	0.036	0.15
Sn	0.11±0.02	0.047	0.050	0.15	0.047	0.031	0.12
Sb	0.07±0.04	0.045	0.047	0.14	0.045	0.040	0.16
I	0.12±0.02	0.045	0.048	0.14	0.045	0.042	0.17
Ta	0.10±0.05	0.045	0.047	0.15	0.045	0.045	0.18
W	0.14±0.02	0.046	0.048	0.15	0.046	0.044	0.18
Au	0.04±0.02	0.046	0.049	0.15	0.048	0.047	0.19
Hg	0.13±0.05	0.048	0.050	0.15	0.057	0.045	0.18
Pb	0.13±0.04	0.045	0.047	0.15	0.058	0.043	0.18
Bi	0.14±0.04	0.044	0.045	0.14	0.056	0.043	0.18

[a]See Sect. 2 for meaning of various calculations.

[b]Extrapolations have been used to obtain values at the highest emission energies, due to large pairing energy corrections. For Be and C pairing energy corrections of 2.5 MeV and 5.0 MeV have been assumed, respectively.

Table IV

Overall comparison of experimental and calculated data for 34 nuclides.

Calc.[a] Nr.	ΔE (MeV)	Exp./Calc. cross section	χ^2	Exp./Calc. f_1-coeff.	χ^2	Exp./Calc. f_2 coeff.	χ^2
1	2-11	0.95[b]	66	0.52[b]	14	3.6[b]	7.0
1	6-11	$0.98^{+0.36}_{-0.26}$[c]	26	$0.76^{+0.33}_{-0.23}$[c]	10	$3.2^{+2.5}_{-1.4}$[c]	4.6
2	2-11	See Calc. 1		0.34[b]	36	2.7[b]	6.0
2	6-11			$0.63^{+0.26}_{-0.18}$[c]	19	$2.5^{+1.5}_{-0.95}$[c]	3.8
3	2-11	See Calc. 1		0.72[b]	7.5	1.10[b]	5.0
3	6-11			$1.03^{+0.45}_{-0.31}$[c]	5.0	$1.00^{+0.78}_{-0.44}$[c]	2.9
4	2-11	1.00[b]	102	0.68[b]	22	4.8[b]	7.3
4	6-11	$1.2^{+1.1}_{-0.6}$[c]	76	$0.82^{+0.41}_{-0.27}$[c]	10	$3.5^{+3.2}_{-1.7}$[c]	4.8
5	2-11	0.92[b]	60	0.74[b]	5.5	5.4[b]	7.8
5	6-11	$0.87^{+0.24}_{-0.19}$[c]	32	$0.97^{+0.27}_{-0.21}$[c]	3.6	$4.1^{+3.1}_{-1.8}$[c]	5.3
6	2-11	See Calc. 5		See Calc. 5		1.3[b]	4.8
6	6-11					$1.0^{+0.77}_{-0.44}$[c]	2.8

[a] See Sect. 2 for meaning of various calculations.

[b] Arithmetic mean value.

[c] Weighted mean values and standard deviations according to lognormal distribution.

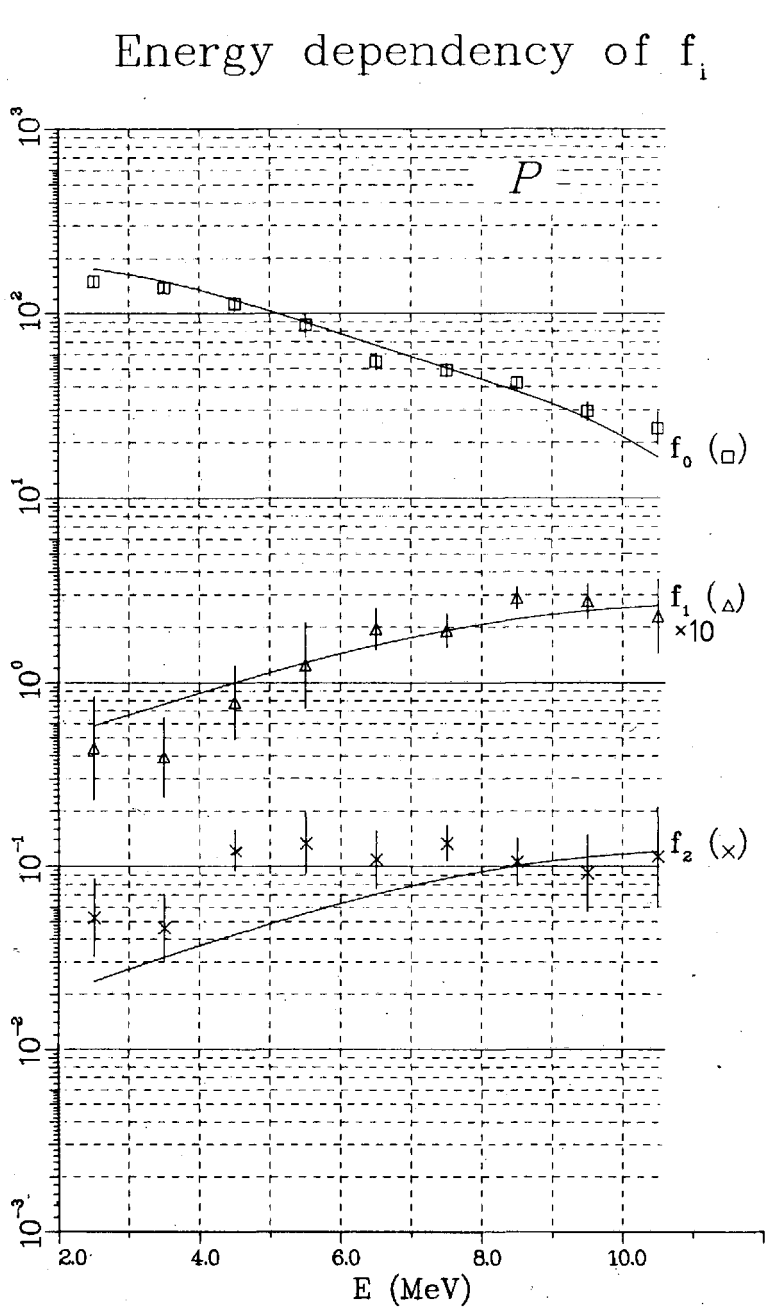

Fig. 1. Experimental and calculated Legendre coefficients as a function of neutron emission energy (c.m. system) for neutron scattering at natural P. The coefficients $f_0 = \sigma_{nn'}$, f_1 and f_2 have been defined in Eq. (1). The vertical scale represents mb/MeV for f_0; f_1 has been multiplied with 10 to avoid interference with f_2. The full curves represent Calc. 3 (fitted global parameters c_1 and c_2).

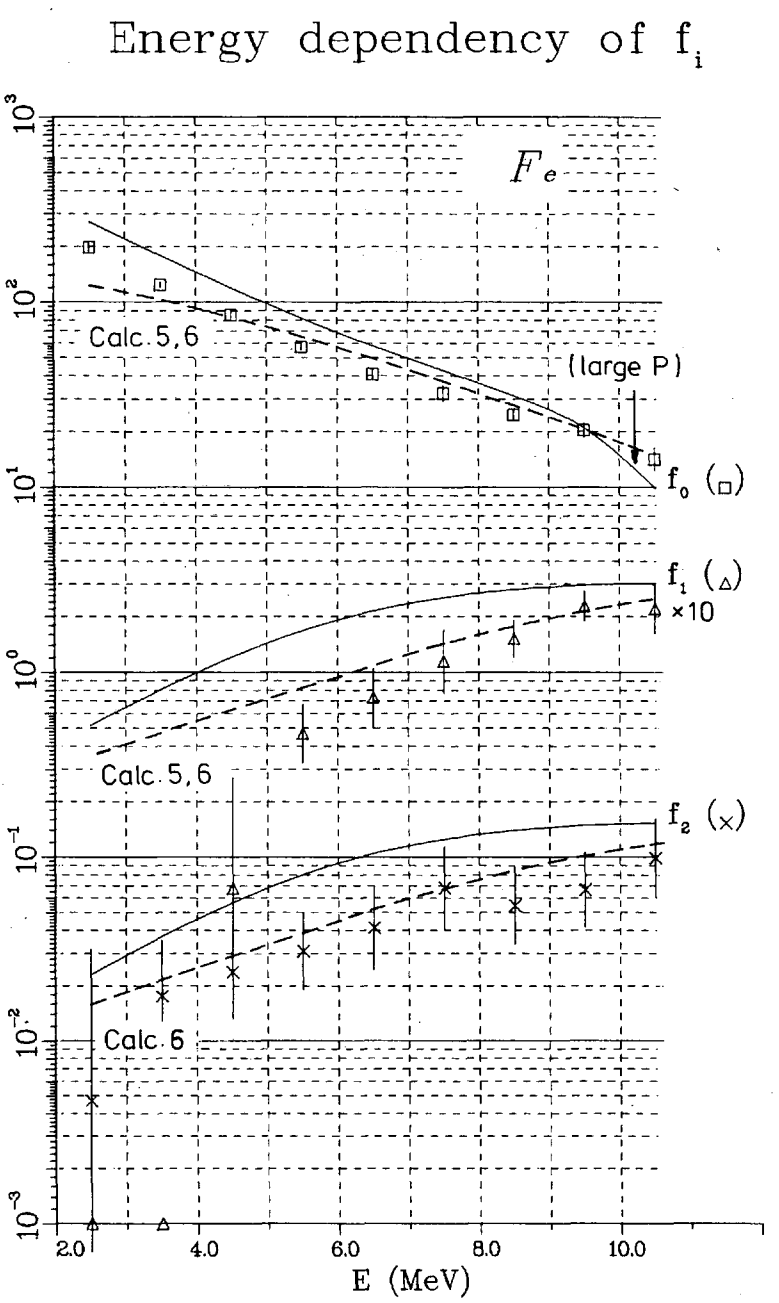

Fig. 2. Experimental and calculated Legendre coefficients for neutron scattering at natural Fe. The full curves represent the results of Calc. 3; the dashed curves were obtained by fitting the final-state level-density parameters (Calcs. 5, 6). See further caption of Fig. 1.

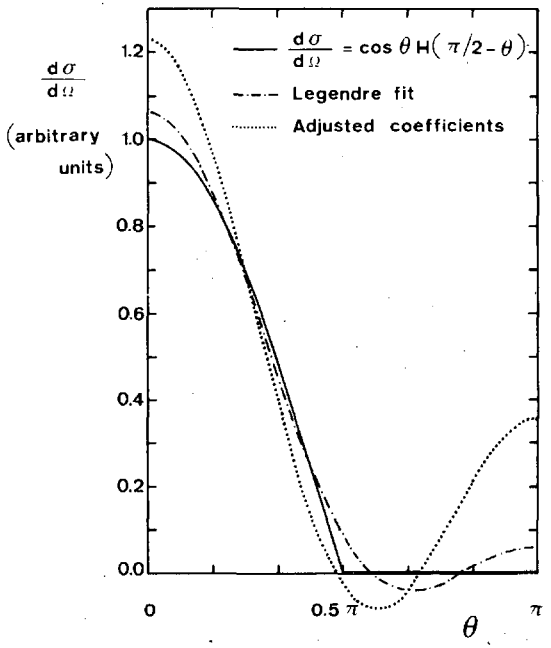

Fig. 3. Angular distribution of adopted scattering kernels. The full curve gives the angular distribution of free nucleon-nucleon scattering as a function of the angle in the lab. system; the dashed-dotted curve is its three-term Legendre polynomial representation with $\mu_0 = 1$, $\mu_1 = 2/3$ and $\mu_2 = 1/4$ ($\beta = 0$). The dotted curve was obtained by multiplying μ_1 and μ_2 with 0.87 and 1.74, respectively, as used in Calc. 3.

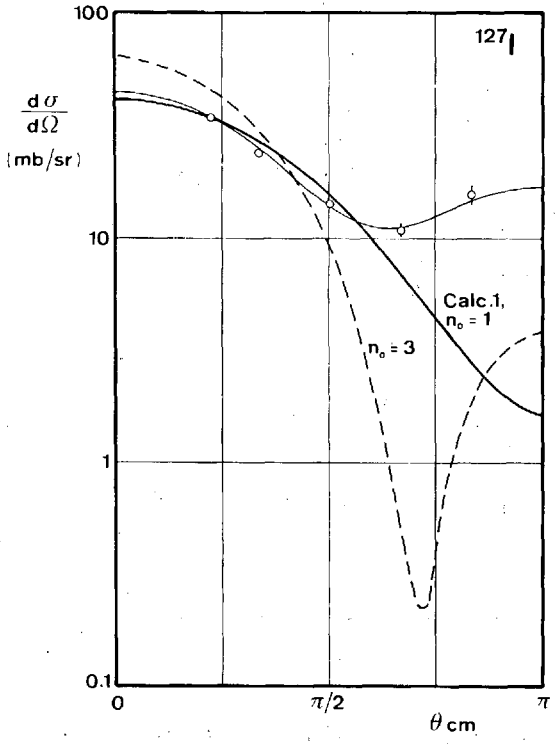

Fig. 4. Simulation of effect of refraction of the incident wave at the nuclear surface by taking $n_0 = 1$ for ^{127}I. The full solid curve represents Calc. 1 (i.e., $n_0 = 1$ and suppressed elastic scattering), whereas the dashed curve was calculated with the same parameters and the usual assumption $n_0 = 3$. Also indicated are the experimental data and their three-term Legendre polynomial fit (full curve). All distributions have been integrated over emission energies from 6 to 11 MeV.

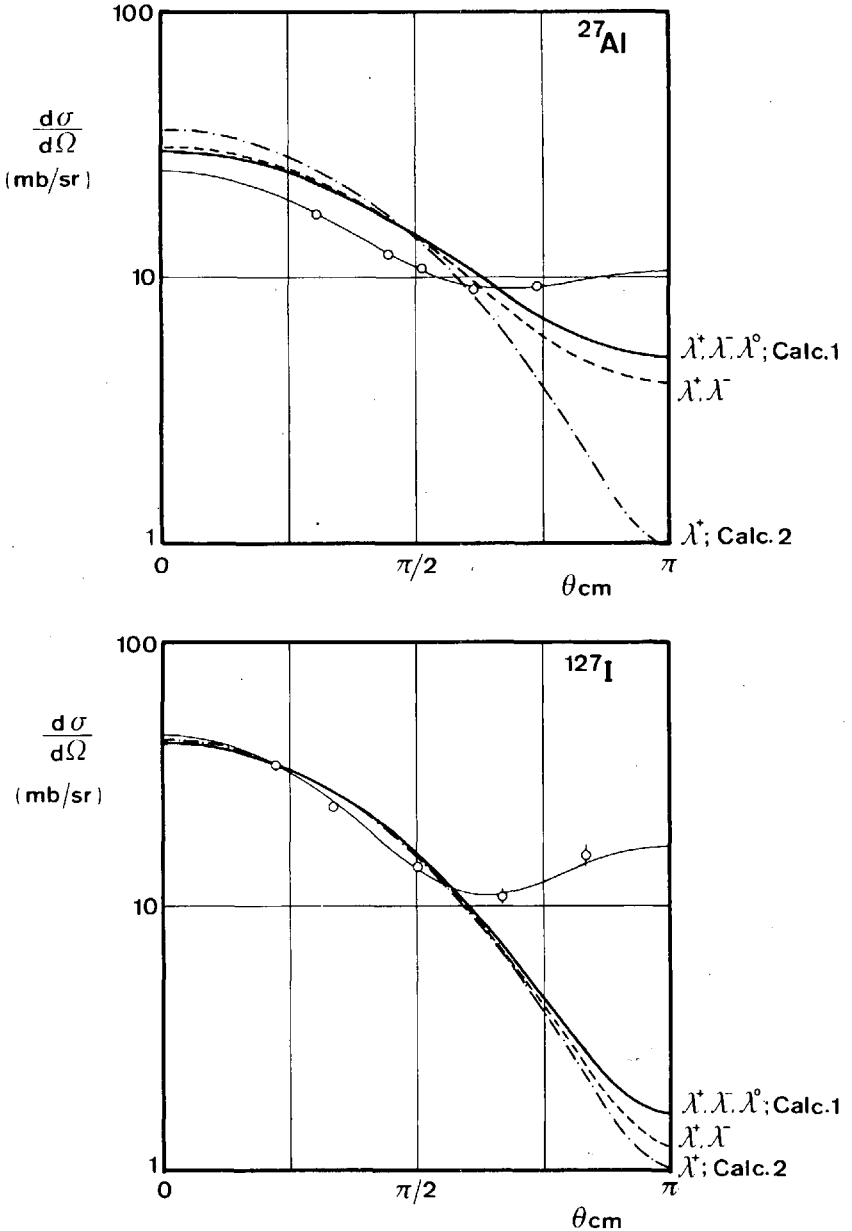

Fig. 5. Effect of "never come back" assumption on angular distributions for ^{27}Al and ^{127}I. The full solid curves represent Calc. 1, taking into account all possible transition rates λ^+, λ^o and λ^-. The dashed-dotted curve was obtained from Calc. 2, neglecting λ^o- and λ^--transitions. The dashed curve was calculated by solving the generalized master equation with $\lambda^o = 0$. See caption of Fig. 4 for further explanation of symbols.

EVALUATION OF NEUTRON CROSS SECTIONS TO 40 MeV FOR $^{54,56}Fe$*

E. D. Arthur and P. G. Young

Theoretical Division
Los Alamos Scientific Laboratory
University of California
Los Alamos, New Mexico 87545

ABSTRACT

Cross sections for neutron-induced reactions on $^{54,56}Fe$ were calculated employing several nuclear models--optical, Hauser-Feshbach, preequilibrium, and DWBA--in the energy range between 3 and 40 MeV. As a prelude to the calculations, the necessary input parameters were determined or verified through analysis of a large body of experimental data both for neutron- and proton-induced reactions in this mass and energy region. This technique also led to cross sections in which the simultaneous influence of available data types added to their consistency and reliability. Calculated cross sections as well as neutron and gamma-ray emission spectra were incorporated into an ENDF evaluation suitable for use to 40 MeV.

INTRODUCTION

As part of an effort to satisfy nuclear data needs for the Fusion Materials Irradiation Test Facility, we performed comprehensive nuclear-model calculations on $^{54,56}Fe$ between 3 and 40 MeV. The results were combined and joined to the existing ENDF/B-V iron evaluation at 3 MeV to produce a new evaluation applicable to 40 MeV that was essentially free of energy balance problems.

Since little experimental data exist for neutron reactions at higher energies (total cross sections are an exception), we relied upon nuclear models--Hauser-Feshbach [1], preequilibrium, optical, and direct reaction--that describe the main mechanisms governing neutron reactions in this mass and energy region. As a first step towards proper use of these models, we determined input parameters

*Work supported by the U.S. Department of Energy.

valid for this calculation. With these parameters we then employed the models in a simultaneous analysis of a large body of available neutron reaction data for iron--cross sections and emission spectra for neutrons, charged particles, and gamma rays. This effort was further aided by the calculation of p + ^{54,56}Fe reaction data at higher energies using these same parameters. In this approach, the many types of available data produce constraints on the calculated results, providing in the end a set of consistent calculated cross sections as well as input parameters tested under varied and stringent conditions. This approach can allow discrepant or inconsistent data sets to be ascertained since it uses, simultaneously, information from several reaction types available at a given incident energy. Thus, unphysical calculations or parameters resulting from the isolated analysis of a given cross section, data type, or experimental result can be largely avoided.

PARAMETERS

We determined values for optical model parameters and gamma-ray strength functions, while for level density or preequilibrium parameters we relied on published results that were generally determined through systematic analysis of a substantial amount of experimental data. We did verify (or modify as needed) these parameters where pertinent data were available, but we did not attempt large-scale or systematic adjustments because of the complexities involved.

We devoted an appreciable effort to determination or verifacation of optical-model and gamma-ray strength function parameters since values were sometimes lacking or were not appropriate to the range of interest in our calculations. Neutron optical parameters received the greatest effort since such parameters must produce realistic formation cross sections for a wide range of energies while providing a reasonable behavior of low-energy transmission coefficients needed in the calculation of reactions such as (n,2n). We determined optical parameters through simultaneous fits to the following neutron data: (1) total cross sections between 2 and 40 MeV, (2) s- and p-wave strength functions and values for the potential scattering radius, (3) elastic scattering angular distributions between 6 and 14 MeV, and (4) reaction cross sections between 5 and 30 MeV. The resulting parameters appear in Table I, while in Figs. 1 and 2 comparisons are made to the total cross section and elastic-scattering angular distributions. Although reasonable agreement was obtained to the quantities listed above, the predicted nonelastic cross section overestimates new results [2] at 40 MeV that were not available for inclusion in our fit. This overprediction led us to renormalize our calculated Hauser-Feshbach cross sections downward by about 10% in this energy region.

Proton and alpha-particle transmission coefficients were calculated from optical parameters based on published sets [3,4] obtained from data fits in this mass and energy range. We adjusted them to better fit low energy data [(p,n) and (α,n) cross sections] and higher energy information (generally, reaction cross sections) that were available. The modification usually took the form of an energy dependence added to the real and/or imaginary well depths. The modified proton and alpha particle parameters also appear in Table I.

Gamma-ray reactions can be important competitors to particle emission, particularly around thresholds. We chose to normalize gamma-ray transmission coefficients (assumed to be of the Brink-Axel [5] giant dipole resonance form) through determination of gamma-ray strength functions by fits to ^{54,56}Fe (n,γ) data. This method avoids problems occurring when this normalization is determined directly from the ratio of the average gamma width, $\langle\Gamma_\gamma\rangle$, and spacing $\langle D\rangle$, for s-wave resonances as is often done for each compound nucleus in these types of calculations. Such $\langle\Gamma_\gamma\rangle$ and $\langle D\rangle$ values are not always reliable, particularly where information for compound systems away from the line of stability must be inferred from their systematic behavior. Gamma-ray strength functions should be more reliable since they vary slowly between nearby nuclei. In fact, the strength function determined for ^{55}Fe and ^{57}Fe were essentially identical, differing only by about 5%.

Parameters for the Gilbert-Cameron [6] level density model used in these calculations were taken from the values of Cook [7] for the level density constant, a, and the pairing energy, Δ. At lower excitation energies a constant temperature expression was used, the parameters of which we adjusted to agree with the cumulative number of discrete levels while joining smoothly to the Fermi-gas form used at higher energies.

For preequilibrium corrections, we applied the master equations model of Kalbach [8] that employs a matrix element for residual two-body interactions whose absolute square depends upon the excitation energy available per exciton as well as the mass of the compound system [9]. The normalization constant was taken to be 160 MeV^3, which is about 20% higher than the value recommended by Kalbach.

Since the preequilibrium and Hauser-Feshbach models do not adequately describe the excitation of collective states in ^{54,56}Fe through neutron inelastic scattering, we performed DWBA calculations for 24 such states. We used deformation parameters, β_ℓ, determined by Mani [10] from 40 MeV inelastic proton scattering on ^{54,56}Fe along with the neutron optical parameters appearing in Table I.

RESULTS AND COMPARISONS TO DATA

Calculations were performed using three nuclear-model codes--(1) DWUCK [11] for DWBA calculations, (2) COMNUC [12] for low energy Hauser-Feshbach calculations with width-fluctuation corrections, and (3) GNASH [13] for higher energy Hauser-Feshbach calculations where preequilibrium corrections were necessary and complex decay chains were followed. In the next few paragraphs, we will compare a portion of the 26 reaction types calculated to experimental data, showing in many cases cross-section values up to 40 MeV.

With the use of evaluated data for shielding and other neutronics purposes, a realistic representation of neutron-emission cross sections, spectra, and angular distributions is of particular importance. Several cross-section types provide the opportunity to evaluate and verify the neutron (and other) parameters used in the calculations as well as indicate features of the data that should be a part of the evaluation if accurate representations are desired. Figure 3 compares the calculated neutron emission spectrum (after incorporation of an appropriate resolution function) to data of Kammerdiener [14]. The lower end of the spectrum consists of evaporation neutrons [mostly from (n,2n) processes] while the middle and upper portions contain preequilibrium neutrons. At the upper part of the spectrum, contributions from discrete levels excited by direct-reaction inelastic scattering are evident both in the data and calculations.

At higher incident energies such emitted neutrons generally become more forward-peaked--not only those resulting from inelastic scattering from discrete levels but also those appearing in the middle and upper continuum regions of the spectrum. Such energy-angle correlations must therefore be incorporated into the evaluated data. Figure 4 compares the DWBA calculated angular distribution to data [15,16] for inelastic scattering from the first excited state of ^{56}Fe by 14.1 MeV neutrons. The agreement indicates the applicability of both the neutron-optical parameters and the β_2 value used as obtained from proton scattering results.

To represent angular distributions of continuum neutrons, we used the phenomological expressions recently determined by Kalbach and Mann [17] from fits to particle-induced reaction data. These expressions rely on information concerning the cross-section fraction resulting from multistep direct and multistep compound processes. We approximated these through use of total preequilibrium and evaporation fractions, respectively. The double-differential cross sections thereby obtained at 14 MeV agree reasonably well with the Hermsdorf angular distribution data [18] measured for natural iron.

Neutron inelastic scattering and emission results on iron are complemented by (n,2n) data measured using large liquid scintilla-

tor tanks. The comparison to such data [19,20] as shown in Fig. 5 provides the opportunity to evaluate several facets of the calculations. To fit the sharp rise near threshold of the (n,2n) cross section accurately, considerable constraint is placed upon the low-energy neutron transmission coefficients as well as the parameters needed to describe competing gamma-ray and charged-particle emission.

Charged-particle production cross sections and spectra resulting from neutron reactions on iron are required for radiation damage calculations and for use in dosimetry applications. An example of the latter data type is the ^{54}Fe (n,p) cross section to which we compare our calculations in Fig. 6. For this nucleus,proton emission accounts for a significant portion of the total reaction cross section (particularly from this reaction), and the agreement indicates the suitability of the proton optical parameters in a case where competition from neutron emission is small.

New opportunities to evaluate calculated (n,np) and (n,pn) cross sections occur from comparison to recently measured proton-production spectra induced by 15-MeV neutrons [21] as shown in Fig. 7 for ^{56}Fe. The agreement at the low energy end of the spectrum indicates a correct calculation of the (n,np) contribution while the agreement for higher secondary energies indicates a proper preequilibrium fraction, particularly with regard to the relative number of protons and neutrons emitted.

Measurements of alpha-production cross sections on iron have been relatively few, consisting mainly of several values of the ^{54}Fe (n,α) cross section at 14 MeV. Recently measurements by Paulsen [22] of the ^{54}Fe (n,α) reaction below 10 MeV and by Grimes et al. [21] of 15-MeV neutron-induced alpha production on ^{54,56}Fe have improved this situation considerably. Our calculations of the ^{54}Fe (n,α) cross section from threshold to 40 MeV are compared to experimental results in Fig. 8. Since total charged-particle production cross sections are needed for radiation damage calculations, we illustrate in Fig. 9 the total production of protons and alphas on ^{54,56}Fe up to 40 MeV. The arrows indicate thresholds for (n,xnp) and (n,xnα) reactions. Comparisons are made to (n,p) or (n,α) data occurring below the first arrow and to the 15-MeV total production cross sections now available.

Gamma-ray production data also play an important role in applications such as shielding calculations. To accurately calculate such data, a detailed gamma-ray cascade model was included and all residual nuclei populated by major reactions were allowed to gamma decay. Quite a large amount of data exist up to 20 MeV, both spectral and production cross sections for discrete lines, that allow the calculations to be further verified. Figures 10 and 11 compare calculations to two such data types--(1) gamma-ray production spectra induced by 14-MeV neutrons as measured by Drake [23] and (2)

the excitation function for production of the 1.238 MeV gamma-ray in ^{56}Fe.

As a supplement to neutron-induced reaction data on iron, we used proton data to provide further checks on parameter sets in energy regions where neutron data are lacking. Figure 12 shows the measured ^{56}Fe (p,n) and (p,2n) cross sections [24,25] to which we compare our calculated results. Through such comparisons, the behavior of proton and neutron transmission coefficients, level density parameters, and preequilibrium corrections can be tested at higher incident energies.

Cross sections for major reactions and production spectra for neutron and gamma-ray emission obtained from these calculations were incorporated into an ENDF-like evaluation extending to 40 MeV. Dosimetry files were provided for $^{54,56}Fe$ while a complete evaluation was provided for natural iron. Below 20 MeV, standard formats and representations were used, making this portion compatible with existing processing and other applications codes. Above 20 MeV, new formats had to be devised to accomodate energy-angle correlations as well as to simplify presentation of data for energies where many reaction channels were open.

REFERENCES

1. W. Hauser and H. Feshbach, Phys. Rev. 87, 336 (1952).

2. I. Zanelli et al., "Measurements of Neutron Total and Non-elastic Cross Sections for C, O, Ca, and Fe," contribution to this Symposium.

3. F. G. Perey, Phys. Rev. 131, 745 (1962).

4. O. F. Lemos, "Diffusion Elastique de Particules Alpha de 21 a 29.6 MeV sur des Noyaux de la Region Ti-Zn," Orsay report, Series A, No. 136 (1972).

5. D. M. Brink, thesis, Oxford University (1955); unpublished; P. Axel, Phys. Rev. 126, 671 (1962).

6. A. Gilbert and A. G. W. Cameron, Can. J. Phys. 43, 1446 (1965).

7. J. L. Cook, H. Ferguson, and A. R. de L. Musgrove, Aust. J. Phys. 20, 447 (1967).

8. C. Kalbach, Z. Phys. A283, 401 (1977).

9. C. Kalbach, Z. Phys. A287, 319 (1978).

10. G. S. Mani, Nucl. Phys. A165, 225 (1977).

11. P. D. Kunz, "DWUCK - A Distorted Wave Born Approximation Program," unpublished.

12. C. L. Dunford, "A Unified Model for Analyses of Compound Nucleus Reactions," AI-AEC-12931, Atomics International (1970).

13. P. G. Young and E. D. Arthur, "GNASH: A Preequilibrium Statistical Model Code for Calculation of Cross Sections and Emission Spectra," LA-6947, Los Alamos Scientific Laboratory (1977).

14. J. L. Kammerdiener, "Neutron Spectra Emitted by ^{239}Pu, ^{238}U, ^{235}U, Pb, Nb, Ni, Fe, Al, and C Irradiated by 14 MeV Neutrons," UCRL-51232, Lawrence Livermore Laboratory (1972).

15. B. E. Leshchenko et al., Sov. J. Nucl. Phys. 15, 5 (1972).

16. M. Hyakutake et al., J. Phys. Soc. Japan 38, 606 (1975).

17. C. Kalbach and F. M. Mann, to be published.

18. D. Hermsdorf et al., "Differentielle Neutronenemissionsquerschitte bei 14.6 MeV Einschussenergie," Dresden report ZFK-277 (1974).

19. J. Frehaut and G. Mosinski, Nuclear Cross Sections and Technology Conference, NBS Special Publication 425 (1975), p. 855.

20. L. R. Veeser, personal communication (1979).

21. S. M. Grimes et al., Phys. Rev. C19, 2127 (1979).

22. A. Paulsen et al., Nucl. Sci. Eng. 72, 113 (1979).

23. D. M. Drake, E. D. Arthur, and M. G. Silbert, Nucl. Sci. Eng. 65, 49 (1978).

24. R. Michel et al., Nucl. Phys. A322, 40 (1979).

25. I. L. Jenkins and A. G. Wain, J. Inorg. Nucl. Chem. 32, 1419 (1970).

TABLE I

Optical Parameters

	r(fm)	a(fm)
Neutrons		
$V(MeV) = 49.747 - 0.4295E - 0.0003E^2$	1.287	0.56
$W_{vol}(MeV) = -0.207 + 0.253E$	1.345	0.47
$V_{SO}(MeV) = 6.2$	1.12	0.47
$W_{SD}(MeV) = 6.053 + 0.074E$	1.3448	0.47
Above 6 MeV		
$W_{SD}(MeV) = 6.497 - 0.325(E-6)$		
Protons		
$V(MeV) = 58.384 - 0.55E$	1.25	0.65
$W_{SD}(MeV) = 13.5 - 0.15E$	1.25	0.47
$V_{SO}(MeV) = 7.5$	1.25	0.47
$r_c(fm) = 1.25$		
Alphas		
$V(MeV) = 193 - 0.15E$	1.37	0.56
$W_{vol}(MeV) = 21 + 0.25E$	1.37	0.56
$r_c(fm) = 1.4$		

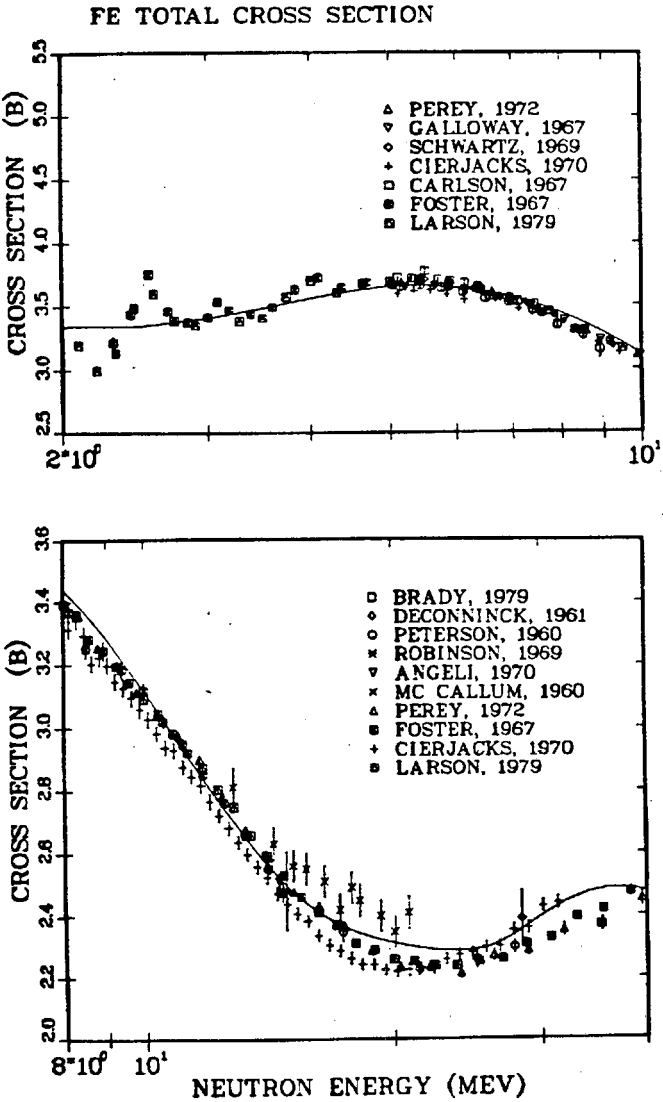

Fig. 1. Total cross-section data and values calculated using the neutron optical parameters of Table I.

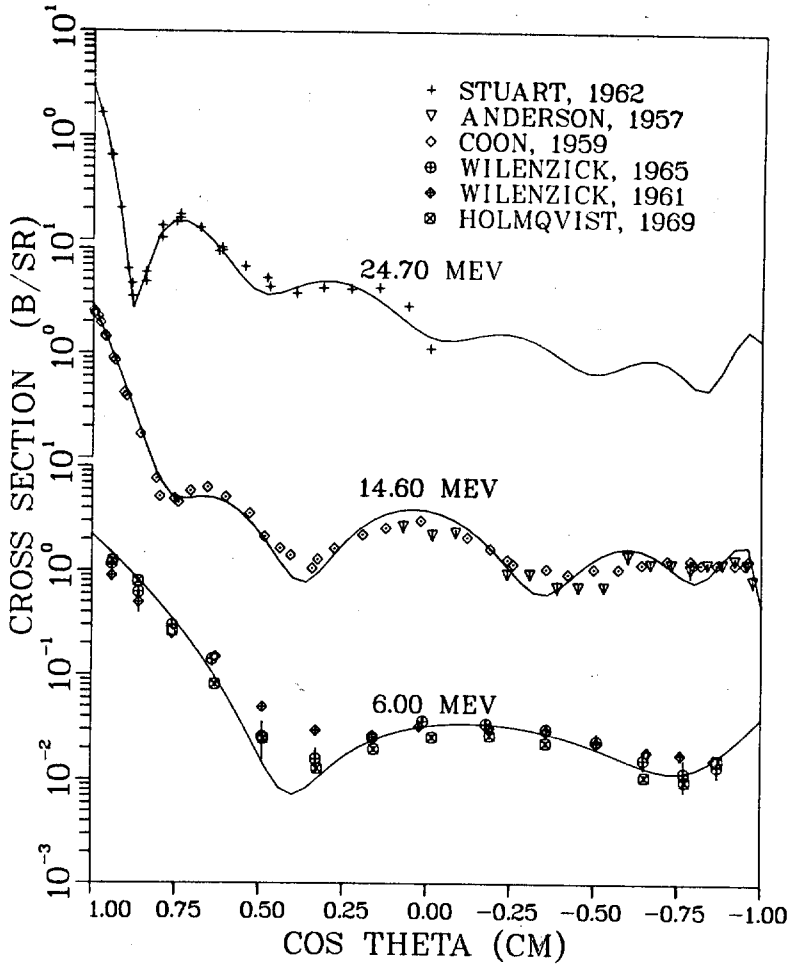

Fig. 2. Experimental and theoretical elastic scattering angular distributions.

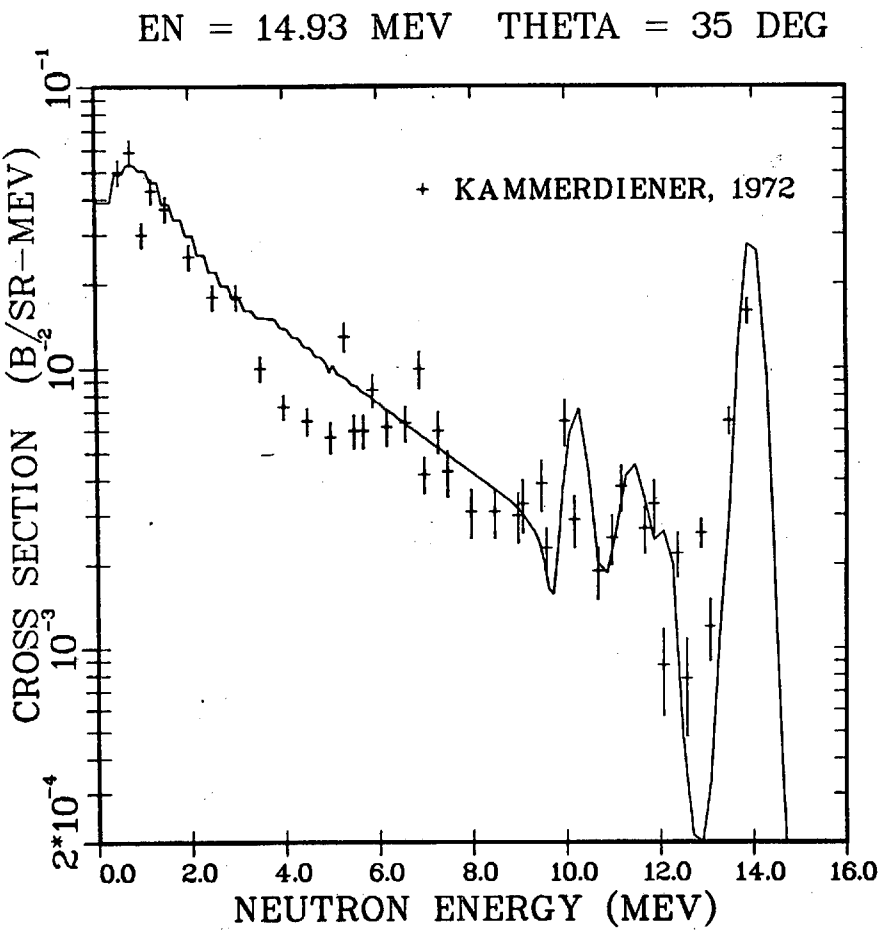

Fig. 3. The calculated neutron emission spectrum induced by 14.9 MeV neutrons is compared to results measured by Kammerdiener.[14]

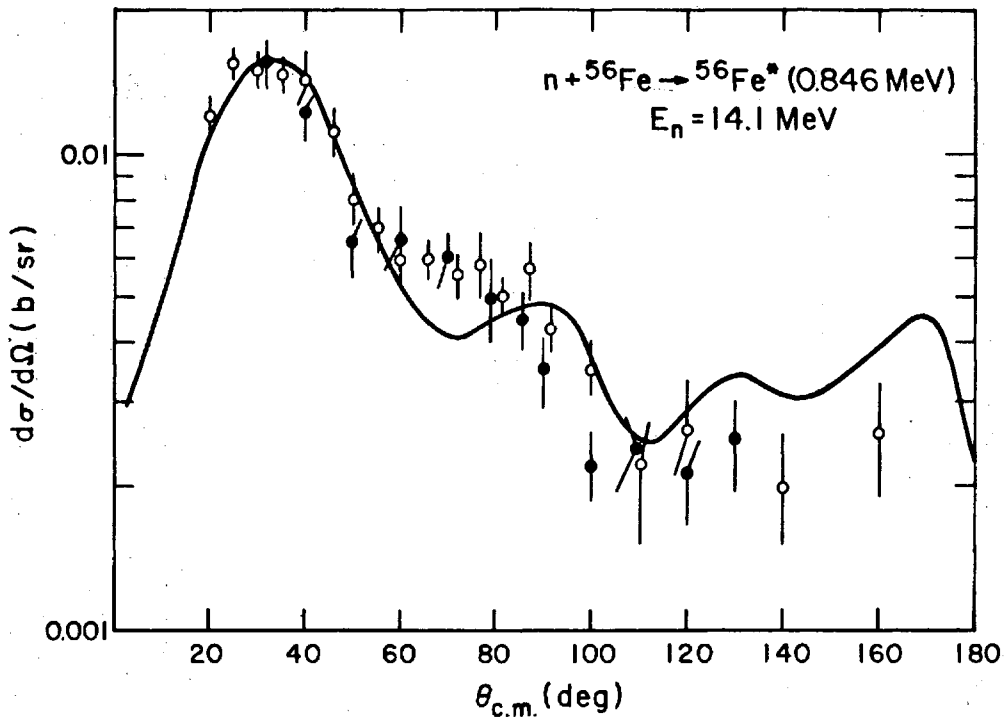

Fig. 4. The theoretical and experimental (closed and open circles are references 15 and 16, respectively) angular distributions for excitation of the 0.846 MeV level in ^{56}Fe by 14 MeV neutrons.

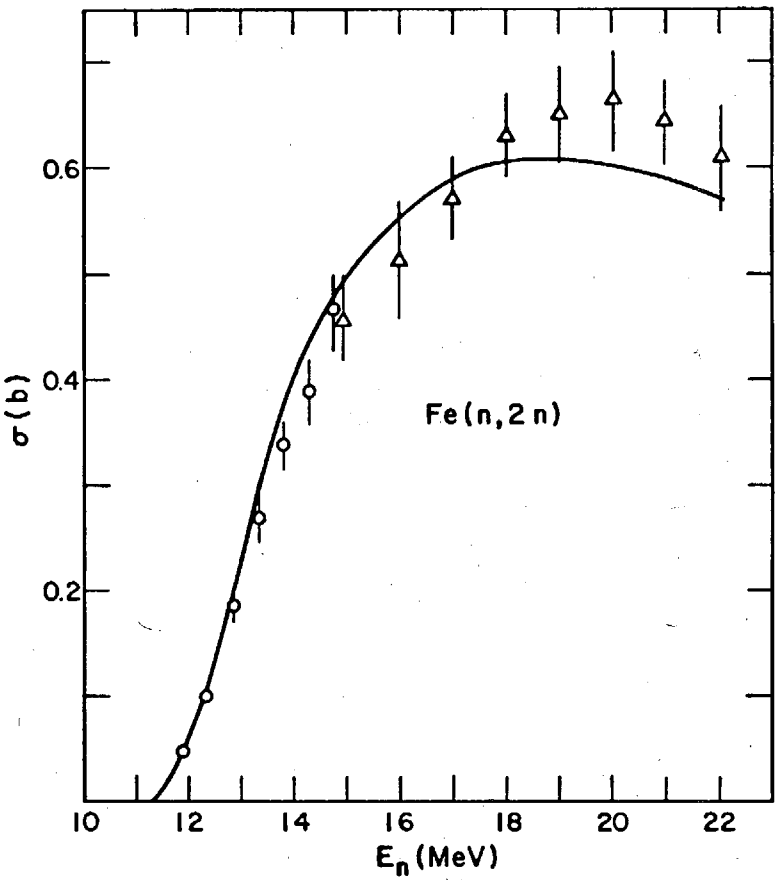

Fig. 5. Calculated and experimental values (circles, Ref. 19; triangles, Ref. 20) for the (n,2n) cross section on natural iron.

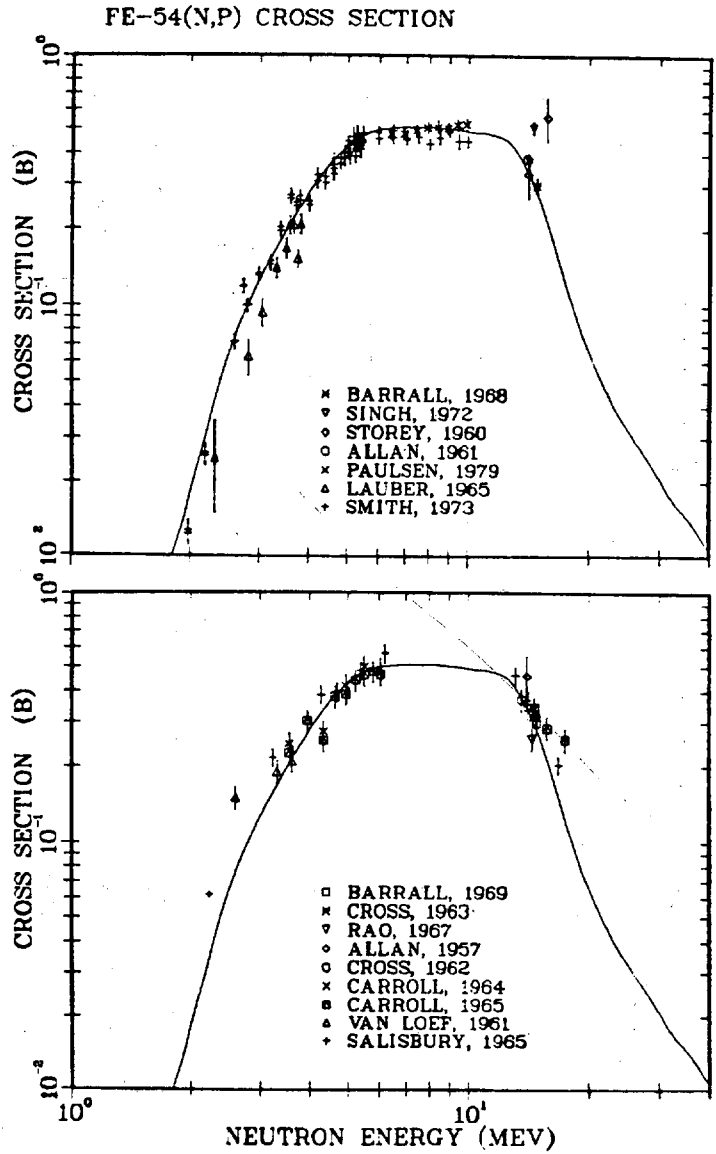

Fig. 6. Theoretical and experimental ^{54}Fe (n,p) cross sections.

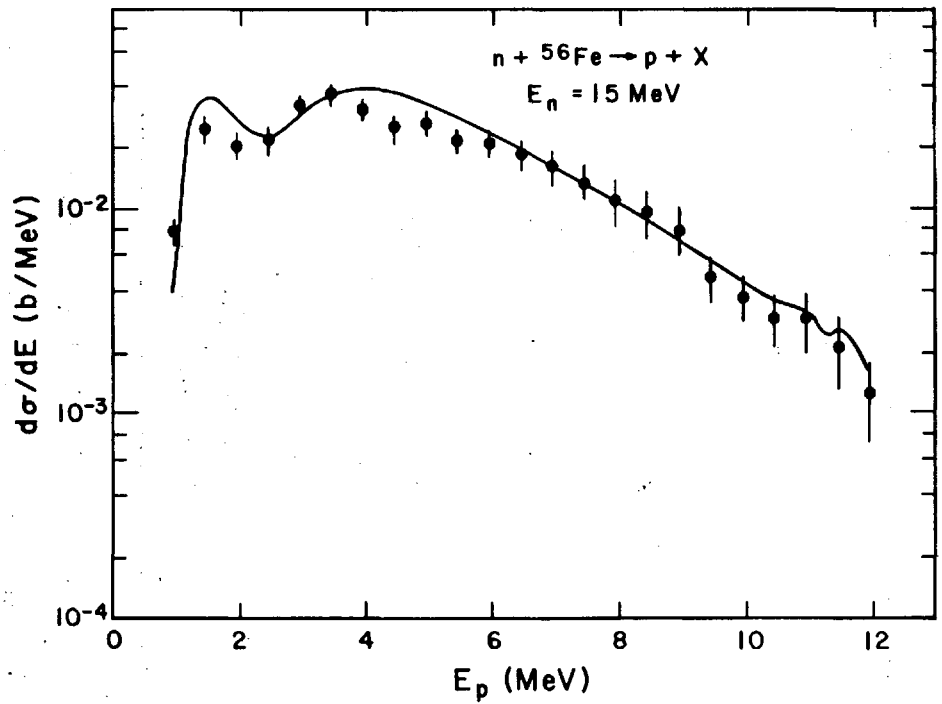

Fig. 7. Calculated values for the proton emission spectrum induced by 15-MeV neutrons on ^{56}Fe are compared to the Grimes[21] data.

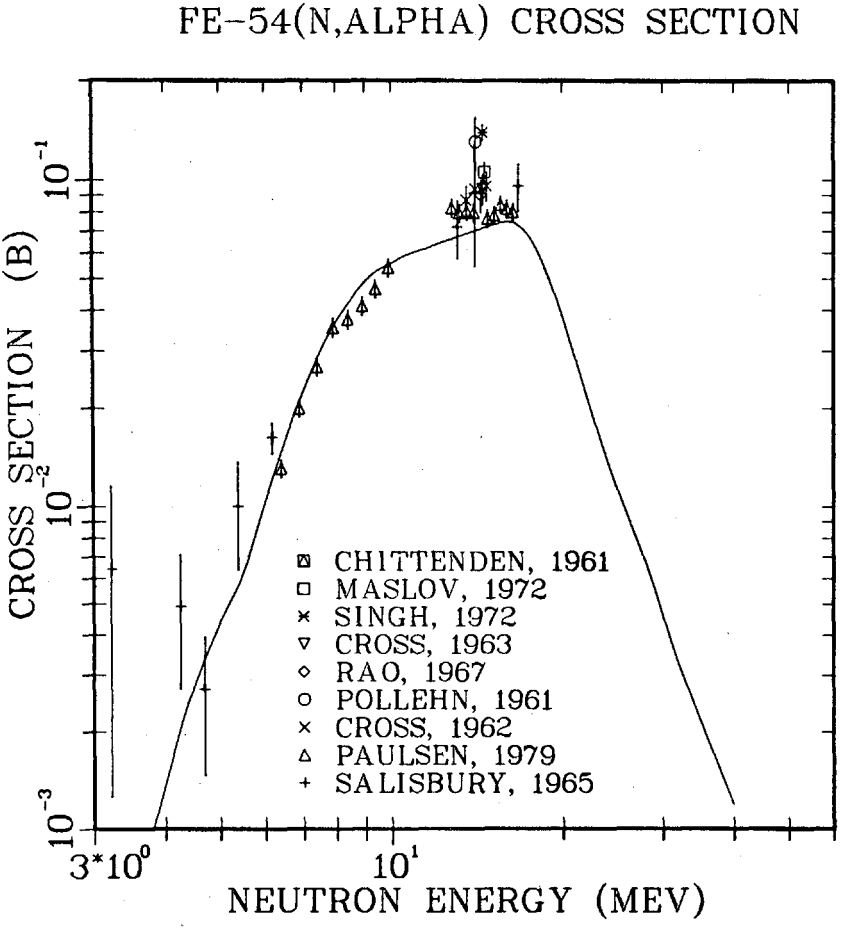

Fig. 8. Theoretical and experimental ^{54}Fe (n,α) values between 3 and 40 MeV.

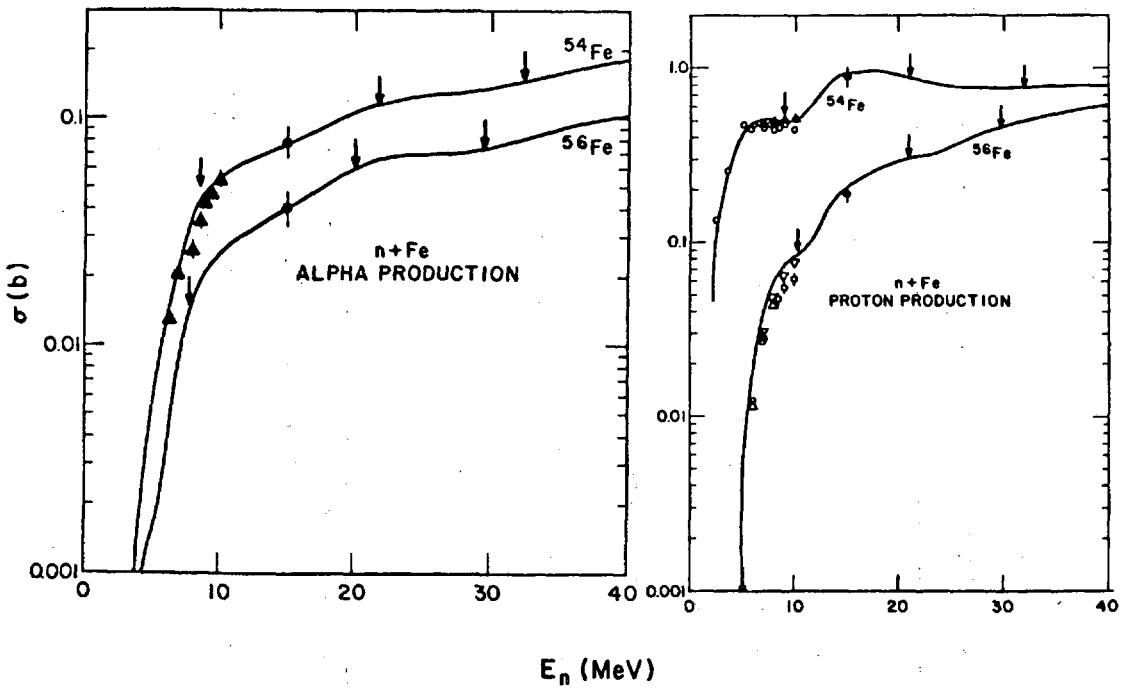

Fig. 9. Total proton- and alpha-production cross sections calculated for ^{54}Fe and ^{56}Fe. The arrows indicate thresholds for (n,xnp) and (n,xnα) reactions.

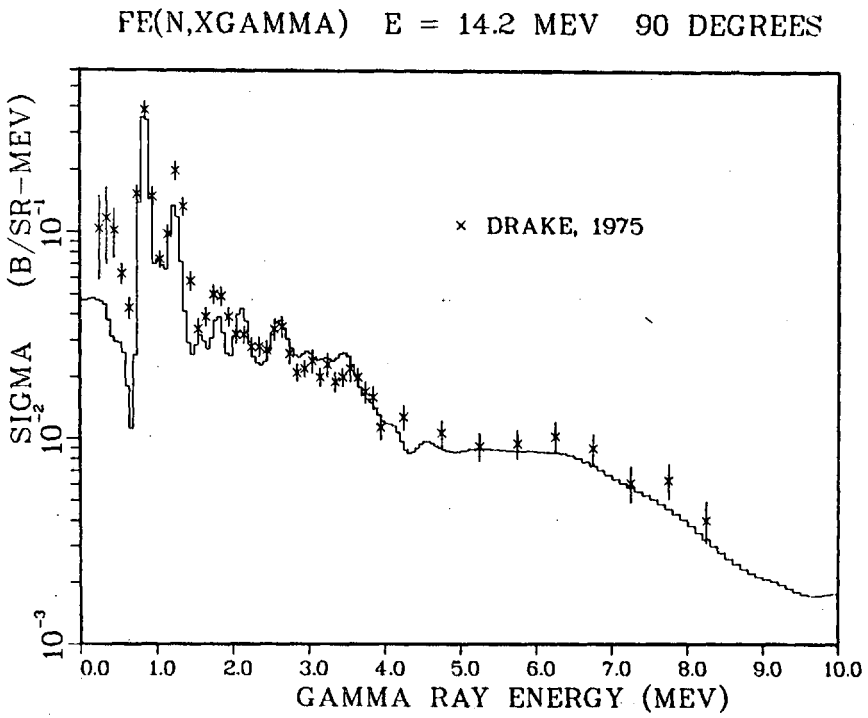

Fig. 10. The calculated gamma-ray production spectrum induced by 14.2 MeV neutrons is compared to data measured by Drake.[23]

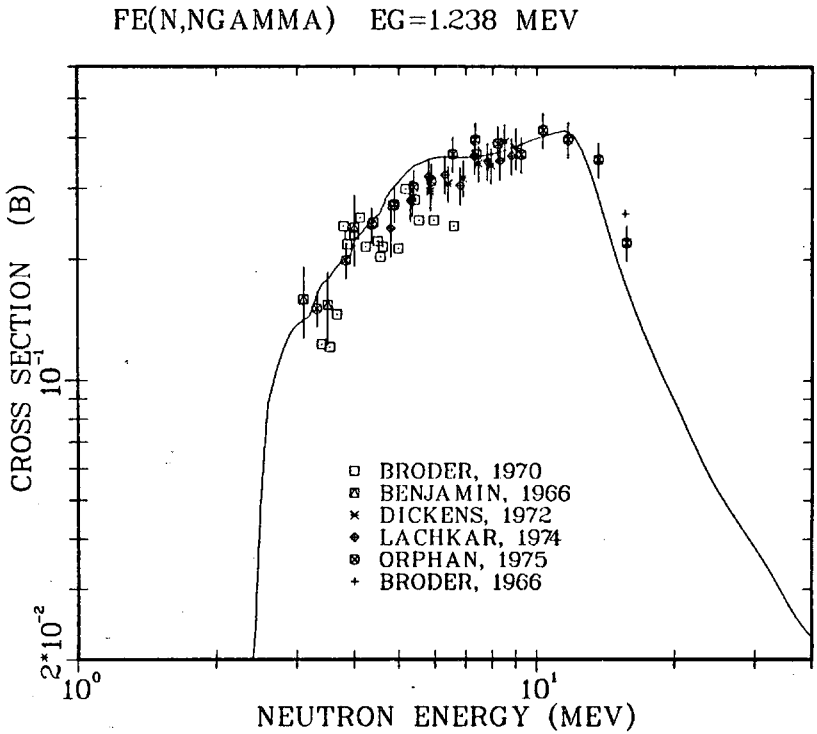

Fig. 11. Theoretical and experimental values for excitation of the 1.238-MeV gamma ray by neutron interactions with iron.

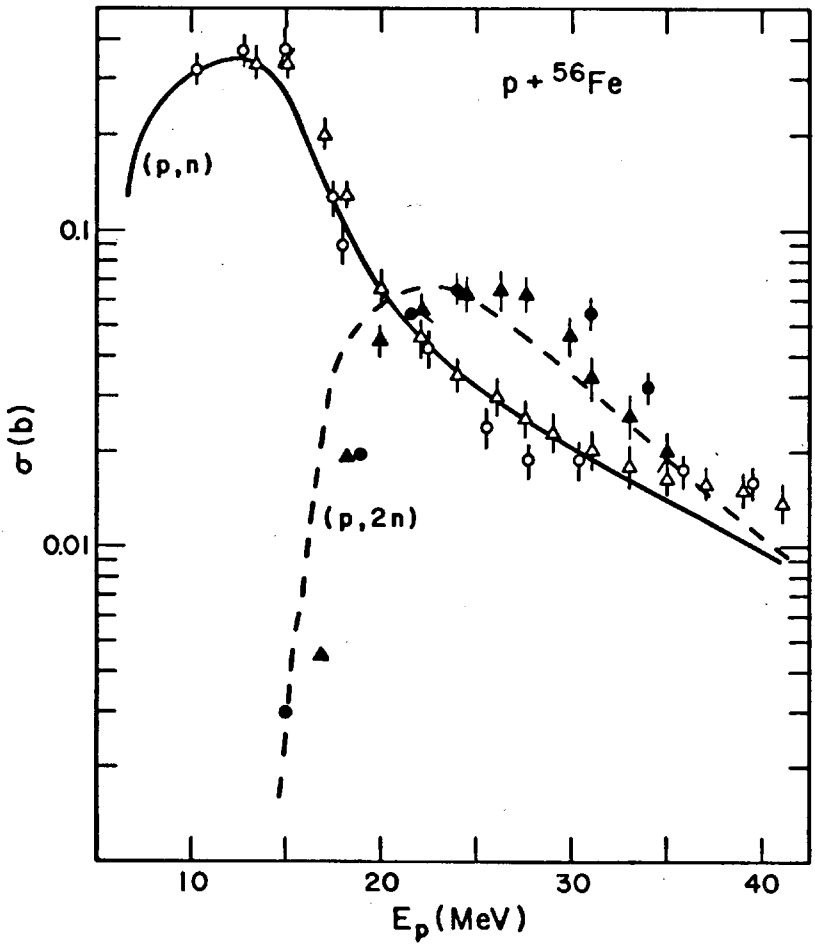

Fig. 12. Calculated and experimental cross sections for ^{56}Fe (p,xn) reactions. (Circles are Ref. 24; triangles are Ref. 25.)

CALCULATION OF ^{59}Co NEUTRON CROSS SECTIONS BETWEEN 3 and 50 MeV*

E. D. Arthur and P. G. Young

Theoretical Division
Los Alamos Scientific Laboratory
University of California
Los Alamos, New Mexico 87545

and

W. K. Matthes

EURATOM CCR
Ispra, Italy

ABSTRACT

Knowledge of the ^{59}Co (n,p), (n,α), and (n,xn) cross sections up to 50 MeV are necessary to satisfy priority dosimetry data needs of the FMIT facility. Since experimental data extend only to 25 MeV in the case of (n,xn) reactions (and lower for the others), we calculated these cross sections as well as those from competing reactions for neutron energies between 3 and 50 MeV. Neutron optical parameters were determined that were valid from several hundreds of keV to 50 MeV. Other parameters were determined or verified through analysis of various experimental data types, thus providing the basis for complete and consistent nuclear model calculations of n + ^{59}Co reactions.

INTRODUCTION

To characterize the neutron environment of samples irradiated in the neutron flux of the Fusion Materials Irradiation Test Facility, dosimetry reaction cross sections must be known to neutron energies of 50 MeV. Since the ^{59}Co (n,p), (n,α), and (n,xn) cross sections represent priority candidates for dosimetry reactions spanning the energy range of interest to materials damage studies, we

*Work supported by the U.S. Department of Energy and EURATOM.

performed calculations of neutron reactions on ^{59}Co between 3 and 50 MeV. In contrast to our earlier work [1] in which cross sections were calculated to 40 MeV using global optical parameter sets, we have devoted a large effort to the determination and verification of parameters suitable for calculations over this energy range. The constraints placed by the data used in this process should result in an improvement in the reliability of the calculated cross sections.

PARAMETER DETERMINATIONS

Our efforts to determine or verify neutron or charged-particle optical parameters generally follow the steps employed in our recent $^{54,56}Fe$ calculations. [2] That is, quite a large effort has been made through fitting techniqes to find neutron optical parameters valid over the entire energy range between several hundred keV and 50 MeV (in this instance). For proton and alpha emission we have generally modified existing parameter sets and then verified their applicability through comparison to independent data types.

To determine our neutron optical parameters, we used ^{59}Co total cross-section data between 0.5 and 30 MeV, supplemented at higher energies by estimates based on iron total cross sections to 50 MeV. Constraints on the low energy behavior of the parameters were achieved through use of s- and p-wave strength functions as well as values for the potential scattering radius. Elastic-scattering angular distribution data were included for neutron energies of 8, 11, and 15 MeV, along with 14-MeV reaction cross sections. Around 40 MeV, an estimate for the reaction cross section was included based on recent data [3] from n + Fe reaction cross-section measurements. For the fit, two energy regions were used with the boundary chosen at 6 MeV. The resulting parameters are shown in Table I. To fit the data, a surface derivative Woods-Saxon potential was used having a positive energy coefficient at low energies with a negative coefficient for energies above 6 MeV. A volume imaginary potential was also used that became dominant for neutron energies above 25 MeV. The calculated total and elastic cross sections are compared to experimental data in Figs. 1-a and 1-b, respectively.

For protons and alphas we used modifed forms, respectively, of the Perey [4] and Lemos [5] global parameter sets that were derived during our n + $^{54,56}Fe$ calculations (see contribution to these proceedings). To further verify them for this problem, we made Hauser-Feshbach calculations of ^{57}Fe (p,n) and ^{55}Mn (α,n) cross sections (with the neutron parameters of Table I) that are compared to data [6-8] in Figs. 2 and 3.

Other quantities required for these calculations consisted mainly of gamma-ray transmission coefficients, level density parameters, and parameters needed for preequilibrium corrections. The latter two parameter types were taken from published values since these result generally from the examination of systematic behavior of pertinent data. We employed the Gilbert-Cameron [9] level density expressions along with the Cook [10] values for Fermi-gas parameters and adjusted constant temperature parameter values to fit (for each nucleus in the calculation) information pertaining to the cumulative number of levels occurring up to a given excitation energy. Since constant-temperature level-density expressions were often employed up to fairly high excitation energies, uncertainties in the level-density expressions, occurring mainly in the Fermi-gas portions, could be minimized.

The matrix normalization constant needed to fix transition rates in the master equations preequilibrium model was taken from the value recommended by Kalbach [11]. The form of the absolute square of this residual two-body matrix element was assumed to be dependent on both the excitation energy available per exciton and the compound system mass [12].

Gamma-ray transmission coefficients were calculated assuming a giant dipole resonance form and were normalized through determination of the gamma-ray stength function by fits to ^{59}Co (n,γ) data. This method eliminates much of the uncertainty occurring from normalization to $2\pi\langle\Gamma_\gamma\rangle/\langle D\rangle$ ratios, especially for nuclei where no such data are available. The ^{60}Co gamma-ray strength function was very similar in magnitude to values we determined for ^{55}Fe and ^{57}Fe. [2]

CALCULATIONS AND RESULTS

The above parameters, along with discrete-level information, were used with three nuclear models--Hauser-Feshbach, preequilibrium, and direct-reaction--that describe the main features of most neutron reactions occurring in this mass and energy region. The main nuclear model codes used for the calculations were COMNUC, [13] GNASH, [14] and DWUCK. [15] In addition to Hauser-Feshbach calculations to which width fluctuations (COMNUC) and preequilibrium corrections (GNASH) were applied, a small direct-reaction component was determined for the first several inelastic levels through DWBA calculations (DWUCK). A weak coupling model for ^{59}Co consisting of a spin 7/2 hole outside a ^{60}Ni core was used along with the assumption of $\ell = 2$ transfer and a value of $\beta_2 = 0.2$. That this model was adequate to represent ^{59}Co direct cross sections was verified by examination of the relative magnitude and shape of 11 MeV proton inelastic scattering data [16] to several low-lying levels.

Figure 4 presents a general overview of the calculated cross sections. Since alpha decay chains were not followed individually except off the main neutron branch, contributions to (n,nα), (n,2nα), etc. cross sections were not ascertained for all components at higher incident energies. However, the effect of this approximation on total alpha production is very small. Also, reactions involving multiple proton emission such as (n,xnyp) ($y \geqslant 2$) were not included since tests performed at 40 MeV indicated that proton emission comprised less than a few percent of the total cross section for decay of a given compound nucleus occurring along the proton branch included in the calculations.

With reference to these cross sections, several general features are noteworthy. At higher energies, reactions involving proton emission such as (n,3np) dominate because of the multiple reaction paths that can produce the final nucleus. Also the compound systems produced along the main neutron decay chain tend to be more proton rich, resulting in less neutron emission. Thus, the (n,4n) reaction that has been suggested for dosimetry uses at higher neutron energies may suffer from a low cross-section value. Reactions such as (n,p), (n,2n), and (n,3n) maintain their cross-section magnitudes without rapid decreases after competing channels become available at higher energies. This results from preequilibrium effects and is well documented from the behavior of (p,xn) and (p,pxn) cross sections in this energy region.

Calculated values for ^{59}Co neutron reactions of dosimetry interest are compared to data in the next several figures. Figure 5 illustrates calculated (n,xn) cross sections with available data [17-21] [(n,2n) and (n,3n) measurements shown here were made using scintillator tanks]. Similarly, in Fig. 6 comparisons are made to ^{59}Co (n,2n) data measured by activation techniques. Both the (n,2n) and (n,3n) threshold energy regions provide an opportunity to verify the low-energy neutron transmission coefficients since emission to discrete states in the residual nucleus dominates here.

The slope of the calculated cross sections, particularly around the (n,2n) threshold, depends strongly upon competition from gamma-ray and charged-particle emission. The fact that the calculations fit the steeply rising cross section around the (n,2n) threshold provides verification of the normalization used for gamma-ray transmission coefficients since the (n,n'γ) reaction competes most strongly there. In the (n,3n) threshold region, such effects are reduced because of increased competition from particle emission through the (n,np) or (n,2n) reactions.

Figure 7 illustrates calculated and experimental values for the ^{59}Co (n,p) reaction. At lower energies, the behavior of the proton transmission coefficients calculated using the modified Perey optical parameters plays an important role in the agreement obtained with the data of Smith [22] (closed circles). At 14 MeV

the calculations fall somewhat lower than the experimental data, most of which cluster around cross-section values of approximately 50-60 mb. Attempts to increase the calculated values in this energy region through adjustment of level density parameters for ^{59}Fe began to disturb the agreement achieved at lower energies. In making such adjustments, the (n,pn) cross section was also increased, adding to the competition to the (n,p) reaction. These two factors made it difficult to adjust these parameters to achieve an increase in the calculated (n,p) values. Potential problems may exist in the relative amounts of proton and neutron emission predicted by the preequilibrium model. However, comparisons of our calculations to available proton emission spectra and (n,p) cross sections for nearby nuclei have resulted in good agreement, particularly between 15 and 20 MeV.

Although (n,np) + (n,pn) reactions are not of interest with respect to dosimetry cross sections, competition from them indirectly affects the calculated (n,2n) and (n,p) cross sections. Figure 8 illustrates our calculated (n,np) and (n,pn) cross section (solid line) and the portion of the reaction leading to the 0.811-MeV gamma ray in ^{58}Fe (dashed line). Also shown are the data of Corcalciuc et al [23] for the production of this gamma ray. The shoulder around 11-13 MeV results from the (n,np) reaction since in the ^{59}Co compound system the proton binding energy is about 3 MeV less than that of the neutron. In this region, the sub-Coulomb barrier behavior of the proton transmission coefficients is important, which led us to compare to low energy ^{57}Fe (p,n) cross sections as shown earlier in Fig. 2. Above 13-14 MeV, the (n,pn) reaction becomes the main contributor to this cross section. Our values (dashed line) agree well with the Corcalciuc data at higher energies but over-estimates it at 16 and 18 MeV. Some problems may exist in these measurements since their results for other reactions [^{56}Fe (n,2nγ) and ^{59}Co (n,2nγ)] appear to be systematically low when compared at these energies to other available data.

Figure 9 illustrates calculated and measured (n,α) cross sections available between 6 and 21 MeV. Although improvements may result from optical parameter adjustments at lower energies, the agreement is reasonable over this wide energy range. In addition to compound and pre-compound processes, we also included pickup and knockout contributions based on empirical expressions developed by Kalbach. [11] The agreement obtained at higher energies provides some verification of these parameterizations.

CONCLUSIONS

Independent data types have been used to determine or verify input parameters for use in comprehensive nuclear-model calculations of neutron reactions on ^{59}Co between 3 and 50 MeV. Results obtained in this manner generally produced good agreement when com-

pared to experimental data, particularly for (n,2n) and (n,3n) reactions up to 22 MeV. Calculated (n,2n) and (n,3n) cross sections should retain significant values at higher energies principally because of preequilibrium effects while the (n,4n) cross section is predicted to be significantly smaller because of competition from reactions involving proton emission. Uncertainty exists for the behavior of the (n,p) cross section above neutron energies of 10-11 MeV since some data are underpredicted by the calculations at 14 MeV. More experimental data (excitation functions) in the energy range from 10 to 20 MeV would be valuable towards solution of this problem. At higher energies, the (n,p) cross section is dominated by preequilibrium effects so that its magnitude remains relatively constant. Finally, the calculated (n,α) values agree reasonably with data up to 21 MeV indicating the reliability of the non-statistical reaction mechanisms used at higher energies.

REFERENCES

1. E. D. Arthur and P. G. Young, in Symposium on Neutron Cross Sections from 10 to 40 MeV, BNL-NCS-50681, Brookhaven National Laboratory, p. 467 (1977).

2. E. D. Arthur and P. G. Young, in Proc. Int. Conf. on Nuclear Cross Sections for Technology, Knoxville, TN (1979).

3. F. P. Brady and J. L. Romero, "Medium Energy Neutron Scattering and Reactions," UCD-CNL-192, UC, Davis report, p. 154 (1979).

4. F. G. Perey, Phys. Rev. 131, 745 (1962).

5. O. F. Lemos, "Diffusion Elastique de Particules Alpha de 21 a 29.6 MeV sur des Noyaux de la Region Ti-Zn," Orsay report, Series A, 136 (1972).

6. C. H. Johnson, A. Galonsky, and C. N. Inskeep, Physics Division Progress Report, ORNL-2910, Oak Ridge National Laboratory, p. 25 (1960).

7. T. Tanaka and M. Furukawa, J. Phys. Soc. Japan 14, 1269 (1959).

8. S. Tanaka et al., J. Phys. Soc. Japan 15, 545 (1960).

9. A. Gilbert and A. G. W. Cameron, Can. J. Phys. 43, 1446 (1965).

10. J. L. Cook, H. Ferguson, and A. R. de L. Musgrove, Aust. J. Phys. 20, 447 (1967).

11. C. Kalbach, Z. Phys. A283, 401 (1977).

12. C. Kalbach, Z. Phys. A287, 319 (1978).

13. C. L. Dunford, "A Unified Model for Analysis of Compound Nucleus Reactions," AI-AEC-12931, Atomics International report (1970).

14. P. G. Young and E. D. Arthur, "GNASH: A Preequilibrium Statistical Model Code for Calculation of Cross Sections and Emission Spectra," LA-6947, Los Alamos Scientific Laboratory report (1977).

15. P. D. Kunz, "DWUCK: A Distorted Wave Born Approximation Program," unpublished.

16. J. K. Dickens, F. G. Perey, and R. J. Silva, "Tabulated Differential Cross Sections for Elastic and Inelastic Scattering of 11 MeV Protons," ORNL-4182, Oak Ridge National Laboratory report (1967).

17. D. Hermsdorf et al., Kernenergie 17, 259 (1974).

18. N. Azziz and J. W. Connelley, Westinghouse report WCAP-7280 (1970).

19. P. Grabmayr and P. Hillie in Proc. Int. Conf. on Neutron Physics and Nuclear Data, Harwell, p. 204 (1978).

20. J. Frehaut and G. Mosinski in Nuclear Cross Sections and Technology, NBS Special Publication NBS 425, p. 855 (1975).

21. L. R. Veeser, E. D. Arthur, and P. G. Young, Phys. Rev. C16, 1791 (1977).

22. D. L. Smith and J. W. Meadows, Nucl. Sci. Eng. 60, 187 (1976).

23. V. Corcalciuc et al., Nucl. Phys. A307, 445 (1978).

TABLE I

$n + {}^{59}Co$ Optical Model Parameters

	r(fm)	a(fm)
$V(MeV) = 47.604 - 0.3636E - 0.0003E^2$	1.2865	0.561
$W_{vol}(MeV) = -0.072 + 0.1475E$	1.3448	0.473
$V_{SO}(MeV) = 6.2$	1.12	0.47
$W_{SD}(MeV) = 8.047 + 0.0805E$	1.3448	0.473
Above 6 MeV		
$W_{SD}(MeV) = 8.53 - 0.2509(E-6)$		

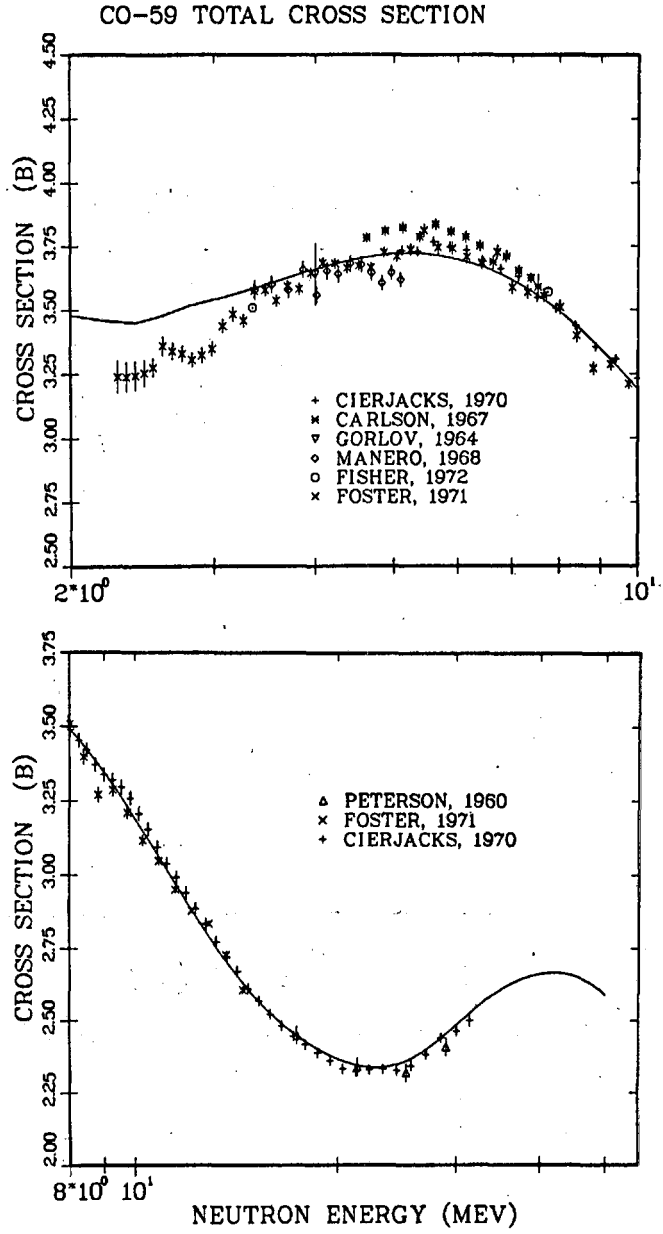

Fig. 1-a. Calculated and experimental values for the n + ^{59}Co total cross section.

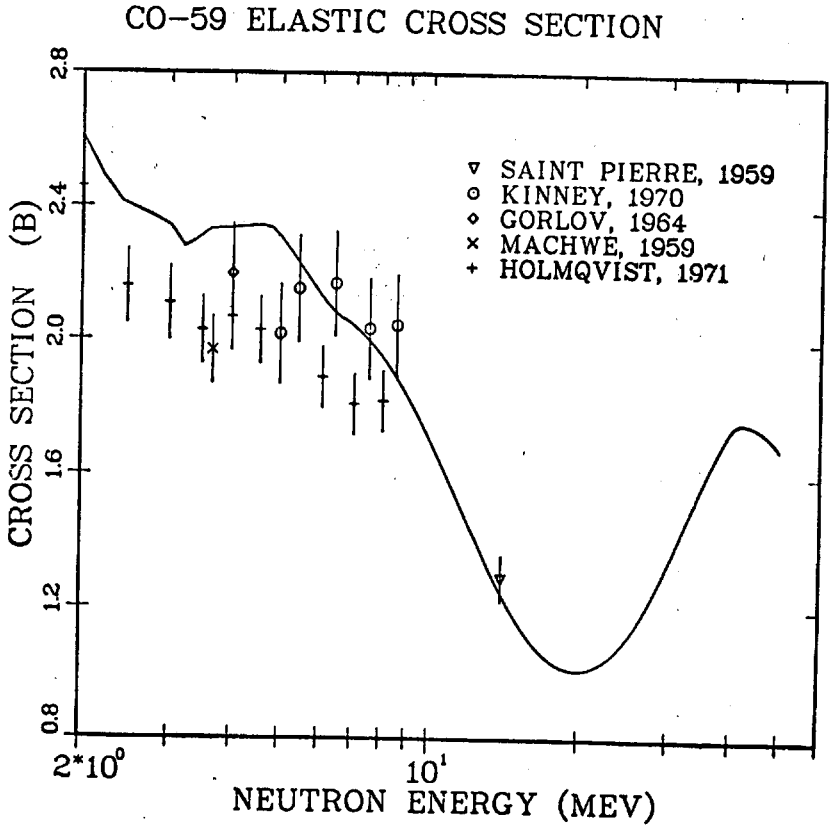

Fig. 1-b. Calculated and experimental cross sections for neutron elastic scattering from ^{59}Co.

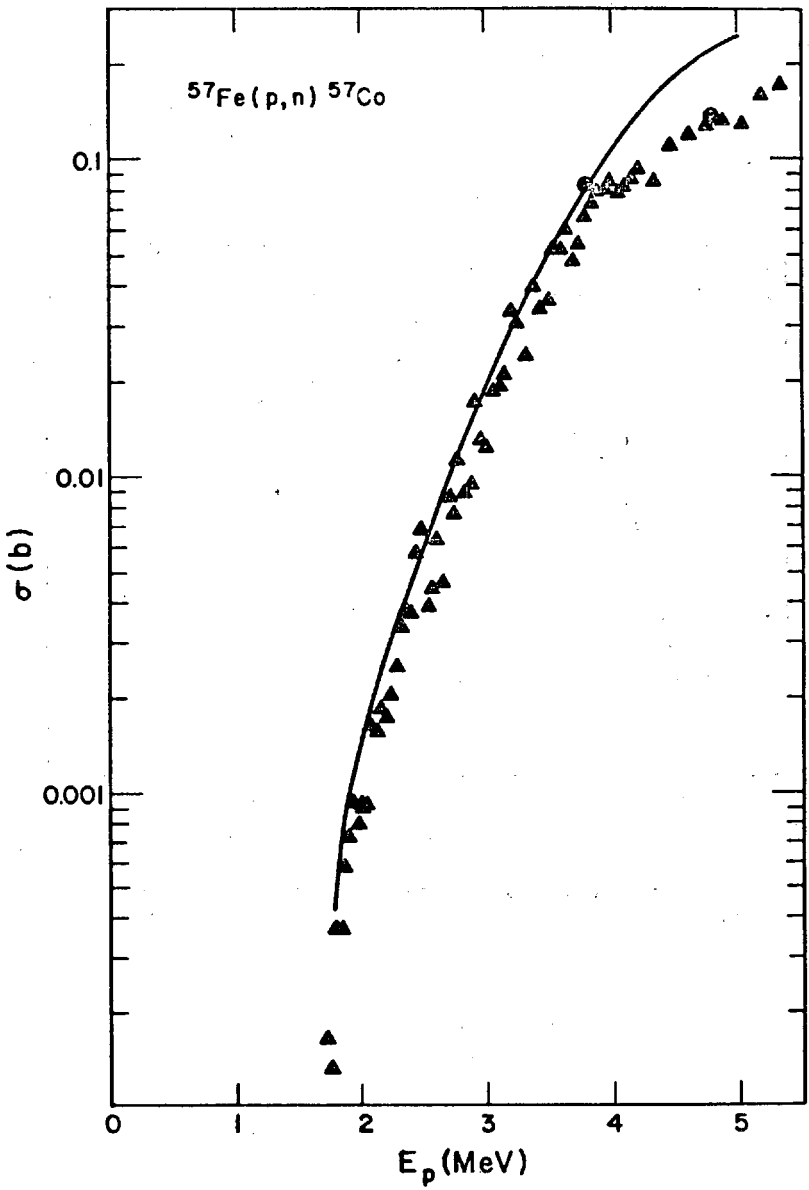

Fig. 2. Calculated and experimental $^{57}Fe(p,n)$ cross-section values. (Crosses are Ref. 6, circles are Ref. 7.)

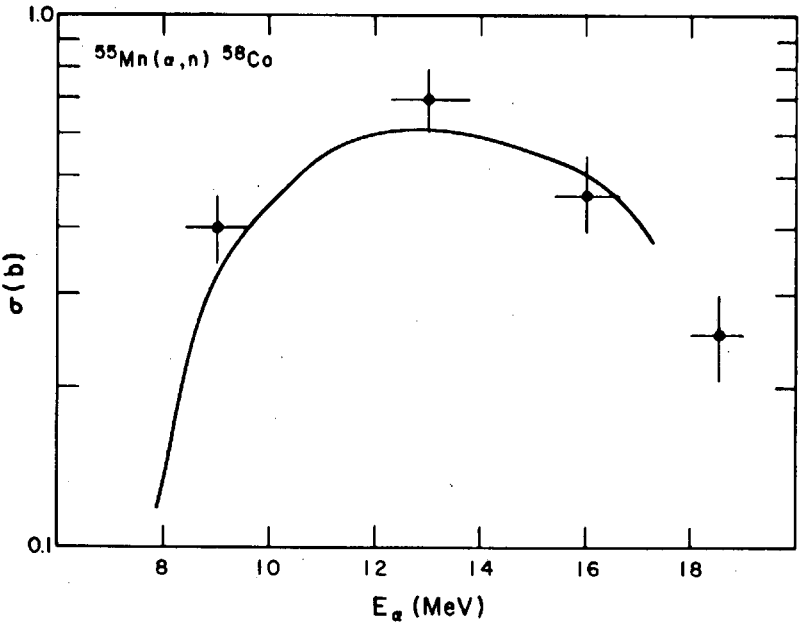

Fig. 3. The Lemos alpha-optical parameters are tested by comparison of calculated ^{55}Mn (α,n) values to experimental data (Ref. 8).

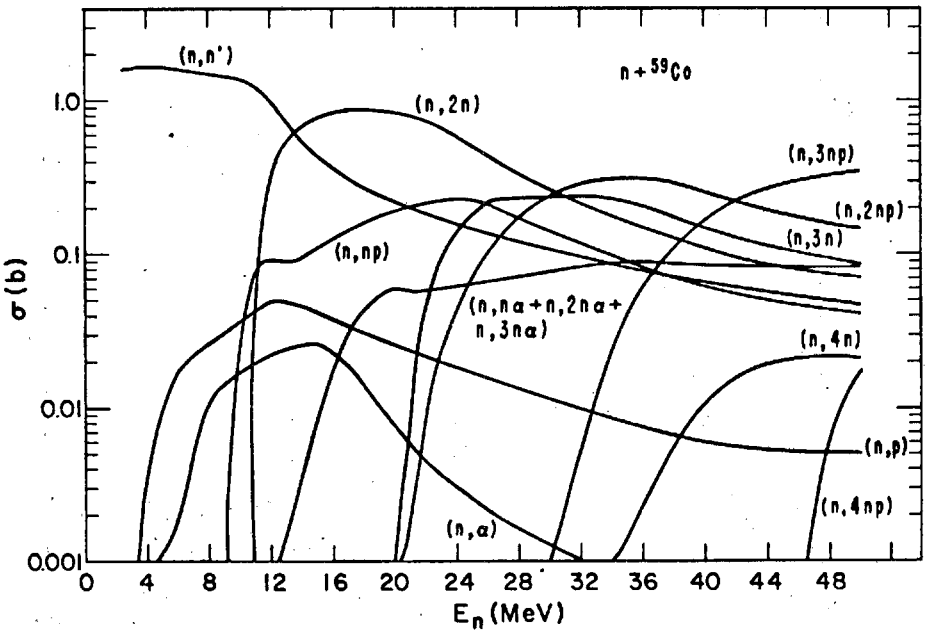

Fig. 4. Trends in cross sections calculated for ^{59}Co.

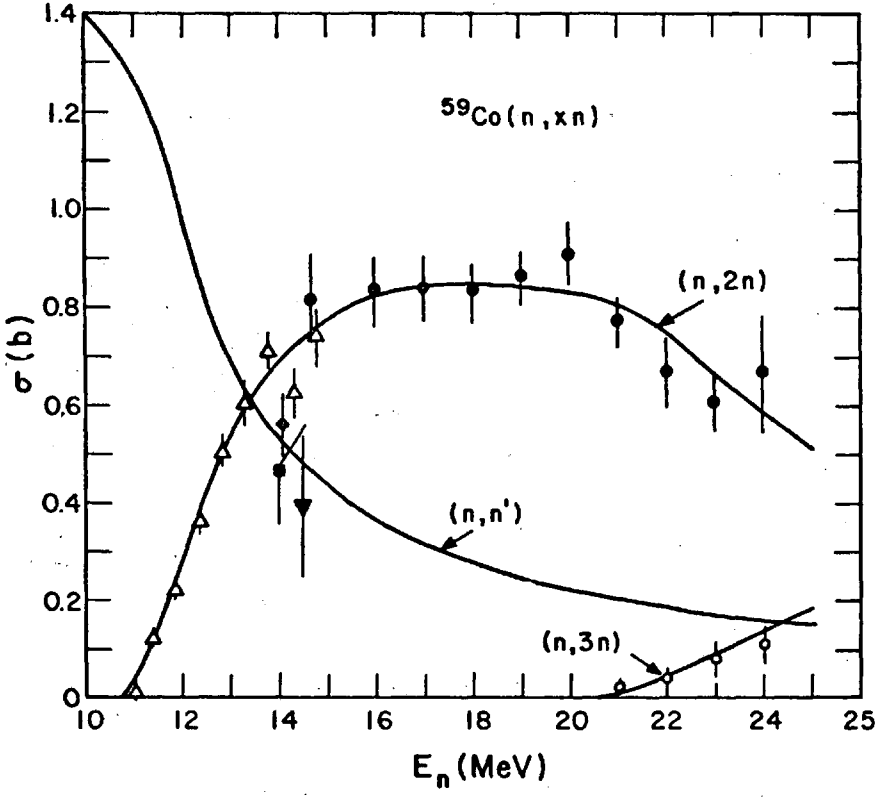

Fig. 5. Calculated and experimental (n,xn) values. For (n,n') reactions, the solid diamond, square, and triangle represent data from Refs. 17-19. The open triangles are (n,2n) data of Frehaut (Ref. 20) while the closed and open circles are (n,2n) and (n,3n) data of Veeser (Ref. 21).

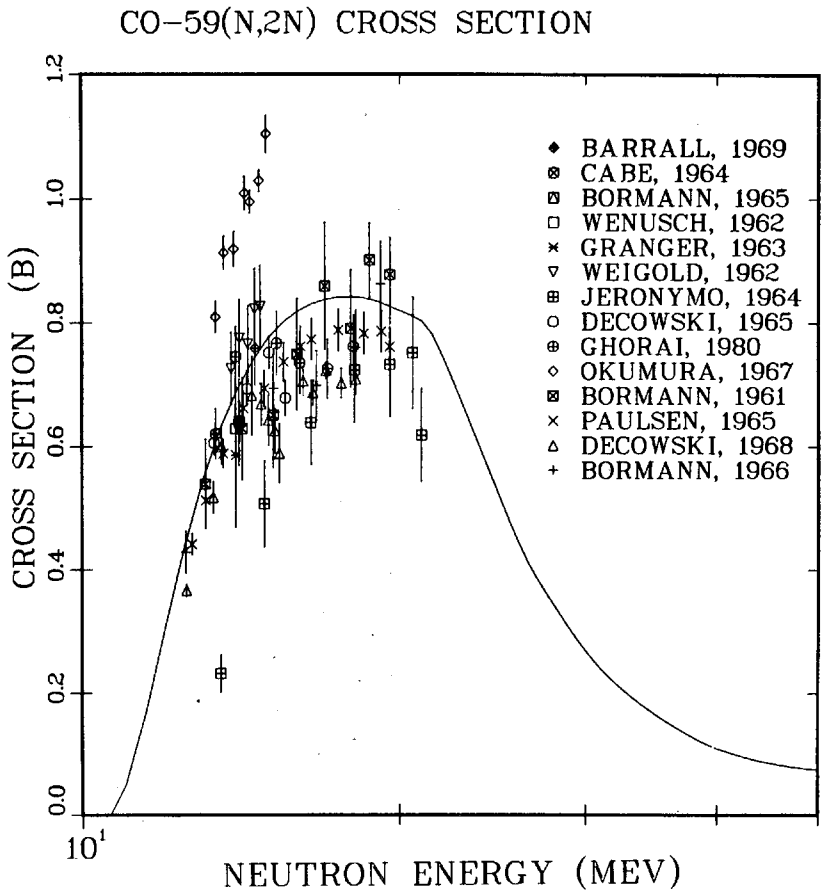

Fig. 6. Results from activation measurements of the ^{59}Co (n,2n) cross section are compared to the theoretical curve.

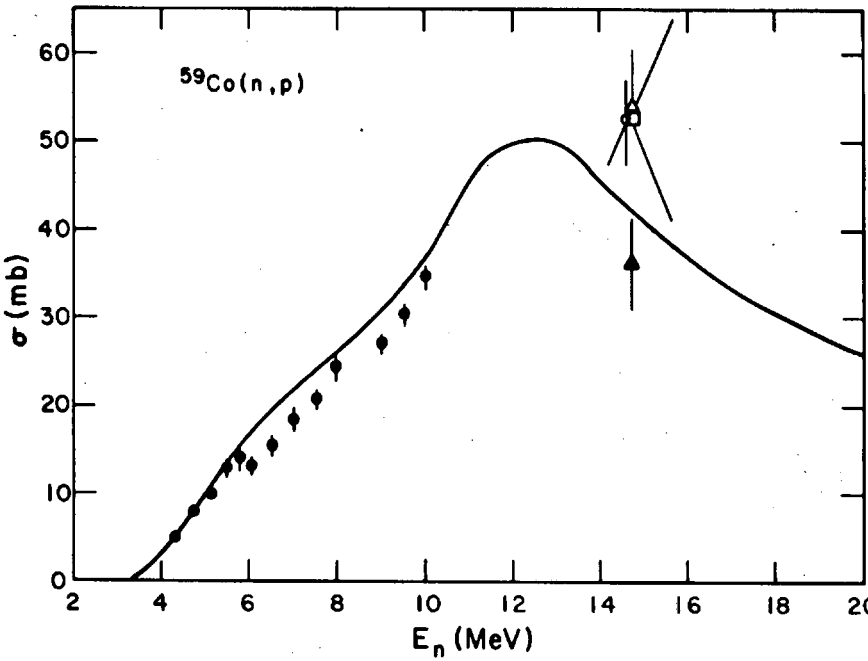

Fig. 7. Calculated and experimental values for the ^{59}Co (n,p) reaction.

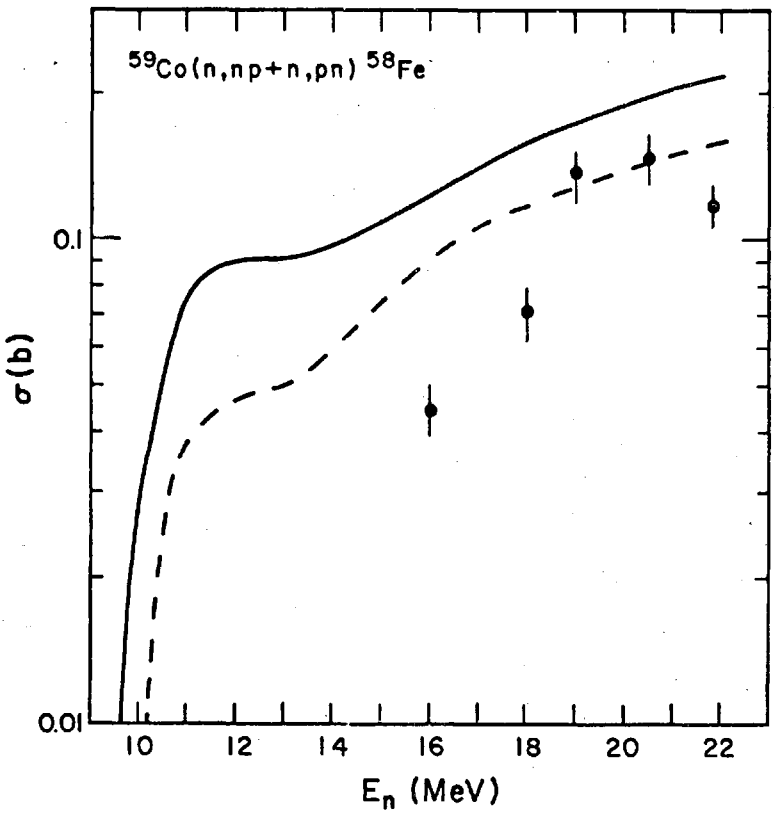

Fig. 8. The total ^{59}Co (n,np) + (n,pn) cross section (solid line) and that leading to the 0.81-MeV ^{58}Fe gamma ray (dashed line) are compared to measurements (Ref. 23) of the production cross section for that gamma ray.

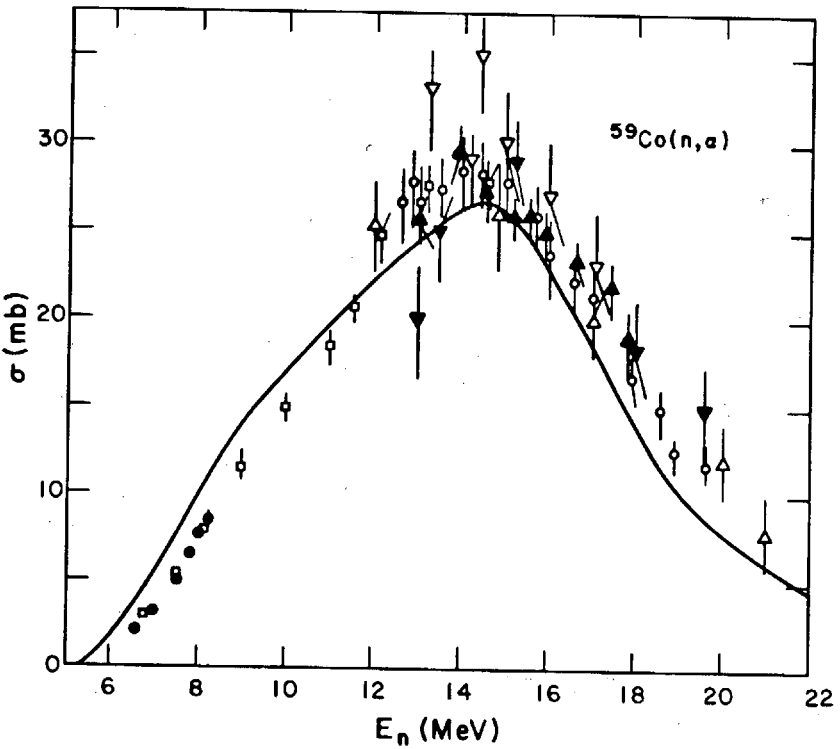

Fig. 9. Calculated and experimental ^{59}Co (n,α) values.

A STUDY OF OPTICAL MODEL PARAMETERS FOR HIGH ENERGY NEUTRON CROSS SECTIONS FROM 5 - 50 MeV IN THE MASS-140 REGION

T. W. Phillips, H. S. Camarda, and R. M. White

Lawrence Livermore Laboratory
University of California
Livermore, California 94550

ABSTRACT

We have begun a study of the neutron optical potential on nuclei near mass-140. In this study we are extending the energy range and improving the precision of previous neutron total cross section measurements. The extended energy range of this measurement reveals maxima and minima in the total cross section which are evidence of the nuclear Ramsauer effect. We employ the 100-MeV linear accelerator to produce a continuum of neutron energies from a Ta-Be conversion target. We use the 250-meter flight path and measure neutron energies by the time-of-flight method. We have obtained transmission data for ^{140}Ce and transmission ratios for ^{142}Ce, ^{141}Pr, and ^{139}La relative to ^{140}Ce. The ^{140}Ce data have a precision of 1-3% and the ratios are obtained with a precision of about .3%. To analyze these total cross section data a computer code has been developed to calculate the total elastic, reaction, and differential elastic scattering cross sections of a neutron interacting with a nucleus. The interaction is represented by a spherically symmetric complex potential which includes spin-orbit coupling. The parameters of this potential have been adjusted to approximate the ^{140}Ce total cross over the energy range from 2.5 to 60 MeV. The energy dependence of these parameters will be described.

INTRODUCTION

Nuclear cross sections which have not been measured are often required to predict the behavior of neutrons in the materials of fusion or fission reactors. In many cases the optical model is

called on to predict these cross sections or model the nucleon-nucleus interaction involved in producing an unmeasured nuclear reaction. An improved understanding of the variation of optical model parameters with energy and nucleon number will increase our confidence in these predictions. As part of a study of the neutron optical model potential we have measured the neutron total cross section of ^{140}Ce and the total cross section ratios for ^{142}Ce, ^{141}Pr, and ^{139}La relative to ^{140}Ce. These measurements were made over an extended energy range with high precision to test the predictions of the optical model. The level of precision, 1-3% in cross section and .3% in ratio, was chosen after using current optical model predictions for nuclei in this mass region to predict the difference for adjacent isotopes. The energy range was chosen to cover two nuclear Ramsauer[1] minima in the cross section. The nuclear Ramsauer effect is due to destructive and constructive interferences between neutron waves transmitted through the nucleus and those diffracted around it. With this energy range and precision we expect to provide a stringent test of the optical model. If it performs well we hope to extract information on the nuclear matter distribution. Since these measurements were only recently completed and the optical model analysis is still in progress, only preliminary conclusions can be drawn on these points.

EXPERIMENT

Considerable care was taken with all facets of experimental technique to achieve high precision over a wide range in energy. The 100 MeV LLL linac provided a contiuum of neutron energies which allowed us to measure the neutron transmission at all energies simultaneously. This source was pulsed at 1440 pps for 10 nanoseconds duration. Neutron energies were determined by the time-of-flight technique over a 250 meter flight path which gave more than adequate energy resolution. This long flight path was used primarily to minimize the background contribution at high energies (i.e. short flight-times) produced by the detector response to the gamma-flash in the neutron target. This background as well as the energy of the accelerator set the upper limit of our energy range.

The detector design was chosen to minimize its response to the gamma flash and maximize its efficiency for high energy neutrons. This design consisted of 16 independent plastic scintillators (each 25 cm x 25 cm x 5 cm) stacked two (2) high and eight (8) deep. A view of the time-of-flight facility is shown in Fig. 1. The neutron producing target was made of water-cooled beryllium plates following a tantalum radiator which converted the electron flux to photons. This target was shown to produce a factor of six (6) improvement in high energy (>10 MeV) neutron flux in comparison with a tantalum neutron target used in other measurements. A study was also made of filters used to reduce the

gamma flash response in the neutron detector. For $^{140}Ce/H$ measurements a 3 cm tungsten filter was required. In the case of the ratio measurements only 1 cm was necessary. The availability or limited quantities of separated isotopes made it necessary to use tight (1 cm dia.) collimation of the neutron beam at the sample position. Powdered oxide targets were prepared by weighing the samples accurately and packing them in hollow aluminum rods milled to precisely the same inside diameter. The ^{140}Ce total cross section was obtained by measuring its transmission relative to hydrogen using an H_2O sample. In all cases the ratio of target thicknesses was chosen to exactly cancel the oxygen contribution in the transmission ratio. The target thicknesses were chosen to give a transmission of $\sim e^{-1}$. This choice minimizes the time needed to achieve a given statistical accuracy at a fixed data rate.

Data rates were limited to one count in ten beam bursts to minimize uncertainties inherent in large dead time corrections. The samples in each ratio measurement were alternately cycled into the neutron beam under computer control. The exposure period was determined by the number of neutron events observed in a monitor detector on a separate neutron flight path as shown in Fig. 1 This cycle length was adjusted to be about 10 minutes to average out systematic variations in the neutron production rate at the source which were not accounted for on the neutron monitor. Neutron flight times were measured by a time digitizer with minimum time resolution set at 4 nanoseconds per channel. Time-of-flight spectra and monitor data were recorded in computer memory for each sample for one cycle. After all samples were exposed, the spectra were recorded on disk, memory was cleared and a new cycle begun. A cumulative spectrum for each sample was also collected to monitor the progress of the experiment. This method of data recording permitted us to discard cycles which had neutron or monitor rates substantially outside the normal statistical fluctuations.

RESULTS

These data were corrected for dead time losses and background events and analyzed to obtain total cross sections or cross section differences. The $^{140}Ce/H$ ratio was analyzed to give the total cross section for ^{140}Ce by using previous measurements of the H cross section.[2] At low neutron (<10 MeV) energies the H cross section is large and contributes about 1% to the uncertainty in the ^{140}Ce total cross section. This uncertainty drops to .2% by 50 MeV and at these energies the uncertainty is dominated by background and statistics.

In Fig. 2 the unfolded cross section of ^{140}Ce is presented. The verticle bars represent the statistical error only. Fig. 3 presents the ^{142}Ce-^{140}Ce cross section difference. In the overlap region of the low and high energy runs these difference cross

sections overlap within statistics. This reproducibility gives us increased confidence in this experimental technique.

OPTICAL MODEL ANALYSIS

A spherically symmetric optical model applicable to these nuclei near a closed shell (N=82) was used to describe these results.

The form of the potential chosen was typical of some optical models,[3] i.e.

$$V_{om} = V_o\, f_1(r) + i\, Wo\, f_2(r) + V_s \left(\frac{\hbar}{M_\pi c}\right)^2 \left|\frac{1}{r}\frac{df_1}{dr}\right| \bar{\sigma}\cdot\bar{\ell}$$

where

$$f_1(r) = \frac{1}{1 + e^{\frac{(r-R)}{a}}}$$

$$R = 1.26\, A^{1/3}\, f$$

$$a = 0.7_f$$

and

$$f_2(r) = e^{-\left[\frac{r-R}{b}\right]^2} \qquad b = 1_f .$$

The calculational procedures used in this study are described elsewhere.[4]

This form of the optical model potential was used in the analysis of neutron total cross sections for a wide range of nuclear masses at 14 MeV by Dukarevich et. al.[5] In our case we cover an extended range of neutron energies which must be accounted for by dependence in the optical model parameters on energy. This energy dependence comes in part from an intrinsic energy dependence in the nucleon interaction and Buck[6] and in part from the approximation of a non-local potential by an equivalent local potential. The energy dependence obtained in our preliminary fit to the ^{140}Ce total cross section is

Real part

$$V_o = -49.9 + 0.32E + (17.-0.111E)\,\frac{N-Z}{A} \quad \text{for } E<25 \text{ MeV}$$

$$V_o = -45.88 + 0.159E + (15.58-0.054E)\,\frac{N-Z}{A} \quad \text{for } E>25 \text{ MeV}$$

Imaginary part

$$W_o = -7.456 + 26.\frac{N-Z}{A} - 1.4\,E \quad \text{for } E<5 \text{ MeV}$$

$$W_o = -16.32\,(1-e^{-E/2.3}) + 26\,\frac{N-Z}{A} \quad \text{for } E>5 \text{ MeV}$$

The fit to our total cross section data is illustrated in Fig. 4. This potential was also used to predict the angular distribution for elastic scattering of neutrons at 7 MeV from ^{142}Nd. Fig. 5 compares our prediction with recent experimental results of G. Haout et. al.[7] We also find our prediction of the total inelastic cross section to be in good agreement with the measurements of Owens and Towle.[8] This agreement is demonstrated in Table I. However we must emphasize the preliminary nature of this potential. If the difference between the optical model prediction described above and our data is compared with the ^{142}Ce-^{140}Ce difference of Figure 3 we find that they are about the same magnitude. Thus further adjustment of the optical model parameters will be necessary before conclusions can be drawn about its ability to predict the precision ratio data. In making such adjustments we will apply constraints dictated by recent theoretical studies[9] and other available data.

SUMMARY

Precision neutron total cross section data have been obtained over an energy range from 2.5 to 60 MeV for ^{140}Ce. Ratios for ^{142}Ce, ^{141}Pr, and ^{139}La relative to ^{140}Ce have been analyzed to determine the differences in these cross sections. A preliminary fit to the ^{140}Ce has been made using a spherically symmetric optical model. Further refinements will be necessary to determine the ability of the optical model to predict the cross section ratios within the constraints of theoretically and experimentally reasonable choices of optical model parameters.

ACKNOWLEDGMENTS

The authors sincerely appreciate the assistance of the LINAC staff in the data taking stage of this experiment. Our appreciation is also extended to Marian E. Smith who coded the optical model calculations for these studies. This work was performed under the auspices of the U.S. Department of Energy by the Lawrence Livermore Laboratory under contract number W-7405-ENG-48.

REFERENCES

1. J. M. PETERSON, Phys. Rev. 125, 955 (1962).

2. E. LOMON and R. WILSON, Phys. Rev. C9, 1329 (1974) and J. BINSTOCK, Phys. Rev. C10, 19 (1974).

3. P. E. HODGSON, Nuclear Reactions and Nuclear Structure, pp. 167-179 (Clarendon Press 1971).

4. M. E. SMITH and H. S. CAMARDA, "Optical Model Calculation of Neutron-Nucleus Scattering Cross Sections" (Lawrence Livermore Laboratory internal report, unpublished, 1979).

5. YU. V. DUKAREVICH, A. N. DYUMIN and D. M. KAMINKER, Nucl. Phys. A92, 433 (1967)

6. F. G. PEREY and B. BUCK, Nucl. Phys. 32, 353 (1962).

7. G. HAOUAT, et. al. Phys. Rev. C20, 78 (1979).

8. R. O. OWENS and T. H. TOWLE, Nucl. Phys. A112, 337 (1968).

9. J. -P. JEUKENNE, A. LEJEUNE, and C. MAHAUX, Phys. Rev. C16, 80 (1977).

TABLE I.

Neutron Energy (MeV)	Optical Model Reaction Cross Section (barns)	Measured Cross Section (barns)
5.0	2.42	2.64 ± .11
6.0	2.40	2.40 ± .09
7.0	2.38	2.30 ± .14

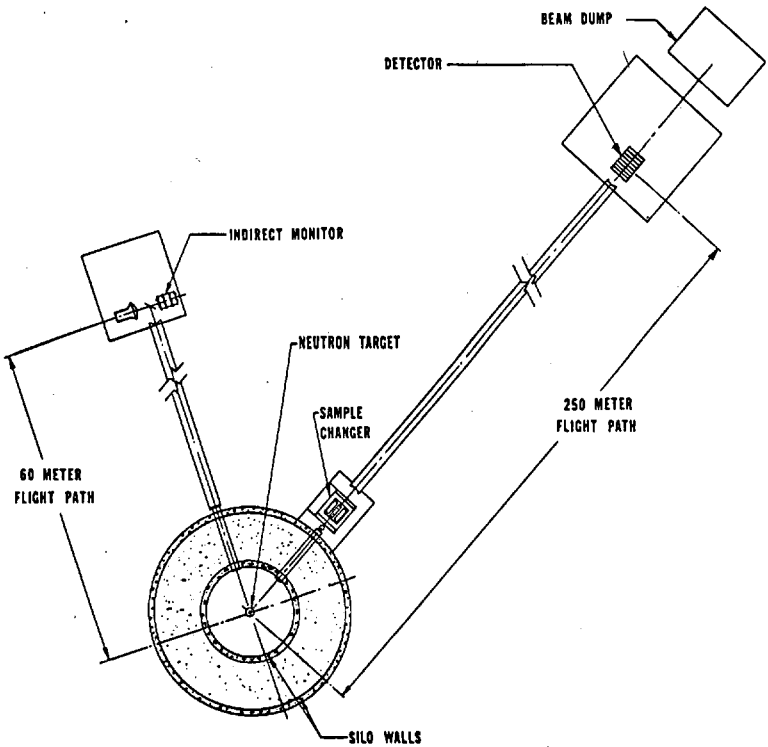

Fig. 1 Plan view of 250 meter T-O-F Facility

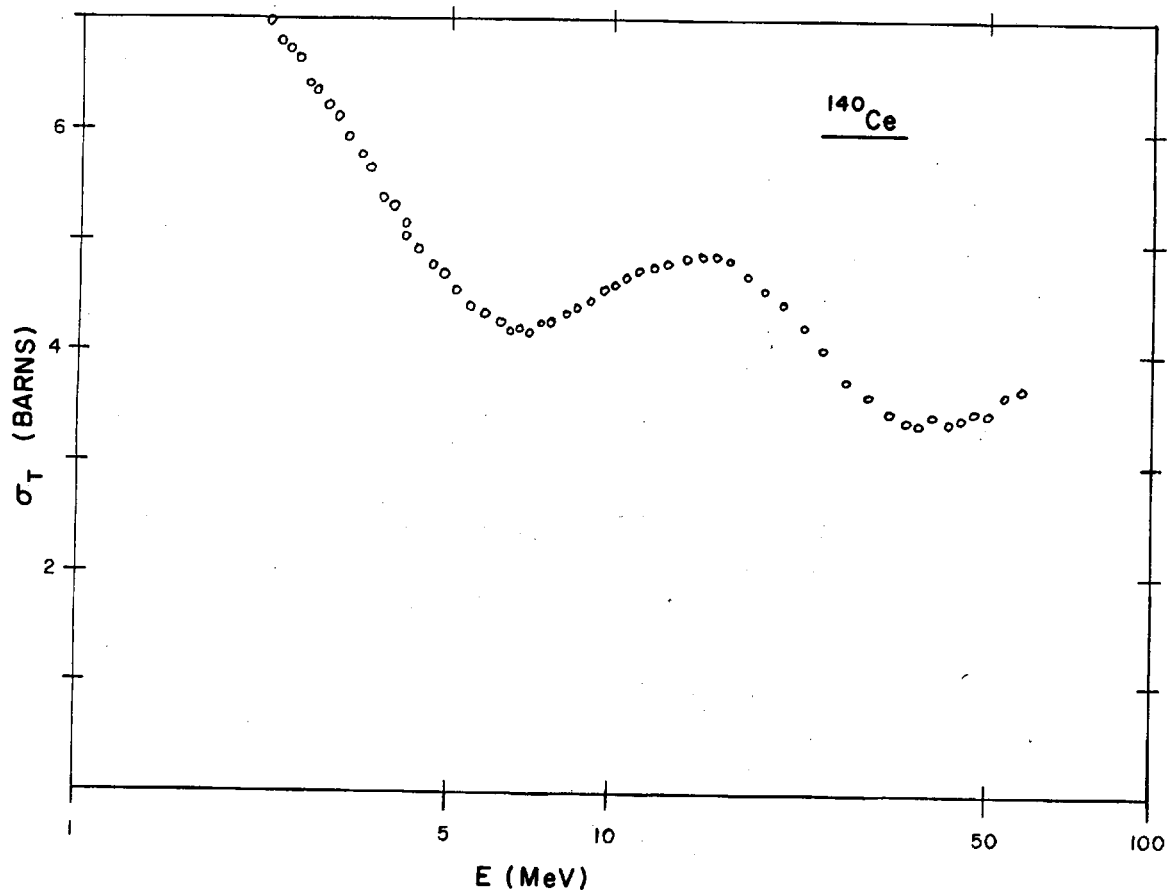

Fig. 2 Experimental total neutron cross section of ^{140}Ce

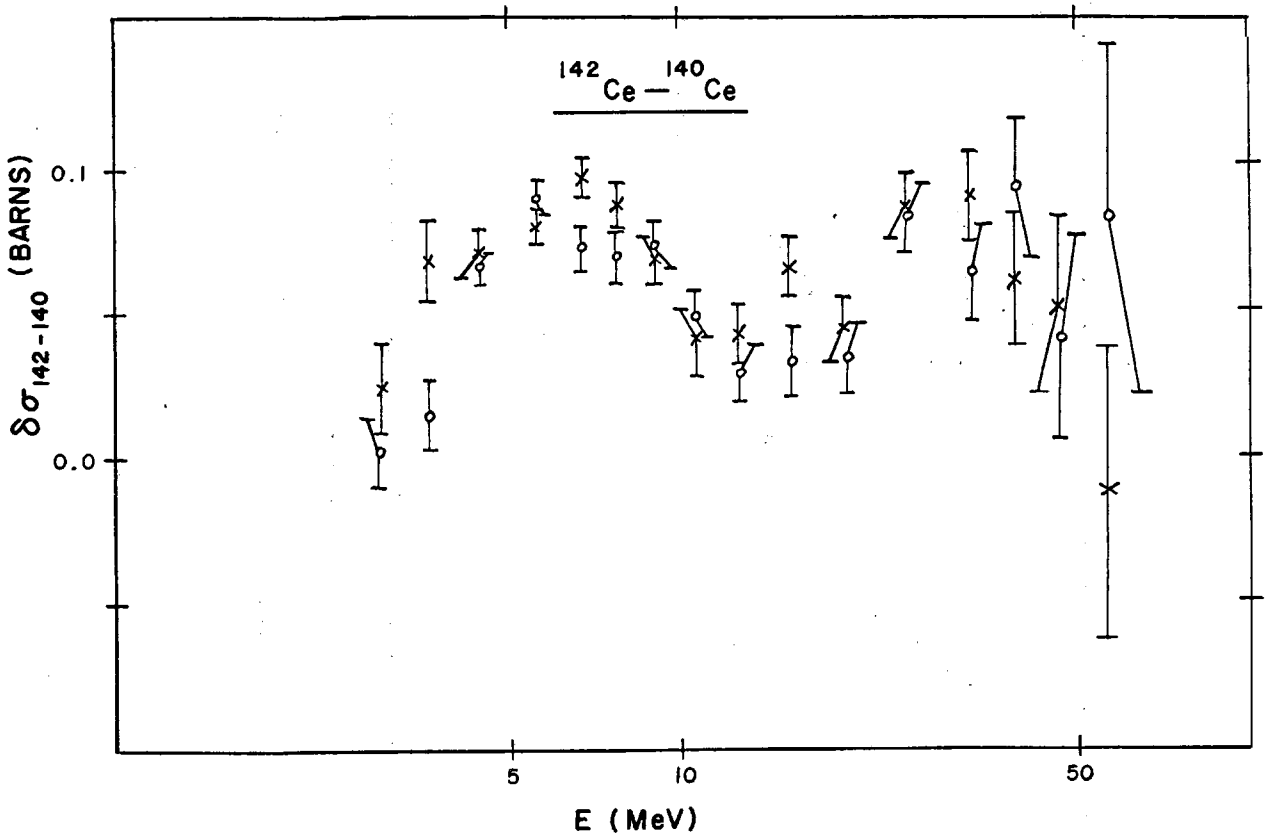

Fig. 3 Experimental difference of total neutron cross sections, ^{142}Ce-^{140}Ce. X-high detector threshold, O-low detector threshold

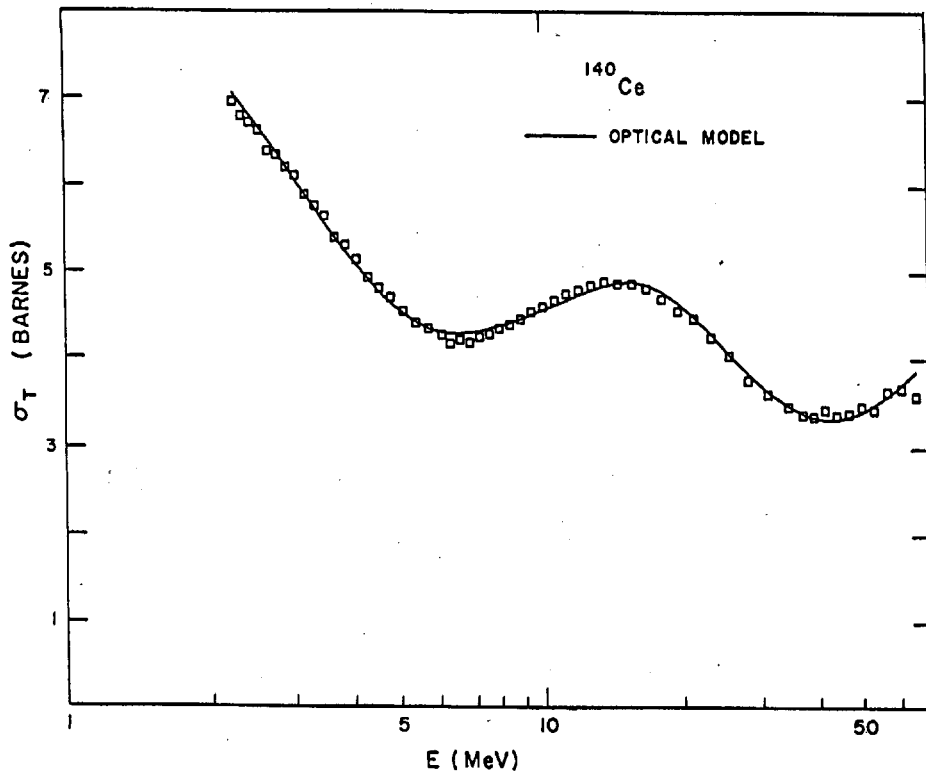

Fig. 4 A comparison of the Optical Model Prediction with the ^{140}Ce neutron total cross section

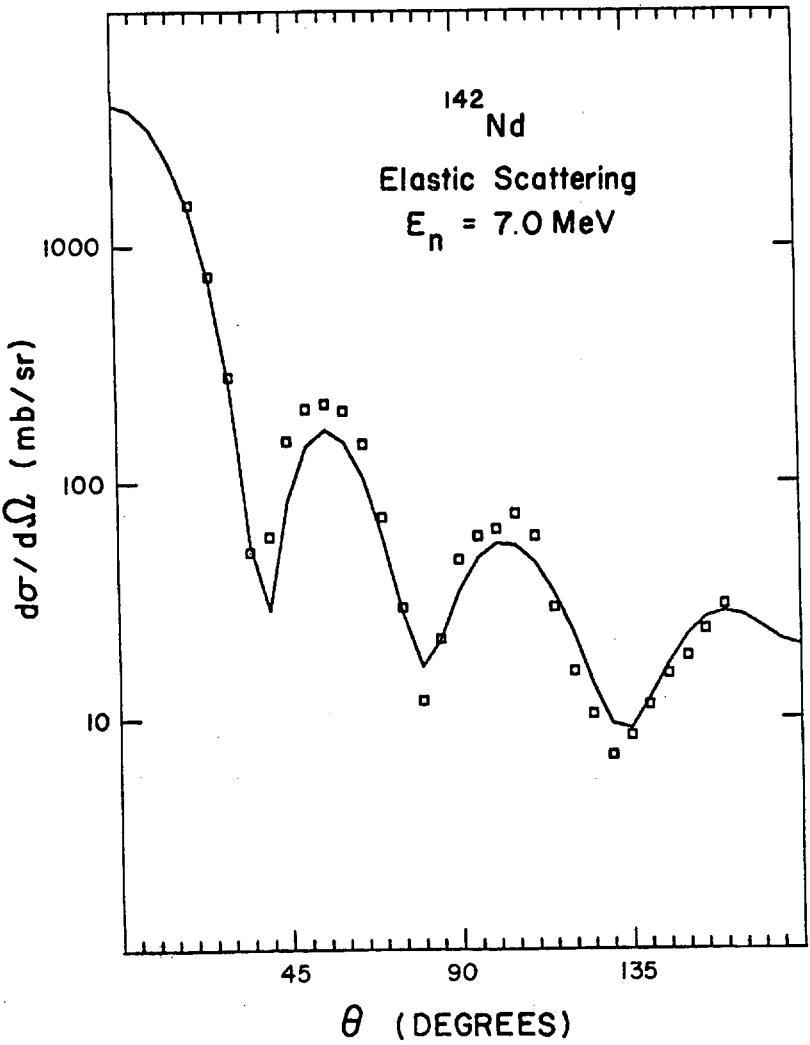

Fig. 5 A comparison of the Optical Model Prediction of the differential Elastic Scattering cross section with experimental data for ^{142}Nd

NEUTRON SCATTERING CROSS SECTIONS FOR ^{232}TH AND ^{238}U INFERRED FROM PROTON SCATTERING AND CHARGE EXCHANGE MEASUREMENTS

L. F. Hansen, S. M. Grimes, B. A. Pohl, C. H. Poppe and C. Wong

Lawrence Livermore Laboratory
Livermore, California 94550 U.S.A.

ABSTRACT

Differential cross sections for the (p,n) reactions to the isobaric analog states (IAS) of ^{232}Th and ^{238}U targets have been measured at 26 and 27 MeV. The analysis of the data has been done in conjunction with the proton elastic and inelastic (2^+, 4^+, 6^+) differential cross sections measured at 26 MeV. Because collective effects are important in this mass region, deformed coupled-channel calculations have been carried out for the simultaneous analysis of the proton and neutron outgoing channels.

We have studied the sensitivity of the calculations to: a) the optical model parameters used in the calculations, b) the shape of the nuclear charge distribution, c) the type of coupling scheme assumed among the levels, d) the magnitude of the deformation parameters and e) the magnitude of the isovector potentials, V_1 and W_1.

A Lane model-consistent analysis of the data has been used to infer optical potential parameters for 6-7 MeV neutrons. The neutron elastic differential cross sections obtained from these calculations are compared with measurements available in the literature; and with results obtained using neutron parameters from global sets reported at these energies.

INTRODUCTION

Neutron data for research applications dealing with reactors, material damage studies, shielding calculations, etc. are often obtained almost completely from optical model (OM) calculations, because of the lack of systematic measurements of neutron cross sections for many elements. In the last couple of years some good data on neutron elastic scattering have become available [1,2]; however, most of the measurements above 10 MeV are for

spherical nuclei, $40 \leq A \leq 208$, (due to limitations in the experimental resolution) for neutron energies about $\geq$ 10 MeV. Only a few good resolution measurements exist [3,4] for deformed nuclei and these are for neutron energies lower than 4 MeV.

The parameters needed to generate the OM potentials are obtained mainly from "global" (smooth dependence on mass number, energy and neutron excess for a wide range of A and E) sets available in the literature [5,6,7]. These OM parameters (OMP) do a reasonable job in predicting the overall trend of the neutron cross sections; but when the calculations are compared with available measurements, for a given A value and neutron energy, E_n, it is found that in order to improve the agreement, the values of the parameters need to be optimized. In order to correct the deficiencies of the "global sets", two more limited sets have been published recently: 1) the Ohio set [1], where the parameters have been fitted for neutron energies between 7 and 26 MeV for spherical nuclei (to minimize the strong coupling dependence of the parameters); 2) the Los Alamos set [8], where the parameters have been optimized for the actinide region, for the neutron energy range of 10 keV $\leq E_n \leq$ 10 MeV.

In the absence of good neutron data which will allow a test of the OM calculations, it has been proposed [9,10,11], based on the Lane-model [12] of the nucleon-nucleus OM potential, that only measurements of proton scattering and charge exchange (p,n) reactions to isobaric analog states (IAS), at the appropriate energy, are needed to generate neutron OMP for a given nucleus. This approach has proved to be very successful when applied to light [9] and intermediate [10,11] nuclei. Schery et al. [13] extended this technique to heavier nuclei, Au, Ph, Bi, and Th; they analyzed their (p,n) IAS measurements with a Lane-model OP, using proton scattering parameters obtained for Pb. The differential elastic neutron cross sections inferred from their analysis were in poorer agreement with neutron measurements available for these nuclei, than similar comparisons obtained earlier for lighter nuclei [10,11]. Several possible explanations were given by the authors [13] to account for their poor results: breakdown of the isospin symmetry of the Lane-potential for higher Z values; the inadequacy of the proton parameters for predicting OMP at the low equivalent neutron energies resulting for these nuclei (for these A values, the Coulomb displacement energy is close to $\sim$ 20 MeV); the possible existence of resonances in the proton scattering data for Pb (from which the proton OMP were obtained) at the energies of their (p,n) measurements, 25.8 MeV, which would invalidate the smooth energy dependence of the proton OMP used in their analysis.

We have recently measured the (p,n) IAS cross sections for ^{181}Ta, ^{197}Au, ^{209}Bi, ^{232}Th and ^{238}U at 26 and 27 MeV; for ^{232}Th and ^{238}U, we also have measurements [14] of elastic and inelastic proton scattering at 26 MeV. Accordingly, in this paper we will discuss only the results for these two nuclei. (At a later date we will report on the analysis of Ta, ^{197}Au and ^{209}Bi which is in

progress.) We have carried out a Lane model-consistent analysis of the proton scattering and (p,n) IAS data using a deformed channel-coupled calculation, which includes the proton, (p,n), and neutron channels simultaneously.

The neutron elastic differential cross sections for ^{232}Th and ^{238}U at 7 MeV, calculated with the OMP obtained from this analysis of the measurements, agree quite well with the existing neutron measurements [15,16], as well as with calculations carried out with neutron parameter sets [8] which have been optimized for this mass and energy region. We feel that the main reason for the difference in the quality of the agreement obtained between our results and those of Schery et al. [13], results from the fact that these authors, in their DWBA type calculations, did not take into account the importance of collective effects in this mass region.

Our results seem to confirm: first, that the charge independence of the nuclear optical potential, postulated by Lane, holds equally well at these higher Z values as in the lower mass regions [9,10,11]. Secondly, that coupling effects are very important through most of the periodic table and cannot be left out of the calculational analysis without a penalty in the quality of the results.

EXPERIMENTAL METHOD

The measurements of the (p,n) reactions were done with 26 and 27 MeV protons, accelerated by the Lawrence Livermore Laboratory cyclograaff. The emitted neutrons were detected using the neutron time-of-flight facility [17], where sixteen NE 213 scintillator detectors (11.4 cm diam. by 5.1 cm long), covering the angular region from 3° to 159° permitted a simultaneous measurement of the complete neutron angular distribution between these angles. Pulse shape discrimination was employed to reduce the time-independent gamma background, and a flight path of 10.8 m was used.

The targets were self-supporting foils of 15.0 mg/cm^2 thickness and 2.54 cm diameter. No separation between the ground state analog neutrons and those from the 2^+ and 4^+ collective levels was possible. The poor resolution was not necessarily the result of the experimental parameter conditions, target thickness (a thinner target could have been used) and beam width, but resulted from the intrinsic width of the ground state analog, $\sim$250 keV which is larger than the excitation energy of 2^+ and 4^+ excited states. The extraction of the cross sections was done by computer fits to the peaks using a Gaussian shape. The choice of a Gaussian versus a Breit-Wigner shape is justified in this case due to the large contribution to the peak width from the target thicknesses and beam width ($\sim$2 ns). The presence of a large background resulting from fission neutrons, makes extraction of the peak areas rather difficult. This accounts for the large errors in the measured cross sections, especially so at the largest angles. The increase

of 1 MeV in the incident proton energy, from 26 to 27 MeV increased the ratio of analog to fission neutrons in the measured spectrum, facilitating somewhat the extraction of the peaks from the fission neutrons. (The shape of the background adjacent to the peaks was assumed to be linear.) This effect, together with much longer running times for the 27 MeV data (28000 μC were collected in 16-hour runs), explains the smaller errors obtained for these data.

CALCULATIONAL METHOD

The proton elastic scattering, the inelastic differential cross sections to the 2^+, 4^+ and 6^+ collective levels, and the charge exchange (p,n) data, were analyzed using the standard Tamura [18] coupled-channel (CCOM) formalism. It was assumed that the Th and U targets are rigid rotators with permanently deformed mass and charge distributions. The deformed OM potentials were generated by replacing the real, imaginary and Coulomb radii by

$$R(\theta) = r_0 A^{1/3}[1+\sum_{\lambda}\beta_\lambda Y_{\lambda 0}(\theta)]$$

where the symbols have standard definitions [18].

The calculations, performed with the Oregon State coupled-channel code [19], were done in three stages: 1) A CCOM calculation was carried out for the elastic and inelastic proton measurements at 26 MeV, which provided the best set of proton OMP. 2) The (p,n) IAS differential cross sections measured at 26 MeV were analyzed in conjunction with the proton data to determine the best values for the isobaric potentials V_1 and W_1. The neutron potentials used in these calculations were generated from the proton potentials obtained in stage 1, (corrected by the values found for V_1 and W_1), in a Lane-consistent manner. The (p,n) angular distributions to the IAS were also calculated with neutron parameters obtained from prescribed global sets [1,8] for the purposes of comparison. 3) A CCOM calculation for the neutron scattering from ^{232}Th and ^{238}U at ∿7 MeV was carried out using the neutron potentials derived from stages 1 and 2. The 2^+ and 4^+ inelastic levels were included in this calculation and their cross sections were added to the ground state values for comparison with the measured neutron scattering angular distributions [15,16]. (These measurements did not resolve the contributions from the low lying inelastic levels.) The cross sections for the 2^+, and in less degree, for the 4^+ levels become comparable in magnitude to the elastic cross section for angles $\theta \gtrsim 60°$.

DISCUSSION OF RESULTS

Proton Calculations

Details of the CCOM analysis for the proton data at 26 MeV are given elsewhere [14]. Here only the main features of the calculations will be pointed out: a) Two sets of OM parameters were tried in these calculations, Becchetti-Greenlees (BG) [7] and Menet et al. [20]. This last set, obtained for high energy protons $30 \leq E_p \leq 60$ MeV gave a better fit to the data at the backward angles, and for this reason was preferred over the BG set. The values of the parameters for these two sets are rather close (Table I), except in the dependence of the imaginary potential on energy (this is expected, since BG values were obtained for an energy range of $10 \leq E_p \leq 50$ MeV). b) The calculations included all quadrupole (β_2), hexadecapole (β_4), and sextupole (β_6) couplings for levels up to J = 8. c) The value of the imaginary potential used in the CC analysis was 70% of the one given in Table I, in order to reproduce the magnitude of the non-elastic cross section, obtained from the spherical OM calculation using the full value of W. d) The values of the deformation parameters β_2, β_4, and β_6 (Table II) were taken from the literature [21,22], with minor adjustment to account for differences in the values of r_R and a_R.

Figures 1 and 2 show the measured and calculated cross sections for ^{232}Th and ^{238}U respectively. In these calculations, the charge distribution was assumed to be given by a homogeneous distribution with $r_c = 1.25$, and the Coulomb deformation parameters were taken to be equal to the nuclear deformation parameters. A Fermi distribution for the charge, with the values of the geometrical and deformation parameters taken from Bemis et al. [23], gave slightly better agreement with the measurements, especially for the 2^+ level where the slope of the angular distribution from forward to backward angles is better reproduced [14].

Calculations of the (p,n) reactions to the IAS

The CCOM analysis included all the couplings among the levels up to J = 4 for the target and final nucleus (because of limitations of the code, only 8 levels could be included; for this reason, J has to be lowered from 8 to 4). Figure 3 shows the coupling scheme among the levels used in the calculations.

From the comparison between the calculated and measured (p,n) cross sections, it was evident that the values of the isobaric potentials, $V_1 = 26.4$ and $W_1 = 15.5$ MeV, in the Menet set were too large. A better agreement with the measurements was obtained using BG values, $V_1 = 24$ and $W_1 = 12$ (an additional reduction of 10 to 15% in these values would bring the calculations and measurements in much better agreement, as indicated by the 27-MeV measurements). The BG values for V_1 and W_1 were used with the Menet potentials, V and W_D; the magnitude of the V_0 and W_{D0} terms

were corrected accordingly in order to conserve the total strength of the Menet potentials given by the expressions in Table I.

The OMP for neutrons of energies between 6 and 7 MeV, were derived from Menet's potential. Because this potential was obtained for protons with energies $E_p \geq 30$, the ratio of volume to surface imaginary potentials and their energy dependence was not adequate to calculate cross sections for these low energy neutrons. For this reason, the magnitudes of W_V and W_D were obtained from BG expressions for these potentials. Figures 4 and 5 show a comparison between the measured and calculated (p,n) IAS angular distribution at 26 and 27 MeV. Since the (p,n) measurements did not resolve the 2^+ and 4^+ from the ground state transition, the calculated curve represents the sum of the cross sections to these three levels. In Table III are listed the magnitude of the calculated cross sections at 27 MeV for the (p,n) transitions to the 0^+, 2^+ and 4^+ analog state; their sum is compared with the experimental value obtained from a Legendre polynomial fit to the measured (p,n) IAS angular distribution. No comparison is made for the 26-MeV data because of the large experimental errors. Calculations carried out with the neutron potentials obtained by Madland and Young [8], which have been optimized for these mass and energy regions, are also shown in Figs. 4 and 5 and the integrated cross sections are listed in Table III.

Neutron Scattering Calculations

CC calculations for 7 MeV neutrons scattered from ^{232}Th and ^{238}U were done using the OMP derived from the analysis of the proton scattering and (p,n) data in Sections I and II. In Fig. 6 the calculations are compared with the measurements of Batchelor et al. [15], at 7 MeV for ^{232}Th and ^{238}U. As discussed earlier, the calculated curves correspond to the sum of the values of the elastic differential cross sections and the values of the inelastic cross sections from the 2^+ and 4^+. The calculations with the Los Alamos OMP set are shown for comparison purposes. Both calculations reproduce the measurements fairly well with the modified Menet potentials giving slightly better fits.

To underline the need for carrying out coupled-channel calculations when calculating elastic scattering cross sections from deformed nuclei, Fig. 7 shows the calculated angular distributions for ^{232}Th, obtained from a spherical OM calculations. The agreement between the measurements and calculations for each of the neutron potential sets used (Menet, LASL and OHIO), is worse than the one obtained with the CC calculations (Fig. 6).

CONCLUSIONS

In the present work we have derived optical model parameters for $\sim$7 MeV neutrons for ^{232}Th and ^{238}U, from the analysis of the proton scattering data at 26 MeV, and the charge exchange (p,n)

measurements at 26 and 27 MeV for these nuclei. (The Coulomb displacement energy, Δ_C, is about 20 MeV.) A coupled-channel optical model calculation (CCOM) has been carried out for the (p,p), (p,n) and (n,n) reactions using consistent Lane-model optical potentials in the simultaneous analysis of the coupled proton and neutron channels. The neutron elastic scattering calculated with the above parameters compared quite well with measurements, and with calculations carried out with OP from global sets [1,8] for neutron scattering. These latter parameters have been optimized after an extensive search to fit neutron data over a larger range of mass and energy.

The present results support the theoretical assumption that the isospin symmetry of the Lane-model potential works as well at high Z values, as it does [10,11] for nuclei with $Z \leq 50$.

It must be pointed out that in the present analysis, no effort was made to optimize, through search of the parameters, the neutron potential derived from the calculations fit to the (p,p) and (p,n) measurements. The neutron potential was obtained directly from Menet's proton potentials for ^{232}Th and ^{238}U, using the Lane formalism. Two corrections were necessary: 1) From the fits to the (p,n) data it was found that the values for the isobaric potentials, V_1 = 26.4 MeV and W_1 = 15.5 MeV, given by Menet were too large. Becchetti and Greenlees [7] values for V_1 = 24 and W_1 = 12 MeV, were substituted in the Menet expressions for the real and surface absorption potentials, adjusting accordingly the values of V_0 and W_{0D}, to maintain constant the value of the potentials V_R and W_D, as given by Menet. (In spite of the rather large errors of our (p,n) data, the overall trend of the calculations indicate that a further reduction of $\sim$10 to 20% in the values of V_1 and W_1 could give a better fit to the data). 2) For the low energy neutrons, the energy dependence of the imaginary potential was not adequate (Menet's potential set was obtained from protons for energies $30 \leq E_p \leq 60$) and the values of W_D were calculated from BG relations for W.

The overall good agreement obtained in the fits to the proton scattering measurements [14] at 26 MeV, the present (p,n) data at 26 and 27 MeV, and the (n,n_0) data [15,16] at 7 MeV is the result of taking into account the strong coupling effects among the levels, by a CC calculation with deformed OM potentials. The proton and neutron potentials used in the calculations were consistent with the Lane model.

To test further the validity of the Lane model for proton and neutron scattering for these high Z nuclei, we have performed a CCOM calculation (not shown in the present work) for the elastic and inelastic proton measurements [14] at 26 MeV, with proton potentials derived from the neutron sets given by Ohio [1] and LASL [8]. The calculations, carried out with potentials calculated for an equivalent energy of $\sim$7 MeV ($E = E_p - \Delta_C$), did a rather poor job in fitting the data. By recalculating the magnitude of the imaginary potentials, without the Coulomb correction term as suggested by Rapaport [24], the agreement with the

measurements improves noticably, but is yet poorer than the one obtained with the proton potentials of the Menet set. Further calculations are in progress to determine if the CCOM calculations with the imaginary potentials, obtained for an "intermediate energy" between the 7 and 26 MeV (equivalent to assuming that Coulomb correction term in the absorbing part of the potential is only a fraction of the Coulomb displacement energy) could result in better agreement with the data. A better understanding of the energy dependence of the imaginary part of the optical potential may be required to answer this question definitively.

ACKNOWLEDGMENTS

Work performed under the auspices of the U.S. Department of Energy by Lawrence Livermore Laboratory under contract no. W-7405-ENG-48.

REFERENCES

1. J. Rapaport, W. Kulkarni, R. W. Finlay, Nucl. Phys. 330, 15 (1979) (see other reference in this paper).

2. S. Elkadi, A. Beyerte, C. Gould, A. McDermott, R. Pedroni, P. Thambidurai, C. E. Nelson, F. O. Purser, W. Seagondollar and R. L. Walter, BAPS 24, 866 (1979).

3. J. Lachkar, Proceedings of the conference on Neutron Phys. and Nucl. Data, Harwell, Sept. 1978, pp 136-155.

4. G. H. R. Kegel et al., Univ. of Lowell, Reports to the DOE Nuclear Data Comm. April 1978, BNL-NCS 24273.

5. D. Wilmore and P. E. Hodgson, Nucl. Phyd. 55, 673 (1964).

6. L. Rosen, J. G. Beery, A. S. Goldhaber and E. H. Auerbach, Ann. Phys. 34, 96 (1965).

7. F. D. Becchetti and G. W. Greenlees, Phys. Rev. 182, 1190 (1969).

8. D. G. Madland and P. G. Young, Proceedings of the Conference on Neutron Phys. and Nucl. Data, Harwell, Sept. 1979, pp 349-354.

9. J. D. Anderson and H. F. Lutz, UCRL-14955 (1966).

10. J. D. Carlson, D. A. Lind and C. D. Zafiratos, Phys. Rev. Lett. 30, 99 (1973).

11. D. M. Patterson, R. R. Doering and Aaron Galonsky, Nucl. Phys. A263, 261 (1976).

12. A. M. Lane, Phys. Rev. Lett. 8, 171, (1962); Nucl. Phys. 35, 676 (1962).

13. S. D. Schery, D. A. Lind, H. W. Fielding and C. S. Zafiratos, Nucl. Phys. A 234, 109 (1974).

14. L. F. Hansen, I. D. Proctor, D. W. Heikkinen and V. A. Madsen, BAPS 23, 927, (1978). A complete text has been written for publication in the Phys. Rev.

15. R. Batchelor, W. B. Gilboy and J. H. Towle, Nucl. Phys. 65, 236 (1965).

16. W. E. Kinney and F. G. Perey, ORNL-4804, UC-79d.

17. J. C. Davis, J. D. Anderson, E. K. Freytag and D. R. Rawles, Trans. Nucl. Sci. 20, 213 (1973).

18. T. Tamura, Rev. of Mod. Phys. 37, 679 (1965).

19. M. J. Stomp, F. A. Schmittroth and V. A. Madsen, USAEC Technical Report, Contract No. AT(45-1)-222 (unpublished).

20. J. J. H. Menet, E. E. Gross, J. J. Malanify, and A. Tucker, Phys. Rev. C4, 1114 (1971).

21. C. H. King, J. E. Finck, G. M. Crawley, J. A. Nolen, Jr., and R. M. Ronningen, Phys. Rev. C 20, 2084 (1979).

22. J. M. Moss, Y. D. Terrien, R. M. Lombard, C. Brassard, and J. M. Loiseaux, Phys. Rev. Lett. 26, 1488 (1971).

23. C. E. Bemis, Jr., F. K. McGowan, J. L. C. Ford, Jr., W. T. Milner, P. H. Stelson and R. L. Robinson, Phys. Rev. C 8, 1466 (1973).

24. J. Rapaport, private communication.

TABLE I

Proton Global Potentials for $10 \leqslant E_p \leqslant 100$

Parameters	Bechetti-Greenlees	Menet et al.
V [MeV]	$54.0-0.32E+0.4Z/A^{1/3}+24\xi$	$49.9-0.22E+0.4Z/A^{1/3}+26.4\xi$
W_V [MeV]	$0.22E-2.7$	$1.2+0.09E$
W_D [MeV]	$11.8-0.25E+12\xi$	$4.2-0.05E+15.5\xi$
V_{SO}[MeV]	6.20	6.04
r_R	1.17	1.16
a_R	0.75	0.75
r_I	1.32	1.37
a_I	$0.51+0.7\xi$	$0.74-0.008E+1.0\xi$
r_{SO}	1.01	1.064
a_{SO}	0.75	0.78
r_C	1.25	1.25

TABLE II

Deformation Parameters Used in the CC Calculations

(A calculation of the multipole moments of the potential distribution are given in Ref. 14.)

	^{232}Th	^{238}U
β_2	0.215	0.220
β_4	0.060	0.045
β_6	0	-0.010

TABLE III

Target	Calculation [mb]				Measurement [mb]
	σ_{0^+}	σ_{2^+}	σ_{4^+}	$\sum_{0^+}^{4^+}$	
^{232}Th	3.24	3.03	0.40	6.67[a]	6.48 ± 0.65
	3.55	3.13	0.44	7.12[b]	
^{238}U	2.90	2.70	0.54	6.14[a]	
	3.36	3.16	0.69	7.20[b]	6.36 ± 0.64
	2.50	2.54	0.51	5.55[c]	

a) The neutron potentials have been derived from Menet et al (see text).
b) The neutron potentials are from Ref. 8.
c) The neutron potentials are from Ref. 1.

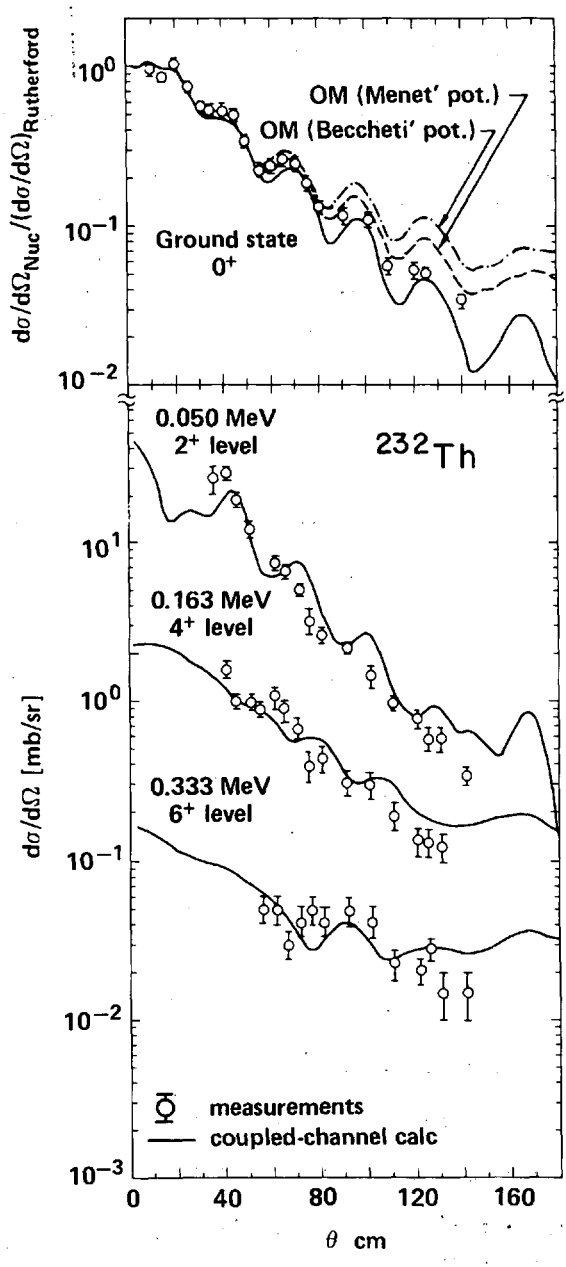

Figure 1. Measurements and coupled-channel calculations for 26-MeV protons scattered from ^{232}Th (Ref. 14).

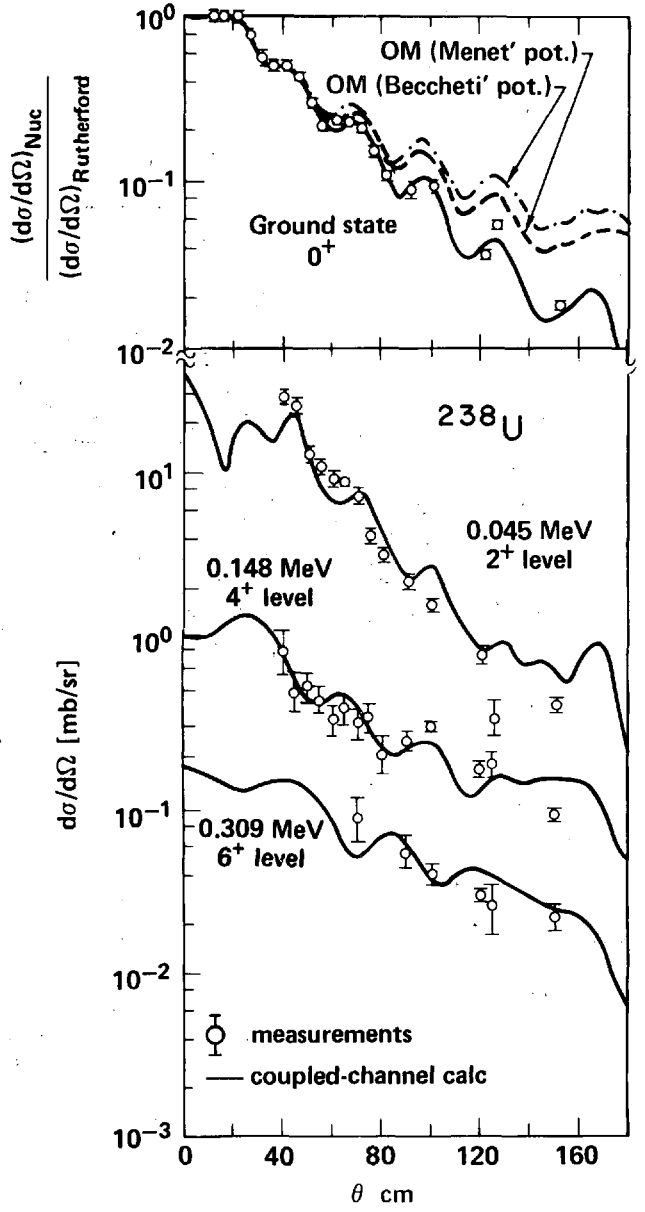

Figure 2. Measurements and coupled-channel calculations for 26-MeV protons scattered from ^{238}U (Ref. 14).

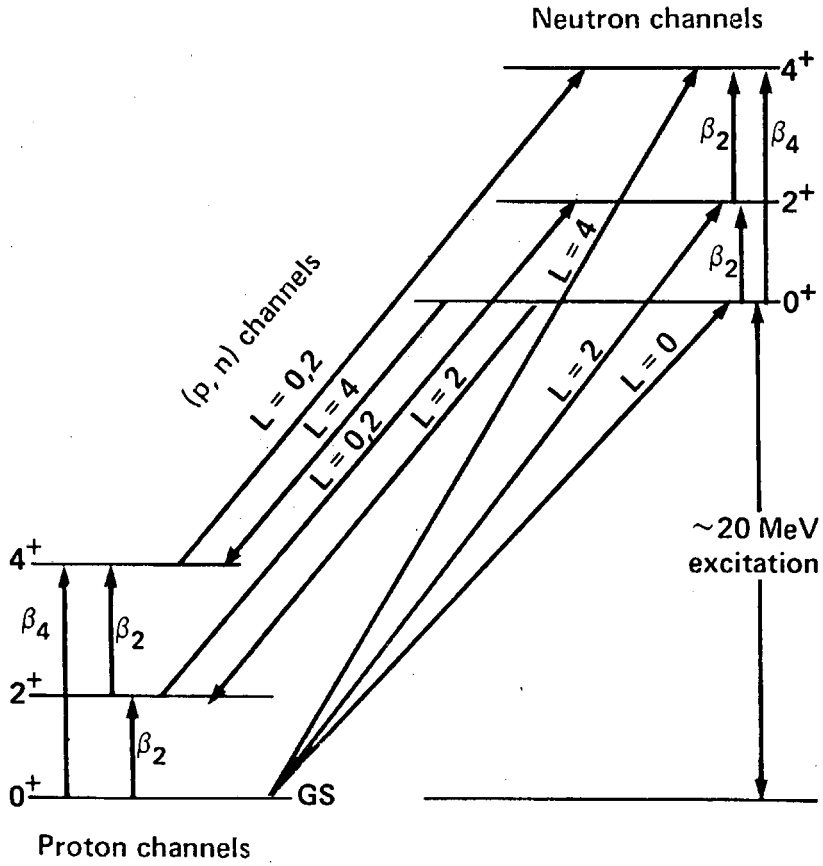

Figure 3. Coupling scheme used in the CC calculations for the proton scattering and charge exchange reactions from ^{232}Th and ^{238}U.

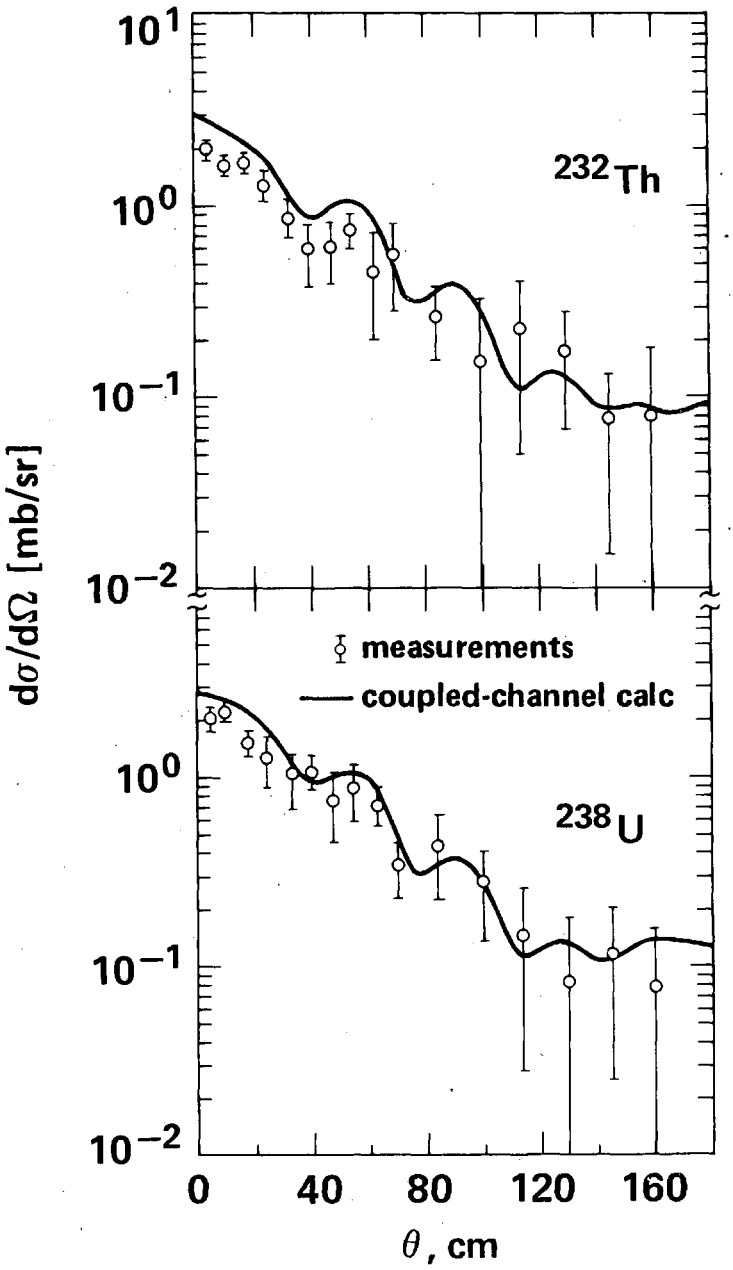

Figure 4. Comparison between the measurements and CC calculations for the (p,n) IAS reaction in ^{232}Th and ^{238}U at 26 MeV. The neutron potentials are those obtained from the consistent Lane analysis of the proton scattering and (p,n) ISA measurements.

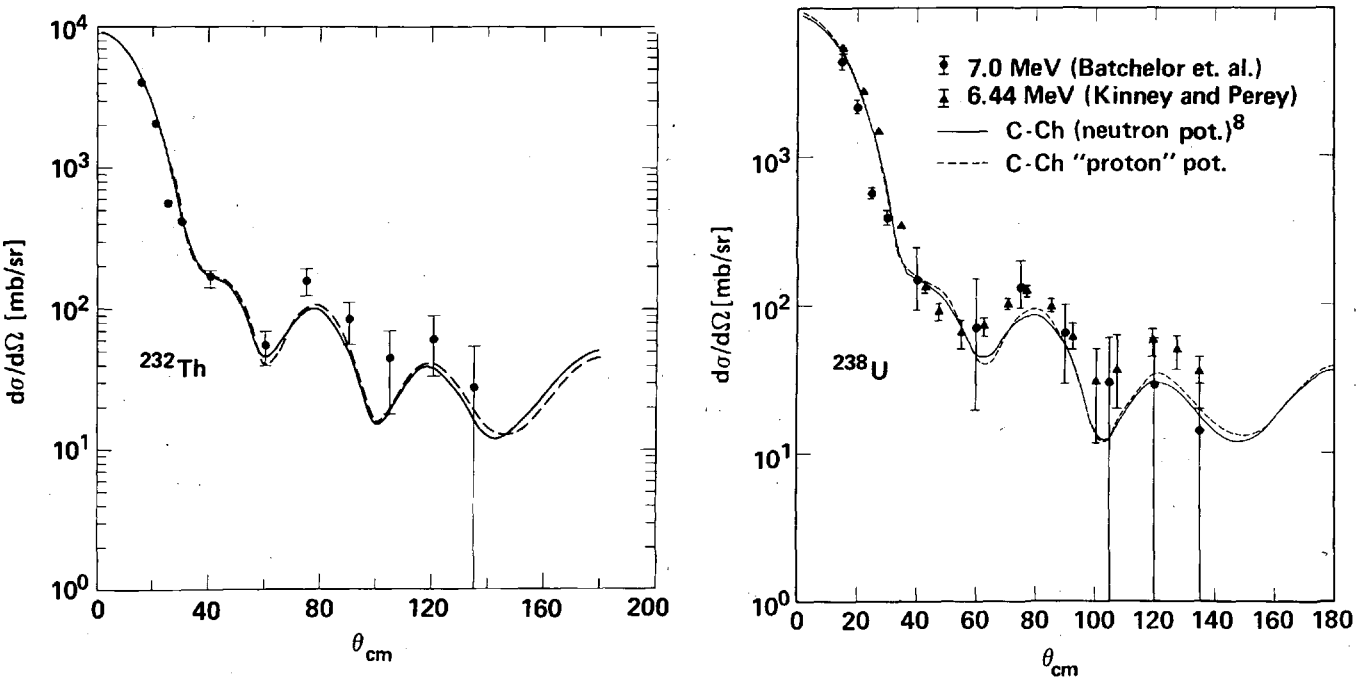

Figure 5. Comparison between the measurements and CC calculation for the (p,n) IAS reaction in ^{232}Th and ^{238}U at 27 MeV. ---- neutron potentials derived from the (p,p) and (p,n) IAS data. —— neutron potentials from Ref. 8.

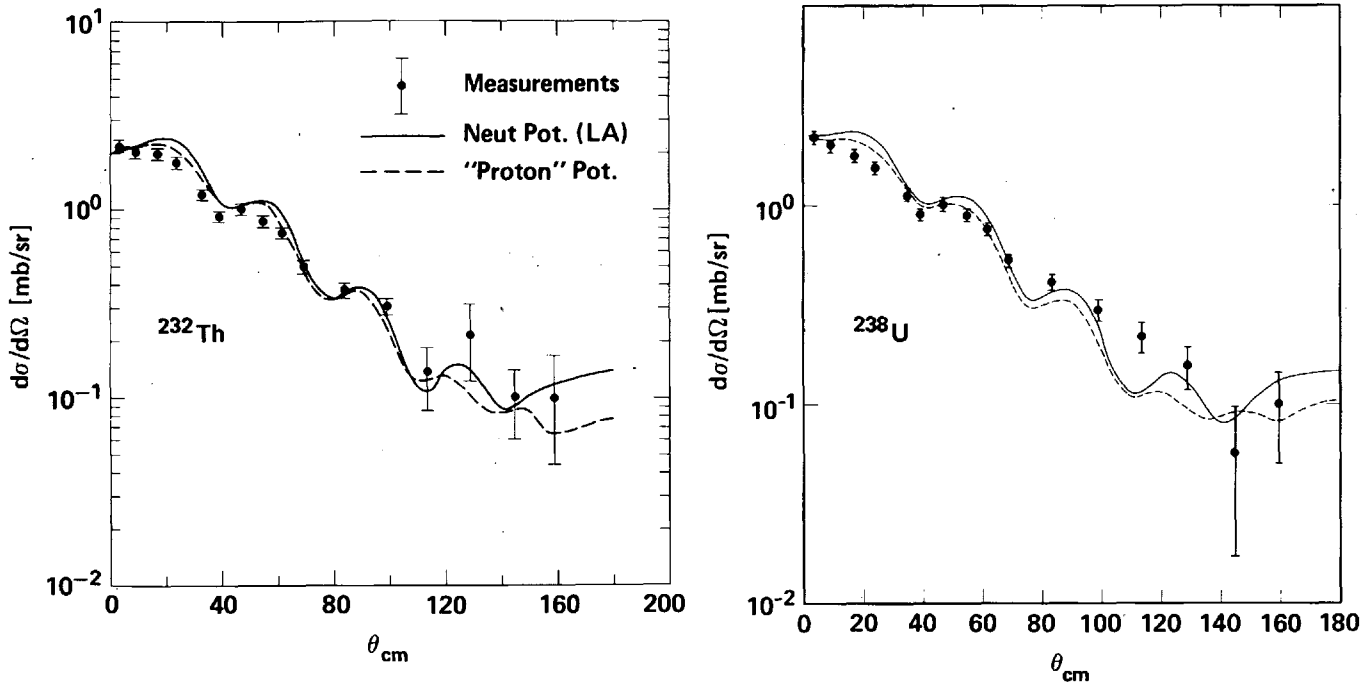

Figure 6. CC calculations of the neutron scattering for ^{232}Th and ^{238}U at 7 MeV. ---- neutron potentials derived from the (p,p) and (p,n) IAS data. ——— neutron potentials from Ref. 8. The measurements are from Refs. 15 and 16.

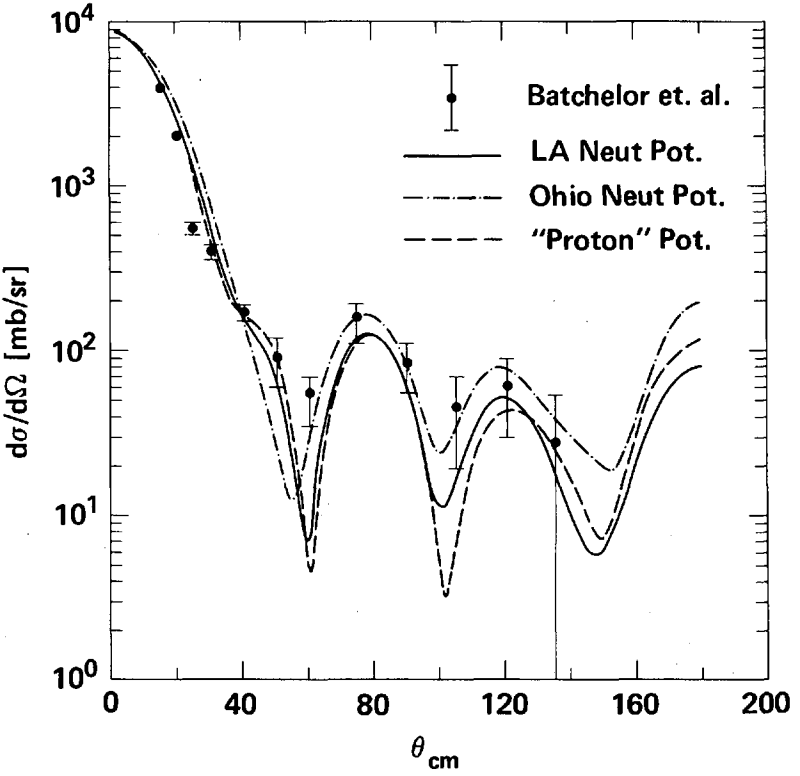

Figure 7. Spherical OM calculations for the neutron elastic scattering from ^{232}Th and ^{238}U at 7 MeV. ---- neutron potentials derived from the (p,p) and (p,n) IAS data. -.-.-. neutron potentials from Ref. 1. —— neutron potentials from Ref. 8. Measurements from Ref. 15.

MEASURED AND EVALUATED BISMUTH CROSS SECTIONS FOR FUSION-FISSION HYBRID REACTORS*+

A. Smith, P. T. Guenther and D. L. Smith

Argonne National Laboratory
Argonne, Illinois 60439, U.S.A.

and

R. J. Howerton

Lawrence Livermore Laboratory
Livermore, California 94550, U.S.A.

ABSTRACT

A comprehensive evaluated nuclear data file for elemental bismuth is presented in the ENDF format. This file is particularly tailored to the needs of the fusion-fission hybrid designer. The file is based upon the present measurements and model, together with those previously reported in the literature. The measured neutron total cross sections extend from 1.2-4.5 MeV with accuracies of ≈1%. Neutron-differential-elastic-scattering cross sections are measured from 1.5-4.0 MeV at energy intervals of ≤0.2 MeV over the angular range 20-160 deg. Concurrently, differential cross sections for the inelastic-neutron excitation of states at 895±15, 1606±14, 2590±15, 2762±29, 3022±21 and 3144±15 keV are determined. The experimental results are used to develop an optical-statistical model descriptive of the measured values and forming a foundation for the evaluation.

INTRODUCTION

It has been suggested that the fusion-fission hybrid concept represents a nuclear-energy system of considerable potential [2].

---

*A detailed description of this work including a numerical listing of the file is given in Ref. 1.

+This work supported by the U.S. Department of Energy.

One aspect of the strategy of such systems is the production of fissile fuel for subsequent burning in LWR or other conventional fission reactors. In this concept the hybrid itself is largely free of fission products with their attendent problems while, at the same time, it provides a rich source of fissile material. With this concept neutron economy is essential and means to multiply the intensity of the primary fusion-neutron source are sought. It has been suggested that one alternative is a bismuth blanket about the primary fusion source as the very large bismuth (n;2n) cross section provides an effective "eta" approaching that of a fissionable multiplier [3]. In addition, bismuth and its alloys have attractive low-melting points and heat-transfer properties.

The above concepts have not been widely examined due to the unavailability of a generally-accepted bismuth evaluated data file for use in neutronic calculations. The provision of such a file is impeded by the sparsity of microscopic nuclear data upon which to base it. The present work was undertaken with the objective of providing the requisite comprehensive evaluated data file in the widely-used ENDF format. As a part of this effort, basic microscopic nuclear-data measurements and associated interpretations were undertaken in order to strengthen the essential physical foundation. Subsequent portions of this paper outline the experimental and analytical portions of this work and the derivation of the evaluated file. A detailed discussion is given in Ref. 1.

EXPERIMENTAL METHODS

The measurement samples were machined into right circular cylinders from ingots of chemically pure elemental bismuth. Two transmission samples were used, each having a diameter of 2.5 cm. The lengths were 2 cm and 4 cm. Neutrons passed through the samples in the axial direction. The scattering samples were 2 cm in diameter and 2 cm long with neutrons incident upon the lateral surface.

The neutron total cross sections were deduced from the measured transmissions of approximately monoenergetic neutrons through the measurement samples in a conventional manner. Concurrent measurements of the neutron total cross sections of elemental carbon assured the fidelity of the measurement system. The details of the method and the particular apparatus have been described extensively elsewhere [1].

The neutron scattering measurements were made using the pulsed-beam time-of-flight technique and the 10-angle scattering apparatus at the Argonne Fast Neutron Generator. Scattered-neutron flight paths were 5.0 to 5.5 m. Relative sensitivities of the hydrogenous neutron detectors were determined by observation of neutrons emitted at the spontaneous fission of ^{252}Cf [4]. The normalization of the relative detector sensitivities was determined by the observation of neutrons scattered from hydrogen in a polyethylene sample. Thus all of the measured neutron-scattering

cross sections were determined relative to the well known H(n,n) cross sections [5]. Concurrent with the bismuth measurements, carbon-scattering cross sections were determined in order to verify the performance of the measurement system. The experimental results were corrected for perturbations due to beam attenuation, multiple events and the angular resolution of the apparatus using a combination of monte-carlo and analytical computational techniques.

EXPERIMENTAL RESULTS

Neutron Total Cross Sections

The measurements extended from ≈1.2 to 4.5 MeV in steps of ≲50 keV. Incident-neutron energy resolutions were 35-50 keV. The measurements were made in a redundent manner with repeated sweeps over the experimental energy range using the two measurement samples outlined above. The statistical accuracies of the individual measured values were in the range of 1-3%. Systematic uncertainties are believed to be much smaller. The results were averaged over intervals of the 100 keV to obtain the final results shown in Fig. 1.

The present measured values are in good agreement with the previously reported results of Refs. 6-9 as illustrated by the comparisons in Fig. 1. The differences between equivalent averages constructed from the various data sets is ≲2% throughout the range of the present experiment.

Neutron Elastic-scattering Cross Sections

Data, measured over the incident-energy range ≈1.5 to 4.0 MeV, were sorted into incident-energy intervals of ≲100 keV and combined to obtain composite angular distributions at the mean energy of the sorting interval. This procedure assumed that the cross sections did not vary significantly over the 100 keV intervals. The assumption is very good at the higher measured energies but somewhat less suitable at the lowest measured energies where fluctuations are clearly evident in the total-neutron cross section (Fig. 1). The incident-neutron resolutions varied from ≈20 to 50 keV and the scattered neutron resolutions were sufficient to clearly distinguish the elastic-neutron group from all known inelastic-neutron components. The individual measurements involved the concurrent determination of ten or twenty differential values distributed over the angular range ≈20 to 160 deg. The relative scattering angles were known to ±0.5 deg and the absolute angular scale was determined to ≈1.0 deg. The accuracies of the individual differential values varied depending upon the care taken during the particular measurement. In the best cases the differential-cross-section uncertainties were ≈5% and in the poor cases ≈10%. A measure of the validity of these uncertainties was the consistency

of the results obtained over a several-year period with various experimental configurations.

The experimental results are summarized in Fig. 2. In some of the lower-energy cases there appeared to be systematic differences between distributions obtained at widely separated times and subsequently combined to form the composite distributions of Fig. 2. These differences could easily be expected from the fluctuations evident in the neutron total cross sections. Even so, the results are generally consistent to well within the respective uncertainties. The angle-integrated neutron elastic-scattering cross sections were obtained from fitting an eight-order Legendre-polynomial series by least-squares to the measured differential values. The resulting angle-integrated cross sections are believed known to ≈5%. They were consistent with the measured neutron total and inelastic-scattering cross sections to well within the respective experimental uncertainties.

The present measured values can be compared with the few previously-reported results. The agreement with the relatively-extensive set of data reported by Tanaka et al. [10] is generally very good. The lower-energy (i.e. 1.5 MeV) values of the present work extrapolate very nicely to the somewhat lower-energy values ($\bar{E}$= 1.45 MeV) of Smith et al. [6]. There is good agreement with the single distributions of Beyster et al. [11], Gordov et al. [12], and Becker et al. [13]. The results of Pasechnik et al. [14], Popov [15], Brugger et al. [16] and Snowdon et al. [17] are not particularly consistent with those of the present work.

Neutron-inelastic-scattering Cross Sections

Differential-inelastic cross-section measurements were made over the scattered-neutron angular range of ≈20-160 deg. A total of six inelastically-scattered neutron groups was observed at a number of incident energies and scattering angles. The corresponding excitation energies were determined from the measured flight times, flight paths and incident neutron energies. Average excitation energies were determined from the individual measured values and the corresponding uncertainties defined as the RMS deviation of the individual values from the average. The resulting excitation energies are 895±15, 1606±14, 2590±15, 2762±29, 3022±21 and 3144±15 keV. A comparison of these measured values with the levels reported in the literature [18] indicated that the first two excitations corresponded to discrete levels while the remainder were the result of contributions from a number of previously reported levels.

All of the observed differential-inelastic-neutron distributions were essentially isotropic. The angle integrated inelastic-neutron cross sections corresponding to the various excitations were determined by least-square fitting the observed differential distributions with low-order legendre-polynomial expansions (e.g. with second-order expansions). The resulting angle-integrated cross sections are shown in Fig. 3. The respective uncertainties

were governed by the same factors applicable to the elastic-scattering measurements. In addition, the experimental resolution was not complete in those cases where the observed neutron group consisted of a number of closely-spaced components. In the best cases the uncertainties associated with the angle-integrated inelastic-scattering cross sections were in the 5-10% range with the larger uncertainties in those cases where the definition of the inelastically-scattered neutron groups was less suitable. Beyond the experimental uncertainties associated with the measurements there may be some residual effects from the physical fluctuations evident, for example, in high-resolution neutron total cross section measurements.

There are a few previously-reported experimental results that can be compared with the present experimental values. The present work extrapolates reasonably well to the lower-energy results of Smith et al. [6] and of Tanaka et al. [10] and to the higher-energy values of Weddell [19]. The present work is in relatively good agreement with the values of Degtyarev et al. [20] and, to a lesser extent, with the results of Cranberg and Levin [21]. The present results are not consistent with the results of Eliot et al. [22].

OPTICAL-STATISTICAL MODEL

A simple spherical model was assumed. This assumption is reasonably justified as ^{209}Bi consists of only one proton added to the doubly-closed shell at A=208. Throughout the energy range of the present experiments compound-nucleus processes were a consideration. These were calculated using the procedures of Moldauer [23]. In doing so the excitation of states to energies of $\approx$3.0 MeV was explicitly treated using the spin and parity assignments of Ref. 18. Where no explicit assignment was given, estimates were made. The excitation of higher-energy levels was treated as a statistical continuum following the concepts of Gilbert and Cameron [24]. The calculations were carried out using the computer program ABAREX-2 [23]. The choice of model parameters was entirely based upon χi-square fitting the measured differential-elastic-scattering distributions as described in Ref. 1. The resulting potential parameters are given in Table I. They are similar to those reported elsewhere in the literature. The potential provides a quantitative description of the measured differential elastic-scattering cross sections as illustrated in Fig. 2. There are some deviations between measured and calculated values at a few and, primarily, lower energies. This is not surprising as the total cross section shows fluctuating structure into the several MeV region that was not clearly averaged in the elastic-scattering measurements. The calculated neutron total cross sections agree with the measured values throughout the present experimental range to within $\lesssim$3%. The largest differences are in the region of 2.5 to 3.0 MeV where the calculated values are systematically lower

than the measured quantities by ≈3%. This is a peculiar energy region where the neutron total cross section, as observed in three entirely independent measurements displays an unusual and broad structure with a periodicity of several hundred keV as shown in Fig. 1. The present model cannot reproduce such structure and it is in the same energy region where the measured and calculated elastic-scattering distributions are somewhat different.

In view of the above, the present potential was accepted as an adequate basis for subsequent interpretations of neutron inelastic scattering and for the extrapolations and interpolations requisite to the comprehensive evaluation.

The calculation of neutron-inelastic-scattering cross sections using the above model was inhibited by a lack of knowledge of the spins and parities of the levels involved. Given this situation only the excitation of the first four observed groups was explicitly calculated and the higher energy excitations were lumped into the continuum contribution. The results of the calculations are compared with the measured values in Fig. 3. Generally the calculated results agree with the measured values to within at least 10-20% and in some cases the agreement is much better. Again, the incident energy region 2.5-3.0 MeV, that where the neutron total cross section is somewhat anomolous, tends to be a problem area. The excitation of the third group is somewhat over-predicted, possibly suggesting some uncertainty in the reported spins and parities of the underlying levels. However, the calculated inelastic-scattering cross sections were considered acceptable and suitable for subsequent use in the extrapolations requisite to the evaluation.

EVALUATION

Throughout this evaluation the emphasis was on an evaluated data file for high-energy (e.g. fusion-fission hybrid) applications. Therefore, while attention was given to low-energy resonance properties, they were not dealt with in great detail and, in particular, the resonance region is described by point-wise data rather than resonance parameters. Those particularly interested in resonance parameters should consult Ref. 25. The file is in the ENDF format and has been transmitted to the National Nuclear Data Center, Brookhaven National Laboratory.

Neutron Total Cross Sections

Below 100 keV the available good-resolution data is largely confined to the work of the Columbia Group, i.e. Singh et al. [26]. From 0.1 to 0.2 MeV the experimental data base consisted of the good resolution results of Singh et al. [25] and of Nichols et al. [27]. From 0.2 to 1.0 MeV the data base consisted of the high resolution results of Cierjacks et al. [7]. The evaluated neutron total cross sections from 1.0 to 20.0 MeV were based upon the

present results, those of Cierjacks et al. [7], of Carlson and Barschall [9] and of Foster and Glasgow. [8]. The final evaluated total cross sections are outlined in Fig. 4.

Neutron Elastic-scattering Cross Sections

For neutron energies of $\lesssim$3.0 MeV the elastic-scattering cross sections were dictated by the differences between evaluated neutron total cross sections and the non-elastic cross sections. At higher energies not all of the partial cross sections are well known and thus the evaluated elastic-scattering cross sections were based upon the predictions of the above model, slightly adjusted to bring exact agreement with the evaluated neutron total cross sections and to improve the agreement with the measured differential elastic-scattering distributions reported at higher energies.

Neutron Inelastic-scattering Cross Sections

The discrete neutron-evaluated-inelastic-scattering cross sections were based upon the present six observed neutron groups. The evaluation followed the eye-guides of Fig. 3 which are consistent with the experimental data base as outlined above. Model calculations were used to extrapolate the measured results from 4-5 MeV to 10 MeV where the individual excitation cross sections were assumed to be zero.

The magnitude of the continuum-inelastic-scattering component was derived from the difference between the measured neutron-total cross sections and the other partial cross sections (largely elastic scattering, (n;2n) and (n;3n) cross sections) with guidance from the systematics derived from the results of the LLL pulsed sphere measurements.

The relative magnitudes of the various inelastic components are indicated in Fig. 5.

Neutron Radiative-capture Cross Sections

A notable feature of the neutron interaction with bismuth is the generally very small radiative capture cross section. The thermal value is only 33 mb and the resonance integral 0.19 b.[25]. As a consequence of this fact, the lack of experimental resonance information, and the high-energy motivation of this evaluation, no attempt was made to give detailed capture resonance parameters. The small cross section values are approximated only with broad energy-averaged values. The evaluation follows the thermal value of Ref. 25 and assumes a 1/v behavior at low energies. This low-energy region is matched to the higher-energy experimental results as summarized in Ref. 28.

The (n;2n') Reaction

The present evaluation is based primarily on the experimental data of Frehaut and Mosinski [29] and Vesser et al. [30] (see Fig. 6). The evaluated 14 MeV cross section of Body and Csikai [31] is plotted on Fig. 6 and lies very close to our evaluated curve. Another weighted average of 14 MeV data, reported by Kondaiah [32] lies ~10% above our curve. Other reported results shown in Fig. 6 are described in Ref. 1.

The above reaction and the following (n;3n') reaction essentially dominate the non-elastic cross section above approximately 14 MeV. Using these two components, as independently evaluated in these two sections, an unusual "bump" would appear in the non-elastic cross section at about 17 MeV suggesting that the composite contributions of (n;2n') and (n;3n') cross sections are too large by about 10% over a several MeV region. Therefore the comprehensive evaluation renormalizes the individual evaluated (n;2n') and (n;3n') components downward by approximately 10% near 14 MeV so as to give a reasonably smooth non-elastic cross section. The source of the anomolous "bump" appears to be in the measured results of Ref. 30. A systematic error in that set of measurements of approximately 10% in this narrow energy region would easily account for the observed anomaly.

The (n;3n') Reaction

The (n;3n') reaction on ^{209}Bi leads to ^{207}Bi with a half life of 38 y and has a Q-value of -14.36 MeV. Nearly 100% of all ^{207}Bi decays produce a 0.570 MeV gamma ray; in fact, calibrated ^{207}Bi sources can be obtained from the U.S. National Bureau of Standards. Nevertheless, no activation data are available for this reaction. The only experimental data available are the values from Vesser et al. [30].

(n;X) Reactions

Elemental bismuth consists of only one quasi-stable isotope, ^{209}Bi ($t_{1/2} = 2 \times 10^{18}$Y). There are a number of neutron-induced charged-particle-emitting reactions that are energetically possible, over the neutron energy range of the present evaluation. Most of these reactions are uncertain but very probably of small cross section.

There are four reported (n,p) reaction cross sections for ^{209}Bi. All of these were measured at ~14 MeV. The weighted average of these data corresponds to 0.89 mb at 14.5 MeV. There are no data on bismuth at other energies; however, there are experimental data defining the excitation function for the $^{197}Au(n,p)^{197}Pt$ reaction. Since the mass and atomic number for gold are not far removed from bismuth, and the (n,p) reaction Q-values are similar, we decided to use the shape for gold from BNL-325 [28] and normalize it to our average 14.5 MeV point for

bismuth to provide an estimate of the excitation function for the $^{209}Bi(n,p)\ ^{209}Pb$ reaction up to ~20 MeV.

Some data from activation measurements of the (n',α) reaction are available for the region around 14 MeV. The (n;α) cross sections for heavy elements are known to be anomalously large when viewed from the point of view of the statistical theory of nuclear reactions. This effect is explained by the direct reaction mechanism. Shell effects are also clearly evident in systematic surveys of 14 MeV (n;α) reaction data. Our evaluation in this region is a weighted average of the activation data which gives 0.64 mb at 14.7 MeV.

From the compilations of Chatterjee [33] and JAERI-1252 [34], it is apparent that the (n;n',p) cross section is considerably < 1 mb in this mass region. For this reason, we make no attempt to provide an evaluation for this reaction.

Data on other (n;n',α) reactions for heavy nuclei, available from JAERI-1252 [34], are generally consistent with the present evaluation, though it must be kept in mind that there are pronounced shell effects which influence the Q-values and cross sections for this process.

Very few data are available on the (n;t), (n;^{3}He), (n;d), (n;n',d), (n;n',^{3}He) and (n;n',t) reactions for any elements let alone ^{209}Bi. In view of the limited available data on these exotic reactions, and the fact that the cross sections are small, we have not attempted to evaluate them and consider them to be negligible in the present work.

Photon-Production

For incident neutron energies less than the threshold for inelastic scattering the only photon producing process is the neutron capture reaction. For this lower energy range photon production was dealt with by using a multiplicity and spectrum as measured by Rasmussen et al. [35] The multiplicity was set to zero at 0.9 MeV. The photons produced by the capture reaction were subsumed into the (n,Xγ) process for incident neutron energies greater than 0.9 MeV.

For incident neutron energies equal to or greater than 0.9 MeV, the method of Perkins, Haight and Howerton [36] was used to calculate cross sections and spectra for the (n,Xγ) process. In the absence of detailed experimental data this method has the advantage of conserving energy on the average between secondary neutrons and photons.

ACKNOWLEDGEMENTS

The authors are indebted to a number of individuals at Lawrence Livermore Laboratory and Argonne National Laboratory for their contributions to various aspects of this work. The authors are particularly appreciative of the assistance provided by Dr. E. Pennington.

REFERENCES

1. A. SMITH et al., Argonne Natl. Lab. Report, ANL/NDM-51 (1980), in press.

2. Final Report of Ad-Hoc Experts Group on Fusion, J. Foster, Chairman, DOE Report, DOE/ER-0008 (1978).

3. Fusion-Fission Hybrid Study Summary Report, Argonne National Laboratory Report (1978), unpublished.

4. A. SMITH, P. GUENTHER and R. SJOBLOM, Nucl. Instr. and Methods, 140, 397(1977).

5. J. HOPKINS and G. BREIT, Nucl. Data, A9, 137(1971).

6. A. SMITH et al., Nucl. Sci. and Eng., 41, 63(1970).

7. S. CIERJACKS, et al., Kernforschungzentrum Karlsruhe Report, KFK-1000 (1968), as revised.

8. D. FOSTER and D. GLASGOW, Phys. Rev., C3, 576(1971).

9. A. CARLSON and H. BARSCHALL, Phys. Rev., 104, 1319(1956).

10. S. TANAKA et al., Nucl. Phys., 179, 513 (1972). This data and the present results appear consistent with those of M. A. Etemad, National Bureau of Standards Pub., NBS-425, Vol. II, 871(1975).

11. J. R. BEYSTER, M. WALT and W. SALMI, Phys. Rev., 104, 1319 (1956).

12. G. GORDOV, N. LEBEDEVA and V. MOROZOV, Doklady Akad Nauk (USSR) 158, 574(1964).

13. R. BECKER, W. GUIDON and G. SMITH, Nucl. Phys., 89, 154(1966).

14. M. Pasechnik et al., Inter. Conf. on Atoms for Peace, Geneva (1958) Vol. 15, United Nations Press.

15. V. POPOV, Atomnaya Energiya, 3, 498(1957).

16. H. BRUGGER et al., Helv. Phys. Acta, 28331 (1955).

17. S. C. SNOWDON and W. D. WHITEHEAD, Phys. Rev., 94, 1267(1954).

18. Nuclear Data Sheets for A = 209, M. J. Martin Compiler (1970).

19. J. B. WEDDELL, Phys. Rev., 104, 1069(1956).

20. YU. G. DEBTYAREV and A. PROTOPOPOV, Atomnaya Energiya, 23, 568(1967).

21. L. CRANBERG and J. LIVIN, Phys. Rev., 103, 343(1956).

22. E. ELIOT et al., Phys. Rev., 94, 144(1954).

23. P. A. MOLDAUER, Private Communication (1979).

24. A. GILBERT and A.G.W. CAMERON, Can. Jour. Phys., 43, 1446(1965).

25. Neutron Cross Sections, Vol - 1, S. Mughabghab and D. Garber, Brookhaven National Laboratory Report, BNL-325, 3rd. Ed., (1973).

26. U. N. SINGH, Phys. Rev., C13, 124(1976).

27. P. NICHOLS, E. BILPUCH and H. NEWSON, Ann. Phys., 8, 250(1959).

28. Neutron Cross Sections, Vol. 2, D. Garber and R. Kinsey, Brookhaven National Laboratory Report, BNL-355, 3rd Ed. (1973).

29. J. FREHAUT and G. MOSINSKI, Proc. Conf. on Nucl. Cross Sections and Tech., National Bureau of Standards Publication, NBS-425, 855(1975).

30. L. VEESER, E. ARTHUR and P. YOUNG, Phys. Rev., C16, 1792(1977), Also E. Arthur, Private Communication (1979).

31. Z. BODY and J. CSIKAI, Atom. Energy Rev., 11, 153(1973).

32. E. KONDAIAH, J. Phys. Ap. Math. Nucl. Gen., 7, 1457(1974).

33. A. CHATTERJEE, Nucleonics, 23, 112(1965).

34. "Table of Nuclear Reactions and Subsequent Radioactive Decays Induced by 14 MeV Neutrons," Japan Atomic Energy Research Institute Report, JAERI-1252, Ed. K. Yamamoto, (1977).

35. N. C. RASMUSSEN, et al., "Line and Continuum Gamma-Ray Yields from Thermal-Neutron Capture in 75 Elements," GA-10248 (1970).

36. S. T. PERKINS, R. C. HAIGHT, and R. J. HOWERTON, Nucl. Sci. and Eng., 57, 1(1975).

TABLE I.

Spherical Optical-Model Parameters

Real Potential[a]	
Strength (V)	43.296 MeV
Radius (R_o^V)[b]	1.300 F
Diffuseness (a^V)	0.58 F
VR_o^2	73.17 MeV · F^2
Imaginary Potential[c]	
Strength (W)	11.91 MeV
Radius (R_o^W)	1.320 F
Diffuseness (a^W)	0.20 F
Wa^W	2.382 MeV · F
Spin-orbit Potential[d]	
Strength (V_{so})	4.35 MeV

[a] Saxon form.

[b] All radii given in the form $R = R_o A^{1/3}$.

[c] Saxon derivative form.

[d] Thomas form.

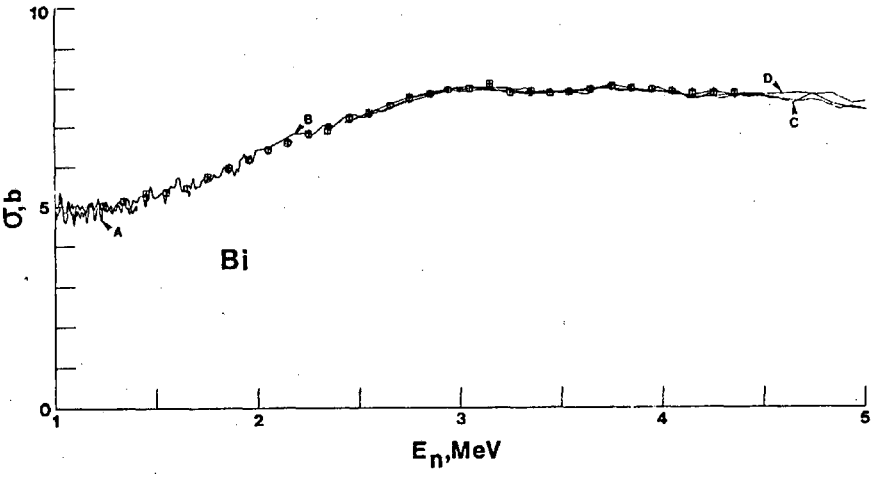

Fig. 1. Measured neutron total cross sections of elemental bismuth. The present results are indicated by circular and square data points. Curves indicate previously reported values as follows; A = Ref. 6, B = Ref. 7, C = Ref. 8 and D = Ref. 9.

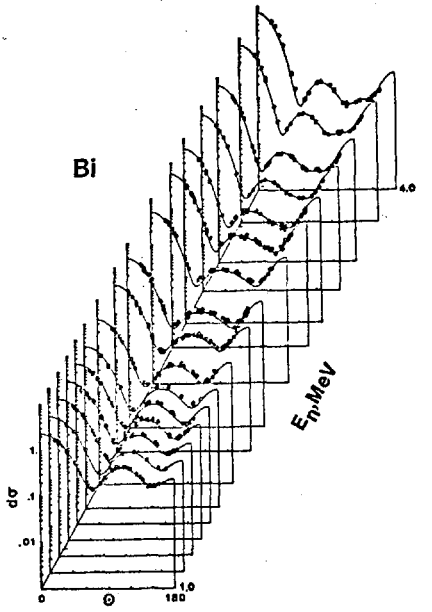

Fig. 2. Differential elastic-scattering cross sections of elemental bismuth. The present measured values are indicated by data points. Curves denote the results of model calculations as discussed in the text.

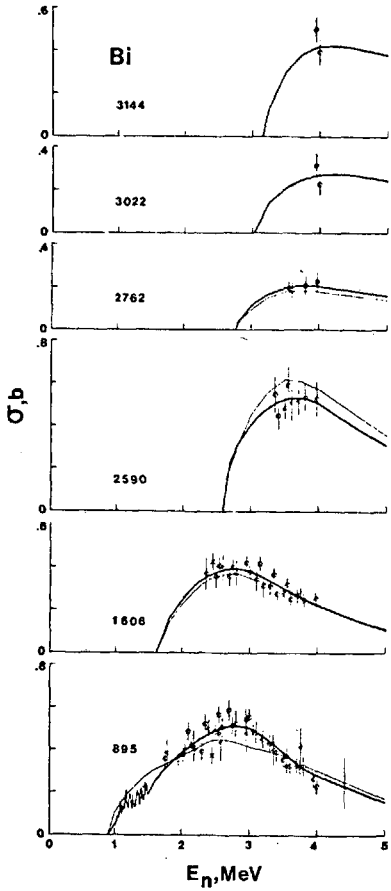

Fig. 3. Inelastic-neutron excitation cross sections of bismuth. The present experimental results are indicated by circular data points. The corresponding observed excitation energies are given in each section of the figure in keV. The heavy curves are "eye-guides" constructed through the available experimental information. The light curves indicate the result of model calculations as described in the text. Previously reported experimental values are denoted by symbols referenced as follows: D = Ref. 20, + = Ref. 19, X = Ref. 21, and ◇ = Ref. 10

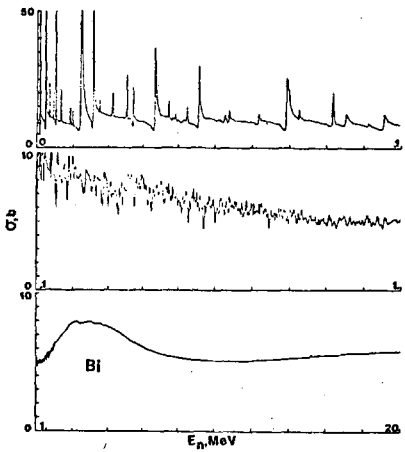

Fig. 4. Evaluated neutron total cross sections of elemental bismuth.

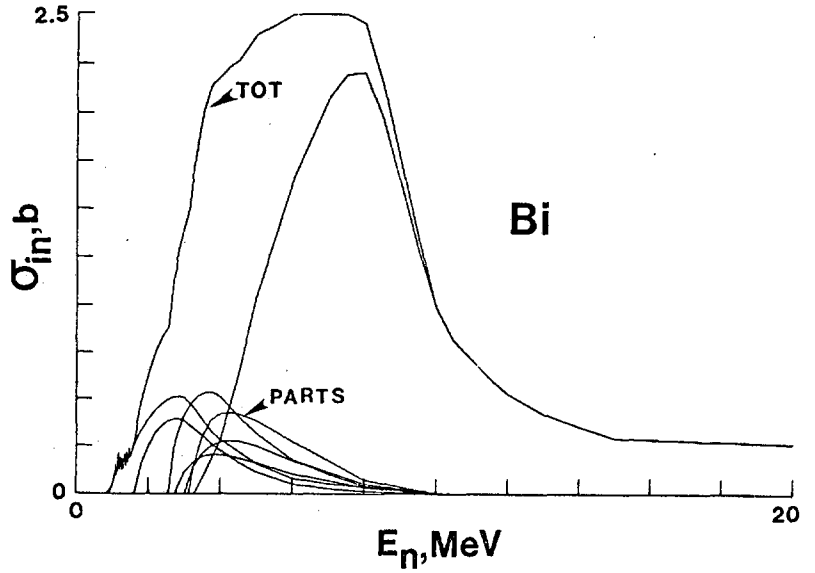

Fig. 5. Evaluated neutron-inelastic-scattering cross sections of elemental bismuth.

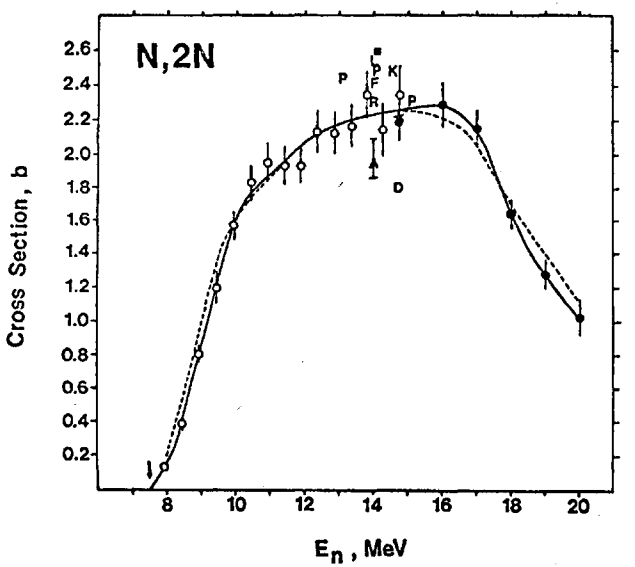

Fig. 6. Experimental, evaluated and calculated cross sections for the $^{209}Bi(n;2n')^{208}Bi$ reaction. Solid curve is present evaluation, dashed curve calculations of Ref. 30. Data symbols are defined in Ref. 1.

PREDICTION OF HEAVY ELEMENT FISSION BARRIER FEATURES FOR MULTIPLE CHANCE NEUTRON CROSS-SECTION CALCULATIONS

UCRL-84370

R. Y. Cusson*, W. M. Howard†
H. W. Meldner†, and P. Möller††

*Consultant to LLL, permanent address: Physics Dept., Duke University, Durham, NC 27706.

†University of California, Lawrence Livermore Laboratory, Livermore, CA 94550

††Present address: Dept. of Math. Physics, Lund University, Box 725, S-22007, Lund, Sweden.

ABSTRACT

A state of the art calculation of even, odd, and even-odd heavy neutron-rich element fission barriers and neutron binding energies is described. The range $76 \leq Z \leq 100$, $118 \leq N \leq 184$ is selected for applications to ICF burnup. Some techniques for exploring multi-dimensional parameter spaces on the computer are discussed. Contour maps of fission barriers and neutron binding energies are shown.

Heavy element production calculations via neutron capture processes in laser fusion pellets or underground thermonuclear explosions require extensive knowledge of the nuclear properties of a broad range of neutron-rich heavy elements. Such knowledge is also needed for the burnup of radioactive wastes in ICF pellets by a neutron spectrum centered near 14 MeV and extending to 20 MeV, a process which has recently been considered [1] for nuclear waste management.

For these highly neutron-rich nuclei, the neutron emission threshold decreases to a few MeV, so that up to fourth or higher chance fission

competition may be required, in the above bombarding energy range. These calculations use statistical theory methods as implemented in the TNG code of Fu.[2] One of the more important inputs for these codes is a set of consistent neutron binding energies and multiple barrier heights for the relevant elements of a chain.

We have calculated fission barriers and ground state masses for some 2000 elements with $76 \leq Z \leq 100$ and $118 \leq N \leq 184$ (for even, odd, and odd-even nuclei) using the well-known macroscopic- microscopic model. The single-particle energies and pairing correlations come from the modified oscillator potential while the droplet model supplies the macroscopic energy. The calculation closely follows the corresponding one discussed in References 3 and 4, where additional references can be found. The present effort includes a zero-point energy of about 0.5 MeV, ε_2, ε_3, ε_4, and ε_5 degrees of freedom and γ degrees of freedom when appropriate and to this extent represents the state of the art for this type of fission barrier modeling. This technique was found [3,4] to predict fission barriers in good agreement with the available data. Here, however, we must keep in mind that we are extending the calculation to a wide range of nuclei not available to ordinary experiment. Some caution will therefore be in order when interpreting the results of actinide burnup predictions.

One major uncertainty in this calculation of fission barriers and particle emission thresholds for neutron-rich heavy elements is the value of the surface asymmetry term in the expression for the macroscopic energy; that is, how rapidly the surface energy is reduced as a function of increasing neutron number. For the calculations reported here, we chose the droplet model for the macroscopic energy. A recent evaluation employing a "new macroscopic" model [5] finds that the surface energy is reduced much less rapidly as a function of increasing neutron number than predicted by the droplet model. This effect will mean that the fission thresholds may decrease less rapidly as a function of neutron number than our calculations suggest. A new calculation of fission barriers employing this macroscopic model is underway.

As in References 3,4, we first determine the saddle points and minima by considering symmetric elongation and necking coordinates only (ε_2 & ε_4). For $\varepsilon_2 \leq 0.65$ we next determine the decrease in the calculated fission barrier heights arising from the

mass-asymmetric (ε_3 & ε_5) deformations. In the lower region $0 \leq \varepsilon \leq 0.60$ the decrease of the (ε_2,ε_4) fission barriers comes mostly from the γ degree of freedom rather than the (ε_3, ε_5) ones; only the γ deformations are therefore considered there. Still, we see that for each nucleus three two-dimensional potential energy surfaces are calculated. Since thousands of nuclei have been considered, it was necessary to develop computer codes using novel techniques for finding saddle points and minima and for merging the results from the three surfaces into a single one-dimensional fission barrier curve. These codes are now briefly described.

The minima and saddle points are to be determined from a 10 x 10 table containing energies vs. ε_2 and ε_4. A fine grid of about 50 x 120 points is generated by interpolation of the starting table. At each point on the grid one looks at the eight nearest neighbors to determine the sign of the change in the function from the chosen point and its neighbors. Some typical results are shown in Figure 1.

- - -	+ + +	+ + +	+ + +	+ + +
- 0 -	+ 0 +	+ 0 -	+ 0 -	+ 0 -
- - -	+ + +	+ - +	- + +	+ - -
(1a)	(1b)	(1c)	(1d)	(1e)

Figure 1

The configuration (1a) shows that our current point is a maximum point, while (1b) indicates a minimum. Next (1c) and (1d) represent saddle points while (1e) is a point on a slope and is therefore discarded. By identifying the patterns in this manner, all minima and saddle points were found. The required path consists of those points ordered by increasing value of ε_2, for the (ε_2, ε_4) case, and so on for the other surfaces.

To merge the results from the three surfaces we start with the fission path in the symmetric (ε_2, ε_4) surface. Then for $\varepsilon_2 \leq 0.60$ we next replace the symmetric peaks and minima by the corresponding saddles and minima in the (γ, (ε_3, $\varepsilon_4(\varepsilon_2)$)) plane, provided they have lower energy. For $\varepsilon_2 \leq 0.65$ a similar procedure for the (ε_3, ε_5 (ε_2,ε_4)),(ε_2, ε_4 (ε_2)) plane. Here the independent variables of the plane are ε_3 and ε_2; ε_4 depends on ε_2 as in the first

minimization and ε_5 is taken to be the one which minimizes the energy for the given ε_2 ε_4 pairs. When one adds details pertaining to file and table generation the merging programs represents some 1000 FORTRAN statements. Since our original aim was to find the minimal path in the five-dimensional ε_2, γ, ε_3, ε_4, ε_5 space, a task which could easily get out of hand, the present solution is relatively fast and simple to apply.

The results to be published [6] include two detailed tables. One table gives the fission barrier height, particle separation energies, and the beta decay energies for each nucleus. The second table gives the structure of the nuclear potential energy surface for each nucleus, including the energy and shape for each maximum and minimum. These results are summarized in Figures 2 and 3.

Figure 2 is a contour plot of the neutron separation energy for even nuclei in the region $76 \leq Z \leq 100$ and $140 \leq N \leq 184$. The number onthe contour line is the separation energy in MeV. One observes the standard decrease in neutron binding energy as a function of increasing neutron number. An unusual features of this plot is the presence of local maxima and minima near $Z = 96$ and $N = 166$, 170 and 176. These features are due to large ground state shape changes upon emission of a single neutron.

Figure 3 is a contour plot of the fission barrier height (including 0.5 MeV zero-point energy) for even nuclei in the region $76 \leq Z \leq 100$ and $140 \leq N \leq 184$. Again the distance between contours is 0.5 MeV and the integer contours are labelled in MeV. One observes the well-known "Bay of Pigs" features at $A \approx 92$ and $160 \leq N \leq 176$. This arises as a result of the changing Nilsson energy levels configurations in this region, and can have a profound effect on the production of heavy neutron-rich elements in a thermonuclear environment, as well as on burnup in ICF, thus underscoring the importance of understanding the detailed structure of these heavy elements.

Additional details and the full table of results will be published [6] in Atomic and Nuclear Data Tables. Multiple chance fission calculations using these tables are currently in progress.[7]

REFERENCES

1. H. W. Meldner and W. M. Howard, "Burning Nuclear Wastes in Fusion Reactors," UCRL-82969, Inter-

national Conference on Cross-Sections for Nuclear Technology, Oak Ridge, October 1979.

2. C. Y. Fu, Atomic and Nuclear Data Tables 17 (1976) 127; see also this conference.

3. P. Möller and J. R. Nix, Proc. Third IAEA Symp. on Physics and Chemistry of Fission, Rochester 1973 (IAEA, Vienna, 1974) Vol. 1, p. 103; R. Bengtson, R. Bolen, and S. E. Larsson, "Stability of Elements in the r-Process Region," Physics Scripta 10A (1974) 142.

4. S. E.Larsson and G. Leander, ibid p. 177.

5. P. Möller and J. R. Nix, "Calculation of Nuclear Masses with a Folded-Yukawa Single Particle Potential and a Yukawa-plus-Exponential Macroscopic Model," Los Alamos Preprint, LA-UR-80-813 (1980).

6. W. M. Howard and P. Möller, Atomic and Nuclear Data Tables (to be published).

7. R. Y. Cusson, H. W. Meldner, and W. M. Howard (to be published).

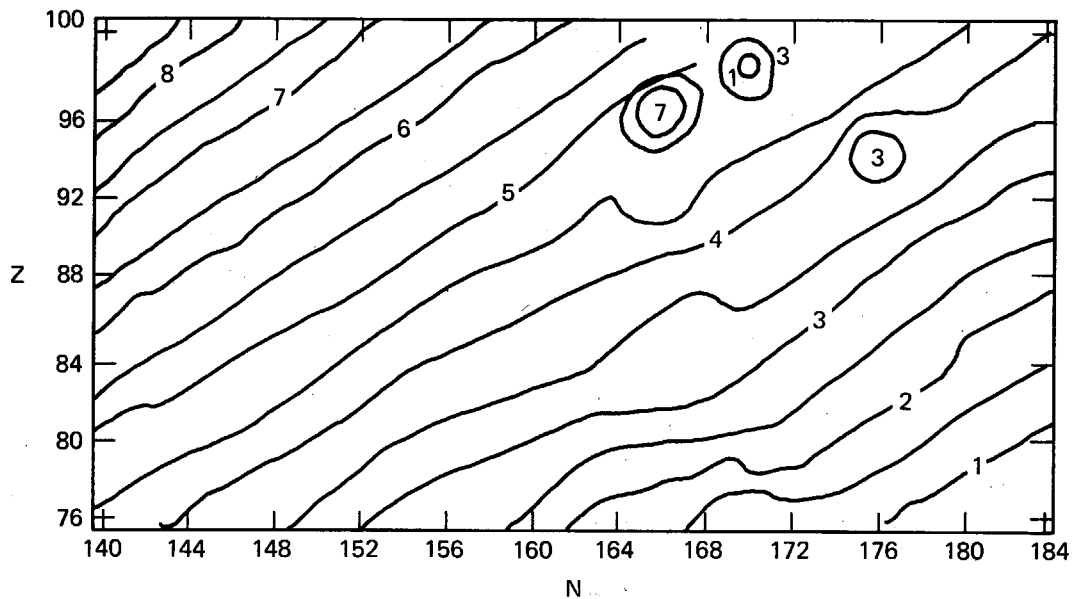

Figure 2. Contour Plot of the Neutron Separation Energy for Even Nuclei in the Region $76 \leq Z \leq 100$ and $140 \leq N \leq 184$

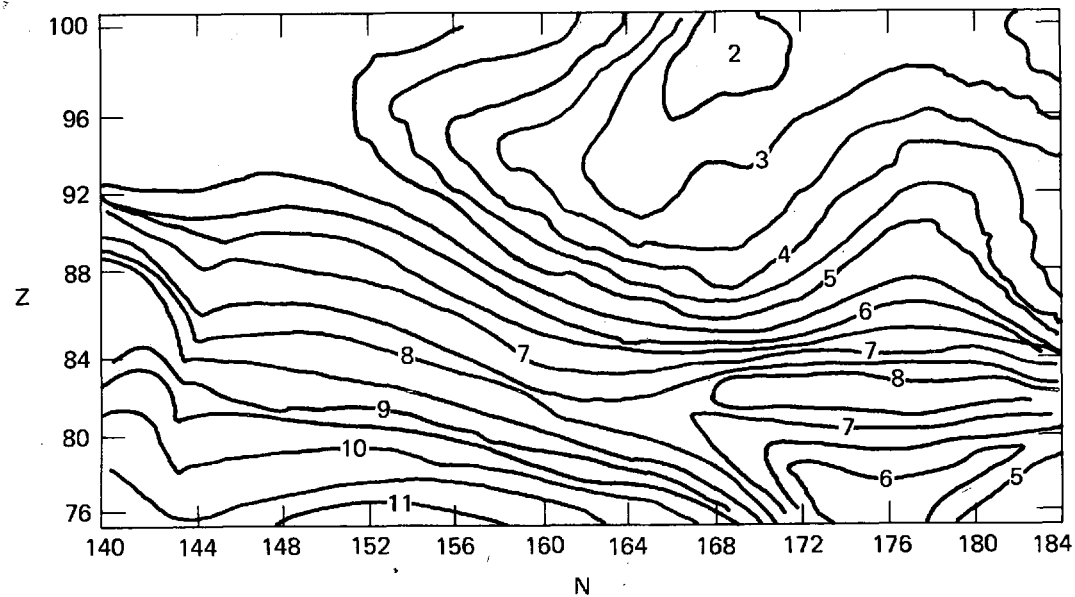

Figure 3. Contour Plot of the Fission Barrier Height (Including 0,5 MeV Zero-Point Energy) for Even Nuclei in the Region $76 \leq Z \leq 100$ and $140 \leq N \leq 184$.

CINDA INDEX.

Gail Joan Wyant.

Element S	A	Quantity	Energy (eV) Min	Max	Type	Documentation Ref	Vol	Page	Date	Lab	Comments
H	001	TOTAL XSECT	5.0+6	2.0+8	Expt	80BNL		301	780	LAS	Lisowski+TOF,TRNS.GRPH.CFD OTHS,ENDF
H	001	TOTAL XSECT	5.0+5	6.0+7	Revw	80BNL		277	780	ORL	Larson.2 EXPTS.GRPH.CFD OTHS.
H	002	DIFF ELASTIC	9.0+6	1.1+7	Revw	80BNL		389	780	OHO	Randers-Pehrson+ANAL P SPEC TBC.NDG.
HE	003	N,GAMMA	6.0+6	1.4+7	Expt	80BNL		259	780	TNL	Walter+ANGDISTS 90 DEG.NDG
HE	004	GAMMA,N	6.0+6	1.4+7	Expt	80BNL		259	780	TNL	Walter+FROM (N,G) MEAS.GRPH,CFD OTHS
LI	006	NEUT EMISSN	1.0+7		Revw	80BNL		215	780	LAS	Browne+REVIEW.REFS GVN.GRPH FOR 2ANG
LI	007	INELST GAMMA	1.0+5	2.0+7	Revw	80BNL		277	780	ORL	Larson.REVIEW.NDG.SEE ORNL REPORT.
LI	007	NEUT EMISSN		1.4+7	Revw	80BNL		215	780	LAS	Browne+REVIEW.REFS GVN.GRPH FOR 2ANG
LI	007	NEUT EMISSN	1.0+6	2.0+7	Revw	80BNL		277	780	ORL	Larson.REVIEW.NDG.SEE ORNL REPORT
LI	007	N,N PROTON	1.4+7	1.5+7	Expt	80BNL		245	780	LRL	Haight+PRELIMINARY MEAS.NDG.
LI	007	N,DEUTERON	1.4+7		Expt	80BNL		245	780	LRL	Haight+MEAS TBC.NDG.
LI	007	N,N TRITON	4.0+6	1.6+7	Revw	80BNL		215	780	LAS	Browne+REVIEW.REFS GVN.GRPH OF REFS.
LI	007	N,N TRITON	1.4+7		Expt	80BNL		245	780	LRL	Haight+MEAS TBC.NDG.
BE	009	DIFF ELASTIC	1.1+7	1.5+7	Revw	80BNL		259	780	TNL	Walter+LANE MDL CALCS.GRPHS.TBC.
BE	009	POLARIZATION	1.1+7	1.5+7	Revw	80BNL		259	780	TNL	Walter+LANE MDL CALCS.GRPHS.TBC.

Element S	A	Quantity	Energy (eV) Min	Max	Type	Documentation Ref	Vol	Page	Date	Lab	Comments
BE	009	POLARIZATION	7.0+6	1.7+7	Revw	80BNL		259	780	TNL	Walter+ANAL PWR DISTRIB.NDG.TBC.
BE	009	DIFF INELAST	1.5+7		Theo	80BNL		711	780	RCN	Gruppelaar+SPEC,ANGDIST.CALC VS EXPT
BE	009	NEUT EMISSN	1.0+7	1.4+7	Revw	80BNL		215	780	LAS	Browne+REVIEW.REFS GVN.NDG.
BE	009	NEUT EMISSN	1.5+7		Theo	80BNL		711	780	RCN	Gruppelaar+EMISSION SPEC CALC VS EXP
BE	009	N,PROTON	1.4+7		Expt	80BNL		245	780	LRL	Haight+MEAS TBC.NDG.
BE	009	N,TRITON	1.3+7	1.5+7	Expt	80BNL		413	780	TOH	Hino+6ES.0.478 MEV CS.TBL,SPEC,GRPHS
BE	009	N,ALPHA REAC	NDG		Expt	80BNL		289	780	AI	Kneff+CS MEAS TO BE ANALYZED.NDG.
BE	009	N,ALPHA REAC	1.4+7		Expt	80BNL		245	780	LRL	Haight+MEAS TBC.NDG.
B		N,N PROTON	1.4+7		Expt	80BNL		245	780	LRL	Haight+MEAS TBC.NDG.
B	010	DIFF ELASTIC	8.0+6	1.4+7	Revw	80BNL		259	780	TNL	Walter+GRPH.EXPT MEAS CFD OPTMDL.
B	010	NONEL GAMMA	5.0+5	1.4+7	Revw	80BNL		215	780	LAS	Browne+REVIEW.REFS GVN.NDG.
B	010	NEUT EMISSN	1.0+7	1.4+7	Revw	80BNL		215	780	LAS	Browne+REVIEW.REFS GVN.NDG.
B	010	N,ALPHA REAC	NDG		Expt	80BNL		289	780	AI	Kneff+CS MEAS TO BE ANALYZED.NDG.
B	011	DIFF ELASTIC	9.0+6	1.4+7	Revw	80BNL		259	780	TNL	Walter+GRPH.EXPT MEAS CFD OPTMDL.TBC
B	011	NONEL GAMMA	7.0+6	1.4+7	Revw	80BNL		215	780	LAS	Browne+REVIEW.REFS GVN.NDG.

Element S	A	Quantity	Energy (eV) Min	Max	Type	Documentation Ref	Vol	Page	Date	Lab	Comments
B	011	NEUT EMISSN	1.0+7	1.4+7	Revw	80BNL		215	780	LAS	Browne+REVIEW.REFS GVN.NDG.
B	011	N,PROTON	1.4+7		Expt	80BNL		245	780	LRL	Haight+MEAS TBC.NDG.
B	011	N,DEUTERON	1.4+7		Expt	80BNL		245	780	LRL	Haight+MEAS TBC.NDG.
B	011	N,ALPHA REAC	NDG		Expt	80BNL		289	780	AI	Kneff+CS MEAS TO BE ANALYZED.NDG.
B	011	N,ALPHA REAC	1.4+7		Expt	80BNL		245	780	LRL	Haight+MEAS TBC.NDG.
C	012	TOTAL XSECT	5.0+7		Expt	80BNL		313	780	DAV	Zanelli+TOF,TRNS.50.4 MEV CS.
C	012	TOTAL XSECT	1.0+7	5.0+7	Revw	80BNL		215	780	LAS	Browne+REVIEW.MEAS DO NOT AGREE.GRPH
C	012	TOTAL XSECT	5.0+6	2.0+8	Expt	80BNL		301	780	LAS	Lisowski+TOF,TRNS.GRPH.CFD OTHS,ENDF
C	012	TOTAL XSECT	5.0+5	8.0+7	Revw	80BNL		277	780	ORL	Larson.ORELA.TRNS AT 40 MEV GVN.
C	012	DIFF ELASTIC	4.0+7		Revw	80BNL		215	780	LAS	Browne+REVIEW.PRELIM MEAS.NDG.
C	012	DIFF ELASTIC	4.0+7		Revw	80BNL		375	780	OHO	Finlay+STATUS SINCE MAY 77.REFS GVN
C	012	POLARIZATION	7.0+6	1.7+7	Revw	80BNL		259	780	TNL	Walter+ANAL PWR DISTRIB.NDG.TBC.
C	012	DIFF INELAST	1.5+7		Theo	80BNL		711	780	RCN	Gruppelaar+SPEC,ANGDIST.CALC VS EXPT
C	012	NONELASTIC	4.0+7	5.0+7	Expt	80BNL		313	780	DAV	Zanelli+2ES.TRANS.GRPH.CFD OPTMDL.
C	012	NONELASTIC	4.0+7	5.0+7	Revw	80BNL		215	780	LAS	Browne+REVIEW.NDG.GT 15PC PRECISION

Element S	A	Quantity	Energy (eV) Min	Max	Type	Documentation Ref	Vol	Page	Date	Lab	Comments
C	012	INELST GAMMA	1.0+5	2.0+7	Revw	80BNL		277	780	ORL	Larson.REVIEW.NDG.SEE ORNL REPORT.
C	012	INELST GAMMA	1.3+7	1.5+7	Expt	80BNL		413	780	TOH	Hino+6ES.4.43 MEV CS.TBL,SPEC,GRPHS
C	012	NEUT EMISSN	1.4+7		Revw	80BNL		215	780	LAS	Browne+REVIEW.REFS GVN.NDG.
C	012	NEUT EMISSN	1.5+7		Theo	80BNL		711	780	RCN	Gruppelaar+EMISSION SPEC CALC VS EXP
C	012	N,PROTON	2.7+7	6.1+7	Expt	80BNL		331	780	DAV	Subramanian+3ES.DIF.ANGINTEG CFD MDL
C	012	N,PROTON	1.4+7	1.5+7	Expt	80BNL		245	780	LRL	Haight+PRELIMINARY MEAS.NDG.
C	012	N,N PROTON	2.7+7	6.1+7	Expt	80BNL		331	780	DAV	Subramanian+3ES.DIF.ANGINTEG CFD MDL
C	012	N,DEUTERON	2.7+7	6.1+7	Expt	80BNL		331	780	DAV	Subramanian+3ES.DIFF SPECTRA 39.7MEV
C	012	N,DEUTERON	1.4+7	1.5+7	Expt	80BNL		245	780	LRL	Haight+PRELIMINARY MEAS.NDG.TBC.
C	012	N,N DEUTERON	2.7+7	6.1+7	Expt	80BNL		331	780	DAV	Subramanian+3ES.DIFF SPECTRA 39.7MEV
C	012	N,TRITON	2.7+7	6.1+7	Expt	80BNL		331	780	DAV	Subramanian+3ES.DIFF SPECTRA 39.7MEV
C	012	N,N TRITON	2.7+7	6.1+7	Expt	80BNL		331	780	DAV	Subramanian+3ES.DIFF SPECTRA 39.7MEV
C	012	N,HE3 REACTN	2.7+7	6.1+7	Expt	80BNL		331	780	DAV	Subramanian+3ES.DIFF SPECTRA 39.7MEV
C	012	N,ALPHA REAC	NDG		Expt	80BNL		289	780	AI	Kneff+CS MEAS TO BE ANALYZED.NDG.
C	012	N,ALPHA REAC	2.7+7	6.1+7	Expt	80BNL		331	780	DAV	Subramanian+3ES.DIF.ANGINTEG CFD MDL

Element S	A	Quantity	Energy (eV) Min	Max	Type	Documentation Ref	Vol	Page	Date	Lab	Comments
C	012	N,ALPHA REAC	4.0+7		Revw	80BNL		215	780	LAS	Browne+REVIEW.INITIAL MEAS.NDG.TBC.
C	012	N,ALPHA REAC	9.0+6	4.0+7	Revw	80BNL		215	780	LAS	Browne+REVIEW.REFS GVN.NDG.
C	012	N,ALPHA REAC	1.4+7	1.5+7	Expt	80BNL		245	780	LRL	Haight+PRELIMINARY MEAS.NDG.TBC.
C	012	N,ALPHA REAC	9.3+6		Revw	80BNL		389	780	OHO	Randers-Pehrson+ANGDIST.NDG.TBC.
C	012	N,N ALPHA	1.1+7		Revw	80BNL		389	780	OHO	Randers-Pehrson+CONTINUUM GRPH.TBC.
C	013	N,GAMMA	6.0+6	1.4+7	Expt	80BNL		259	780	TNL	Walter+ANGDISTS 90 DEG.GRPH
N	014	N,GAMMA	6.0+6	1.4+7	Expt	80BNL		259	780	TNL	Walter+ANGDISTS 90 DEG.NDG
N	014	NONEL GAMMA	1.0+5	2.0+7	Revw	80BNL		277	780	ORL	Larson.REVIEW.NDG.SEE ORNL REPORT.
N	014	N,PROTON	2.7+7	6.1+7	Expt	80BNL		331	780	DAV	Subramanian+3ES.DIF.ANGINTEG CFD MDL
N	014	N,PROTON	1.4+7		Expt	80BNL		245	780	LRL	Haight+MEAS TBC.NDG.
N	014	N,N PROTON	2.7+7	6.1+7	Expt	80BNL		331	780	DAV	Subramanian+3ES.DIF.ANGINTEG CFD MDL
N	014	N,DEUTERON	2.7+7	6.1+7	Expt	80BNL		331	780	DAV	Subramanian+3ES.DIF SPEC AT 60.7MEV.
N	014	N,DEUTERON	1.4+7		Expt	80BNL		245	780	LRL	Haight+MEAS TBC.NDG.
N	014	N,N DEUTERON	2.7+7	6.1+7	Expt	80BNL		331	780	DAV	Subramanian+3ES.DIF SPEC AT 60.7MEV.
N	014	N,TRITON	2.7+7	6.1+7	Expt	80BNL		331	780	DAV	Subramanian+3ES.DIF SPEC AT 60.7MEV.

Element S	A	Quantity	Energy (eV) Min	Max	Type	Documentation Ref	Vol	Page	Date	Lab	Comments
N	014	N,N TRITON	2.7+7	6.1+7	Expt	80BNL	331	780	DAV		Subramanian+3ES.DIF SPEC AT 60.7MEV.
N	014	N,HE3 REACTN	2.7+7	6.1+7	Expt	80BNL	331	780	DAV		Subramanian+3ES.DIF SPEC AT 60.7MEV.
N	014	N,ALPHA REAC	2.7+7	6.1+7	Expt	80BNL	331	780	DAV		Subramanian+3ES.DIF.ANGINTEG CFD MDL
N	014	N,ALPHA REAC	1.4+7		Expt	80BNL	245	780	LRL		Haight+MEAS TBC.NDG.
0	016	TOTAL XSECT	1.0+7	5.0+7	Revw	80BNL	215	770	LAS		Browne+REVIEW.MEAS DO NOT AGREE.GRPH
0	016	TOTAL XSECT	5.0+5	6.0+7	Revw	80BNL	277	780	ORL		Larson.ORELA.TRNS AT 40 MEV GVN.
0	016	DIFF ELASTIC	2.0+7	2.6+7	Revw	80BNL	215	780	LAS		Browne+REVIEW.10-15PC PRECISION.NDG
0	016	DIFF ELASTIC	2.4+7		Revw	80BNL	375	780	OHO		Finlay+GRPH.MEAS CFD OPTMDL CALCS.
0	016	DIFF INELAST	2.4+7		Revw	80BNL	375	780	OHO		Finlay+GRPH.FIRST,SECOND EXC STATES.
0	016	NONELASTIC	4.0+7	5.0+7	Expt	80BNL	313	780	DAV		Zanelli+2ES.TRANS.GRPH.CFD OPTMDL.
0	016	NONELASTIC	4.0+7	5.0+7	Revw	80BNL	215	780	LAS		Browne+REVIEW.10-15PC PRECISION.NDG
0	016	NONEL GAMMA	1.0+5	2.0+7	Revw	80BNL	277	780	ORL		Larson.REVIEW.NDG.SEE ORNL REPORT.
0	016	N,PROTON	2.7+7	6.1+7	Expt	80BNL	331	780	DAV		Subramanian+3ES.DIF.ANGINTEG CFD MDL
0	016	N,PROTON	1.4+7		Expt	80BNL	245	780	LRL		Haight+MEAS TBC.NDG.
0	016	N,DEUTERON	2.7+7	6.1+7	Expt	80BNL	331	780	DAV		Subramanian+3ES.DIF SPEC AT 60.7MEV.

Element S	A	Quantity	Energy (eV) Min	Max	Type	Documentation Ref	Vol	Page	Date	Lab	Comments
0	016	N,DEUTERON	1.4+7		Expt	80BNL		245	780	LRL	Haight+MEAS TBC.NDG.
0	016	N,TRITON	2.7+7	6.1+7	Expt	80BNL		331	780	DAV	Subramanian+3ES.DIF SPEC AT 60.7MEV.
0	016	N,HE3 REACTN	2.7+7	6.1+7	Expt	80BNL		331	780	DAV	Subramanian+3ES.DIF SPEC AT 60.7MEV.
0	016	N,ALPHA REAC	NDG		Expt	80BNL		289	780	AI	Kneff+CS MEAS TO BE ANALYZED.NDG.
0	016	N,ALPHA REAC	2.7+7	6.1+7	Expt	80BNL		331	780	DAV	Subramanian+3ES.DIF.ANGINTEG CFD MDL
0	016	N,ALPHA REAC	1.4+7		Expt	80BNL		245	780	LRL	Haight+MEAS TBC.NDG.
0	018	DIFF ELASTIC	2.4+7		Revw	80BNL		375	780	OHO	Finlay+GRPH.MEAS CFD OPTMDL CALCS.
0	018	DIFF INELAST	2.4+7		Revw	80BNL		375	780	OHO	Finlay+GRPH.MEAS CFD DWBA,CCBA MDLS.
F	019	NONEL GAMMA	1.0+5	2.0+7	Revw	80BNL		277	780	ORL	Larson.REVIEW.NDG.SEE ORNL REPORT.
F	019	N,PROTON	1.4+7		Expt	80BNL		245	780	LRL	Haight+MEAS TBC.NDG.
F	019	N,DEUTERON	1.4+7		Expt	80BNL		245	780	LRL	Haight+MEAS TBC.NDG.
F	019	N,ALPHA REAC	NDG		Expt	80BNL		289	780	AI	Kneff+CS MEAS TO BE ANALYZED.NDG.
F	019	N,ALPHA REAC	1.4+7		Expt	80BNL		245	780	LRL	Haight+MEAS TBC.NDG.
NA	023	DIFF INELAST	1.5+7		Theo	80BNL		711	780	RCN	Gruppelaar+SPEC,ANGDIST.CALC VS EXPT
NA	023	NONEL GAMMA	1.0+5	2.0+7	Revw	80BNL		277	780	ORL	Larson.REVIEW.NDG.SEE ORNL REPORT.

Element S	A	Quantity	Energy (eV) Min	Max	Type	Documentation Ref	Vol	Page	Date	Lab	Comments
NA	023	NEUT EMISSN	1.5+7		Theo	80BNL		675	780	ORL	Fu.MULTI-STEP H-F CALC CFD EXPT.GRPH
NA	023	NEUT EMISSN	1.5+7		Theo	80BNL		711	780	RCN	Gruppelaar+EMISSION SPEC CALC VS EXP
MG		DIFF INELAST	1.5+7		Theo	80BNL		711	780	RCN	Gruppelaar+SPEC,ANGDIST.CALC VS EXPT
MG		INELST GAMMA	1.0+5	2.0+7	Revw	80BNL		277	780	ORL	Larson.REVIEW.NDG.SEE ORNL REPORT.
MG		NONEL GAMMA	1.0+5	2.0+7	Revw	80BNL		277	780	ORL	Larson.REVIEW.NDG.SEE ORNL REPORT.
MG		NEUT EMISSN	1.5+7		Theo	80BNL		711	780	RCN	Gruppelaar+EMISSION SPEC CALC VS EXP
AL	027	TOTAL XSECT	2.0+6	8.0+7	Revw	80BNL		277	780	ORL	Larson.ORELA.TRNS AT 40 MEV GVN.
AL	027	DIFF ELASTIC	2.0+7	2.6+7	Revw	80BNL		215	780	LAS	Browne+REVIEW.5-10PC PRECISION.NDG.
AL	027	DIFF INELAST	1.5+7		Theo	80BNL		711	780	RCN	Gruppelaar+SPEC,ANGDIST.CALC VS EXPT
AL	027	NONEL GAMMA	1.0+5	2.0+7	Revw	80BNL		277	780	ORL	Larson.REVIEW.NDG.SEE ORNL REPORT.
AL	027	NEUT EMISSN	1.0+6	2.0+7	Revw	80BNL		215	780	LAS	Browne+REVIEW.REFS GVN.NDG.
AL	027	NEUT EMISSN	1.0+6	2.0+7	Revw	80BNL		277	780	ORL	Larson.REVIEW.NDG.SEE ORNL REPORT
AL	027	NEUT EMISSN	1.5+7		Theo	80BNL		711	780	RCN	Gruppelaar+EMISSION SPEC CALC VS EXP
AL	027	N,PROTON	1.5+7		Revw	80BNL		215	780	LAS	Browne+REVIEW.SPEC,ANGDISTS.NDG.REFS
AL	027	N,DEUTERON	1.5+7		Revw	80BNL		215	780	LAS	Browne+REVIEW.SPEC,ANGDISTS.NDG.REFS

Element S	A	Quantity	Energy (eV) Min	Max	Type	Documentation Ref	Vol	Page	Date	Lab	Comments
AL	027	N,TRITON	3.0+7		Expt	80BNL		539	780 JUL		Qaim+CS GVN.20 PCT ERROR
AL	027	N,ALPHA REAC	1.5+7		Expt	80BNL		289	780 AI		Kneff+CS FOR 13 NUCLIDES.TBL.CFD.
AL	027	N,ALPHA REAC	1.5+7		Revw	80BNL		215	780 LAS		Browne+REVIEW.SPEC,ANGDIST.CS TBL.
AL	027	N,ALPHA REAC	3.0+7		Expt	80BNL		539	780 JUL		Qaim+INTEG MEAS CFD CS FROM EXCIT FN
SI		TOTAL XSECT	1.0+7	5.0+7	Revw	80BNL		215	780 LAS		Browne+REVIEW.MEAS DO NOT AGREE.GRPH
SI		TOTAL XSECT	2.0+6	8.0+7	Revw	80BNL		277	780 ORL		Larson.ORELA.TRNS AT 40 MEV GVN.
SI		DIFF ELASTIC	2.0+7	2.6+7	Revw	80BNL		215	780 LAS		Browne+REVIEW.10-15PC PRECISION.NDG
SI		DIFF ELASTIC	2.0+7	2.6+7	Revw	80BNL		215	780 LAS		Browne+REVIEW.5-10PC PRECISION.NDG.
SI		DIFF INELAST	2.0+7	2.6+7	Revw	80BNL		215	780 LAS		Browne+REVIEW.NDG.BIB REFS.
SI		DIFF INELAST	7.5+6	1.2+7	Revw	80BNL		259	780 TNL		Walter+CONTINUUM EMISSION SPEC TBD.
SI		DIFF INELAST	1.5+7		Theo	80BNL		711	780 RCN		Gruppelaar+SPEC,ANGDIST.CALC VS EXPT
SI		NONEL GAMMA	1.0+5	2.0+7	Revw	80BNL		277	780 ORL		Larson.REVIEW.NDG.SEE ORNL REPORT.
SI		NEUT EMISSN	1.5+7		Theo	80BNL		711	780 RCN		Gruppelaar+EMISSION SPEC CALC VS EXP
SI		N,ALPHA REAC	NDG		Expt	80BNL		289	780 AI		Kneff+CS MEAS TO BE ANALYZED.NDG.
SI	028	DIFF ELASTIC	2.0+7	4.0+7	Revw	80BNL		375	780 OHO		Finlay+STATUS SINCE MAY 77.REFS GVN

Element S	A	Quantity	Energy (eV) Min	Max	Type	Documentation Ref	Vol	Page	Date	Lab	Comments
SI	028	DIFF ELASTIC	1.0+7		Expt	80BNL		421	780	TUD	Pilz+TOF.GRPH ANGDIST CFD MDL CALCS.
SI	028	DIFF INELAST	2.6+7		Revw	80BNL		375	780	OHO	Finlay+STATUS SINCE MAY 77.REFS GVN.
SI	028	DIFF INELAST	1.0+7		Expt	80BNL		421	780	TUD	Pilz+TOF.GRPH ANGDIST CFD MDL CALCS.
P	031	DIFF INELAST	1.5+7		Theo	80BNL		711	780	RCN	Gruppelaar+CS CALC VS EXPT.LEG COEFS
P	031	NEUT EMISSN	1.5+7		Theo	80BNL		711	780	RCN	Gruppelaar+EMISSION SPEC CALC VS EXP
S		DIFF INELAST	1.5+7		Theo	80BNL		711	780	RCN	Gruppelaar+SPEC,ANGDIST.CALC VS EXPT
S		NEUT EMISSN	1.5+7		Theo	80BNL		711	780	RCN	Gruppelaar+EMISSION SPEC CALC VS EXP
S	032	DIFF ELASTIC	2.0+7	4.0+7	Revw	80BNL		375	780	OHO	Finlay+STATUS SINCE MAY 77.REFS GVN
S	032	DIFF INELAST	2.2+7	2.6+7	Revw	80BNL		375	780	OHO	Finlay+STATUS SINCE MAY 77.REFS GVN.
CA		TOTAL XSECT	3.5+7	5.0+7	Expt	80BNL		313	780	DAV	Zanelli+TOF,TRNS.3E.TBL,GRPH.CFD.
CA		TOTAL XSECT	1.0+7	5.0+7	Revw	80BNL		215	780	LAS	Browne+REVIEW.MEAS DO NOT AGREE.GRPH
CA		TOTAL XSECT	2.0+6	8.0+7	Revw	80BNL		277	780	ORL	Larson.ORELA.TRNS AT 40 MEV GVN.
CA		DIFF ELASTIC	2.0+7	2.6+7	Revw	80BNL		215	780	LAS	Browne+REVIEW.10-15PC PRECISION.NDG
CA		DIFF INELAST	1.5+7		Theo	80BNL		711	780	RCN	Gruppelaar+SPEC,ANGDIST.CALC VS EXPT
CA		NONELASTIC	4.0+7	5.0+7	Revw	80BNL		215	780	LAS	Browne+REVIEW.10-15PC PRECISION.NDG

Element S	A	Quantity	Energy (eV) Min	Max	Type	Documentation Ref	Vol	Page	Date	Lab	Comments
CA		NONEL GAMMA	1.0+5	2.0+7	Revw	80BNL		277	780	ORL	Larson.REVIEW.NDG.SEE ORNL REPORT.
CA		NEUT EMISSN	1.5+7		Theo	80BNL		711	780	RCN	Gruppelaar+EMISSION SPEC CALC VS EXP
CA	040	TOTAL XSECT	8.0+6	2.0+7	Eval	80BNL		675	780	ORL	Fu.EVAL FOR ENDF REDONE.14.6MEV GRPH
CA	040	DIFF ELASTIC	2.0+7	4.0+7	Revw	80BNL		375	780	OHO	Finlay+STATUS SINCE MAY 77.REFS GVN.
CA	040	POLARIZATION	7.0+6	1.7+7	Revw	80BNL		259	780	TNL	Walter+ANAL PWR DISTRIB.NDG.TBC.
CA	040	NONELASTIC	4.0+7	5.0+7	Expt	80BNL		313	780	DAV	Zanelli+2ES.TRANS.GRPH.CFD OPTMDL.
CA	040	N,GAMMA	8.0+6	2.0+7	Eval	80BNL		675	780	ORL	Fu.EVAL FOR ENDF REDONE.14.6MEV GRPH
CA	040	N,GAMMA	6.0+6	1.4+7	Expt	80BNL		259	780	TNL	Walter+ANGDISTS 90 DEG.NDG
CA	040	INELST GAMMA	8.0+6	2.0+7	Eval	80BNL		675	780	ORL	Fu.ENDF EVAL REDONE.GRPHS FOR 2 ES.
CA	040	NEUT EMISSN	8.0+6	2.0+7	Eval	80BNL		675	780	ORL	Fu.EVAL FOR ENDF REDONE.14.6MEV GRPH
CA	040	N,PROTON	8.0+6	2.0+7	Eval	80BNL		675	780	ORL	Fu.EVAL FOR ENDF REDONE.14.6MEV GRPH
CA	040	N,ALPHA REAC	8.0+6	2.0+7	Eval	80BNL		675	780	ORL	Fu.EVAL FOR ENDF REDONE.14.6MEV GRPH
SC	045	N2N REACTION	1.2+7	1.5+7	Expt	80BNL		399	780	BRC	Frehaut+TOF.NORM REL U238 NF.CS TBL.
TI		DIFF INELAST	1.5+7		Theo	80BNL		711	780	RCN	Gruppelaar+SPEC,ANGDIST.CALC VS EXPT
TI		NONEL GAMMA	2.0+6	2.0+7	Revw	80BNL		215	780	LAS	Browne+REVIEW.REFS GVN.GRPH.

Element S	A	Quantity	Energy (eV) Min	Max	Type	Documentation Ref	Vol	Page	Date	Lab	Comments
TI		NONEL GAMMA	1.0+5	2.0+7	Revw	80BNL		277	780	ORL	Larson.REVIEW.NDG.SEE ORNL REPORT.
TI		N2N REACTION	1.0+7	1.5+7	Expt	80BNL		399	780	BRC	Frehaut+TOF.NORM REL U238 NF.CS TBL.
TI		NXN REACTION	1.0+6	2.0+7	Revw	80BNL		277	780	ORL	Larson.REVIEW.NDG.SEE ORNL REPORT
TI		NEUT EMISSN	1.4+7		Expt	80BNL		343	780	IRK	Vonach+ANGINTEG SPEC.TBL,GRPH.CFD.
TI		NEUT EMISSN	1.5+7		Theo	80BNL		711	780	RCN	Gruppelaar+EMISSION SPEC CALC VS EXP
TI		N,PROTON	1.5+7		Revw	80BNL		215	780	LAS	Browne+SPEC,ANGDISTS.NDG.REFS
TI		N,DEUTERON	1.5+7		Revw	80BNL		215	780	LAS	Browne+SPEC,ANGDISTS.NDG.REFS
TI		N,ALPHA REAC	1.5+7		Expt	80BNL		289	780	AI	Kneff+CS FOR 13 NUCLIDES.TBL.CFD.
TI		N,ALPHA REAC	1.5+7		Revw	80BNL		215	780	LAS	Browne+REVIEW.SPEC,ANGDIST.CS TBL.
TI	046	N2N REACTION	3.0+7		Expt	80BNL		539	780	JUL	Qaim+ACT.CS VERSUS ASSYM PAR GRPH.
TI	046	N,PROTON	1.5+7		Expt	80BNL		245	780	LRL	Haight+GRPH.SECOND CHANCE P EMISSION
TI	046	N,PROTON	3.0+7		Expt	80BNL		539	780	JUL	Qaim+INTEG MEAS CFD CS FROM EXCIT FN
TI	046	N,ALPHA REAC	NDG		Expt	80BNL		289	780	AI	Kneff+CS MEAS TBD.NDG.
TI	046	N,ALPHA REAC	1.5+7		Revw	80BNL		215	780	LAS	Browne+REVIEW.PROD CS.TBL.
TI	047	NXN REACTION	3.0+7		Expt	80BNL		539	780	JUL	Qaim+ACT.(N,3N) CS.SYSTEMATICS TBD.

Element S	A	Quantity	Energy (eV) Min	Max	Type	Documentation Ref	Vol	Page	Date	Lab	Comments
TI	047	N,PROTON	3.0+7		Expt	80BNL	539	780	JUL		Qaim+ACT.CS VS ASSYMETRY PAR.GRPH.
TI	047	N,N PROTON	3.0+7		Expt	80BNL	539	780	JUL		Qaim+(N,D)+(N,NP).CS VS ASSYMETRY.
TI	047	N,DEUTERON	3.0+7		Expt	80BNL	539	780	JUL		Qaim+(N,D)+(N,NP).CS VS ASSYMETRY.
TI	047	N,ALPHA REAC	NDG		Expt	80BNL	289	780	AI		Kneff+CS MEAS TBD.NDG.
TI	048	N,PROTON	1.5+7		Expt	80BNL	245	780	LRL		Haight+GRPH.SECOND CHANCE P EMISSION
TI	048	N,PROTON	3.0+7		Expt	80BNL	539	780	JUL		Qaim+ACT.CS VS ASSYM PAR GRPH.
TI	048	N,N PROTON	3.0+7		Expt	80BNL	539	780	JUL		Qaim+(N,D)+(N,NP).CS VS ASSYMETRY.
TI	048	N,DEUTERON	3.0+7		Expt	80BNL	539	780	JUL		Qaim+(N,D)+(N,NP).CS VS ASSYMETRY.
TI	048	N,ALPHA REAC	NDG		Expt	80BNL	289	780	AI		Kneff+CS MEAS TBD.NDG.
TI	048	N,ALPHA REAC	1.5+7		Revw	80BNL	215	780	LAS		Browne+REVIEW.PROD CS.TBL.
TI	049	N,PROTON	3.0+7		Expt	80BNL	539	780	JUL		Qaim+ACT.CS VS ASSYM PAR GRPH.
TI	049	N,N PROTON	3.0+7		Expt	80BNL	539	780	JUL		Qaim+(N,D)+(N,NP).CS VS ASSYMETRY.
TI	049	N,DEUTERON	3.0+7		Expt	80BNL	539	780	JUL		Qaim+(N,D)+(N,NP).CS VS ASSYMETRY.
TI	049	N,ALPHA REAC	NDG		Expt	80BNL	289	780	AI		Kneff+CS MEAS TBD.NDG.
TI	050	N,PROTON	3.0+7		Expt	80BNL	539	780	JUL		Qaim+ACT.CS VS ASSYM PAR.GRPH.

Element S	A	Quantity	Energy (eV) Min	Max	Type	Documentation Ref	Vol	Page	Date	Lab	Comments
TI	050	N,N PROTON	3.0+7		Expt	80BNL	539	780	JUL		Qaim+(N,D)+(N,NP).CS VS ASSYMETRY.
TI	050	N,DEUTERON	3.0+7		Expt	80BNL	539	780	JUL		Qaim+(N,D)+(N,NP).CS VS ASSYMETRY.
TI	050	N,ALPHA REAC	NDG		Expt	80BNL	289	780	AI		Kneff+CS MEAS TBD.NDG.
TI	050	N,ALPHA REAC	3.0+7		Expt	80BNL	539	780	JUL		Qaim+ACT.CS VS ASSYM PAR GRPH.
V	051	DIFF INELAST	1.5+7		Theo	80BNL	711	780	RCN		Gruppelaar+SPEC,ANGDIST.CALC VS EXPT
V	051	NONEL GAMMA	1.0+5	2.0+7	Revw	80BNL	277	780	ORL		Larson.REVIEW.NDG.SEE ORNL REPORT.
V	051	N2N REACTION	1.1+7	1.5+7	Expt	80BNL	399	780	BRC		Frehaut+TOF.NORM REL U238 NF.CS TBL.
V	051	NEUT EMISSN	1.5+7		Theo	80BNL	711	780	RCN		Gruppelaar+EMISSION SPEC CALC VS EXP
V	051	N,PROTON	1.5+7		Revw	80BNL	215	780	LAS		Browne+REVIEW.SPEC,ANGDISTS.NDG.REFS
V	051	N,PROTON	3.0+7		Expt	80BNL	539	780	JUL		Qaim+ACT.CS VS ASSYM PAR GRPH.
V	051	N,DEUTERON	1.5+7		Revw	80BNL	215	780	LAS		Browne+REVIEW.SPEC,ANGDISTS.NDG.REFS
V	051	N,HE3 REACTN	3.0+7		Expt	80BNL	539	780	JUL		Qaim+ACT.CS GVN.SYSTEMATICS TBD.
V	051	N,ALPHA REAC	NDG		Expt	80BNL	289	780	AI		Kneff+CS MEAS TO BE ANALYZED.NDG.
V	051	N,ALPHA REAC	1.5+7		Revw	80BNL	215	780	LAS		Browne+REVIEW.SPEC,ANGDIST.CS TBL.
V	051	N,ALPHA REAC	3.0+7		Expt	80BNL	539	780	JUL		Qaim+ACT.CS VS ASSYM PAR GRPH.

Element S	A	Quantity	Energy (eV) Min	Max	Type	Documentation Ref	Vol	Page	Date	Lab	Comments
V	051	N,N ALPHA	3.0+7		Expt	80BNL		539	780	JUL	Qaim+ACT.CS GVN.SYSTEMATICS TBD.
CR		TOTAL XSECT	2.0+6	8.0+7	Revw	80BNL		277	780	ORL	Larson.GRPH.CFD OTH MEAS.
CR		DIFF INELAST	1.5+7		Revw	80BNL		215	780	LAS	Browne+REVIEW.NDG.BIB REFS.
CR		DIFF INELAST	7.5+6	1.2+7	Revw	80BNL		259	780	TNL	Walter+CONTINUUM EMISSION SPEC TBD.
CR		DIFF INELAST	1.5+7		Theo	80BNL		711	780	RCN	Gruppelaar+SPEC,ANGDIST.CALC VS EXPT
CR		NONEL GAMMA	1.0+5	2.0+7	Revw	80BNL		277	780	ORL	Larson.REVIEW.NDG.SEE ORNL REPORT.
CR		N2N REACTION	1.0+7	1.5+7	Expt	80BNL		399	780	BRC	Frehaut+TOF.NORM REL U238 NF.CS TBL.
CR		NEUT EMISSN	1.4+7		Expt	80BNL		343	780	IRK	Vonach+ANGINTEG SPEC.TBL,GRPH.CFD.
CR		NEUT EMISSN	1.5+7		Theo	80BNL		711	780	RCN	Gruppelaar+EMISSION SPEC CALC VS EXP
CR		N,PROTON	1.5+7		Revw	80BNL		215	780	LAS	Browne+SPEC,ANGDISTS.NDG.REFS
CR		N,PROTON	1.5+7		Revw	80BNL		245	780	LRL	Haight+CS TBL.REVIEW.
CR		N,DEUTERON	1.5+7		Revw	80BNL		215	780	LAS	Browne+SPEC,ANGDISTS.NDG.REFS
CR		N,DEUTERON	1.5+7		Revw	80BNL		245	780	LRL	Haight+CS TBL.REVIEW
CR		N,TRITON	3.0+7		Expt	80BNL		539	780	JUL	Qaim+CS GVN.20 PCT ERROR
CR		N,ALPHA REAC	1.5+7		Expt	80BNL		289	780	AI	Kneff+CS FOR 13 NUCLIDES.TBL.CFD.

Element S	A	Quantity	Energy (eV) Min	Max	Type	Documentation Ref	Vol	Page	Date	Lab	Comments
CR		N,ALPHA REAC	1.5+7		Revw	80BNL		215	780	LAS	Browne+REVIEW.SPEC,ANGDISTS.NDG.REFS
CR		N,ALPHA REAC	1.5+7		Revw	80BNL		245	780	LRL	Haight+CS TBL.REVIEW
CR	050	N2N REACTION	3.0+7		Expt	80BNL		539	780	JUL	Qaim+ACT.CS VS ASSYM PAR.GRPH.
CR	050	NXN REACTION	3.0+7		Expt	80BNL		539	780	JUL	Qaim+ACT.(N,3N) CS.SYSTEMATICS TBD.
CR	050	N,PROTON	1.5+7		Revw	80BNL		245	780	LRL	Haight+CS TBL.P SPEC GRPH.CFD CALCS.
CR	050	N,DEUTERON	1.5+7		Revw	80BNL		245	780	LRL	Haight+CS TBL.REVIEW.
CR	050	N,ALPHA REAC	NDG		Expt	80BNL		289	780	AI	Kneff+CS MEAS TBD.NDG.
CR	050	N,ALPHA REAC	1.4+7	1.5+7	Revw	80BNL		215	780	LAS	Browne+REVIEW.ANG-INTEG SPEC.GRPH
CR	050	N,ALPHA REAC	1.5+7		Revw	80BNL		245	780	LRL	Haight+CS TBL.A SPEC GRPH.CFD CALCS.
CR	052	N2N REACTION	3.0+7		Expt	80BNL		539	780	JUL	Qaim+ACT.CS VS ASSYM PAR GRPH.
CR	052	N,PROTON	1.5+7		Revw	80BNL		245	780	LRL	Haight+CS TBL.P SPEC GRPH.CFD CALCS.
CR	052	N,PROTON	3.0+7		Expt	80BNL		539	780	JUL	Qaim+ACT.CS VS ASSYMETRY PAR.GRPH.
CR	052	N,DEUTERON	1.5+7		Revw	80BNL		245	780	LRL	Haight+CS TBL.REVIEW.
CR	052	N,ALPHA REAC	NDG		Expt	80BNL		289	780	AI	Kneff+CS MEAS TBD.NDG.
CR	052	N,ALPHA REAC	1.5+7		Revw	80BNL		215	780	LAS	Browne+REVIEW.ANG-INTEG SPEC.GRPH

Element S	A	Quantity	Energy (eV) Min	Max	Type	Documentation Ref	Vol	Page	Date	Lab	Comments
CR	052	N,ALPHA REAC	1.5+7		Revw	80BNL		245	780	LRL	Haight+CS TBL.A SPEC GRPH.CFD CALCS.
CR	053	NXN REACTION	3.0+7		Expt	80BNL		539	780	JUL	Qaim+ACT.(N,3N) CS.SYSTEMATICS TBD.
CR	053	N,PROTON	3.0+7		Expt	80BNL		539	780	JUL	Qaim+ACT.CS VS ASSYM PAR GRPH.
CR	053	N,N PROTON	3.0+7		Expt	80BNL		539	780	JUL	Qaim+(N,D)+(N,NP).CS VS ASSYMETRY.
CR	053	N,DEUTERON	3.0+7		Expt	80BNL		539	780	JUL	Qaim+(N,D)+(N,NP).CS VS ASSYMETRY.
CR	053	N,HE3 REACTN	3.0+7		Expt	80BNL		539	780	JUL	Qaim+ACT.CS GVN.SYSTEMATICS TBD.
CR	053	N,ALPHA REAC	NDG		Expt	80BNL		289	780	AI	Kneff+CS MEAS TBD.NDG.
CR	054	N,N PROTON	3.0+7		Expt	80BNL		539	780	JUL	Qaim+(N,D)+(N,NP).CS VS ASSYMETRY.
CR	054	N,DEUTERON	3.0+7		Expt	80BNL		539	780	JUL	Qaim+(N,D)+(N,NP).CS VS ASSYMETRY.
CR	054	N,ALPHA REAC	NDG		Expt	80BNL		289	780	AI	Kneff+CS MEAS TBD.NDG.
CR	054	N,ALPHA REAC	3.0+7		Expt	80BNL		539	780	JUL	Qaim+ACT.CS VS ASSYM PAR GRPH.
CR	415	N,TRITON	3.0+7		Expt	80BNL		539	780	JUL	Qaim+STAINLESS STEEL CS.+-20PCT.
MN	055	DIFF INELAST	1.5+7		Theo	80BNL		711	780	RCN	Gruppelaar+SPEC,ANGDIST.CALC VS EXPT
MN	055	NONEL GAMMA	1.0+5	2.0+7	Revw	80BNL		277	780	ORL	Larson.REVIEW.NDG.SEE ORNL REPORT.
MN	055	N2N REACTION	3.0+7		Expt	80BNL		539	780	JUL	Qaim+ACT.CS VS ASSYM PAR GRPH.

Element S	A	Quantity	Energy (eV) Min	Max	Type	Documentation Ref	Vol	Page	Date	Lab	Comments
MN	055	NEUT EMISSN	1.5+7		Theo	80BNL		711	780	RCN	Gruppelaar+EMISSION SPEC CALC VS EXP
MN	055	N,PROTON	3.0+7		Expt	80BNL		539	780	JUL	Qaim+ACT.CS VS ASSYM PAR GRPH.
MN	055	N,TRITON	3.0+7		Expt	80BNL		539	780	JUL	Qaim+CS GVN.20 PCT ERROR
MN	055	N,ALPHA REAC	NDG		Expt	80BNL		289	780	AI	Kneff+CS MEAS TO BE ANALYZED.NDG.
MN	055	N,ALPHA REAC	3.0+7		Expt	80BNL		539	780	JUL	Qaim+ACT.CS VS ASSYM PAR GRPH.
FE		EVALUATION	3.0+6	4.0+7	Eval	80BNL		731	780	LAS	Arthur+3 MDL CALCS.GRPHS.CFD EXPTS.
FE		TOTAL XSECT	3.5+7	5.0+7	Expt	80BNL		313	780	DAV	Zanelli+TOF,TRNS.3E.TBL,GRPH.CFD.
FE		TOTAL XSECT	1.0+7	5.0+7	Revw	80BNL		215	770	LAS	Browne+REVIEW.MEAS DO NOT AGREE.GRPH
FE		TOTAL XSECT	5.0+5	8.0+7	Revw	80BNL		277	780	ORL	Larson.2 EXPTS.GRPH.CFD OTHS.
FE		DIFF ELASTIC	2.0+7	2.6+7	Revw	80BNL		215	780	LAS	Browne+REVIEW.10-15PC PRECISION.NDG
FE		DIFF ELASTIC	2.0+7	2.6+7	Revw	80BNL		215	780	LAS	Browne+REVIEW.5-10PC PRECISION.NDG.
FE		DIFF INELAST	7.5+6	1.2+7	Revw	80BNL		259	780	TNL	Walter+3ES.PRELIM GRPH EXCIT FN.TBC.
FE		DIFF INELAST	1.5+7		Theo	80BNL		711	780	RCN	Gruppelaar+CS CALC VS EXPT.LEG COEFS
FE		NONELASTIC	4.0+7	5.0+7	Revw	80BNL		215	780	LAS	Browne+REVIEW.10-15PC PRECISION.NDG
FE		NONEL GAMMA	1.0+5	2.0+7	Revw	80BNL		277	780	ORL	Larson.REVIEW.NDG.SEE ORNL REPORT.

Element S	A	Quantity	Energy (eV) Min	Max	Type	Documentation Ref	Vol	Page	Date	Lab	Comments
FE		N2N REACTION	1.2+7	1.5+7	Expt	80BNL		399	780	BRC	Frehaut+TOF.NORM REL U238 NF.CS TBL.
FE		NEUT EMISSN	1.0+7	1.2+7	Revw	80BNL		215	780	LAS	Browne+REVIEW.REFS GVN.GRPH FOR 6ANG
FE		NEUT EMISSN	1.4+7		Expt	80BNL		343	780	IRK	Vonach+ANGINTEG SPEC.TBL,GRPH.CFD.
FE		NEUT EMISSN	1.5+7		Theo	80BNL		711	780	RCN	Gruppelaar+EMISSION SPEC CALC VS EXP
FE		N,PROTON	1.5+7		Revw	80BNL		215	780	LAS	Browne+SPEC,ANGDISTS.NDG.REFS
FE		N,PROTON	1.5+7		Revw	80BNL		245	780	LRL	Haight+CS TBL.REVIEW.
FE		N,DEUTERON	1.5+7		Revw	80BNL		215	780	LAS	Browne+SPEC,ANGDISTS.NDG.REFS
FE		N,DEUTERON	1.5+7		Revw	80BNL		245	780	LRL	Haight+CS TBL.REVIEW
FE		N,TRITON	3.0+7		Expt	80BNL		539	780	JUL	Qaim+CS GVN.20 PCT ERROR
FE		N,ALPHA REAC	1.5+7		Expt	80BNL		289	780	AI	Kneff+CS FOR 13 NUCLIDES.TBL.CFD.
FE		N,ALPHA REAC	1.5+7		Revw	80BNL		215	780	LAS	Browne+REVIEW.SPEC,ANGDIST.CS TBL.
FE		N,ALPHA REAC	1.5+7		Revw	80BNL		245	780	LRL	Haight+CS TBL.REVIEW
FE	054	EVALUATION	3.0+6	4.0+7	Eval	80BNL		731	780	LAS	Arthur+3 MDL CALCS.GRPHS.CFD EXPTS.
FE	054	DIFF ELASTIC	8.0+6	1.4+7	Revw	80BNL		259	780	TNL	Walter+EXPT COMPLETED AT TNL.NDG.TBC
FE	054	POLARIZATION	1.0+7	1.4+7	Revw	80BNL		259	780	TNL	Walter+ANAL PWR DISTRIB.NDG.GRPH.CFD

Element S	A	Quantity	Energy (eV) Min	Max	Type	Documentation Ref	Vol	Page	Date	Lab	Comments
FE	054	N2N REACTION	3.0+7		Expt	80BNL		539	780	JUL	Qaim+ACT.CS VERSUS ASSYM PAR GRPH.
FE	054	N,PROTON	1.2+7	1.7+7	Revw	80BNL		215	780	LAS	Browne+REVIEW.ACT.NDG.
FE	054	N,PROTON	1.5+7		Revw	80BNL		245	780	LRL	Haight+CS TBL.P SPEC GRPH.CFD CALCS.
FE	054	N,PROTON	3.0+7		Expt	80BNL		539	780	JUL	Qaim+ACT.CS VS ASSYMETRY PAR.GRPH.
FE	054	N,DEUTERON	1.5+7		Revw	80BNL		245	780	LRL	Haight+CS TBL.REVIEW.
FE	054	N,ALPHA REAC	NDG		Expt	80BNL		289	780	AI	Kneff+CS MEAS TO BE ANALYZED.NDG.
FE	054	N,ALPHA REAC	1.2+7	1.7+7	Revw	80BNL		215	780	LAS	Browne+REVIEW.ANG-INTEG SPEC.GRPH
FE	054	N,ALPHA REAC	1.5+7		Revw	80BNL		245	780	LRL	Haight+CS TBL.A SPEC GRPH.CFD CALCS.
FE	054	N,ALPHA REAC	3.0+7		Expt	80BNL		539	780	JUL	Qaim+ACT.CS VS ASSYM PAR GRPH.
FE	056	EVALUATION	3.0+6	4.0+7	Eval	80BNL		731	780	LAS	Arthur+3 MDL CALCS.GRPHS.CFD EXPTS.
FE	056	DIFF ELASTIC	8.0+6	1.4+7	Revw	80BNL		259	780	TNL	Walter+GRPH.EXPT MEAS CFD OPTMDL.
FE	056	DIFF INELAST	1.6+7	2.2+7	Revw	80BNL		215	780	LAS	Browne+REVIEW.NDG.BIB REFS.
FE	056	NONELASTIC	4.0+7	5.0+7	Expt	80BNL		313	780	DAV	Zanelli+2ES.TRANS.GRPH.CFD OPTMDL.
FE	056	NXN REACTION	1.5+7		Theo	80BNL		675	780	ORL	Fu.(N,XN).MULTISTEP H-F CALC CFD EXP
FE	056	N,PROTON	1.5+7		Revw	80BNL		245	780	LRL	Haight+CS TBL.P SPEC GRPH.CFD CALCS.

Element S	A	Quantity	Energy (eV) Min	Max	Type	Documentation Ref	Vol	Page	Date	Lab	Comments
FE	056	N,PROTON	1.5+7		Theo	80BNL		675	780	ORL	Fu.(N,XP).MULTISTEP H-F CALC CFD EXP
FE	056	N,PROTON	3.0+7		Expt	80BNL		539	780	JUL	Qaim+ACT.CS VS ASSYMETRY PAR.GRPH.
FE	056	N,DEUTERON	1.5+7		Revw	80BNL		245	780	LRL	Haight+CS TBL.REVIEW.
FE	056	N,ALPHA REAC	NDG		Expt	80BNL		289	780	AI	Kneff+CS MEAS TO BE ANALYZED.NDG.
FE	056	N,ALPHA REAC	1.2+7	1.7+7	Revw	80BNL		215	780	LAS	Browne+REVIEW.ANG-INTEG SPEC.GRPH
FE	056	N,ALPHA REAC	1.5+7		Revw	80BNL		245	780	LRL	Haight+CS TBL.A SPEC GRPH.CFD CALCS.
FE	056	N,ALPHA REAC	1.5+7		Theo	80BNL		675	780	ORL	Fu.(N,XA).MULTISTEP H-F CALC CFD EXP
FE	057	N,ALPHA REAC	NDG		Expt	80BNL		289	780	AI	Kneff+CS MEAS TO BE ANALYZED.NDG.
FE	058	N,ALPHA REAC	NDG		Expt	80BNL		289	780	AI	Kneff+CS MEAS TO BE ANALYZED.NDG.
FE	415	N,TRITON	3.0+7		Expt	80BNL		539	780	JUL	Qaim+STAINLESS STEEL CS.+-20PCT.
CO	059	TOTAL XSECT	2.0+6	1.0+7	Theo	80BNL		751	780	LAS	Arthur+OPTMDL CALC CFD EXPTS.GRPHS.
CO	059	ELASTIC SCAT	8.0+6	4.0+7	Theo	80BNL		751	780	LAS	Arthur+OPTMDL CALC CFD EXPTS.GRPHS.
CO	059	TOT INELAST	1.0+7	2.5+7	Theo	80BNL		751	780	LAS	Arthur+OPTMDL CALC CFD EXPTS.GRPHS.
CO	059	DIFF INELAST	1.5+7		Theo	80BNL		711	780	RCN	Gruppelaar+SPEC,ANGDIST.CALC VS EXPT
CO	059	N2N REACTION	Tr	2.5+7	Revw	80BNL		215	780	LAS	Browne+REVIEW.10-20PC PRECISION.NDG

Element S	A	Quantity	Energy (eV) Min	Max	Type	Documentation Ref	Vol	Page	Date	Lab	Comments
CO	059	N2N REACTION	1.1+7	2.5+7	Theo	80BNL		751	780	LAS	Arthur+OPTMDL CALC CFD EXPTS.GRPHS.
CO	059	N2N REACTION	1.1+7	1.5+7	Expt	80BNL		399	780	BRC	Frehaut+TOF.NORM REL U238 NF.CS TBL.
CO	059	N2N REACTION	3.0+7		Expt	80BNL		539	780	JUL	Qaim+ACT.CS VS ASSYM PAR GRPH.
CO	059	NXN REACTION	Tr	2.4+7	Revw	80BNL		215	780	LAS	Browne+REVIEW.(N,3N) MEAS.NO (N,4N)
CO	059	NXN REACTION	2.0+7	5.0+7	Theo	80BNL		751	780	LAS	Arthur+OPTMDL CALCS CFD EXPTS.GRPHS.
CO	059	NXN REACTION	3.0+7		Expt	80BNL		539	780	JUL	Qaim+ACT.(N,3N) CS.SYSTEMATICS TBD.
CO	059	NEUT EMISSN	1.5+7		Theo	80BNL		711	780	RCN	Gruppelaar+EMISSION SPEC CALC VS EXP
CO	059	N,PROTON	2.6+6	1.5+7	Revw	80BNL		215	780	LAS	Browne+REVIEW.MEAS CFD.TBL 14 MEV
CO	059	N,PROTON	3.0+6	5.0+7	Theo	80BNL		751	780	LAS	Arthur+OPTMDL CALCS CFD EXPTS.GRPHS.
CO	059	N,PROTON	3.0+7		Expt	80BNL		539	780	JUL	Qaim+ACT.CS VS ASSYM PAR GRPH.
CO	059	N,N PROTON	1.0+7	2.0+7	Theo	80BNL		751	780	LAS	Arthur+(N,NP)+(N,PN).OPTMDL VS EXPT.
CO	059	N,TRITON	3.0+7		Expt	80BNL		539	780	JUL	Qaim+CS GVN.20 PCT ERROR
CO	059	N,ALPHA REAC	NDG		Expt	80BNL		289	780	AI	Kneff+CS MEAS TO BE ANALYZED.NDG.
CO	059	N,ALPHA REAC	3.0+6	5.0+7	Theo	80BNL		751	780	LAS	Arthur+OPTMDL CALCS CFD EXPTS.GRPHS.
CO	059	N,ALPHA REAC	3.0+7		Expt	80BNL		539	780	JUL	Qaim+ACT.CS VS ASSYM PAR GRPH.

Element S	A	Quantity	Energy (eV) Min	Max	Type	Documentation Ref	Vol	Page	Date	Lab	Comments
NI		TOTAL XSECT	2.0+6	8.0+7	Revw	80BNL		277	780	ORL	Larson.GRPH.CFD OTH MEAS.
NI		DIFF ELASTIC	2.0+7	2.6+7	Revw	80BNL		215	780	LAS	Browne+REVIEW.5-10PC PRECISION.NDG.
NI		DIFF INELAST	7.5+6	1.2+7	Revw	80BNL		259	780	TNL	Walter+CONTINUUM EMISSION SPEC.NDG.
NI		DIFF INELAST	1.5+7		Theo	80BNL		711	780	RCN	Gruppelaar+SPEC,ANGDIST.CALC VS EXPT
NI		NONEL GAMMA	1.0+5	2.0+7	Revw	80BNL		277	780	ORL	Larson.REVIEW.NDG.SEE ORNL REPORT.
NI		NONEL GAMMA	1.0+5	2.0+7	Revw	80BNL		277	780	ORL	Larson.REVIEW.NDG.SEE ORNL REPORT.
NI		NEUT EMISSN	1.0+7	1.4+7	Revw	80BNL		215	780	LAS	Browne+REVIEW.REFS GVN.GRPH FOR 1ANG
NI		NEUT EMISSN	1.4+7		Expt	80BNL		343	780	IRK	Vonach+ANGINTEG SPEC.TBL,GRPH.CFD.
NI		NEUT EMISSN	1.5+7		Theo	80BNL		711	780	RCN	Gruppelaar+EMISSION SPEC CALC VS EXP
NI		N,PROTON	1.5+7		Revw	80BNL		215	780	LAS	Browne+REVIEW.SPEC,ANGDISTS.GRPH.
NI		N,PROTON	1.5+7		Revw	80BNL		245	780	LRL	Haight+CS TBL.P EMISSION SPEC.
NI		N,DEUTERON	1.5+7		Revw	80BNL		215	780	LAS	Browne+REVIEW.SPEC,ANGDISTS.NDG.REFS
NI		N,DEUTERON	1.5+7		Revw	80BNL		245	780	LRL	Haight+CS TBL.REVIEW
NI		N,TRITON	3.0+7		Expt	80BNL		539	780	JUL	Qaim+CS GVN.20 PCT ERROR
NI		N,ALPHA REAC	1.5+7		Expt	80BNL		289	780	AI	Kneff+CS FOR 13 NUCLIDES.TBL.CFD.

Element S	A	Quantity	Energy (eV) Min	Max	Type	Documentation Ref	Vol	Page	Date	Lab	Comments
NI		N,ALPHA REAC	1.5+7		Revw	80BNL		215	780	LAS	Browne+REVIEW.SPEC,ANGDIST.CS TBL.
NI		N,ALPHA REAC	1.5+7		Revw	80BNL		245	780	LRL	Haight+CS TBL.REVIEW
NI	058	DIFF ELASTIC	2.4+7		Revw	80BNL		375	780	OHO	Finlay+GRPH.MEAS CFD OPTMDL CALCS.
NI	058	DIFF ELASTIC	8.0+6	1.4+7	Revw	80BNL		259	780	TNL	Walter+EXPT COMPLETED AT TNL.NDG.TBC
NI	058	POLARIZATION	1.0+7		Revw	80BNL		259	780	TNL	Walter+ANAL PWR DISTRIB.NDG.TBC.
NI	058	DIFF INELAST	2.4+7		Revw	80BNL		215	780	LAS	Browne+REVIEW.NDG.BIB REFS.
NI	058	DIFF INELAST	2.4+7		Revw	80BNL		375	780	OHO	Finlay+GRPH.MEAS CFD DWBA,CCBA MDLS.
NI	058	N2N REACTION	3.0+7		Expt	80BNL		539	780	JUL	Qaim+ACT.CS VERSUS ASSYM PAR GRPH.
NI	058	NXN REACTION	3.0+7		Expt	80BNL		539	780	JUL	Qaim+ACT.(N,3N) CS.SYSTEMATICS TBD.
NI	058	N,PROTON	1.5+7		Revw	80BNL		245	780	LRL	Haight+CS TBL.P SPEC GRPH.CFD CALCS.
NI	058	N,PROTON	8.0+6	1.1+7	Revw	80BNL		389	780	OHO	Randers-Pehrson+PRELIM SPEC.TBC.
NI	058	N,PROTON	3.0+7		Expt	80BNL		539	780	JUL	Qaim+ACT.CS VS ASSYMETRY PAR.GRPH.
NI	058	N,N PROTON	3.0+7		Expt	80BNL		539	780	JUL	Qaim+(N,D)+(N,NP).CS VS ASSYMETRY.
NI	058	N,DEUTERON	1.5+7		Revw	80BNL		245	780	LRL	Haight+CS TBL.REVIEW.
NI	058	N,DEUTERON	3.0+7		Expt	80BNL		539	780	JUL	Qaim+(N,D)+(N,NP).CS VS ASSYMETRY.

Element S	A	Quantity	Energy (eV) Min	Max	Type	Documentation Ref	Vol	Page	Date	Lab	Comments
NI	058	N,ALPHA REAC	1.5+7		Expt	80BNL		289	780	AI	Kneff+CS FOR 13 NUCLIDES.TBL.CFD.
NI	058	N,ALPHA REAC	1.5+7		Revw	80BNL		215	780	LAS	Browne+REVIEW.ANG-INTEG SPEC.GRPH
NI	058	N,ALPHA REAC	1.5+7		Revw	80BNL		245	780	LRL	Haight+CS TBL.A SPEC GRPH.CFD CALCS.
NI	058	N,ALPHA REAC	8.0+6	1.1+7	Revw	80BNL		389	780	OHO	Randers-Pehrson+PRELIM SPEC.TBC.
NI	060	DIFF ELASTIC	2.4+7		Revw	80BNL		375	780	OHO	Finlay+GRPH.MEAS CFD OPTMDL CALCS.
NI	060	DIFF ELASTIC	8.0+6	1.4+7	Revw	80BNL		259	780	TNL	Walter+EXPT COMPLETED AT TNL.NDG.TBC
NI	060	DIFF INELAST	2.4+7		Revw	80BNL		215	780	LAS	Browne+REVIEW.NDG.BIB REFS.
NI	060	DIFF INELAST	2.4+7		Revw	80BNL		375	780	OHO	Finlay+GRPH.MEAS CFD DWBA,CCBA MDLS.
NI	060	N,PROTON	1.5+7		Revw	80BNL		245	780	LRL	Haight+CS TBL.P SPEC GRPH.CFD CALCS.
NI	060	N,PROTON	3.0+7		Expt	80BNL		539	780	JUL	Qaim+INTEG MEAS CFD CS FROM EXCIT.FN
NI	060	N,DEUTERON	1.5+7		Revw	80BNL		245	780	LRL	Haight+CS TBL.REVIEW.
NI	060	N,ALPHA REAC	1.5+7		Expt	80BNL		289	780	AI	Kneff+CS FOR 13 NUCLIDES.TBL.CFD.
NI	060	N,ALPHA REAC	1.5+7		Revw	80BNL		215	780	LAS	Browne+REVIEW.ANG-INTEG SPEC.GRPH
NI	060	N,ALPHA REAC	1.5+7		Revw	80BNL		245	780	LRL	Haight+CS TBL.A SPEC GRPH.CFD CALCS.
NI	061	N,ALPHA REAC	1.5+7		Expt	80BNL		289	780	AI	Kneff+CS FOR 13 NUCLIDES.TBL.CFD.

Element S	A	Quantity	Energy (eV) Min	Max	Type	Documentation Ref	Vol	Page	Date	Lab	Comments
NI	062	N,ALPHA REAC	1.5+7		Expt	80BNL		289	780	AI	Kneff+CS FOR 13 NUCLIDES.TBL.CFD.
NI	064	N,ALPHA REAC	1.5+7		Expt	80BNL		289	780	AI	Kneff+CS FOR 13 NUCLIDES.TBL.CFD.
NI	415	N,TRITON	3.0+7		Expt	80BNL		539	780	JUL	Qaim+STAINLESS STEEL CS.+-20PCT.
CU		TOTAL XSECT	2.0+6	8.0+7	Revw	80BNL		277	780	ORL	Larson.ORELA.TRNS AT 40 MEV GVN.
CU		DIFF ELASTIC	NDG		Revw	80BNL		215	780	LAS	Browne+REVIEW.10 PC PRECISION.NDG.
CU		DIFF INELAST	7.5+6	1.2+7	Revw	80BNL		259	780	TNL	Walter+CONTINUUM EMISSION SPEC.NDG.
CU		DIFF INELAST	1.5+7		Theo	80BNL		711	780	RCN	Gruppelaar+SPEC,ANGDIST.CALC VS EXPT
CU		NONEL GAMMA	1.0+5	2.0+7	Revw	80BNL		277	780	ORL	Larson.REVIEW.NDG.SEE ORNL REPORT.
CU		N2N REACTION	1.0+7	1.5+7	Expt	80BNL		399	780	BRC	Frehaut+TOF.NORM REL U238 NF.CS TBL.
CU		NXN REACTION	1.0+6	2.0+7	Revw	80BNL		277	780	ORL	Larson.REVIEW.NDG.SEE ORNL REPORT
CU		NEUT EMISSN	1.0+6	2.0+7	Revw	80BNL		215	780	LAS	Browne+REVIEW.REFS GVN.GRPH FOR 1ANG
CU		NEUT EMISSN	1.4+7		Expt	80BNL		343	780	IRK	Vonach+ANGINTEG SPEC.TBL,GRPH.CFD.
CU		NEUT EMISSN	1.5+7		Theo	80BNL		711	780	RCN	Gruppelaar+EMISSION SPEC CALC VS EXP
CU		N,PROTON	1.5+7		Revw	80BNL		215	780	LAS	Browne+SPEC,ANGDISTS.NDG.REFS
CU		N,PROTON	1.5+7		Revw	80BNL		245	780	LRL	Haight+CS TBL.REVIEW.

Element S	A	Quantity	Energy (eV) Min	Max	Type	Documentation Ref	Vol	Page	Date	Lab	Comments
CU		N,DEUTERON	1.5+7		Revw	80BNL		215	780	LAS	Browne+SPEC,ANGDISTS.NDG.REFS
CU		N,DEUTERON	1.5+7		Revw	80BNL		245	780	LRL	Haight+CS TBL.REVIEW
CU		N,ALPHA REAC	1.5+7		Expt	80BNL		289	780	AI	Kneff+CS FOR 13 NUCLIDES.TBL.CFD.
CU		N,ALPHA REAC	1.5+7		Revw	80BNL		215	780	LAS	Browne+REVIEW.SPEC,ANGDISTS.NDG.REFS
CU		N,ALPHA REAC	1.5+7		Revw	80BNL		245	780	LRL	Haight+CS TBL.REVIEW
CU	063	DIFF ELASTIC	8.0+6	1.4+7	Revw	80BNL		259	780	TNL	Walter+GRPH.EXPT MEAS CFD OPTMDL.
CU	063	N2N REACTION	3.0+7		Expt	80BNL		539	780	JUL	Qaim+ACT.CS VS ASSYM PAR GRPH.
CU	063	N2N REACTION	3.0+7		Expt	80BNL		539	780	JUL	Qaim+ACT.CS VS ASSYM PAR.GRPH.
CU	063	NXN REACTION	3.0+7		Expt	80BNL		539	780	JUL	Qaim+ACT.(N,3N) CS.SYSTEMATICS TBD.
CU	063	N,PROTON	1.5+7		Expt	80BNL		245	780	LRL	Haight+CS TBL.REVIEW.
CU	063	N,DEUTERON	1.5+7		Revw	80BNL		245	780	LRL	Haight+CS TBL.REVIEW.
CU	063	N,ALPHA REAC	1.5+7		Expt	80BNL		289	780	AI	Kneff+CS FOR 13 NUCLIDES.TBL.CFD.
CU	063	N,ALPHA REAC	1.5+7		Revw	80BNL		215	780	LAS	Browne+REVIEW.ANG-INTEG.GRPH,TBL
CU	063	N,ALPHA REAC	1.5+7		Revw	80BNL		245	780	LRL	Haight+CS TBL.A SPEC GRPH.CFD CALCS.
CU	065	DIFF ELASTIC	8.0+6	1.4+7	Revw	80BNL		259	780	TNL	Walter+EXPT COMPLETED AT TNL.NDG.TBC

Element S	A	Quantity	Energy (eV) Min	Max	Type	Documentation Ref	Vol	Page	Date	Lab	Comments
CU	065	POLARIZATION	1.0+7	1.4+7	Revw	80BNL		259	780	TNL	Walter+ANAL PWR DISTRIB.NDG.GRPH.CFD
CU	065	N2N-REACTION	3.0+7		Expt	80BNL		539	780	JUL	Qaim+ACT.CS VS ASSYM PAR GRPH.
CU	065	N,PROTON	1.5+7		Revw	80BNL		245	780	LRL	Haight+CS TBL.P SPEC GRPH.CFD CALCS.
CU	065	N,PROTON	3.0+7		Expt	80BNL		539	780	JUL	Qaim+ACT.CS VS ASSYM PAR.GRPH.
CU	065	N,PROTON	3.0+7		Expt	80BNL		539	780	JUL	Qaim+INTEG MEAS CFD CS FROM EXCIT FN
CU	065	N,DEUTERON	1.5+7		Revw	80BNL		245	780	LRL	Haight+CS TBL.REVIEW.
CU	065	N,ALPHA REAC	1.5+7		Expt	80BNL		289	780	AI	Kneff+CS FOR 13 NUCLIDES.TBL.CFD.
CU	065	N,ALPHA REAC	1.5+7		Revw	80BNL		215	780	LAS	Browne+REVIEW.ANG-INTEG.GRPH,TBL
CU	065	N,ALPHA REAC	1.5+7		Revw	80BNL		245	780	LRL	Haight+CS TBL.A SPEC GRPH.CFD CALCS.
CU	065	N,N ALPHA	3.0+7		Expt	80BNL		539	780	JUL	Qaim+ACT.CS GVN.SYSTEMATICS TBD.
ZN		DIFF INELAST	1.5+7		Theo	80BNL		711	780	RCN	Gruppelaar+SPEC,ANGDIST.CALC VS EXPT
ZN		NONEL GAMMA	1.0+5	2.0+7	Revw	80BNL		277	780	ORL	Larson.REVIEW.NDG.SEE ORNL REPORT.
ZN		NEUT EMISSN	1.4+7		Expt	80BNL		343	780	IRK	Vonach+ANGINTEG SPEC.TBL,GRPH.CFD.
ZN		NEUT EMISSN	1.5+7		Theo	80BNL		711	780	RCN	Gruppelaar+EMISSION SPEC CALC VS EXP
GA		DIFF INELAST	1.5+7		Theo	80BNL		711	780	RCN	Gruppelaar+SPEC,ANGDIST.CALC VS EXPT

Element S	A	Quantity	Energy (eV) Min	Max	Type	Documentation Ref	Vol	Page	Date	Lab	Comments
GA		N2N REACTION	1.0+7	1.5+7	Expt	80BNL		399	780	BRC	Frehaut+TOF.NORM REL U238 NF.CS TBL.
GA		NEUT EMISSN	1.5+7		Theo	80BNL		711	780	RCN	Gruppelaar+EMISSION SPEC CALC VS EXP
AS	075	N2N REACTION	1.1+7	1.5+7	Expt	80BNL		399	780	BRC	Frehaut+TOF.NORM REL U238 NF.CS TBL.
SE		DIFF INELAST	1.5+7		Theo	80BNL		711	780	RCN	Gruppelaar+SPEC,ANGDIST.CALC VS EXPT
SE		NEUT EMISSN	1.5+7		Theo	80BNL		711	780	RCN	Gruppelaar+EMISSION SPEC CALC VS EXP
SE	076	N2N REACTION	1.2+7	1.5+7	Expt	80BNL		399	780	BRC	Frehaut+TOF.NORM REL U238 NF.CS TBL.
SE	078	N2N REACTION	1.1+7	1.5+7	Expt	80BNL		399	780	BRC	Frehaut+TOF.NORM REL U238 NF.CS TBL.
SE	080	N2N REACTION	1.0+7	1.5+7	Expt	80BNL		399	780	BRC	Frehaut+TOF.NORM REL U238 NF.CS TBL.
SE	082	N2N REACTION	1.0+7	1.5+7	Expt	80BNL		399	780	BRC	Frehaut+TOF.NORM REL U238 NF.CS TBL.
BR		DIFF INELAST	1.5+7		Theo	80BNL		711	780	RCN	Gruppelaar+SPEC,ANGDIST.CALC VS EXPT
BR		NEUT EMISSN	1.5+7		Theo	80BNL		711	780	RCN	Gruppelaar+EMISSION SPEC CALC VS EXP
Y	089	N2N REACTION	1.2+7	1.5+7	Expt	80BNL		399	780	BRC	Frehaut+TOF.NORM REL U238 NF.CS TBL.
ZR		DIFF INELAST	1.5+7		Theo	80BNL		711	780	RCN	Gruppelaar+SPEC,ANGDIST.CALC VS EXPT
ZR		N2N REACTION	8.0+6	1.5+7	Expt	80BNL		399	780	BRC	Frehaut+TOF.NORM REL U238 NF.CS TBL.
ZR		NEUT EMISSN	1.4+7		Expt	80BNL		343	780	IRK	Vonach+ANGINTEG SPEC.TBL,GRPH.CFD.

Element S	A	Quantity	Energy (eV) Min	Max	Type	Documentation Ref	Vol	Page	Date	Lab	Comments
ZR		NEUT EMISSN	1.5+7		Theo	80BNL		711	780	RCN	Gruppelaar+EMISSION SPEC CALC VS EXP
ZR		N,ALPHA REAC	NDG		Expt	80BNL		289	780	AI	Kneff+CS MEAS TO BE ANALYZED.NDG.
ZR	088	N2N REACTION	1.2+7	2.0+7	Revw	80BNL		641	780	LRL	Gardner+CS CALC CFD EXPT.GRPH.
ZR	089	N2N REACTION	1.0+7	2.0+7	Revw	80BNL		641	780	LRL	Gardner+CS CALC CFD EXPT.GRPH.
ZR	090	TOT INELAST	1.2+7	2.0+7	Revw	80BNL		641	780	LRL	Gardner+COMNUC CALC VS STAPRE.GRPH.
ZR	090	N2N REACTION	8.0+6	2.0+7	Revw	80BNL		641	780	LRL	Gardner+COMNUC CALC VS STAPRE.GRPH.
ZR	090	N,PROTON	8.0+6	2.0+7	Revw	80BNL		641	780	LRL	Gardner+COMNUC CALC VS STAPRE.GRPH.
ZR	090	N,N PROTON	1.1+7	2.0+7	Revw	80BNL		641	780	LRL	Gardner+COMNUC CALC VS STAPRE.GRPH.
ZR	090	N,ALPHA REAC	1.2+7	2.4+7	Revw	80BNL		641	780	LRL	Gardner+COMNUC CALC VS STAPRE.GRPH.
ZR	090	N,N ALPHA	1.2+7	2.4+7	Revw	80BNL		641	780	LRL	Gardner+COMNUC CALC VS STAPRE.GRPH.
NB	093	DIFF INELAST	7.5+6	1.2+7	Revw	80BNL		259	780	TNL	Walter+CONTINUUM EMISSION SPEC TBD.
NB	093	DIFF INELAST	1.5+7		Theo	80BNL		711	780	RCN	Gruppelaar+SPEC,ANGDIST.CALC VS EXPT
NB	093	NONEL GAMMA	1.0+5	2.0+7	Revw	80BNL		277	780	ORL	Larson.REVIEW.NDG.SEE ORNL REPORT.
NB	093	N2N REACTION	9.4+6	1.5+7	Expt	80BNL		399	780	BRC	Frehaut+TOF.NORM REL U238 NF.CS TBL.
NB	093	N2N REACTION	3.0+7		Expt	80BNL		539	780	JUL	Qaim+INTEG MEAS CFD CS FROM EXCIT FN

Element S	A	Quantity	Energy (eV) Min	Max	Type	Documentation Ref	Vol	Page	Date	Lab	Comments
NB	093	N2N REACTION	3.0+7		Expt	80BNL		539	780 JUL		Qaim+ACT.CS VS ASSYM PAR.GRPH.
NB	093	NXN REACTION	1.0+6	2.0+7	Revw	80BNL		277	780 ORL		Larson.REVIEW.NDG.SEE ORNL REPORT
NB	093	NEUT EMISSN	1.4+7		Expt	80BNL		343	780 IRK		Vonach+ANGINTEG SPEC.TBL,GRPH.CFD.
NB	093	NEUT EMISSN	1.5+7		Theo	80BNL		711	780 RCN		Gruppelaar+EMISSION SPEC CALC VS EXP
NB	093	N,PROTON	1.5+7		Revw	80BNL		215	780 LAS		Browne+SPEC,ANGDISTS.NDG.REFS
NB	093	N,DEUTERON	1.5+7		Revw	80BNL		215	780 LAS		Browne+SPEC,ANGDISTS.NDG.REFS
NB	093	N,TRITON	3.0+7		Expt	80BNL		539	780 JUL		Qaim+CS GVN.20 PCT ERROR
NB	093	N,ALPHA REAC	NDG		Expt	80BNL		289	780 AI		Kneff+CS MEAS TO BE ANALYZED.NDG.
NB	093	N,ALPHA REAC	1.4+7	1.5+7	Revw	80BNL		215	780 LAS		Browne+REVIEW.SPEC,ANGDIST.CS TBL.
NB	093	N,ALPHA REAC	3.0+7		Expt	80BNL		539	780 JUL		Qaim+ACT.CS VS ASSYM PAR.GRPH.
NB	093	LVL DENSITY	NDG		Revw	80BNL		641	780 LRL		Gardner+SPIN CUT OFF PARS.GRPH.
MO		NONEL GAMMA	1.0+5	2.0+7	Revw	80BNL		277	780 ORL		Larson.REVIEW.NDG.SEE ORNL REPORT.
MO		N2N REACTION	8.0+6	1.5+7	Expt	80BNL		399	780 BRC		Frehaut+TOF.NORM REL U238 NF.CS TBL.
MO		NEUT EMISSN	1.4+7		Revw	80BNL		215	780 LAS		Browne+REVIEW.REFS GVN.NDG.
MO		NEUT EMISSN	1.4+7		Expt	80BNL		343	780 IRK		Vonach+ANGINTEG SPEC.TBL,GRPH.CFD.

Element S	A	Quantity	Energy (eV) Min	Max	Type	Documentation Ref	Vol	Page	Date	Lab	Comments
MO		N,ALPHA REAC	NDG		Expt	80BNL		289	780	AI	Kneff+CS MEAS TO BE ANALYZED.NDG.
MO	092	DIFF ELASTIC	2.6+7		Revw	80BNL		375	780	OHO	Finlay+STATUS SINCE MAY 77.REFS GVN.
MO	092	N,PROTON	1.4+7	1.5+7	Expt	80BNL		245	780	LRL	Haight+PRELIMINARY MEAS.NDG.
MO	092	N,DEUTERON	1.4+7	1.5+7	Expt	80BNL		245	780	LRL	Haight+PRELIMINARY MEAS.NDG.
MO	092	N,ALPHA REAC	NDG		Expt	80BNL		289	780	AI	Kneff+CS MEAS TO BE ANALYZED.NDG.
MO	092	N,ALPHA REAC	1.4+7	1.5+7	Expt	80BNL		245	780	LRL	Haight+PRELIMINARY MEAS.NDG.
MO	092	N,ALPHA REAC	3.0+7		Expt	80BNL		539	780	JUL	Qaim+ACT.CS VS ASSYM PAR GRPH.
MO	092	N,ALPHA REAC	3.0+7		Expt	80BNL		539	780	JUL	Qaim+ACT.CS VS ASSYM PAR.GRPH.
MO	094	N,PROTON	1.4+7	1.5+7	Expt	80BNL		245	780	LRL	Haight+P SPEC AT 90 DEG.
MO	094	N,DEUTERON	1.4+7	1.5+7	Expt	80BNL		245	780	LRL	Haight+PRELIMINARY MEAS.NDG.
MO	094	N,ALPHA REAC	NDG		Expt	80BNL		289	780	AI	Kneff+CS MEAS TO BE ANALYZED.NDG.
MO	094	N,ALPHA REAC	1.4+7	1.5+7	Expt	80BNL		245	780	LRL	Haight+PRELIMINARY MEAS.NDG.
MO	095	N,PROTON	1.4+7	1.5+7	Expt	80BNL		245	780	LRL	Haight+PRELIMINARY MEAS.NDG.
MO	095	N,DEUTERON	1.4+7	1.5+7	Expt	80BNL		245	780	LRL	Haight+PRELIMINARY MEAS.NDG.
MO	095	N,ALPHA REAC	NDG		Expt	80BNL		289	780	AI	Kneff+CS MEAS TO BE ANALYZED.NDG.

Element S	A	Quantity	Energy (eV) Min	Max	Type	Documentation Ref	Vol	Page	Date	Lab	Comments
MO	095	N,ALPHA REAC	1.4+7	1.5+7	Expt	80BNL		245	780	LRL	Haight+PRELIMINARY MEAS.NDG.
MO	096	DIFF ELASTIC	2.6+7		Revw	80BNL		375	780	OHO	Finlay+STATUS SINCE MAY 77.REFS GVN.
MO	096	N,PROTON	1.4+7	1.5+7	Expt	80BNL		245	780	LRL	Haight+PRELIMINARY MEAS.NDG.
MO	096	N,PROTON	3.0+7		Expt	80BNL		539	780	JUL	Qaim+ACT.CS VS ASSYM PAR GRPH.
MO	096	N,N PROTON	3.0+7		Expt	80BNL		539	780	JUL	Qaim+(N,D)+(N,NP).CS VS ASSYMETRY.
MO	096	N,DEUTERON	1.4+7	1.5+7	Expt	80BNL		245	780	LRL	Haight+PRELIMINARY MEAS.NDG.
MO	096	N,DEUTERON	3.0+7		Expt	80BNL		539	780	JUL	Qaim+(N,D)+(N,NP).CS VS ASSYMETRY.
MO	096	N,ALPHA REAC	NDG		Expt	80BNL		289	780	AI	Kneff+CS MEAS TO BE ANALYZED.NDG.
MO	096	N,ALPHA REAC	1.4+7	1.5+7	Expt	80BNL		245	780	LRL	Haight+PRELIMINARY MEAS.NDG.
MO	096	N,ALPHA REAC	3.0+7		Expt	80BNL		539	780	JUL	Qaim+ACT.CS VS ASSYM PAR.GRPH.
MO	097	N,N PROTON	3.0+7		Expt	80BNL		539	780	JUL	Qaim+(N,D)+(N,NP).CS VS ASSYMETRY.
MO	097	N,DEUTERON	3.0+7		Expt	80BNL		539	780	JUL	Qaim+(N,D)+(N,NP).CS VS ASSYMETRY.
MO	097	N,ALPHA REAC	NDG		Expt	80BNL		289	780	AI	Kneff+CS MEAS TO BE ANALYZED.NDG.
MO	098	DIFF ELASTIC	2.6+7		Revw	80BNL		375	780	OHO	Finlay+STATUS SINCE MAY 77.REFS GVN.
MO	098	N,N PROTON	3.0+7		Expt	80BNL		539	780	JUL	Qaim+(N,D)+(N,NP).CS VS ASSYMETRY.

Element S	A	Quantity	Energy (eV) Min	Max	Type	Documentation Ref	Vol	Page	Date	Lab	Comments
MO	098	N,DEUTERON	3.0+7		Expt	80BNL	539	780	JUL		Qaim+(N,D)+(N,NP).CS VS ASSYMETRY.
MO	098	N,ALPHA REAC	3.0+7		Expt	80BNL	539	780	JUL		Qaim+ACT.CS VS ASSYM PAR GRPH.
MO	100	DIFF ELASTIC	2.6+7		Revw	80BNL	375	780	OHO		Finlay+STATUS SINCE MAY 77.REFS GVN.
MO	100	N,ALPHA REAC	NDG		Expt	80BNL	289	780	AI		Kneff+CS MEAS TO BE ANALYZED.NDG.
RH	103	N2N REACTION	1.0+7	1.5+7	Expt	80BNL	399	780	BRC		Frehaut+TOF.NORM REL U238 NF.CS TBL.
AG		NONEL GAMMA	1.0+5	2.0+7	Revw	80BNL	277	780	ORL		Larson.REVIEW.NDG.SEE ORNL REPORT.
AG		NEUT EMISSN	1.4+7		Expt	80BNL	343	780	IRK		Vonach+ANGINTEG SPEC.TBL,GRPH.CFD.
CD		DIFF INELAST	1.5+7		Theo	80BNL	711	780	RCN		Gruppelaar+SPEC,ANGDIST.CALC VS EXPT
CD		NEUT EMISSN	1.5+7		Theo	80BNL	711	780	RCN		Gruppelaar+EMISSION SPEC CALC VS EXP
IN		DIFF INELAST	1.5+7		Theo	80BNL	711	780	RCN		Gruppelaar+SPEC,ANGDIST.CALC VS EXPT
IN		NEUT EMISSN	1.5+7		Theo	80BNL	711	780	RCN		Gruppelaar+EMISSION SPEC CALC VS EXP
SN		DIFF INELAST	7.5+6	1.2+7	Revw	80BNL	259	780	TNL		Walter+CONTINUUM EMISSION SPEC TBD.
SN		DIFF INELAST	1.5+7		Theo	80BNL	711	780	RCN		Gruppelaar+SPEC,ANGDIST.CALC VS EXPT
SN		NONEL GAMMA	1.0+5	2.0+7	Revw	80BNL	277	780	ORL		Larson.REVIEW.NDG.SEE ORNL REPORT.
SN		NEUT EMISSN	1.4+7		Revw	80BNL	215	780	LAS		Browne+REVIEW.REFS GVN.NDG.

Element S	A	Quantity	Energy (eV) Min	Max	Type	Documentation Ref	Vol	Page	Date	Lab	Comments
SN		NEUT EMISSN	1.4+7		Expt	80BNL		343	780	IRK	Vonach+ANGINTEG SPEC.TBL,GRPH.CFD.
SN		NEUT EMISSN	1.5+7		Theo	80BNL		711	780	RCN	Gruppelaar+EMISSION SPEC CALC VS EXP
SN		N,ALPHA REAC	NDG		Expt	80BNL		289	780	AI	Kneff+CS MEAS TO BE ANALYZED.NDG.
SN	112	N,ALPHA REAC	NDG		Expt	80BNL		289	780	AI	Kneff+CS MEAS TBD.NDG.
SN	114	N,ALPHA REAC	NDG		Expt	80BNL		289	780	AI	Kneff+CS MEAS TBD.NDG.
SN	115	N,ALPHA REAC	NDG		Expt	80BNL		289	780	AI	Kneff+CS MEAS TBD.NDG.
SN	116	DIFF INELAST	2.4+7		Revw	80BNL		215	780	LAS	Browne+REVIEW.NDG.BIB REFS.
SN	116	DIFF INELAST	2.4+7		Revw	80BNL		375	780	OHO	Finlay+STATUS SINCE MAY 77.REFS GVN.
SN	116	N,ALPHA REAC	NDG		Expt	80BNL		289	780	AI	Kneff+CS MEAS TBD.NDG.
SN	117	N,ALPHA REAC	NDG		Expt	80BNL		289	780	AI	Kneff+CS MEAS TBD.NDG.
SN	118	DIFF ELASTIC	2.4+7		Revw	80BNL		375	780	OHO	Finlay+STATUS SINCE MAY 77.REFS GVN.
SN	118	N,ALPHA REAC	NDG		Expt	80BNL		289	780	AI	Kneff+CS MEAS TBD.NDG.
SN	119	N,ALPHA REAC	NDG		Expt	80BNL		289	780	AI	Kneff+CS MEAS TBD.NDG.
SN	120	N,ALPHA REAC	NDG		Expt	80BNL		289	780	AI	Kneff+CS MEAS TBD.NDG.
SN	122	N,ALPHA REAC	NDG		Expt	80BNL		289	780	AI	Kneff+CS MEAS TBD.NDG.

Element S	A	Quantity	Energy (eV) Min	Max	Type	Documentation Ref	Vol	Page	Date	Lab	Comments
SN	124	DIFF ELASTIC	2.4+7		Revw	80BNL		375	780	OHO	Finlay+STATUS SINCE MAY 77.REFS GVN.
SN	124	N,ALPHA REAC	NDG		Expt	80BNL		289	780	AI	Kneff+CS MEAS TBD.NDG.
SB		DIFF INELAST	1.5+7		Theo	80BNL		711	780	RCN	Gruppelaar+SPEC,ANGDIST.CALC VS EXPT
SB		NEUT EMISSN	1.5+7		Theo	80BNL		711	780	RCN	Gruppelaar+EMISSION SPEC CALC VS EXP
I	127	DIFF INELAST	1.5+7		Theo	80BNL		711	780	RCN	Gruppelaar+SPEC,ANGDIST.CALC VS EXPT
I	127	NEUT EMISSN	1.5+7		Theo	80BNL		711	780	RCN	Gruppelaar+EMISSION SPEC CALC VS EXP
BA		NEUT EMISSN	1.4+7		Expt	80BNL		343	780	IRK	Vonach+ANGINTEG SPEC.TBL,GRPH.CFD.
LA	139	TOTAL XSECT	2.5+6	6.0+7	Expt	80BNL		769	780	LRL	Phillips+TRNS.REL CE-140 OPTMDL.NDG
CE	140	TOTAL XSECT	2.5+6	6.0+7	Expt	80BNL		769	780	LRL	Phillips+TRNS.GRPH.OPTMDL ANAL
CE	142	TOTAL XSECT	2.5+6	6.0+7	Expt	80BNL		769	780	LRL	Phillips+TRNS.REL CE-140 OPTMDL.GRPH
PR	141	TOTAL XSECT	2.5+6	6.0+7	Expt	80BNL		769	780	LRL	Phillips+TRNS.REL CE-140 OPTMDL.NDG
ND	142	DIFF ELASTIC	7.0+6		Theo	80BNL		769	780	LRL	Phillips+OPTMDL CALC CFD EXPT.GRPH
ND	142	TOT INELAST	5.0+6	7.0+6	Theo	80BNL		769	780	LRL	Phillips+OPTMDL CALC CFD EXPT.3E.TBL
ND	142	N2N REACTION	1.0+7	1.5+7	Expt	80BNL		399	780	BRC	Frehaut+TOF.NORM REL U238 NF.CS TBL.
ND	144	N2N REACTION	8.2+6	1.5+7	Expt	80BNL		399	780	BRC	Frehaut+TOF.NORM REL U238 NF.CS TBL.

Element S	A	Quantity	Energy (eV) Min	Max	Type	Documentation Ref	Vol	Page	Date	Lab	Comments
ND	146	N2N REACTION	8.0+6	1.5+7	Expt	80BNL		399	780	BRC	Frehaut+TOF.NORM REL U238 NF.CS TBL.
ND	146	NXN REACTION	1.5+7	1.5+7	Expt	80BNL		399	780	BRC	Frehaut+(N,3N).TOF.REL U238 NF.TBL.
ND	148	N2N REACTION	8.0+6	1.5+7	Expt	80BNL		399	780	BRC	Frehaut+TOF.NORM REL U238 NF.CS TBL.
ND	148	NXN REACTION	1.4+7	1.5+7	Expt	80BNL		399	780	BRC	Frehaut+(N,3N).TOF.REL U238 NF.TBL.
ND	150	N2N REACTION	8.0+6	1.5+7	Expt	80BNL		399	780	BRC	Frehaut+TOF.NORM REL U238 NF.CS TBL.
ND	150	NXN REACTION	1.3+7	1.5+7	Expt	80BNL		399	780	BRC	Frehaut+(N,3N).TOF.REL U238 NF.TBL.
SM	148	N2N REACTION	8.6+6	1.5+7	Expt	80BNL		399	780	BRC	Frehaut+TOF.NORM REL U238 NF.CS TBL.
SM	150	N2N REACTION	8.6+6	1.5+7	Expt	80BNL		399	780	BRC	Frehaut+TOF.NORM REL U238 NF.CS TBL.
SM	152	N2N REACTION	8.6+6	1.5+7	Expt	80BNL		399	780	BRC	Frehaut+TOF.NORM REL U238 NF.CS TBL.
SM	154	N2N REACTION	8.4+6	1.5+7	Expt	80BNL		399	780	BRC	Frehaut+TOF.NORM REL U238 NF.CS TBL.
EU	151	N2N REACTION	8.4+6	1.5+7	Expt	80BNL		399	780	BRC	Frehaut+TOF.NORM REL U238 NF.CS TBL.
GD	155	N2N REACTION	6.9+6	1.5+7	Expt	80BNL		399	780	BRC	Frehaut+TOF.NORM REL U238 NF.CS TBL.
GD	156	N2N REACTION	8.4+6	1.5+7	Expt	80BNL		399	780	BRC	Frehaut+TOF.NORM REL U238 NF.CS TBL.
GD	157	N2N REACTION	6.9+6	1.5+7	Expt	80BNL		399	780	BRC	Frehaut+TOF.NORM REL U238 NF.CS TBL.
GD	158	N2N REACTION	8.4+6	1.5+7	Expt	80BNL		399	780	BRC	Frehaut+TOF.NORM REL U238 NF.CS TBL.

Element S	A	Quantity	Energy (eV) Min	Max	Type	Documentation Ref	Vol	Page	Date	Lab	Comments
GD	160	N2N REACTION	7.9+6	1.5+7	Expt	80BNL		399	780	BRC	Frehaut+TOF.NORM REL U238 NF.CS TBL.
GD	160	NXN REACTION	1.4+7	1.5+7	Expt	80BNL		399	780	BRC	Frehaut+(N,3N).TOF.REL U238 NF.TBL.
TM	169	N2N REACTION	8.4+6	1.5+7	Expt	80BNL		399	780	BRC	Frehaut+TOF.NORM REL U238 NF.CS TBL.
LU	175	N2N REACTION	8.0+6	1.6+7	Revw	80BNL		641	780	LRL	Gardner+LU174 ISOMER RATIO CALC.CURV
LU	175	N2N REACTION	8.4+6	1.5+7	Expt	80BNL		399	780	BRC	Frehaut+TOF.NORM REL U238 NF.CS TBL.
TA	181	DIFF ELASTIC	NDG		Expt	80BNL		781	780	LRL	Hansen+(P,N)MEAS.DEL FROM OPTMDL.NDG
TA	181	DIFF INELAST	1.5+7		Theo	80BNL		711	780	RCN	Gruppelaar+SPEC,ANGDIST.CALC VS EXPT
TA	181	NONEL GAMMA	1.0+5	2.0+7	Revw	80BNL		277	780	ORL	Larson.REVIEW.NDG.SEE ORNL REPORT.
TA	181	N2N REACTION	8.4+6	1.5+7	Expt	80BNL		399	780	BRC	Frehaut+TOF.NORM REL U238 NF.CS TBL.
TA	181	NEUT EMISSN	1.4+7		Expt	80BNL		343	780	IRK	Vonach+ANGINTEG SPEC.TBL,GRPH.CFD.
TA	181	NEUT EMISSN	1.5+7		Theo	80BNL		711	780	RCN	Gruppelaar+EMISSION SPEC CALC VS EXP
W		DIFF ELASTIC	NDG		Revw	80BNL		215	780	LAS	Browne+REVIEW.10 PC PRECISION.NDG.
W		DIFF INELAST	7.5+6	1.2+7	Revw	80BNL		259	780	TNL	Walter+CONTINUUM EMISSION SPEC TBD.
W		DIFF INELAST	1.5+7		Theo	80BNL		711	780	RCN	Gruppelaar+SPEC,ANGDIST.CALC VS EXPT
W		NONEL GAMMA	1.0+5	2.0+7	Revw	80BNL		277	780	ORL	Larson.REVIEW.NDG.SEE ORNL REPORT.

Element S	A	Quantity	Energy (eV) Min	Max	Type	Documentation Ref	Vol	Page	Date	Lab	Comments
W		N2N REACTION	8.0+6	1.5+7	Expt	80BNL		399	780	BRC	Frehaut+TOF.NORM REL U238 NF.CS TBL.
W		NEUT EMISSN	1.4+7		Revw	80BNL		215	780	LAS	Browne+REVIEW.REFS GVN.NDG.
W		NEUT EMISSN	1.4+7		Expt	80BNL		343	780	IRK	Vonach+ANGINTEG SPEC.TBL,GRPH.CFD.
W		NEUT EMISSN	1.5+7		Theo	80BNL		711	780	RCN	Gruppelaar+EMISSION SPEC CALC VS EXP
W		N,ALPHA REAC	NDG		Expt	80BNL		289	780	AI	Kneff+CS MEAS TO BE ANALYZED.NDG.
W	182	N2N REACTION	8.2+6	1.5+7	Expt	80BNL		399	780	BRC	Frehaut+TOF.NORM REL U238 NF.CS TBL.
W	182	N,ALPHA REAC	NDG		Expt	80BNL		289	780	AI	Kneff+CS MEAS TBD.NDG.
W	183	N2N REACTION	7.4+6	1.5+7	Expt	80BNL		399	780	BRC	Frehaut+TOF.NORM REL U238 NF.CS TBL.
W	183	N,ALPHA REAC	NDG		Expt	80BNL		289	780	AI	Kneff+CS MEAS TBD.NDG.
W	184	N2N REACTION	7.7+6	1.5+7	Expt	80BNL		399	780	BRC	Frehaut+TOF.NORM REL U238 NF.CS TBL.
W	184	NXN REACTION	1.5+7		Expt	80BNL		399	780	BRC	Frehaut+(N,3N).TOF.REL U238 NF.TBL.
W	184	N,ALPHA REAC	NDG		Expt	80BNL		289	780	AI	Kneff+CS MEAS TBD.NDG.
W	186	N2N REACTION	7.4+6	1.5+7	Expt	80BNL		399	780	BRC	Frehaut+TOF.NORM REL U238 NF.CS TBL.
W	186	NXN REACTION	1.4+7	1.5+7	Expt	80BNL		399	780	BRC	Frehaut+(N,3N).TOF.REL U238 NF.TBL.
W	186	N,ALPHA REAC	NDG		Expt	80BNL		289	780	AI	Kneff+CS MEAS TBD.NDG.

Element S	A	Quantity	Energy (eV) Min	Max	Type	Documentation Ref	Vol	Page	Date	Lab	Comments
PT		N2N REACTION	8.0+6	1.5+7	Expt	80BNL		399	780	BRC	Frehaut+TOF.NORM REL U238 NF.CS TBL.
AU	197	TOTAL XSECT	2.0+6	8.0+7	Revw	80BNL		277	780	ORL	Larson.ORELA.TRNS AT 40 MEV GVN.
AU	197	DIFF ELASTIC	NDG		Expt	80BNL		781	780	LRL	Hansen+(P,N)MEAS.DEL FROM OPTMDL.NDG
AU	197	DIFF INELAST	1.5+7		Theo	80BNL		711	780	RCN	Gruppelaar+SPEC,ANGDIST.CALC VS EXPT
AU	197	NONEL GAMMA	1.0+5	2.0+7	Revw	80BNL		277	780	ORL	Larson.REVIEW.NDG.SEE ORNL REPORT.
AU	197	N2N REACTION	8.4+6	1.5+7	Expt	80BNL		399	780	BRC	Frehaut+TOF.NORM REL U238 NF.CS TBL.
AU	197	NEUT EMISSN	1.4+7		Expt	80BNL		343	780	IRK	Vonach+ANGINTEG SPEC.TBL,GRPH.CFD.
AU	197	NEUT EMISSN	1.5+7		Theo	80BNL		711	780	RCN	Gruppelaar+EMISSION SPEC CALC VS EXP
AU	197	N,ALPHA REAC	1.5+7		Expt	80BNL		289	780	AI	Kneff+CS FOR 13 NUCLIDES.TBL.CFD.
HG		DIFF INELAST	1.5+7		Theo	80BNL		711	780	RCN	Gruppelaar+SPEC,ANGDIST.CALC VS EXPT
HG		NEUT EMISSN	1.5+7		Theo	80BNL		711	780	RCN	Gruppelaar+EMISSION SPEC CALC VS EXP
TL	203	N2N REACTION	8.4+6	1.5+7	Expt	80BNL		399	780	BRC	Frehaut+TOF.NORM REL U238 NF.CS TBL.
TL	205	N2N REACTION	8.4+6	1.5+7	Expt	80BNL		399	780	BRC	Frehaut+TOF.NORM REL U238 NF.CS TBL.
PB		TOTAL XSECT	2.0+6	8.0+7	Revw	80BNL		277	780	ORL	Larson.ORELA.TRNS AT 40 MEV GVN.
PB		DIFF INELAST	7.5+6	1.2+7	Revw	80BNL		259	780	TNL	Walter+CONTINUUM EMISSION SPEC.NDG.

Element S	A	Quantity	Energy (eV) Min	Max	Type	Documentation Ref	Vol	Page	Date	Lab	Comments
PB		DIFF INELAST	1.5+7		Theo	80BNL		711	780	RCN	Gruppelaar+SPEC,ANGDIST.CALC VS EXPT
PB		NONEL GAMMA	1.0+5	2.0+7	Revw	80BNL		277	780	ORL	Larson.REVIEW.NDG.SEE ORNL REPORT.
PB		N2N REACTION	7.4+6	1.5+7	Expt	80BNL		399	780	BRC	Frehaut+TOF.NORM REL U238 NF.CS TBL.
PB		NEUT EMISSN	1.0+7	1.2+7	Revw	80BNL		215	780	LAS	Browne+REVIEW.REFS GVN.GRPH FOR 1ANG
PB		NEUT EMISSN	1.4+7		Expt	80BNL		343	780	IRK	Vonach+ANGINTEG SPEC.TBL,GRPH.CFD.
PB		NEUT EMISSN	1.5+7		Theo	80BNL		711	780	RCN	Gruppelaar+EMISSION SPEC CALC VS EXP
PB		N,ALPHA REAC	NDG		Expt	80BNL		289	780	AI	Kneff+CS MEAS TO BE ANALYZED.NDG.
PB	204	N,ALPHA REAC	NDG		Expt	80BNL		289	780	AI	Kneff+CS MEAS TBD.NDG.
PB	206	N2N REACTION	8.4+6	1.5+7	Expt	80BNL		399	780	BRC	Frehaut+TOF.NORM REL U238 NF.CS TBL.
PB	206	N,ALPHA REAC	NDG		Expt	80BNL		289	780	AI	Kneff+CS MEAS TBD.NDG.
PB	207	N2N REACTION	7.4+6	1.5+7	Expt	80BNL		399	780	BRC	Frehaut+TOF.NORM REL U238 NF.CS TBL.
PB	207	N,ALPHA REAC	NDG		Expt	80BNL		289	780	AI	Kneff+CS MEAS TBD.NDG.
PB	208	TOTAL XSECT	5.0+6	2.0+8	Expt	80BNL		301	780	LAS	Lisowski+TOF,TRNS.GRPH.CFD OTHS,ENDF
PB	208	DIFF ELASTIC	2.0+7	4.0+7	Revw	80BNL		375	780	OHO	Finlay+STATUS SINCE MAY 77.REFS GVN.
PB	208	DIFF ELASTIC	1.0+7		Revw	80BNL		259	780	TNL	Walter+EXPT COMPLETED AT TNL.NDG.TBC

Element S	A	Quantity	Energy (eV) Min	Max	Type	Documentation Ref	Vol	Page	Date	Lab	Comments
PB	208	POLARIZATION	1.0+7		Revw	80BNL		259	780	TNL	Walter+ANAL PWR DISTRIB.NDG.TBC.
PB	208	DIFF INELAST	2.6+7		Revw	80BNL		375	780	OHO	Finlay+STATUS SINCE MAY 77.REFS GVN.
PB	208	N,GAMMA	6.0+6	1.4+7	Expt	80BNL		259	780	TNL	Walter+ANGDISTS 90 DEG.NDG
PB	208	N2N REACTION	7.9+6	1.5+7	Expt	80BNL		399	780	BRC	Frehaut+TOF.NORM REL U238 NF.CS TBL.
PB	208	N,ALPHA REAC	NDG		Expt	80BNL		289	780	AI	Kneff+CS MEAS TBD.NDG.
BI	209	EVALUATION	1.0-5	2.0+7	Eval	80BNL		799	780	ANL	Smith+ENDF FORMAT.GRPHS.CFD EXPTS.
BI	209	TOTAL XSECT	1.2+6	4.5+6	Expt	80BNL		799	780	ANL	Smith+TRNS.50 KEV RSLN.GRPH.CFD OTHS
BI	209	ELASTIC SCAT	1.5+6	4.0+6	Expt	80BNL		799	780	ANL	Smith+TOF,20-160DEG.INTEG.NDG.
BI	209	DIFF ELASTIC	1.5+6	4.0+6	Expt	80BNL		799	780	ANL	Smith+TOF,20-160DEG.GRPH.CFD OTHS
BI	209	DIFF ELASTIC	NDG		Expt	80BNL		781	780	LRL	Hansen+(P,N)MEAS.DEL FROM OPTMDL.NDG
BI	209	DIFF INELAST	1.0+6	4.0+6	Expt	80BNL		799	780	ANL	Smith+20-160 DEG.ANGINTEG GRPHS.CFD.
BI	209	DIFF INELAST	1.5+7		Theo	80BNL		711	780	RCN	Gruppelaar+SPEC,ANGDIST.CALC VS EXPT
BI	209	N2N REACTION	8.0+6	1.5+7	Expt	80BNL		399	780	BRC	Frehaut+TOF.NORM REL U238 NF.CS TBL.
BI	209	NEUT EMISSN	1.4+7		Expt	80BNL		343	780	IRK	Vonach+ANGINTEG SPEC.TBL,GRPH.CFD.
BI	209	NEUT EMISSN	1.5+7		Theo	80BNL		711	780	RCN	Gruppelaar+EMISSION SPEC CALC VS EXP

Element S	A	Quantity	Energy (eV) Min	Max	Type	Documentation Ref	Vol	Page	Date	Lab	Comments
TH	232	TOTAL XSECT	5.0+6	2.0+8	Expt	80BNL		301	780	LAS	Lisowski+TOF,TRNS.GRPH.CFD OTHS,ENDF
TH	232	DIFF ELASTIC	7.0+6		Expt	80BNL		781	780	LRL	Hansen+(P,N)MEAS.OPTMDL DEL.TBL,GRPH
TH	232	NONEL GAMMA	1.0+5	2.0+7	Revw	80BNL		277	780	ORL	Larson.REVIEW.NDG.SEE ORNL REPORT.
U	238	TOTAL XSECT	5.0+6	2.0+8	Expt	80BNL		301	780	LAS	Lisowski+TOF,TRNS.GRPH.CFD OTHS,ENDF
U	238	DIFF ELASTIC	7.0+6		Expt	80BNL		781	780	LRL	Hansen+(P,N)MEAS.OPTMDL DEL.TBL,GRPH
U	238	N2N REACTION	6.9+6	1.5+7	Expt	80BNL		399	780	BRC	Frehaut+TOF.NORM REL U238 NF.CS TBL.
U	238	NXN REACTION	1.2+7	1.5+7	Expt	80BNL		399	780	BRC	Frehaut+(N,3N).TOF.REL U238 NF.TBL.
PU	242	TOTAL XSECT	5.0+6	2.0+8	Expt	80BNL		301	780	LAS	Lisowski+TOF,TRNS.GRPH.CFD OTHS,ENDF
MANY		DIFF ELASTIC	2.0+7	4.0+7	Revw	80BNL		375	780	OHO	Finlay+PARTIAL SURVEY SINCE MAY 77
MANY		DIFF INELAST	2.0+7	4.0+7	Revw	80BNL		375	780	OHO	Finlay+PARTIAL SURVEY SINCE MAY 77
MANY		N2N REACTION	TR	1.5+7	Expt	80BNL		399	780	BRC	Frehaut+SYSTEMATICS.50 ELEMENTS.
MANY		N2N REACTION	3.0+7		Expt	80BNL		539	780	JUL	Qaim+SYSTEMATICS FOR 11 ELEMENTS
MANY		NXN REACTION	3.0+7		Expt	80BNL		539	780	JUL	Qaim+(N,3N)11 ELEMENT SYSTEMATICS
MANY		NEUT EMISSN	1.4+7		Expt	80BNL		343	780	IRK	Vonach+17 ELEMENTS.TBLS,GRPHS.CFD.
MANY		N,PROTON	3.0+7		Expt	80BNL		539	780	JUL	Qaim+SYSTEMATICS FOR 11 ELEMENTS.

Element S	A	Quantity	Energy (eV) Min	Max	Type	Documentation Ref	Vol	Page	Date	Lab	Comments
MANY		N,N PROTON	3.0+7		Expt	80BNL	539	780	JUL		Qaim+(N,D)+(N,NP).SYSTEMATICS
MANY		N,DEUTERON	3.0+7		Expt	80BNL	539	780	JUL		Qaim+(N,D)+(N,NP).SYSTEMATICS
MANY		N,HE3 REACTN	3.0+7		Expt	80BNL	539	780	JUL		Qaim+SYSTEMATICS FOR 11 ELEMENTS.
MANY		N,ALPHA REAC	3.0+7		Expt	80BNL	539	780	JUL		Qaim+SYSTEMATICS FOR 11 ELEMENTS.
MANY		N,N ALPHA	3.0+7		Expt	80BNL	539	780	JUL		Qaim+SYSTEMATICS FOR 11 ELEMENTS.

CHARGED PARTICLE REACTION INDEX.

T. W. Burrows.

Be-9(p,x)n relative thick target yield(E;theta)
CRC Revw Conf 80BNL 1 147 80 1.0+1 2.5+1 Lone+ TBL. CURV. LOW-E N(0.3-2.3MEV).

Be-9(p,inelastic+n)Be-8 relative thick target yield(E;theta)
CRC Revw Conf 80BNL 1 147 80 1.5+1 Lone+ APP. 30PRCNT OF LOW-E N YLD.

Be-9(p,inelastic)Be-9 sigma(E;theta)
TNL Revw Conf 80BNL 1 259 80 1.1+1 1.5+1 Walter+ CURV. EXPT+LANE MODEL.

Be-9(p,inelastic)Be-9 polarization (E;theta)
TNL Revw Conf 80BNL 1 259 80 1.1+1 1.6+1 Walter+ CURV. EXPT+LANE MODEL.

Be-9(p,n)B-9 sigma(E;theta)
TNL Revw Conf 80BNL 1 259 80 1.1+1 1.6+1 Walter+ CURV. EXPT+LANE MODEL.

Be-9(p,n)B-9 polarization (E;theta)
TNL Revw Conf 80BNL 1 259 80 1.1+1 1.6+1 Walter+ CURV. EXPT+LANE MODEL.

C-12(p,inelastic)C-12 sigma(E;E';theta)
TNL Theo Conf 80BNL 2 689 80 4.0+1 Kalbach+ CURV. MSD AND MSC CFD EXPT.

C-13(p,inelastic)C-13 sigma(E;theta)
TNL Revw Conf 80BNL 1 259 80 NDG Walter+ NDG. LANE MODEL APPROACH.

C-13(p,n)N-13 sigma(E;theta)
TNL Revw Conf 80BNL 1 259 80 NDG Walter+ NDG. LANE MODEL APPROACH.

N-15(p,inelastic)N-15 sigma(E;theta)
TNL Revw Conf 80BNL 1 259 80 NDG Walter+ NDG. LANE MODEL APPROACH.

N-15(p,n)O-15 sigma(E;theta)
TNL Revw Conf 80BNL 1 259 80 NDG Walter+ NDG. LANE MODEL APPROACH.

O-18(p,inelastic)O-18 sigma(E;theta)

OHO	Revw	Conf	80BNL	1 375	80	2.4+1		Finley+ CURV. 1.98MEV LVL. CFD (N,N').

Al-27(p,x)n sigma(E;theta)

LAS	Revw	Conf	80BNL	1 169	80	5.0+0	8.0+2	Russell+ NDG.

Fe-54(p,alpha)Mn-51 sigma(E;E';theta)

TNL	Theo	Conf	80BNL	2 689	80	1.5+1		Kalbach+ CURV. MSD AND MSC CFD EXPT.

Fe-54(p,He3)Mn-52 sigma(E;E';theta)

TNL	Theo	Conf	80BNL	2 689	80	2.4+1		Kalbach+ CURV. MSD AND MSC CFD EXPT.

Fe-54(p,inelastic)Fe-54 sigma(E;E';theta)

TNL	Theo	Conf	80BNL	2 689	80	1.0+1	6.2+1	Kalbach+ CURV. MSD AND MSC CFD EXPT.

Fe-54(p,inelastic)Fe-54 sigma(E;E';theta) Legendre coefficient expansion x sigma(E)

TNL	Theo	Conf	80BNL	2 689	80	6.2+1		Kalbach+ CURV. MSD AND MSC CFD EXPT.

Fe-56(p,2n)Co-55 sigma(E)

LAS	Eval	Conf	80BNL	2 731	80	1.5+1	4.0+1	Arthur+ CURV. CALC. CFD EXPT.

Fe-56(p,n)Co-56 sigma(E)

LAS	Eval	Conf	80BNL	2 731	80	3.0+0	4.0+1	Arthur+ CURV. CALC. CFD EXPT.

Fe-57(p,n)Co-57 sigma(E)

LAS	Theo	Conf	80BNL	2 751	80	1.8+0	5.0+0	Arthur+ CURV. H-F CALC. CFD EXPT.

Ni-62(p,inelastic)Ni-62 sigma(E;E')

LRL	Revw	Conf	80BNL	2 641	80	1.4+1		Gardner. CURV. CALC. CFD. EXPT(SPRINZAK

Ni-62(p,inelastic)Ni-62 sigma(E;E';theta)

LRL	Revw	Conf	80BNL	2 641	80	1.2+1		Gardner. CURV. 75DEG. CALC. CFD EXPT.

Cu-0(p,x)n sigma(E;theta)
LAS Revw Conf 80BNL 1 169 80 5.0+0 8.0+2 Russell+ NDG.

Nb-93(p,n)Mo-93 sigma(E;theta)
LRL Revw Conf 80BNL 2 641 80 4.9+1 Gardner. CURV. CC CALC. CFD. EXPT.

Rh-103(p,n)Pd-103 sigma(E;E';theta)
TNL Theo Conf 80BNL 2 689 80 5.5+0 Kalbach+ CURV. MSD AND MSC CFD EXPT.

Ag-107(p,n)Cd-107 sigma(E;E';theta)
TNL Theo Conf 80BNL 2 689 80 1.8+1 Kalbach+ CURV. MSD AND MSC CFD EXPT.

In-0(p,x)n sigma(E;theta)
LAS Revw Conf 80BNL 1 169 80 5.0+0 8.0+2 Russell+ NDG.

Sn-120(p,alpha)In-117 sigma(E;E';theta)
TNL Theo Conf 80BNL 2 689 80 5.0+1 Kalbach+ CURV. MSD AND MSC CFD EXPT.

Sn-120(p,t)Sn-118 sigma(E;E';theta)
TNL Theo Conf 80BNL 2 689 80 3.6+1 Kalbach+ CURV. MSD AND MSC CFD EXPT.

Sn-120(p,d)Sn-119 sigma(E;E';theta)
TNL Theo Conf 80BNL 2 689 80 4.0+1 Kalbach+ CURV. MSD AND MSC CFD EXPT.

Sn-120(p,inelastic)Sn-120 sigma(E;E';theta)
TNL Theo Conf 80BNL 2 689 80 2.5+1 5.5+1 Kalbach+ CURV. MSD AND MSC CFD EXPT.

Ta-0(p,x)n thick target yield(E;E';theta)
LAS Revw Conf 80BNL 1 169 80 8.0+2 Russell+ CURV. 90 DEG. EXPT+CALC.

Ta-0(p,x)n thick target yield(E;theta)
LAS Revw Conf 80BNL 1 169 80 5.0+0 4.0+2 Russell+ NDG. 90 DEGREES.

Ta-181(p,n)W-181 sigma(E;E';theta)

LRL	Exth	Conf	80BNL	2	781	80	2.6+1	2.7+1	Hansen+ NDG. IAR. ANALYSIS IN PROGRESS.

W-0(p,x)n thick target yield

LAS	Revw	Conf	80BNL	1	169	80	NDG		Russell+ NDG.

W-0(p,x)n raw thick target yield

LAS	Revw	Conf	80BNL	1	169	80	8.0+2		Russell+ TBL. PRELIM. FERFICON.

W-0(p,x)n thick target yield(E;E';theta)

LAS	Revw	Conf	80BNL	1	169	80	8.0+2		Russell+ CURV. 90 DEG. EXPT+CALC.

W-0(p,x)n thick target yield(E;theta)

LAS	Revw	Conf	80BNL	1	169	80	5.0+0	4.0+2	Russell+ NDG. 90 DEGREES.

W-0(p,x)n product yield

ANL	Expt	Abst	80BNL	1	111	80	3.0+2	5.0+2	Carpenter+ NDG. ZING-P. INDIRECT.

W-0(p,x)n partial thick target yield

LAS	Revw	Conf	80BNL	1	169	80	8.0+2		Russell+ TBL. CALC. EN LT 20 MEV.

Au-197(p,inelastic)Au-197 sigma(E;E';theta)

TNL	Theo	Conf	80BNL	2	689	80	2.0+1		Kalbach+ CURV. MSD AND MSC CFD EXPT.

Au-197(p,n)Hg-197 sigma(E;E';theta)

LRL	Exth	Conf	80BNL	2	781	80	2.6+1	2.7+1	Hansen+ NDG. IAR. ANALYSIS IN PROGRESS.

Pb-0(p,x)n sigma(E;E';theta)

KFK	Expt	Conf	80BNL	1	201	80	5.9+2		Cierjacks+ CURV. 5CM INTO TRGT. CFD LAS
	Expt	Conf	80BNL	1	201	80	TR	5.9+2	Cierjacks+ CURV. VS. DEPTH IN TARGET.
	Expt	Conf	80BNL	1	201	80	5.9+2		Cierjacks+ NDG. 30-150DEG. VAR. DEPTHS.

```
Pb-0(p,x)n   thick target yield(E;E';theta)
   KFK  Expt  Conf  80BNL    1 201      80  5.9+2       Cierjacks+ CURV. 90DEG. 30CM DEPTH.
        Expt  Conf  80BNL    1 201      80  1.1+3       Cierjacks+ NDG. PLANNED AT SATURN.

Pb-0(p,x)n   relative thick target yield(E;E';theta)
   KFK  Expt  Conf  80BNL    1 201      80  5.9+2 6.0+2 Cierjacks+ CURV. CALC(PRELIM)+EXPT.

Pb-0(p,x)n   thick target yield
   LAS  Revw  Conf  80BNL    1 169      80  NDG         Russell+ NDG.

Pb-0(p,x)n   sigma(E;theta)
   LAS  Revw  Conf  80BNL    1 169      80  5.0+0 8.0+2 Russell+ NDG.

Pb-0(p,x)n   raw thick target yield
   CRC  Revw  Conf  80BNL    1 155      80  4.8+2       Fraser+ TBL. FERFICON. H2O CAPT/PROTON.
        Revw  Conf  80BNL    1 155      80  5.2+2 9.5+2 Fraser+ CURV. BNL COSMO. CRC CALC.
   LAS  Revw  Conf  80BNL    1 169      80  8.0+2       Russell+ TBL. PRELIM. FERFICON.

Pb-0(p,x)n   partial thick target yield
   TOK  Expt  Jour  NIM  151   493      78  5.2+1       Nakamura+TBL.EXP.+RENRM.FRWRD HEMI.EN>5
   LAS  Revw  Conf  80BNL    1 169      80  8.0+2       Russell+ TBL. CALC. EN LT 20 MEV.

Pb-0(p,x)H-1   sigma(E;E';theta)
   KFK  Expt  Conf  80BNL    1 201      80  5.9+2       Cierjacks+ CURV. 90DEG. 5CM DEPTH.
        Expt  Conf  80BNL    1 201      80  5.9+2       Cierjacks+ NDG. 30-150DEG. VAR. DEPTHS.

Pb-208(p,inelastic)Pb-208   sigma(E;E';theta)
   LRL  Revw  Conf  80BNL    2 641      80  6.2+1       Gardner. CURV. NSDR APPROACH CFD EXPT

Bi-209(p,alpha)Pb-206   sigma(E;E';theta)
   TNL  Theo  Conf  80BNL    2 689      80  4.0+1       Kalbach+ CURV. MSD AND MSC CFD EXPT.
```

Bi-209(p,n)Po-209 sigma(E;E';theta)
LRL Exth Conf 80BNL 2 781 80 2.6+1 2.7+1 Hansen+ NDG. IAR. ANALYSIS IN PROGRESS.

Th-232(p,x)n thick target yield
LAS Revw Conf 80BNL 1 169 80 NDG Russell+ NDG.

Th-232(p,x)n partial thick target yield
LAS Revw Conf 80BNL 1 169 80 NDG Russell+ NDG.

Th-232(p,x)n raw thick target yield
CRC Revw Conf 80BNL 1 155 80 4.8+2 Fraser+ TBL. FERFICON. H20 CAPT/PROTON.
LAS Revw Conf 80BNL 1 169 80 8.0+2 Russell+ TBL. PRELIM. FERFICON.

Th-232(p,inelastic)Th-232 sigma(E)
LRL Exth Conf 80BNL 2 781 80 2.6+1 2.7+1 Hansen+ TBL. EXPT. AND CC MODEL.

Th-232(p,inelastic)Th-232 partial sigma(E)
LRL Exth Conf 80BNL 2 781 80 2.6+1 2.7+1 Hansen+ TBL. CC MODEL.

Th-232(p,inelastic)Th-232 sigma(E;theta)
LRL Exth Conf 80BNL 2 781 80 2.6+1 Hansen+ TBL. EXPT. AND CC MODEL.

Th-232(p,elastic)Th-232 sigma(E;theta)
LRL Exth Conf 80BNL 2 781 80 2.6+1 Hansen+ TBL. EXPT. AND CC MODEL.

Th-232(p,n)Pa-232 sigma(E;theta)
LRL Exth Conf 80BNL 2 781 80 2.6+1 2.7+1 Hansen+ TBL. EXPT. AND CC MODEL.

U-0(p,x)n thick target yield(E;E';theta)
KFK Expt Conf 80BNL 1 201 80 1.1+3 Cierjacks+ NDG. PLANNED AT SATURN.

U-0(p,x)n product yield

ANL	Expt	Abst	80BNL	1	111	80	3.0+2	5.0+2	Carpenter+ NDG. ZING-P. INDIRECT.

U-238(p,x)n thick target yield

LAS	Revw	Conf	80BNL	1	169	80	8.0+2		Russell+ TBL. CALC. EN LT 20 MEV.

U-238(p,x)n partial thick target yield

LAS	Revw	Conf	80BNL	1	169	80	8.0+2		Russell+ TBL. CALC. EN LT 20 MEV.

U-238(p,x)n raw thick target yield

CRC	Revw	Conf	80BNL	1	155	80	4.8+2		Fraser+ TBL. FERFICON. H20 CAPT/PROTON.
	Revw	Conf	80BNL	1	155	80	5.2+2	9.5+2	Fraser+ CURV. BNL COSMO. CRC CALC.
LAS	Revw	Conf	80BNL	1	169	80	8.0+2		Russell+ TBL. PRELIM. FERFICON.

U-238(p,x)n sigma(E;theta)

LAS	Revw	Conf	80BNL	1	169	80	5.0+0	8.0+2	Russell+ NDG.

U-238(p,x)n relative thick target yield(E;E';theta)

CRC	Revw	Conf	80BNL	1	155	80	4.8+2		Fraser+ CURV. NMTC CALC. CFD FISS. SPEC

U-238(p,x)n thick target yield(E;E')

ANL	Revw	Conf	80BNL	1	75	80	5.0+2		Greenwood. CURV. MOCKUP OF IPNS.

U-238(p,inelastic)U-238 partial sigma(E)

LRL	Exth	Conf	80BNL	2	781	80	2.6+1	2.7+1	Hansen+ TBL. CC MODEL.

U-238(p,inelastic)U-238 sigma(E)

LRL	Exth	Conf	80BNL	2	781	80	2.6+1	2.7+1	Hansen+ TBL. EXPT. AND CC MODEL.

U-238(p,inelastic)U-238 sigma(E;theta)

LRL	Exth	Conf	80BNL	2	781	80	2.6+1		Hansen+ TBL. EXPT. AND CC MODEL.

U-238(p,elastic)U-238 sigma(E;theta)
LRL Exth Conf 80BNL 2 781 80 2.6+1 Hansen+ TBL. EXPT. AND CC MODEL.

U-238(p,n)Np-238 sigma(E;theta)
LRL Exth Conf 80BNL 2 781 80 2.6+1 2.7+1 Hansen+ TBL. EXPT. AND CC MODEL.

U-238(p,fission)mass distribution fission yield
BNL Theo Conf 80BNL 1 133 80 3.0+2 Takahashi. CURV. INTRANUCL. CASCADE. CF

U-238(p,fission)mass distribution nu n
BNL Theo Conf 80BNL 1 133 80 3.0+2 Takahashi. CURV. INTRANUCL. CASCADE. CF

U-oxi(p,x)n raw thick target yield
CRC Revw Conf 80BNL 1 155 80 4.8+2 Fraser+ TBL. FERFICON. H20 CAPT/PROTON.

Np-238(p,fission)mass distribution primary fission yield
BNL Theo Conf 80BNL 1 133 80 9.9+0 3.0+2 Takahashi. CURV. INTRANUCL. CASCADE. CF

Np-238(p,fission)mass distribution fission yield
BNL Theo Conf 80BNL 1 133 80 9.9+0 3.0+2 Takahashi. CURV. INTRANUCL. CASCADE. CF

systematics(p,inelastic) sigma(E;theta) Legendre coefficient expansion x sigma(E)/4pi
TNL Theo Conf 80BNL 2 689 80 NDG Kalbach+ CURV. MSD AND MSC PROCESSES.

systematics(p,alpha) sigma(E;theta) Legendre coefficient expansion x sigma(E)/4pi
TNL Comp Conf 80BNL 2 689 80 NDG Kalbach+ CURV. MSD AND MSC PROCESSES.

Li-0(d,x)gamma thick target yield
HED Revw Conf 80BNL 2 495 80 3.5+1 Johnson+ NDG. WEAK LOW-E. DONE AT DAVIS

Li-0(d,x)gamma thick target yield(E;E';theta)
HED Revw Conf 80BNL 2 495 80 3.5+1 Johnson+ NDG. WEAK LOW-E. DONE AT DAVIS

Li-0(d,x)n thick target yield(E;E';theta)									
	HED	Theo	Conf	80BNL	2	517	80	1.5+1 4.0+1	Mann+ TBL. CURV. DATA USED IN FIT.
		Theo	Conf	80BNL	2	517	80	3.5+1	Mann+ TBL. SEMI-CLASS. MOD. CFD DAVIS
	DAV	Expt	Conf	80BNL	1	99	80	3.5+1	Johnson+ CURV. 0-150 DEGREES. 1-50 MEV.
		Expt	Conf	80BNL	1	99	80	3.5+1	Johnson+ CURV. 45 DEGREES. 0-2.5 MEV.
	HED	Revw	Conf	80BNL	2	431	80	3.5+1	Carter+ CURV.FRM DAV.SHIELD DESIGN IMP.
	HED	Revw	Conf	80BNL	2	495	80	3.5+1	Johnson+ CURV. 8 ANGLES. FROM DAVIS.
Li-0(d,x)n thick target yield(E;theta)									
	DAV	Expt	Conf	80BNL	1	99	80	3.5+1	Johnson+ TBL. 0-150 DEGREES. 2 N THRESH
		Expt	Conf	80BNL	1	99	80	3.5+1	Johnson+ CURV. 0-150 DEGREES. INTED.
Li-0(d,x)n thick target yield									
	DAV	Expt	Conf	80BNL	1	99	80	3.5+1	Johnson+ 3.0E+11 N/SEC.
Li-0(d,x)H-1 thick target yield(E;E';theta)									
	HED	Revw	Conf	80BNL	2	495	80	3.5+1	Johnson+ NDG. CALCULATED.
Li-0(d,x)isotopic distribution thick target yield									
	HED	Revw	Conf	80BNL	2	495	80	TR 3.5+1	Johnson+ NDG. STACKED-FOILS. AT DAVIS.
Li-0(d,x)isotopic distribution sigma(E)									
	HED	Revw	Conf	80BNL	2	495	80	TR 3.5+1	Johnson+ NDG. STACKED-FOILS. AT DAVIS.
Li-6(d,x)n thick target yield(E;E';theta)									
	DAV	Expt	Conf	80BNL	1	99	80	3.5+1	Johnson+ 30PERCENT LESS THAN NAT.(PREL)
Li-6(d,2p)He-6 sigma(E)									
	HED	Revw	Conf	80BNL	2	553	80	NDG	Gold+ NDG. FOR FMIT LI FLOW DOSIMETRY.
Li-6(d,n)Be-7 sigma(E)									
	HED	Revw	Conf	80BNL	2	553	80	NDG	Gold+ NDG. FOR FMIT LI FLOW DOSIMETRY.

Li-7(d,x)He-6 sigma(E)									
	HED	Revw	Conf	80BNL	2	553	80	NDG	Gold+ NDG. FOR FMIT LI FLOW DOSIMETRY.
Li-7(d,p)Li-8 sigma(E)									
	HED	Revw	Conf	80BNL	2	553	80	NDG	Gold+ NDG. FOR FMIT LI FLOW DOSIMETRY.
Li-7(d,2n)Be-7 sigma(E)									
	HED	Revw	Conf	80BNL	2	553	80	NDG	Gold+ NDG. FOR FMIT LI FLOW DOSIMETRY.
Be-9(d,x)n relative thick target yield(E;theta)									
	CRC	Revw	Conf	80BNL	1	147	80	1.0+1 2.5+1	Lone+ TBL. CURV. LOW-E N(0.3-2.3MEV).
Be-9(d,x)n thick target yield(E;E';theta)									
	CRC	Revw	Conf	80BNL	1	147	80	1.2+1	Lone+ CURV. THETA=0. E=1-16 MEV.
	HED	Revw	Conf	80BNL	2	495	80	1.6+1 5.0+1	Johnson+NDG.FOR FMIT.FRM MEULDER+(1975)
	RI	Expt	Conf	80BNL	1	113	80	3.0+1	Kneff+ CURV. 0-60DEG. 30CM. RADIOMETRIC
	HED	Revw	Conf	80BNL	2	459	80	4.0+1	Doran+CURV.15 DEG.ORIC.CFD UNFOLDED SPC
	ANL	Revw	Conf	80BNL	1	75	80	4.0+1	Greenwood. CURV. 0-90 DEG. ORNL.
		Revw	Conf	80BNL	1	75	80	3.0+1	Greenwood.CURV.0DEG. 3.4+15.6MM. DAVIS
Be-9(d,x)n product yield(E;E';theta)									
	CRC	Revw	Conf	80BNL	1	147	80	1.2+1	Lone+ CURV. THCKNSS=0.55 RANGE. THETA=0
Be-9(d,x)n thick target yield(E;theta)									
	HED	Revw	Conf	80BNL	2	495	80	1.6+1 5.0+1	Johnson+NDG.FOR FMIT.FRM MEULDER+(1975)
	ANL	Revw	Conf	80BNL	1	75	80	4.0+1	Greenwood. TBL. TYPICAL FLUX ERR. ORNL.
Be-9(d,inelastic+n)Be-8 relative thick target yield(E;theta)									
	CRC	Revw	Conf	80BNL	1	147	80	1.5+1	Lone+ APP. 4PRCNT OF LOW-E N YLD.
Be-9(d,inelastic+n)Be-8 partial thick target yield(E;E';theta)									
	CRC	Revw	Conf	80BNL	1	147	80	5.0+0 2.4+1	Lone+CURV.700KEV PK. GOOD SHAPE. LOW YL

C-0(d,x)isotopic distribution sigma(E)
HED Revw Conf 80BNL 2 495 80 TR 3.5+1 Johnson+ NDG. STACKED-FOILS. AT DAVIS.

C-0(d,x)isotopic distribution thick target yield
HED Revw Conf 80BNL 2 495 80 TR 3.5+1 Johnson+ NDG. STACKED-FOILS. AT DAVIS.

C-12(d,x)n thick target yield(E;theta)
HED Revw Conf 80BNL 2 495 80 1.6+1 5.0+1 Johnson+NDG.FOR FMIT.FRM MEULDER+(1975)

C-12(d,x)n thick target yield(E;E';theta)
HED Revw Conf 80BNL 2 495 80 1.6+1 5.0+1 Johnson+NDG.FOR FMIT.FRM MEULDER+(1975)

Na-23(d,x)isotopic distribution sigma(E)
HED Revw Conf 80BNL 2 495 80 TR 3.5+1 Johnson+ NDG. PLANNED AT DAVIS.

Na-23(d,x)isotopic distribution thick target yield
HED Revw Conf 80BNL 2 495 80 TR 3.5+1 Johnson+ NDG. PLANNED AT DAVIS.

Al-27(d,x)isotopic distribution thick target yield
HED Revw Conf 80BNL 2 495 80 TR 3.5+1 Johnson+ NDG. STACKED-FOILS. AT DAVIS.

Al-27(d,x)isotopic distribution sigma(E)
HED Revw Conf 80BNL 2 495 80 TR 3.5+1 Johnson+ NDG. STACKED-FOILS. AT DAVIS.

Ca-0(d,x)isotopic distribution thick target yield
HED Revw Conf 80BNL 2 495 80 TR 3.5+1 Johnson+ NDG. PLANNED AT DAVIS.

Ca-0(d,x)isotopic distribution sigma(E)
HED Revw Conf 80BNL 2 495 80 TR 3.5+1 Johnson+ NDG. PLANNED AT DAVIS.

Cr-0(d,x)isotopic distribution sigma(E)
HED Revw Conf 80BNL 2 495 80 TR 3.5+1 Johnson+ NDG. PLANNED AT DAVIS.

Cr-0(d,x)isotopic distribution thick target yield
HED Revw Conf 80BNL 2 495 80 TR 3.5+1 Johnson+ NDG. PLANNED AT DAVIS.

Mn-55(d,x)isotopic distribution thick target yield
HED Revw Conf 80BNL 2 495 80 TR 3.5+1 Johnson+ NDG. PLANNED AT DAVIS.

Mn-55(d,x)isotopic distribution sigma(E)
HED Revw Conf 80BNL 2 495 80 TR 3.5+1 Johnson+ NDG. PLANNED AT DAVIS.

Fe-0(d,x)isotopic distribution sigma(E)
HED Revw Conf 80BNL 2 495 80 TR 3.5+1 Johnson+ NDG. STACKED-FOILS. AT DAVIS.

Fe-0(d,x)isotopic distribution thick target yield
HED Revw Conf 80BNL 2 495 80 TR 3.5+1 Johnson+ NDG. STACKED-FOILS. AT DAVIS.

Ni-0(d,x)isotopic distribution thick target yield
HED Revw Conf 80BNL 2 495 80 TR 3.5+1 Johnson+ NDG. STACKED-FOILS. AT DAVIS.

Ni-0(d,x)isotopic distribution sigma(E)
HED Revw Conf 80BNL 2 495 80 TR 3.5+1 Johnson+ NDG. STACKED-FOILS. AT DAVIS.

Ni-58(d,inelastic)Ni-58 sigma(E;E';theta)
TNL Theo Conf 80BNL 2 689 80 3.0+1 Kalbach+ CURV. MSD AND MSC CFD EXPT.

Cu-0(d,x)n thick target yield(E;theta)
HED Revw Conf 80BNL 2 495 80 1.6+1 5.0+1 Johnson+NDG.FOR FMIT.FRM MEULDER+(1975)

Cu-0(d,x)n thick target yield(E;E';theta)
HED Revw Conf 80BNL 2 495 80 1.6+1 5.0+1 Johnson+NDG.FOR FMIT.FRM MEULDER+(1975)

Cu-0(d,x)isotopic distribution thick target yield
HED Revw Conf 80BNL 2 495 80 1.5+1 4.0+1 Johnson+ CURV. 9 PRODUCTS. PRELIM(DAVIS

Cu-0(d,x)isotopic distribution sigma(E)
HED Revw Conf 80BNL 2 495 80 TR 3.5+1 Johnson+ NDG. STACKED-FOILS. AT DAVIS.

Cu-63(d,alpha)Ni-61 sigma(E;E';theta)
TNL Theo Conf 80BNL 2 689 80 2.8+1 Kalbach+ CURV. MSD AND MSC CFD EXPT.

Mo-0(d,x)n thick target yield(E;theta)
HED Revw Conf 80BNL 2 495 80 1.6+1 5.0+1 Johnson+NDG.FOR FMIT.FRM MEULDER+(1975)

Mo-0(d,x)n thick target yield(E;E';theta)
HED Revw Conf 80BNL 2 495 80 1.6+1 5.0+1 Johnson+NDG.FOR FMIT.FRM MEULDER+(1975)

Mo-0(d,x)isotopic distribution thick target yield
HED Revw Conf 80BNL 2 495 80 TR 3.5+1 Johnson+ NDG. STACKED-FOILS. AT DAVIS.

Mo-0(d,x)isotopic distribution sigma(E)
HED Revw Conf 80BNL 2 495 80 TR 3.5+1 Johnson+ NDG. STACKED-FOILS. AT DAVIS.

Ta-181(d,x)n thick target yield(E;E';theta)
HED Revw Conf 80BNL 2 495 80 1.6+1 5.0+1 Johnson+NDG.FOR FMIT.FRM MEULDER+(1975)

Ta-181(d,x)n thick target yield(E;theta)
HED Revw Conf 80BNL 2 495 80 1.6+1 5.0+1 Johnson+NDG.FOR FMIT.FRM MEULDER+(1975)

Au-197(d,x)n thick target yield(E;E';theta)
HED Revw Conf 80BNL 2 495 80 1.6+1 5.0+1 Johnson+NDG.FOR FMIT.FRM MEULDER+(1975)

Au-197(d,x)n thick target yield(E;theta)
HED Revw Conf 80BNL 2 495 80 1.6+1 5.0+1 Johnson+NDG.FOR FMIT.FRM MEULDER+(1975)

Au-197(d,x)isotopic distribution sigma(E)
HED Revw Conf 80BNL 2 495 80 TR 3.5+1 Johnson+ NDG. STACKED-FOILS. AT DAVIS.

Au-197(d,x)isotopic distribution thick target yield

HED	Revw	Conf	80BNL	2	495	80	TR	3.5+1	Johnson+ NDG. STACKED-FOILS. AT DAVIS.

Pb-0(d,x)isotopic distribution thick target yield

HED	Revw	Conf	80BNL	2	495	80	TR	3.5+1	Johnson+ NDG. STACKED-FOILS. AT DAVIS.

Pb-0(d,x)isotopic distribution sigma(E)

HED	Revw	Conf	80BNL	2	495	80	TR	3.5+1	Johnson+ NDG. STACKED-FOILS. AT DAVIS.

Pb-208(d,alpha)Tl-206 sigma(E;E';theta)

TNL	Theo	Conf	80BNL	2	689	80	5.0+1		Kalbach+ CURV. MSD AND MSC CFD EXPT.

Th-232(d,inelastic)Th-232 sigma(E;E';theta)

TNL	Theo	Conf	80BNL	2	689	80	4.0+1		Kalbach+ CURV. MSD AND MSC CFD EXPT.

Li-6(t,x)n relative sigma(E;E';theta)

CRC	Exth	Conf	80BNL	1	193	80	1.1+0		Lone+ CURV. 0 DEGREES. LI6F TRGT.

Li-7(t,x)n relative sigma(E;E';theta)

CRC	Exth	Conf	80BNL	1	193	80	1.1+0		Lone+ CURV. 0 DEGREES.

Ni-62(He3,d)Cu-63 sigma(E;E';theta)

TNL	Theo	Conf	80BNL	2	689	80	1.1+1		Kalbach+ CURV. MSD AND MSC CFD EXPT.

C-12(alpha,inelastic)C-12 sigma(E;E';theta)

TNL	Theo	Conf	80BNL	2	689	80	2.0+1		Kalbach+ CURV. MSD AND MSC CFD EXPT.

Mn-55(alpha,n)Co-58 sigma(E)

LAS	Theo	Conf	80BNL	2	751	80	8.0+0	1.8+1	Arthur+ CURV. H-F CALC. CFD EXPT.

Fe-54(alpha,inelastic)Fe-54 sigma(E;E';theta)

TNL	Theo	Conf	80BNL	2	689	80	1.1+1	4.5+1	Kalbach+ CURV. MSD AND MSC CFD EXPT.

Fe-54(alpha,t)Co-55 sigma(E;E';theta)
TNL Theo Conf 80BNL 2 689 80 2.6+1 Kalbach+ CURV. MSD AND MSC CFD EXPT.

Fe-54(alpha,p)Co-57 sigma(E;E';theta)
TNL Theo Conf 80BNL 2 689 80 1.7+1 4.0+1 Kalbach+ CURV. MSD AND MSC CFD EXPT.

Co-59(alpha,p)Ni-62 sigma(E;E';theta)
TNL Theo Conf 80BNL 2 689 80 3.2+1 Kalbach+ CURV. MSD AND MSC CFD EXPT.

Ni-61(alpha,p)Cu-64 sigma(E;E';theta)
TNL Theo Conf 80BNL 2 689 80 2.5+1 Kalbach+ CURV. MSD AND MSC CFD EXPT.

Rh-103(alpha,p)Pd-106 sigma(E;E';theta)
TNL Theo Conf 80BNL 2 689 80 2.0+1 Kalbach+ CURV. MSD AND MSC CFD EXPT.